

Advances in Liquid-Jet Photoelectron Spectroscopy:

Determination of Absolute Energetics
and
Probing Chirality in Solution

Inaugural-Dissertation
to obtain the academic degree
Doctor rerum naturalium (Dr. rer. nat.)

Submitted to the Department of
Biology, Chemistry, Pharmacy
of Freie Universität Berlin

by

Sebastian Malerz (M.Sc.)

Berlin, May 2022



FRITZ-HABER-INSTITUT MAX-PLANCK-GESELLSCHAFT

This thesis was performed from July 2017 to May 2022, in the Molecular Physics Department at the Fritz-Haber-Institut der Max-Planck Gesellschaft in Berlin, under the supervision of Dr. Bernd Winter and Prof. Dr. Gerard J. M. Meijer.

1st reviewer: Prof. Dr. Gerard J. M. Meijer
(and doctor father)

2nd reviewer: Prof. Dr. Eckart Rühl

Advisor: Dr. Bernd Winter

Disputation: Berlin, 28.09.2022

Abstract

This doctoral thesis reports on recent developments in photoelectron spectroscopy from the liquid phase, with a prime focus on the electronic structure of liquid water and aqueous solutions. The enabling technique is liquid-jet photoelectron spectroscopy (LJ-PES), which combines state-of-the-art high-pressure-compatible electron analyzers with an in-vacuo liquid microjet. This technique is often applied in conjunction with soft-X-ray photons delivered from synchrotron-radiation facilities. In this work, I will also present data obtained with a laboratory helium-discharge source, providing XUV photon energies. There were three main objectives at the beginning of my thesis: (1) the application of photoelectron circular dichroism (PECD) to the liquid phase, (2) exploring how electron scattering in aqueous solution can disturb native photoelectron peaks, and (3) the development of experimental methods that allow the determination of accurate energetics of solutions, which largely refers to the ability to determine accurate valence and core-level electron binding energies from both liquid water and solutes. In addition, I have participated in several other studies with associated topics, although not immediately relevant for above-mentioned topics (1) to (3). These studies will be briefly described at the end of this thesis in Chapter 3.

My first project (1), the application of PECD to the liquid phase, with a particular emphasis on chiral (biologically relevant) molecules in water, has started at a time where PECD has been well established for isolated (gas-phase) molecules. PECD manifests as a forward-backward asymmetry of the photoelectron emission intensity from chiral molecules, measured with respect to the propagation direction of circularly polarized light (CPL). No analogous studies in liquid-phase environments have been reported to date and were not even possible with existing equipment. Challenged by this lack of tools, and in the light of the importance of chirality in aqueous-phase biological systems and the relevance in the context of chiral pharmaceuticals, I set out to construct and build a unique apparatus that would allow to explore PECD in liquid phase. Its realization would be an expansion of the LJ-PES technique, now extending to the detection of the forward-backward asymmetry using a specialized geometry when ionizing the liquid jet with CPL. The result is the *EASI* apparatus (acronym for Electronic structure from Aqueous Solutions and Interfaces) and the

demonstration of the very first PECD measurements from the liquid phase, exemplified for a liquid fenchone beam and the amino acid alanine in aqueous solution. In both cases, PECD was explored upon carbon core-level (near-threshold) ionization. A technical article describing *EASI*, its concepts and performance, and another article on liquid-fenchone PECD resulting from these efforts have been published (Paper I and Paper V). Additional, not-yet-published results from aqueous-phase alanine will be presented briefly in the results section (Chapter 3.3).

Project (2) is intimately connected with PECD measurements as it investigates the effect of electron scattering in solution at low-to-very-low kinetic energies, which is the energy range where PECD is expected to be largest. As it turns out, this is exactly the region where quasi-elastic electron (small-energy-loss vibrational) scattering occurs, which can severely disturb the native photoelectron peaks of interest. It is noted that the successful combination of tunable XUV light with the detection of low-kinetic-energy LJ-PE spectra had been hampered for experimental reasons. Thus, our study is the first to actually quantify the role and importance of these scattering effects in water and aqueous solutions, enabling the determination of a critical kinetic-energy value below which an undistorted photoelectron spectrum cannot be measured. Details, including mechanistic aspects of electron scattering and implications for future PES studies from liquids are described in Paper II. A prerequisite to characterize low-energy processes is the ability to detect even those electrons that have lost all their energy and thus are left with an almost zero kinetic energy. In the PE spectrum, such electrons accumulate at the low-energy cut-off, a quantity (barely considered previously) which is also of great importance for the novel route to determine accurate energetics from solutions, project (3).

The concept underpinning project (3) is the application of PES methodology that has been commonly used for condensed-matter studies but barely considered for liquid water. In fact, almost all reported LJ-PES studies, since the beginning about 20 years ago, have adopted a molecular-physics description of liquid water. That is, aqueous-phase spectra have been essentially described in terms of molecular orbitals just as the respective gas-phase counterparts. Additional energy shifts and peak broadenings with respect to the gas-phase spectra are mainly described as a perturbation of the intrinsic molecular electronic structure,

and have been assigned to liquid-water electronic screening as well as to hydrogen-bonding-induced effects on the orbital symmetry, respectively. Similarly, ionization energies have exclusively been referenced to gas-phase PE features, which are inevitably measured together in PE spectra from the liquid phase due to evaporation. A critical consequence of this approach, which implies referencing detected liquid-phase energies to known water gas-phase (ionization) energies, is that the measured energy value depends on particular experimental conditions due to additional unwanted electric fields present in a typical LJ-PES experiment. Briefly, the liquid-jet surface is charged by electrokinetic charging, from molecular surface dipoles, or upon ionization of solutions with insufficient electrical conductivity. Hence, under all practical experimental conditions, there will be an electric field between the liquid jet and the electron detector. Photoelectrons originating from ionization of water gas-phase molecules surrounding the liquid jet will vary in kinetic energy because of acceleration or deceleration under the influence of the present field, depending on the distance of birth from the jet. Disentangling these contributions is very complex and generally is not even attempted in typical LJ-PES experiments; instead, a predetermined ionization energy for prominent liquid features has been used to define the energy scale of a measured spectrum with possibly large associated errors of this approach. The new approach does not at all rely on the gas phase but rather uses the intrinsic liquid-phase low-energy cut-off as a reference. Then, with an accurately known photon energy, one can precisely determine both solute and solvent electron binding energies. We were thus able to determine the accurate energy value for liquid water's leading orbital (HOMO), which has been controversially discussed in the literature. More importantly, though, the new method enables the measurement of water's electronic-structure changes induced by solute for the first time, since this energy-referencing method does not require assuming solvent PE features as fixed in energy. This achievement has cumulated in the publication of Paper III and IV, and a summary will be provided in the results section (Chapter 3.2). In conjunction with the new referencing schemes, additional energy referencing with respect to the Fermi energy has been attempted, which promises an accurate determination of the work function of liquid water and aqueous solutions. At the end of this thesis (Chapter 4), I evaluate and discuss the challenge of characterizing the Fermi level of liquid water and aqueous solutions, thus bridging the gap between liquid- and solid-phase PES.

Another study I was actively involved in, but less closely related to the main objectives of my thesis is the electronic-structure characterization of glucose as a function of pH. This particular LJ-PES study focused on the identification of electronic-structure changes of the anomeric center when scanning the pH range across the acidity constant, pK_a , by investigating the site- and energy-specific signature of the carbon 1s spectrum. I briefly explain the motivation of this study and ongoing related studies in the framework of chirality in aqueous phase in the results section (Chapter 3.4). The results of this study are published in Paper VI.

The second side project was the investigation of *non-local* electronic relaxation processes upon 1s ionization of divalent and trivalent metal cations in water. This followed up on a long and ongoing interest of our group in identifying, for instance, intermolecular / interatomic Coulombic decay (ICD) processes in liquid water and aqueous solutions, and relates observed spectral information to hydrogen bonding (including nuclear dynamics) and general solution structure properties. The individual ICD features show a high selectivity for specific water ionization channels and are considered to reflect the hydration water molecules, which is possible due to the nature of ICD to involve molecules in vicinity of the excited system. A short summary of this published study (Paper VII) is also provided in the results section (Chapter 3.5).

Another study that relates less closely to the main objectives of my thesis includes the development of a liquid flatjet, which essentially forms a flat leaf of two laminarly co-flowing aqueous solutions and thus a liquid–liquid interface. The motivation for those experiments is described in the results section (Chapter 3.6). For example, an application of a flatjet for the determination of chemical kinetics (exemplified for the luminol – hydrogen peroxide chemical reaction in water) – not using PES though – is explained, which summarizes results that we published in Paper VIII.

Zusammenfassung

Diese Doktorarbeit thematisiert die neuesten Entwicklungen im Bereich der Photoelektronen-Spektroskopie in der flüssigen Phase. Das Hauptaugenmerk liegt dabei auf den elektronischen Strukturen von flüssigem Wasser und wässrigen Lösungen. Das hierfür angewendete Verfahren ist die sogenannte Flüssigkeitsstrahl-Photoelektronen-Spektroskopie (Liquid-Jet Photoelectron Spectroscopy, LJ-PES), welches modernste Elektronenanalysatoren mit einem flüssigen mikrometergroßen Strahl im Vakuum kombiniert. Dieses Verfahren wird häufig in Verbindung mit weicher Röntgenstrahlung (Soft X-rays) angewendet, die von Elektronenspeicherringen (Synchrotrons) erzeugt wird.

In dieser Arbeit werden zudem Daten gezeigt und diskutiert, die mit einer Helium-Plasmaquelle und somit mit ultravioletter Röntgenstrahlung (XUV) im Labor gemessen wurden. Am Anfang meiner Doktorarbeit standen drei Hauptziele: (1) Die Anwendung des sogenannten Photoelektronen-Zirkulardichroismus (Photoelectron Circular Dichroism, PECD) in flüssiger Phase, (2) Studien zur Elektronenstreuung in wässriger Lösung und damit verbundenen Störungen von nativen Photoelektronen-Signalen und (3) die Entwicklung experimenteller Methoden, die durch die Bestimmung genauer Valenz- und Innerschalen-Bindungsenergien von flüssigem Wasser sowie von gelösten Stoffen die Bestimmung der genauen (Bindungs-)Energien von Lösungen ermöglichen sollen. Darüber hinaus habe ich an mehreren anderen Studien mit verwandten Themen teilgenommen, die jedoch für die oben genannten Themen (1) bis (3) nicht unmittelbar relevant sind. Diese Studien werden am Ende dieser Arbeit kurz beschrieben.

Das erste Projekt (1), die Anwendung von PECD in flüssiger Phase mit besonderem Schwerpunkt auf chiralen (biologisch relevanten) Molekülen im Wasser, begann, als PECD für isolierte (Gasphasen-)Moleküle bereits etabliert war. PECD manifestiert sich als eine Vorwärts-Rückwärts-Asymmetrie der Photoelektronen-Emissionsintensität von chiralen Molekülen, gemessen in Bezug auf die Ausbreitungsrichtung der Photonen des dafür genutzten zirkular polarisierten Lichtes (Circularly Polarized Light, CPL). Bisher wurden keine analogen Studien in wässriger Phase in der Literatur erwähnt. Darüber hinaus waren solche Studien mit den vorhandenen technischen Mitteln nicht durchführbar. Angesichts des

Mangels einer entsprechenden experimentellen Methode und im Hinblick auf die Bedeutung der Chiralität für biologische Systeme in wässriger Phase sowie deren Relevanz im Zusammenhang mit chiralen Pharmazeutika konstruierte und baute ich eine einzigartige Apparatur, die es ermöglicht, PECD in flüssiger Phase zu untersuchen. Die Entwicklung dieser Apparatur und deren Funktionsweise im Rahmen meiner Doktorarbeit ist eine bedeutende Erweiterung der LJ-PES-Technik: Ein Flüssigkeitsstrahl wird mit CPL ionisiert und die Vorwärts-Rückwärts-Asymmetrie der Photoelektronen-Intensität wird unter Verwendung einer speziellen Geometrie detektiert. Das Ergebnis ist die *EASI*-Apparatur (Akronym für Electronic Structure from Aqueous Solutions and Interfaces) und die Demonstration der allerersten PECD-Messungen aus der flüssigen Phase am Beispiel eines flüssigen Fenchon-Jets und der Aminosäure Alanin in wässriger Lösung. In beiden Fällen wurde PECD nach einer Innerschalen-Ionisation von Kohlenstoff (nahe der Ionisationsschwelle) untersucht. Ein technisch-wissenschaftliches Paper, welches die Konzepte und Möglichkeiten von *EASI* beschreibt, sowie ein weiteres Paper über PECD von flüssigem Fenchon, sind hieraus hervorgegangen und veröffentlicht (Paper I und Paper V). Weitere, noch nicht publizierte Ergebnisse von Alanin in wässriger Phase werden darüber hinaus kurz im Ergebnisteil (Kapitel 3.3) vorgestellt.

Projekt (2) ist sehr eng mit den PECD-Messungen verbunden, da es den Effekt der Elektronenstreuung in Lösungen bei sehr geringen kinetischen Energien untersucht und der beobachtbare PECD-Effekt in diesem unteren Energiebereich voraussichtlich am größten sein wird. Wie sich herausstellte, tritt in diesem Bereich quasi-elastische Elektronenstreuung (Vibrationsstreuung mit geringem Energieverlust) auf, die das native Photoelektronen-Signal signifikant stören kann. Erst die erfolgreiche Kombination von ultravioletter Röntgenstrahlung mit der Fähigkeit, emittierte Elektronen aus Flüssigkeitsstrahlen mit sehr niedrigen kinetischen Energien zu detektieren, ermöglichte solche Messungen. Somit ist unsere Studie die erste, die die Rolle und Bedeutung dieser Streueffekte quantifiziert und die die Bestimmung eines kritischen kinetischen Energiewertes ermöglicht. Unterhalb dieses Energiewertes kann ein unverzerrtes Photoelektronen-Spektrum nicht gemessen werden. Einzelheiten, einschließlich mechanistischer Aspekte der Elektronenstreuung und Implikationen für zukünftige Photoelektronen-Studien aus Flüssigkeiten, werden in Paper II ausführlich beschrieben. Eine Voraussetzung für die Charakterisierung solch

niederenergetischer Prozesse ist die Fähigkeit auch solche Elektronen zu detektieren, die ihre gesamte Energie verloren haben und daher mit einer kinetischen Energie nahe Null gemessen werden. In einem Photoelektronen-Spektrum finden sich solche Elektronen an der sogenannten niederenergetischen Untergrenze (Low-Energy Cut-off). Diese Größe, die bisher in Flüssigkeiten kaum Beachtung fand, ist essenziell für die neuartige Methode zur Bestimmung genauer Energien aus Lösungen, was wiederum für Projekt (3) von großer Bedeutung ist.

Das zugrunde liegende Konzept von Projekt (3) ist die Anwendung einer PES-Methodik, die üblicherweise für Studien an kondensierter Materie verwendet wird, jedoch für flüssiges Wasser kaum in Betracht gezogen wurde. Tatsächlich haben fast alle publizierten LJ-PES-Studien seit Beginn dieser Experimente vor etwa 20 Jahren eine molekularphysikalische Beschreibung von flüssigem Wasser verwendet. Dabei wurden Spektren in wässriger Phase im Wesentlichen in Form von Molekülorbitalen beschrieben, die aus der Gasphase bekannt waren. Auftretende Energieverschiebungen und Signalverbreiterungen in der Flüssigkeitsphase im Vergleich zur Gasphase wurden hauptsächlich als Störung der intrinsischen molekularen elektronischen Struktur beschrieben. Sie wurden zudem der Elektronen-Abschirmung in flüssigem Wasser sowie den durch Wasserstoffbrückenbindungen induzierten Effekten auf die Orbitalsymmetrie zugeordnet. In ähnlicher Weise wurden Ionisierungsenergien der flüssigen Phase ausschließlich auf Photoelektronen-Merkmale der Gasphase bezogen, die aufgrund der Verdampfung des Flüssigkeitsstrahls im Vakuum zwangsläufig zusammen mit den Photoelektronen-Merkmalen aus der flüssigen Phase gemessen werden. Jedoch ist der gemessene Energiewert der Gasphase, der als Referenz für die Energiewerte der Flüssigphase genutzt wurde, aufgrund von unerwünschten elektrischen Feldern, die typischerweise bei einem LJ-PES Experiment auftreten, stark abhängig von den experimentellen Bedingungen. Zusammenfassend gilt: Die Oberfläche des Flüssigkeitsstrahls wird durch elektrokinetische Aufladung von molekularen Oberflächendipolen oder bei der Ionisierung von Lösungen mit unzureichender elektrischer Leitfähigkeit aufgeladen. Daher besteht unter allen praktischen experimentellen Bedingungen ein elektrisches Feld zwischen dem Flüssigkeitsstrahl und dem Elektronen-Detektor. Die kinetische Energie der Photoelektronen, die aus der Ionisation der Wassermoleküle aus der den Flüssigkeitsstrahl umgebenden Gasphase stammen, variiert

aufgrund von Abbremsung und Beschleunigung unter dem Einfluss des vorhandenen Feldes in Abhängigkeit der Entfernung zum Flüssigkeitsstrahl. Das Quantifizieren dieser Beiträge ist sehr komplex und wird im Allgemeinen in typischen LJ-PES-Experimenten nicht durchgeführt. Stattdessen wurde eine vorbestimmte Ionisationsenergie für die Photoelektronen-Signale von flüssigem Wasser verwendet, um die Energieskala eines gemessenen Spektrums mit möglichst kleinen experimentellen Fehlern zu definieren.

Der neue Ansatz bezieht sich nicht auf die Gasphase, sondern verwendet die intrinsische niederenergetische Untergrenze der Flüssigphase als Referenz. Somit kann man mit einer genau bekannten Photonenenergie sowohl die Elektronenbindungsenergien des gelösten Stoffes als auch des Lösungsmittels genau bestimmen. Damit konnte der in der Literatur kontrovers diskutierte Energiewert für das höchste besetzte Molekülorbital (Highest Occupied Molecular Orbital, HOMO) von flüssigem Wasser bestimmt werden. Noch wichtiger ist jedoch, dass die neue Methode zum ersten Mal die Messung von Änderungen der elektronischen Struktur von Wasser, die durch gelöste Stoffe induziert werden, ermöglicht. Hintergrund dafür ist, dass diese Methode nicht die Annahme voraussetzt, dass die PE-Merkmale der gemessenen Lösungsmittel-Photoelektronen-Spektren energiefixiert sein müssen. Die Ergebnisse dieser Methodik sind in Paper III und IV veröffentlicht und eine Zusammenfassung wird im Ergebniskapitel (Kapitel 3.2) dargestellt. In Verbindung mit der neuen Methode zur Referenzierung genauer Energien in wässrigen Lösungen wurde eine zusätzliche Energie-Referenzierung bezüglich der Fermi-Energie untersucht, die eine genaue Bestimmung der Austrittsarbeit von flüssigem Wasser und wässrigen Lösungen ermöglicht. Am Ende von Kapitel 3.2 und in Kapitel 4 bewerte und diskutiere ich die Hürden, die überwunden werden mussten, um das Fermi-Niveau in Bezug auf flüssigen Wasser zu charakterisieren und somit die Lücke zwischen Flüssig- und Festphasen-PES zu schließen.

Eine weitere Studie, an der ich aktiv beteiligt war, die aber weniger eng mit den Hauptzielen dieser Doktorarbeit zusammenhängt, ist die Charakterisierung der elektronischen Struktur von Glucose als Funktion des pH-Werts. Diese spezielle LJ-PES-Studie konzentrierte sich auf die Identifizierung von Änderungen der elektronischen Struktur des anomeren Zentrums bei unterschiedlichen pH-Werten, nahe des pK_a -Wertes, indem die orts- und energiespezifische Signatur des Kohlenstoff-Innerschalen-Spektrums untersucht wurde. Die Ergebnisse dieser

Studie sind in Paper VI publiziert. Darüber hinaus erläutere ich kurz die Motivation zu dieser Arbeit und zu weiteren, derzeit laufenden Arbeiten im Hinblick auf die Chiralität in wässriger Phase im Ergebniskapitel (Kapitel 3.4).

Die Untersuchung nicht-lokaler elektronischer Relaxationsprozesse bei 1s-Ionisation von zwei- und dreiwertigen Metall-Kationen in Wasser, war eine weitere Studie, bei der ich eng involviert war. Dieses Projekt resultierte aus einem langen und anhaltenden Interesse unserer Forschungsgruppe, intermolekulare / interatomare Coulomb-Zerfallsprozesse (Interatomic / Intermolecular Coulombic Decay, ICD) in flüssigem Wasser und wässrigen Lösungen zu identifizieren und somit Rückschlüsse auf die Struktur der Wasserstoffbrückenbindungen (einschließlich Kerndynamik) und allgemein der molekularen Struktur von Wasser und wässrigen Lösungen aus den spektralen Informationen zu ziehen. Die einzelnen ICD-Merkmale zeigen eine sehr hohe Selektivität für spezifische Wasserionisationskanäle und man geht davon aus, dass diese Kanäle die Wassermoleküle der Hydratationshülle widerspiegeln, da es mittels ICD möglich ist, Moleküle in direkter Nähe des angeregten Systems mit einzubeziehen. Eine kurze Zusammenfassung dieser publizierten Studie (Paper VII) findet sich auch im Ergebnisteil dieser Arbeit (Kapitel 3.5).

Eine weitere Studie, die weniger eng mit den Hauptzielen meiner Dissertation zusammenhängt, ist die Entwicklung eines flüssigen Flachstrahls, der im Wesentlichen ein flaches Blatt aus zwei laminar zusammenströmenden wässrigen Lösungen ist und so eine Grenzfläche von zwei (verschiedenen) Flüssigkeiten bildet. Die Motivation für Studien an diesem planaren Flüssigkeitssystem wird in Kapitel 3.6 beschrieben. Unter anderem wird eine Anwendung des Flachstrahls zur Bestimmung der chemischen Reaktionskinetik am Beispiel der chemischen Reaktion von Luminol mit wässriger Wasserstoffperoxid-Lösung gezeigt; allerdings nicht unter Verwendung von Photoelektronen-Spektroskopie. Die Ergebnisse dieser Studie wurden in Paper VIII veröffentlicht.

List of Abbreviations

| | |
|----------------------|---------------------------------------------------------------------------------------------------|
| AO | Atomic Orbital |
| APPLE | Advanced Planar Polarized Light Emitter |
| (e)BE | (electron) Binding Energy |
| BESSY | Berliner Elektronenspeicherring-Gesellschaft für Synchrotronstrahlung m.b.H. |
| BG | Background |
| CCD | Charge-Coupled Device |
| CPL (<i>l / r</i>) | Circularly Polarized Light (<i>left / right</i>) |
| CS | Cross Section |
| DESY | Deutsche Elektronen-Synchrotron |
| DFT | Density Functional Theory |
| EA | Electron Analyzer |
| EAL | Effective Attenuation Length |
| EASI-(setup) | Electronic structure from Aqueous Solutions and Interfaces |
| E_F | Fermi Energy |
| (e)KE | (electron) Kinetic Energy |
| ERC | European Research Council |
| ESCA | Electron Spectroscopy of Chemical Analysis |
| ETMD | Electron-Transfer-Mediated-Decay |
| FJ | FlatJet |
| H-Bond / HB | Hydrogen Bond |
| HOMO | Highest Occupied Molecular Orbital |
| HPLC | High Performance / Pressure Liquid Chromatography |
| $h\nu$ | Photon Energy ($E_{\text{photon}} = h\nu = \frac{hc}{\lambda}$) with c for the speed of light |
| ICD | Intermolecular Coulombic Decay |
| IE | Ionization Energy |
| IR | Infrared |
| LET | Low (Kinetic) Energy Tail |

| | |
|-------------------|----------------------------------------------|
| LJ | Liquid Jet |
| LJ-PES | Liquid Jet-Photoelectron Spectroscopy |
| LN ₂ | Liquid Nitrogen |
| LPL | Linearly Polarized Light |
| LUMO | Lowest Unoccupied Molecular Orbital |
| MCP | Microchannel Plate |
| MD | Molecular Dynamics |
| MFP (IMFP / EMFP) | Mean Free Pathway (Inelastic / Elastic) |
| MO | Molecular Orbital |
| PAD | Photoelectron Angular Distribution |
| PECD | Photoelectron Circular Dichroism |
| PEEK | Polyether Ether Ketone |
| PES | Photoemission or Photoelectron Spectroscopy |
| PETRA | Positron-Elektron-Tandem-Ring-Anlage at DESY |
| RIXS | Resonant Inelastic X-ray Scattering |
| RHF | Restricted Hartree-Fock |
| SSHG | Surface Second-Harmonic Generation |
| STR | (as subscript) Streaming |
| UHV | Ultra-High Vacuum |
| UV | Ultraviolet |
| VB | Valence Band |
| VIE | Vertical Ionization Energy |
| VSFG | Vibrational Sum Frequency Generation |
| WFT | Wave Function Theory |
| XAS | X-ray Absorption Spectroscopy |
| XES | X-ray Emission Spectroscopy |
| XPS | X-ray Photoelectron Spectroscopy |

List of Publications

The work presented in my written thesis is based on the following published papers:

- I. A setup for studies of photoelectron circular dichroism from chiral molecules in aqueous solution
S. Malerz, H. Haak, F. Trinter, A. B. Stephansen, C. Kolbeck, M. Pohl, U. Hergenhahn, G. Meijer, and B. Winter.
Rev. Sci. Instrum. 2022, 93, 015101-015116.
DOI: [10.1063/5.0072346](https://doi.org/10.1063/5.0072346)
- II. Low-energy constraints on photoelectron spectra measured from liquid water and aqueous solutions
S. Malerz, F. Trinter, U. Hergenhahn, A. Ghrist, H. Ali, C. Nicolas, C.-M. Saak, C. Richter, S. Hartweg, L. Nahon, C. Lee, C. Goy, D. M. Neumark, G. Meijer, I. Wilkinson, B. Winter, and S. Thürmer.
Phys. Chem. Chem. Phys. 2021, 23, 8246-8260.
DOI: [10.1039/d1cp00430a](https://doi.org/10.1039/d1cp00430a)
- III. Accurate vertical ionization energy and work function determinations of liquid water and aqueous solutions
S. Thürmer, S. Malerz, F. Trinter, U. Hergenhahn, C. Lee, D. M. Neumark, G. Meijer, B. Winter, and I. Wilkinson.
Chem. Sci. 2021, 12, 10558-10582.
DOI: [10.1039/d1sc01908b](https://doi.org/10.1039/d1sc01908b)
- IV. Quantitative electronic structure and work-function changes of liquid water induced by solute
B. Credidio, M. Pugini, S. Malerz, F. Trinter, U. Hergenhahn, I. Wilkinson, S. Thürmer, and B. Winter.
Phys. Chem. Chem. Phys. 2022, 24, 1310-1325.
DOI: [10.1039/d1cp03165a](https://doi.org/10.1039/d1cp03165a)
- V. Photoelectron circular dichroism in angle-resolved photoemission from liquid fenchone
M. Pohl,* S. Malerz,* F. Trinter, C. Lee, C. Kolbeck, I. Wilkinson, S. Thürmer, D. M. Neumark, L. Nahon, I. Powis, G. Meijer, B. Winter, and U. Hergenhahn
Phys. Chem. Chem. Phys. 2022, 24, 8081-8092.
DOI: [10.1039/d1cp05748k](https://doi.org/10.1039/d1cp05748k)

* Shared authorship. Authors contributed equally.

- VI. Following in Emil Fischer's footsteps: a site-selective probe of glucose acid-base chemistry
S. Malerz,* K. Mudryk,* L. Tomaník, D. Stemer, U. Hergenbahn, T. Buttersack, F. Trinter, R. Seidel, W. Quevedo, C. Goy, I. Wilkinson, S. Thürmer, P. Slavíček, and B. Winter.
J. Phys. Chem. A 2021, 125, 6881-6892.
DOI: [10.1021/acs.jpca.1c04695](https://doi.org/10.1021/acs.jpca.1c04695)
- VII. Probing aqueous ions with non-local Auger relaxation
G. Gopakumar,* E. Muchová,* I. Unger, S. Malerz, F. Trinter, G. Öhrwall, F. Lipparini, B. Mennucci, D. Céolin, C. Caleman, I. Wilkinson, B. Winter, P. Slavíček, U. Hergenbahn, and O. Björneholm.
Phys. Chem. Chem. Phys. 2022, 24, 8661-8671.
DOI: [10.1039/d2cp00227b](https://doi.org/10.1039/d2cp00227b)
- VIII. Imaging of Chemical Kinetics at the Water – Water Interface in a Free-Flowing Liquid Flat-Jet
H. C. Schewe,* B. Credidio,* A. M. Ghrist,* S. Malerz, C. Ozga, A. Knie, H. Haak, G. Meijer, B. Winter, and A. Osterwalder
J. Am. Chem. Soc. 2022, 144, 7790-7795.
DOI: [10.1021/jacs.2c01232](https://doi.org/10.1021/jacs.2c01232)

Publications less closely related to the thesis

- IX. Specific *versus* non-specific interactions of indole in water revealed by X-ray photoemission spectroscopy
L. He, S. Malerz, F. Trinter, S. Trippel, L. Tomaník, M. Belina, P. Slavíček, B. Winter, and J. Küpper.
Submitted.
- X. Valence and Core-Level X-ray Photoelectron Spectroscopy of a Liquid Ammonia Microjet
T. Buttersack, P. E. Mason, R. S. McMullen, T. Martinek, K. Brezina, D. Hein, H. Ali, C. Kolbeck, C. Schewe, S. Malerz, B. Winter, R. Seidel, O. Marsalek, P. Jungwirth, and S. E. Bradforth.
J. Am. Chem. Soc. 2019, 141, 1838-1841.
DOI: [10.1021/jacs.8b10942](https://doi.org/10.1021/jacs.8b10942)

* Shared authorship. Authors contributed equally.

Tabel of Content

| | | |
|---------|------------------------------------------------------------------------------------------------------------------|----|
| 1. | Introduction | 1 |
| 1.1 | Outline of the thesis..... | 9 |
| 2. | Methods and concepts..... | 11 |
| 2.1 | History of photoelectron spectroscopy | 11 |
| 2.2 | Principles of photoelectron spectroscopy | 13 |
| 2.3 | Electronic relaxation processes – second-order emission processes..... | 19 |
| 2.4 | A typical photoemission spectrum of water | 25 |
| 2.5 | Electron scattering and mean free path | 31 |
| 2.6 | Photoelectron angular distribution and photoelectron circular dichroism | 37 |
| 2.7 | Circularly polarized radiation at a synchrotron light source | 43 |
| 2.8 | Experimental LJ-PES setup – all components | 47 |
| 2.8.1 | Photoelectron spectroscopy of liquids – a brief historical overview..... | 47 |
| 2.8.2 | <i>EASI</i> – technical concerns and realizations..... | 51 |
| 2.8.2.1 | Liquid-microjet setup – the HPLC pumps | 51 |
| 2.8.2.2 | Liquid-microjet setup – manufacturing of quartz-glass nozzles | 53 |
| 2.8.2.3 | Liquid-microjet setup – catcher and ice crusher..... | 55 |
| 2.8.2.4 | Liquid-microjet setup – differential pumping stage and setup alignment..... | 59 |
| 3. | Summary of the main experiments and their results..... | 61 |
| 3.1 | Low-energy constraints on photoelectron spectra from liquid water and aqueous solutions | 61 |
| 3.2 | Accurate vertical ionization energy and work function determinations of liquid water and aqueous solutions | 65 |
| 3.3 | Photoelectron circular dichroism in angle-resolved photoemission from liquid fenchone | 69 |
| 3.4 | Following in Emil Fischer’s Footsteps: A Site-Selective Probe of Glucose Acid-Base Chemistry | 73 |
| 3.5 | Probing aqueous-phase ions <i>via non-local</i> core-level electronic relaxation | 77 |
| 3.6 | Perspectives of flatjets in LJ-PES..... | 81 |
| 4. | Conclusion and Outlook..... | 85 |

5. References..... 91

6. Appendix: Reprints of published papers 99

Paper I:

A setup for studies of photoelectron circular dichroism from chiral molecules in aqueous solution

Paper II:

Low-energy constraints on photoelectron spectra measured from liquid water and aqueous solutions

Paper III:

Accurate vertical ionization energy and work function determinations of liquid water and aqueous solutions

Paper IV:

Quantitative electronic structure and work-function changes of liquid water induced by solute

Paper V:

Photoelectron circular dichroism in angle-resolved photoemission from liquid fenchone

Paper VI:

Following in Emil Fischer's footsteps: A site-selective probe of glucose acid-base chemistry

Paper VII:

Probing aqueous ions with non-local Auger relaxation

Paper VIII:

Imaging of chemical kinetics at the water-water interface in a free-flowing liquid flat-jet

Curriculum Vitae i

Statutory Declaration iii

Acknowledgment..... v

1. Introduction

Water is the most common liquid in our daily life and covers more than two-thirds of Earth's surface. We use it for drinking, cooking, cleaning, and cooling, and we usually barely think about how strongly this small molecule affects our environment and life every day. Water occurs in all of its three phases on Earth under normal conditions, be it as vapor in the atmosphere, as a liquid in oceans and rivers, or as ice in clouds and glaciers. Water, or in a much broader sense, aqueous solutions encompass us everywhere, visibly and invisibly, for instance in microscopic living systems. Most of the chemical and biological processes are promoted by water, and all life forms on Earth require water.^[1-4]

The study of water has been and continues to be an extremely active research field, with ever advancing experimental tools and theoretical methods to understand its many properties, including an astonishingly large number of anomalies which are absent in chemical analogues like TeH_2 , SeH_2 , or H_2S .^[5] It would seem surprising that the seemingly small and simple water molecule, H_2O , is capable of such versatile and unique behaviour. Arguably, most familiar is the density anomaly at 4 °C. At this temperature, water has its highest density which makes ice swim on liquid water. Altogether, there are more than 70 reported anomalies which can be categorized in phase, density, material, thermodynamical, and physical anomalies.^[2] Most of them are attributed to the interaction between the (partially positive) hydrogen atoms and the (partially negative) oxygen atom. This hydrogen bond (H-bond) network between the water molecules ties them together, and the characteristics of these weak bonds are responsible for the behaviour of water in all of its physical states.

Naturally, there is thus a large demand to gain a detailed molecular-level understanding of water's H-bonding interactions and associated chemical and structure aspects. This includes how water and its H-bonding-network are affected by atomic or molecular solutes. Water consists of one oxygen atom binding to two hydrogen atoms, with a 104.45° angle between the hydrogen atoms, resulting from the repulsion of the non-bonding electron pairs of oxygen;^[5-6] the electronic structure of the H_2O molecule will be detailed later. The fact that the electronegativity of oxygen is 1.7 times higher than for hydrogen (Pauling scale) leads to an

uneven charge distribution which is responsible for an electric dipole moment toward the oxygen atom of 1.85 D (Debye), the basis for H-bond formation.^[7]

A wide range of spectroscopic and theoretical methods were used to characterize electronic and structure aspects of liquid water and aqueous solutions on the molecular level, both in the bulk solution and at the solution—air / vacuum interface.^[8] Experimental methods include electronic and vibrational spectroscopy, spanning a wide range of excitation / ionization energies, and detection of electrons, neutrons, and light, respectively, over a large energy range, depending on the property to be explored. Here, I highlight those aspects which are most relevant in the context of my thesis. Classical vibrational spectroscopic methods, *e.g.*, infrared (IR) and Raman spectroscopy, are powerful tools to experimentally probe the structure and dynamics of bulk water. The stretching vibration of the hydroxyl in liquid water was shown to be sensitive to the distribution of hydrogen-bonded structures. This enables to access information on, *e.g.*, bond angles, number of H-bonds, and their strength.^[9-10] Experimentally, electronic structure of liquid water and aqueous solutions has been successfully determined using several local-probe X-ray techniques, and one distinguishes those detecting emitted (X-ray) photons and those detecting emitted electrons.^[11] The former studies include total and dispersed X-ray detection, typically referred to as total X-ray absorption (simply XAS), X-ray emission (XES), near-edge X-ray absorption fine structure (NEXAFS), and specifically resonant inelastic X-ray scattering (RIXS).^[4, 12] Both regular XAS and RIXS are highly complementary to electron-emission techniques which access X-ray absorption spectra *via* total or partial electron yields;^[13] the latter implies the detection of Auger-electron channels. Electron detection is also the method which I have applied in my studies. Specifically, photoelectron spectroscopy (PES) – also being highly element- and environment-sensitive – can access electron binding energies from both water solvent and solute. Furthermore, PES has the potential to be tuneable to being fairly surface-sensitive. This nicely complements several non-linear optical methods, particularly nonlinear (optical) vibrational spectroscopic methods like vibrational sum-frequency generation (VSFG) and surface second-harmonic generation (SSHG) on OH and OD, revealing information about the H-bonding network and its dynamics as well as on the orientation of the molecules on the surface.^[14] The exceptionally large surface sensitivity of these methods results from the symmetry breaking associated with the (solution – air / vacuum) interface;^[15] note though that

such experiments were typically performed under near-ambient pressure conditions, and spectral contributions due to solution impurities cannot be ruled out.^[12]

A prerequisite to understand the properties of water is a unifying picture of water's structure at ambient conditions, from temperatures below freezing up to boiling. This requires the development of suitable computational techniques – hand-in-hand with the development of experimental techniques – that can describe the structure of the H-bond network in water. Importantly, structure models must account for the dynamics due to the fluctuating H-bonds, in addition to the local excitations involving breaking and forming of H-bonds, but also in the form of collective excitations leading to density fluctuations.^[4] The accuracy to which this can be accomplished depends on how accurately the molecular interactions and the overall system dynamics are described in the computer simulations, and this depends on the computational approaches used, which I will describe very briefly. Two main groups can be distinguished, depending on how the potential energy surface is described, 'force-field' methods and '*ab initio*' approaches, as recently reviewed in Ref. 16. In the former case, a set of predefined analytical functions represents the underlying potential energy surface as a function of the corresponding molecular coordinates. In the '*ab initio*' approaches, water PE spectra are obtained "on the fly" by performing quantum chemical calculations to solve the electronic time-independent Schrödinger equation for a given molecular configuration. A further distinction of the latter approach is if it is based on wave function theory (WFT) or on density functional theory (DFT). No matter which representation is being used, the nuclear dynamics can then be described classically by Newton's equations of motion, or at the quantum mechanical level by solving the corresponding nuclear time-dependent Schrödinger equation (using grid methods, wave packets, semiclassical approaches, and methods built upon Feynman's path-integral formalism).

In my thesis, I focus on the characterization of the electronic structure of liquid water and aqueous solutions using photoelectron spectroscopy, also referred to as photoemission spectroscopy (PES). Such experiments have become possible after the invention of the vacuum liquid-jet technique, enabling electrons emitted from the liquid to be detected without perturbing collisions with gas-phase water molecules surrounding the (highly volatile) water target. Since the early systematic experiments on liquid water and aqueous solutions about

20 years ago, liquid-jet photoelectron spectroscopy (LJ-PES) has evolved into a well-recognized active modern research field, with the corresponding setups now being available in many laboratories worldwide. The majority of experiments has been performed with soft X-rays from synchrotron-radiation facilities, and more recently also laser-based high-harmonic light sources have been used.^[17] Here, I am not considering laser-based time-resolved PES studies, typically using up to 6 eV photon energy (~200 nm wavelength) and often applied to explore the nature and energetics of the solvated (hydrated) electron in water. Common LJ-PES experiments typically aimed at determining valence and core-level electron binding energies of water solvent and solute. Valence energetics can be connected to chemical reactivity in solution. Yet, the majority of experiments had focused on the detection of core-level spectra, often exploiting the so-called chemical shifts. That method can be used, for instance, to explore oxidation states, chemical bonding of an atom, or molecular dissociation equilibria, often as a function of solute concentration or solution pH.^[18] This is due to the core-level binding energies being highly element- and site-specific. It is also common practice to make use of the probing-depth sensitivity of X-ray photoelectron spectroscopy, assisted by an interpretation of the intensities of measured photoelectron peaks. Such sensitivity results from the kinetic-energy-dependent electron-scattering processes in solution. One can then characterize the spatial distribution of the various solution constituents with regard to the solution—vacuum interface^[19-20], or access photoelectron angular distributions (PADs).^[21-22] All of these measurements are based on the detection of emitted (direct) photoelectrons and probe the system's electronic ground state. Direct PES in the aqueous phase has been extensively reviewed.^[8, 11-12, 18]

LJ-PES comprises yet another large class of processes, namely second-order electron emission, associated with the electronic relaxation typically following core-level ionization. It is thus more suited to rather use the term photoemission instead of photoelectron spectroscopy, to include all processes, such as the well-known *local* Auger-electron relaxation process. Arguably, less familiar are *non-local* autoionization decays occurring in weakly bound systems, such as hydrogen-bonded or van-der-Waals-bonded systems. The Auger process typically leads to a doubly charged final state with the charges localized at the initially ionized atom of a given species. In contrast, *non-local* autoionization results in a two-hole state which is delocalized over the initially ionized (molecular) species and (in the case of solution) the

solvation shell, stabilized by the Coulomb energy resulting from the separation of the two positive charges. These so-called interatomic / intermolecular Coulombic decay (ICD) processes in liquid water and clusters, as well as the related *non-local* processes, have recently been comprehensively reviewed.^[23]

My work is, however, largely concerned with the detection of direct photoelectrons from liquid water and aqueous solutions, and, as one important topic, addresses the determination of accurate electron binding energies (BEs) of solvent and solute. In all previous LJ-PES works, electron binding energies were determined with reference to the accurately known (lowest) ionization energy of the free water molecule, *i.e.*, energies from the liquid phase were obtained as the energetic difference between the measured liquid- and gas-phase peaks. However, this gas-liquid energy shift is typically neither constant nor universal. It may vary in case the liquid surface gets charged. Several sources of such charging can be identified, but their quantification is almost elusive. Therefore another, more robust experimental method was direly needed. In fact, a condensed-matter based description of liquid water's electronic structure would seem more appropriate and offers the potential to access explicit surface and interfacial properties such as solution work functions. Although the latter aspect is not always straightforward to apply, the measurement of the so-called spectral low-energy cut-off from solution, which is a crucial element of the new approach, enables an absolute and accurate determination of solute and solvent energies, without relying on the gas-phase energy reference. Most important consequence is that we are now able, for the first time, to determine, *e.g.*, the solute-induced changes of the water electronic structure on an absolute scale, and, likewise, we can quantify solute binding energies as a function of solute concentration.

Another major aspect, also barely considered in the previous LJ-PES literature, is the role of scattering of photoelectrons in solution, here explored in liquid water. Of particular concern is the scattering of low-energy electrons. In that case, the photoelectron spectrum overlaps with a strong low-energy tail, the onset of which corresponds to photoelectrons emitted with nearly zero kinetic energy from the liquid. On the one hand, this low-energy cut-off is very useful, allowing for instance aforementioned condensed-matter-based protocol for binding-energy calibration. But on the other hand, given the origin of this tail, which is associated with quasi-elastic electron scattering due to vibrational excitations, electron-scattering processes

will severely disturb native (original) photoelectron spectral shapes and peak energies. This prevents the determination of accurate solvent and solute BEs below approximately 15 eV electron kinetic energy. It thus puts a limit on the applicable photon-energy range (with respect to a given ionization threshold) to LJ-PES studies with a number of important consequences that I will discuss below. It should also be noted that electron scattering is intimately connected with the probing depth into the solution, a quantity that remains to be accurately determined, and a reliable route for which has not yet been identified. Moreover, elastic scattering will change the propagation direction of the electrons, thus resulting in a measured PAD that is more isotropic than the genuine one, and different from the respective intrinsic molecule-specific PAD. Electron scattering is a central aspect of my work, and I will provide a good amount of background information. As mentioned above, it is the energy-dependent electron scattering that enables aforementioned depth-profiling, *i.e.*, probing different depths from the surface simply by varying the photon energy, and it specifically provides the opportunity to observe the layered interface structure of surface-active species.^{[21-}

22, 24]

My thesis explores yet another previously not addressed photoelectron process from aqueous solution or any liquid sample, namely photoelectron circular dichroism (PECD) of chiral molecules, with the potential to uniquely and sensitively connect molecular electronic structure to chirality. It manifests in a feature of the PAD that only occurs for chiral molecules, namely a forward-backward asymmetry in the photoelectron emission intensity relative to the light propagation axis, and requires the use of circularly polarized light. PECD has been intensively explored for isolated chiral molecules, and was also found in clusters and nanoparticles. Studies included single-photon ionization and multi-photon processes and associated time-resolved ultrafast studies.^[25-35] The demonstration of PECD in liquid phase, driven by its large relevance to life sciences in aqueous environments, where hydration and chiral recognition are fundamental biochemical processes, has arguably been the major challenge of my thesis work. As I will detail in the results chapters, the largest challenge in detecting PECD, which has a large cross section only near the ionization threshold and hence requires probing low electron kinetic energies, is the strong signal overlap with the large signal from the low-energy scattering tail. In order to perform LJ-PECD studies from aqueous phase, a dedicated and unique experimental setup was needed. Its design, manufacturing,

and commissioning, all largely under my lead management, made up for a large fraction of the time required to prepare this thesis work. Experimental and technical details as well as the basic formalism describing PADs – regular and chiral-specific ones – will be presented below.

1.1 Outline of the thesis

Chapter 2, which is divided into six sub-chapters, provides the essential scientific and technical background information so that the subsequently presented results can be appreciated without consulting the large available literature. I include descriptions of synchrotron light sources, the new liquid-jet PES setup (based on Paper I), *EASI*, the liquid-jet technique with a brief historical review, and the main concepts of photoelectron spectroscopy. The latter includes electron-scattering processes in liquid water as well as the role of photoelectron angular distributions with emphasis on the chiral anisotropy parameter. Chapter 3 reviews results that I have obtained during my doctoral research, particularly on those topics that have been published, see Papers I-VIII, attached in the appendix. Specifically, Chapter 3.1, based on Paper II, discusses the nature of the low-energy tail in the photoelectron spectra from neat liquid water and aqueous solutions and shows that the large probability for vibrational (small)-energy losses by low-kinetic-energy electrons leads to the distortion of native PE spectra. Chapter 3.2, based on Paper III and IV, presents the novel approach applying condensed-matter concepts to liquid-jet photoelectron spectroscopy (LJ-PES) that enables the accurate determination of solvent and solute electron binding energies. I explain the need for measuring the low-energy cut-off from aqueous phase, as well as how this ability can be further extended to access explicit solution interfacial properties by the formal introduction of the Fermi energy. Chapter 3.3 reports on first-ever PECD experiments from liquid phase, exemplified here for carbon 1s core-level ionization of fenchone which is a liquid at room temperature, based on Paper I and V. Studying that sample is convenient as a fenchone liquid jet can be operated as routinely as water liquid jets. In the subsequent Chapter 3.4, I present the very first systematic LJ-PES measurements from a sugar aqueous solution, based on Paper VI. My interest in that study relates to the anomeric effect, although Paper VI is rather the demonstration of LJ-PES application to glucose aqueous solution. I will show that PES is ideally suited to identify the sites that change their charge state as a function of pH, and I will conclude with briefly discussing how to “freeze” the anomeric center, using methylated glucose. Observed considerable differences in both the carbon core-level and valence PE spectra for α - and β -glucose can be associated with the different chemical reactivity of the two anomers. Chapter 3.5 presents *non-local* autoionization measurements, specifically intermolecular Coulombic decay (ICD), of a series of aqueous-phase isoelectronic cations

following 1s core-level ionization, based on Paper VII. We identify the ICD contribution to the K-edge Auger-electron spectrum and use a so-called core-hole-clock analysis to estimate the associated ICD timescales. This study shows that Auger decay and ICD spectroscopy represent a powerful tool for the exploration of intra- and inter-molecular decay processes. At the very end, in Chapter 3.6 which is based on Paper VIII, I describe an important technical accomplishment in flatjet generation, based on the collision of two cylindrical microjets of different aqueous solutions. Potential applications of such a structure in vacuum will be discussed.

2. Methods and concepts

In this chapter, essential concepts are discussed, which are necessary for understanding the research methodology and results of this thesis. First, a few historical landmarks through the evolution of photoelectron / photoemission spectroscopy are given. Then, I introduce the general theory, followed by dedicated chapters providing necessary methods and concepts of photoemission. Later, more specialized sub-chapters will detail photoelectron angular distributions (PADs) and their origin. A particular focus is on the special case of PADs from chiral molecules, applying circularly polarized light, referred to as photoelectron circular dichroism (PECD). Furthermore, I give a description of some main components of the *EASI* setup, which was used for most measurements of my thesis. This additional information is beyond what is covered in the related Paper I, and will also provide a brief hands-on how to perform a liquid-jet photoelectron spectroscopy (LJ-PES) experiment.

2.1 History of photoelectron spectroscopy

As early as 1839, Alexandre Edmond Becquerel, father of the Nobel Prize laureate Antoine Henri Becquerel, observed that charge carriers are transferred between two electrodes immersed in an electrolyte when just one electrode is irradiated with light. This so-called “Becquerel effect” was the starting point for further investigations and developments which ultimately would lead to photoelectron spectroscopy (PES).^[36-37] Similar to Becquerel, Heinrich Hertz described the removal of electrons from a solid body by short-wave radiation in 1886 and established the photoelectric effect. He recognized that a charged metal plate discharged faster when exposed to light. One year later, Wilhelm Hallwachs, former student of Hertz, investigated Hertz’s observation further and noticed that the amount of the emitted (photo-)electrons is proportional to the intensity of the impinging light. Moreover, he observed that the kinetic energy (KE) of the emitted photoelectrons depends on the frequency of the incident light.^[38-39] Because of his investigations, the photoelectric effect was also known as “Hallwachs effect” for a period of time but was not fully understood.^[40]

It was not until 1905 that Albert Einstein succeeded in theoretically explaining the effect based on Planck's law of radiation. Planck proposed that light consists of tiny packages of energy (quanta) and each package carries an energy, $E = h\nu$, which is proportional to the frequency ν of the corresponding electromagnetic wave. Einstein invoked the concept of the light quantum (later known as photon, a term introduced by Lewis 1926)^[41] and received the Nobel Prize in Physics in 1921 for his theoretical work on the photoelectric effect.^[42] Over the next decades, new techniques were developed using the photoelectric effect to investigate the electronic, structural, and chemical properties of matter and gave new insights into the structure of matter or reactivity of chemical reactions. Photoelectron spectroscopy is arguably the most direct technique to investigate structures, (chemical) environment, reactivity, and electronic effects of atoms and molecules. Only relatively recently, the technique was extended to water and aqueous solutions and helped to open the doors to inferring chemical and biochemical processes in liquids on the molecular level. The history of the development of the liquid-jet technique is provided later, in Chapter 2.8.1.

2.2 Principles of photoelectron spectroscopy

Photoemission* spectroscopy (PES) has emerged as a powerful technique to investigate the electronic structure of atoms and molecules in solid, gaseous as well as liquid samples. A distinctive feature of PES is the ability to selectively probe individual atomic / molecular orbitals, which distinguishes this method from many other spectroscopic techniques. In addition, sensitive probing of the environment is possible by identifying core-level chemical shifts as a result of the bonding behavior (*i.e.*, changes in orbital energy imposed by the chemical environment).^[43-45] Electrons are emitted after ionization by (often monochromatic) electromagnetic radiation of frequency ν , carrying the photon energy $h\nu$. The directly measured quantity is the ionization potential, I , (or rather the binding energy, BE) which describes the minimum required energy to remove an electron from an atomic / molecular orbital. Utilizing an approximation, called *Koopmanns' theorem*, we can connect the ionization potential directly to the orbital energy of a specific orbital of the initial atom / molecule:^[46]

$$I_{\text{Orbital}} = -\varepsilon_{\text{Orbital}} \quad (\text{eq. 1})$$

In other words, we can connect our measured property directly to the internal electronic structure of the matter under study. In reality, *Koopmanns' theorem* neglects several effects such as relaxation of the remaining electrons as well as relativistic and correlation effects.^[47] Thus, obtained PE spectra contain information on the molecular orbital energies but also show changes in the molecular geometry caused by electron removal from specific orbitals. The character of the orbitals – bonding, antibonding, or non-bonding – may be revealed by the specific shape of the bands in a spectrum.^[46]

An equal or greater amount of energy than the BE must be invested to liberate an electron from its bound state – an atomic / molecular orbital or energy level – and promote it into the vacuum, *i.e.*, $h\nu > \text{BE}$. Any excess energy above the BE is converted into kinetic energy ($KE = \frac{1}{2}m_e v_e^2$) of the emitted photoelectron. This relation is expressed in the photoelectric law (also compare Figure 1a):^[48]

* Photoemission includes all primary and any emitted electrons by other, second-order processes, *e.g.*, Auger decay. Whereas the term photoelectron usually means the detected photoelectron originate out of a first-order process.

$$BE = h\nu - KE \quad (\text{eq. 2})$$

However, for condensed matter like solids, electron binding energies are provided with respect to a different energy reference, the Fermi energy. The Fermi level is usually equilibrated throughout all materials in contact, which makes it often a convenient energy reference in the condensed phase (with complications in liquids, see later). Accordingly, the BE is defined as the energy to promote an electron from a bound state to the Fermi level inside the matter. However, for the electron to leave the matter and be expelled into vacuum additional energy is required. This sample-specific ionization threshold is referred to as the work function, Φ . In this definition, eq. 2 is rewritten as (see also Figure 1b):

$$BE = h\nu - KE - \Phi \quad (\text{eq. 3})$$

In general, the exact value of the work function is unknown, and thus it is often difficult to compare values between these two definitions (*i.e.*, between gaseous and condensed-phase measurements). To obtain BEs of condensed-phase samples, the energetic position of the Fermi level in the PE spectrum can be determined and used as energy reference. While this is very convenient for metals, where the Fermi level is occupied with electrons and thus accessible for PES, it is troublesome for semiconductors and isolators where the Fermi level is residing in an energy gap devoid of electrons. This topic is explored further in Chapter 3.1 and 3.2, which are based on Paper III and IV. For now, we will concern ourselves with isolated atoms or molecules.

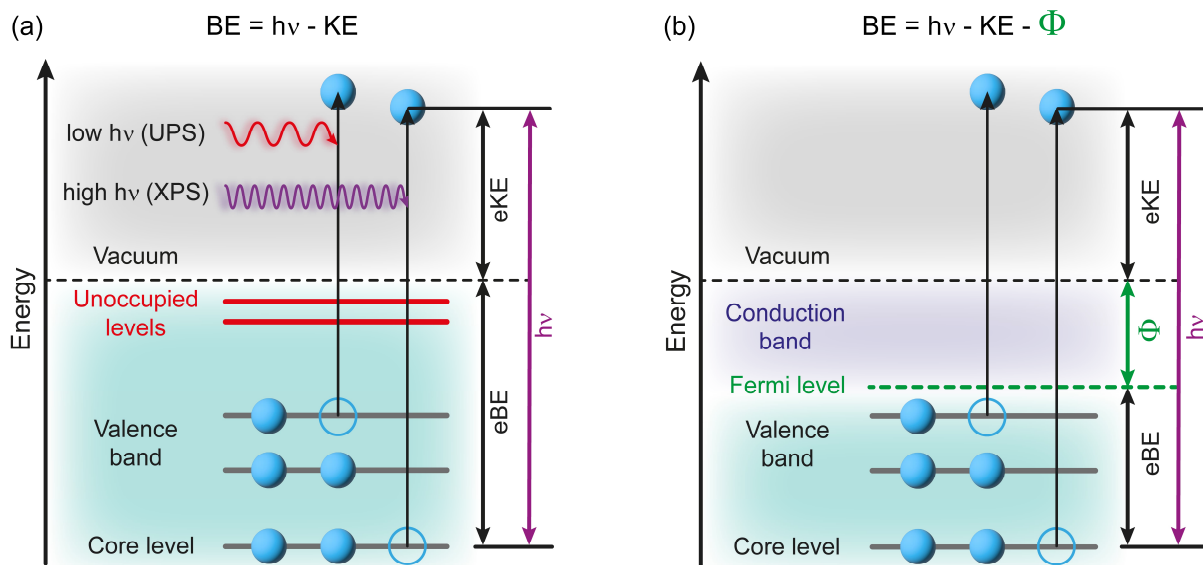


Figure 1: Schematic energy-level diagram of a direct ionization process of the gaseous phase (a) and of the condensed phase (b). The full circles represent electrons (core and valence electrons), the open circles the “holes” after ionization.

In more general terms, the ground – or initial – state of the PE process represents an N -electron state in a relaxed geometry. The (direct) PE process results in an $N-1$ -electron final state with a vacancy in one of the atom shells plus a freely propagating photoelectron. Thus, the PE process reflects a transition from the initial to the final state, and the total energy between these two states is expressed as the BE. As PE spectroscopy only measures the KE of an outgoing photoelectron, it is, strictly speaking, impossible to gain direct information about the initial state and instead a spectrum contains information about the behavior of the system during the ionization (this will involve so-called final-state effects). Both initial and final state depend on the environment of the ionized entity, which appears as a unique fingerprint in the spectrum. However, we have established in equation 1 and 2, that, with a few approximations, the obtained KE is a useful measure of the initial electronic structure, and the ionic system as well as final-state effects can be considered additional corrections.

After electron emission, the system seeks to adapt to the positive hole left behind. As a consequence, the system undergoes nuclear and / or electronic structure rearrangements within the new ionic potential. The PE process is assumed to be instantaneous (this is termed *sudden approximation*). In reality, it takes place on the femto- to attosecond timescale (depending on the KE of the electron), which is orders of magnitudes faster than any atomic movements, and thus the sudden approximation usually holds.^[49-51] Or in other words, the

time needed for the electron to leave the system depends on the energy of the photoelectron, and this approximation is better for higher KE. For an interacting N -electron system, the *sudden approximation* assumes that the photoelectron is decoupled from the $N-1$ -electron state, so that the electron does not carry information about the latter.^[12, 52] Moreover, it is assumed that the orbital configuration, the spatial distribution, and the energies between the initial N -electron state and the final $N-1$ state do not change during the ionization process (also called *frozen-orbital approximation*). This is the basis for the equality of the orbital energy and the BE (also known as *Koopmans' BE*) established in eq. 1. A different approach viable for low-KE electrons is the so-called *adiabatic approximation*.^[53] When the photoelectron leaves the ionized entity slowly, it recognizes the electronic relaxation of the remaining electrons to adapt to the changed effective atomic / molecular potential in a self-consistent way.^[54] The final state differs from the initial state by the reorganization energy (from the relaxation process) as well as correlation and relativistic effects. Especially the reorganization energy is a crucial parameter for a better understanding of chemical reactions.

Now turning to the interpretation of a measured PE spectrum, we first have to realize that the intensity of peaks in a measured spectrum is affected by a number of factors. First, there are experimental factors such as the acceptance angle of the analyzer or electron transmission rate, which is most often summarized a single parameter T_{det} , the illuminated / detected area of the sample $A_{surface}$, and the photon flux F_{photon} . Then, there are physical factors: The ionization cross section (CS) of the probed orbital $\sigma_{orbital}$, the sample or atom density ρ_{sample} , and the probing depth, which is represented by the still-to-be-discussed inelastic mean free path (IMFP), λ_{in} . The measured intensity I can be expressed as:^[19, 49]

$$I_{detection} = T_{det} \cdot A_{surface} \cdot F_{photon} \cdot \sigma_{orbital} \cdot \rho_{sample} \cdot \lambda_{in} \quad (\text{eq. 4})$$

In general, most of these parameters are quantitatively unknown and the intensity in a PE spectrum remains somewhat arbitrary. Thus, absolute intensities are typically not accessible and only a qualitative interpretation of spectra is possible. One can, however, exploit the fact that most parameters are fixed, which makes it possible to quantify relative intensities (of *e.g.*, between different orbitals) or changes in intensity when one parameter is changed (*e.g.*, density). The photoionization CS, $\sigma_{orbital}$, describes the probability of photoionization upon

interaction of an entity with an incident photon, and is dependent on the photon energy and the polarization of the incident light. Note that for liquids, which of course includes water and aqueous solutions, accurate ionization CS values are not available, which limits studies to relative changes. The IMFP, which is related to electron scattering, and photoionization CS will be described in more detail in Chapter 2.5.

If the incoming photon energy is not sufficient to ionize but carries an energy value resonant with the energy difference between an occupied and unoccupied atomic / molecular orbital, absorption takes place and promotes an electron into the higher unoccupied level. The system becomes excited, which, however unlike ionization, will leave the charge state of the system unchanged. So-called secondary processes can occur both after emission of the primary electron upon ionization and resonant excitation, which are explained in the next section.

2.3 Electronic relaxation processes – second-order emission processes

After X-ray irradiation, the system is left in an excited state with a core-level hole present. This state inevitably decays with a characteristic lifetime, where an electron from a higher energy level fills the core hole. This leads to a plethora of so-called second-order processes. These second-order processes may even involve other neighbouring atoms or molecules in the condensed phase, which reveal themselves with a unique fingerprint in PE spectra, as we see later. We can thus distinguish between *local*, within a molecule / atom, and *non-local* processes, which involves surrounding entities.^[55-56]

First, I will explain *local* processes, which take place within a single atom or molecule. This is the only type of process that can occur in isolated, non-interacting systems. The energy can dissipate in two different ways:

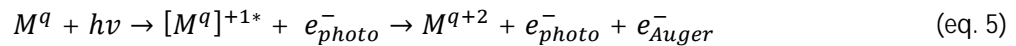
- i. Emission of a photon, which increases in probability for heavier elements,^[57]
or
- ii. Emission of another electron as a result of autoionization[†],^[58-59] which is the dominating process for light elements.^[60-61]

The latter is termed *normal Auger decay*[‡] ^[62-63] and leaves the system in a doubly charged state (2+) with two holes (2h-state) in the valence band, as illustrated in Figure 2a. After ionizing deep core levels, several Auger decays can take place: After the core vacancy is filled with an electron from an intermediate state, this new vacancy will be filled with an electron from a higher orbital, and so on. This *Auger-electron cascade* continues until the system remains in a relaxed, (n+1) h-state, with n being the number of Auger processes leading to this state. The KE of the direct photoelectron depends on the incident photon energy, $h\nu$, whereas the KE of the Auger electron only depends on the involved energy levels and is thus independent of the exciting photon energy, but in turn carries a specific fingerprint of the ionized system. This is true for all processes discussed in this chapter. Thus, Auger electron peaks occur at the same KE in PE spectra independent of the photon energy, whereas direct PE peaks shift with a

[†] In general, autoionization is a process in which a system ionizes without any outside influences.

[‡] *Auger decay* was first observed by Lise Meitner and later described by Pierre Auger. Lise Meitner's contribution was not well noted at the time. In honour of her work, nowadays this process is also termed *Auger-Meitner-effect*.

changing photon energy. The Auger process for a molecule M with a given charge q can be described as



with $[M^q]^*$ as the intermediate excited state. The resulting KE of the Auger electron can be estimated from the binding energy (BE) of the incurred core-hole BE^C , the hole-filling electron BE^F , and the emitted electron BE^E :^[64]

$$KE_{Auger} \approx BE_{binding}^C - BE_{binding}^F - BE_{binding}^E \quad (\text{eq. 6})$$

This approximation is never exact and KE_{Auger} depends on other energy terms like hole-hole Coulomb repulsions or changes due to nuclear relaxation processes during the core-hole lifetime.^[65] Typically, *Auger decay* is denoted by labels of the involved shells in the X-ray notation, like KLL, with a vacancy in the K-shell and autoionization from the L-shell.

Auger decay can still occur when the photon energy is not sufficient to ionize the entity but instead resonant with the energy difference between an occupied and unoccupied energy level. In this case, the electron is promoted into an unoccupied state (e.g., the lowest unoccupied molecule orbital, LUMO) and, as before, leaves a vacancy in the core level. Thus, we have the right conditions for *Auger decay*. In this 'resonant' Auger process, de-excitation leaves only a singly charged (1+) final state with one hole (1h-state) in the valence band. Now two decay processes can follow, depicted in Figure 2b and c, respectively. In the so-called *spectator Auger* process, a valence electron fills the core hole as before. Now the extra excited electron screens the ionic potential, which reduces the Coulomb attraction and increases the KE of the outgoing Auger electron, as illustrated in Figure 2b. Alternatively, the excited electron itself can also fall back into the core hole. In this *participator Auger*, shown in Figure 2c, the outgoing electron gets almost the full energy of the initial photon. This process is very similar to a direct PE process, but with the delay of the lifetime of the excited state and possible final-state effects, which can lead to an imprint of the final state or the onset of nuclear dynamics onto the PE signal. Nevertheless, a deeper discussion of this topic is beyond the aim of this chapter and is not related to my thesis.

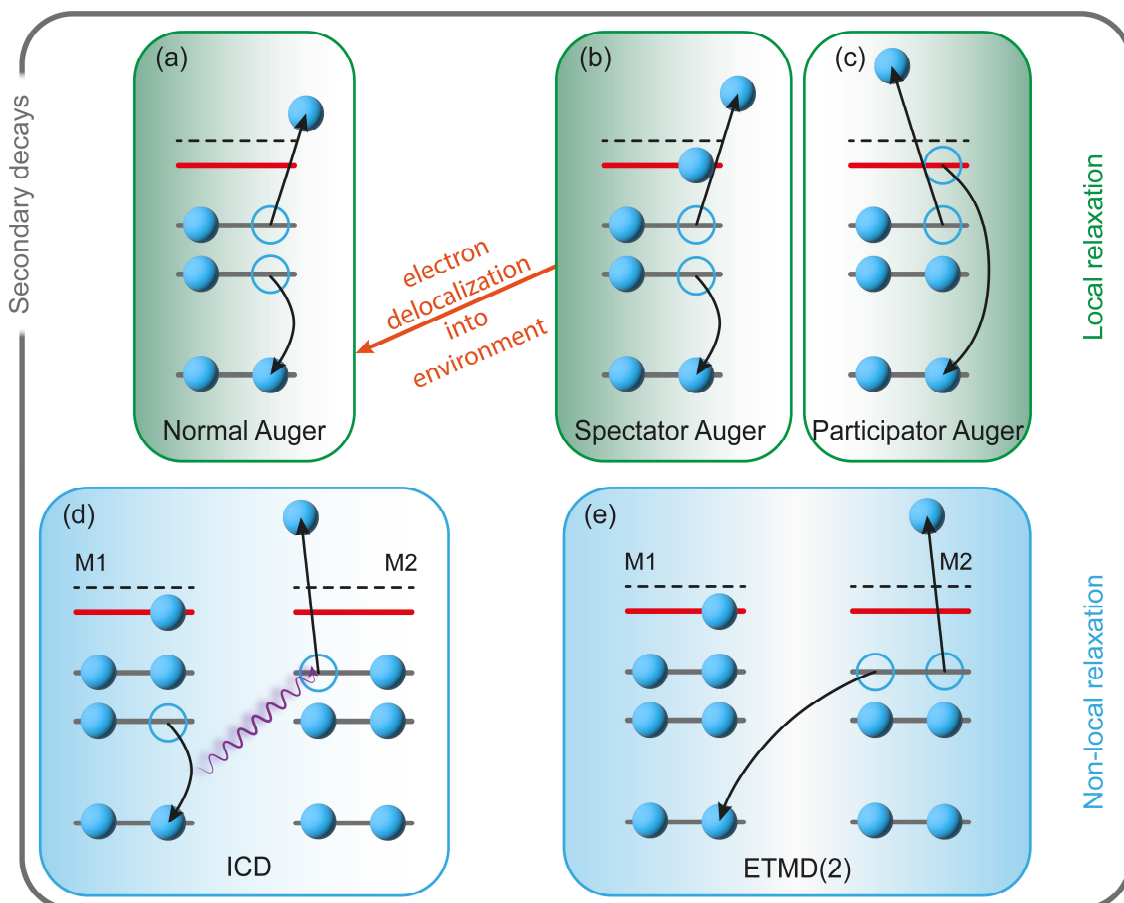
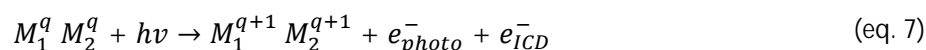


Figure 2: Schematic energy-level diagrams for **local** (a-c) and **non-local** (d-e) decays. Red lines represent unoccupied orbitals and blue circles represent holes. *Normal Auger* decay (a) occurs as a result of ionization. Resonant excitation leads to *spectator* (b) and *participator Auger* decay (c). The released electron gains KE as compared to a *local Auger* electron due to the reduced Coulomb attraction *via* electron screening. In the condensed phase, an excited electron can **delocalize** (orange arrow) from its weakly bound state to the environment within the core-hole lifetime.^[66-68] The subsequent decay resembles *normal Auger* decay because of the absence of the screening electron.^[68] A specific *non-local* decay mechanism is interatomic / intermolecular Coulomb decay (ICD) (d), where the excess energy is transferred to a neighbouring molecule in close vicinity, which is in turn ionized. Again, the Coulomb attraction is reduced, which leads to an increased KE of the Auger electron. Electron-transfer mediated decay (ETMD) (e) is instead a process where the core hole is filled by an electron from a neighbouring entity. The released energy is used to ionize the electron donor itself, denoted as ETMD(2), or a third molecule, ETMD(3). In all cases, the KE of the released electron is independent of the initial photon energy.

All processes described so far can occur in both the gas phase and the condensed phase. Now, we turn to processes which are limited to weakly interacting systems, *e.g.*, van-der-Waals interaction or H-bonds, where the presence of nearby entities can considerably alter the decay process and additional processes can occur by involving neighbouring atoms and molecules. These *non-local* processes occur in systems, where atoms / molecules are in vicinity to each other and possibly share a (directional) connection such as hydrogen bonding (*e.g.*, in water). Such additional decay channels are shown in Figure 2d and e. *Non-local* decay causes charge separation between multiple separated molecules or atoms, which is mediated either by

electron or energy transfer. First, for the resonant excitation processes described above, it is now possible that the excited electron delocalizes into the environment, shown as an orange arrow in Figure 2. This delocalization reverts the intermediate state back to that of the *normal* Auger process, and thus the energetics are the same. The percentage of *normal* Auger signal for resonant excitation can be seen as an indication of the time scale for electron delocalization since the electron has to delocalize before the decay happens (*i.e.*, within the core-hole lifetime).^[66-68]

Energy may be transferred from a molecule M_1 to a neighbouring molecule M_2 in close vicinity during decay, where the latter is ionized. This so-called interatomic / intermolecular Coulomb decay (ICD) results in a final state, where both positive charges are located on two separate, neighbouring molecules,^[56, 69] and can be expressed as:



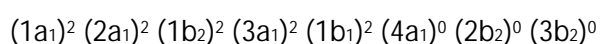
The KE of the emitted ICD electron is larger than the respective Auger decay electron, because of the reduced Coulombic energy in the system.^[23] The efficiency of the energy transfer depends on the distance R between the energy donor and the acceptor *via* R^{-6} . However, in the case of an orbital overlap, the probability of ICD depends exponentially on the distance. The fact that ICD only involves the nearest neighbours makes it very sensitive to intermolecular distances and is a powerful tool to study the structure of the solvation shell around solutes. ICD is a fast relaxation process on a sub-100 fs scale and depends strongly on the number or the nearest neighbours. The more neighbours, the faster the process, which makes ICD interesting for probing hydrogen-bond strength and solvent structure.^[23, 70-71] Nevertheless, experimental observation of ICD is challenging due to the fact that ICD is obscured by all the other occurring processes, *e.g.*, *local* Auger decay and charge transfer via nuclear dynamics. Instead of refilling the vacancy with an electron from the same molecule, an electron from a neighbouring molecule can refill the hole. In this so-called electron-transfer-mediated decay (ETMD) process, the released energy is either used to ionize the electron donor itself, or a third species; referred to as ETMD(2) and as ETMD(3), respectively (numbers in brackets indicate, how much molecules are involved). Like for Auger decay and ICD, a reduced Coulombic repulsion is reflected in a change of KE of the emitted ETMD electron, *i.e.*, it is possible to

experimentally distinguish between ETMD(2) and ETMD(3) *via* their KE signature in the spectrum. Like for ICD, ETMD becomes more likely and relevant with smaller distance between the involved molecules, however, ETMD is much less probable than ICD. This is due to the fact that ETMD requires orbital overlap, which makes ETMD much less probable and much more difficult to detect. Thus, the effect was first observed in systems where ICD and *local* Auger decay were energetically impossible or highly unfavoured.^[56, 72] ETMD was found to be significant for systems with a large orbital overlap in highly coordinated systems like Ar in a Kr-Ar-Kr trimer.^[72] A first observation in aqueous solution has been reported for solvated Li ions,^[73-74] which showed that ETMD can be a sensor for the species residing in the first solvation shell thanks to the unique energetic fingerprint for each entity involved in the process.

2.4 A typical photoemission spectrum of water

Pure water is dielectric, *i.e.*, has very low conductivity. This is a hindrance for PE spectroscopy: Not only must the sample be properly grounded to maintain the same potential; an insufficient conductivity may also lead to charge-up of the sample because of the large number of released photoelectrons. For these reasons, usually a small amount of salt is added to the liquid to assure sufficient electric conductivity. Thus, referring to 'neat water' implies that always a small amount of salt, usually 2 - 50 mM, has been dissolved.

Water itself is a simple molecule consisting of two hydrogen atoms covalently bonded with a central oxygen atom under an angle of 104.45° , whereas the distance between the hydrogens and the oxygen is 95.8 pm.^[6] The angle deviates from the tetrahedral angle of 109° because of the repulsion of two lone pairs (in sp^3 hybridization) of the oxygen. The electronegativity of oxygen is 1.667 times higher than that of hydrogen (Pauling scale), which leads to an uneven charge distribution over the molecule. The resulting dipole for a free water molecule with an electric dipole moment of 1.84 D (Debye) is the basis for H-bonding.^[2, 12, 75] The symmetry of the planar water molecule is C_{2v} : The molecule has a twofold rotational symmetry (C_2), *i.e.*, rotating the molecule around the z-axis by 180° yields the same orientation. The denotation v indicates the two vertical mirror planes without sign change of the molecule. Adopting the C_{2v} symmetry, the electronic configuration of an isolated water molecule in the ground state is:^[2, 76-77]



The molecular orbitals (MO) are labelled with respect to their symmetry, whereby identical symmetries are distinguished by leading numbers, starting with 1 at the highest BE. Within this conventional description, the water $1b_1$ MO is associated with the lowest-BE electrons. Beside this fully symmetrical a_1 orbital, we observe b_1 and b_2 orbitals, which change sign by mirroring in the molecular plane, and in the perpendicular plane, respectively.

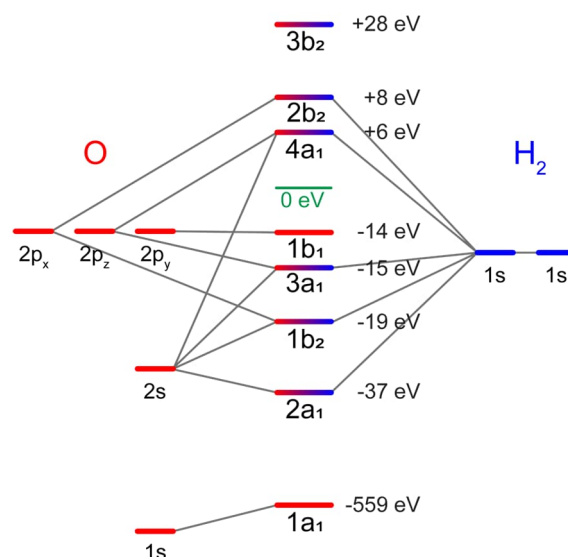


Figure 3: Calculated energy diagram of the five occupied and the lowest three unoccupied molecular orbitals of an isolated water molecule (gas phase). Molecular orbitals (MOs) are represented as a linear combination of the atomic orbitals (AOs). The highest occupied MO (HOMO), $1b_1$, is formed by the two oxygen lone pairs. Given BEs in eV are theoretical calculated. Figure adopted from Ref. 2.

Figure 3 shows the calculated energy diagram from an isolated water molecule, taken from Ref. 2. It was calculated using the restricted Hartree-Fock (RHF) method with the 6-31 G** basis set. The first five molecular orbitals (MO) are filled with two electrons each. For the $1a_1$ and the $1b_1$, all electrons are originating from the oxygen, which leads to a full oxygen 1s character. Moreover, the lowest (core-)orbital, $1a_1$, does not participate in any bonding and is labelled usually just as O 1s in the literature. The other three (antibonding) orbitals above the 0-eV threshold are empty and are not observed in PE spectra. PE spectra are often separated in two regions, depending on the used spectroscopic method and available photon energy, the valence-band region (8 - 35 eV BE) and the core-level region (535 - 545 eV BE). The former contains $(2a_1)^2$, $(1b_2)^2$, $(3a_1)^2$, and $(1b_1)^2$, and the latter contains just the $(1a_1)^2$.

Usually, the very same orbital description is used for PE spectra from liquid water. This is rooted in the fact that all orbitals are still present and discernible in measured spectra. Here, the liquid environment can be seen as a perturbation of the molecule's electronic structure (or orbital symmetry).^[78-79] Yet, the almost purely molecular description of liquid water is unsatisfactory, and we strived to move towards a description more in line with PE spectroscopy from condensed phase, such as solids (see later).^[78] Furthermore, PE spectra of liquids always contain signal contributions from the gas phase due to the inevitable evaporation from the liquid's exposed surface in vacuum. A way to separate the signals of the

gas phase from the liquid phase is to apply a bias voltage.^[78, 80-82] For biased PES experiments, the liquid is connected to a power supply by inserting a conductive metal junction into the PEEK tubing which carries the liquid to the nozzle (see Paper I)^[81]; the liquid jet is otherwise insulated from the apparatus. With a bias voltage applied to the liquid, the entire liquid-phase spectrum experiences a rigid energy shift, equivalent to the negative voltage. The photoelectrons originating from the gas phase experience less acceleration in the field gradient established between the liquid jet and the detector orifice, depending on their position of origin. This reduced effect of the bias voltage with distance from the liquid surface leads to an, on average, much smaller shift and smears out the gas-phase signal. As a result, the liquid-phase PE spectrum can be obtained essentially free from overlapping gas-phase signal. However, there will always be some residual gas-phase contribution, because some gas-phase molecules will reside directly above the surface and thus experience the full bias potential.^{[78,}

81, 83]

In Figure 4, a spectrum of the valence band and core-level region of liquid water is shown under a biased condition (in blue; -32 V bias). Here, the energy axis is already converted to BE, *i.e.*, presented after removing any shift from the bias voltage and converting the measured kinetic energy into a calibrated binding energy scale; this energy calibration process is explained in detail in Paper III. The pure gas-phase spectrum is shown in grey, and was obtained when measuring the water vapor above the liquid surface or a water vapor stream introduced into the vacuum chamber. A typically unbiased liquid-water spectrum is a combination of both individual components (shown in red).

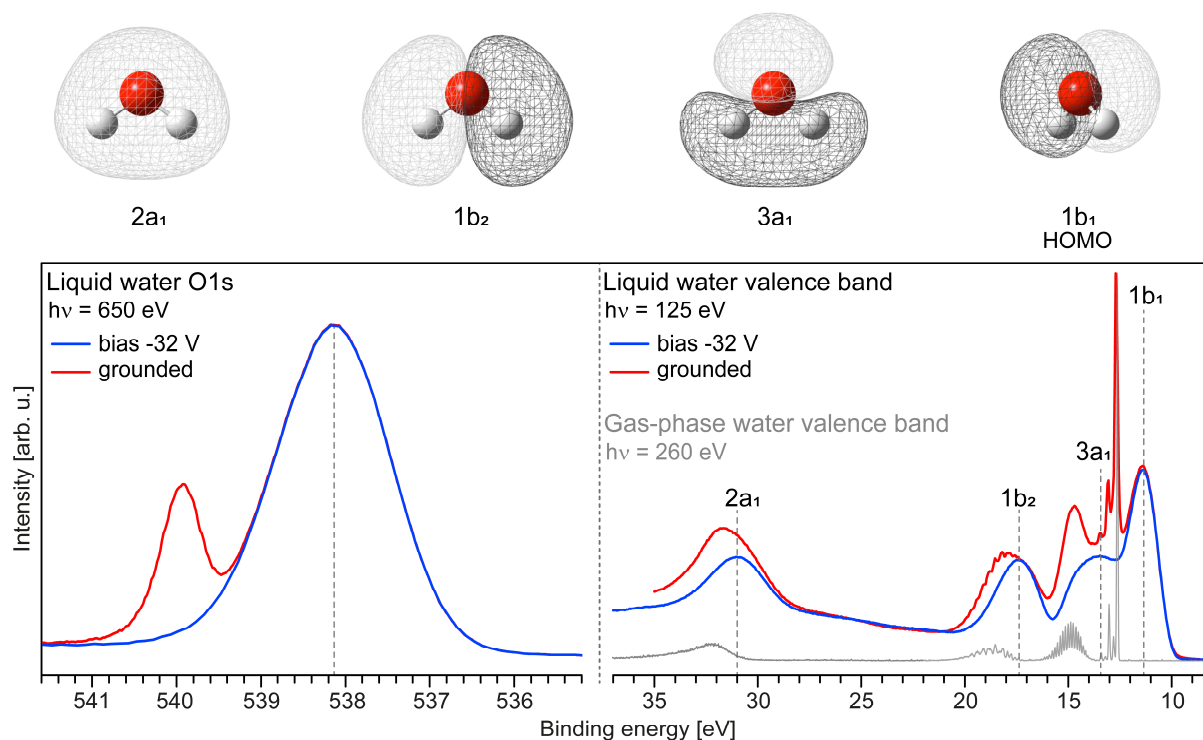


Figure 4: The top panel shows the calculated electron-density contours of the MOs of the water valence band, taken from Ref. 76. The lower panel shows PE spectra of liquid water in **blue**, measured at the UE42 beamline at BESSY II. A spectrum of the valence band is shown to the right and the O 1s peak is shown to the left; both spectra were measured without any gas-phase contribution by applying a bias of -32 V. For the detailed procedure, see Papers I – IV.^[78, 80-81, 83] For comparison, grounded spectra of water are shown in **red**, measured at beamline P04 at DESY at $h\nu = 125$ eV, where the additional gas-phases contribution can be clearly identified. All occupied water orbitals in the valence band ($1b_1$, $3a_1$, $1b_2$, and $2a_1$) are visible and labeled. The BE scale was calibrated to 11.33 eV of water $1b_1$, and to 538.1 eV BE for the O 1s.^[78, 84] A pure water gas-phase spectrum is shown in **grey** for comparison. Here, a large number of sharp peaks, which are due to excitation of different vibrational modes during the ionization process, are resolved for the $3a_1$ and $1b_2$ orbitals. The BE scale for the gas phase was calibrated to 539.9 eV^[77] for water's O 1s and to 12.612 eV^[85] for the ($v = 0$) peak of the valence band's $1b_1$ orbital.

Usually, the flowing liquid beam from a non-conductive solution is already electrically charged by electrokinetic charging. This is caused by disruption of an electric double layer created at the interface between the inner wall of the nozzle / PEEK tube and the flowing liquid,^[86-87] *i.e.*, the engendered Stern layer of ions, bounded on the inner wall of the nozzle, is sheared off by the mobile liquid phase. As a consequence, the flowing mobile phase carries counterions away and creates a streaming electric current, I_{Str} , as well as a corresponding streaming potential, Φ_{Str} .^[86] This unwanted electrokinetic charging disturbs the emitted photoelectrons on their way to the analyzer, which leads to energy shifts and peak-broadening. Another inevitable potential in the experiment to consider is the contact potential, which originates from the difference in work function of the sample (the liquid jet) and of the apparatus. This potential, with unknown magnitude, is further modified by adsorption of

water molecules on all surfaces in the interaction chamber over time, which leads to energy shifts up to several hundreds of meV over a time period of several hours, depending on the pressure in the chamber during the measurement. However, with just the right amount of salt concentration in conjunction with a well-defined jet diameter, flow rate, and under stable temperature conditions, it has been shown that the streaming potential can be tuned in a way to yield field-free conditions, *i.e.*, zero effective potential, between the jet and the analyzer.^{[78,}

86, 88]

In the past, liquid-phase spectra were energy-referenced to their respective gas-phase counterparts, for which the ionization energy is known with high accuracy (*e.g.*, the BE of the $1b_1$). However, due to the presence of aforementioned parasitic potentials, this procedure is prone to errors, and an accurate energy reference cannot be achieved in general. In some special cases, where field-free conditions can be engineered, such gas-phase referencing may be used to determine BEs of a solution. However, in practice, achieving such conditions is highly unpractical and even impossible for most aqueous solutions. Thus, the absolute BE of water's $1b_1$ was under debate.^[89-92] Implementation of a robust method for an absolute energy referencing of BEs from water and aqueous solutions was one main goal of my work. With this method it was possible to determine the accurate BE of water (described in detail in Paper III and IV)^[78, 83] as 11.33 eV for the $1b_1$ and 538.10 eV for the $1a_1$ (O 1s),^[78] to be briefly summarized in Chapter 3.2.

Compared to the gas phase, liquid water's peaks are shifted by 1.2-1.9 eV to lower BE (see Figure 4). This solvation shift occurs because of dielectric screening and intermolecular interactions with neighbouring water molecules in the liquid.^[12, 93-96] Moreover, peaks are broader because of a large distribution of different configurations between water molecules, leading to a slightly different energy for each individual molecule. Strong orbital interaction in the hydrogen-bonded network leads to a split of the $3a_1$ peak into a bonding ($3a_{1H}$) and a non-bonding ($3a_{1L}$) contribution. This peak splitting is also observed for ice and is less pronounced for liquid water.^[97]

2.5 Electron scattering and mean free path

In general, the propensity to interact or scatter from matter is very high for free electrons, which is the reason for the need to maintain ultra-high vacuum conditions during a PES experiment. The distance an electron can travel through the matter before undergoing a scattering event, the so-called mean free path (MFP), is highly dependent on the molecular density. The inelastic MFP (IMFP), λ_{in} , describes the average distance which an electron of a given energy can travel before undergoing inelastic scattering, *i.e.*, scattering with loss of some of its kinetic energy.^[19] Similarly, the elastic mean free path (EMFP) describes the average distance traveled before undergoing elastic scattering (involving no or an insignificant amount of energy loss). Electron scattering attenuates the PE signal, *i.e.*, an electron which loses sufficient energy *via* scattering is removed from the respective peak's signal. Also, inelastic scattering leads to the appearance of a background signal at lower kinetic energies than the respective peak signal. The IMPF is an important factor, which for example determines the surface sensitivity of the experiment, and will be discussed in more detail below.

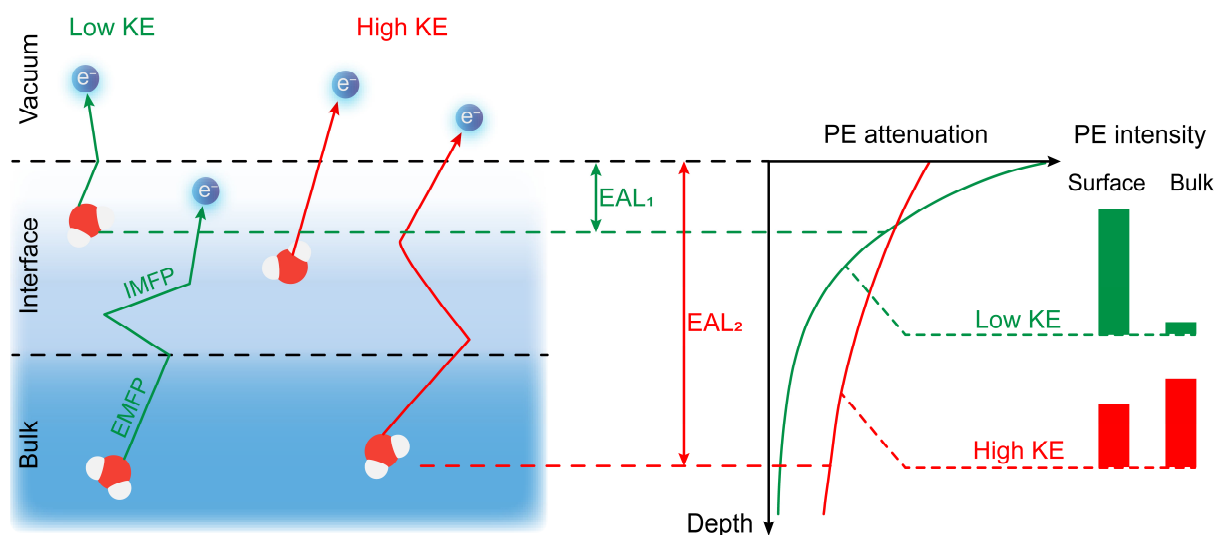


Figure 5: Illustration of the effective attenuation length (EAL) as well as the inelastic and elastic mean free path ways (IMFP and EMFP) in condensed matter. The emitted electrons undergo elastic scattering (no energy loss), and inelastic scattering (involves energy loss); the latter causes an attenuation of the PE signal. The PE signal is attenuated exponentially with the probing depth (interface / surface vs. bulk probing). Because of lower ionization cross sections (CS) at higher kinetic energies (KE), the red curve starts lower due to less signal attenuation. Figure adapted from Ref. 98.

Depending on the incident photon energy, and in turn the resulting kinetic energy after ionization, the IMPF and with it the escape depth of the electrons vary. This makes it possible

to tune the probing depth by varying the photon energy to scan over different interfacial layers, which is termed depth probing. This enables the study of species which are located at specific depths such as surfactants,^[83] hydrophobic / hydrophile functional groups,^[99-101] or polarizable ions.^[20, 102] With the knowledge of the IMPF behavior an interpretation of the probing depth is possible, and would enable, *e.g.*, determination of solute density profiles at the aqueous solution interface.^[19] However, determining the exact depth where the electrons originate is challenging and several hurdles need to be overcome.

While the IMFP is in general strongly material-dependent, for most solid metals very similar qualitative observations were made: At an eKE of 50-100 eV, the IMFP is between ~5 to ~10 Å, with a steep increase towards lower KEs and a moderate increase towards higher energies. Values of ~20 Å for eKE ~ 1000 eV and ~30 Å around eKE ~ 2000 eV were determined. The characteristic shape of the resulting IMFP plot is often referred as universal curve in textbooks.^[49] The reason for this somewhat surprising similarity for different metals is the simple fact that inelastic scattering is mainly driven by plasmon excitations within the metal, which is rather independent of the specific material. However, for most materials the shape of the IMFP curve varies considerably. For liquids in particular, the IMFP is rather unexplored, because direct measurements are challenging. While the MFP for liquid water is especially important, as its value determines the energy deposition by electrons into the liquid and thus governs topics like radiation damage and shielding,^[12, 18, 66, 84, 103-104] no consensus has been reached, particularly at low kinetic energies. This is exemplified in Figure 6, which plots representative experimental and theoretical results for the IMFP of water. Disagreement especially at eKEs below 100 eV is apparent. Several hurdles make the determination of the IMPF curve for water difficult which are detailed in the following.

First, only the so-called *effective attenuation length* (EAL), which describes the, on average, shortest distance from a starting point where the photoelectron is generated to the surface, is accessible in the experiment (not though for water as I will detail below). The PE signal is an average over depth from the surface and all scattering processes. Electrons originating from a region close to the surface are more likely to get detected by the analyzer with less scattering contribution compared to electrons from deeper layers, which undergo more scattering events and are thus attenuated in intensity. Assuming a uniform density for an isotropic system, and

that the PE signal attenuates exponentially with depth (compare Figure 5), the EAL can in principle be extracted from the photon-energy-dependent variation of the PE signal.^[105-106] However, the EAL is only equal to the IMFP in the limiting case that there is no elastic scattering.^[19] Any elastic scattering (angular deflection) of the electrons elongates the traveling distance before an inelastic scattering event happens. Thus, the EAL can be significantly shorter than the IMFP, if elastic scattering is significant, as shown in Figure 5. Thus, a better understanding of elastic scattering (and its variation with energy) is mandatory to get access to the IMFP.

For solids, different methods are available to determine the EAL.^[19, 105, 107] One common method is the overlay technique, where a thin film with a known thickness is sputtered onto the probing substrate under ultra-high-vacuum conditions. Electrons emitted from the substrate travel through the thin film, and the resulting PE signal attenuation is monitored as a function of the film thickness. Obviously, the creation of a well-defined liquid thin film under high-vacuum conditions is impossible, because of evaporation and freezing, and maintaining a defined thickness of a given liquid film is prevented by surface tension, gravitational pull, and other factors altering the liquid's shape. Still, several indirect methods have been applied to extract the IMFP of water, which however are somewhat in disagreement with each other and with theory at low kinetic energies (compare Figure 6).^[19, 21, 91] Here, the fact that elastic and inelastic scattering processes have different effects was exploited. With the former, electrons maintain their initial KE, but change direction. This will affect ('smear out') an initial electron angular distribution and affect angular-distribution measurements. With the latter, the electron loses some of its KE by transferring an amount of energy to the impacted molecule / atom, exciting or even ionizing it. Thus, the relative amount of elastic vs. inelastic scattering could be estimated by angle-resolved measurements.

A promising new technology in this regard may be the development of the flat liquid sheet, which was one goal of my work and is lined out in Paper I and VIII. While not yet used for this purpose, a flat liquid surface promises to remove ambiguity due to the take-off angle from the surface inevitably introduced with a cylindrical jet, and may give a much more consistent relation between PE signal intensity and EAL, and thus IMFP.

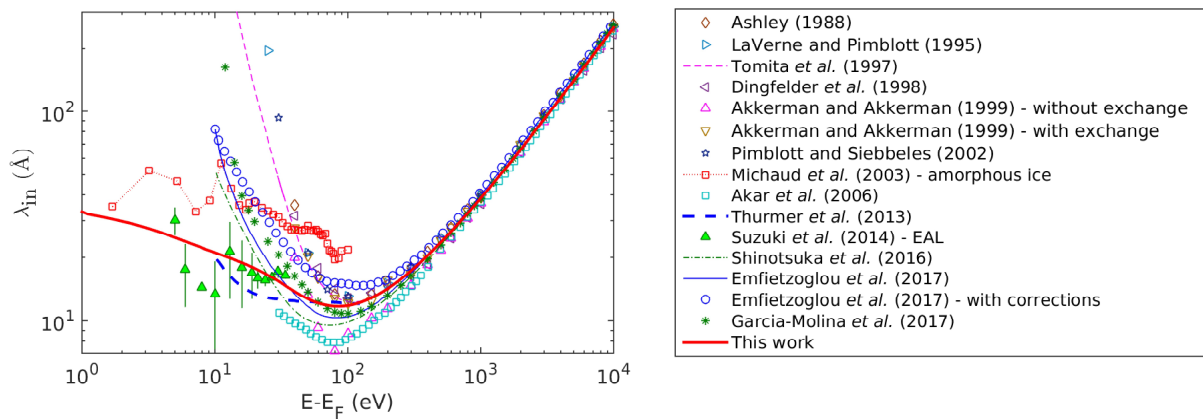


Figure 6: Inelastic mean free path (IMFP) curves for liquid water as a function of electron energy. Energies are stated with respect to the Fermi level. At high energies (>250 eV) studies are in agreement. At lower energies, a discrepancy between experiment and theory as well as different theoretical models still exists. Figure taken and adapted from Ref. 108.

Nevertheless, at higher KEs, and thus with higher photon energies, it can be assumed that the EAL increases and more electrons escape from deeper layers (bulk), which then dominate the PE signal.^[98] This makes depth probing a viable technique at X-ray energies. Yet, experiments at lower energies in the UV regime are in dire need of a detailed understanding of the MFP and how electrons escape the condensed phase. Experimentally, the differentiation between elastic and inelastic scattering is not straightforward at these energies, especially for very small energy losses, remaining within the peak width. These are low-energy excitations such as rotational or vibrational excitation. Various types of energy loss can occur depending on the KE of the electron.^[109-110] While elastic scattering can be neglected when one is not interested in angular distributions (see later), inelastic scattering needs to be accounted for a correct interpretation of PE spectra. This becomes crucial for very-low-KE electrons in liquid water which is discussed in Paper II and Chapter 3.1, but will be briefly addressed in the next paragraph.

If the electron's KE approaches just a few eV, *electronic* inelastic scattering channels (channels involving excitation and ionization of an atom or molecule) become energetically unfeasible, since the energy 'gap' for electronic excitation is about ~8 eV in water.^[89, 111] Thus, other quasi-elastic[§] processes, *e.g.*, vibration or rotation, start to dominate. This strongly affects peak intensities and shapes in a PE spectrum at these energies, since intensities are strongly

[§] The term "quasi-elastic" describes a process, in which only a very small portion of energy is transferred and thus makes it indistinguishable from elastic scattering (no energy transfer) in the experiment.

diminished but also obscured by a rising scattering-background signal at approximately the same energetic position as the original peak.^[80] As a consequence, BEs cannot be accurately extracted from a spectrum, when too low photon energies are used. The rapid decrease in nascent, direct PE peak intensity and a rise of the underlying background signal is observed especially below a photoelectron KE of ~ 10 - 14 eV, as shown in Figure 7a where the corresponding peak areas of the water $1b_1$, $3a_1$, $1b_2$, and $2a_1$ orbitals as a function of the KE are plotted. This range coincides with the transition from electronic to vibrational inelastic scattering channels as shown in Figure 7b.^[80] Here, the kinetic-energy region above 15-20 eV is dominated by electronic excitation / dissociation and ionization of the impacted water molecule, since the energy of the electron is sufficient to reach these final states. However, if the kinetic energy falls below 10-15 eV, these channels close, and instead energy is transferred into vibration (bending and stretching modes). This enhances quasi-elastic scattering and leads to a distortion of the nascent PE signals, as the energy loss is still within the width of the peak itself (about 1-2 eV for water peak features)^[89].

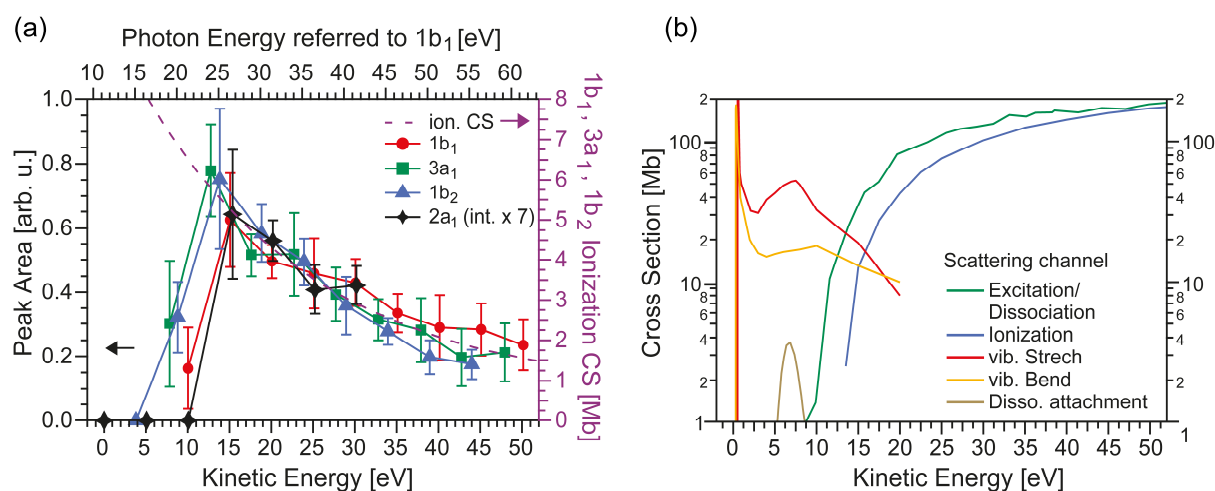


Figure 7: (a) Intensity of liquid water valence photoelectron peaks (left y-axis) in comparison with ionization cross section data (right y-axis). Peak areas of the $1b_1$ (red circles), $3a_1$ (green squares; sum of double-peak), $1b_2$ (blue triangles), and $2a_1$ (black diamonds) direct photoelectron features are plotted versus electron kinetic energy. The gas-phase ionization cross section, shown as purple dashed line, is averaged over the $1b_1$, $3a_1$, and $1b_2$ molecular orbitals; peak areas follow this trend until an energy of about 10-15 eV, where the peak signal declines steeply. The top axis shows the photon energy specifically corresponding to the $1b_1$ orbital ionization channel for comparison. (b) Ionization cross sections of different electron-scattering channels for the water gas-phase molecule. A region of dominating electronic scattering above 15 eV transitions to mostly vibrational scattering within a 10-15 eV energy window, leading to a large amount of quasi-elastic scattering below 10 eV. Figure taken from Paper II.

As a final note, electrons in liquid-jet experiments actually travel through two regimes, namely the liquid itself and the surrounding vapor. However, we found that the latter usually has only a negligible effect on the PE spectrum unless the vapor density is very high.^[80]

2.6 Photoelectron angular distribution and photoelectron circular dichroism

First angle-resolved PES measurements of gas-phase species have been conducted in the 1930s,^[112] which were intended to gain more information about molecular orbitals or photoionization dynamics of atoms.^[113] These experiments were limited to single-photon ionization at fixed wavelengths of an isotropic sample. Although several theoretical models had been developed, the results were just of qualitative nature at first.^[114] This changed dramatically with the development of new models and new imaging detectors with spatial resolution, which made photoelectron angular distribution (PAD) measurements a viable tool for the gas phase. The PAD describes detected PE intensities of a certain band as a function of the angle between a principal symmetry axis and the emitted electron. The principal symmetry axis corresponds to the electric-field vector \vec{E} or the light-propagation vector \vec{k} , for linearly and circularly polarized light, respectively. In the case of aligned molecules, the symmetry axis of the molecule itself also becomes important. Essentially, PADs reveal the symmetry of the probed orbital and can thus be used to study the orbital character and molecular structure as well as dynamics (in time-resolved experiments).

For linearly polarized light (LPL) and achiral, randomly oriented targets, the angular-distribution function can be expressed as (in its well-known form as derived by Cooper and Zare):^[21, 53, 113, 115]

$$I(\varphi) \propto 1 + \beta P_2(\cos \varphi) \quad (\text{eq. 8})$$

under the restriction of single-photon photoionization within the dipole approximation. Here, $P_2(x) = (3x^2 - 1)/2$ is the second-order Legendre polynomial which provides the non-isotropic part of the overall distribution and φ is the angle between the linearly polarized light vector \vec{E} and the direction of the emitted photoelectron. The anisotropy parameter β , can range from $-1 \leq \beta \leq +2$ (i.e., $\sin^2(\varphi)$ to $\cos^2(\varphi)$) and specifies the magnitude of the emission anisotropy. Equation 8 possesses mirror symmetry about the principal symmetry axis which is in the case of LPL the polarization vector \vec{E} .^[81] The anisotropy parameter itself is independent of φ , but depends on the excitation energy and the probed orbital. In Figure 8, a polar plot of eq. 8 for selected anisotropy parameters between -1 to 2 is shown, which

exemplifies the expected relative PE intensity when measured from each direction. For example, the PE intensity at 90° is zero and maximum at 0° or 180° when $\beta = +2$. In the special case that $\varphi = \arccos(\sqrt{1/3}) \approx 54.7^\circ$ (the so-called *magic angle*), the measured intensity for any transition becomes independent of its β value and is proportional to its total cross section.^[81] This angle is useful for comparing PE signal intensities and determining, *e.g.*, relative sample compositions. Equation 8 was derived by Cooper and Zare with the assumption that the initial state can be described by a defined angular momentum and, strictly speaking, only applies to atoms with a closed shell.^[113, 115]

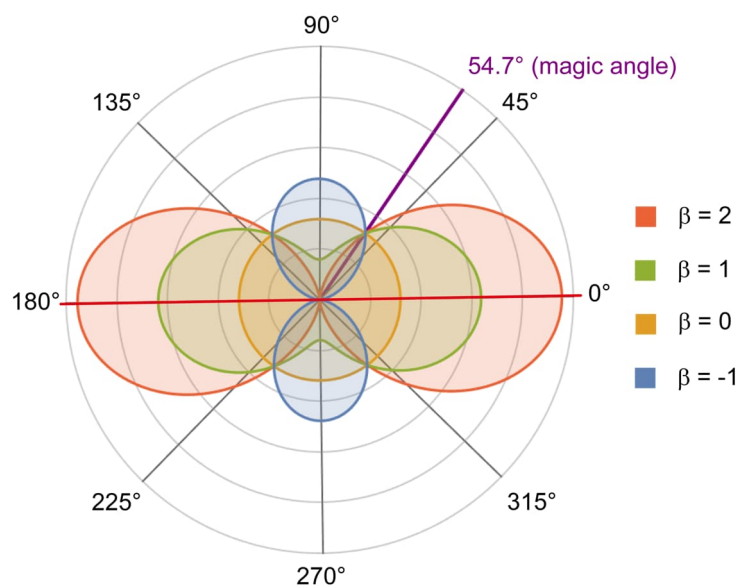


Figure 8: Polar plot of equation 8 for several beta values ranging $-1 \leq \beta \leq +2$ for linearly polarized light. The *magic angle* at 54.7° is given in purple, which indicates the angle where the PE intensity becomes β -independent. For example, for $\beta = 2$, the intensity is zero for the plane perpendicular to the polarization vector and maximum in the polarization vector plane (indicated by the red line). Figure adapted from Ref. 116.

Absorption of a photon leads to a change of $\Delta l = \pm 1$ according to the selection rules in the dipole approximation. For example, the closed 1s orbital of an atom has an angular momentum, l , of zero, which leads to p -wave ($l = 1$) character of the emitted electron, and corresponds to $\beta = 2$. For higher orbitals, both $\Delta l = +1$ and $\Delta l = -1$ contributions will mix, which is more difficult to interpret.

For circularly polarized light (CPL) a similar expression governs the PAD:

$$I(\theta) \propto 1 - \frac{\beta}{2} P_2(\cos \theta) \quad (\text{eq. 9})$$

with θ defined as the angle between the emitted photoelectron and the photon-propagation vector \vec{k} . A more general but less prevalent expression of both equation eq. 8 and eq. 9 can be given:^[25, 27, 117-120]

$$I_p(\theta) \propto 1 + b_1^p P_1(\cos\theta) + b_2^p P_2(\cos\theta) \quad (\text{eq. 10})$$

Here, $P_1(x) = x$ is the first-order Legendre polynomial. The equation is given for CPL, denoted with the used angle θ , being the angle between the direction of the emitted electron and the photon-propagation axis.^[118] For LPL, θ is replaced by φ . The photoionization dynamics is given by the anisotropy coefficients b_n^p and depends on the polarization state p , with $p = 0$ for LPL, and the radial-dipole amplitudes between the ionized and the initial state of the molecule. For left- or right-handed circularly polarized light, l -CPL or r -CPL, the values for the polarization state are $p = +1$ and $p = -1$, respectively, following the optical convention and the restriction to single photoionization of randomly oriented targets.^[118, 120-121] For the $P_2(\cos\theta)$ term, this leads to $\beta = b_2^0 = -2b_2^{\pm 1}$.^[27] Moreover, for achiral molecules, b_1^0 is zero and $b_1^{\pm 1}$ also vanishes, which reduces eq. 10 to the more common and well-known forms of eq. 8 and eq. 9.^[81, 120]

A special case occurs when chiral molecules are ionized with CPL. Here, b_1^p no longer vanishes and switches sign with respect to the polarization of the incident light: $b_1^{+1} = -b_1^{-1}$.^[81, 117, 119-120] As an alternative to switching the polarization, b_1^p also changes sign when changing the handedness of the molecule, *e.g.*, switching between enantiomers of a sample.^[25, 117] This so-called photoelectron circular dichroism (PECD) is an intense forward-backward asymmetry with respect to the light's propagation axis when a chiral molecule is ionized by CPL and arises from pure electric-dipole interaction, whereas the highest intensity is observed at $\theta = 0^\circ$ or 180° for $P_1(\cos\theta) = \cos\theta$ (compare eq. 10).^[35, 119] Although predicted more than 45 years ago by Ritchie *et al.*,^[117] it took until the year 2000 for the first realistic calculations and until 2001 for the first experimental report.^[25-26, 122] Since then, many single-photon gas-phase studies of biologically relevant molecules (*e.g.*, camphor, fenchone, or alanine)^[30-32, 123] have

shown the large potential of probing molecular chirality,^[30] revealing its sensitivity to the electronic structure,^[32] molecular conformation,^[34, 118] vibrational excitation,^[33, 124] structural isomerism,^[35, 125] clustering and chemical substitution.^[126-128] PECD is thus a powerful tool for probing chirality of randomly oriented chiral molecules. As a far goal, PECD promises to enable the study of chiral molecules in aqueous solution to investigate possible origins of the symmetry-breaking mechanism responsible for life's homochirality and thus the origin of life.^[129-130] Although PECD from chiral gas-phase molecules is large, the effect is expected to be reduced for liquid samples, because of electron scattering, which is discussed in detail in Paper I and V.^[81-82] Also, additional factors need to be taken into account such as the presence of a surface^[131] and the possible spatial ordering of molecules^[8].

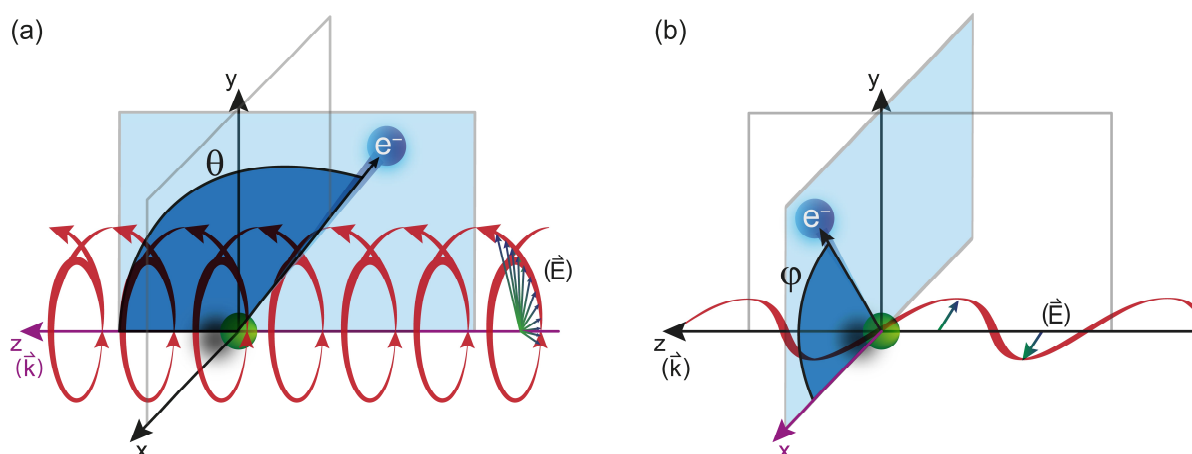


Figure 9: Schematic drawing of the symmetry axes and respective angles for experiments using circularly polarized light (CPL) (a) and linearly polarized light (LPL) in the horizontal plane (b). The interaction region with the liquid-jet target is shown in green. Panel (a) shows the backward-scattering geometry (backward with respect to \vec{k}) used for all PECD measurements, where the angle θ is spanned between the propagation direction (wave vector \vec{k}) of the CPL and the electron-detection axis. (b) The angle ϕ is spanned between the electric-field vector \vec{E} and the electron-detection axis, shown here in the plane perpendicular to the floor plane (dipole plane). Figure taken from Paper I.^[81]

So far, a suitable experimental apparatus for studying PECD from liquid phase was not available. With the development of the *EASI* setup (short for: Electronic structure from Aqueous Solutions and Interfaces), PECD from a liquid was demonstrated for the first time (Paper I and V). The *EASI* setup represents the first dedicated apparatus to study PECD in liquids. Due to its unique geometry and compact design, the apparatus is ideal to measure both PAD and PECD at synchrotron light sources with variable polarization. The possible

detection directions and respective angles along the principal symmetry axes are shown in Figure 9 (measurement geometry for PECD and PAD in panels (a) and (b), respectively). Here, the principal symmetry axis is highlighted in purple, whereas the detection plane and angle of *EAS*'s analyzer are shown in light and dark blue, respectively. Because the liquid-jet target strongly attenuates X-rays, the analyzer needs to tilt towards the light propagation vector \vec{k} .

2.7 Circularly polarized radiation at a synchrotron light source

PECD manifests itself as a forward-backward asymmetry with respect to the light's propagation axis when a chiral molecule is ionized by CPL.^[35, 119] For this reason, it is essential to have a source of circularly polarized X-rays with a handedness controlled by the user. *EASI* was designed to determine PADs and PECD of molecules in the liquid state, and was optimized to make an efficient use of the P04 beamline at the PETRA III synchrotron-radiation source at DESY in Hamburg. This beamline, equipped with an *advanced planar polarized light emitter*, APPLE, undulator, provides left- and right-handed CPL with a high reproducibility and a high degree of circular polarization. This is necessary to reveal the PECD effect in liquids, which is assumed to be small.^[81-82] The fact that synchrotron radiation, providing high photon flux and allowing for tight focussing, is crucial, in particular for LJ-PECD measurements makes it worthwhile to give a brief overview on how circularly polarized synchrotron radiation is generated and how the polarization is changed.

A synchrotron light source provides electromagnetic radiation in a broad wavelength regime. The emitted photon energy can be obtained by the energy loss of a charged particle, *e.g.*, an electron, under acceleration and bending of its trajectory.^[132-133] In an actual electron storage ring for synchrotron-radiation production, a relativistic electron beam is bent by auxiliary compounds like undulators, wigglers, or just bending magnets, by deflection in a magnetic field.^[133] To generate high-energy photons within the bending process, electrons in the storage ring are accelerated to kinetic energies in the GeV regime. At the P04 beamline of PETRA III, an APPLE II undulator (Sasaki type)^[134] is used to generate the highly brilliant** synchrotron radiation in the range between 250-3000 eV photon energy.^[135]

An undulator bends the electron path multiple times in an alternating pattern of magnets, and produces a line spectrum which is the result of a high overlap of all radiation cones. Due to this overlap, interferences occur which lead to a higher brilliance and higher photon flux at 'peaks' in the frequency spectrum (undulator harmonics).^[133] However, since the output profile peaks at only a few limited photon energies, with almost no intensity in-between,

** The brilliance describes the effects of the spatial (radiation cross section and solid angle) and the temporal coherence (time and bandwidth interval) of a light source.

adjustment of the undulator's magnetic field is required if different photon energies are desired. This is achieved by changing the physical gap between the top and bottom magnet rows (a smaller gap increases the field strength), which makes it possible to shift the harmonics in energy. The produced synchrotron radiation is usually highly polarized, where the polarization of the electric-field vector of the emitted light figuratively 'follows the electron motion'. Thus, at the center axis of a planar undulator completely linearly polarized light in the horizontal plane is observed.^[136]

To perform angle-resolved PE measurements with a hemispherical electron analyzer (HEA), rotation of the analyzer is unfeasible since it would require maintaining the target in the same spot with micro-meter precision. Instead, the APPLE II undulator makes it possible to alter the polarization of the light by shifting of its magnet rows in a specific pattern, which provides circularly polarized light and linearly polarized light^{††} at any orientation of the polarization ellipse. For this, the top and bottom permanent magnet arrays of an APPLE II undulator are split into two separately adjustable rows, which can be shifted along the center axis of the undulator, altering the magnetic field lines and thus bending the trajectories of the passing electrons.^[137]

The period λ is given by four permanent magnets arranged in a Halbach array as shown in Figure 10. The diagonally opposing magnet rows, S_1 and S_3 , can be shifted axially parallel or anti-parallel to introduce and tune the strength of a horizontal magnetic-field component, which in turn affects the electron trajectory in vertical direction in addition to the horizontal bending motion. Depending on the relative magnetic strength and phase of the horizontal and vertical components, any desired polarization of the emitted light can be generated.^[132, 137-138] If all arrays are in-phase (Figure 10a), linearly horizontally polarized light is emitted. Shifting the array rows S_1 and S_3 in parallel in the same direction (parallel mode, Figure 10b) by half a period length ($\lambda/2$) yields a fully horizontal magnetic field (vertical component is zero) and thus linearly vertically polarized light is obtained.

^{††} Note that linear polarization is currently not possible at beamline P04 because of issues with a high heat load on the first mirror.

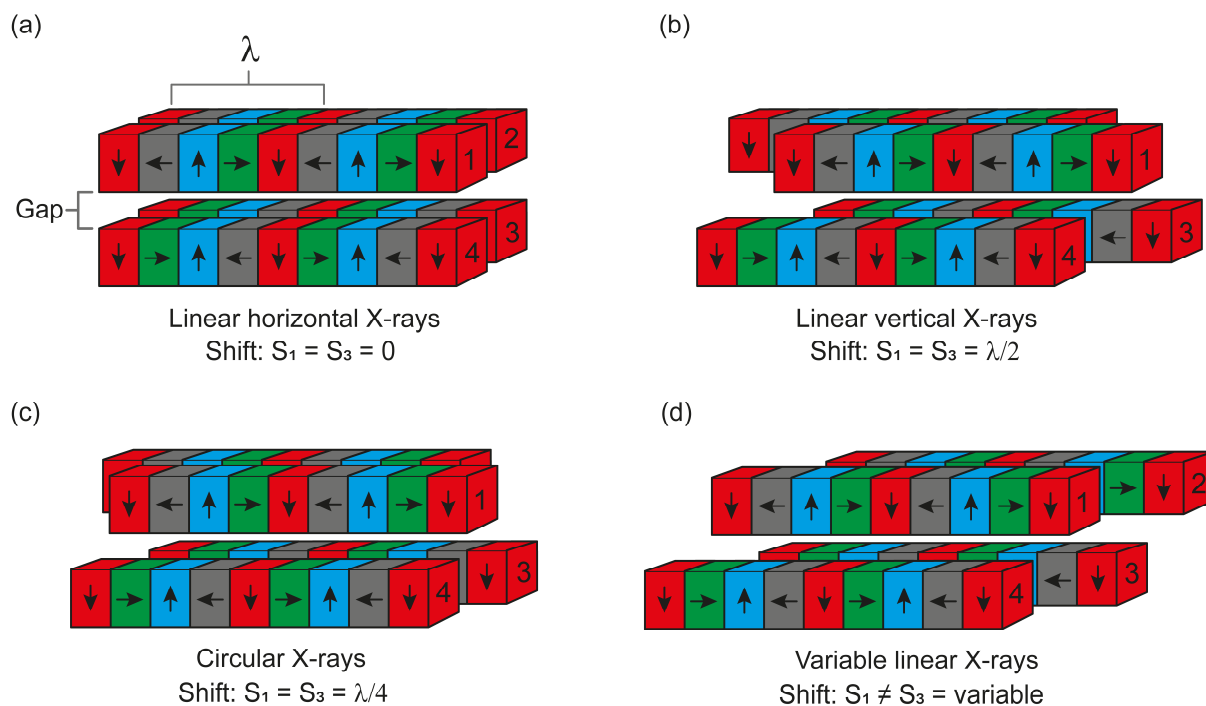


Figure 10: Schematic drawing of the parallel (panels a, b, c) and anti-parallel (panel d) modes of an APPLE II undulator (so-called Sasaki type)^[134]. To obtain either (a) horizontally polarized (shift = 0), (b) vertically polarized (shift = $\lambda/2$), or (c) right-handed circularly polarized (shift = $\lambda/4$) X-rays, two diagonally opposite rows (S_1 and S_3) of the four Halbach magnet array rows are shifting in parallel. A negative shift of $-\lambda/4$ leads to left-handed circularly polarized X-rays at beamline P04 (not shown here).^[81] To obtain (d) linearly polarized light with an angle of the polarization at values intermediate between 0 and 90°, the upper and lower half-rows are shifted antiparallel to each other.

By shifting the array rows S_1 and S_3 parallel in the same direction by $\lambda/4$, as shown in Figure 10c, the electrons are forced to a helical rotational motion which leads to circularly polarized X-rays. For variable linearly polarized X-rays, the rows are shifted in opposite directions (antiparallel mode) as shown in Figure 10d. In result, any polarization with respect to the undulator plane is achievable. Note that shifts in-between 0 and $\lambda/2$ reduce the effective magnetic field strength due to the altered array geometry, which leads to a drift of the harmonics and thus lowers the effective photon flux at the photon-energy setting used in the monochromator. To compensate for this, the magnetic field strength can be re-adjusted by changing the undulator gap, or by a simultaneous shift of the two upper magnet arrays (S_1 and S_2) with respect to the two lower magnet arrays (S_3 and S_4), which is usually used for energy adjustment of CPL.^[139] However, the gap has a lower (physical) limit, and as a consequence, the usable energy range is further limited in polarization-dependent measurements with an APPLE II undulator.

By changing the linear polarization angle and by the possibility to generate *left*- and *right*-handed CPL, APPLE undulators are powerful tools for PAD and PECD measurements. By our first measurements on gas-phase fenchone at beamline P04, we identified that a negative shift of the opposing magnetic arrays of the APPLE II undulator at P04 corresponds to *l*-CPL by comparing measured asymmetries to previous gas-phase fenchone results. Before that the absolute sign of the handedness of P04 radiation was not known.^[31, 81]

2.8 Experimental LJ-PES setup – all components

After the theoretical details have been explained, a brief technical realization of a typical PES experiment and some hands-on insights will be given in the next sections. I will summarize insights on how to build up a liquid-jet PES experiment and how to improve it. The aim of the chapter is not to provide a detailed technical description of *EASI*, rather it is supposed to serve as a text-based, small tour around the setup with additional information beyond Paper I. Beginning with a brief historical overview through the evolution of liquid-jet PES, which ends with the methods used presently, the following Chapter 2.8.2 is based mostly on the first part of Paper I and focuses on the technical and methodical development of my LJ setup and on the advantages of *EASI*. The scientific outcome of Paper I is discussed separately in subsections in Chapter 3.

2.8.1 Photoelectron spectroscopy of liquids – a brief historical overview

Photoelectron spectroscopy is a highly surface-sensitive analysis method which needs well-maintained ultra-high vacuum (UHV) conditions. In principle, the main obstacle for studying electronic processes at liquids and their interfaces is the difficulty inherent in handling liquids in a high vacuum environment. This arguably has been the main reason of the limited availability of PES data from liquids and solutes in the past. Liquids, and in particular volatile liquids like water, have a high vapor pressure and evaporate easily under reduced pressure. Moreover, under high-vacuum conditions, liquids start evaporating strongly until they freeze. Depending on the substance, the vapor pressure of a liquid can be up to hundreds of mbar, which is too high even for modern electron analysers. Additionally, high vapor density over / around the liquid phase impairs the emitted photoelectrons on their trajectories and causes scattering, which may lead to loss of KE and thus an attenuation and broadening (depending on the KE) of the nascent PE signal. As a consequence, several attempts were necessary to render liquid PES feasible.

Photoelectron spectroscopy (PES) was well established in the 1970s for solids, gases, and vapors from liquids. However, PES measurements from neat, highly volatile liquids like water

were challenging at this time due to many inherent properties of liquids, *e.g.*, high vapor pressure. To overcome the evaporation hurdles in the early studies of liquid PES and to bring them into an UHV environment, different approaches were attempted in the past, illustrated in Figure 11. The first approach was a liquid-beam arrangement by Hans and Kai Siegbahn, which bears surprising similarities to the nowadays well-established liquid-microjet setup, shown in Figure 11a.^[140] This method provides a sample continuously renewed by a recirculating system to prevent radiation damage of the sample and to reduce the amount of needed sample, which is similar to a recently reported approach of a catcher system for liquid microjets.^[141] Moreover, this method enabled the separation of the gas / vapor and liquid signals in XPS spectra and was used for the first electron spectroscopy for chemical analysis (ESCA) studies of liquids.^[66, 140, 142]

Another approach to introduce a liquid as a thin film into vacuum was the so-called wetted metal wire. A metal wire was running down from a bobbin through a reservoir with the liquid sample. After the wire was covered with the sample, it ran up into the interaction region of the incident X-rays and the detector axis, shown in Figure 11b. This method was more suitable for PES studies because the control of the thickness of the liquid surface was more effective.^[142] A later approach used plates or cylindrical-shaped objects (trundles) immersed in the liquid reservoir and rotated about their axis, as shown in Figure 11c. One variant used a conically shaped metal trundle for ESCA, shown in the right panel of Figure 11c.^[142] Yet, another variant employed a rotating plate or wheel, made of stainless steel^[143] or quartz glass^[144]. Auxiliary, a sapphire crystal was used as a scrape-off skimmer to provide a thin liquid layer and to reduce the vapor pressure.^[145] For all approaches above, cooling down the liquid samples reduces the vapor pressure significantly and increases the spectral resolution. Moreover, the metal of the entrance slit of the electron analyzer is warmer than the cooled liquid, which prevents condensation of the vapor on it and thus prevents energy broadening and energy shifts of the signal.^[142] Furthermore, the charging of low-conductivity liquids by the electron-emission process was reduced by the restriction to very thin liquid films on metallic carriers. Nevertheless, an additional disadvantage of the metallic carrier plates and wires is their reactivity with some liquids like acids, which leads to undesired gas formation and reaction products. Despite the huge advantages of the feasibility of liquid PES, however, all these techniques were still challenging to handle, especially due to the requirement of UHV

conditions. Without a sufficient or suitable treatment of the liquid (*e.g.*, adding high amounts of salt to reduce the vapor pressure), the feasibility of liquid studies was limited to non-volatile liquids, and water, for example, was inaccessible.

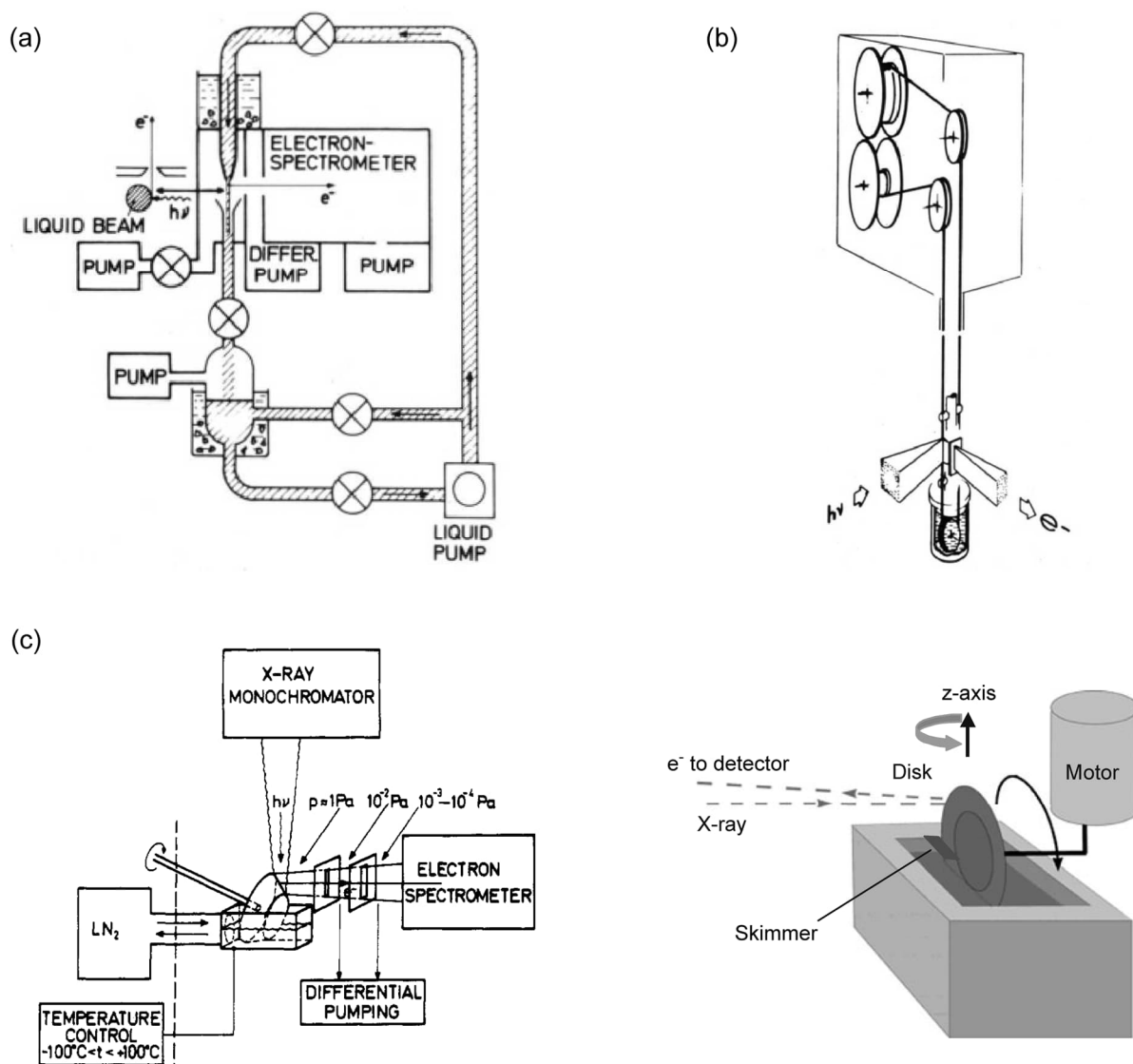


Figure 11: Schematic drawings of different approaches and arrangements used to provide liquid samples for PE spectroscopy. Panel (a) shows the liquid-beam arrangement with a recirculation setup. Panel (b) shows the wetted-metal-wire approach, which provides a continuous transport of the liquid into the interaction region, usually combined with a cooled sample reservoir to lower the vapor pressure. The conical trundle with a chilled liquid reservoir (left), and the wetted-wheel arrangement (right) are shown in (c). For the wetted-wheel approach, a sapphire skimmer is used to produce a thin liquid layer and thus to reduce the vapor pressure. Panels (a), (b) and the left side of (c) are taken from H. Siegbahn^[142], the right side of panel (c) is taken from Wang and Morgner^[145].

However, to investigate catalytic reactions or electronic effects between a metallic or even conductive substrate and liquid electrolytes, these so-called "dip and pull" methods are still

in use today and are a good approach in conjunction with new ambient pressure PES (APPES) for a direct probe of the solid-liquid interface.^[146-147]

A major experimental breakthrough was achieved in 1997 with the development of the liquid microjet by Faubel *et al.* and marks the groundwork for the astonishing revival of liquid PES and of my own research on liquids.^[12, 66, 148-149] Faubel's approach was based on a fast-flowing liquid jet that he had developed in 1988 to study the collision-free evaporation of a small amount of water sample into vacuum.^[66, 150-151] To generate the microjet, the liquid samples were pressurized in a cylinder with helium or another noble gas up to 1-10 bar and subsequently released through a small orifice, usually a circular platinum-iridium aperture plate with an opening of 5-30 μm .^[150] In the following years, many advances were made on the LJ system to resolve difficulties of handling the He-pressurized setups and the inability to change the liquid during a running experiment. Another approach was the use of huge syringe pumps, which reduced the technical effort, however, a change between different solvents was still a critical situation during a running experiment. Nowadays liquid microjets in vacuum are still produced by pushing a liquid through a micrometer-sized orifice. Usually, a quartz nozzle with a diameter of 15-30 μm is used, connected over a polyether ether ketone (PEEK) tubing with a high performance liquid chromatography (HPLC) pump. Despite the huge advantage in handling by using HPLC pumps, there are still technical concerns to keep in mind to realize a LJ-PES experiment.

Although the first approach by K. and H. Siegbahn was similar to the method used today, the decisive step to establish liquid PES was the technical feasibility to manufacture micrometer-sized orifices for the liquid microjets. The resulting significant reduction of the required liquid which results in a considerable reduction of the vapor load and the development of nowadays near-ambient-pressure hemispherical electron analyzers (HEAs) were the key points compared to the approach of K. and H. Siegbahn.

2.8.2 *EASI* – technical concerns and realizations

In this subsection, which is based on Paper I, I will provide additional information about the main components of the *EASI* (Electronic structure from Aqueous Solutions and Interfaces) setup. I will give an overview of the technical and practical hurdles and constraints I had to overcome to realize different experimental approaches in my thesis employing LJ-PES. I will point out the benefits of some technical approaches and give some useful advice for further experimental approaches. At first, I will explain some improvements I made to the standard LJ approach used in my thesis, followed by a detailed description of some main components of *EASI*.

2.8.2.1 Liquid-microjet setup – the HPLC pumps

By pushing a liquid or solvent through a circular, micrometer-sized hole, a cylindrical liquid microjet is formed. In my thesis, in-house made quartz-glass capillaries of ~30 mm length with inner-diameters between 10-30 μm were used. To pressurize the liquid through the nozzle, I used commercial HPLC pumps (Shimadzu LC-20AD) combined with a solvent inline degasser (Shimadzu DGU-20A_{5R}), which is connected *via* a polyether ether ketone (PEEK) tubing with the nozzle. In addition, the liquid samples were degassed with an ultrasonic bath prior to use to support the inline-degasser unit. Each pump is equipped with a four-channel solvent valve, which makes it possible to connect four samples at the same time and easily switch between them, thus reducing the time for changing between samples significantly. As a backup, two of these pumps were connected *via* a 3-way valve in order to make it easier to interchange them in case of any malfunction, or to increase just the availability of samples. Each solution was filtered before entering the vacuum chamber. To prevent nozzle clogging, a 10 μm suction filter in each sample reservoir was used, followed by a 5 μm filter located directly downstream of the double pistons of the HPLC pump. Additionally, before the sample enters the vacuum chamber, two micrometer-pore size inline filters, located 60 cm and 300 cm upstream of the nozzle, were used. Notably, the inline filters are mounted directly after valves or other moveable parts in the tubing, to filter insoluble particles originating from

these parts. The choice of the used pore size and the used frit material of the inline filters depends on the experimental conditions. For highly acidic and basic liquids, PEEK and stainless-steel frits were used, respectively. Titanium frits, however, are usable for both, acidic and basic solutions in a moderate pH regime of 2-13.

An important ingredient of a successful LJ-PES experiment is the HPLC pump in use. As there are different types of HPLC pumps on the market, it required several tests of different double-piston pumps in order to find the most suitable option. One property turned out to be most important: Both pistons must have the same size (area and volume) to maintain a stable liquid jet. Other pumps with a main and smaller supporting piston, in which the supporting piston takes over when the main piston reaches its upper and lower dead points, showed clearly observable periodic spatial oscillations of the jet ('pulsing'), and thus an unstable laminar flow region was formed. However, even with two identical pistons, a small amount of pulsing of the laminar region was still observed due to the low backpressure at the pistons from the jet site. Pulsing becomes even more critical in flatjet experiments, where two identical, cylindrical jets are colliding at a certain angle to form a chain of planar surfaces ('leaves'). To overcome the pulsing issue in both cases, I constructed a liquid supply line made up of short (few tens of cm) PEEK tubing sections with inner diameters of 250 μm and of 500 μm connected to each other. I also inserted two 20 cm long sections of Teflon[®] tubing with an inner diameter of 1.2 to 3.2 mm. The empirically found damping-line approach reduced the pulsing effectively down to a degree where it could not be observed anymore, probably due to the different stiffness of the tubing materials used and due to the alternating diameters. The efficiency of this scheme was empirically found to improve for a higher number of tube sections alternating between smaller and larger diameters. On the other hand, with more tubing, the total distance between the nozzle and the pump increases, which leads to an increase in the amount of time it takes until a new sample enters the vacuum chamber. For each experiment, a compromise between sample performance and pulsing needs to be figured out.

2.8.2.2 Liquid-microjet setup – manufacturing of quartz-glass nozzles

Almost all measurements in my thesis were performed with liquid jets formed by quartz-glass capillaries. However, at the beginning of the measurements for Paper III, I used a self-made design to use a platinum-iridium (PtIr) disc with an inner diameter of 30 μm and an outer diameter of 2 mm; shown in Figure 12, and similar to the earlier approaches by Faubel *et al.*^[149] to determine the absolute vertical ionization energies (VIEs) of liquid water. Besides the formation of the jet, the platinum-iridium disc could be used to refer measured energies to the Fermi edge.

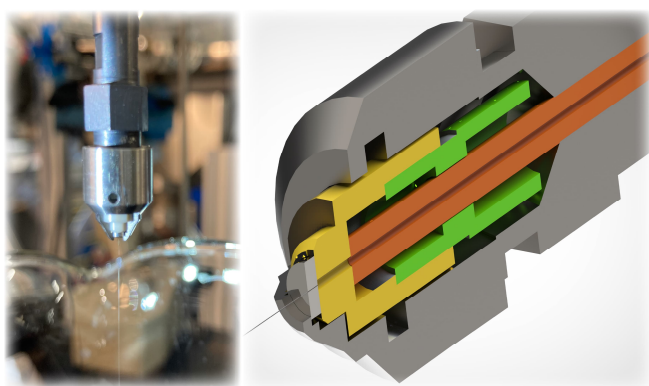


Figure 12: Photograph (left) and rendered cross-section graphic (right) of the first experimental approach to refer vertical ionization energy (VIE) using a PtIr disc. The liquid is expanded through a thin PtIr-disc which is held on ground potential of the setup. A sector of the titanium mount has been cut out in order to enable the recording of PES of the PtIr disc to determine its Fermi edge. We assume that its Fermi edge is aligned with one of the liquids flowing through the PtIr disc. However, since water is a semiconductor, its Fermi edge is not directly measurable.

Nevertheless, this relatively bulky design led to an inhomogeneous electric-field distribution in front of the analyser cone, and thus to a reduction of the spectral resolution. As a consequence, a conventional liquid jet produced by a glass-capillary nozzle, where the liquid was in electrical contact with a gold wire as a reference (see Paper III for more details), was used.

To manufacture quartz-glass nozzles with an inner diameter of 10-60 μm was crucial for my experiments and in this section, I will give guidance regarding this task. All quartz-glass nozzles used during my thesis were made in-house at our institute by the following procedure: To fabricate the nozzles, quartz-glass capillaries of 100 mm length and with an inner diameter of 1 mm and an outer diameter of 3 mm, which are melted down in the middle were purchased commercially (company Hilgenberg). A thinned-out section of the capillary was produced by melting it in the middle and stretching it axially by the manufacturer. The capillaries were cut in the middle and subsequently sanded down until the desired diameter

of the orifice was reached. To avoid clogging by the use of sandpaper (3000-8000 corns per cm²), water is pushed into the capillary during sander process from the back site. The diameter and the shape of the orifice is determined by the use of a measuring microscope. The last and most critical step is the flame annealing of the sanded surface to round the edges of the opening. Without the annealing process, the liquid microjet does not form a laminar flow region. Finally, the opening and the diameter are controlled again with a measuring microscope and the nozzle is shortened to a total length of ~30 mm. To avoid clogging by dust, the nozzles were stored in a water/isopropanol mixture (70:30; v/v).

2.8.2.3 Liquid-microjet setup – catcher and ice crusher

By releasing a liquid microjet into vacuum, a laminar region of several millimetres extension is formed, followed by a turbulent region which results in droplet formation and ends with the freezing of the droplets to ice. The length of the important laminar region strongly depends on the liquid (viscosity, surface tension, *etc.*). Under the conditions of our experiment, water shows a laminar region of 5 to 10 mm, whereas isopropanol for example shows a laminar region of up to 30 mm under otherwise similar conditions (nozzle diameter, flow rate). To maintain the vacuum conditions indispensable for a PES experiment, the liquid jet needs to be collected in some form downstream of the interaction region. The simplest approach of a LJ catcher is a steel pipe immersed in LN₂ into which the jet propagates after some centimetres of travel. Another variant is a LN₂-filled steel cylinder, which is arranged to block the trajectory of the jet some centimetres downstream. Both of these approaches work in practice, but after a certain operating time often ice needles start to form and grow opposite to the flow direction towards the glass capillary. This effect is more readily observed with higher salt concentrations and may crucially limit the measurement time available for a liquid sample. As already mentioned in Paper I, I developed a motorized rotating cutting blade, called ice crusher, which is mounted between the jet and the catcher to mechanically cut growing ice needles as they grow. Moreover, it turns out that the rotating, kitchen-mixer like device nebulizes the liquid very effectively which leads to a reduction in needle growth and, for a cold trap arranged perpendicular to the jet, to a homogeneous coverage of the cooled surface. With that device in place, the time between venting and cleaning cycles of the *EASI* setup increases significantly and the decrease of the pump efficiency of the cold surface by saturation is slowed down. In Figure 13, a rendered technical drawing shows details of the ice crusher.

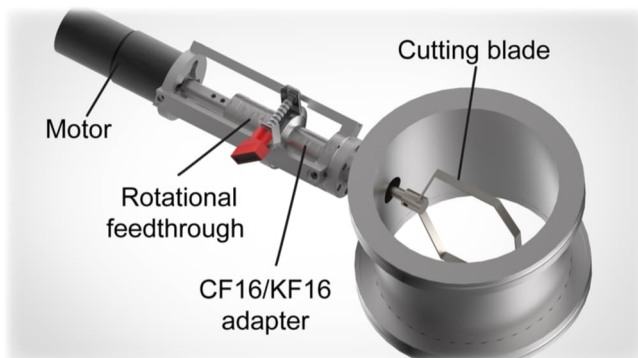


Figure 13: Rendered drawing of the ice crusher. The main body consist of a standard ISO-K 100 tube with a CF16 port to mount the crusher unit. The rotational motion is produced by a high-torque electric motor available commercially, and is transferred via a rotary feedthrough.

The electric motor is connected *via* a customized connector to a commercial KF16 rotational feedthrough, which is mounted sidewise with an KF16-to-CF16 adapter on the CF16 side port of the used ISO-K 100 tube.^{††} A titanium rod holding the cutting-bladed crusher head is mounted at the feedthrough on the vacuum side. The used electrical motor is commercially available and contains a standard housing which allows an easy exchange. In the different measurement orientations of *EASI*, different sizes and makes of the jet catcher are used. By the use of a longer titanium rod, a simple adaption of the crusher to other tube diameters is possible. However, after several hours of measuring, an ice layer grows on the inner side of the ISO-K tube at the position of the cutting blade frame, which can block the rotational motion. To overcome the potential blocking, the edges of the cutting blade are sharpened to cut off the growing ice layers. As an alternative, low-voltage heating tapes can be connected with an electric power supply and mounted around the ISO-K tube to prevent the formation of the ice layer. By using the crusher, the measuring time is only limited by the surface area of the cold trap.

For the sake of completeness, I would like to mention another technique to collect the liquid jet, which is an improved approach to the first LJ-PES setup of K. and H. Siegbahn,^[140] and has been described in the literature.^[141] We have tested this same approach using a commercially available (Microliquids design, now Advanced Microfluidic Systems GmbH—AdMiSys)^[152] catcher / recirculation unit facing the jet after 5-10 mm of free flow. Then the liquid is injected into the orifice of a heated cone made of non-magnetic metal. The trapped liquid is removed

^{††} The CF16 side port is a left-over of a previous design of the catcher, where I used an old CF16 feedthrough with an edged-welded bellow. Note that in general such bellows are not suitable for constant rotations in the same direction.

from the catcher by a membrane pump over a Woulfe bottle which is immersed in an ice bath to condense the liquid vapor.

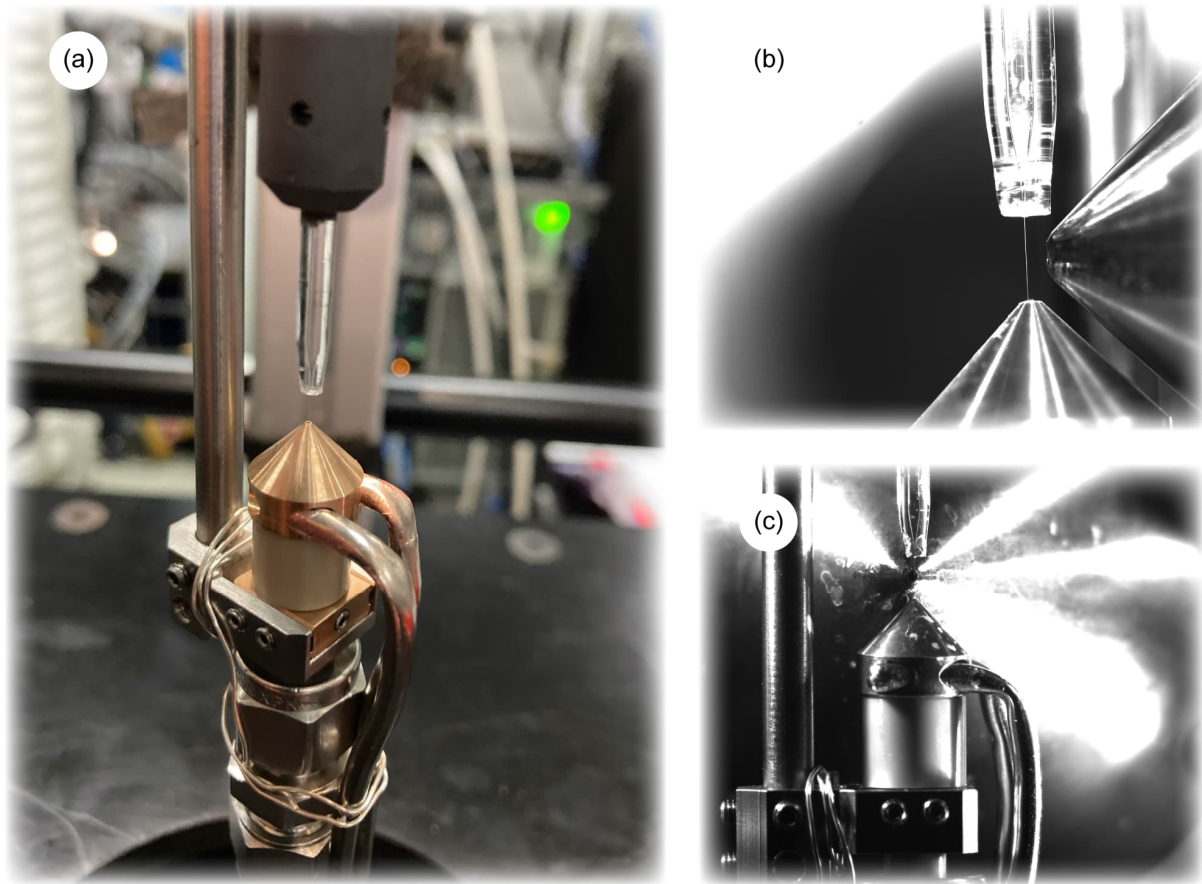


Figure 14: Photographs of the one-port catcher unit which was used for some experiments. It is possible to adjust and test the alignment between jet and catcher outside of the vacuum chamber (a). The copper tip is heated up with a thermoelement and heat pipes. Even when using the catcher, a small distance to the HEA skimmer (0.8 mm) can be maintained (b). The whole catcher unit is mounted by clamps and an additional titanium rod on the housing of the regular jet. A silver wire, winding around the holding rod and the heat pipes maintains electrical contact of the assembly to the HEA (a, c). All parts were made of titanium, rhodium, PEEK, or copper.

To successfully collect the liquid jet and to maintain the vacuum conditions for extended measurements the jet has to be aligned properly to the catcher opening. Both units are mounted on a high precision x-y-z translation stage to facilitate the adjustment of the liquid sample to the analyser and photon beam. In order to preserve the relative adjustment between jet and catcher opening, I have constructed a mounting clamp which connects the latter with the liquid-jet nozzle holder. Two degrees of freedom (translation and rotation) of the catcher cone allow to fix it in a position in which the jet centrally enters into its opening. These adjustments can be done outside of the vacuum, before the unit is inserted into the *EASI* sample region as a whole. To pump the catcher liquid out of the catcher, the tubing of the

catcher is guided through a suitable cluster flange and is connected with a Woulfe bottle and a membrane pump to pump out the liquid. Additionally, the cluster flange contains an electrical feedthrough to connect a power supply for heating up the catcher cone to prevent ice formation. Beyond the technical drawing in Figure 5 of Paper I, I provide three photographs of my realization of a one-port catching unit in Figure 14.

2.8.2.4 Liquid-microjet setup – differential pumping stage and setup alignment

For synchrotron-radiation experiments with a liquid or even with a flatjet, a pressure differential has to be maintained between the LJ setup and the beamline. The latter requires a vacuum of 10^{-9} mbar or better. To face these conditions with the typical residual pressure of 10^{-5} to 10^{-3} mbar in a liquid-jet or flatjet experiment, respectively, we designed a novel, modular, and highly efficient differential pumping stage (DP) for *EASI*. With a total length of just 355 mm and the capability to maintain an upstream vacuum of 10^{-9} mbar even for near-ambient pressure experiments in the interaction chamber (IC) of *EASI*, the DP does not exceed the frame of the setup. Thus, the only constraint is the overall dimension of the setup frame itself. A detailed and rendered technical drawing of the DP is given in Paper I, Figure 4. A notable feature of the DP is the capability to switch between a three-stage and a two-stage operation mode. By mounting an inset, indicated in green in Figure 4 in Paper I, the initial two-chamber enclosure is separated into three chambers in total. The reason for that design was to provide space for additional filters, photodiodes, or other devices in the stage at the high-vacuum side of the two-stage arrangement (without the inset). Both stages have almost the same volume and each is equipped with a cooling trap. Nevertheless, the pumping efficiency and the resulting vacuum gradient worsens compared to the three-stage arrangement. To improve the pumping efficiency, the stainless-steel capillaries mounted at each stage can be exchanged.

Usually, we use 20 mm long capillaries with diameters of 8 mm, 5 mm, and 3 mm (from the low- to the high-vacuum side) in the three-stage arrangement. To facilitate the alignment to the synchrotron radiation, each end of the capillaries facing the beamline is coated with fluorescing powder. Additionally, adjustable feet at the DP allow an adjustment independent from the setup. The setup itself, with its total weight of ~1250 kg, is adjusted with the help of three compressed-air feet, standing on glass plates. The arrangement of the feet retraces a triangle nook facing the beamline. By applying 6-8 bar of air pressure on the feet, the setup starts to levitate just a few μm over the planar glass surfaces and is easily movable. To align the setup properly with regard to the synchrotron-light focus, a gold wire (coated with fluorescence powder), the liquid jet, or even a single-crystal cerium (III)-doped yttrium aluminum garnet (YAG:Ce) screen can be used at the entrance to the HEA. However, at

different beamlines aligning procedures differ and also depend on local conditions and experimental requirements. Thus, a generally applicable procedure cannot be given. To ensure that the setup is well aligned for LJ experiments, the final fine-adjustment is done by measuring a liquid-water spectrum with defined conditions, *e.g.*, pass energy, energy range, photon energy.

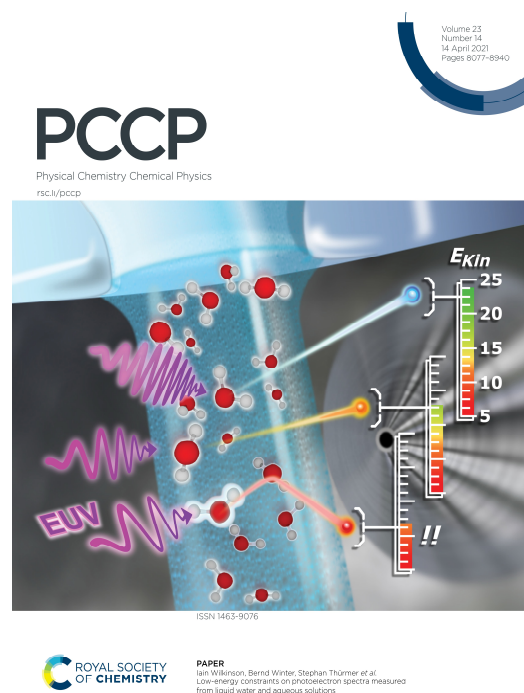
3. Summary of the main experiments and their results

In this chapter, the results and findings from each Paper (I-VIII) are summarized separately. On the first pages of Chapter 3.1, 3.2, 3.3, and 3.4, I present the respective journal cover arts made by our group. For Chapter 3.5 and 3.6, the table-of-content figure and an illustrative photograph is shown, respectively. Background information, which is not contained in the respective papers but necessary for a good understanding of the publications are provided in Chapter 2.

3.1 Low-energy constraints on photoelectron spectra from liquid water and aqueous solutions ^{II}

In the introduction, I have mentioned that the use of the term 'photoelectron spectrum' can be misleading since spectra typically contain electron contributions not only from the direct photoionization but also from second-order processes (see also Chapter 2.3 and 3.5) as well as from the various electron-scattering processes a (photo-) electron encounters when moving through the aqueous solution, from its place of origin until crossing the liquid–vacuum interface. Our study presented in Paper II focusses exactly on this latter aspect, exploring conditions where

electron inelastic scattering, notably electron–water collisions, in liquid water and in aqueous solutions can severely distort the true ("genuine") photoelectron spectrum to the point that



^{II} This chapter is based on the publication:

S. Malerz, F. Trinter, U. Hergenhausen, A. Ghrist, H. Ali, C. Nicolas, C.-M. Saak, C. Richter, S. Hartweg, L. Nahon, C. Lee, C. Goy, D. M. Neumark, G. Meijer, I. Wilkinson, B. Winter, and S. Thürmer.

Phys. Chem. Chem. Phys., 2021, 23, 8246-8260.

DOI: [10.1039/d1cp00430a](https://doi.org/10.1039/d1cp00430a)

energetics (electron binding energies) can be no longer directly inferred by the measurement. Only with the assistance of complex theoretical modelling of electron scattering in liquid water, the reconstruction of the original PE spectrum can be accomplished. This severe scattering effect occurs especially for low electron kinetic energies, whereas at high-enough electron kinetic energies (and correspondingly high-enough photon energies) photoelectron peak shapes are essentially unaffected. The reason is directly connected to the fact that liquid water is a large-band-gap semiconductor, with a band gap of approximately 8.9 eV, implying that the minimum energy required to ionize liquid water must be approximately of this magnitude.^[153-155] This reflects in the vanishing probability for electronic scattering channels (ionization, excitation, or dissociation) when going from high to low electron kinetic energies (eKEs), near 7 eV (smallest electronic excitation due to electronic states in the band gap).^[111, 156-157] However, at the same time, for eKE < 8-15 eV intermolecular vibrational inelastic-scattering channels open up with considerable probabilities (see Figure 2c of Paper II, and the sketch in Figure 15), corresponding to ~10-900 meV energy losses.

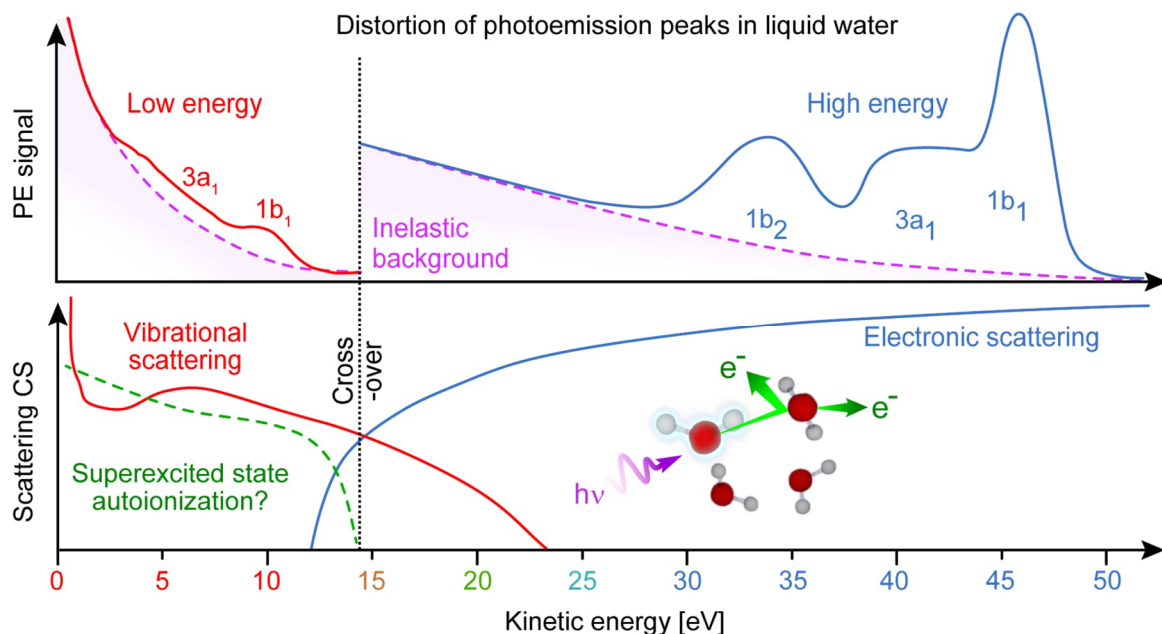


Figure 15: Schematical sketch of the distortion of photoemission peaks in liquid water. At eKE of 10-14 eV, vibrational scattering channels dominate. Top: The local signal background grows underneath the PE peak of interest to the point that the peak completely disappears in the scattering background signal. Bottom: Scattering cross section depending on the eKE.

Because these energy losses are so small, these quasi-elastic scattering processes will contribute to the signal of a narrow spectral region around the base of a given PE peak. As a

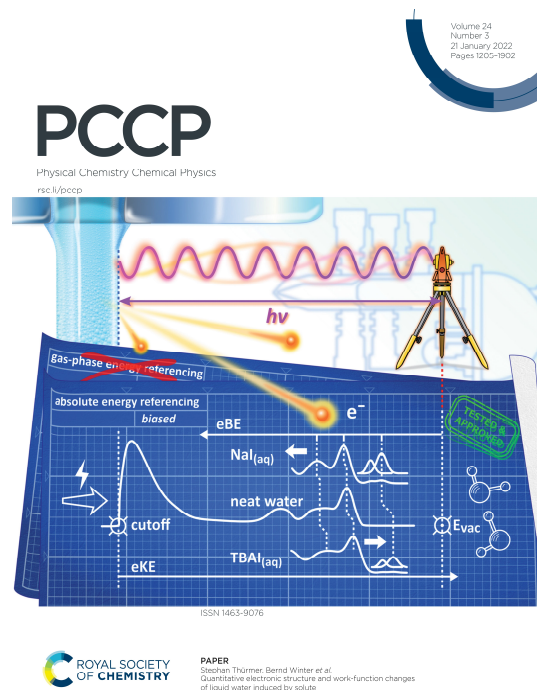
consequence, a local signal background will grow underneath the PE peak of interest to the point that the peak completely disappears in the (scattering) background signal. For liquid water and sufficiently dilute aqueous solutions, we have determined an approximately 10-14 eV eKE limit below which quantitative analysis of PE peaks becomes unreliable, and correspondingly both solute and solvent eBEs cannot be accurately determined. In Paper II, implications for typical laser experiments (where few-eV photoelectrons have been generated) are discussed. The situation is very different for the higher eKEs where only electronic channels are relevant. Since electronic excitations require energies > 7 eV, any occurring scattered electrons must have KEs which are at least 7 eV lower than the respective photoelectron peak. This is a large-enough energy separation not having a noticeable effect on the shape and energy position of the PE peak of interest.

Another important aspect addressed in Paper II is the nature of the low-energy tail (LET) that inevitably accompanies a PE spectrum from condensed matter due to the described scattering processes. Clearly, in typical gas-phase PES experiments, where species densities are considerably lower, such a scattering tail does not exist. This has important implications for performing liquid-phase PES experiments near the ionization threshold, including LJ-PECD, as I explain in detail in Chapter 3.3 when discussing PECD measurements from liquid fenchone as well as of aqueous solutions. I like to close this short chapter by pointing out that the detection and qualitative interpretation of the LET (composed of scattered initial electrons and newly generated electrons; see details in Paper II) was also a substantial accomplishment and laid the groundwork for the measurement of absolute electron binding energies from aqueous solutions.

3.2 Accurate vertical ionization energy and work function determinations of liquid water and aqueous solutions^{II}

LJ-PES application for the determination of the electronic structure of liquid water and aqueous solutions developed into an active multidisciplinary research field, and it may surprise that several most fundamental properties, such as accurate solvent and solute electron binding energies and solution work function, were not accessible. During my doctoral research, I devoted a considerable amount of time to enable such measurements aiming at the determination of these quantities. This led to the publication of Paper III and IV. The need for this undertaking is

best conveyed by realizing that in all previous LJ-PES studies (since more than 20 years) liquid-phase eBEs have been obtained with reference to the known BE of gas-phase water. A deficiency that has been long realized is that the energetic difference between gas- and given liquid-phase species in the LJ-PES spectrum is not constant, and this approach is condemned to be inaccurate. This is due to charging of the liquid jet, which can happen for various reasons, including electrokinetic charging (and associated steaming potential) and surface molecular dipoles, explained in detail in Paper III. The essential point is that charge affects the electric potential of the liquid jet, which in turn leads to an electric field between the jet and the electron detector. As illustrated in Figure 16, this implies that the KE of water gas-phase



^{II} This chapter is based on the publications:

1. S. Thürmer, S. Malerz, F. Trinter, U. Hergenbahn, C. Lee, D. M. Neumark, G. Meijer, B. Winter, and I. Wilkinson.
Chem. Sci. 2021, 12, 10558-10582.
DOI: [10.1039/d1sc01908b](https://doi.org/10.1039/d1sc01908b)
2. B. Credidio, M. Pugini, S. Malerz, F. Trinter, U. Hergenbahn, I. Wilkinson, S. Thürmer, and B. Winter.
Phys. Chem. Chem. Phys. 2022, 24, 1310-1325.
DOI: [10.1039/d1cp03165a](https://doi.org/10.1039/d1cp03165a)

molecules measured in a LJ-PES experiment will depend on the position between jet and analyzer where a given molecule has been ionized; this leads to energy shifts and broadening of the gas-phase spectrum.

Thus, it is not surprising that there has been quite an intense debate about the correct value of the lowest (vertical) ionization energy of liquid water, $VIE_{\text{water},1}$ (compare Chapter 2), with reported values ranging between 11.16 eV and 11.31 eV, with a recent outlier of 11.67 eV.^[86, 89-90, 158] This debate has come to an end with the development of our method that does not rely on the gas-phase reference, and the elaborate introduction of this method as well as the necessary background information is detailed in Paper III.

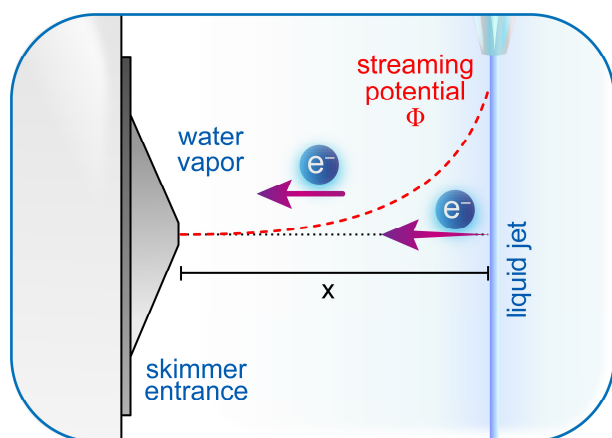


Figure 16: Schematic sketch of the streaming potential originating from the jet. Kinetic energy of electrons resulting from ionization of gaseous water molecules depend on their position (x) between the jet and the skimmer entrance of the analyzer. This leads to energy shifts and peak broadening.

Briefly, a concept well known in solid-state PE spectroscopy, the determination of the low-energy cut-off and simultaneously measured PE spectrum (at a precisely known photon energy), provides three energies, zero energy, solute / solvent KE, and maximum KE (here, vacuum level). One crucial experimental requirement is the application of a (negative) bias voltage to the liquid jet which enables spectral separation of the low-energy cut-offs from the liquid sample and the detector. From these quantities, we can accurately determine a given solute and solvent eBE with respect to the vacuum level; a discussion of the relevant vacuum level in a liquid-jet experiment is provided in Paper III. I like to stress that with the new method, we can for the first time determine solute-induced changes of the water electronic structure. In all previous LJ-PES measurements from solutions, solute BEs had to be determined with respect to the BEs of liquid water, which used to be $VIE = 11.12$ eV. Of course, this is a rather meaningless procedure but had been accepted for many years in lack of a suitable experimental approach. This has now indeed changed as demonstrated in Paper IV

for two show-case solutions, NaI (sodium iodide) and TBAI (tetrabutylammonium iodide) in aqueous solution. These are the first studies to quantitatively track the water electronic-structure changes as a function of solute concentration. Both Paper III and IV address yet another novel aspect, namely the perspective to experimentally access solution work functions. Here, the comparison between mentioned solutions is particularly interesting, with TBAI being a strong surfactant while NaI does exhibit a by far smaller propensity for the solution–vacuum interface. Hence, one can expect in the former case a surface dipole which would reflect in larger energy shift of the water $1b_1$ energy (as compared to the NaI solution). Indeed, a large energy shift, up to ~ 700 meV toward lower BEs upon increasing concentration to saturation is found for TBAI. A smaller shift, up to ~ 300 meV, and in the opposite direction is obtained for NaI solution when increasing the concentration from zero to 8 M. I am not detailing these findings here, and I rather conclude by pointing out that this information alone is insufficient to attribute observed spectral shifts to the changes of work function.

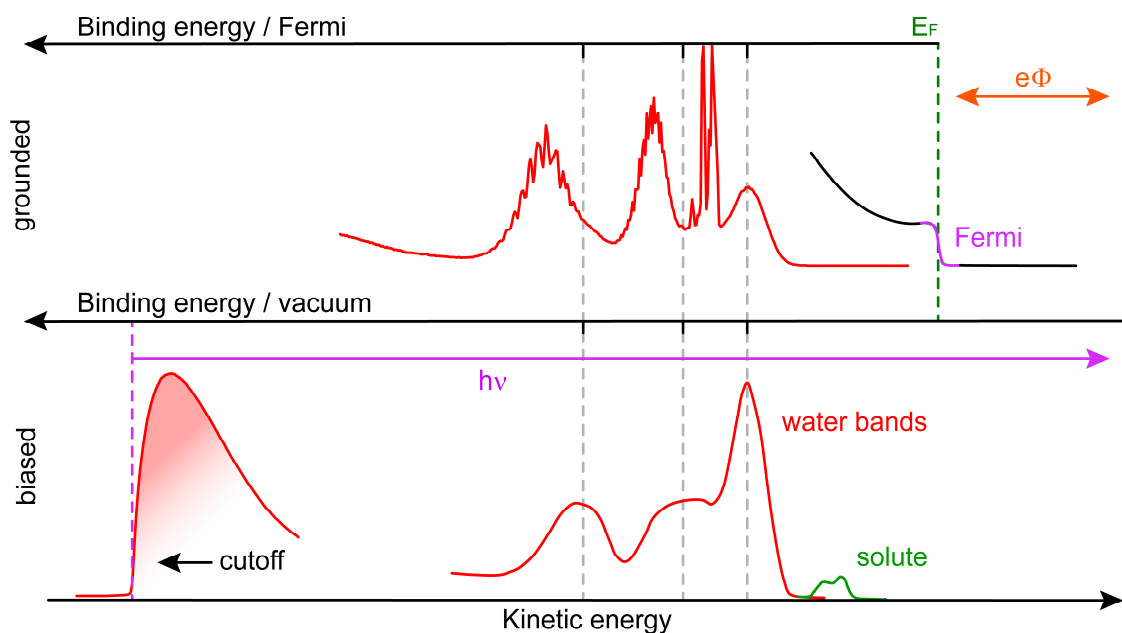


Figure 17: Schematic sketch of the introduction of the Fermi energy, E_F , to aqueous solution. The work function, $e\Phi$, is indicated as the difference between the vacuum energy and the Fermi energy.

This requires the conceptual introduction of a Fermi energy, E_F , to water and aqueous solution; as shown in the sketch of Figure 17, the work function, $e\Phi$, is the difference between the vacuum energy and E_F . The principal idea and challenges of such an approach are

explained in great detail in Paper III. There is intense work in progress in our group to further develop LJ-PES with regard to accessing explicit condensed-matter properties which are not captured in the molecular-physics description of liquid water.

3.3 Photoelectron circular dichroism in angle-resolved photoemission from liquid fenchone^{II}

One of the main motivations to build the new *EASI* setup was the idea to distinguish between chiral substances on the molecular and electronical level in liquids with photoelectron spectroscopy, specifically, photoelectron circular dichroism (PECD). Previously, this effect had been demonstrated for chiral gas-phase molecules.^[25, 27, 29, 117, 122, 159] PECD describes a forward-backward asymmetry in the angle-resolved photoelectron flux after ionization of a chiral sample with circularly polarized light (CPL). It can thus be observed as

a difference of the PE intensity between two measurements, where either the handedness of the sample or that of the light is swapped;^[25-26, 31, 81] see Chapter 2.6 for the relevant background information.

For chiral gas-phase molecules^[27, 29, 31-32, 122-123, 125] and even for clusters and nanoparticles,^[123, 127, 160] many studies have been performed in the past. Yet, PECD from liquids composed of chiral constituents had not been attempted by the time I started my work. For this purpose, we have designed the new *EASI* instrument with a good transmission even for low-kinetic-energy



^{II} This chapter is based on the publications:

1. S. Malerz, H. Haak, F. Trinter, A. B. Stephansen, C. Kolbeck, M. Pohl, U. Hergenbahn, G. Meijer, and B. Winter. *Rev. Sci. Instrum.* 2022, 93, 015101-015116. DOI: [10.1063/5.0072346](https://doi.org/10.1063/5.0072346)
2. M. N. Pohl, *S. Malerz,* F. Trinter, C. Lee, C. Kolbeck, I. Wilkinson, S. Thürmer, D. M. Neumark, L. Nahon, I. Powis, G. Meijer, B. Winter, and U. Hergenbahn. *Phys. Chem. Chem. Phys.* 2022, 24, 8081-8092. DOI: [10.1039/d1cp05748k](https://doi.org/10.1039/d1cp05748k)

* Shared authorship. Authors contributed equally.

electrons under near-ambient pressure conditions, described in Paper I, with additional information in Chapter 2.8.2. Our first PECD experiment with *EASI* was performed from previously well-studied gas-phase fenchone, both enantiomers, to test the performance of our new setup. Using fenchone was particularly motivated by the fact that fenchone at room temperature is a liquid, and operation of a liquid jet is almost as straight-forward as for liquid water. There has been an understanding that liquid fenchone would thus be an ideal chiral liquid to begin with, prior to exploring the solutions of our prime interest, *i.e.*, chiral molecules in aqueous phase, to be briefly detailed at the end of this chapter. The observed C 1s photoelectron lines of 1R-fenchone are shown as measured in Figure 18a. A significant difference in the PE signal intensity is found between the two helicities, which is in good agreement with the literature (see Table 1, Paper I). Combined with a higher resolution and a shorter acquisition time, the *EASI* setup indeed demonstrates its feasibility for PECD experiments in the gas phase.

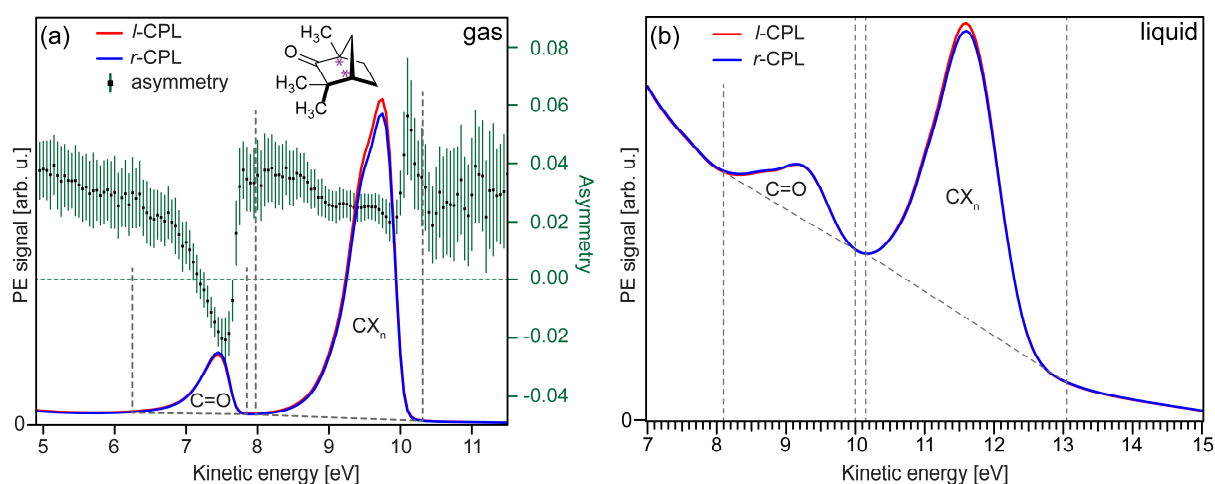


Figure 18: Photoelectron spectra of 1R-fenchone. (a) Gas phase spectra as measured at 300 eV photon energy with *l*- and *r*-CPL. The chiral centers of fenchone are labeled with * in the molecular sketch. Vertical and nearly horizontal lines indicate area intervals used for peak-area determination and the respective background. Note, the ostensibly higher intensity of the CX_n line originates from an apparatus asymmetry. The corrected asymmetry is indicated as green curve (see Paper I for details). (b) PE spectra from the liquid at 302 eV photon energy. The large background signal (dashed line) arises from electron scattering in the liquid. Spectra were normalized to equal total area to visually suppress a small, non-essential variation of the background height when changing helicity.

Analogous measurements from liquid fenchone can be expected to be more difficult because of electron scattering, which is ubiquitous for PES from condensed-phase samples as discussed in Chapter 3.1 and Paper II. A representative C 1s spectrum of liquid 1R-fenchone, measured at 302 eV photon energy (*i.e.*, 2 eV larger than shown in Figure 18a, for reasons

explained in the manuscript) is shown in Figure 18b. This spectrum contains the large signal background, the low-energy-tail, LET, which complicates the analysis of the PECD effect. Yet, as in the gas phase, also in the liquid phase of 1R-fenchone, an intensity difference between both light helicities is observable. By using the same principal analysis method as for the gas phase, and analysing spectra measured at multiple near-threshold photon energies, the asymmetry for the liquid is found to be approximately 2.5 times smaller.

An initially unexpected complication in the analysis of the LJ-PE spectra from fenchone is the fact that gas- and liquid-phase contributions cannot be readily distinguished because of almost perfect spectral overlap. This is very different from other previously studied liquids.^[84, 161-163] To estimate the gas contribution to the PE signal of the total spectrum (liquid plus gaseous) fenchone, a bias voltage was applied (see Chapter 2.4 and Paper I for details) which shifts only the liquid-phase components to higher kinetic energies, while the gas-phase contributions smear out. This spectral separation is shown in Figure 19a. Note though that the actual PECD measurements were all done for a grounded liquid jet.

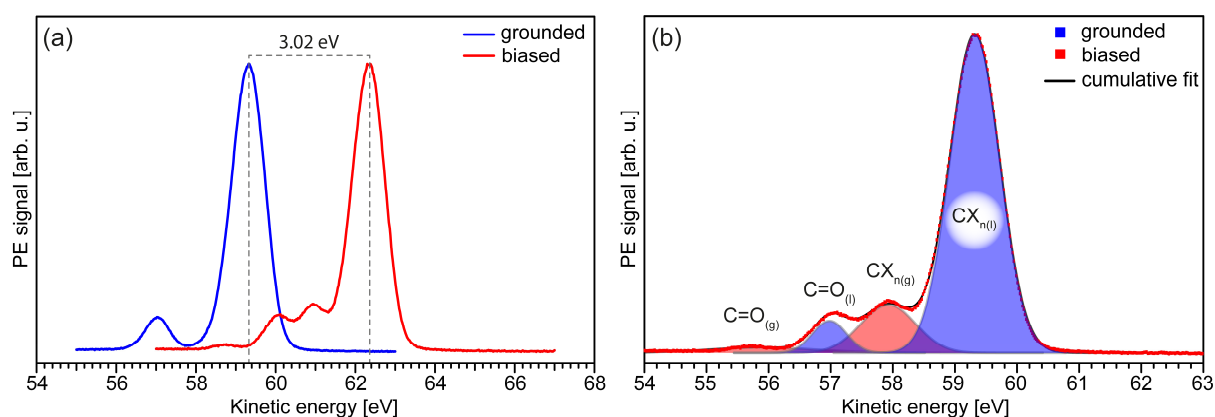


Figure 19: (a) C 1s photoelectron spectra from liquid 1R-fenchone recorded at 350 eV photon energy for a grounded liquid jet (in blue) and with an effective bias voltage of -3.02 V. Both the gas- and liquid-phase peaks are affected by the bias voltage, but electrons from the gaseous species experience less overall acceleration in the less negative electric potential some distance away from the liquid jet, which results in a peak separation of ~ 1.3 eV between the peaks of both phases. (b) The spectrum from the biased jet has been shifted by -3.02 eV such that the liquid-phase peaks overlap for the unbiased and biased spectra. Intensities are normalized to yield the same height of the main peak.

In a follow-up experiment, we started an investigation of the PECD effect from the amino acid alanine in aqueous solution, again detecting the C 1s peaks. As shown in Figure 20, different C 1s intensities were observed between *l*- and *r*-CPL for both enantiomers of a 0.5 M alanine aqueous solution at pH 10 where only the anionic form exists. Unlike fenchone, there is no

gas phase for alanine in the liquid jet experiment which facilitates the data analysis to some extent. However, the steep water-LET background in the alanine experiment, is again challenging and the analysis is still in progress. Yet, our results suggest that a considerably large PECD effect exists; representative spectra measured at 306 eV photon energy are shown in Figure 20. Analogous measurements from zwitterionic and cationic alanine aqueous solutions are currently performed to explore the effect of charge state on PECD. The analysis of the data is complex and is still ongoing, facing many of the issues reported in Paper III and briefly discussed in Chapter 3.2. Since I have not yet reached a convincing enough conclusion regarding the quantitative aspects of the PECD effect – including the comparison between cationic, zwitterionic, and anionic alanine in water – I will not present those data in more detail in my written thesis.

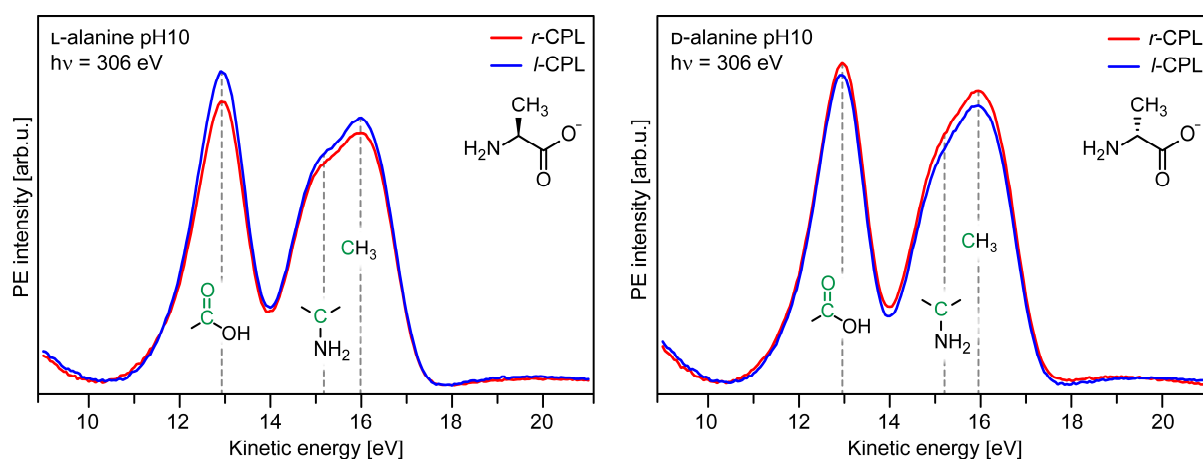


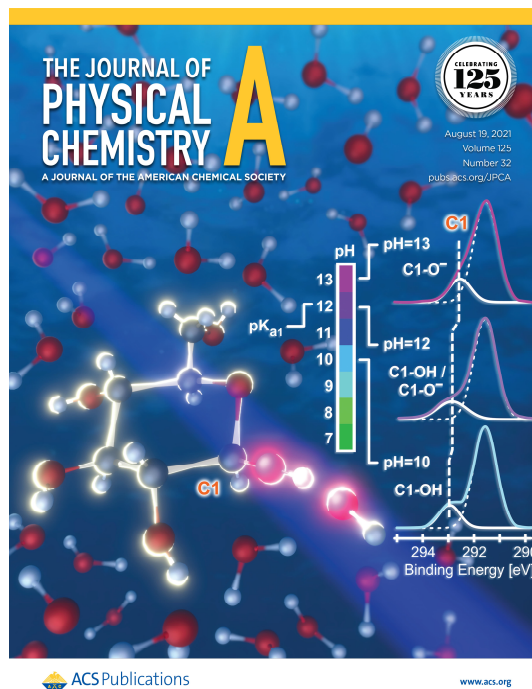
Figure 20: C 1s PE spectra of a 0.5 M L-alanine (left) and a 0.5 M D-alanine (right) aqueous solution at 306 eV photon energy. Both spectra were recorded under the same conditions. A background was subtracted from all spectra. For the left-handed enantiomer (left), the *l*-CPL provides a higher intensity and *vice versa*. Spectral labels indicate the carbon group leading to the respective peaks.

Naturally, our initial studies will be extended to other biologically relevant chiral molecules, including the anomeric effect in sugars; see following chapter.

3.4 Following in Emil Fischer's Footsteps: A Site-Selective Probe of Glucose Acid-Base Chemistry^{II}

In the previous Chapter 3.3, I have reported on the first-ever PECD measurements from the liquid phase, exemplified for neat fenchone and aqueous-phase alanine. I next report on related studies aiming to probe the effects of chirality on the electronic structure on the anomeric effect in sugars. I begin with a preparatory C 1s study of glucose as a function of solution pH, which lead to Paper VI, and then briefly comment on follow-up studies that are currently in progress.

A major motivation that led to the work presented in Paper VI was to achieve the site-specific electronic-structure characterization of a sugar in aqueous solution, here 1 M α -D-glucose, upon variation of pH using LJ-PES. A sketch of the molecular structure of protonated and deprotonated glucose is presented in Figure 21a, denoted as glucose⁰ and glucose⁻, respectively. Surprisingly, this is the first-ever core-level LJ-PES study from any sugar dissolved in water. A valence-band study has been published by Schroeder *et al.*^[164] focusing only on the first (vertical) ionization energy, not as a function of pH though. The present work on α -D-glucose aqueous solution includes both C 1s core-level and valence-band spectra of the protonated glucose⁰ and deprotonated glucose⁻ species by varying solution pH from 2 to 13. For the valence-band spectral region, spectra measured at pH values below and above the first acid dissociation constant, $pK_{a1} = 12.2$, reveal a change in glucose's lowest ionization



^{II} This chapter is based on the publication:

S. Malerz,* K. Mudryk,* L. Tomaník, D. Stemer, U. Hergenhausen, T. Buttersack, F. Trinter, R. Seidel, W. Quevedo, C. Goy, I. Wilkinson, S. Thürmer, P. Slavíček, and B. Winter.
J. Phys. Chem. A, 2021, 125, 6881-6892.
DOI: [10.1021/acs.jpca.1c04695](https://doi.org/10.1021/acs.jpca.1c04695)

* Shared authorship. Authors contributed equally.

energy upon the deprotonation of neutral glucose (glucose⁰) and the subsequent emergence of its anionic counterpart (glucose⁻). Note that the pK_{a1} value of 12.2, obtained here from C 1s core-level energies (see below), is in great agreement with titration-based values from the literature.^[165-167] However, valence ionization does not reveal the specific sites of the molecule that are being protonated / deprotonated depending on solution pH. Such site specificity is uniquely accessed from the C 1s core-level chemical shifts (see Chapter 2.2), enabling the spectroscopic determination of the pK_{a1} value.

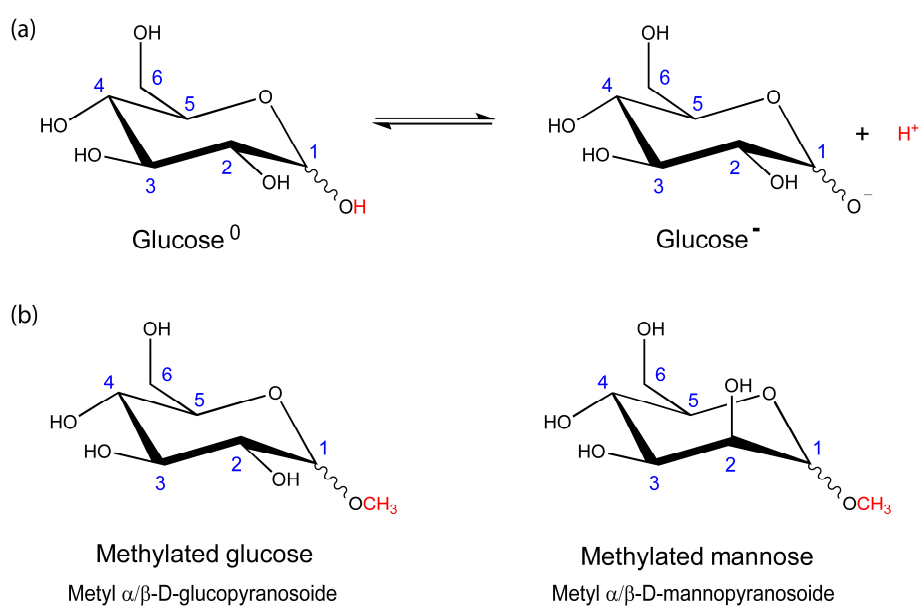


Figure 21: Schematics of the six-membered closed ring of protonated (glucose⁰) and deprotonated glucose (glucose⁻) in aqueous solution (a). A zig-zag line at the anomeric centre indicates the possible axial and equatorial position of the substituent, given as α or β , respectively. Schematics of methylated sugars (b), left for glucose, right for mannose. Due to electronic hindrances caused by the methyl group, mutarotation does not take place.

Specifically, the C 1s data reveal a considerably higher binding energy, at 292.9 eV, of the C1 carbon (at C-OH; see Figure 21a) associated with protonation, as shown in Figure 22. Here, I only show results obtained at pH 10 and 13 which correspond to 100% population of neutral and anionic glucose. Upon deprotonation, the C1 peak shifts to approximately 0.4 eV lower binding energy, yielding a BE of 292.5 eV, due to the larger electron density at the respective carbon site given the deprotonation of the associated hydroxyl group. The spectral assignment, including the close-lying energies of the C2 to C6 carbon sites, is supported by high-level electronic-structure calculations performed by our theory partners in Prague, the Petr Slavíček group (for details, see Paper VI and associated supplementary information).

Each of the modelled spectra was obtained from calculated VIEs at optimized geometries with an empirical broadening scheme. The combination of experimental and theoretical approaches confirms that at pK_{a1} deprotonation occurs almost exclusively at the C1 site. Our LJ-PES approach can be readily applied for the determination of the deprotonation site of sugars, glycans, or even of polyprotic organic acids.

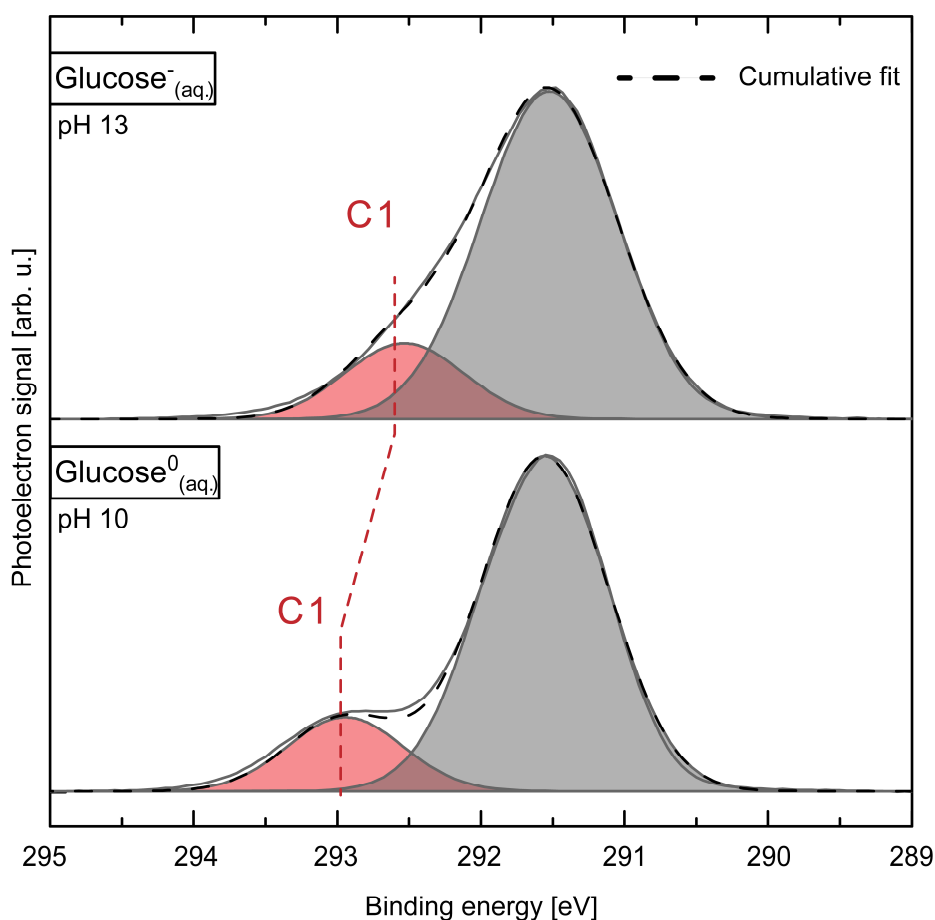


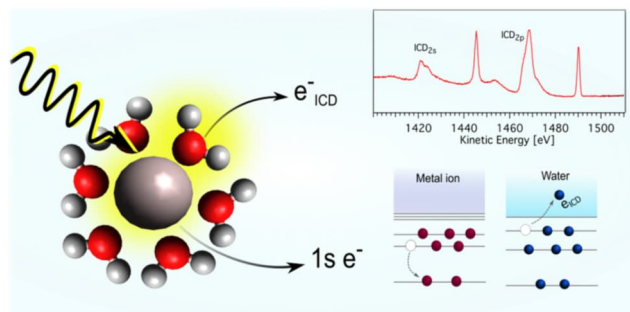
Figure 22: PES spectra of 1 M glucose aqueous solutions at pH 10 and 13, measured at 850 eV photon energy. The dashed lines indicate the cumulative Gaussian fits. The anomeric C1 is indicated in red, C2–C6 are shown in grey, respectively. The BE scale is calibrated by using liquid water's O 1s core level BE, which is the commonly applied procedure in LJ-PES.^[84]

It is noteworthy to mention that α -glucose (studied here) converts into β -glucose by a mechanism called mutarotation *via* a ring-opening reaction;^[168-170] however, their PE spectra are indistinguishable. In several recent explorative studies, we have looked for temporal C 1s spectral changes associated with the occurrence of the aldose form as part of the ring-opening. As of now, these studies are inconclusive though.

Another follow-up study we have started is to 'freeze' each anomeric form, and thus to facilitate probing of anomer-specific electronic-structure photoelectron fingerprints. For that we set out to perform experiments analogous to those in Paper VI, but now using methylated α - and β -glucose and mannose derivatives, as depicted in Figure 21b. Preliminary results indicate a selectivity to the anomer-specific electronic structure observed in the valence band. However, the analysis is not yet complete and additional measurements are required. The accurate characterization of both valence and core-level electron structure and its extension to other sugars will greatly improve our understanding of carbohydrate acid-base chemistry, the anomeric-effect itself, and anomer-specific chemical reactivity.

3.5 Probing aqueous-phase ions *via non-local* core-level electronic relaxation^{II}

In the introduction and in Chapter 2.3, I had mentioned that a photoemission spectrum can contain contributions from the direct photoionization (denoted as photoelectron spectroscopy) and from second-order electronic relaxation

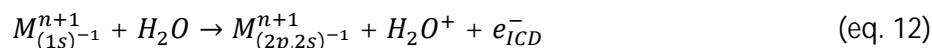


processes including *local* and *non-local* decay processes. The following is a brief summary of an experiment which I have been involved in, exploring *non-local* autoionization channels, specifically intermolecular Coulombic decay (ICD), of a series of aqueous-phase isoelectronic cations, Na^+ , Mg^{2+} , and Al^{3+} , upon core-level ionization. Although related studies have been performed previously,^[23] the peculiarity here is to explore the processes occurring for a metal cation surrounded by its water hydration shell rather than for a water molecule containing metallic ions in its solvation shell; the latter studies have been reported.^[171] Moreover, here we initiated ICD upon the deep 1s ionization for all three mentioned metals. Previous attempts have not been successful due to too low signal. However, with *EASI* at the P04 beamline at DESY high enough signal intensities can be obtained. By ionizing the 1s level of a central metal ion, the obtained autoionization spectra can be more clearly assigned compared to measurements when ionizing a 2p level, which leads to numerous final states and thus a more complicated interpretation of the results.^[23, 56, 69] The processes of ionization and generation of the ICD electron are sketched in Figure 23, and expressed in equations 11 and 12, respectively.

^{II} This chapter is based on the publication:

G. Gopakumar,* E. Muchová,* I. Unger, S. Malerz, F. Trinter, G. Öhrwall, F. Lipparini, B. Mennucci, D. Céolin, C. Caleman, I. Wilkinson, B. Winter, P. Slavíček, U. Hergenhahn, and O. Björneholm.
Phys. Chem. Chem. Phys., 2022, 24, 8661-8671.
DOI: [10.1039/d2cp00227b](https://doi.org/10.1039/d2cp00227b)

* Shared authorship. Authors contributed equally.



Regarding the second step (eq. 12), the actual relaxation of the core hole, we distinguish whether the hole is being refilled by the 2s or 2p level; the respective emitted ICD electron is then denoted ICD_{2s} or ICD_{2p}. One motivation for this work was to explore how different strengths of the ion–water interactions (intermolecular distances, as ICD scales with 1/R⁶, with R being the distance between the interacting entities) is reflected in the probability for ICD to occur. The largest ICD signal intensity was found for the Al³⁺ cation, followed by Mg²⁺, and no ICD signal is observed for the weakly solvent-bound Na⁺ ion.

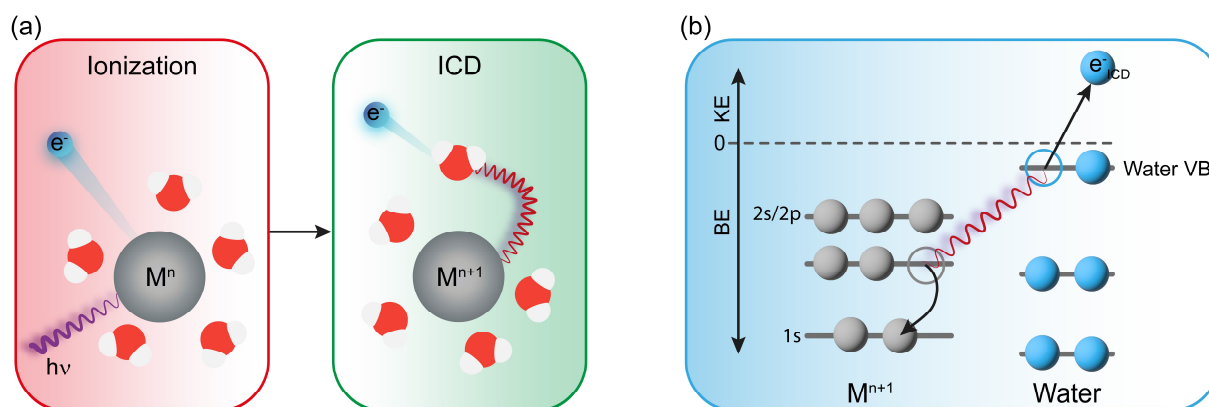


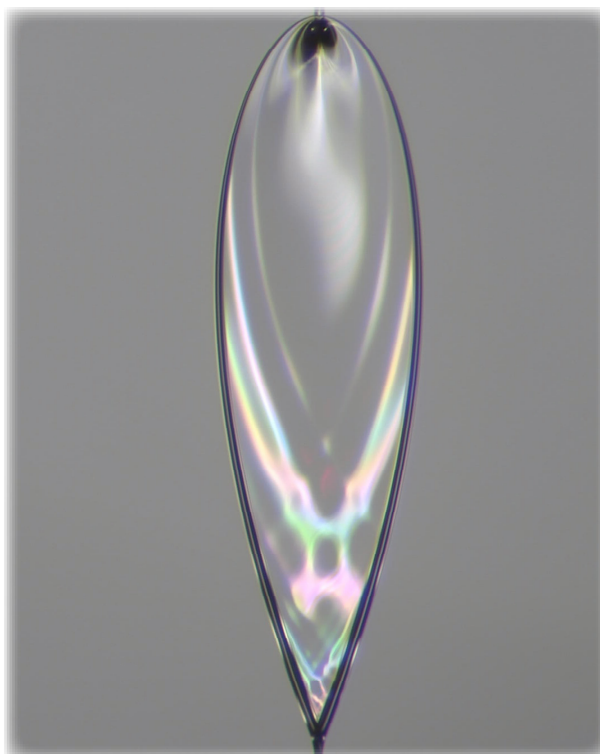
Figure 23: (a) Sketch of the ionization of a metal center (Mⁿ) and the subsequent energy transfer to a surrounding water molecule. By ionizing the metal cation, a photoelectron is emitted and the core vacancy is filled up by an electron from the L-shell. The released energy is transferred to a surrounding water molecule, leading to the emission of an electron (e_{ICD}⁻). (b) A schematic energy diagram of the metal ICD process.

Calculations by our theory partner group, led by Petr Slavíček (Prague), performing *ab initio* electronic-structure calculations and molecular dynamics (MD) simulations, assisted in assigning all spectral features. This includes the electrons due to the *local* Auger decay, the direct photoelectrons (giving rise to relatively sharp lines), and the small intensity from ICD electrons, containing a signature of the water valence band. From an estimate of the ratio of the Auger signal to the ICD signal intensities, applying what is known as core-hole-clock analysis,^[172-173] we estimate ICD timescales of approximately 34 fs for Al³⁺ and 76 fs for Mg²⁺. The individual ICD features, originating from the relaxation involving either the 2s or 2p

levels of the cations and mostly water valence states (compare Figure 23b), show a high selectivity for specific water ionization channels. In fact, the ICD spectral substructure may be considered to reflect the photoelectron spectrum of exclusively the hydration water, an information not accessible otherwise. This becomes possible due to the nature of ICD to involve nearest neighbors of the initially ionized site. The largest ICD signal arises from transitions including the $3a_1$ level of (hydration) water which, in accordance with the calculations, is caused by the orbital overlap between the water valence states and the cation. The orientation of the water molecules toward the cation enhances the orbital overlap of water's $3a_1$ orbital, whereas the water $1b_1$ and $1b_2$ orbital overlaps are disfavored. However, ICD channels that lead to $1b_2$ orbital emission appear to be favored in the specific cases of Mg^{2+} and Al^{3+} ICD_{2s} processes relative to ICD_{2p} , indicating that also the electronic structure of the core-hole-excited species plays a role. But this is not further explained here. Note that contributions from the counterion (Cl^-)-states were found to play a minor role in both Mg and Al solutions, in agreement with MD simulations of the solution structure.

3.6 Perspectives of flatjets in LJ-PES^{II}

I have also been involved in developing a novel flatjet design that is compact enough to match the spatial constraints of the new *EASI* setup. Our interest in flatjets lies, for instance in their potential application in molecular-beam scattering of a liquid (planar) surface.^[174] In that case scattering conditions are much better defined than in the case of a cylindrical jet. Another interest in the planar geometry is that molecular surface dipoles probed in a PES experiment can be associated with a single orientation of the solution surface, rather than a curved



surface which would average over 0° to 90° (compare Paper III) with respect to the electron detection. In other words, the curvature of a cylindrical jet implies that the measured photoelectron spectrum is an integration over all take-off angles of all emitted photoelectrons relative to water's surface normal. Different arrangements exist to produce planar liquid surfaces. One possibility is the crossing and impinging of two identical cylindrical jets under an angle of ~40° to 50°. This forms a chain of few-micron-thin leaf-shaped sheets, each bound by a relatively thick fluid rim, where consecutive sheet planes are perpendicular to each other (see Figure 1 in Paper VIII). The stability and geometry of the leaf chain is promoted by

^{II} This chapter is based on the publication:

1. [S. Malerz](#), H. Haak, F. Trinter, A. B. Stephansen, C. Kolbeck, M. Pohl, U. Hergenhausen, G. Meijer, and B. Winter. *Rev. Sci. Instrum.* 2022, 93, 015101-015116.
DOI: [10.1063/5.0072346](https://doi.org/10.1063/5.0072346)
2. H. C. Schewe,* B. Credidio,* A. M. Ghrist,* [S. Malerz](#), C. Ozga, A. Knie, H. Haak, G. Meijer, B. Winter, and A. Osterwalder.
J. Am. Chem. Soc. 2022, 144, 7790-7795.
DOI: [10.1021/jacs.2c01232](https://doi.org/10.1021/jacs.2c01232)

* Shared authorship. Authors contributed equally.

solution properties such as surface tension and viscosity, and by system parameters such as the flow rate and the jet diameter.^[175]

Our works on flatjets have resulted in two publications. One of them, Paper I, reports on a first proof-of-principal PES experiment from water and NaI aqueous solution, performed with the new *EASI* setup in the laboratory, and using a He-discharging lamp ($h\nu = 40.814$ eV). This study demonstrates the feasibility to use flatjets in PES spectroscopy, and opens the way to a large number of experiments with much higher photon flux and much smaller focal size, obtained, *e.g.*, at synchrotron-light facilities. It would include the systematic measurement of PADs, which can be compared with the ones from cylindrical jet. One other aspect is the generation of a flatjet with each face consisting of a different solution, not only for PES as I describe next.

The second publication, Paper VIII, reports on a study where we have crossed two cylindrical liquid jets from different solutions, with the aim to explore how solutions mix upon first impingement. In order to track the mixing, we have chosen to study a chemical reaction that signals the encounter of species from both solutions. Our specific choice was the reaction of luminol and hydrogen peroxide by crossing a luminol aqueous solution of different concentrations (from 6-34 mmol) with a 10% H₂O₂ aqueous solution, leading to an excited intermediated transient structure that decays by chemiluminescence (CL). This CL was detected perpendicular to the leaf surface using a charge-coupled device (CCD) camera that collected the emitted light from the entire leaf. The spatially varying light intensity can be assigned to areas where mixing has occurred, and we can also assign a time scale down the leaf (in the direction of the jet flow) to interpret the observed CL intensity distribution across the leaf, not only of the first one. We find that the mixing occurs primarily by diffusion between two laminar co-flowing solutions, separated by their mutual interface. Paper VIII discusses in great detail how our experiment can be used to study the reaction kinetics between two solutions. Inspired by these findings we have performed several PES measurements from flatjets, measured with soft-X-rays at the synchrotron-light facility BESSY II, and thus well extending on the flatjet spectra reported in Paper VIII. Indeed, each face yields a different photoelectron spectrum, each essentially reproducing the one from the respective cylindrical single-jet solution.

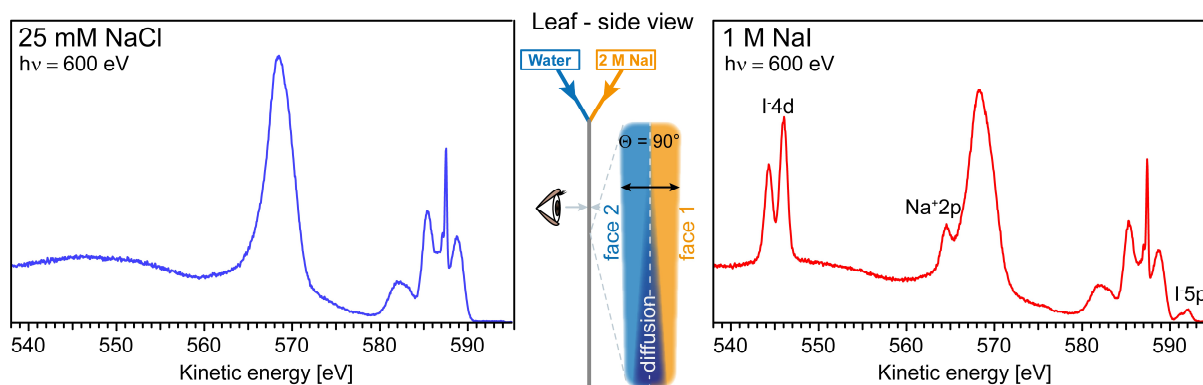


Figure 24: Center: Schematic side-view of the first leaf of a flatjet generated by two colliding cylindrical jets of same size and velocity (approximately 100 m/s) but different aqueous solutions, 25 mM NaCl, and 1 M NaI. Left: Extended valence PE spectrum with the NaCl solution facing the electron detector. Right: NaI solution faces the detector. Photoelectron peaks due to Na⁺ and I⁻ are labelled.

As a demonstration I show in Figure 24 the spectra from a flatjet made from colliding a 25 mM NaCl aqueous solution with a 1 M NaI aqueous solution cylinder jet. Notably, the I-4d and I-5p features from the NaI side are not observable on the water site. We can envision the enormous potential for subsequent studies, in particular when applying bias voltages, identical or different, at the single jets before collision. I also like to point out that this novel liquid – liquid-interface system will have a large potential for applying earlier mentioned photon-out X-ray spectroscopy (*e.g.*, XAS or RIXS) to study the physical and chemical interactions of two liquids.

4. Conclusion and Outlook

In my thesis, I presented several explorative studies and results taking advantage of the unique design of the *EASI* setup for liquid-microjet photoemission spectroscopy, which I have developed. By virtue of its compact footprint, the apparatus can be shipped to synchrotron-light facilities or other laboratories, which gives it a broad flexibility in the use of excitation energies and other properties of the radiation source.

My first study has provided new insights into the inherent growth of the electron inelastic-scattering background, universal to photoemission spectra from liquids, and the effect of inelastic scattering on the nascent PE signal. As it turns out, a change in the electron-scattering mechanism below kinetic energies of ~ 10 - 14 eV causes any photoelectron peak to diminish with a simultaneous rise of the background signal (due to the quasi-elastic scattering associated with small-energy vibrational losses) which makes it impossible to extract undisturbed PE features. Thus, quantitative analysis of PE peaks becomes unreliable, and correspondingly both solute and solvent electron binding energies (eBEs) cannot be accurately determined in this low-kinetic-energy region.

I have determined the absolute accurate binding energy for water's highest occupied molecular orbital (HOMO), $1b_1$, using a newly developed method by which the energies of electronic states in a liquid are measured relative to the zero-kinetic-energy cut-off in the electron spectrum. We find an average eBE of 11.33 ± 0.03 eV for neat water with respect to the vacuum level, which is now determined completely independent from any gas-phase references; this latter method had been known to suffer from charging of the jet surface, and hence making the gas-phase PE spectral features shift and broaden depending on the experimental conditions. Additionally, by carefully creating potential-free conditions, we determined water's lowest binding energy of 6.60 eV with respect to the Fermi energy. For the (core-level) O $1s$ state, by applying the same referencing approach at a much higher photon energy of $h\nu = 650$ eV, we were able to extract a value of 538.10 eV for the binding energy with respect to the vacuum level. We also quantified the absolute energetics of aqueous solutions as a function of solute concentration for the first time, exemplified for sodium iodide (NaI) and the surfactant tetrabutylammonium iodide (TBAI). This shows that the presented

method, based on the cut-off measurement, is a viable method to determine absolute ionization energies for both solute and solvent states, and makes the previously common, but unsatisfactory gas-phase energy-referencing method obsolete. Furthermore, our new method promises direct access to surface and interfacial properties of liquid water and aqueous solutions with the ability to access both changes in work function (surface-specific) and bulk electronic structure.

A third major result of my thesis is a feasibility study on the detection of photoelectron circular dichroism (PECD) from a liquid with the new *EASI* setup, which became possible due to its unique detection geometry. The study of PECD on chiral species in a liquid environment was arguably the main motivation for the development and construction of the *EASI* setup. Here, among other goals, we aimed to specifically adapt to the technical environment of the P04 soft-X-ray beamline at the PETRA III synchrotron-radiation facility. This enabled us to successfully perform the first PECD measurement from a liquid, exemplified for liquid fenchone as a prototypical chiral system. Analysis of spectra of the two enantiomers of fenchone, obtained as a function of photon energy and alternating helicity of the circularly polarized synchrotron radiation, revealed for the first time the existence of PECD in liquid phase. Follow-up studies on PECD in aqueous solutions, in particular aqueous-phase alanine, are ongoing and the first preliminary results reveal the huge potential of this method to investigate the electronic and geometric structure of biomolecules in their native environment. By investigating electronic energy levels of biologically relevant chiral molecules, *e.g.*, sugars or even small proteins, I envision to gain a deeper understanding of chiral-recognition processes, and thus a deeper understanding of biochemical reactions in aqueous solution as well as of the role played by specific solvation effects, both at the surface and in bulk solution.

Furthermore, I have initiated a first exploratory study of PE spectra from a sugar – here glucose – in aqueous solution as a function of pH, also presented in this thesis. Aiming at characterizing site-specific changes of the electronic structure depending on the protonation state of glucose in aqueous solution, we demonstrated the capability to access the solution pK_a value using photoemission spectroscopy. This new approach can be considered a ‘photoemission spectroscopy titration’ method. In particular, we studied the C 1s core-level PE spectra of glucose, and identified energy shifts specifically associated with the C1 site of

the molecule, assisted by electronic-structure calculations. We also determined a pK_a value of 12.2 for the anomeric hydroxyl group at the C1 site just from the PE spectra alone, which is in good agreement with the literature. Though, other than in the literature, we observed no significant differences for the acidity constant between glucose's two anomeric forms. In that first study, however, it was not possible to determine pK_a values for the other acidic hydroxyl groups (C2 to C5) due to the high acidity of the anomeric center -OH. In the future, by protecting the anomeric hydroxyl with a suitable ester (*via* esterification), we envision to determine the pK_a values associated with the other hydroxyl groups. One other aspect to be further explored in upcoming studies is attempting to track the mutarotation of glucose (compare Chapter 3.4) recording C 1s PE spectra as a function of time, with the goal to detect the small C 1s signal of CHO of the transient aldose group. With the ability to observe interconverting reactions, *e.g.*, mutarotation of pyranoses as a consequence of ring-chain tautomerism, new perspectives will open up regarding biochemical interactions like cell-cell communication. Further, by investigating biorelevant systems, *e.g.*, amino acids, and proteins in their native aqueous environment, new insights of biologically relevant chiral recognition can be unveiled.

Regarding my side projects, the good energy resolution of *EASI* in combination with the well-adapted P04 beamline at PETRA III, DESY, enabled high-resolution *non-local* Auger spectroscopic measurements from isoelectronic metal cations after 1s core-level ionization of the metal center. Here, intermolecular Coulombic decay (ICD) of the aqueous-phase isoelectronic cations Na^+ , Mg^{2+} , and Al^{3+} was investigated. For the first time, ICD was probed after 1s core-level ionization of a metallic center, which makes the resulting spectra less complex as compared to 2p ionization. By comparing the ICD *versus* Auger signal intensity, a so-called core-hole-clock analysis based on the natural lifetime of the core hole with timescales of 34 fs and 76 fs, respectively, for Al^{3+} and Mg^{2+} inner-shell ICD was conducted. We were also able to assign individual ICD features to specific ionization channels of water, and access, thanks to the propensity of ICD to involve the nearest neighbors of the ionized species, the electronic-structure properties of just the hydration water molecules, *i.e.*, those directly surrounding the metal center. Analogous studies from other metal ions are planned to particularly explore the details that drive the probability of the different ICD channels; one useful aspect here will be the comparison with solvents other than water, *i.e.*, alcohols.

Another rewarding side study was the generation of a flatjet, made by colliding two cylindrical jets from different solutions, and the characterization of such a laminarly co-flowing liquid-liquid system, both in air and in vacuum. The main finding was that the solutions do not mix within the first leaf of the chain of leaves; mixing only occurs within the leaf boundaries, the rims. This provides novel possibilities for studying reaction kinetics, exploiting the built-in time scale of the liquid flow, which we have exemplified for the chemical reaction between hydrogen peroxide and luminol. In that case the actual reaction was observed by detecting chemiluminescence emitted from the surface of the leaf where the two reactants have encountered each other. This experiment was not done in vacuum. However, in another study, we used the same design to generate a vacuum flatjet upon mixing two different aqueous solutions. We showed that the two faces of the first leaf yield different PE spectra, each essentially representing the PE spectrum one measures from a single jet from the respective solution. In ongoing experiments, we now explore the effect of an applied bias (allowing for differential voltages) on the impinging single jets in the PE spectra from both sides of the flatjet. Flatjets may also open up interesting new perspectives for PAD measurements. As a side note, double-faced flatjets are a unique system for future studies of the liquid—liquid interface on the microscopic level; the X-ray photon-out technique or transmission would be predestinated techniques to follow up on these routes.

In summary, I have achieved several technical and scientific accomplishments with considerable impact on the wider field of (aqueous) solution, interfacial and bulk, electronic-structure properties. On the technical side, I have built a LJ-PES setup, improved existing techniques, and developed several flatjets of different design. With these tools, I was able to perform measurements that enabled the determination of solution absolute and accurate energetics, which led to a better understanding of the electron scattering in water and aqueous solutions, important for the interpretation of measured PE spectra. These studies have also laid the ground work to access typical condensed-matter properties of water and aqueous solutions, such as the work function. Furthermore, I provided the experimental and technical platform that allowed to extent LJ-PES to LJ-PECD. The latter I have successfully demonstrated, and with that paved the way for the systematic exploration of this important electronic-structure-based chiral effect which is truly crucial for biologically relevant systems. Finally, the successful application of LJ-PES to flatjets, both single-phase and

two-solution-faces, provides novel experimental possibilities for advanced PAD measurements (now from a planar surface), and perhaps for a field-induced manipulation of the liquid surface when applying a bias voltage. There are many other open potential routes for the future, including time-resolved LJ-PES, probing light-induced molecular chirality in aqueous solution, bridging to quantities obtained in electrochemistry, or applying LJ-PES for exploring the mechanistic aspects underlying molecular-beam scattering of a (planar) liquid surface.

5. References

- [1] C. P. McKay, *Proc. Natl. Acad. Sci. U.S.A.* 2014, *111*, 12628-12633.
- [2] M. F. Chaplin, *Anomalous properties of water*, https://water.lsbu.ac.uk/water/water_anomalies.html, 02.02.2022
- [3] W. Good, *J. Theor. Biol.* 1973, *39*, 249-276.
- [4] L. G. M. Pettersson, R. H. Henchman, and A. Nilsson, *Chem. Rev.* 2016, *116*, 7459-7462.
- [5] E. Brini, C. J. Fennell, M. Fernandez-Serra, B. Hribar-Lee, M. Lukšič, and K. A. Dill, *Chem. Rev.* 2017, *117*, 12385-12414.
- [6] A. G. Császár, G. Czakó, T. Furtenbacher, J. Tennyson, V. Szalay, S. V. Shirin, N. F. Zobov, and O. L. Polyansky, *J. Chem. Phys.* 2005, *122*, 214305.
- [7] S. Piana, A. G. Donchev, P. Robustelli, and D. E. Shaw, *J. Phys. Chem. B* 2015, *119*, 5113-5123.
- [8] R. Dupuy, C. Richter, B. Winter, G. Meijer, R. Schlögl, and H. Bluhm, *J. Chem. Phys.* 2021, *154*, 060901.
- [9] J. B. Asbury, T. Steinel, K. Kwak, S. A. Corcelli, C. P. Lawrence, J. L. Skinner, and M. D. Fayer, *J. Chem. Phys.* 2004, *121*, 12431-12446.
- [10] M. L. Cowan, B. D. Bruner, N. Huse, J. R. Dwyer, B. Chugh, E. T. J. Nibbering, T. Elsaesser, and R. J. D. Miller, *Nature* 2005, *434*, 199-202.
- [11] T. Fransson, Y. Harada, N. Kosugi, N. A. Besley, B. Winter, J. J. M. Rehr, L. G. Pettersson, and A. Nilsson, *Chem. Rev.* 2016, *116*, 7551-7569.
- [12] B. Winter, and M. Faubel, *Chem. Rev.* 2006, *106*, 1176-1211.
- [13] R. Golnak, S. I. Bokarev, R. Seidel, J. Xiao, G. Grell, K. Atak, I. Unger, S. Thürmer, S. G. Aziz, O. Kühn, B. Winter, and E. F. Aziz, *Sci. Rep.* 2016, *6*, 24659.
- [14] Q. Du, R. Superfine, E. Freysz, and Y. R. Shen, *Phys. Rev. Lett.* 1993, *70*, 2313-2316.
- [15] G. Gonella, E. H. G. Backus, Y. Nagata, D. J. Bonthuis, P. Loche, A. Schlaich, R. R. Netz, A. Kühnle, I. T. McCrum, M. T. M. Koper, M. Wolf, B. Winter, G. Meijer, R. K. Campen, and M. Bonn, *Nat. Rev. Chem.* 2021, *5*, 466-485.
- [16] G. A. Cisneros, K. T. Wikfeldt, L. Ojamäe, J. Lu, Y. Xu, H. Torabifard, A. P. Bartók, G. Csányi, V. Molinero, and F. Paesani, *Chem. Rev.* 2016, *116*, 7501-7528.
- [17] J. Nishitani, Y.-I. Yamamoto, C. W. West, S. Karashima, and T. Suzuki, *Sci. Adv.* 2019, *5*, eaaw6896.
- [18] R. Seidel, B. Winter, and S. E. Bradforth, *Annu. Rev. Phys. Chem.* 2016, *67*, 283-305.
- [19] N. Ottosson, M. Faubel, S. E. Bradforth, P. Jungwirth, and B. Winter, *J. Electron Spectrosc. Relat. Phenom.* 2010, *177*, 60-70.
- [20] S. Ghosal, J. C. Hemminger, H. Bluhm, B. S. Mun, E. L. D. Hebenstreit, G. Ketteler, D. F. Ogletree, F. G. Requejo, and M. Salmeron, *Science* 2005, *307*, 563-566.

- [21] S. Thürmer, R. Seidel, M. Faubel, W. Eberhardt, J. C. Hemminger, S. E. Bradforth, and B. Winter, *Phys. Rev. Lett.* 2013, *111*, 173005.
- [22] R. Dupuy, J. Filser, C. Richter, R. Seidel, F. Trinter, T. Buttersack, C. Nicolas, J. Bozek, U. Hergenbahn, H. Oberhofer, B. Winter, K. Reuter, and H. Bluhm, *Phys. Chem. Chem. Phys.* 2022, *24*, 4796-4808.
- [23] T. Jahnke, U. Hergenbahn, B. Winter, R. Dörner, U. Fröhling, P. V. Demekhin, K. Gokhberg, L. S. Cederbaum, A. Ehresmann, A. Knie, and A. Dreuw, *Chem. Rev.* 2020, *120*, 11295-11369.
- [24] S. Gozem, R. Seidel, U. Hergenbahn, E. Lugovoy, B. Abel, B. Winter, A. I. Krylov, and S. E. Bradforth, *J. Phys. Chem. Lett.* 2020, *11*, 5162-5170.
- [25] I. Powis, *J. Chem. Phys.* 2000, *112*, 301-310.
- [26] I. Powis, *J. Phys. Chem. A* 2000, *104*, 878-882.
- [27] G. A. Garcia, L. Nahon, M. Lebeck, J.-C. Houver, D. Doweck, and I. Powis, *J. Chem. Phys.* 2003, *119*, 8781-8784.
- [28] I. Powis, E. E. Rennie, U. Hergenbahn, O. Kugeler, and R. Bussy-Socrate, *J. Phys. Chem. A* 2003, *107*, 25-34.
- [29] U. Hergenbahn, E. E. Rennie, O. Kugeler, S. Marburger, T. Lischke, I. Powis, and G. Garcia, *J. Chem. Phys.* 2004, *120*, 4553-4556.
- [30] I. Powis, in *Adv. Chem. Phys.* (Ed.: S. A. Rice), 138, 2008, pp. 267-329.
- [31] V. Ulrich, S. Barth, S. Joshi, U. Hergenbahn, E. Mikajlo, C. J. Harding, and I. Powis, *J. Phys. Chem. A* 2008, *112*, 3544-3549.
- [32] I. Powis, C. J. Harding, G. A. Garcia, and L. Nahon, *ChemPhysChem* 2008, *9*, 475-483.
- [33] G. A. Garcia, L. Nahon, S. Daly, and I. Powis, *Nat. Commun.* 2013, *4*, 2132.
- [34] G. A. Garcia, L. Nahon, C. J. Harding, and I. Powis, *Phys. Chem. Chem. Phys.* 2008, *10*, 1628-1639.
- [35] L. Nahon, G. A. Garcia, and I. Powis, *J. Electron Spectrosc. Relat. Phenom.* 2015, *204*, 322-334.
- [36] J. B. Gough, *Becquerel, Alexander-Edmond, Vol. 1*, Charles Coulston Gillispie, New York, 1970.
- [37] J. Schubert, *Physikalische Effekte, Vol. 2*, Physik-Verlag, 1984.
- [38] W. Hallwachs, *Ann. Phys.* 1888, *269*, 301-312.
- [39] W. Hallwachs, *Ann. Phys.* 1888, *270*, 731-734.
- [40] G. Zoltan, *Phys. Z.* 1912, *13*, 454-460.
- [41] N. V. Pope, in *The Present Status of the Quantum Theory of Light, in Honour of Professor Jean-Pierre Vigiér, Vol. 80*, York Univ, Toronto, Canada, 1995, pp. 495-502.
- [42] NobelPrize.org, *The Nobel Prize in Physics 1921*, <https://www.nobelprize.org/prizes/physics/1921/einstein/facts/>, 13.12.2021
- [43] K. Siegbahn, *Rev. Mod. Phys.* 1982, *54*, 709-728.

- [44] U. Gelius, *J. Electron Spectrosc. Relat. Phenom.* 1974, 5, 985-1057.
- [45] O. Travnikova, K. J. Børve, M. Patanen, J. Söderström, C. Miron, L. J. Sæthre, N. Mårtensson, and S. Svensson, *J. Electron Spectrosc. Relat. Phenom.* 2012, 185, 191-197.
- [46] J. H. D. Eland, *Photoelectron Spectroscopy: An Introduction to Ultraviolet Photoelectron Spectroscopy in the Gas Phase*, Elsevier, 1983.
- [47] T. Koopmans, *Physica* 1934, 1, 104-113.
- [48] A. Einstein, *Ann. Phys.* 1905, 322, 132-148.
- [49] S. Hüfner, *Photoelectron Spectroscopy: Principles and Applications*, Springer Berlin, 1995.
- [50] C.-W. Jiang, A.-P. Fang, D. Zhao, H.-R. Li, R.-H. Xie, and F.-L. Li, *Int. J. Photoenergy* 2014, 2014, 597165.
- [51] A. H. Zewail, *J. Phys. Chem. A* 2000, 104, 5660-5694.
- [52] S. D. Kevan, and E. Rotenberg, *J. Electron Spectrosc. Relat. Phenom.* 2001, 117-118, 57-70.
- [53] V. Schmidt, *Electron Spectrometry of Atoms using Synchrotron Radiation*, Cambridge University Press, Cambridge, 2009.
- [54] J. Stöhr, R. Jaeger, and J. J. Rehr, *Phys. Rev. Lett.* 1983, 51, 821-824.
- [55] L. S. Cederbaum, J. Zobeley, and F. Tarantelli, *Phys. Rev. Lett.* 1997, 79, 4778-4781.
- [56] U. Hergenhahn, *J. Electron Spectrosc. Relat. Phenom.* 2011, 184, 78-90.
- [57] A. L. Ankudinov, W. T. Elam, J. R. Sieber, and J. J. Rehr, *X-Ray Spectrom.* 2006, 35, 312-318.
- [58] P. L. Geissler, C. Dellago, D. Chandler, J. Hutter, and M. Parrinello, *Science* 2001, 291, 2121-2124.
- [59] P. Natalis, P. Penntreau, L. Longton, and J. E. Collin, *Chem. Phys.* 1982, 73, 191-201.
- [60] J. M. Hollas, *Moderne Methoden in der Spektroskopie*, 1995.
- [61] M. O. Krause, *J. Phys. Chem. Ref. Data* 1979, 8, 307-327.
- [62] L. Meitner, *Z. Phys.* 1922, 11, 35-54.
- [63] P. Auger, *J. Phys. Radium* 1925, 6, 205-208.
- [64] T. Schuelke, in *Encyclopedia of Tribology* (Eds.: Q. J. Wang, Y.-W. Chung), Springer US, Boston, MA, 2013, pp. 149-154.
- [65] F. A. Settle, *Handbook of Instrumental Techniques for Analytical Chemistry*, Prentice Hall PTR, Upper Saddle River, New Jersey, 1997.
- [66] B. Winter, *Nucl. Instrum. Methods Phys. Res., Sect. A* 2009, 601, 139-150.
- [67] B. Winter, U. Hergenhahn, M. Faubel, O. Björneholm, and I. V. Hertel, *J. Chem. Phys.* 2007, 127, 094501.
- [68] D. Nordlund, H. Ogasawara, H. Bluhm, O. Takahashi, M. Odelius, M. Nagasono, L. G. M. Pettersson, and A. Nilsson, *Phys. Rev. Lett.* 2007, 99, 217406.
- [69] C. P. Schwartz, S. Fatehi, R. J. Saykally, and D. Prendergast, *Phys. Rev. Lett.* 2010, 105, 198102.

- [70] S. Barth, S. Marburger, O. Kugeler, V. Ulrich, S. Joshi, A. M. Bradshaw, and U. Hergenbahn, *Chem. Phys.* 2006, *329*, 246-250.
- [71] S. Thürmer, M. Ončák, N. Ottosson, R. Seidel, U. Hergenbahn, S. E. Bradforth, P. Slavíček, and B. Winter, *Nat. Chem.* 2013, *5*, 590-596.
- [72] M. Pernpointner, N. V. Kryzhevoi, and S. Urbaczek, *J. Chem. Phys.* 2008, *129*, 024304.
- [73] I. Unger, R. Seidel, S. Thürmer, M. N. Pohl, E. F. Aziz, L. S. Cederbaum, E. Muchová, P. Slavíček, B. Winter, and N. V. Kryzhevoi, *Nat. Chem.* 2017, *9*, 708-714.
- [74] M. N. Pohl, C. Richter, E. Lugovoy, R. Seidel, P. Slavíček, E. F. Aziz, B. Abel, B. Winter, and U. Hergenbahn, *J. Phys. Chem. B* 2017, *121*, 7709-7714.
- [75] S. A. Clough, Y. Beers, G. P. Klein, and L. S. Rothman, *J. Chem. Phys.* 1973, *59*, 2254-2259.
- [76] P. Hunt, *Molecular Orbitals and Population Analysis*, http://www.huntresearchgroup.org.uk/teaching/teaching_comp_chem_year4/L7_bonding.pdf, 07.02.2022
- [77] R. Sankari, M. Ehara, H. Nakatsuji, Y. Senba, K. Hosokawa, H. Yoshida, A. De Fanis, Y. Tamenori, S. Aksela, and K. Ueda, *Chem. Phys. Lett.* 2003, *380*, 647-653.
- [78] S. Thürmer, S. Malerz, F. Trinter, U. Hergenbahn, C. Lee, D. M. Neumark, G. Meijer, B. Winter, and I. Wilkinson, *Chem. Sci.* 2021, *12*, 10558-10582.
- [79] B. Winter, R. Weber, I. V. Hertel, M. Faubel, P. Jungwirth, E. C. Brown, and S. E. Bradforth, *J. Am. Chem. Soc.* 2005, *127*, 7203-7214.
- [80] S. Malerz, F. Trinter, U. Hergenbahn, A. Ghrist, H. Ali, C. Nicolas, C. M. Saak, C. Richter, S. Hartweg, L. Nahon, C. Lee, C. Goy, D. M. Neumark, G. Meijer, I. Wilkinson, B. Winter, and S. Thürmer, *Phys. Chem. Chem. Phys.* 2021, *23*, 8246-8260.
- [81] S. Malerz, H. Haak, F. Trinter, A. B. Stephansen, C. Kolbeck, M. Pohl, U. Hergenbahn, G. Meijer, and B. Winter, *Rev. Sci. Instrum.* 2022, *93*, 015101.
- [82] M. N. Pohl, S. Malerz, F. Trinter, C. Lee, C. Kolbeck, I. Wilkinson, S. Thürmer, D. M. Neumark, L. Nahon, I. Powis, G. Meijer, B. Winter, and U. Hergenbahn, *Phys. Chem. Chem. Phys.* 2022, *24*, 8081-8092.
- [83] B. Credidio, M. Pugini, S. Malerz, F. Trinter, U. Hergenbahn, I. Wilkinson, S. Thürmer, and B. Winter, *Phys. Chem. Chem. Phys.* 2022, *24*, 1310-1325.
- [84] B. Winter, E. F. Aziz, U. Hergenbahn, M. Faubel, and I. V. Hertel, *J. Chem. Phys.* 2007, *126*, 124504.
- [85] S. Y. Truong, A. J. Yench, A. M. Juarez, S. J. Cavanagh, P. Bolognesi, and G. C. King, *Chem. Phys.* 2009, *355*, 183-193.
- [86] N. Kurahashi, S. Karashima, Y. Tang, T. Horio, B. Abulimiti, Y.-I. Suzuki, Y. Ogi, M. Oura, and T. Suzuki, *J. Chem. Phys.* 2014, *140*, 174506.
- [87] J. O'm Bockris, M. A. V. Devanathan, and K. Müller, *Proc. R. Soc. London, Ser. A* 1963, *274*, 55-79.
- [88] G. R. Wiese, R. O. James, and T. W. Healy, *Discuss. Faraday Soc.* 1971, *52*, 302-311.

- [89] B. Winter, R. Weber, W. Widdra, M. Dittmar, M. Faubel, and I. V. Hertel, *J. Phys. Chem. A* 2004, *108*, 2625-2632.
- [90] C. F. Perry, P. Zhang, F. B. Nunes, I. Jordan, A. von Conta, and H. J. Wörner, *J. Phys. Chem. Lett.* 2020, *11*, 1789-1794.
- [91] Y.-I. Suzuki, K. Nishizawa, N. Kurahashi, and T. Suzuki, *Phys. Rev. E* 2014, *90*, 010302(R).
- [92] Y. Tang, H. Shen, K. Sekiguchi, N. Kurahashi, T. Mizuno, Y.-I. Suzuki, and T. Suzuki, *Phys. Chem. Chem. Phys.* 2010, *12*, 3653-3655.
- [93] S. Barth, M. Ončák, V. Ulrich, M. Mucke, T. Lischke, P. Slavíček, and U. Hergenbahn, *J. Phys. Chem. A* 2009, *113*, 13519-13527.
- [94] A. P. Gaiduk, M. Govoni, R. Seidel, J. H. Skone, B. Winter, and G. Galli, *J. Am. Chem. Soc.* 2016, *138*, 6912-6915.
- [95] M. N. Pohl, E. Muchová, R. Seidel, H. Ali, S. Sršeň, I. Wilkinson, B. Winter, and P. Slavíček, *Chem. Sci.* 2019, *10*, 848-865.
- [96] N. Ottosson, K. J. Børve, D. Spångberg, H. Bergersen, L. J. Sæthre, M. Faubel, W. Pokapanich, G. Öhrwall, O. Björneholm, and B. Winter, *J. Am. Chem. Soc.* 2011, *133*, 3120-3130.
- [97] K. Nishizawa, N. Kurahashi, K. Sekiguchi, T. Mizuno, Y. Ogi, T. Horio, M. Oura, N. Kosugi, and T. Suzuki, *Phys. Chem. Chem. Phys.* 2011, *13*, 413-417.
- [98] S. Thürmer, doctoral thesis, Universität Potsdam (Potsdam), 2012.
- [99] M. A. Brown, M. Faubel, and B. Winter, *Annu. Rep. Prog. Chem. Sect. C: Phys. Chem.* 2009, *105*, 174-212.
- [100] T. Lewis, M. Faubel, B. Winter, and J. C. Hemminger, *Angew. Chem. Int. Ed. Engl.* 2011, *50*, 10178-10181.
- [101] T. Lewis, B. Winter, A. C. Stern, M. D. Baer, C. J. Mundy, D. J. Tobias, and J. C. Hemminger, *J. Phys. Chem. C* 2011, *115*, 21183-21190.
- [102] A. C. Stern, M. D. Baer, C. J. Mundy, and D. J. Tobias, *J. Chem. Phys.* 2013, *138*, 114709.
- [103] A. Nilsson, T. Tokushima, Y. Horikawa, Y. Harada, M. P. Ljungberg, S. Shin, and L. G. M. Pettersson, *J. Electron Spectrosc. Relat. Phenom.* 2013, *188*, 84-100.
- [104] H. Nikjoo, D. Emfietzoglou, T. Liamsuwan, R. Taleei, D. Liljequist, and S. Uehara, *Rep. Prog. Phys.* 2016, *79*, 116601.
- [105] A. Jablonski, and C. J. Powell, *J. Electron Spectrosc. Relat. Phenom.* 1999, *100*, 137-160.
- [106] A. Jablonski, and C. J. Powell, *J. Phys. Chem. Ref. Data* 2020, *49*, 033102-033144.
- [107] R. L. Kurtz, N. Usuki, R. Stockbauer, and T. E. Madey, *J. Electron Spectrosc. Relat. Phenom.* 1986, *40*, 35-58.
- [108] H. T. Nguyen-Truong, *J. Phys.: Condens. Matter* 2018, *30*, 155101.
- [109] Y. Itikawa, and N. Mason, *J. Phys. Chem. Ref. Data* 2005, *34*, 1-22.
- [110] I. Plante, and F. A. Cucinotta, *New J. Phys.* 2009, *11*, 063047.

- [111] J. M. Heller Jr., R. N. Hamm, R. D. Birkhoff, and L. R. Painter, *J. Chem. Phys.* 1974, *60*, 3483-3486.
- [112] E. O. Lawrence, and M. A. Chaffee, *Phys. Rev.* 1930, *36*, 1099-1100.
- [113] K. L. Reid, *Annu. Rev. Phys. Chem.* 2003, *54*, 397-424.
- [114] B. Ritchie, *J. Chem. Phys.* 1975, *63*, 1351-1359.
- [115] J. Cooper, and R. N. Zare, *J. Chem. Phys.* 1968, *48*, 942-943.
- [116] J. B. Martins, Doctoral thesis, Sorbonne Université (Paris), 2021.
- [117] B. Ritchie, *Phys. Rev. A* 1976, *13*, 1411-1415.
- [118] M. Tia, B. Cunha de Miranda, S. Daly, F. Gaie-Levrel, G. A. Garcia, L. Nahon, and I. Powis, *J. Phys. Chem. A* 2014, *118*, 2765-2779.
- [119] M. H. M. Janssen, and I. Powis, *Phys. Chem. Chem. Phys.* 2014, *16*, 856-871.
- [120] C. J. Harding, E. Mikajlo, I. Powis, S. Barth, S. Joshi, V. Ulrich, and U. Hergenhahn, *J. Chem. Phys.* 2005, *123*, 234310.
- [121] M. Born, and E. Wolf, *Principles of Optics: Electromagnetic Theory of Propagation, Interference and Diffraction of Light*, 7th ed., Cambridge University Press, Cambridge, 1999.
- [122] N. Böwering, T. Lischke, B. Schmidtke, N. Müller, T. Khalil, and U. Heinzmann, *Phys. Rev. Lett.* 2001, *86*, 1187-1190.
- [123] L. Nahon, G. A. Garcia, H. Soldi-Lose, S. Daly, and I. Powis, *Phys. Rev. A* 2010, *82*.
- [124] M. M. Rafiee Fanoood, H. Ganjitabar, G. A. Garcia, L. Nahon, S. Turchini, and I. Powis, *ChemPhysChem* 2018, *19*, 921-933.
- [125] L. Nahon, L. Nag, G. A. Garcia, I. Myrgorodska, U. Meierhenrich, S. Beaulieu, V. Wanie, V. Blanchet, R. Géneaux, and I. Powis, *Phys. Chem. Chem. Phys.* 2016, *18*, 12696-12706.
- [126] M. Stener, G. Fronzoni, D. Di Tommaso, and P. Decleva, *J. Chem. Phys.* 2004, *120*, 3284-3296.
- [127] I. Powis, S. Daly, M. Tia, B. Cunha de Miranda, G. A. Garcia, and L. Nahon, *Phys. Chem. Chem. Phys.* 2014, *16*, 467-476.
- [128] G. A. Garcia, H. Dossmann, L. Nahon, S. Daly, and I. Powis, *Phys. Chem. Chem. Phys.* 2014, *16*, 16214-16224.
- [129] M. Tia, B. Cunha de Miranda, S. Daly, F. Gaie-Levrel, G. A. Garcia, I. Powis, and L. Nahon, *J. Phys. Chem. Lett.* 2013, *4*, 2698-2704.
- [130] D. G. Blackmond, *Cold Spring Harb. Perspect. Biol.* 2010, *2*, a002147.
- [131] A. Schild, M. Peper, C. Perry, D. Rattenbacher, and H. J. Wörner, *J. Phys. Chem. Lett.* 2020, *11*, 1128-1134.
- [132] H. Wiedemann, *Synchrotron Radiation Physics*, Springer, 2020.
- [133] A. Hofmann, *The Physics of Synchrotron Radiation*, Cambridge University Press, 2004.

- [134] M. Calvi, C. Camenzuli, E. Prat, and T. Schmidt, *J. Synchrotron Radiat.* 2017, 24, 600-608.
- [135] Deutsches Elektronen-Synchrotron DESY, *P04 Variable Polarization XUV Beamline*, https://photon-science.desy.de/facilities/petra_iii/beamlines/p04_xuv_beamline/index_eng.html, 29.01.2022
- [136] G. Brown, K. Halbach, J. Harris, and H. Winick, *Nucl. Instrum. Methods Phys. Res.* 1983, 208, 65-77.
- [137] S. Sasaki, *Nuclear Instruments & Methods in Physics Research Section a-Accelerators Spectrometers Detectors and Associated Equipment* 1994, 347, 83-86.
- [138] S. Lidia, and R. Carr, *Nucl. Instrum. Methods Phys. Res., Sect. A* 1994, 347, 77-82.
- [139] H. Wang, P. Bencok, P. Steadman, E. Longhi, J. Zhu, and Z. Wang, *J. Synchrotron Radiat.* 2012, 19, 944-948.
- [140] H. Siegbahn, and K. Siegbahn, *J. Electron Spectrosc. Relat. Phenom.* 1973, 2, 319-325.
- [141] J. W. Riley, B. Wang, M. A. Parkes, and H. H. Fielding, *Rev. Sci. Instrum.* 2019, 90, 083104.
- [142] H. Siegbahn, *J. Phys. Chem.* 1985, 89, 897-909.
- [143] R. Moberg, F. Bökman, O. Bohman, and H. O. G. Siegbahn, *J. Chem. Phys.* 1991, 94, 5226-5232.
- [144] P. Delahay, and K. Von Burg, *Chem. Phys. Lett.* 1981, 83, 250-254.
- [145] C. Wang, and H. Morgner, *Microchim. Acta* 2010, 171, 415-422.
- [146] S. Axnanda, E. J. Crumlin, B. Mao, S. Rani, R. Chang, P. G. Karlsson, M. O. Edwards, M. Lundqvist, R. Moberg, P. Ross, Z. Hussain, and Z. Liu, *Sci. Rep.* 2015, 5, 9788.
- [147] M. Favaro, F. F. Abdi, E. J. Crumlin, Z. Liu, R. van de Krol, and D. E. Starr, *Surfaces* 2019, 2, 78-99.
- [148] M. Faubel, B. Steiner, and J. P. Toennies, *J. Electron Spectrosc. Relat. Phenom.* 1998, 95, 159-169.
- [149] M. Faubel, B. Steiner, and J. P. Toennies, *J. Chem. Phys.* 1997, 106, 9013-9031.
- [150] M. Faubel, S. Schlemmer, and J. P. Toennies, *Z. Phys. D: At., Mol. Clusters* 1988, 10, 269-277.
- [151] M. Faubel, and T. Kisters, *Nature* 1989, 339, 527-529.
- [152] MicroLiquids, now *Advanced Microfluidic Systems GmbH – AdMiSys*, <https://admisys-gmbh.com/>, 03.08.2021
- [153] C. Adriaanse, J. Cheng, V. Chau, M. Sulpizi, J. VandeVondele, and M. Sprik, *J. Phys. Chem. Lett.* 2012, 3, 3411-3415.
- [154] A. Bernas, C. Ferradini, and J. P. JayGerin, *Chem. Phys.* 1997, 222, 151-160.
- [155] A. P. Gaiduk, T. A. Pham, M. Govoni, F. Paesani, and G. Galli, *Nat. Commun.* 2018, 9, 247.

- [156] F. Williams, S. P. Varma, and S. Hillenius, *J. Chem. Phys.* 1976, *64*, 1549-1554.
- [157] T. W. Marin, I. Janik, D. M. Bartels, and D. M. Chipman, *Nat. Commun.* 2017, *8*, 15435.
- [158] R. Signorell, and B. Winter, *Phys. Chem. Chem. Phys.* 2022.
- [159] B. Ritchie, *Phys. Rev. A* 1976, *14*, 359-362.
- [160] S. Hartweg, G. A. Garcia, D. K. Božanić, and L. Nahon, *J. Phys. Chem. Lett.* 2021, *12*, 2385-2393.
- [161] C.-M. Saak, I. Unger, B. Brena, C. Caleman, and O. Björneholm, *Phys. Chem. Chem. Phys.* 2019, *21*, 15478-15486.
- [162] J. P. Bruce, K. Zhang, S. G. Balasubramani, A. R. Haines, R. P. Galhenage, V. K. Voora, F. Furche, and J. C. Hemminger, *J. Phys. Chem. B* 2021, *125*, 8862-8868.
- [163] T. Buttersack, P. E. Mason, R. S. McMullen, T. Martinek, K. Brezina, D. Hein, H. Ali, C. Kolbeck, C. Schewe, S. Malerz, B. Winter, R. Seidel, O. Marsalek, P. Jungwirth, and S. E. Bradforth, *J. Am. Chem. Soc.* 2019, *141*, 1838-1841.
- [164] C. A. Schroeder, E. Pluhařová, R. Seidel, W. P. Schroeder, M. Faubel, P. Slavíček, B. Winter, P. Jungwirth, and S. E. Bradforth, *J. Am. Chem. Soc.* 2015, *137*, 201-209.
- [165] F. Urban, and P. A. Shaffer, *J. Biol. Chem.* 1932, *94*, 697-715.
- [166] F. Urban, and R. D. Williams, *J. Biol. Chem.* 1933, *100*, 237-241.
- [167] B. E. Lewis, and V. L. Schramm, *J. Am. Chem. Soc.* 2003, *125*, 7872-7877.
- [168] J. Buddrus, *Grundlagen der Organischen Chemie, Vol. 4*, de Gruyter Studium.
- [169] K. P. C. Vollhardt, and N. E. Schore, *Organische Chemie, Vol. 5*, Wiley-VCH, Weinheim, 2011.
- [170] J. Clayden, N. Greeves, and S. Warren, *Organische Chemie, Vol. 2*, Springer Spektrum, 2012.
- [171] N. Ottosson, G. Öhrwall, and O. Björneholm, *Chem. Phys. Lett.* 2012, *543*, 1-11.
- [172] O. Björneholm, A. Nilsson, A. Sandell, B. Hernnäs, and N. Mårtensson, *Phys. Rev. Lett.* 1992, *68*, 1892-1895.
- [173] A. Föhlisch, P. Feulner, F. Hennies, A. Fink, D. Menzel, D. Sanchez-Portal, P. M. Echenique, and W. Wurth, *Nature* 2005, *436*, 373-376.
- [174] C. Lee, M. Pohl, I. Ramphal, W. Yang, B. Winter, B. Abel, and D. Neumark, ChemRxiv 2022, 10.26434/chemrxiv-2022-fxn xv, This content is a preprint and has not been peer-reviewed.
- [175] M. Ekimova, W. Quevedo, M. Faubel, P. Wernet, and E. T. J. Nibbering, *Struct. Dyn.* 2015, *2*, 054301.

6. Appendix: Reprints of published papers

In this chapter, the aforementioned Paper I-VIII are presented in their published layout. All reprints are unchanged and shown as published.

Paper I



A setup for studies of photoelectron circular dichroism from chiral molecules in aqueous solution

Cite as: Rev. Sci. Instrum. 93, 015101 (2022); doi: 10.1063/5.0072346

Submitted: 22 September 2021 • Accepted: 14 December 2021 •

Published Online: 10 January 2022





View Online



Export Citation



CrossMark

Sebastian Malerz,¹ Henrik Haak,¹  Florian Trinter,^{1,2}  Anne B. Stephansen,^{1,a)} Claudia Kolbeck,^{1,b)} Marvin Pohl,^{1,c)} Uwe Hergenhan,¹  Gerard Meijer,¹  and Bernd Winter^{1,d)} 

AFFILIATIONS

¹ Molecular Physics Department, Fritz-Haber-Institut der Max-Planck-Gesellschaft, Faradayweg 4-6, 14195 Berlin, Germany

² FS-PETRA-S, Deutsches Elektronen-Synchrotron (DESY), Notkestraße 85, 22607 Hamburg, Germany

^{a)} **Current address:** Seaborg Technologies, Titangade 11, 2200 Copenhagen, Denmark.

^{b)} **Current address:** sonUtec GmbH, Mittlere-Motsch-Straße 26, 96515 Sonneberg, Germany.

^{c)} **Current address:** Department of Chemistry, University of California, Berkeley, CA 94720, USA.

^{d)} **Author to whom correspondence should be addressed:** winter@fhi-berlin.mpg.de

ABSTRACT

We present a unique experimental design that enables the measurement of photoelectron circular dichroism (PECD) from chiral molecules in aqueous solution. The effect is revealed from the intensity difference of photoelectron emission into a backward-scattering angle relative to the photon propagation direction when ionizing with circularly polarized light of different helicity. This leads to asymmetries (normalized intensity differences) that depend on the handedness of the chiral sample and exceed the ones in conventional dichroic mechanisms by orders of magnitude. The asymmetry is largest for photon energies within several electron volts above the ionization threshold. A primary aim is to explore the effect of hydration on PECD. The modular and flexible design of our experimental setup *EASI* (Electronic structure from Aqueous Solutions and Interfaces) also allows for detection of more common photoelectron angular distributions, requiring distinctively different detection geometries and typically using linearly polarized light. A microjet is used for liquid-sample delivery. We describe *EASI*'s technical features and present two selected experimental results, one based on synchrotron-light measurements and the other performed in the laboratory, using monochromatized He-II α radiation. The former demonstrates the principal effectiveness of PECD detection, illustrated for prototypic gas-phase fenchone. We also discuss the first data from liquid fenchone. In the second example, we present valence photoelectron spectra from liquid water and NaI aqueous solution, here obtained from a planar-surface microjet (flatjet). This new development features a more favorable symmetry for angle-dependent photoelectron measurements.

© 2022 Author(s). All article content, except where otherwise noted, is licensed under a Creative Commons Attribution (CC BY) license (<http://creativecommons.org/licenses/by/4.0/>). <https://doi.org/10.1063/5.0072346>

I. INTRODUCTION

A. General considerations

Photoelectron spectroscopy (PES) studies from liquids and particularly from water and aqueous solutions, mostly in conjunction with a liquid microjet,^{1,2} have contributed tremendously to our current understanding of the aqueous-phase electronic structure. An experimental focus has been on core-level PES,^{2,3} with far less studies directed at the lowest ionization energies, although the latter govern chemical reactivity.^{4,5} Core-level spectra, typically measured with tunable soft-x-ray photons from synchrotron radiation beamlines,

have identified chemical shifts of solutes, pH-dependent protonation and de-protonation,^{6–8} solvent and solute interfacial depth profiles,^{9,10} as well as several non-local electronic relaxation processes, such as intermolecular Coulombic decay (ICD).¹¹ In most of these studies, electrons with some tens to hundreds of eV kinetic energy (KE) were detected. Single-photon ionization-threshold phenomena in the aqueous phase, corresponding to generation of photoelectrons with kinetic energies typically smaller than 20 eV, have barely been addressed.¹² This is despite their significant relevance, including the increase in photoionization cross sections near an ionization edge, the yet to be demonstrated liquid-phase

post-collision interaction (PCI),^{13,14} or the potential presence of photoelectron circular dichroism (PECD)^{15–19} in the ionization of liquids. Enabling the exploration of near-threshold ionization phenomena, and particularly aqueous-phase PECD, has been a major motivation to build *EASI* (Electronic structure from Aqueous Solutions and Interfaces), a unique, versatile liquid-microjet photoelectron spectroscopy setup.

Our interest in PECD is motivated by the fact that it uniquely connects the molecular electronic structure to chirality.¹⁵ The effect manifests as a forward–backward asymmetry in the photoelectron emission intensity from chiral molecules, measured with respect to the propagation direction \vec{k} of circularly polarized light (CPL), the sign of which depends on the helicity of the ionizing radiation (*left* or *right*-handed, *l*-CPL or *r*-CPL). The magnitude of PECD is expressed via the chiral anisotropy parameter b_1 . Furthermore, the PECD mechanism is solely based on electric dipole transition amplitudes, which leads to much stronger effects than found in conventional circular dichroism methods.¹⁹ Since chirality is a universal property, and of particular importance for biochemically relevant complexes in aqueous solution, it is highly desirable to quantify PECD in an aqueous environment and understand the molecules' possible chiral imprint on their solvation shells.

The principal geometry of a PECD measurement is illustrated in Fig. 1(a). However, application to the liquid phase requires that several experimental and technical hurdles are overcome, calling for novel and dedicated experimental designs. For gas-phase targets, PECD studies can be readily and very efficiently performed with a velocity map imaging (VMI) spectrometer,²⁰ which provides high electron collection efficiency by simultaneous and angle-resolved acquisition of the electron signal in all emission directions. However, currently available VMI spectrometers are not compatible with liquid jets for several reasons: (1) A liquid jet represents a dielectric

filament of improperly defined charge state, thus introducing undesired electric-field perturbations near the actual ionization region. (2) For sole geometrical reasons, VMI cannot image the full photoelectron angular distribution (PAD) from a cylindrical jet since photoelectrons born inside the solution engage in multiple electron-scattering processes, mostly with water molecules.¹² These electrons may even be directed away from the liquid–vacuum interface into the solution, or if reaching the detector, they will contribute to a signal background that will be difficult to quantify. Using a planar liquid microjet (see Sec. III B) might be advantageous since electrons would be detected from a single surface orientation rather than from a curved surface. Admittedly though, an increased water vapor pressure from a flatjet is likely to result in additional disturbing electron scattering. (3) An additional, more technical complication arises from the considerable background vapor pressure in a liquid-jet (LJ) experiment, which for highly volatile water and aqueous solutions may well be in the $\sim 10^{-3}$ mbar (for the flatjet) to 10^{-5} mbar range. Correspondingly, the successful implementation of the VMI technique with a liquid-jet target remains a challenging technical goal. A first approach toward a technical realization has been attempted very recently for non-electrically conductive solutions. Yet, particularly the consequences of electron scattering in the liquid phase have been barely elaborated on.²¹ The same challenges hold for COLTRIMS-type setups, which also have a history of providing important results on gas-phase PECD²² but have yet to be implemented with liquid-phase targets.

Here, we take a more conventional, simpler, and currently feasible approach by using a state-of-the-art hemispherical electron analyzer (HEA) equipped with a differentially pumped pre-lens section (capable of near-ambient pressure experiments)² and mounted in a geometry compliant with the requirements of PECD detection. Magnetic fields in the region where the liquid jet is

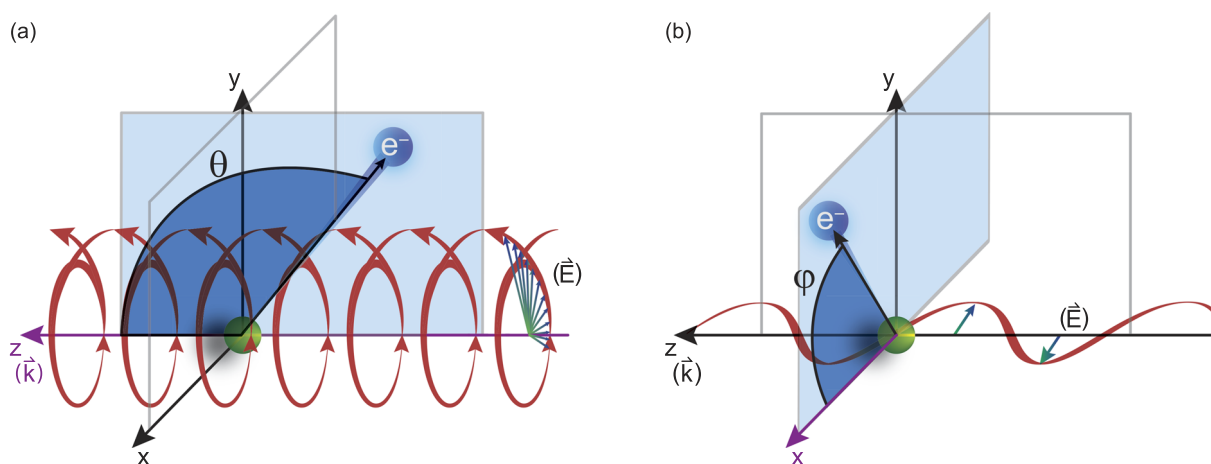


FIG. 1. Sketch of the relevant principal symmetry axes and respective angles for PES experiments using circularly polarized light (a) or linearly (horizontally) polarized light (b); also see Eqs. (1)–(3). The green circle indicates the ionization region. In panel (a), the important parameter is the angle θ spanned between the propagation direction (wave vector, \vec{k}) of the circularly polarized light and the electron detection axis, shown here for detection in the direction opposite to \vec{k} (backward-scattering geometry). In panel (b), the important parameter is the angle φ spanned between the electric field vector \vec{E} and the electron detection axis, shown here in the plane perpendicular to the floor plane and the photon propagation direction (dipole plane).

ionized are carefully shielded by a full μ -metal encasement, enabling the detection of photoelectrons and elastically and inelastically scattered electrons down to near-zero-eV kinetic energy with quantitative accuracy,^{12,23} as required for studying any (near) ionization-threshold phenomena. This includes the measurement of the low-energy cutoff and low-energy tail in a water or aqueous-solution PE spectrum.^{12,23} In addition, in gas-phase studies, PECD was found to be most prominent at electron kinetic energies smaller than ~ 15 eV.^{15–19}

A major drawback imposed by the *geometric* constraints in a liquid-jet experiment is that the dichroic effect, resulting in different intensities emitted in forward and backward directions, cannot be directly and simultaneously measured. Instead, the signal intensity, obtained at a (necessarily) fixed detection angle of our hemispherical electron analyzer, has to be collected for alternating CPL helicity. A similar detection scheme has been previously used to demonstrate core-level PECD in the gas phase.²⁴ Yet, extension to liquid-jet PECD (LJ-PECD) experiments entails major technical considerations and developments, which will be detailed below.

A suitable radiation source for our PECD experiments is the synchrotron radiation delivered from a helical undulator (e.g., APPLE-II).^{25,26} However, the flexible design of *EASI* also enables PAD measurements to be carried out using linearly polarized synchrotron radiation. For this purpose, *EASI* is devised to detect signals within the plane perpendicular to the propagation of the light [“dipole plane,” see Fig. 1(b)] at three alternative fixed detection angles: 0° (horizontal, in the floor plane, parallel to the polarization vector), 54.7° (magic angle), and 90° (perpendicular to the floor and polarization vector). These optional geometries are relevant when only linear horizontal polarization is available, which is the case for many beamlines at synchrotron-light facilities. Photoelectrons from most orbitals are emitted preferentially in the direction of the polarization vector,²⁷ while electrons from Auger or ICD processes typically feature an isotropic emission pattern.²⁸ Then, choosing the 0° -geometry for photoelectrons and 90° -geometry for Auger electrons will yield relatively larger intensities of the respective spectral ranges. The 54.7° -geometry is used to explicitly suppress any angular distribution effects (see below), for instance, when comparing relative signal intensities from ionization of different orbitals for quantitative analysis of relative solute concentration. If linear polarization with a variable orientation of the polarization ellipse is available, any detection angle within 0° – 90° can be realized for any of the three geometries, and photoelectron angular distributions (PADs) can be fully mapped out allowing for a determination of the common (dipolar) anisotropy parameter, β , from aqueous solution of both the water solvent and solute. This parameter can reveal hydrogen-bonding-induced orbital structural changes at the solution–vacuum interface²⁹ and also provides insight into the molecular structure at such interfaces.³⁰

In the following, we will describe the overall design of *EASI* and its components, including the main technical specifications and its principal detection geometries. We close by presenting experimental results to highlight the performance of *EASI*. These include core-level PECD measurements from gas- and liquid-phase fenchone and regular valence PE spectra obtained from a planar microjet (flatjet) using unpolarized He-II α (40.814 eV) radiation. It is useful though to first review the aforementioned anisotropy parameters, which are relevant for PAD and specifically PECD experiments.

B. Photoelectron angular distributions in single-photon ionization

The directional anisotropy of the photoemission process from molecules has played a decisive role in the conceptual design of *EASI*. We, therefore, review here the main aspects determining PADs. We restrict ourselves to single-photon photoionization of a randomly oriented target within the dipole approximation by light in a pure polarization state p , with $p = +1$ designating *l*-CPL in the sense of the optical convention, $p = 0$ linear, and $p = -1$ corresponding to *r*-CPL.^{24,31} The PAD describes differential photoelectron intensities as a function of the angle between a principal symmetry axis and the detection direction. In the case of unpolarized light or CPL, the symmetry axis is the light-propagation direction \vec{k} [Fig. 1(a)], whereas for linearly polarized light (LPL), it is the direction of the electric field vector \vec{E} [Fig. 1(b)]. In the following, we distinguish these cases by denoting the respective angles as θ and φ .

PADs are uniquely connected with several important electronic-structure properties, for instance, photoionization dynamics, based on interfering photoelectron partial waves. Coupling of the electron and photon angular momenta introduces certain symmetry properties and constraints. These symmetry conditions of the experiment determine which terms in the angular distribution function contribute to the PAD. In the following we restrict ourselves to the electric dipole approximation. The influence of magnetic and higher-order electric multipoles on the PADs of linear molecules for single-photon photoionization at photon energies below 1 keV was experimentally found to be small.^{32,33} We expect the same also for chiral-specific non-dipole terms, as derived in Ref. 34. This has been discussed in some detail in Ref. 35. The angular distribution function for perfectly linearly polarized light (LPL) can then be written in the form^{36–38}

$$I(\varphi) \propto 1 + \beta P_2(\cos \varphi), \quad (1)$$

where $P_2(x)$ is the second-order Legendre polynomial which provides the non-isotropic part of the overall distribution and φ is the angle between the linear polarization vector \vec{E} and the direction of photoelectron emission [Fig. 1(b)]. The anisotropy parameter β is constrained to values $-1 \leq \beta \leq +2$ specifying the magnitude of the emission anisotropy, which ranges from a pure $\cos^2(\varphi)$ to a $\sin^2(\varphi)$ form, and therefore possesses mirror symmetry about the principal symmetry axis which is always the polarization vector. For CPL, the PAD is governed by a similar expression (valid only for non-chiral targets, see below),

$$I(\theta) \propto 1 - \frac{\beta}{2} P_2(\cos \theta), \quad (2)$$

with θ defined as the angle between the photon propagation vector \vec{k} and the direction of photoelectron emission [see Fig. 1(a)]. The second Legendre polynomial has a zero crossing at $x = \cos(54.7^\circ)$. At this particular (magic) angle, the measured differential cross section for any transition will become independent of its β -value and thus proportional to its total cross section.

Less widely recognized is that these equations are just special (though common) sub-cases of a more general expression,^{39,40}

$$I_p(\theta) \propto 1 + b_1^p P_1(\cos \theta) + b_2^p P_2(\cos \theta). \quad (3)$$

The equation is written with the understanding that the variable θ is replaced by φ in the linearly polarized case. The coefficients b_n^p are determined by the photoionization dynamics and depend on the photon polarization state p and the radial dipole amplitudes between the molecular initial and ionized state. For the $P_2(x)$ terms, this leads to the relation $\beta = b_2^0 = -2b_2^{\pm 1}$. Moreover, $b_1^0 = 0$, while $b_1^{\pm 1}$ also vanishes for achiral molecules; in such circumstances, this general expression (3) reduces to the well-known former forms (1) and (2).

Particularly relevant for the present work is that for the specific case of a chiral molecule ionized with CPL, the $P_1(x)$ (first-order Legendre polynomial) coefficients no longer vanish for symmetry reasons.³⁹ Furthermore, they switch signs with respect to a change of light polarization: $b_1^{+1} = -b_1^{-1}$. The same change in sign of the $b_1^{\pm 1}$ coefficient is also encountered upon changing the enantiomer.^{39,40} As $P_1(\cos\theta) = \cos\theta$, the largest asymmetry (largest PECD effect) can be observed at $\theta = 0^\circ$ (or 180°). This is, however, elusive for a non-gaseous sample because of the existence of a liquid-gas interface and the associated electron scattering inside the liquid.¹² On the other hand, the PECD asymmetry vanishes in the dipole plane (at $\theta = 90^\circ$), which is the standard (and only) electron detection arrangement realized in currently existing LJ-PES setups. The extension to off-dipole plane detection [Fig. 1(a)] was hence the main motivation for constructing a new setup.

II. EXPERIMENTAL

A. EASI—General features

EASI is a state-of-the-art setup for angle-resolved photoelectron spectroscopy from a liquid microjet, typically used in conjunction with monochromatic linearly or circularly polarized extreme ultraviolet (XUV) to soft-x-ray radiation. For laboratory experiments, also (essentially) unpolarized radiation from a monochromatized helium plasma-discharge source, yielding the He-I α (21.218 eV), He-I β (23.087 eV), He-I γ (23.743 eV), He-II α (40.814 eV), He-II β (48.372 eV), or He-II γ (51.017 eV) emission lines, can be used. Figure 2(a) presents the principal arrangement of the EASI instrument for the case of electron detection in the floor plane—which is one of the geometries suited for b_2 PAD measurements—and using variable linearly polarized light (LPL). This is the standard configuration for laboratory experiments with He-I/II radiation and the most compact form adopted when moving EASI between the home laboratory and synchrotron-radiation facilities. In Fig. 2(b), a rendered graphic of EASI in its unique position for LJ-PECD experiments with CPL is shown. Here, the HEA (detection axis, green arrow) is tilted away from the propagation direction of the CPL [red arrow; compare Fig. 1(a)], forming an angle of $\theta = 130^\circ$. At this angle, the PECD asymmetry, $\sim(I_{+1}(\theta) - I_{-1}(\theta))$, will

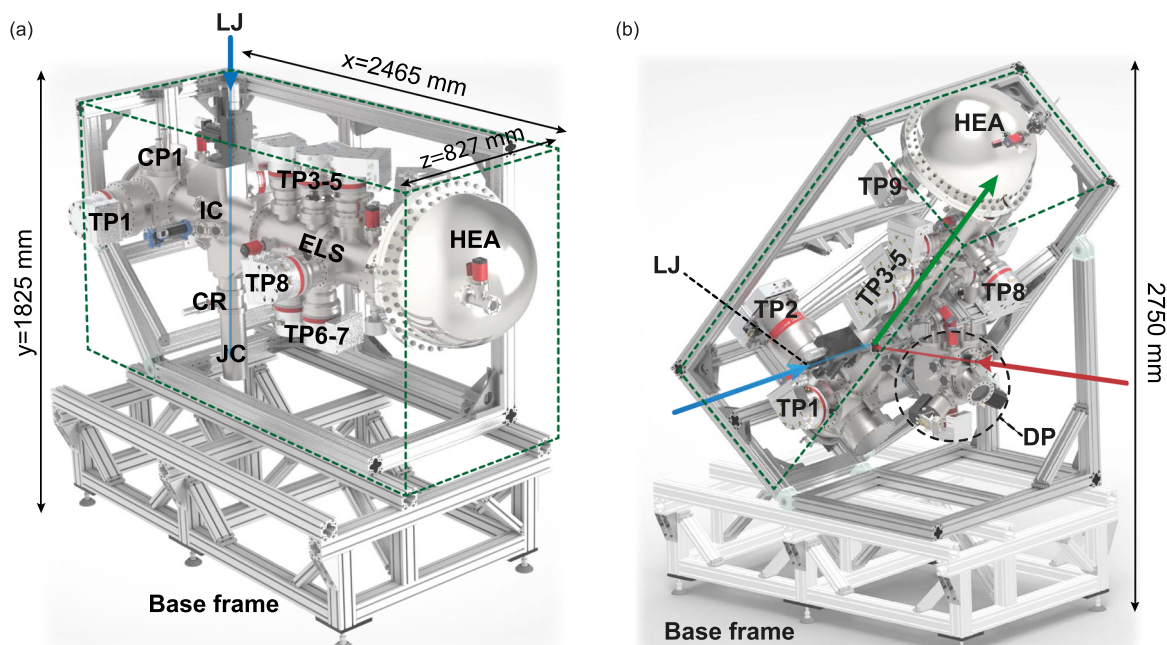


FIG. 2. Rendered drawing of EASI in its most compact (smallest enclosed volume, travel) arrangement (a) and in its “PECD-arrangement” with $\theta = 130^\circ$ (b). In the orientation shown in (a), the liquid jet (blue arrow) travels from top to bottom. The jet direction is parallel to the entrance slit into the hemisphere. In (b), the jet enters horizontally; the HEA unit is now rotated 90° about the lens axis (green arrow) such that the entrance slit is again parallel to the jet. The most important components are labeled as follows: Interaction Chamber (IC); Electron Lens System (ELS); Hemispherical Electron Analyzer (HEA); Turbomolecular Pump (TP#); Cryo Pump (CP); Ice Crusher (CR); Liquid Jet (LJ); and Jet Catching Unit (JC). The Differential Pumping (DP) stage will be shown in more detail in Fig. 4, and the mounted VUV He-discharge light source can be seen in Fig. 6. The total weight of EASI is 1232 kg; the weight of the base frame is 232 kg. Transformation between the EASI default configurations is facilitated by the compact cuboidal frame (indicated by green dashed lines), containing the core of EASI, which can be detached from its base frame to be freely moved in space. For each setting, a different side (face) of the cuboid sits on the lower base frame. The interaction region, i.e., point of ionization, is at the same vertical distance from the floor in any orientation. Lifting, tilting, and rotating the cuboid unit is typically crane-assisted.

be reduced by a factor of $|\cos(130^\circ)| \cong 0.64$ from its maximum value at $\theta = 0^\circ$ or 180° . Due to spatial constraints, especially the dimension (size) of the HEA unit and the extension of synchrotron radiation beamline components, it was technically impossible to implement the analyzer at a smaller θ -angle. Note that positioning the HEA to detect PECD electrons in the forward direction (i.e., at $\theta = 50^\circ$) is not an option because electrons cannot be detected from the far side of the liquid-jet target. This is due to the combination of strong light absorption in the dense liquid and the small electron escape depth,^{1,12} the latter making PES distinctively surface sensitive.

Our detection angle of 130° is close to a zero crossing of the second Legendre polynomial at $\theta = 180^\circ - 54.7^\circ = 125.3^\circ$ [$P_2(\cos 125.3^\circ) = 0$], with the important and favorable side effect that the angular dependence of the electron intensity on the dipolar parameter β is suppressed [Eq. (2)]. This is indeed crucial when using CPL in this “PECD” setup for achiral targets, allowing for a meaningful comparison of signal intensities arising from ionization of orbitals of different symmetry. A common application is to quantify relative intensities of different core-level peaks, often in the context of mapping solvent and solute species’ distributions in solution.^{1,2}

The aforementioned two other *EASI* configurations, corresponding to $\varphi = 54.7^\circ$ (magic angle) and 90° detection within the dipole plane [compare Fig. 1(b)], i.e., in combination with horizontally LPL, are sketched in Fig. 3. As explained above, measuring at just the magic angle is advantageous for many routine studies, while for some measurements, it is desirable to maximize or minimize relative signal contribution from a particular orbital symmetry, and this is best realized by choosing either $\varphi = 0^\circ$ or 90° .

The modular concept of *EASI* allows for a fairly easy transformation between the various geometries. In each configuration, suitable ports allow the photon beam as well as the liquid jet to enter the interaction chamber such that the ionization spot is at the same height from the floor, not requiring any height re-adjustment at a given beamline. However, when changing between

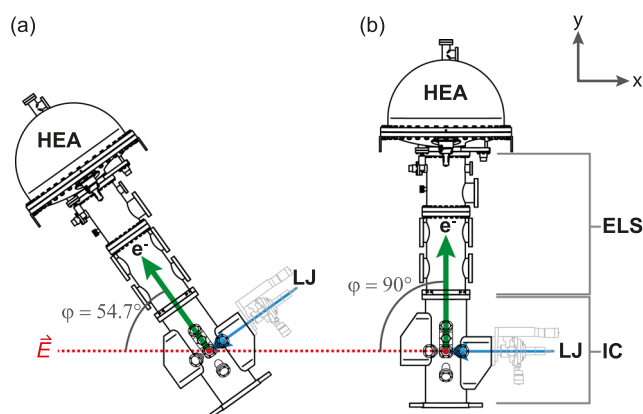


FIG. 3. Sketches showing *EASI* without the cuboidal frame in the $\varphi = 54.7^\circ$ (a) and $\varphi = 90^\circ$ (b) configurations in the x - y (dipolar) plane defined in Fig. 1(b). As in Fig. 2, in each configuration, electrons are detected perpendicular to the flow direction of the liquid jet. Red dots indicate the ionization point associated with synchrotron radiation propagating perpendicular to the figure plane, towards the observer. The horizontal electric field vector \vec{E} (in the case of horizontally LPL) is also indicated.

configurations, the system must be vented, and several components must be re-arranged or rotated. Typically, for a given experimental run period of several days or longer, a single setting is used. Switching to another setting can be completed within 3–4 h with the help of a crane, and the experiment can be resumed. Our experiments do not require any bake-out. Moreover, while the main experimental chamber is vented, the pressure inside the HEA and in the section containing the electron lens system is allowed to increase into the low mbar range. The necessary high-vacuum conditions for a LJ-PES experiment can be re-established within ~ 5 min.

We now consider Fig. 2(a) in more detail, identifying the main components of the setup. These are (i) the interaction vacuum chamber (IC), which houses the liquid microjet (LJ) and is equipped with multiple cryo- (CP) and turbomolecular pumps (TP#) (their number, #, varies upon experimental demand); (ii) the electron detector, consisting of a differentially pumped electron pre-lens system (ELS) for near-ambient-pressure operation and the hemispherical electron analyzer (HEA); (iii) a multistage differential pumping unit (DP) that is only used for studies at synchrotron facilities; and (iv) a helium-discharge, high-intensity vacuum ultraviolet (VUV) source, only mounted for laboratory studies. A description of the most-relevant components will be provided in the following subsections (Secs. II B–II F).

B. Interaction chamber

The custom-made 211-mm-diameter and 600-mm long cylindrical IC is made of grade 304 corrosion-resistant steel. A total of 11 ConFlat (CF) ports of size CF40 and four ports of size CF100 are arranged on the outer surface of the IC such that they point toward the interaction center of the chamber. Different ports can be used for photons to enter or to mount a cylindrical or flat-surface liquid microjet and the respective jet-catcher unit depending on the specific *EASI* geometric arrangement. The intended occupancy of the ports in a given geometry is indicated in Figs. 2 and 3 by the red (photon-beam axis), green (electron-detection axis), and blue (LJ-flow axis) arrows/dots.

In order to effectively shield induced magnetic fields and the Earth’s magnetic field at the interaction point (red dots in Fig. 3), which is of major concern for the quantitative detection of low-kinetic-energy electrons, we mounted an additional μ -metal superalloy shielding (μ SH), a cylindrical inset within the cylindrical IC that forms an inner layer over its entire length. Typical magnetic fields measured at the interaction point of liquid jet and light are $\sim 0.5 \mu\text{T}$ for the horizontal and $0.3 \mu\text{T}$ for the vertical components. The μ SH incorporates 13 30-mm and two 40-mm diameter holes on its surface, positioned such that the ports on the IC have an unobstructed view on the interaction point. The two larger ports are used for the liquid jet and provide enough space for its positioning. Fixations of the μ SH shield are made of titanium. At one end, the IC connects via a CF200 flange to the magnetic shield of the lens system of the analyzer, giving *EASI* the elongated appearance. A view into the IC and the μ SH, along the cylinder and electron detection axis of the hemispherical energy analyzer, is shown in Fig. 6(a).

In order to achieve a sufficient vacuum base pressure in the IC, $\sim 5 \cdot 10^{-5}$ mbar for typical liquid-jet experiments, two turbomolecular pumps [TP1 and TP2; see Fig. 2(a)] are mounted ~ 400 mm downstream of the analyzer orifice. TP1 is a 1360 l/s (Pfeiffer ATH 1603 M) TP, and TP2 is a 790 l/s (Pfeiffer HiPace[®] 800 M) TP. Each

TP is backed by one corrosion-resistant 10 l/s scroll pump (Edwards xDS35i C). Main pumping of the evaporating liquid jet is, however, accomplished by at least one additional cryo pump (CP). When operating a cylindrical microjet in the laboratory, we use a single CP, consisting of a cylindrical liquid-nitrogen (LN₂) trap made of stainless steel with a surface area of ~1000 cm². This is CP1 in Fig. 2(a). The pumping speed of CP1 for water vapor is ~10 000 l/s for a pristine trap surface,⁴¹ i.e., exceeding the capacity of TP1 and TP2 by nearly an order of magnitude. If required, for instance, when operating a liquid flatjet with much higher evaporation rates and for synchrotron-light experiments, up to three LN₂-traps can be added. Alternatively, a recirculating system for liquid collection can be used instead of a liquid-nitrogen cold trap, as we detail in Sec. II E.

C. Electron detection

The electron analyzer used with *EASI*, a Scienta Omicron HiPP-3, is a high-energy-resolution state-of-the-art HEA with 200 mm central radius of the hemisphere. It has rather similar properties as its predecessor, which has been described in detail previously.⁴² Here, we review the main features and highlight several new ones. One characteristic is the separate pre-lens that provides efficient differential pumping, in conjunction with two further differential-pressure stages within the HiPP-3 lens system, and the electron optics for PES imaging. The HEA can operate over a large pressure range, including typical 10⁻⁴ to 10⁻⁵ mbar pressures under standard liquid-jet conditions, but also sustaining pressures as high as 5–30 mbar in the IC. This enables the probing of liquid surfaces other than those associated with liquid jets or jets within some gaseous (near-ambient-pressure) environment. To provide the required vacuum conditions, each stage of the electron lens is pumped by two 255 l/s turbomolecular pumps (Pfeiffer HiPace 300 M), labeled TP3, TP4, etc., in Fig. 2(a), with each given pair of TPs being backed by one 10 l/s scroll pump (Edwards xDS35i C).

The pre-lens is equipped with a small front aperture (orifice or skimmer, representing the first differential pumping stage) at the tip of a graphite-covered titanium analyzer cone, that permits electrons to enter the analyzer. The opening angle of the front cone is 45° [see Fig. 6(b) below], which is sufficiently steep to position the liquid jet in close proximity. The slim front-cone design also provides sufficient space for the exit capillary of the He-discharge source, requiring a short working distance (see below).

Different orifice sizes are available, although we almost exclusively use an 800- μ m orifice for liquid-jet experiments. This small opening allows for an elevated maximum pressure in the IC and at the same time effectively protects the lens system from contamination arising from the volatile-sample environment. The acceptance angle is $\sim\pm 15^\circ$, with the accurate value depending on the retardation ratio, eKE/E_p (see below). In all cases, this angle is smaller than the $\pm 26.6^\circ$ geometric acceptance for the nearly point-sized liquid-jet sample in front of the 800- μ m orifice. The HiPP-3 analyzer is capable of covering a ~2–1500 eV electron kinetic-energy detection range. Extension to even higher kinetic energies can be achieved when using a higher-voltage power supply. The (pre-)lens design—having a first skimmer followed by a second one—enables operation of the analyzer in two different modes, the swift acceleration mode and the normal transmission mode. For realization of the former, the second skimmer is held at a potential, while it is grounded for the normal

mode. In the swift mode, electrons are thus accelerated as soon as they enter the analyzer, which greatly reduces the inelastic scattering of the photoelectrons with the dense water-gas environment, thus enhancing the transmission at near-ambient-pressure conditions. In addition, this mode increases the angular acceptance (an aspect less relevant when using a small entrance-cone orifice) in both ultra-high vacuum and mbar pressure conditions. In combination, this leads to an increase in signal of up to a factor of ten compared to traditional lens modes.

The energy resolution and the electron transmission are determined by the size of the entrance slit into the hemisphere (selectable between 0.1 and 4.0 mm using nine different straight slits) and by the pass energy, E_p , with the latter being restricted to pre-set values depending on the lens mode used. For instance, in the transmission mode, E_p can be selected from 20, 50, 100, 200, and 500 eV, covering an electron kinetic-energy range of 20–1500 eV. With 20 eV pass energy and 500 eV kinetic energy, an energy resolution better than 15 meV full width at half maximum (FWHM) is specified; note, however, that in the case of aqueous solutions, most PES peaks are considerably wider due to an intrinsic distribution of hydration/solvation configurations of different energies. Other available modes include the angular ($\pm 9^\circ$ parallel angular range; 100–1500 eV kinetic-energy range) and spatial (20–1500 eV kinetic-energy range) modes. The latter mode is specified to achieve a spatial resolution $<10 \mu\text{m}$ for kinetic energies below 1200 eV. For measurements from a cylindrical liquid microjet, the spatial mode is of little relevance, but this mode will be exploited in upcoming characterizations of planar microjets where several properties (including jet thickness, solute concentration, and temperature) might vary when probing the liquid sheet along the flow direction.^{43,44}

Another unique lens mode of the HiPP-3 is the UPS upgrade, which enables low-kinetic-energy measurements with high energy resolution and a simultaneous increase of electron transmission. This adds the following features: energy resolution <5 meV FWHM at 5 eV pass energy and 10 eV kinetic energy; pass energies 2, 5, 10, and 20 eV; kinetic-energy ranges of near-zero to 60 eV (UPS mode), near-zero to 100 eV (angular mode), and near-zero to 20 eV (spatial mode). It is the former mode, typically using $E_p = 20$ eV, which is indispensable for the near-threshold measurements, i.e., the main mission of *EASI*. Here, the detection of electron energies smaller than E_p is accomplished by a custom-made lens table developed by Scienta Omicron.

The actual electron detector unit at the exit of the hemisphere consists of a stack of two 40 mm-diameter microchannel plates (MCPs) in a Chevron arrangement, combined with a phosphor screen (type P46) to image the position of electron hits in two dimensions. The screen image is recorded through a viewport by a CCD camera (Basler scA 1400-17gm; acquiring 17 frames per second) placed outside of the vacuum vessel. A rectangular section of this image is divided into a maximum of 1064 energy channels in the energy-dispersive and 1000 channels in the non-dispersive direction, which for some lens modes corresponds to a spatial or angular coordinate at the interaction center. The camera may either count illuminated pixels above a certain threshold to determine the number of detected electrons (pulse-counting-mode) or generate the spectrum from interpreting the gray-scale levels of the CCD image (ADC-mode). To obtain the absolute count rate from the recorded ADC spectra, a calibration factor (multiple counting factor, MCF)

must be determined before measurements, individually for each pass energy. In routine operation, we use the gray-scale mode.

D. Differential pumping chamber

In synchrotron-radiation measurements employing a liquid jet, a highly efficient differential pumping unit (DP) must be placed between the IC and the beamline, since in the latter a pressure requirement of 10^{-9} to 10^{-10} mbar usually must be met (as compared to the typical 10^{-4} to 10^{-5} mbar pressure in the IC or considerably worse, 10^{-3} mbar, in the case of flatjets or near-ambient-pressure studies). For EASI, we designed a novel highly compact three-stage DP, which is shown in Fig. 4. The total length is only 355 mm, allowing accommodation of this unit even at beamlines with a relatively short focal length. Each stage is pumped separately. The first one, close to the interaction chamber (low-vacuum side), is pumped by one 255 l/s TP (Pfeiffer HiPace 300 M), while

the other two stages are each pumped by one 90 l/s TP (Leybold TURBOVAC 90i). All three pumps are backed by a single 10 l/s scroll pump (Edwards xDS35i C). In order to increase the pumping speed and to more efficiently pump water vapor, we additionally use two LN₂ traps (cryo pumps; CP in Fig. 4), each with a surface area of ~ 580 cm². With that, we maintain a 10^{-9} to 10^{-10} mbar pressure in the connecting beamline chamber even for mbar-range pressure in the IC.

The photon beam propagates through the DP via three 20-mm long stainless-steel capillaries, which connect the stages. On the high- and low-vacuum sides, we use a capillary of 3 and 8 mm inner diameter, respectively; the capillaries can be easily exchanged if required by the experimental conditions. To aid alignment of the whole unit, we coated the ends of the capillaries facing the beamline with fluorescence powder (Honeywell LUMINUX Green B 43-3), and the green-glowing spot allows the position of the light beam to be tracked and observed through dedicated viewports (VPs).

Two further elements for beam monitoring are mounted inside the IC: a retractable gold mesh (Precision Eforming, 333 LPI) for quantitative monitoring of the photon flux shortly downstream of the interaction point and a YAG:Ce screen for visual inspection of the photon beam shape.

E. Liquid jets and alignment

Vacuum liquid microjets are produced by pushing water (or other solvents or solutions) through a micrometer-sized orifice into vacuum.^{1,4,46} We usually use 15–30 μm inner-diameter quartz-glass capillaries of ~ 3 cm length, made in-house, to obtain cylindrical microjets. At times, we also use platinum plates (30 μm inner diameter; 2 mm outer diameter), similar to what has been reported in our early LJ-PES studies.^{47,48} Resulting jet velocities are in the 20–80 ms^{-1} range, depending on the given experimental conditions. More recently, we have also generated planar-surface microjets by colliding two cylindrical jets at a suitable angle, analogous to the design described in Ref. 44. Several different capillary materials, including quartz, have been tested. In the exemplary photoelectron spectra from a liquid-water planar jet which will be presented below, 65- μm inner-diameter polyether ether ketone (PEEK) tubes were used, at a 46° collision angle.

The liquid to be pushed through the capillary is pumped through PEEK interconnected tubing of different inner diameters, 130 and 800 μm , by a high-performance liquid chromatography pump (HPLC; Shimadzu LC-20AD), equipped with four inlets to accommodate quick switching between different solutions. A sketch of our standard liquid-jet setup is shown in Fig. 5(a). The HPLC takes in filtered solutions channeled via an in-line Shimadzu DGU-20A_{5R} degasser to enable the simultaneous preparation of different solutions. The high-pressure side of the HPLC is connected to the jet holder via ~ 5 m of PEEK tubing, which is interrupted by several Teflon[®] inter-connecting tubing segments of different inner diameter, as experience showed this to dampen occasional oscillatory throughput variations of the HPLC operating in the low-pressure regime. Under these conditions, typical flow rates are 0.4 ml/min up to 1.5 ml/min, corresponding to 5–30 bars pressure in the tubing for (cylindrical) liquid-jet experiments at solution temperatures of 10 °C. In a given set of experiments, the flow rate is typically constant, adjusted by HPLC backing pressure, which depends on

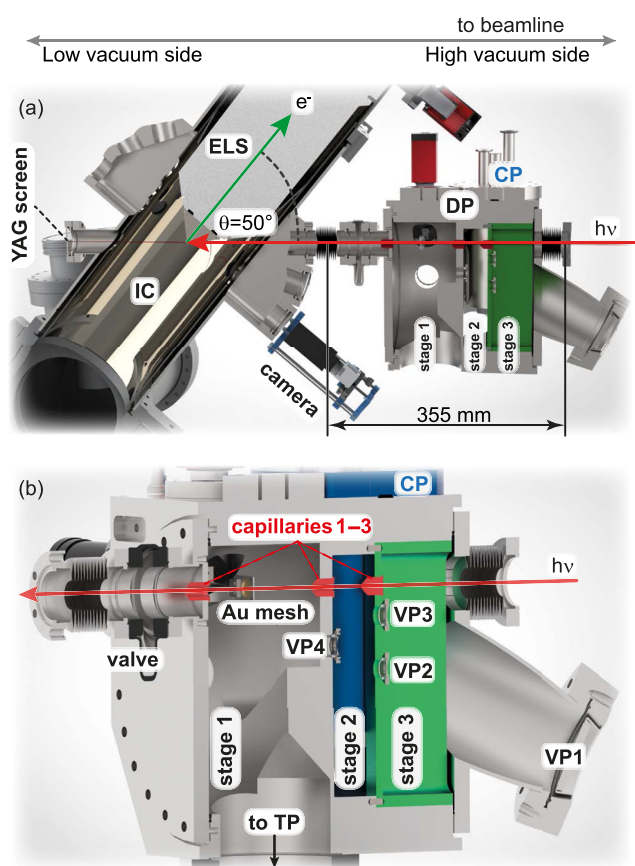


FIG. 4. (a) Sketch of the differential pumping unit (DP), including dimensions and mounting orientation onto the IC in the “PECD” configuration [compare Fig. 2(b)]. (b) Close-up view of the DP. The main components are labeled as introduced in the text: stages 1–3; view ports 1–4 (VP1, VP2, etc.); capillaries 1–3; camera; and cryo pumps (CPs; only one can be seen from this viewing angle). A single-crystal cerium (III)-doped yttrium aluminum garnet (YAG:Ce) screen of 0.1 mm thickness and 20 mm diameter is placed on the far side of the IC for visual inspection of the beam position, as it emits visible light when hit by UV light or x rays.⁴⁵

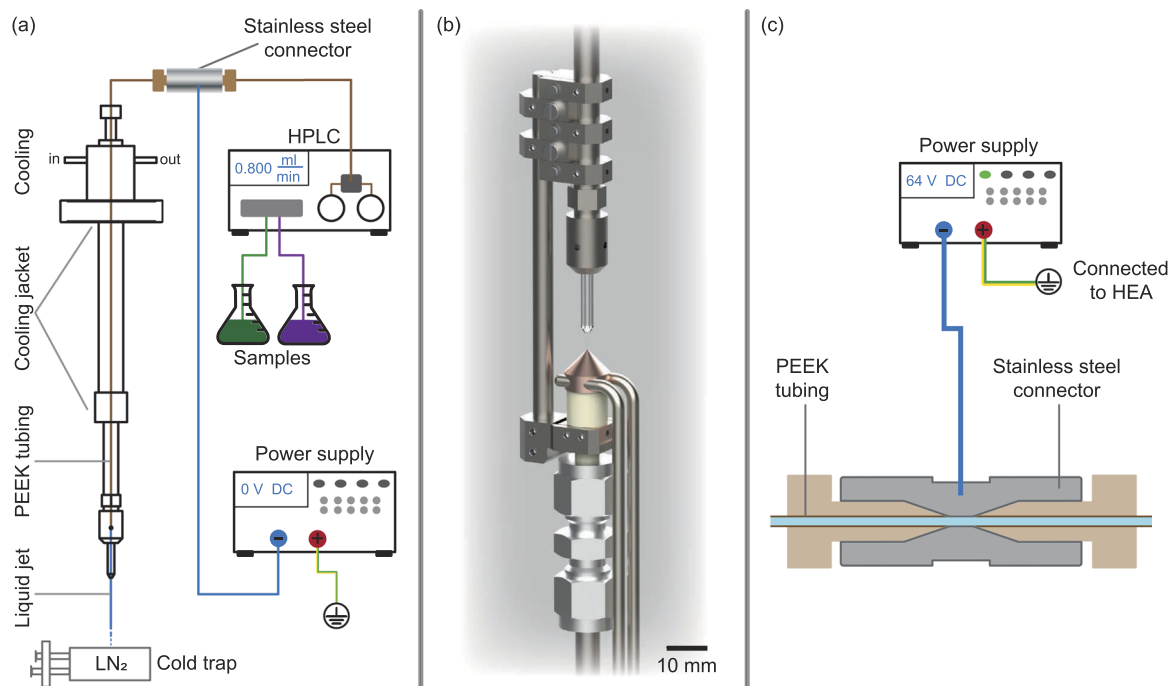


FIG. 5. (a) Schematic of the standard liquid-jet setup, showing the jet rod, HPLC pump, liquid-nitrogen cold trap, and electric connections for biasing or grounding the liquid jet. (b) Rendered graphic of a liquid-jet catcher/recirculation unit. The liquid-jet-injecting glass capillary and the jet catching cone with 500 μm orifice at <7 mm distance from the capillary tip in the direction of the flowing jet are mounted on a common support. Mutual jet and catcher positions are mechanically adjustable. The bronze catcher cone is typically held at 80 $^{\circ}\text{C}$ (associated heat pipes are shown) to prevent clogging of its orifice upon water ice formation; details of pumping on the catcher side are not shown. This slim and compact design (using several components of Microfluidics design, now Advanced Microfluidic Systems GmbH—AdMiSys)⁴⁹ fits into the same ports of the cylindrical shielding (μSH) used for jet operation without a recirculating unit. (c) Schematic of the stainless-steel connector which is in contact with the aqueous solution. For grounding the liquid jet, the connector is linked to the grounded HEA, and for biasing the jet, the connector is electrically linked to a power supply on a common ground with the HEA.

solution viscosity and temperature as well as jet diameter. Control and stabilization of the jet temperature is accomplished by flowing a water–ethanol volume mixture (30:70) through a cooling jacket of the jet rod. Toward this end, a closed-flow temperature-stabilized cycle is maintained by a chiller unit (Julabo CORIO CD-200F). Typically, the temperature is set between 4 and 20 $^{\circ}\text{C}$ depending on the experiment. A small but unquantified difference of the set temperature to the actual temperature at the point of expansion may occur because the cooling jacket ends few centimeters before the actual nozzle.

In vacuum, the produced laminar liquid microjet quickly cools by evaporation. Eventually, it disintegrates into droplets and freezes, and the resulting spray is collected downstream of the flow. For a jet traveling horizontally, we typically use a regular LN₂ cold trap of similar design as the cryo pumps described above.^{3,47} In case the jet travels vertically from top to bottom [see Fig. 2(a)], it is terminated by a steel cylinder submerged in a liquid-nitrogen bath. A noteworthy technical detail is that at some suitable position, ~ 100 mm upstream of the respective catching unit, a motorized rotating wire-frame, with a shape resembling a kitchen mixer, is placed [CR in Fig. 2(a)]. This unit nebulizes the liquid flow and prevents ice needles growing back from the cold-trap surface toward the jet capillary, i.e., opposite to the flow direction. This also helps to maintain a rather homogeneous coverage of the cold surface which slows down the

decrease in pump efficiency and considerably extends the available measurement time between venting-and-cleaning cycles.

The liquid-jet rod, the supporting metallic unit for a cylindrical single jet, consists of an inner tube with a socket to hold the quartz capillary, PEEK tubing, and an upstream connector [see Fig. 5(a)]. These parts are sleeved with an outer tube to stabilize the construction, also acting as a jacket for the coolant liquid. This whole unit, a modified Microfluidics design (now Advanced Microfluidic Systems GmbH—AdMiSys),⁴⁹ is mounted on a high-precision x-y-z-manipulator (Hositrاد, MA2000 series). All parts of the jet-assembly unit that immerse into the magnetically shielded region of the IC are made of titanium or other non-magnetic materials, typically tungsten, copper, or aluminum. Parts (except for the quartz capillary) in the vicinity of the ionization region have been graphite-coated to assure a common electric potential. All of these parts are fully electrically insulated from the liquid sample solutions. As mentioned above, we can alternatively operate the liquid jet as a recirculating system, based on collecting the liquid jet before freezing. Our system is similar to those previously reported,^{50,51} consisting of a catcher, of ~ 1 cm³ size, made of bronze which is connected via stainless-steel tubing to a solution reservoir container; see schematic in Fig. 5(b). The liquid jet shoots into the 500- μm orifice of the cone of the catcher after <7 mm travel in vacuum. The advantage of a recirculating unit, other than recycling or

recovering the solution, is the reduction of pressure in the main IC and, even more important for our experiments, the deposition of volatile species from the solution on the chamber walls can be reduced to achieve more temporally stable vacuum conditions.

Given the micrometer-sized diameter of the liquid jet, highly accurate positioning of the jet is mandatory and is accomplished using a high-precision *x-y-z* manipulator (Hositräd, MA2000 series), modified by the manufacturer to achieve a spatial resolution of $2.5\ \mu\text{m}$ with a repeatability of $1.25\ \mu\text{m}$. To visually monitor the liquid-microjet performance and its position, we use two Basler acA2440-35- μm cameras in combination with suitable telescopes. One camera (equipped with a NAVITAR NMV-100 objective and a 15-mm spacer) is aligned to the rotational symmetry axis of the electron-analyzer lens and observes whether the liquid jet is centered in front of the HEA first skimmer. The typical jet-to-skimmer distance is 500–800 μm to match the imaging distance of the HEA lens system; at the same time, this distance corresponds to a suitable electron transfer length between the liquid jet and analyzer at the typical 10^{-4} to 10^{-5} mbar water vapor pressure in the IC.¹ A view seen by this camera, although in the presence of a flatjet sample, is shown in Fig. 6(a). The other camera (combined with a RICOH FL-BC7528-9M objective) is directed at the jet and the HEA entrance cone at an angle perpendicular to the detection axis (see Fig. 4). With this combination of two cameras, we can accurately re-position the jet for each measurement, in any of *EASIS*'s geometric arrangements.

In order to obtain meaningful liquid-jet photoelectron spectra, we have to assure that the solutions have a sufficient electrical conductivity. Neat liquid water and many aqueous solutions containing no ions are, however, poorly conductive, and a tiny amount of salt needs to be added, as discussed previously.¹ Another effect of salt addition is the compensation of electrokinetic charging of the jet surface.^{52,53} In a related context, molecular dipoles at the solution surface can also give rise to surface charging. Any quantitative information on the energetics [absolute binding energies (BE)] of the ionized solute and solvent then requires that the jet is either properly grounded to the HEA or that a stable bias voltage is applied, as recently discussed.^{12,23} To connect the liquid jet to the electrostatic potential of the analyzer, we have inserted a stainless-steel through-connector (as used with HPLCs) in the high-pressure side of the PEEK line, at a few tens of millimeters upstream of the liquid-jet holder. This design, detailed in Fig. 5(c), turned out to provide a much lower contact resistance compared to earlier versions, in which the electrical contact to the solution was provided by a gold wire. For PES experiments from a biased liquid jet, the solution is fully electrically insulated from any other potential and only connected to a high-precision power supply. We use a Rohde & Schwarz HMP 4030 high-precision voltage source or for higher voltages (60–300 V) a Delta Electronics ES 0300-0.45 power supply.

F. Helium lamp

A helium plasma-discharge source (Scienta Omicron VUV5k) enables LJ-PES valence measurements in the laboratory. Here, we greatly benefit from the aforementioned HEA VUV lens-mode. This combination has been recently applied to determine absolute lowest ionization energies of water and solutes.^{23,54} The VUV5k, equipped with differential pumping, is operated with helium 6.0, and liquid

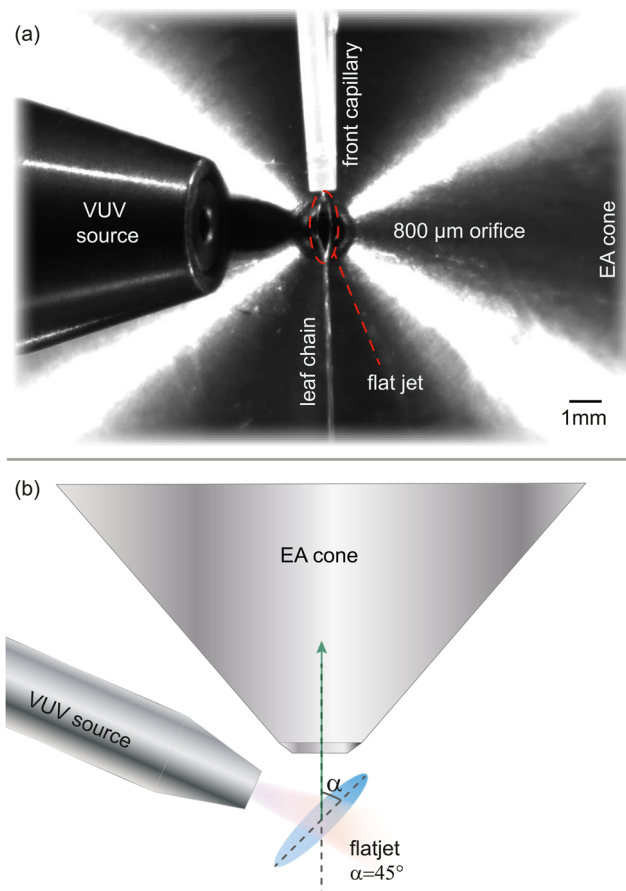


FIG. 6. (a) Photograph of the view into the IC along the lens axis of the HEA and centered on the analyzer cone with its 800- μm orifice. In front of the orifice, a water flatjet, 1.2 mm long and 0.6 mm wide, is seen. The thickness of the jet is ~ 20 – $25\ \mu\text{m}$. A subsequent chain of pairwise orthogonal leaves, forming downstream along the flow direction, is not resolved by the camera used here for jet alignment. The flatjet is formed by two colliding cylindrical jets, each with $65\ \mu\text{m}$ inner diameter and a 46° collision angle; simultaneously changing the diameters of the cylindrical jets can be used to adjust the size and thickness of the planar jet. Above the flatjet, one of the two PEEK capillaries generating the colliding cylindrical jets can be seen. At the left-hand side, the focusing capillary, receiving light from the VUV discharge source, is shown at a working distance of ~ 5 mm. The angle between the detector axis and the VUV photon beam is 110° . (b) Schematic of a top view of the same situation, showing the angle α between the surface plane of the first flatjet leaf and the direction of electron detection.

nitrogen-cooling of the connecting gas-line removes water residuals and contaminant gases. A given discharge line—we primarily use He-I α (21.218 eV), He-II α (40.814 eV), and He-II β (48.372 eV)—is selected by an $80 \times 30\ \text{mm}^2$ toroidal grating with 1200 lines/mm. The monochromatic radiation is then directed into a collimating 300- μm -inner-diameter (75-mm-long) glass capillary, producing a $300 \times 300\ \mu\text{m}^2$ focus at 5 mm focal length, which corresponds to the distance between capillary exit and liquid jet (see Fig. 6). The total photon flux at the ionization region, without grating and focusing capillary implemented, is $\sim 3 \cdot 10^{14}$ photons/s, and the flux of the focused He-I α photon beam, using the 300- μm capillary,

is specified as $\sim 1.8 \cdot 10^{11}$ photons/s. The He-II α photon flux is $\sim 1 \cdot 10^{10}$ photons/s. Both values are sufficient to acquire high-quality LJ-PE spectra,¹² an example of which will be presented below. The He light source is dismantled when performing experiments with synchrotron radiation.

III. EASI PERFORMANCE

This section presents selected aspects of the EASI instrument performance, exemplified for two applications that qualitatively extend the liquid-phase photoemission studies that had been reported hitherto. We first underpin the feasibility of studying liquid-phase PECD using EASI. In the second example, we present the outer-valence spectra of neat liquid water and of a sodium-iodide aqueous solution, here recorded from a planar liquid microjet.

A. PECD in the C 1s spectrum of gaseous and liquid fenchone

Fenchone is a chiral organic molecule, a terpene, consisting of a six-membered carbon ring stabilized by an additional carbon bridge, which contains two stereo centers, as depicted in the inset of Fig. 7. A single ring site is double-bonded to an oxygen (carbonyl group). The chiral centers are located at the positions connecting the ring and bridge; these sites are labeled with * in Fig. 7. This rigid structure of the molecule makes fenchone a suitable, prototypical system for studies of PECD, as isomerism plays a minor role; isomerism might otherwise considerably complicate the interpretation of observed emission asymmetries. After the discovery of a significant gas-phase PECD in its C 1s spectrum,¹⁸ fenchone has been used in a number of valence-level PECD studies^{55,56} as well as for exploration of more sophisticated dichroic effects upon multi-photon excitation.^{57–61}

Another noticeable aspect in the present context is that fenchone is a liquid at room temperature, with somewhat higher viscosity than liquid water, and ~ 10 -times lower vapor pressure at room temperature. Although the formation of a liquid-fenchone jet is almost as straightforward as for water, the immiscibility of fenchone with water requires that all surfaces of the jet setup in contact with the liquid must be completely water-free to avoid clogging of the quartz capillary. Unlike water, fenchone is a nonpolar molecule, which has important consequences for the interpretation of liquid-jet spectra, as discussed below.

Commercial samples of (1R, 4S)-(-)-fenchone (Sigma-Aldrich, $\geq 98\%$ purity) and (1S, 4R)-(+)-fenchone (Sigma-Aldrich, $\geq 98\%$ purity) were used in our experiments. To avoid charging of the jet (compare Sec. II E), the conductivity of liquid fenchone was increased by adding tetrabutyl-ammonium nitrate salt (TBAN) to 75 mM concentration to the liquid. We used liquid flow rates between 0.7 and 1.0 ml/min through a 28 μm glass capillary; the bath temperature upstream of the nozzle was set to 10 $^\circ\text{C}$. Very similar conditions are applied in typical LJ-PES studies from water and aqueous solutions. The liquid jet was kept at ground potential, unless otherwise stated. Experiments were conducted at the soft-x-ray beamline P04 of the PETRA III storage ring.⁶² Opposite-helicity C 1s PE spectra were sequentially recorded, repeatedly

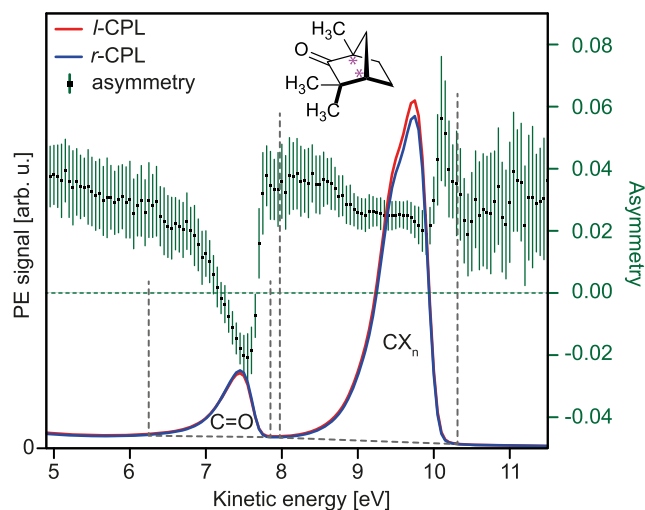


FIG. 7. Photoelectron spectra of gaseous 1R-fenchone recorded at a photon energy of 300 eV with *left-* and *right-* handed circularly polarized light, referred to the left-hand side y-axis. The asymmetry, A , of the spectra derived for every data point (symbols) is referred to the right-hand side y-axis and is not symmetric about zero because the intensities of the two different photon beams are not identical, see text for details. Two chemically shifted C 1s components near 7.4 eV (C=O site) and 9.7 eV kinetic energy (all $-\text{CX}_n$ sites; X includes carbon and hydrogen atoms) with different asymmetry are seen. The chiral centers of fenchone are labeled with * in the molecular sketch. Vertical and nearly horizontal lines indicate area intervals used for peak area determination and the respective background, see text for details. Error bars of the asymmetry designate the standard deviation of the mean values derived from the variation of the individual sweeps. The modulation of A near 10 eV kinetic energy, exhibiting a small minimum toward smaller A values with a sharp overshoot at slightly higher kinetic energy, arguably results from minute differences of the peak profiles, reflecting the slight disturbances from fluctuating potentials of a charged liquid jet in the present experiment.

switching between *l-* and *r-*CPL with helicity $p = +1, -1$ (we follow the “optical” convention).³¹ A fairly large x-ray focal spot size, 180 μm horizontal (parallel to the liquid jet) and 30–40 μm vertical, was deliberately chosen in order to minimize electron signal sweep-to-sweep fluctuations that may arise from small liquid-jet instabilities. We collected between 10 and 30 spectral sweeps for each helicity of the radiation, with the acquisition time of a single sweep being between 30 and 60 s. The HEA was operated in the novel VUV lens mode at a pass energy of 20 eV. As the absolute helicity of the undulator radiation had not been previously determined, this information could be inferred in the present study. We identified that a negative shift of the opposing magnetic arrays of the APPLE-II undulator at the P04 beamline corresponds to *l-*CPL by comparing measured asymmetries (see Fig. 7) to previous gas-phase fenchone results.¹⁸

1. Gas-phase fenchone C 1s spectra

C 1s PE spectra from gas-phase 1R-fenchone, collected from the surroundings of the liquid jet at 300 eV photon energy, are presented in Fig. 7. Signal intensities in this figure are displayed as measured. Photon energies in the present work were calibrated by a standard procedure which fixes the grating pitch angle for specular reflection and are estimated to have ± 0.2 eV accuracy in the energy

range studied. Measured kinetic energies were corrected to match the binding energies (BE) of the two main peaks, previously reported in Ref. 18. Note that the photon energy of 300 eV corresponds to ~ 7.4 eV kinetic energy of the photoelectron due to ionization of the carbonyl carbon (~ 292.6 eV BE) at which the largest PECD effect has been reported.¹⁸ Two spectrally well-separated peaks are observed in Fig. 7, which are in very good agreement with earlier results.¹⁸ The more intense peak near 9.7 eV KE (~ 290.3 eV BE) and denoted as $-CX_n$ arises from the nine energetically overlapping carbons featuring C–C or C–H bonds. The small peak is due to C 1s ionization of the carbonyl group (C=O). An important implication of the gas-phase work on core-level PECD is that the emergence of a measurable asymmetry generally is not restricted to atoms forming the chiral center of a molecule.³⁵ A PECD effect for the C=O group may therefore be expected and is discussed in detail in Ref. 18.

The intensities of spectra obtained with *l*-CPL and *r*-CPL are displayed as measured in Fig. 7. For a meaningful discussion of their intensity differences, it is useful to discuss them in a normalized form. We, therefore, display the channel-by-channel asymmetry A , defined as $(I(l\text{-CPL}) - I(r\text{-CPL})) / (I(l\text{-CPL}) + I(r\text{-CPL}))$. This quantity shows a fairly constant behavior over the $-CX_n$ peaks and a strong trend toward the opposite sign of A in the region of the non-chiral C=O carbon (Fig. 7). In order to further interpret these results, we make use of the finding of Ulrich *et al.*¹⁸ that the combined intrinsic asymmetry of the $-CX_n$ peaks cancels out to a good approximation. Indeed, within the error bars, it is hardly different from the background asymmetry. We can then use our measured value of A , which corresponds to the observed overall shift of A by about ~ 0.025 toward positive values, to quantify the instrumental asymmetry which is caused by a slight imbalance between intensities of the APPLE-II undulator at positive and negative shift. In the work of Ulrich *et al.*,¹⁸ a sophisticated scheme involving rapid alternation between two beams of opposite helicity, produced in a twin undulator, was used to achieve cancellation of these apparatus effects.²⁴ However, the asymmetry of negative sign for the carbonyl C 1s does arise from PECD.

Below, we will discuss its values, corrected such that the apparatus asymmetry of the $-CX_n$ peaks vanishes. A similar procedure was used in an early work on gas-phase core-level PECD.³⁵ The low-kinetic-energy flanks of both peaks are caused by the unresolved vibrational structure.⁶³ The slight increase in the value of A along both flanks toward lower kinetic energies is caused by a small constant background present in both spectra but with slightly different intensity, the influence of which increases with decreasing signal intensity.

In Table I, we compare results for the intrinsic chiral asymmetry parameter $b_1^{+1} = A / \cos(130^\circ)$ extracted from the spectra shown in Fig. 7, and additional measurements at photon energies of 301, 302, and 305 eV after correction for the instrumental asymmetry, to results in the literature. Here we have neglected a β -dependent correction factor in the relation between A and b_1^{+1} , which is near unity in our geometry.¹⁸ Measurements from both enantiomers were directly compared at 300 eV in the gaseous phase and at 302 eV for the liquid (yet to be discussed in detail). Values of b_1^{+1} in the present work were determined from peak areas minus a linear background between the respective vertical lines shown in Fig. 7.

The results of our few-photon-energy measurements and of the respective literature values, presented in Table I, are found to be in reasonable agreement. Note that both experiments reveal the change in sign of b_1^{+1} for 7.4 eV kinetic energy (300 eV photon energy) when switching between the two fenchone enantiomers. We also point out that the fenchone $-CX_n$ peak is somewhat better resolved in the present study, exhibiting a more structured peak top. Combined with much faster data acquisition, this opens the perspective to study sub-structures within the $-CX_n$ peak of fenchone or of congested line systems of other chiral molecules.

2. Liquid fenchone C 1s spectra

Turning now to analogous measurements from liquid fenchone, we expect that quantification of PECD will be complicated by (photo)electron scattering which occurs in any condensed matter system. Inelastic and quasi-inelastic scattering leads to the formation of an intense background at low kinetic energies,¹² which inevitably

TABLE I. PECD parameter b_1^{+1} of the carbonyl C 1s photoemission line of both enantiomers of fenchone measured at different photon energies. Results for the gaseous phase are compared to Ref. 18. Literature values in parentheses were obtained by interpolation between the nearest reported energies. An uncertainty of ~ 0.004 – 0.007 in the values for b_1^{+1} is found from the sweep-to-sweep fluctuations in our study and corresponds to the approximate size of error bars shown in Ref. 18. 1R-fenchone is used as a shorthand notation for (1R, 4S)-(–)-fenchone and 1S-fenchone for (1S, 4R)-(+)–fenchone. The value given for liquid-phase fenchone has not been corrected for the presence of gaseous components; see the main body of the text for details.

| Phase | Enantiomer | KE (eV) | $h\nu$ (eV) | b_1^{+1} (this work) | b_1^{+1} (Ref. 18) |
|--------------------|-------------|---------|-------------|------------------------|----------------------|
| Gaseous | 1R-fenchone | 7.4 | 300 | 0.067(6) | 0.069, 0.086 |
| | 1S-fenchone | 7.4 | 300 | –0.084(5) | –0.072, –0.078 |
| | 1S-fenchone | 8.4 | 301 | –0.085(7) | (–0.070) |
| | 1S-fenchone | 9.4 | 302 | –0.050(4) | (–0.045) |
| | 1R-fenchone | 12.4 | 305 | 0.019(4) | 0.032 |
| Liquid + gas-phase | 1R-fenchone | 9.4 | 302 | 0.02 | ... |
| | 1S-fenchone | 9.4 | 302 | –0.02 | ... |

overlaps with photoelectron peaks when measured near a given photoionization threshold energy (as is the case here). We have recently shown for neat liquid water that the presence of such scattering channels significantly perturbs the native photoelectron peak shape and also affects the peak center position, making a meaningful determination of the energetics futile below ~ 10 eV kinetic energy.¹² An exact value of this limiting kinetic energy for liquid fenchone has not been determined, but, indeed, the existence of a strong scattering background is a major challenge for PECD measurements from liquid fenchone and aqueous solution alike.

C 1s PE spectra of a grounded liquid jet from 1R-fenchone, measured at 302 eV photon energy with *l*- and *r*-CPL, respectively, are shown in Fig. 8. At this photon energy, the lower-kinetic-energy C 1s peak of C=O from liquid fenchone can still be resolved at ~ 9.5 eV KE atop of the inelastic background. At a slightly lower photon energy of 300 eV, as used for the measurements on gas-phase fenchone (Fig. 7), the C 1s peak of C=O could not well be separated from the large scattering background (not shown here), illustrating the detrimental impact of electron scattering at these low energies. Noticeably, the liquid-phase spectra exhibit a similar effect of the CPL helicity on the intensity. Again, the main C 1s peak exhibits higher intensity for *l*-CPL originating from the same instrumental effect, but the respective flipped intensities of the C=O peak are only revealed upon spectral analysis. Performing the analogous analysis as for the gas phase, we find the respective liquid-phase asymmetry values which are presented in Table I. These values have the same sign as the gas-phase asymmetries but are smaller by a factor of ~ 2.5 . Quantitative results strongly depend on the exact choice of the background model though, with one possible approach sketched in Fig. 8. A more elaborate analysis will be presented in a forthcoming work. We also note that our simple analysis does not account for possible ordering of molecules at the liquid–vacuum interface, in which case the angular distributions may be affected considerably.³⁸ Such

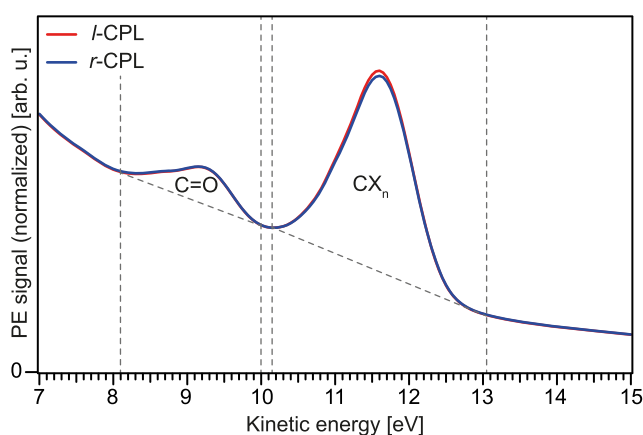


FIG. 8. C 1s photoelectron spectra from liquid 1R-fenchone recorded at a photon energy of 302 eV with left and right circularly polarized light. The liquid-fenchone temperature was stabilized to 10 °C. The large background signal (dashed line) arises from electron scattering in the liquid. Spectra were normalized to equal total area to visually suppress a small, non-essential variation of the background height when changing helicity.

a contribution cannot be quantified here, but a previous PAD study from liquid water⁶⁴ suggests that for a cylindrical liquid jet, orientation effects average out, and PADs can be well described using the expression for randomly oriented species.

An additional problem, not anticipated at the beginning of this study, is the fact that fenchone gas- and liquid-phase spectral features appear at very similar kinetic (or binding) energies. This is not the case for the core-level ionization of water, where the gas-phase O 1s peak occurs at ~ 1.8 eV lower kinetic energies than the corresponding liquid-phase O 1s peak maximum.⁶⁵ The absence of an energy shift between the liquid and the gaseous component in the case of a grounded fenchone jet reflects the nonpolar nature of this molecule and is evidence that intermolecular interactions in the liquid phase are very weak. This makes the quantification of liquid-phase PECD more complicated, as a quantitative subtraction of the overlapping gas-phase signal contribution is required. The vapor pressure of fenchone, however, is much lower than the one of water, with 0.3 and 0.7 mbar at temperatures of 10 and 20 °C, which is the stabilized temperature of our sample cooling bath and the estimated maximum of the actual temperature at the glass capillary, respectively.⁶⁶ Corresponding values for water are 12.3 and 23.4 mbar. For a pure water jet, a gas-phase component as small as 5% of the total water O 1s signal can be obtained when the light focus matches the liquid-jet diameter. We aimed to find the analogous gas-phase contribution in the liquid fenchone C 1s spectrum in a separate experiment.

Gas- and liquid-phase PE signals can be separated spectrally by applying an electric bias voltage to the liquid-fenchone jet. Only the liquid-phase features experience the full energy shift from the applied potential. The gas-phase spectrum, on the other hand, experiences a smaller energy shift accompanied by spectral broadening since the strength of the accelerating field decreases with distance from the liquid jet, and electrons from the gaseous species pick up less energy on average.²³ In Fig. 9(a), we show a PE spectrum from 1R-fenchone, measured with a grounded liquid jet at a considerably higher photon energy of 350 eV (blue trace), using *l*-CPL. At this energy, the photoelectron spectrum is well separated from the electron scattering background tail, and the $-CX_n$ peak maximum now occurs at 59.3 eV kinetic energy, as measured without any energy correction applied. The PE spectrum from the biased liquid jet [red trace in Fig. 9(a)] exhibits four, instead of two, peaks, with the main CX_n peak shifted by 3.02 eV toward higher kinetic energy. This energy shift is considerably smaller than the actual applied bias voltage of -10 V, implying resistive losses. Overall, we observe two liquid-phase peaks at 60.6 and 58.3 eV KE, and two less intense peaks separated from the former by 1.3 eV in KE each, i.e., at 59.3 and 57.0 eV KE. We assign these two peaks as the gas-phase components. In Fig. 9(b), the biased spectrum (red dots) is shifted by 3.02 eV toward lower KE to show the liquid-phase contribution atop of the original, unbiased measurement (blue dots). We note that such rigid spectral shifts cannot be properly energy-referenced here as this would require the additional measurement of the liquid's low-energy cutoff, as discussed in Ref. 23. The observed 1.3-eV spectral separation between the liquid- and gas-phase peaks can be assigned to the difference in accelerating field strength directly at the liquid surface (for electrons originating from the liquid phase) compared to some distance away from the liquid-fenchone jet (for electrons from the gas phase). The bias-induced peak separation, therefore,

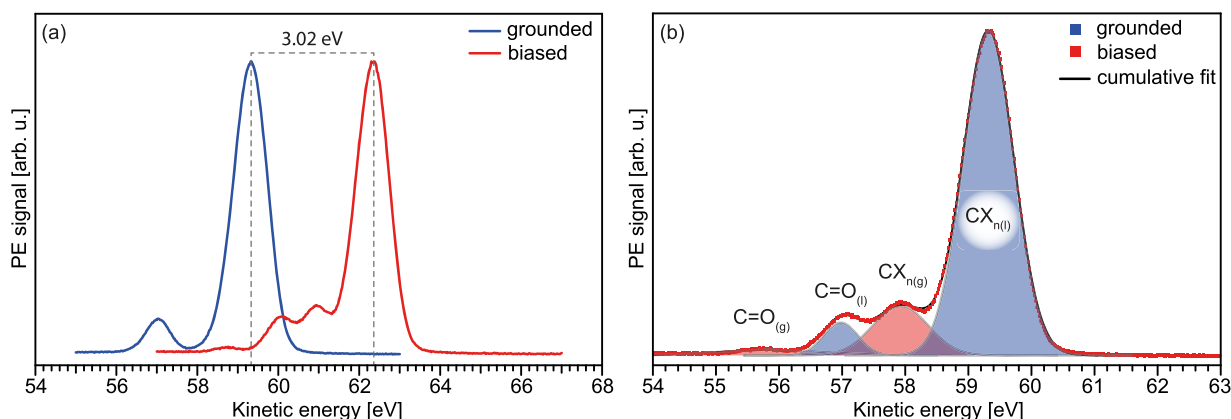


FIG. 9. (a) C 1s photoelectron spectra from liquid 1R-fenhone recorded at a photon energy of 350 eV for a grounded liquid jet (in blue) and with an effective bias voltage of -3.02 V. Both the gas and liquid-phase peaks are affected by the bias voltage, but electrons from the gaseous species experience less overall acceleration in the less negative electric potential some distance away from the liquid jet, which resulted in a peak separation of ~ 1.3 eV between the peaks of both phases. (b) The spectrum from the biased jet has been shifted by -3.02 eV such that the liquid-phase peaks overlap for the unbiased and biased spectra. Intensities are displayed to yield the same height of the main peak. See the main text for details.

enables us to quantify the relative gas- and liquid-phase signal contributions in our PECD measurements under the given experimental conditions. For a relatively large focal spot size present in this experiment [$180 \mu\text{m}$ horizontal size, $75(\pm 10) \mu\text{m}$ vertical size], we find a gas-phase contribution of $\sim 14\%$, inferred from a peak-area analysis. This implies that the observed PECD effect contains some contributions from the gas phase and that the pure liquid-phase effect is likely smaller than stated in Table I. If we assume 14% -gas-phase signal contribution in our liquid-phase spectra, we arrive at a corrected b_1^{+1} value with a magnitude between 0.010 and 0.012 at 302 eV for pure liquid fenhone. We believe that this estimate of the reduction in the value of b_1^{+1} is conservative for two reasons: (1) The actual liquid-fenhone measurements were done with a smaller vertical focus size of $30\text{--}40 \mu\text{m}$ (and thus a reduced gas-phase fraction). (2) At similar conditions to the ones at which the gas-phase contribution for fenhone was determined, we find a gas-phase contribution of only 11% for a water jet. This last result is at odds with expectations from the relative partial gas pressures of the two solutions but is additional evidence that our experiment provides an upper bound for the fenhone gas-phase fraction.

A quantitative analysis of the background shape and the gas-phase contribution to the measured liquid asymmetries is beyond the scope of this work and will be presented in a separate publication. Although values given in Table I should grossly reflect the magnitude of the PECD effect, more accurate values remain to be determined.

In upcoming studies, we will also explore aqueous solutions, initially of chiral amino acids, where we aim to characterize the potential role of interaction with solvation-shell water molecules on PECD. Studying such aqueous solutions has the benefit that the solute contributes minimally to the gas-phase spectrum. Furthermore, future PECD studies from solution will need to address possible interfacial molecular alignment, which to some extent can be explored by comparative measurements from a planar (flat) liquid jet.

B. Valence spectra from a liquid water flatjet obtained with He-II α radiation

Over the years, several studies reported valence photoelectron spectra from liquid water.^{48,67–69} However, to the best of our knowledge, all previously reported measurements were performed from a cylindrical liquid microjet. Indeed, cylindrical jets are easier to operate, and the smaller surface area results in a lower water-vapor background pressure; with a cylindrical jet installed, we achieve 10^{-5} mbar in the IC of EASI. In conjunction with a micrometer-sized focus of the photon beam, approximately matching the liquid-jet diameter, almost pure liquid-phase photoelectron spectra can be obtained, with gas-phase contributions as low as 5% , as mentioned earlier.^{53,70}

Yet, the curvature of a cylindrical jet implies that the measured photoelectron spectrum is an integration over all take-off angles of the photoelectrons relative to the water surface. Information related to a specific orientation of water or solvent molecules at the surface, as observed in other techniques,^{71–76} is thus lost. Specifically, regarding PAD measurements from a cylindrical liquid jet, elastic electron scattering^{12,64} will contribute differently to the measured photoelectron signal intensity, which will be dependent on the unresolved take-off angle.

Being able to perform PAD measurements from a planar water surface of sub- $20 \mu\text{m}$ thickness is therefore highly desirable and has motivated us to construct a flatjet system compatible with the spatial constraints of the EASI interaction chamber (see Sec. II E). With this system, we also expect to step into novel future applications for flatjets in PES (and other x-ray spectroscopies), which are currently emerging. This would include their use in a (to be developed) liquid-jet velocity map imaging detector (LJ-VMI) or in non-linear-optical studies requiring a flat and clean solution surface, and potentially in the context of gas–liquid–surface interaction experiments, and even exploring liquid–liquid interfaces. Another very recently discussed issue is the ability to access solution work functions²³ which would

also greatly benefit from a planar surface for the same reasons. Yet, it remains to be explored to what extent the higher gas-phase density above the flatjet surface affects the native liquid-phase PADs.

In Fig. 10(a), we show valence PE spectra from a water flatjet (see details in the caption) measured with 40.814 eV (He-II α) radiation in the EASI laboratory arrangement. Results are presented for three take-off angles [see Fig. 6(b)], $\alpha = 30^\circ$, 45° , and 60° , with

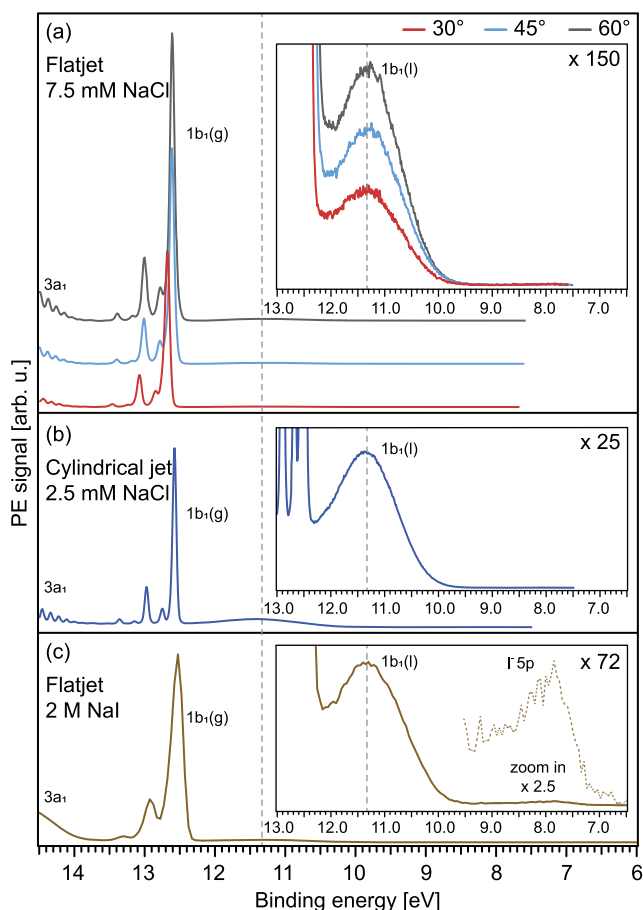


FIG. 10. (a) $1b_1$ valence PE spectra from a liquid water (with 7.5 mM NaCl) flatjet measured with He-II α radiation (40.814 eV) at angles $\alpha = 30^\circ$, 45° , and 60° ; see Fig. 6 and Sec. II E for experimental details. The broad small peak at 11.33 eV binding energy²³ (shown enlarged in the inset) is due to liquid water, $1b_1(l)$, and all other spectral contributions largely arise from ionization of gas-phase water, $1b_1(g)$. (b) PE spectrum as above but replacing the flatjet by a 28- μm -diameter cylindrical jet. Note that lower salt concentration, 2.5 mM NaCl, is needed to compensate for electrokinetic charging. This is due to different capillary materials and flow rates used for cylindrical vs flatjets. (c) Spectrum from a flatjet, as in the upper panel, at $\alpha = 45^\circ$ but from a high-concentration 2 M NaI aqueous solution, exhibiting a weak I⁻ 5p (aq.) signal near 8.2 eV binding energy. For convenience, the spectrum was shifted such that the water $1b_1(l)$ peaks of all spectra shown in the figure align at the same binding energy of 11.33 eV; note that the true water $1b_1(l)$ energy for this particular solution is 11.38 eV.⁵⁴ The small energy shift and increase of width of the gas-phase peak from the concentrated aqueous solution arises from surface charges and hence from an electric field between flatjet surface and electron analyzer.

respect to the flatjet surface; implicitly, rotating the flatjet at a fixed analyzer position also changes the angle of the incident photon beam relative to the water surface. We display only the region of ionization of water's highest-occupied molecular orbital (HOMO), $1b_1$. The spectra are dominated by the vibrationally resolved $1b_1(g)$ gas-phase signal contributions, originating at 12.6 eV,⁷⁷ and the $1b_1(l)$ emission from liquid water gives rise to a small signal at the lowest binding energy, shifted here to occur at 11.33 eV.²³ A zoom into the $1b_1(l)$ region is shown in the inset of Fig. 10(a). An observed relative increase of the liquid-phase signal of $\sim 20\%$ for a larger detection angle (toward normal emission from the surface) results from the larger illuminated surface area for increasing grazing incidence angles. For comparison, Fig. 10(b) shows a PE spectrum from a cylindrical 28- μm -diameter liquid-water jet, again measured using He-II α radiation. One observes an ~ 7 – 8 -times decrease in the gas-to-liquid signal ratio due to the—relatively—reduced evaporation from the cylindrical jet. This is accompanied by an approximately 10-fold increase in water vapor pressure when exchanging the cylindrical jet for the flatjet (without additional cryo-pumping). The overall large gas-phase signal in all spectra of Fig. 10 results from the much larger focal size of the He-II photon beam compared to the jet diameter and light foci available at synchrotron-radiation beamlines.

We note that the ability to achieve vibrational resolution of the gas-phase PE spectrum of water implies that electric fields between the liquid jet and the electron detector have been quantitatively compensated, referred to as field-free conditions. In the case of the cylindrical jet, this was accomplished by dissolving 2.5 mM NaCl in water, while for the flatjet, a higher concentration of 7.5 mM was needed due to the different capillary materials and flow rates employed; see the associated comment in Sec. II E. Establishing field-free electron detection conditions from water microjets and the implications thereof are discussed in Ref. 23.

The most important conclusion from Fig. 10(a) is that measurements of PE spectra from aqueous-solution flatjets are straightforward and can be routinely conducted even in the laboratory using a commercial (differentially pumped) He-discharge VUV source. More generally, routine lab-based LJ-PES measurements are very feasible and useful as we have recently demonstrated in a study of absolute ionization energies and solution work function using cylindrical jets.^{23,54} Note also that the 40.814-eV photon energy is just large enough to enable detection of the full liquid-water outer-valence band, including the $1b_2$ and $3a_1$ water orbitals. That is, the kinetic energies of the respective photoelectrons are above the aforementioned 10–12 eV limit, below which the native photoelectron peaks are highly perturbed and cannot be fully resolved. With reference to Fig. 9, we note that application of a bias voltage equally works for a liquid-water flatjet and should enable spectral separation of liquid-phase from gas-phase features. In fact, if the bias voltage is large enough, an essentially gas-phase-free PE spectrum can be obtained, so far demonstrated only for cylindrical jets though.^{23,54} Hence, (disturbing) large gas-phase spectral contributions in Fig. 10 can be expected to be elegantly and almost quantitatively removed. We conclude by presenting a valence PE spectrum from a flatjet from an aqueous solution in Fig. 10(c), exemplified here for 2 M NaI measured with the same 40.814 eV. This particular spectrum was measured for eight minutes, which is sufficient to detect the iodide I⁻ 5p_{1/2} and I⁻ 5p_{3/2} signal.²³ Systematic and high-signal-to-noise

PE spectra from flatjets of different solutions will be presented in an upcoming work.

IV. SUMMARY

We have presented a unique experimental setup, *EASI*, with all major components, that enables PECD and regular PAD measurements, associated with the chiral b_1 and non-chiral b_2 anisotropy parameters, respectively, from liquid microjets of (aqueous) solutions. *EASI*'s principal configurations—one for PECD and three for regular PAD measurements—and how transformation between those configurations is accomplished time-effectively and with rather little effort have been described in detail. Regarding *EASI*'s performance, near-ionization-threshold C 1s photoelectron spectra from 1S- and 1R-gas-phase and liquid fenchone for different helicities of circularly polarized soft x rays have been presented. This aspect of our work shows the feasibility of liquid-jet PECD studies, also highlighting the difficulty of quantifying PECD for a non-polar liquid. Our results encourage studies from chiral molecules in aqueous solutions. With respect to laboratory experiments, conducted in conjunction with a commercial VUV light source, we have presented photoelectron spectra from a planar microjet (flatjet) for the first time, exemplified here for neat liquid water and NaI aqueous solution. Planar jets will play a crucial role in developing the field of PADs from liquid surfaces—but in conjunction with small focal sizes of extreme ultraviolet (XUV) to soft-x-ray beamlines—and also in designing novel efficient detectors, simultaneously collecting signal over a large electron emission angle.

ACKNOWLEDGMENTS

The authors would like to thank Laurent Nahon, Ivan Powis, Stephan Thürmer, and Iain Wilkinson for the many stimulating discussions, particularly in the planning and commissioning phase of *EASI*. We also thank Stephan Thürmer and Iain Wilkinson for critical reading of and comments on this manuscript, as well as their assistance with the collection and processing of the fenchone data. We further acknowledge discussions with Oleg Kornilov and his team regarding the construction of the jet recirculation system. B.W. acknowledges funding from the European Research Council (ERC) under the European Union's Horizon 2020 research and innovation program under Grant Agreement No. GAP 883759—AQUACHIRAL. S.M., U.H., and B.W. acknowledge support from the Deutsche Forschungsgemeinschaft (Grant No. Wi 1327/5-1). F.T. and B.W. acknowledge support from the MaxWater initiative of the Max-Planck-Gesellschaft. All authors acknowledge DESY (Hamburg, Germany), a member of the Helmholtz Association HGF, for the provision of experimental facilities. Parts of this research were carried out at PETRA III and we would like to thank Moritz Hoesch in particular, as well as the whole beamline staff, the PETRA III chemistry laboratory, and crane operators for assistance in using the P04 soft x-ray beamline. Beamtime was allocated for proposal II-20180012 (LTP). Additionally, we thank the FHI workshop for supporting us with the technical realization, especially for last-minute modifications of the setup. We acknowledge discussions with Vincent Lehane (Scienta Omicron, Uppsala, Sweden) for providing a custom-made lens table that enables the quantitative detection of the full low-energy tail of the photoelectrons from liquid jets.

AUTHOR DECLARATIONS

Conflict of Interest

The authors have no conflicts to disclose.

DATA AVAILABILITY

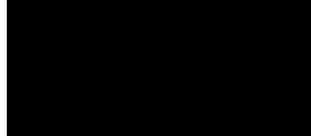
The data that support the findings of this study are openly available at <http://doi.org/10.5281/zenodo.5730418>.

REFERENCES

- ¹B. Winter and M. Faubel, *Chem. Rev.* **106**(4), 1176 (2006).
- ²R. Dupuy, C. Richter, B. Winter, G. Meijer, R. Schlögl, and H. Bluhm, *J. Chem. Phys.* **154**(6), 060901 (2021).
- ³B. Winter, *Nucl. Instrum. Methods Phys. Res., Sect. B* **601**(1–2), 139 (2009).
- ⁴R. Seidel, S. Thürmer, and B. Winter, *J. Phys. Chem. Lett.* **2**(6), 633 (2011).
- ⁵R. Seidel, B. Winter, and S. E. Bradforth, *Annu. Rev. Phys. Chem.* **67**, 283 (2016).
- ⁶S. Malerz, K. Mudryk, L. Tomanik, D. Stemer, U. Hergenhahn, T. Buttersack, F. Trinter, R. Seidel, W. Quevedo, C. Goy, I. Wilkinson, S. Thürmer, P. Slavíček, and B. Winter, *J. Phys. Chem. A* **125**(32), 6881 (2021).
- ⁷N. Ottosson, K. J. Børve, D. Spångberg, H. Bergersen, L. J. Sæthre, M. Faubel, W. Pokapanich, G. Öhrwall, O. Björneholm, and B. Winter, *J. Am. Chem. Soc.* **133**(9), 3120 (2011).
- ⁸D. Nolting, E. F. Aziz, N. Ottosson, M. Faubel, I. V. Hertel, and B. Winter, *J. Am. Chem. Soc.* **129**(45), 14068 (2007).
- ⁹N. Ottosson, M. Faubel, S. E. Bradforth, P. Jungwirth, and B. Winter, *J. Electron Spectrosc. Relat. Phenom.* **177**(2–3), 60 (2010).
- ¹⁰S. Ghosal, J. C. Hemminger, H. Bluhm, B. S. Mun, E. L. D. Hebenstreit, G. Ketteler, D. F. Ogletree, F. G. Requejo, and M. Salmeron, *Science* **307**(5709), 563 (2005).
- ¹¹T. Jahnke, U. Hergenhahn, B. Winter, R. Dörner, U. Fröhling, P. V. Demekhin, K. Gokhberg, L. S. Cederbaum, A. Ehresmann, A. Knie, and A. Dreuw, *Chem. Rev.* **120**(20), 11295 (2020).
- ¹²S. Malerz, F. Trinter, U. Hergenhahn, A. Ghrist, H. Ali, C. Nicolas, C.-M. Saak, C. Richter, S. Hartweg, L. Nahon, C. Lee, C. Goy, D. M. Neumark, G. Meijer, I. Wilkinson, B. Winter, and S. Thürmer, *Phys. Chem. Chem. Phys.* **23**(14), 8246 (2021).
- ¹³P. van der Straten, R. Morgenstern, and A. Niehaus, *Z. Phys. D: At., Mol. Clusters* **8**(1), 35 (1988).
- ¹⁴M. Y. Kuchiev and S. A. Sheinerman, *Usp. Fiz. Nauk* **158**(3), 353 (1989).
- ¹⁵M. H. M. Janssen and I. Powis, *Phys. Chem. Chem. Phys.* **16**(3), 856 (2014).
- ¹⁶L. Nahon, G. A. Garcia, H. Soldi-Lose, S. Daly, and I. Powis, *Phys. Rev. A* **82**(3), 032514 (2010).
- ¹⁷I. Powis, C. J. Harding, S. Barth, S. Joshi, V. Ulrich, and U. Hergenhahn, *Phys. Rev. A* **78**(5), 052501 (2008).
- ¹⁸V. Ulrich, S. Barth, S. Joshi, U. Hergenhahn, E. Mikajlo, C. J. Harding, and I. Powis, *J. Phys. Chem. A* **112**(16), 3544 (2008).
- ¹⁹G. A. Garcia, L. Nahon, C. J. Harding, and I. Powis, *Phys. Chem. Chem. Phys.* **10**(12), 1628 (2008).
- ²⁰A. T. J. B. Eppink and D. H. Parker, *Rev. Sci. Instrum.* **68**(9), 3477 (1997).
- ²¹J. Long, Z. Qiu, J. Wei, D. Li, X. Song, B. Jin, and B. Zhang, *Rev. Sci. Instrum.* **92**(6), 065108 (2021).
- ²²M. Tia, M. Pitzer, G. Kastirke, J. Gatzke, H.-K. Kim, F. Trinter, J. Rist, A. Hartung, D. Trabert, J. Siebert, K. Henrichs, J. Becht, S. Zeller, H. Gassert, F. Wiegandt, R. Wallauer, A. Kuhlins, C. Schober, T. Bauer, N. Wechselberger, P. Burzynski, J. Neff, M. Weller, D. Metz, M. Kircher, M. Waitz, J. B. Williams, L. P. H. Schmidt, A. D. Müller, A. Knie, A. Hans, L. Ben Ltaief, A. Ehresmann, R. Berger, H. Fukuzawa, K. Ueda, H. Schmidt-Böcking, R. Dörner, T. Jahnke, P. V. Demekhin, and M. Schöffler, *J. Phys. Chem. Lett.* **8**(13), 2780 (2017).
- ²³S. Thürmer, S. Malerz, F. Trinter, U. Hergenhahn, C. Lee, D. M. Neumark, G. Meijer, B. Winter, and I. Wilkinson, *Chem. Sci.* **12**(31), 10558 (2021).
- ²⁴C. J. Harding, E. Mikajlo, I. Powis, S. Barth, S. Joshi, V. Ulrich, and U. Hergenhahn, *J. Chem. Phys.* **123**(23), 234310 (2005).

- ²⁵T. Tanaka and H. Kitamura, *Nucl. Instrum. Methods Phys. Res., Sect. A* **449**(3), 629 (2000).
- ²⁶S. Sasaki, *Nucl. Instrum. Methods Phys. Res., Sect. A* **347**(1–3), 83 (1994).
- ²⁷J. J. Yeh and I. Lindau, *At. Data Nucl. Data Tables* **32**(1), 1 (1985).
- ²⁸U. Becker and D. A. Shirley, *VUV and Soft X-Ray Photoionization* (Springer, 1996), pp. 135–180.
- ²⁹S. Gozem, R. Seidel, U. Hergenhanh, E. Lugovoy, B. Abel, B. Winter, A. I. Krylov, and S. E. Bradforth, *J. Phys. Chem. Lett.* **11**(13), 5162 (2020).
- ³⁰T. Lewis, B. Winter, S. Thürmer, R. Seidel, A. B. Stephansen, J. A. Freitas, D. J. Tobias, and J. C. Hemminger, *J. Phys. Chem. C* **123**(13), 8160 (2018).
- ³¹M. Born and E. Wolf, *Principles of Optics: Electromagnetic Theory of Propagation, Interference and Diffraction of Light*, 7th ed. (Cambridge University Press, Cambridge, 1999).
- ³²K. Hosaka, J. Adachi, A. V. Golovin, M. Takahashi, T. Teramoto, N. Watanabe, A. Yagishita, S. K. Semenov, and N. A. Cherepkov, *J. Phys. B: At., Mol. Opt. Phys.* **39**(2), L25 (2006).
- ³³K. Hosaka, J. Adachi, A. V. Golovin, M. Takahashi, T. Teramoto, N. Watanabe, T. Jahnke, T. Weber, M. Schöffler, L. Schmidt, T. Osipov, O. Jagutzki, A. L. Landers, M. H. Prior, H. Schmidt-Böcking, R. Dörner, A. Yagishita, S. K. Semenov, and N. A. Cherepkov, *Phys. Rev. A* **73**(2), 022716 (2006).
- ³⁴B. Ritchie, *Phys. Rev. A* **14**(1), 359 (1976).
- ³⁵U. Hergenhanh, E. E. Rennie, O. Kugeler, S. Marburger, T. Lischke, I. Powis, and G. Garcia, *J. Chem. Phys.* **120**(10), 4553 (2004).
- ³⁶J. Cooper and R. N. Zare, *J. Chem. Phys.* **48**(2), 942 (1968).
- ³⁷V. Schmidt, *Electron Spectrometry of Atoms Using Synchrotron Radiation* (Cambridge University Press, Cambridge, 2009).
- ³⁸K. L. Reid, *Annu. Rev. Phys. Chem.* **54**, 397 (2003).
- ³⁹B. Ritchie, *Phys. Rev. A* **13**(4), 1411 (1976).
- ⁴⁰I. Powis, *J. Chem. Phys.* **112**(1), 301 (2000).
- ⁴¹W. Schwarz, *J. Vac. Sci. Technol. A* **5**(4), 2568 (1987).
- ⁴²J. T. Newberg, J. Åhlund, C. Arble, C. Goodwin, Y. Khalifa, and A. Broderick, *Rev. Sci. Instrum.* **86**(8), 085113 (2015).
- ⁴³J. W. M. Bush and A. E. Hasha, *J. Fluid Mech.* **511**, 285 (2004).
- ⁴⁴M. Ekimova, W. Quevedo, M. Faubel, P. Wernet, and E. T. J. Nibbering, *Struct. Dyn.* **2**(5), 054301 (2015).
- ⁴⁵G. Blasse and A. Bril, *Appl. Phys. Lett.* **11**(2), 53 (1967).
- ⁴⁶M. A. Brown, M. Faubel, and B. Winter, *Annu. Rep. Prog. Chem., Sect. C: Phys. Chem.* **105**, 174 (2009).
- ⁴⁷M. Faubel, B. Steiner, and J. P. Toennies, *J. Chem. Phys.* **106**(22), 9013 (1997).
- ⁴⁸B. Winter, R. Weber, W. Widdra, M. Dittmar, M. Faubel, and I. V. Hertel, *J. Phys. Chem. A* **108**(14), 2625 (2004).
- ⁴⁹MicroLiquids, now Advanced Microfluidic Systems GmbH–AdMiSys, <https://admisys-gmbh.com/>, 2021-08-03.
- ⁵⁰J. W. Riley, B. Wang, M. A. Parkes, and H. H. Fielding, *Rev. Sci. Instrum.* **90**(8), 083104 (2019).
- ⁵¹E. Pellegrin, V. Perez-Dieste, C. Escudero, P. Rejmak, N. Gonzalez, A. Fontseré, J. Prat, J. Fraxedas, and S. Ferrer, *J. Mol. Liq.* **300**, 112258 (2020).
- ⁵²N. Kurahashi, S. Karashima, Y. Tang, T. Horio, B. Abulimiti, Y.-I. Suzuki, Y. Ogi, M. Oura, and T. Suzuki, *J. Chem. Phys.* **140**(17), 174506 (2014).
- ⁵³M. N. Pohl, E. Muchova, R. Seidel, H. Ali, S. Srsen, I. Wilkinson, B. Winter, and P. Slavíček, *Chem. Sci.* **10**(3), 848 (2019).
- ⁵⁴B. Credidio, M. Pugini, S. Malerz, F. Trinter, U. Hergenhanh, I. Wilkinson, S. Thürmer, and B. Winter, “Quantitative electronic structure and work-function changes of liquid water induced by solute,” *Phys. Chem. Chem. Phys.* (published online 2021).
- ⁵⁵L. Nahon, L. Nag, G. A. Garcia, I. Myrgorodska, U. Meierhenrich, S. Beaulieu, V. Wanie, V. Blanchet, R. Géneaux, and I. Powis, *Phys. Chem. Chem. Phys.* **18**(18), 12696 (2016).
- ⁵⁶I. Powis, C. J. Harding, G. A. Garcia, and L. Nahon, *ChemPhysChem* **9**(3), 475 (2008).
- ⁵⁷C. Lux, M. Wollenhaupt, T. Bolze, Q. Liang, J. Köhler, C. Sarpe, and T. Baumert, *Angew. Chem., Int. Ed. Engl.* **51**(20), 5001 (2012).
- ⁵⁸A. Kastner, G. Koumarianou, P. Glodic, P. C. Samartzis, N. Ladda, S. T. Ranecky, T. Ring, S. Vasudevan, C. Witte, H. Braun, H.-G. Lee, A. Senftleben, R. Berger, G. B. Park, T. Schäfer, and T. Baumert, *Phys. Chem. Chem. Phys.* **22**(14), 7404 (2020).
- ⁵⁹A. Kastner, T. Ring, B. C. Krüger, G. B. Park, T. Schäfer, A. Senftleben, and T. Baumert, *J. Chem. Phys.* **147**(1), 013926 (2017).
- ⁶⁰S. Beaulieu, A. Comby, D. Descamps, B. Fabre, G. A. Garcia, R. Géneaux, A. G. Harvey, F. Légaré, Z. Mašín, L. Nahon, A. F. Ordonez, S. Petit, B. Pons, Y. Mairesse, O. Smirnova, and V. Blanchet, *Nat. Phys.* **14**(5), 484 (2018).
- ⁶¹J. Miles, D. Fernandes, A. Young, C. M. M. Bond, S. W. Crane, O. Ghafur, D. Townsend, J. Sá, and J. B. Greenwood, *Anal. Chim. Acta* **984**, 134 (2017).
- ⁶²J. Viehhaus, F. Scholz, S. Deinert, L. Glaser, M. Ilchen, J. Seltmann, P. Walter, and F. Siewert, *Nucl. Instrum. Methods Phys. Res., Sect. A* **710**, 151 (2013).
- ⁶³U. Hergenhanh, *J. Phys. B: At., Mol. Opt. Phys.* **37**(12), R89 (2004).
- ⁶⁴S. Thürmer, R. Seidel, M. Faubel, W. Eberhardt, J. C. Hemminger, S. E. Bradforth, and B. Winter, *Phys. Rev. Lett.* **111**(17), 173005 (2013).
- ⁶⁵B. Winter, E. F. Aziz, U. Hergenhanh, M. Faubel, and I. V. Hertel, *J. Chem. Phys.* **126**(12), 124504 (2007).
- ⁶⁶V. Štejfá, M. Fulem, K. Růžička, and C. Červinka, *J. Chem. Thermodyn.* **79**, 272 (2014).
- ⁶⁷K. Nishizawa, N. Kurahashi, K. Sekiguchi, T. Mizuno, Y. Ogi, T. Horio, M. Oura, N. Kosugi, and T. Suzuki, *Phys. Chem. Chem. Phys.* **13**(2), 413 (2011).
- ⁶⁸M. Faubel, K. R. Siefermann, Y. Liu, and B. Abel, *Acc. Chem. Res.* **45**(1), 120 (2012).
- ⁶⁹A. P. Gaiduk, M. Govoni, R. Seidel, J. H. Skone, B. Winter, and G. Galli, *J. Am. Chem. Soc.* **138**(22), 6912 (2016).
- ⁷⁰P. Slavíček, N. V. Kryzhevoi, E. F. Aziz, and B. Winter, *J. Phys. Chem. Lett.* **7**(2), 234 (2016).
- ⁷¹P. Jungwirth, B. J. Finlayson-Pitts, and D. J. Tobias, *Chem. Rev.* **106**(4), 1137 (2006).
- ⁷²K. B. Eisenthal, *Chem. Rev.* **96**(4), 1343 (1996).
- ⁷³D. Liu, G. Ma, L. M. Levering, and H. C. Allen, *J. Phys. Chem. B* **108**(7), 2252 (2004).
- ⁷⁴S. Gopalakrishnan, D. Liu, H. C. Allen, M. Kuo, and M. J. Shultz, *Chem. Rev.* **106**(4), 1155 (2006).
- ⁷⁵S. M. Baumler and H. C. Allen, in *Physical Chemistry of Gas-Liquid Interfaces*, edited by J. A. Faust and J. E. House (Elsevier, 2018), pp. 105–133.
- ⁷⁶F. Perakis, L. De Marco, A. Shalit, F. Tang, Z. R. Kann, T. D. Kühne, R. Torre, M. Bonn, and Y. Nagata, *Chem. Rev.* **116**(13), 7590 (2016).
- ⁷⁷S. Y. Truong, A. J. Yench, A. M. Juarez, S. J. Cavanagh, P. Bolognesi, and G. C. King, *Chem. Phys.* **355**, 183 (2009).

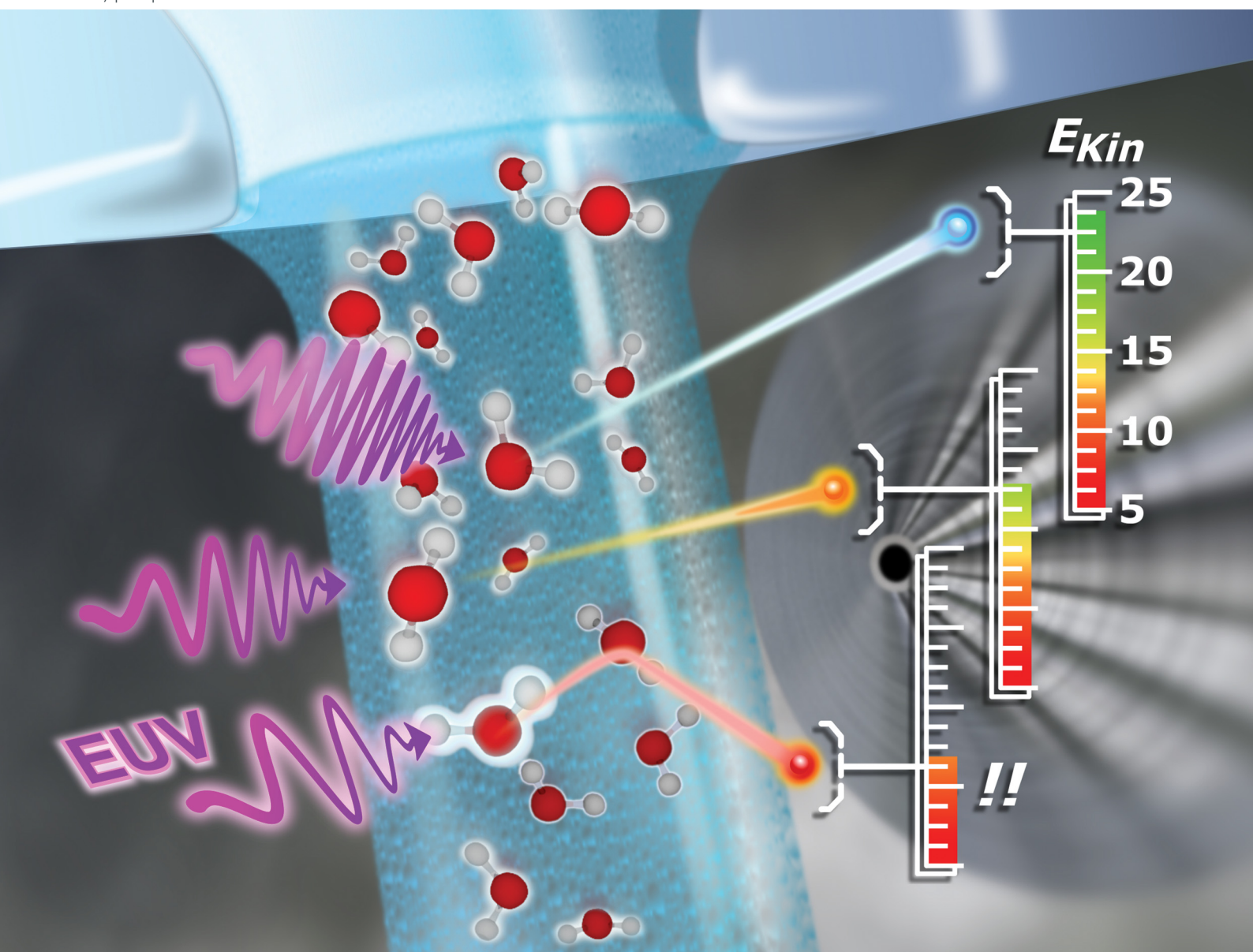
Paper II



PCCP

Physical Chemistry Chemical Physics

rsc.li/pccp



ISSN 1463-9076

PAPER

Iain Wilkinson, Bernd Winter, Stephan Thürmer *et al.*
Low-energy constraints on photoelectron spectra measured
from liquid water and aqueous solutions


 Cite this: *Phys. Chem. Chem. Phys.*,
2021, 23, 8246

Low-energy constraints on photoelectron spectra measured from liquid water and aqueous solutions†

 Sebastian Malerz,^{id a} Florian Trinter,^{id ab} Uwe Hergenbahr,^{id ac} Aaron Ghrist,^{id ad} Hebatallah Ali,^{id ae} Christophe Nicolas,^f Clara-Magdalena Saak,^{id g} Clemens Richter,^{id ac} Sebastian Hartweg,^{id f} Laurent Nahon,^{id f} Chin Lee,^{id ahi} Claudia Goy,^{id j} Daniel M. Neumark,^{id hi} Gerard Meijer,^{id a} Iain Wilkinson,^{id *k} Bernd Winter^{id *a} and Stephan Thürmer^{id *l}

We report on the effects of electron collision and indirect ionization processes, occurring at photo-excitation and electron kinetic energies well below 30 eV, on the photoemission spectra of liquid water. We show that the nascent photoelectron spectrum and, hence, the inferred electron binding energy can only be accurately determined if electron energies are large enough that cross sections for quasi-elastic scattering processes, such as vibrational excitation, are negligible. Otherwise, quasi-elastic scattering leads to strong, down-to-few-meV kinetic energy scattering losses from the direct photoelectron features, which manifest in severely distorted intrinsic photoelectron peak shapes. The associated cross-over point from predominant (known) electronically inelastic to quasi-elastic scattering seems to arise at surprisingly large electron kinetic energies, of approximately 10–14 eV. Concomitantly, we present evidence for the onset of indirect, autoionization phenomena (occurring via superexcited states) within a few eV of the primary and secondary ionization thresholds. These processes are inferred to compete with the direct ionization channels and primarily produce low-energy photoelectrons at photon and electron impact excitation energies below ~15 eV. Our results highlight that vibrational inelastic electron scattering processes and neutral photoexcitation and autoionization channels become increasingly important when photon and electron kinetic energies are decreased towards the ionization threshold. Correspondingly, we show that for neat water and aqueous solutions, great care must be taken when quantitatively analyzing photoelectron spectra measured too close to the ionization threshold. Such care is essential for the accurate determination of solvent and solute ionization energies as well as photoelectron branching ratios and peak magnitudes.

 Received 29th January 2021,
Accepted 23rd February 2021

DOI: 10.1039/d1cp00430a

rsc.li/pccp

^a Molecular Physics Department, Fritz-Haber-Institut der Max-Planck-Gesellschaft, Faradayweg 4-6, 14195 Berlin, Germany.

E-mail: winter@fhi-berlin.mpg.de

^b Institut für Kernphysik, Goethe-Universität, Max-von-Laue-Straße, 60438 Frankfurt am Main, Germany

^c Leibniz Institute of Surface Engineering (IOM), Department of Functional Surfaces, 04318 Leipzig, Germany

^d Department of Chemistry, University of Southern California, Los Angeles, CA 90089, USA

^e Physics Department, Women Faculty for Art, Science and Education, Ain Shams University, Heliopolis, 11757 Cairo, Egypt

^f Synchrotron SOLEIL, L'Orme des Merisiers, St. Aubin, BP 48, 91192 Gif sur Yvette, France

^g Department of Physics and Astronomy, Uppsala University, Box 516, SE-751 20 Uppsala, Sweden

^h Department of Chemistry, University of California, Berkeley, CA 94720, USA

ⁱ Chemical Sciences Division, Lawrence Berkeley National Laboratory, Berkeley, CA 94720, USA

^j Centre for Molecular Waer Science (CMWS), Photon Science, Deutsches Elektronen-Synchrotron (DESY), Notkestraße 85, 22607 Hamburg, Germany

^k Department of Locally-Sensitive & Time-Resolved Spectroscopy, Helmholtz-Zentrum Berlin für Materialien und Energie, Hahn-Meitner-Platz 1, 14109 Berlin, Germany.

E-mail: iain.wilkinson@helmholtz-berlin.de

^l Department of Chemistry, Graduate School of Science, Kyoto University, Kitashirakawa-Oiwakecho, Sakyo-Ku, Kyoto 606-8502, Japan.

E-mail: thuermer@kuchem.kyoto-u.ac.jp

† Electronic supplementary information (ESI) available. See DOI: 10.1039/d1cp00430a



Introduction

The development of liquid-jet photoelectron or more accurately photoemission spectroscopy (LJ-PES) represents a milestone for research on the electronic structure of liquid water and aqueous solutions.^{1–3} Among the quantities of prime interest are solvent and solute lowest vertical ionization energies (VIEs), which measure the energetic cost to detach an electron under equilibrium conditions and thus chart critical parts of the energy landscape that controls chemical reactivity.⁴ Furthermore, core-level binding energies (BEs) are sensitive to covalent bonding interactions^{5–7} and solute charge states,^{8,9} relative peak intensities reveal stoichiometry^{10,11} as well as surface propensity (*via* the so-called depth-probing technique),^{12,13} and resonant signal enhancements can be used, *e.g.*, to increase detection sensitivity.^{5,14,15} These applications rely on extracting photoelectron (PE) peak areas and/or kinetic energies by taking into account experimental factors such as ionization and electron collection geometries, detection efficiency, and/or ionization cross sections (CSs), although the latter are typically unknown in the aqueous phase.

One often unconsidered and almost overlooked aspect when analyzing PE spectra from liquid water is that PE peak profiles and centroid positions may be altered due to inelastic scattering. Although electron-scattering-induced changes in peak positions have been observed for water clusters as a function of their size¹⁶ and for the solvated electron in liquid water,¹⁷ the prevalent assumption made in condensed-phase PE spectroscopy is that PE peaks are associated with directly-produced photoelectrons that have escaped the sample entirely unscattered. Furthermore, it is generally assumed that peaks (and thus the respective electron binding energies) can be extracted by subtraction of some quantifiable inelastically scattered electron ‘background’. However, this is not necessarily the case, as we show here. Indeed, liquid water may seem a favorable case to neglect this electron scattering issue given that inelastic scattering is dominated by electron-impact-induced excitation, neutral dissociation, and ionization at X-ray photoexcitation energies, where photoelectron kinetic energies (eKE) are many tens of electron volts and larger. In fact, for water – a large-band-gap semiconductor^{18–21} – the smallest energy for electronic excitation is approximately 7 eV,^{22–24} implying that signals from electronically scattered electrons appear at eKEs well below the original direct PE peak. Hence, under high photon and eKE conditions, the nascent direct PE feature profiles are essentially unaffected by inelastic scattering processes. However, the situation changes drastically when photon energies are significantly smaller, such that the primary photoelectrons have insufficient energy to excite/ionize water. In such cases, in both the gas- and condensed phase, vibrational scattering pervades^{25–27} and largely determines the scattering-induced changes to the nascent PE spectra. In this article, we will experimentally demonstrate that quasi-elastic scattering similarly leads to photoelectron kinetic energy losses in the liquid-phase, which unlike in the case of high

enough eKEs, for all practical purposes, prevents the measurement of accurate binding energies and peak intensities. Furthermore, at specific excitation energies, we will present evidence for valence autoionization resonances in liquid water. These metastable states appear to be accessed both *via* photon and electron impact excitation close to the primary and secondary ionization thresholds, respectively, competing with direct ionization processes and yielding low-KE primary and secondary electrons. Notably, these processes are found to occur below the expected energetic onsets of aqueous-phase non-local autoionization processes (at ~ 30 eV), in particular Intermolecular Coulombic Decay (ICD).⁸⁵

In a related context, slow electrons play a crucial role in radiation damage in aqueous systems,^{28,29} and hence, the origins and properties of such electrons are essential for understanding, *e.g.*, radiobiological damage. Recently, nascent PE peak distortions have been observed in the low-eKE PE spectra of the hydrated electron, with the distortions being attributed to electron scattering. With the help of detailed scattering models, the nascent (‘genuine’) electron distribution curve could be recovered.¹⁷

Specifically focusing on valence ionization of liquid water, experiments have been performed with table-top lasers, so far covering the 1–60 eV photon energy regime, and with soft-X-ray photons from synchrotron radiation facilities, typically with photon energies not lower than 100 eV. It is the former, lower energy range, and particularly eKEs approaching just a few eV – where the electronic inelastic scattering channels become energetically unfeasible and vibrational and other quasi-elastic processes dominate – that we address in the present work. An associated expectation is that electron binding energies, and particularly the VIE of the lowest energy ionizing transition of liquid water (corresponding to removal of an electron from the leading $1b_1$, highest occupied molecular orbital, denoted as $VIE_{1b_1(0)}$) are not accurately accessible by experiments when too small a photon energy is utilized. This expectation builds on the following basis: At low eKE values, below the electronic excitation threshold of liquid water, the photoelectrons are expected to predominantly engage in vibrational excitations. Focusing on these lowest eKE cases, vibrational scattering processes will produce inelastically scattered background electron signals – most efficiently *via* just few-meV (single-scattering-event) energy losses – that partially spectrally overlap with the primary PE peaks. Furthermore, as is well known in the radiation chemistry community, within 10–30 eV of the photon or electron impact ionization thresholds, metastable neutral state absorption – followed by dissociation and/or indirect autoionization – can be expected to compete with direct photoionization.^{30–32} Such behavior is specifically observed in gas-phase water,³³ and can be expected to occur in liquid water as well.^{30–32} Thus, a quantitative analysis of the direct, primary PE peak parameters is expected to be hampered and potentially prevented as photoexcitation energies, and thus eKEs, are progressively

‡ Photoemission includes primary photoelectrons and any electrons emitted by some second-order process, *e.g.*, Auger decay.

§ Technically, recent laser developments can bridge this energy gap, with high harmonic generation sources routinely providing 100 eV photon energies, and even extending beyond 300 eV in a few laboratories, albeit with additional experimental complexity. See, *e.g.*, ref. 84.



reduced. In line with these expectations, we here demonstrate that in liquid water at eKEs less than 15–20 eV, the nascent, directly-produced PE peaks begin to broaden and become increasingly difficult to isolate as the secondary electron impact ionization threshold and predominantly vibrational scattering regime is approached. Notably, since the inelastic scattering behaviors primarily depend on eKE, they should also be detectable using X-rays to ionize high-binding-energy electrons, provided the specific photon energy is close enough to a core-level ionization threshold. We note that for core-level ionization, additional processes may occur close to the ionization threshold that may further distort the PE peaks (post-collision interaction, PCI,^{34–37} effects are an example), where we ignore such effects here as they are negligible in our exemplary systems. Indeed, the core-level ionization spectra analyzed and discussed below, reveal similar electron scattering signatures as those observed in the vicinity of the valence photoionization and primary photoelectron impact ionization thresholds.

The first part of the present work reports on valence photoemission measurements of liquid water using continuously tunable 10–60 eV photon energies ($h\nu$), which result in photoelectron production in the 0–50 eV KE range. Such LJ-PES experiments have not been technically realized before, and became possible by implementing the wide-energy range VUV/soft X-ray synchrotron radiation beamlines DESIRS and PLÉIADES (both at SOLEIL, St. Aubin) in conjunction with spectrometers that are capable of accurately and efficiently detecting eKEs from aqueous solutions down to nearly-zero electron volts. These studies include threshold measurements of water's fractional PE spectrum produced with photon energies extending below (the centroid of) the $\text{VIE}_{1b_1(l)}$ water ionization, *i.e.*, close to the ionization onset, revealing that the spectra still exhibit peak-like shapes at threshold but that these 'peaks' are almost entirely generated by inelastically scattered directly, and likely indirectly, produced electrons. The second part of this work presents soft-X-ray photon energy results (measured at the UE56-2_PGM1 beamline at the BESSY II synchrotron facility, Berlin) from a 3 M NaCl aqueous solution, with a focus on the Cl 2p PE spectrum, obtained for photon energies within a range of ~ 7 –18 eV above the respective core-level ionization threshold of approximately 202 eV.³⁸ Both sets of experiments aim to determine the lowest photon energy, and hence eKE, that can still be used to reveal accurate (nascent) spectral features, *i.e.*, for which the true (essentially undistorted) PE spectrum can still be extracted. Expressed as eKEs, this minimum energy is found to be approximately 10–14 eV for water, where the PE peak intensities diminish, and widths increase, until towards yet smaller energies, signal from direct photoemission can barely be identified on the large background due to inelastic (including quasi-elastic) scattering, at eKEs approximately < 10 eV. The background signals specifically underlying the primary electron peaks can generally be associated with small energy losses typical, for instance, of intra- and intermolecular vibrational excitations. On a related note, processes which indirectly produce low kinetic energy photoelectrons and associated electronic scattering channels will also be argued to come into effect at these low excitation

energies, something which may be responsible for a surprisingly large background signal peaking near zero eKE. Such signals are found to be consistent with superexcited state^{30–32} population and pre-ionization/autoionization of liquid water, either directly following photoabsorption or through primary photoelectron impact excitation. Our data is analyzed with reference to electron collision cross sections for gas-phase H_2O and the condensed-phase H_2O excitation and ionization literature. Similar scattering behavior is observed from NaCl aqueous solutions, as investigated with soft X-ray radiation and core-level ionization.³⁹ Crucially, our cumulative results allow us to advise that future attempts to measure accurate solute binding energies and peak intensities should be performed at photon energies that are sufficiently in excess of the ionization threshold, where sufficient is here determined to be ~ 30 eV.

Experimental

Measurements of the liquid water valence band were conducted at the PLÉIADES ($h\nu = 20$ –60 eV) and DESIRS ($h\nu = 10$ –25 eV) beamlines⁴⁰ of the SOLEIL synchrotron facility, Paris, using the PLÉIADES liquid-jet source⁴¹ and the EASI (Electronic structure from Aqueous Solutions and Interfaces) liquid-jet PES instrument,⁴² respectively. The electron–electron coincidence measurements from the 3 M NaCl solution were carried out at the UE56-2_PGM1 beamline⁴³ of the BESSY II synchrotron facility, Berlin, using a liquid-jet setup coupled to a magnetic bottle time-of-flight electron analyzer, described elsewhere.⁴⁴ For the liquid-water measurements, a small amount (~ 50 mM) of NaCl salt was added to highly demineralized water (conductivity $\sim 0.2 \mu\text{S cm}^{-1}$) to maintain electrical conductivity and mitigate potentially deleterious sample charging effects.⁴⁵ This is common practice when measuring PE spectra from liquid water.² The 3 M concentration solutions were prepared by dissolving NaCl (Sigma-Aldrich, $\geq 99\%$ purity) in highly demineralized water. For the SOLEIL experiments liquid microjets were generated by injecting liquid water (containing 50 mM NaCl) into the interaction vacuum chamber through 40 μm or 28 μm diameter glass capillaries, at a typical flow rate of 0.8 mL min^{-1} . Experiments with the 3 M NaCl aqueous solution at BESSY II used a 30 μm glass capillary at 1 mL min^{-1} flow rate.

Liquid water PES experiment at PLÉIADES

The measurements were performed using the electromagnetic HU256 undulator and the low-energy 400 lines per mm grating of the beamline. The energy resolution and photon-beam focal spot size (vertical \times horizontal) were approximately 2.5 meV and $50 \times 120 \mu\text{m}^2$, respectively. The energy resolution of the hemispherical electron analyzer (wide-angle lens VG-Scienta R4000) is 50 meV at a pass energy of 50 eV. The electron spectrometer is mounted with the electron detection axis perpendicular to the plane of the electron orbit in the storage ring.⁴⁶ The light traveled orthogonally to both the liquid jet and the electron detection axis, both being perpendicular to each other. The light polarization was set parallel to the spectrometer axis.



While it is unfortunate that measurements could not be conducted in the so-called magic-angle geometry (an angle of 54.7° between the light polarization vector and electron detection axis), which would cancel all intensity variations from the photoelectron angular anisotropy, this has only a minor impact on the results for the following reasons.

Near-equivalent liquid water valence anisotropy parameters, $\beta < 1$, have been measured at photon energies below 60 eV for all open ionization channels (0.51 ± 0.06 for $1b_1^{-1}$, 0.75 ± 0.13 for $3a_1^{-1}$, and 0.46 ± 0.13 for $1b_2^{-1}$ at 35.6 eV⁴⁷ and 0.27 ± 0.07 for $1b_1^{-1}$, 0.24 ± 0.09 for $3a_1^{-1}$, and 0.18 ± 0.06 for $1b_2^{-1}$ at 29.5 eV⁴⁸); PE signal intensity scales with $I \sim 1 + \beta P_2[\cos(\theta)]$, where $P_2[x]$ denotes the second order Legendre polynomial. A parallel alignment ($\theta = 0^\circ$) leads to anisotropy-induced signal variations between the open ionization channels of only $I_{3a_1}/I_{1b_1} \sim 1.16$ and $I_{1b_2}/I_{1b_1} \sim 0.97$ at 35.6 eV (instead of a value of 1), *i.e.*, a slight enhancement of the $3a_1$ feature at most, which is however below our error bars. Using the values for 29.5 eV the signal variation reduces to less than $\sim 8\%$ with $I_{3a_1}/I_{1b_1} \sim 0.98$ and $I_{1b_2}/I_{1b_1} \sim 0.93$.

The liquid jet source is based on a Microliquids© design. Crucially for the experiments discussed here, the liquid jet formed by a 40 μm orifice diameter glass capillary and collected by a heated copper-beryllium catcher was contained within an approximately $7 \times 8 \times 15 \text{ cm}^3$ aluminum enclosure. This box has two 3 mm diameter holes for the synchrotron light to enter and exit, and one 5 mm hole in a titanium piece through which the emitted electrons pass on their way to the hemispherical electron analyzer. When the liquid jet head is inserted, two channels of 1 mm diameter and 5 mm length face the liquid entrance and exit holes, in addition to a 300 μm stainless-steel skimmer facing the titanium hole. The jet is placed at the working distance of the electron analyzer (*i.e.*, at 3.4 cm from the 4 cm diameter entrance aperture), which corresponds to a distance of 1 mm between the entrance of the skimmer and the jet. A spectrometer electron transmission measurement using the liquid jet has not been attempted, and the profile of the true, low-eKE, spectral tail is unknown. However, we take the observed rather constant overall spectral shape upon variation of bias voltage (and hence variation of measured eKE range) as an indication of smooth variations of the transmission function in the eKE range considered here.

The liquid feed to the glass capillary was made of non-conductive PEEK line. A small gold-coated metallic connector located 20 cm up-stream before injection into vacuum was used to electrically ground the jet, or to apply a bias voltage to the sufficiently conductive liquid sample. The jet and catcher were always at the same potential. The bias was applied using a highly stable voltage supply (Delta Elektronika, SM 70 – AR 24). The liquid solution was pushed through the system using a HPLC (Watrex P102) pump.

The differential pumping box was evacuated with an 800 L s^{-1} turbo-molecular pump (Edwards, STPA803C) with a $100 \text{ m}^3 \text{ h}^{-1}$ dry multistage roots backing pump (Adixen, A103P). The spectrometer was pumped with one 600 L s^{-1} and one 450 L s^{-1} turbo-molecular pumps (Edwards, Seiko Seiki STP 600C and STP 450C)

with the beamline $600 \text{ m}^3 \text{ h}^{-1}$ dry multistage roots backing pump (Edwards, GX600n). Both the spectrometer and the liquid jet chamber are equipped with a liquid nitrogen trap (8400 L s^{-1} pumping speed for water). Pressures of 3×10^{-4} mbar and 8×10^{-6} mbar were achieved in the differential pumping stage and the spectrometer chamber, respectively.

Liquid water PES experiment at DESIRS

Experiments at the VUV variable polarization undulator beamline DESIRS⁴⁰ were performed in the 10–25 eV photon energy range with the EASI liquid-jet PES setup,⁴² which is equipped with a Scienta-Omicron HiPP3 differentially pumped hemispherical electron analyzer. This device uses a unique pre-lens system optimized for the detection of low-energy electrons. Unlike in the instrument described in the previous paragraphs, for the measurements at DESIRS the liquid jet was not enclosed. However, the EASI instrument's efficient μ -metal shielding and low-energy lens mode enabled detection of low-energy electrons. Here, the approximately 28 μm diameter liquid microjet was positioned at a 0.5–0.8 mm distance from the 800 μm orifice diameter skimmer at the analyzer entrance. Similarly, a systematic measurement of the electron transmission function has not been attempted with the EASI instrument. The synchrotron light propagation direction was orthogonal to the liquid jet, both lying in the horizontal plane. We used the hemispherical electron analyzer positioned at a 40° angle with respect to the photon beam propagation direction, with its lens lying in a vertical plane, and a vertical polarization of the photon beam. Although the hemispherical electron analyzer alignment with respect to the light polarization axis deviated somewhat from an ideal value in these experiments (40° instead of 54.7° , *i.e.*, the single-photon ionization magic angle), associated effects on the measured ionization-channel-resolved photoelectron yields are expected to be negligible for the following reasons. Analogous to the discussion for the PLÉIADES experiment, the near-equivalent and near-zero liquid-phase water β values measured at photon energies below 30 eV⁴⁸ give anisotropy-induced signal variations of $I_{3a_1}/I_{1b_1} \sim 0.99$ and $I_{1b_2}/I_{1b_1} \sim 0.97$ at 29.5 eV for an angle of $\theta = 40^\circ$, *i.e.*, less than 4%. At lower photon energies, the liquid water anisotropy parameters are expected to monotonically converge to zero and isotropic emission behaviors as the ionization thresholds are approached.⁴⁷ Accordingly, still lower anisotropy-induced signal variations are expected in our threshold ($h\nu \leq 25 \text{ eV}$) ionization experiments.

The pressure in the main chamber was kept at approximately 5×10^{-4} mbar using two turbo-molecular pumps (with a total pumping speed of $\sim 2600 \text{ L s}^{-1}$ for water) and three liquid-nitrogen cold traps (with a total pumping speed of $\sim 35\,000 \text{ L s}^{-1}$ for water). A similar sample delivery design as described above was used to generate the liquid jet, also allowing for the precise application of a bias voltage. The solution was delivered using a Shimadzu LC-20 AD HPLC pump that incorporates a four-channel valve for quick switching between different solutions. The system was equipped with an in-line degasser (Shimadzu DGU-20A5R). The bias voltage was applied using a highly stable Rohde & Schwarz HMP4030 power supply.



All photoemission measurements reported here were conducted in the 10–25 eV photon energy region, using the 200 lines per mm grating of the DESIRS beamline, and with the monochromator exit slit set to 20 μm . These settings yielded an approximately 200 μm horizontal (in the direction of the liquid jet propagation) and 80 μm vertical focus. The energy resolution is exit-slit-limited and given by $\Delta E [\text{eV}] = 1.16 \times 10^{-4} \times E [\text{eV}]$ (for instance, about 2.3 meV at 20 eV). The exit-slit limited photon flux amounted to $\sim 4 \times 10^{11} \text{ ph s}^{-1}$ between 10 and 14 eV, $3 \times 10^{11} \text{ ph s}^{-1}$ at 20 eV, and $8 \times 10^{10} \text{ ph s}^{-1}$ at 25 eV photon energies. The energy resolution of the hemispherical electron analyzer was approximately 30 meV at the implemented pass energy of 5 eV. A few spectra recorded with the same setup, but using a He gas discharge lamp as a laboratory light source are shown in the ESI.†

3 M NaCl coincidence experiment at BESSY II

This experiment was performed with the synchrotron operated in ‘single-bunch’ mode (1.25 MHz light pulse repetition rate). Electrons were detected using a magnetic bottle time-of-flight (TOF) electron analyzer, optimized for the high background pressure encountered in liquid-jet experiments. Details are described elsewhere.⁴⁴ The analyzer was aligned vertically, thus the liquid jet, the synchrotron radiation propagation, and the TOF-axis directions were mutually orthogonal. The polarization vector of the synchrotron radiation was vertical, hence coinciding with the analyzer TOF axis. A small accelerating potential into the analyzer was produced by biasing the tip of the magnet at -2 V ,

and for some spectra measured at 210 and 212 eV photon energy, an additional positive bias voltage was applied to the entrance diaphragm of the spectrometer (facing the liquid jet). Inside the time-of-flight analyzer, electrons were accelerated by a $+2 \text{ V}$ potential to produce flight times below the temporal bunch spacing of the storage ring. Event-based data acquisition was carried out with a multi-hit capable time-to-digital converter with a 60 ps bin width (GPTA, Berlin). Flight times were measured against a clock signal providing the revolution frequency of electrons in the BESSY II storage ring, and converted to kinetic energies using measured reference spectra. A coincidence analysis of the set of events recorded within 60 s per photon energy was performed, in which we retained only electron pairs with a fast electron in the eKE range (taken as 150–200 eV) of the Cl LMM Auger decay and a slow electron of any smaller kinetic energy (‘coincident electrons’). Alternatively, the undiscriminated electron spectrum can be produced from the full set of events.

Results and discussion

Full photoemission spectra from liquid water: $h\nu \geq 20 \text{ eV}$

Fig. 1 presents a series of full photoemission spectra from liquid water obtained at photon energies between 20 and 60 eV. ‘Full’ refers to spectra extending from the kinetic energy of the low-energy cutoff, E_{cut} , at the onset of the large signal tail (appearing at $\text{KE} < 10 \text{ eV}$) generally associated with inelastically

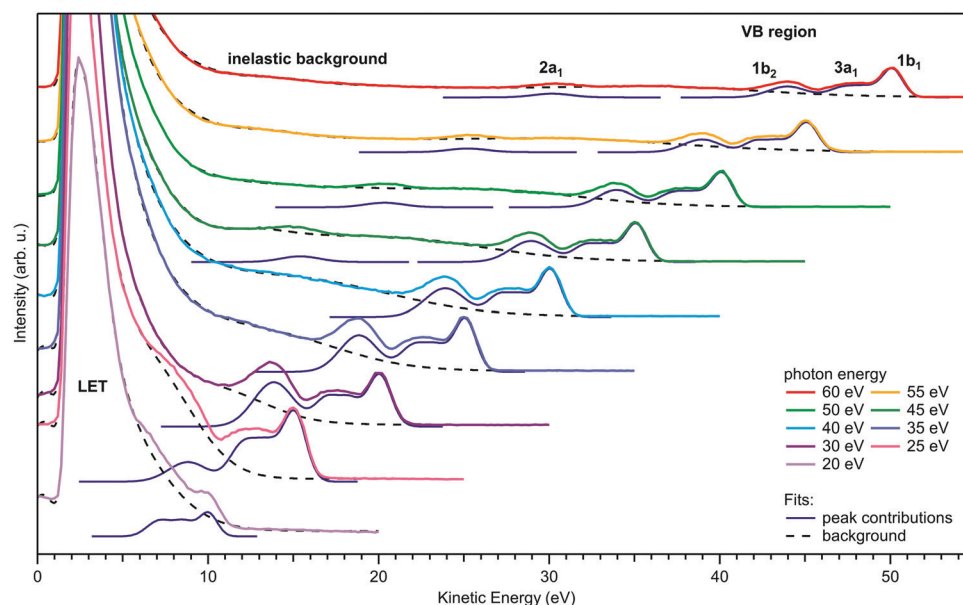


Fig. 1 Valence photoemission spectra from liquid water ionized at photon energies between 20 and 60 eV. Photoelectron peaks due to ionization of the water $1b_1$, $3a_1$, $1b_2$, and $2a_1$ orbitals are labeled. All peaks shift to higher kinetic energy (KE) with increasing photon energy according to $\text{KE} = h\nu - \text{BE}$. The signal associated with the inelastic scattering background is visible to the left of the water photoelectron peaks, and cumulates in the large scattering tail of the inelastic electron energy distribution (here denoted as the LET, low energy tail) curve close to zero KE. This LET curve is exposed by applying a negative bias voltage to the liquid sample, where the nominally applied voltage has been subtracted from the measured KEs to produce the KE scale shown here. Note that the measured cutoff signal will not necessarily coincide with zero KE after such a subtraction (as is the case here); the actual bias at the liquid jet is usually slightly different from that applied at the voltage source due to resistances and charge drops along the bias chain, and the potential presence of additional potentials. All spectra were fit by a series of Gaussians to account for the contributions of the nascent, undisturbed, direct PE peak signal (blue lines) and the inelastic scattering background signal (dashed black lines). See the main text for details.



scattered electrons, up to the lowest-ionization-energy (highest eKE) valence emission feature, assigned to photoemission from the $1b_1$ molecular orbital. All spectra were recorded from a water jet biased at -55 V; the resulting shift in the measured eKEs has been subtracted in Fig. 1 such that the PES spectra appear as if being measured from a grounded jet. The reason for applying a bias voltage is that it allows E_{cut} to be separated from the corresponding low-energy cutoff arising from the electron analyzer itself.⁴⁹ Arguably more important for this study, electron signal contributions from gas-phase water around the liquid jet can be effectively removed from the PES spectra. With the focal size of the photon beam and analyzer being larger than the liquid-jet diameter, gas-phase water molecules will be ionized at different distances from the jet, and thus take up different energies in the electric field between biased jet and grounded electron detector. As a consequence, the gas-phase signal is strongly broadened, and the majority of it is mapped to spectral regions that have no overlap with the liquid features. Hence, after correcting for the bias voltage, a nearly pure PES spectrum from neat liquid water is obtained; the effect is shown in Fig. S1, panel A of the ESI,[†] which presents PES spectra measured with and without applied bias voltage, respectively. Intensities of the spectra in Fig. 1 are displayed as measured, except for intensity corrections to account for small variations in photon flux when changing the photon energy. Note that the intensity maxima of the scattering tails are clipped in Fig. 1, and full-intensity-range spectra are shown in Fig. S2 of the ESI.[†]

In each tier of Fig. 1, we also present peak fits to the water valence spectrum (in blue), where the contributions from the four valence orbitals ($1b_1$, $3a_1$ doublet, $1b_2$, and $2a_1$, marked in the top tier) are cumulatively fit by five Gaussians. We constrained the two $3a_1$ components to have the same height and width.⁵⁰ Additionally, the $1b_2$ - $3a_1$ peak separation for $h\nu = 25$ eV and the $3a_1$ - $1b_1$ separation for $h\nu = 20$ eV were constrained to fit these peaks on top of the steeply sloping background. The valence peaks shift to lower eKEs with decreasing photon energy ($h\nu$) according to $\text{KE} = h\nu - \text{BE}$, where the binding energies (BEs) pertain to the direct ionization energies, VIE, of the respective water molecular orbitals. For $h\nu > 50$ eV, all four valence PE peaks are well visible on a rather smooth background, while for $h\nu < 35$ eV, the valence spectrum resides on top of a background of increasing slope, with the water $2a_1$ peak beginning to become undetectable due to diminishing intensity and overlap with the background signal where the low-energy spectral tail rises steeply. Upon further lowering the photon energy, all other valence peaks sequentially disappear as well, and at $h\nu = 20$ eV, the remaining emission due to water $1b_1$ ionization results in only a small shoulder near 10 eV eKE. Taken together, we observe a sudden decline of the primary, direct PE peak intensities (yet to be justified in detail), counter-balanced by the relative contribution of the underlying inelastically scattered background signal – most likely including indirect electron production at lower energies – rising steeply when the photoelectron eKEs drop below ~ 10 – 14 eV.

The dashed black curves in Fig. 1 represent the contribution from this background signal. Here, we include all broad features

($> \sim 4$ eV full-width half-maximum, FWHM) within this background, and the sharp cutoff is modeled with exponentially modified Gaussians. Note that the Shirley or Tougaard algorithms commonly applied for inelastic background determination in solid-state X-ray PE spectroscopy are not applicable here for several reasons. The simple Shirley method is unsuited for condensed matter with a strongly eKE-dependent scattering probability, which is the case for semiconductors and insulators.⁵¹ The Tougaard algorithm, on the other hand, is only applicable under the conditions of using absolute-intensity-calibrated spectra together with the correct scattering function for the material.⁵² Furthermore, the Tougaard algorithm applies at sufficiently high eKEs, far away from the scattering tail, since this algorithm is incapable of quantifying impact ionization cascades. Neither condition is fulfilled here. Our simple approach to quantify the magnitude of the background signal, particularly that underlying the direct PE peaks, is sufficient and robust, yielding good agreement with available gas-phase photoionization cross sections (CSs), as we will demonstrate below.

Kinetic-energy-dependent composition of the low-energy spectral tail

Before we move on to discuss why photoelectron peaks can be severely distorted in some cases, reflecting the rich ionization and scattering behavior of liquid water, we would like to briefly introduce some terminology describing the overall PE spectral shape, including the background signal extending down to zero eKE. Photoelectrons that lose almost all of their initial energy in various scattering processes will give rise to a low-KE tail, denoted here LET, characteristic for condensed-phase photoemission. It is important to realize that the LET spectrum is generally comprised of primary electrons which have lost energy due to (1) various inelastic scattering processes (inelastically scattered primary electrons), as well as (2) electrons formed in impact-ionization cascades that generate secondary electrons, each having sufficient energy to overcome the surface barrier of the sample; electrons with the smallest energies (quasi-zero kinetic energy) give rise to the steep signal edge at the cutoff. The terms ‘secondary electron energy distribution’ (SEED) or ‘secondary electron emission’, typically used to denote the LET in the condensed-matter PES literature⁵³ as well as in electron microscopy and high-energy physics contexts,^{54,55} are misleading if used to describe low-energy spectra. Specifically, these terms do not account for the contribution to the LET of those direct photoelectrons that have lost energy in processes not involving the generation of another electron. This contribution is indeed sizable in the case of a semiconductor excited at very low photon energies, where the eKE is smaller than the band gap, and hence insufficient to ionize another electron. In such a case, the LET will instead consist to a large extent of the inelastically scattered primary photoelectron distribution, here denoted as IPED. Quantification of the latter is elusive due to our currently incomplete understanding of all contributing scattering processes in liquid water. In fact, there is an ongoing lively discussion about the correct modeling of electron scattering in liquid water, especially for the low-energy regime.⁵⁶



Notably, low-KE electrons may also be produced *via* indirect primary or secondary ionization processes. In the gas phase, at excitation energies up to a few-tens of eV above valence ionization thresholds, direct ionization is known to compete with metastable superexcited state production, with subsequent dissociation and/or indirect (auto-)ionization.^{30–32} The indirect ionization processes occur through the coupling of the aforementioned superexcited states to the ionization continuum, producing electron distributions which can extend from zero eKE to the (coupled photoionized state's) adiabatic ionization threshold, depending on the degrees of internal excitation produced in the residual photoionized species. Such states have been found to play notable roles in the valence ionization dynamics of gas-phase water⁵⁷ and amorphous ice.⁵⁸ However, the degree to which unstable superexcited neutral states contribute to the threshold ionization dynamics of liquid water has yet to be determined. Should indirect ionization channels – associated with initial photoexcitation or primary photoelectron impact excitation – be significant in the near-threshold ionization of liquid water, as in water's other phases, we expect such processes to contribute to the LET signal and potentially to the background electron distributions extending to the primary, directly-produced photoelectron signals.

Our approach to model the aforementioned scattering and potential indirect ionization mechanisms is very simple, using well-established scattering cross sections from gas-phase water and the available water photoabsorption and photoionization literature in an attempt to qualitatively explain our yet-to-be-detailed experimental observations.

Correlation/anti-correlation of water photoelectron signal intensity with ionization and scattering cross sections:

$h\nu \geq 20$ eV

We first determine the signal intensities of all water valence direct PE peaks and of the full (inelastic/indirect ionization) background signal (see Fig. 1) based on Gaussian peak and baseline fits, as introduced above. The resulting direct PE peak fit areas are shown in Fig. 2A on the eKE x -scale associated with each direct PE peak (bottom axis), as well as on a photon-energy x -scale specifically pertaining to the water $1b_1$ ionization channel (top axis). The peak areas are presented as extracted from the fits, except for the $2a_1$ contribution which is scaled up by a factor of 7 to bring its values to approximate overlap with results for the other orbitals. This compensates the smaller $2a_1$ ionization cross section at the employed photon energies.^{59,60} Peak signal intensities are found to increase with decreasing eKE and then exhibit a steep decline to zero in the 5–15 eV eKE region; all orbitals exhibit the same trend fully in line with negligibly small β -induced effects (as explained above). Here, a value of 'zero' means that the direct PE peak is so small or distorted that it can no longer be identified in the spectrum. Notably, the observed smooth signal variation up to the sudden drop scales approximately with the experimental partial photoionization CSs of the gas-phase water orbitals $1b_1$, $3a_1$, and $1b_2$, as concluded based on the matching eKE-dependent photoionization CS curve (purple dashed line).⁶¹ All three orbitals have very similar CSs; we detail how the displayed

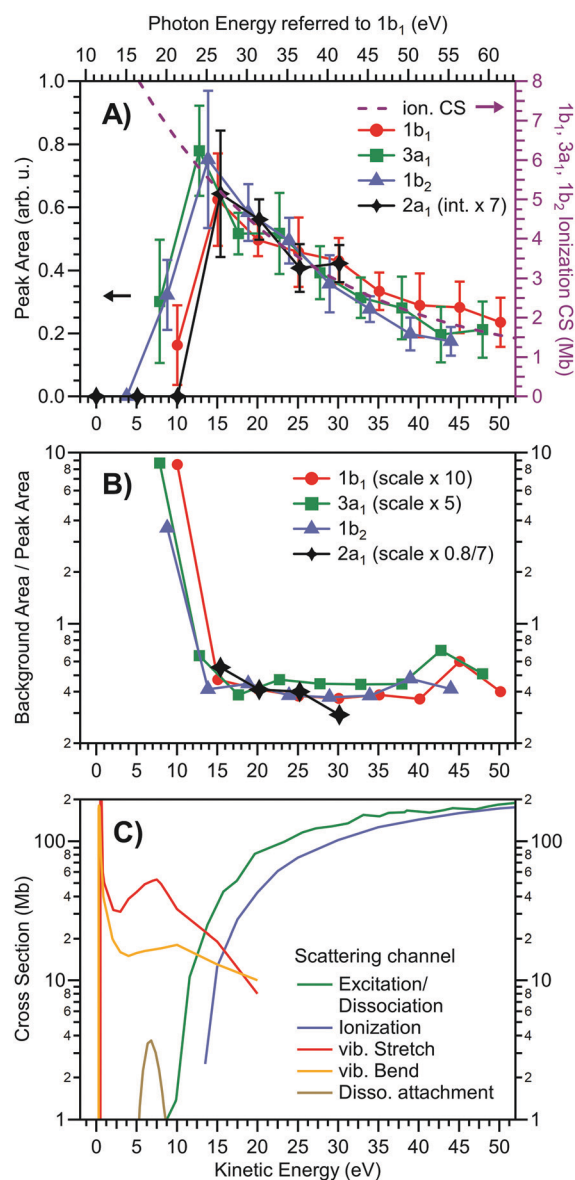


Fig. 2 Intensity of liquid water valence photoelectron peaks and the underlying inelastically scattered background, in comparison with ionization cross section data. Data are derived from the peak fits shown in Fig. 1. (A) Peak areas of the $1b_1$ (red circles), $3a_1$ (green squares; sum of double-peak), $1b_2$ (blue triangles), and $2a_1$ (black diamonds) direct photoelectron features versus electron kinetic energy. The gas-phase ionization cross section, averaged over the $1b_1$, $3a_1$, and $1b_2$ molecular orbitals,⁶¹ is overlaid onto the data as a purple dashed line, and is referred to the y-scale on the right (see text and Fig. S3 in the ESI†). Error bars depict the breadth of results obtained from running a least-squares fit of the spectra with varying model parameters and constraints. The top axis shows the photon energy specifically corresponding to $1b_1$ orbital ionization channel. (B) Inelastically scattered local-background-signal strength at the respective peak position, relative to the peak areas of the signal components shown in A; the background (dashed lines in Fig. 1) was integrated over the range of each peak's FWHM. The scaling factors for the $1b_1$, $3a_1$, and $2a_1$ peaks account for the fact that each peak sits atop a different background because of its relative position in the spectrum, which may include scattering contribution from higher eKEs (see also Fig. S4, ESI†). The ratio of local background signal height versus nascent peak area rises steeply below ~ 13 eV KE. (C) Cross sections of various electron scattering channels for the (gas-phase) H_2O molecule from ref. 25, 69, and 70. Ionization (blue), vibrational stretch (red), and vibrational bend (yellow) from ref. 25; direct dissociation following excitation (green) from ref. 69; dissociative electron attachment (brown) from ref. 70.



CS curve relates to the literature data in Fig. S3 (ESI[†]). Note that in an early LJ-PES publication⁵⁰ a rather large difference between the gas- and liquid-phase water ionization CSs was reported, especially for the 1b₁ and 3a₁ orbital ionization channels. However, these differences may have originated from a combination of overestimating the background using a simple Shirley-type subtraction procedure, uncompensated polarization-dependent intensity variations, and possible variations in the spectrometer transmission function, as discussed in the original publication.⁵⁰

Before discussing the origin of the steep signal drop near 10–14 eV found in Fig. 2A, we additionally analyze the background-to-direct-PE signal ratio, displayed in Fig. 2B; here the background is the local background signal directly underneath the respective primary, directly-produced PE peak. Associated absolute background intensities are presented in Fig. S4 (ESI[†]). The same eKE axis is used as in Fig. 2A. Relative to the peak area, the underlying electron background signal increases in intensity towards low energies. Assuming the background signal originates from the same direct PE channels, we see that it solely scales with eKE but is independent of the ionized orbital. Hence, the background-to-direct-PE signal ratio is constant within our experimental error up until eKE ~ 13 eV. Notably, this is the same eKE region where the change in behavior is observed in Fig. 2A.

In order to explain the sudden changes of behavior observed in Fig. 2A and B, we consider the CSs for the various relevant inelastic electron scattering processes discussed in the literature as a function of eKE, which are shown in Fig. 2C. We deliberately choose the gas-phase CS values²⁵ for this comparison to emphasize that the effect is not exclusively a property of the liquid state, but mainly stems from the fact that the much higher density of liquid water leads to more pronounced scattering. Furthermore, the scattering CSs for aqueous solutions are admittedly less accurately known, with significant variance of the associated values being reported by different research groups.^{56,62,63} This is partially due to the need to invoke additional processes, including several intermolecular vibrational energy transfer processes (over many water molecules) leading for instance to librations, translational displacement, and bending motion of the intermolecular hydrogen-bond coordinate,⁶⁴ all of which participate in the breaking and forming of hydrogen bonds. Rotational motion, on the other hand, is strongly suppressed by the hydrogen-bonding network. Notably, however, none of these details are directly considered in our qualitative signal analysis; we here focus on the cross-over from known electronic to alternative, *e.g.*, vibrational, scattering behaviors occurring in the 10–20 eV eKE region. Indeed, particularly the scattering processes occurring at low eKEs are the most difficult to model in liquid water, although it has been suggested⁵⁶ that these processes and their CSs are very similar to those associated with amorphous ice.²⁷

An important inference from Fig. 2C is that the dominant processes occurring at higher eKEs are the electronic scattering channels (resulting in relatively high-energy losses)^{25,65–69} – *i.e.*, ionization (in blue) and excitation and dissociation (in green) – with the respective (gas-phase) CSs tending towards zero near 10–14 eV eKEs, when the eKEs approach the VIE_{1b₁} threshold and the electronic scattering channels begin to close. Importantly, the

total ionization cross-section data shown in Fig. 2C integrates over direct and any indirect electron-producing channels. It should also be noted that, as compared to the gas phase, the (vertical) valence excitation and ionization energies approach each other in liquid water, with the respective CS curves expected to tend to somewhat different eKE values. In the liquid, the electronic excitation CS curves shift to higher eKEs by ~1 eV, with the direct ionization scattering channel CS curves tending to lower eKE values by about 1–2 eV.⁵⁰ This brings the onsets of the major electronic scattering processes in liquid water closer together and the cumulative electronic inelastic scattering CS towards the lower eKE region characterized by predominant vibrational scattering. Despite these shortcomings, the gas-phase CSs shown in Fig. 2C clearly indicate that upon decreasing the eKE below 10–14 eV, the CSs for vibrational scattering processes, partitioned here into vibrational stretch (in red) and vibrational bends (in orange),²⁵ quickly rise and assume similar values to those of the electronic processes in the case of KEs above the cross-over region. In the following, we will concentrate just on these known scattering processes in water, and later discuss the possibility of additional (so far unexplored) excitation and indirect ionization channels likely contributing in this energy region.

To our knowledge, no (non-vibrational) inelastic scattering processes have been reported to produce few-eV (*i.e.*, LET contributing) electrons following low-KE-electron (0–15 eV) collisions with either gas- or liquid-phase water. Dissociative electron attachment to neutral water molecules (processes of the type e⁻ + H₂O → OH + H⁻),^{69,70} although included in Fig. 2C, is of minor importance here as these excitation channels exclusively act as electron sinks. Furthermore, the respective (gas-phase) CSs (brown curve) are one order of magnitude smaller than their vibrational inelastic scattering counterparts in the 5–10 eV eKE region. The fact that vibrational CSs are so large at the low eKEs (and we do not even refer to the CS spikes in the KE < 2 eV range) would imply that a primary photoelectron produced in this range engages in many quasi-elastic (low-energy) scattering losses which gives rise to a broad signal approximately centered (with higher tendency towards lower eKEs) at the original peak position in the spectrum. In other words, the undisturbed photoelectron peak diminishes in height, since fewer electrons escape from the liquid with their nascent KEs. This is balanced by a build-up of a broad scattering background right underneath the same peak. It can therefore be argued that the observed discontinuities in Fig. 2A and B for eKE < ~13 eV thus reflect the transition from mainly electronic scattering channels to alternative quasi-elastic processes such as those arising through vibrational scattering. Also, dissociative electron attachment and potential indirect autoionization mechanisms may contribute to the diminished primary PE peak areas in the intermediate eKE region, and potentially close to the photoionization threshold. In more practical terms, both Fig. 1 and 2 are quantitative and illustrative demonstrations of, and actually handy reference data showing, the lowest photon energy at which any PE feature from liquid water can still be extracted (essentially) undisturbed by scattering effects. (In a related upcoming publication, we will discuss smaller additional primary PE peak distortions, specifically



slight peak energy shifts, which already set in at eKEs below ~ 30 eV.)

In light of the low-eKE inelastic scattering processes discussed above, we consider the 20 eV photon energy spectrum shown in Fig. 1 in more detail. This corresponds to a <10 eV eKE of the water $1b_1$ peak, which is just below VIE_{1b_1} . Based on Fig. 2C, the LET signal should entirely consist of IPED at a 20 eV photoexcitation energy. Surprisingly, however, this does not seem to be the case. A plot of the (integrated) LET signal intensity divided by the ionization channel-resolved direct valence PE peak areas, presented in Fig. S5 (ESI[†]), reveals a smooth decrease towards lower eKEs as secondary-electron-generating processes diminish. However, below eKEs of ~ 14 eV, a steep rise indicates that an additional high-CS and yet unknown low-KE electron generating process must contribute to the LET signal intensity, a point we will return to below. Nonetheless, we argue that IPED contributions remain large in these low primary eKE regions to some extent because the probability for direct secondary ionization is diminished. If primary electrons cannot engage in high-energy losses, which would essentially remove them from the measurable photoelectron signal (*i.e.*, the electron distribution which has sufficient energy to overcome the aqueous-vacuum surface barrier), they can travel much further in the liquid and undergo many quasi-elastic scattering events. In such a case, the liquid probing depth will significantly increase, *i.e.*, the liquid will become (more) 'transparent' for electrons with KEs below ~ 10 eV. For this reason, LET electron emission from semiconductors, including liquid water, is found to be up to an order of magnitude more intense as compared to that observed from metals. This effect depends on the material's bandgap, E_{gap} , and the electron yield has been found to be highest when $E_{\text{gap}} \sim 7$ eV (compared to 8.9 eV for liquid water¹⁹).⁷¹ Thus, the fraction of IPED *versus* SEED gradually increases as we change the photon energy from 60 to 20 eV (Fig. 1). However, as Fig. S5 (ESI[†]) implies, another type of scattering process, or perhaps an alternative primary but indirect few-eV electron-generating mechanism, must also be included to describe the LET signal change that occurs in the 10–14 eV eKE region. Our current understanding of electron-collision interactions in liquid water for eKE < 14 eV seems to be insufficient, and very likely processes other than vibrational scattering need to be identified and considered in order to explain the observed large LET signal, and perhaps the suddenness of the behavioral changes highlighted in Fig. 2A and B.

Liquid water photoemission spectra: towards $h\nu \leq VIE_{1b_1}$

Although eKEs of approximately 10 eV (referring to the bottom spectrum in Fig. 1) are already too small to support the extraction of undistorted nascent PE peaks, it is instructive to explore photoemission spectra measured at yet smaller photon energies, so as to approach conditions met in a number of previous laser-based experiments. We are particularly interested in cases where $h\nu < 11.3$ eV (*i.e.*, the VIE_{1b_1}). Results are shown in Fig. 3 for the ionization of a liquid-water jet using photon energies between 10–25 eV. As compared to the measurements leading to Fig. 1, a much smaller bias voltage (-4 V) has been applied, implying that the apparent water gas-phase contribution is not as

effectively smeared out. Spectra are displayed such that the leading spectral features exhibit approximately the same peak height; the full intensity scale and presentation of approximate relative signal intensities is displayed in Fig. S6 (ESI[†]). Here, zero energy marks the position of VIE_{1b_1} ($= 11.3$ eV, with a 1.45 eV FWHM⁴⁵) as measured in a high-KE experiment, exemplified by the 25 eV PE spectrum where $1b_1$ ionization still yields a clearly resolved (but already somewhat distorted) peak profile. All other spectra have been shifted analogously by $h\nu - VIE_{1b_1}$, so as to display all spectra on the same relative energy scale with respect to VIE_{1b_1} . Note that for $h\nu \leq 15$ eV the full spectral ranges are captured, while for the 20 and 25 eV spectra E_{cut} is off scale, as is the IPED (and SEED) signal intensity. Spectra measured at the latter two energies were already presented in Fig. 1, but we now observe additional intensity in the -1 to -3 eV range (on our relative energy scale) arising from gaseous water, due to the smaller bias voltage.

By successively lowering the photon energy down to 10 eV, we can track the photoemission distribution resulting from ionizing the full liquid water $1b_1$ valence band down to ionizing just its lowest binding energy component. For example, the PE signal in the 10 eV spectrum of Fig. 3 contributes only to the

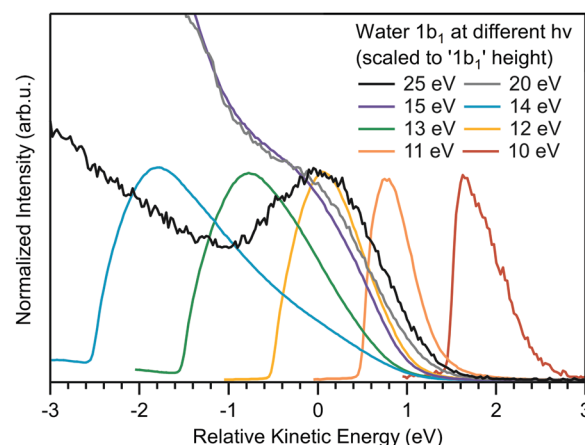


Fig. 3 Photoemission spectra of liquid water obtained for photon energies of 10–25 eV, which covers energies above and below VIE_{1b_1} ($= 11.3$ eV). In the absence of a calibrated transmission function of the electron analyzer, spectra measured at $h\nu = 10$ –14 eV are scaled to yield the same peak heights. Spectra measured at $h\nu = 15$ –25 eV are scaled such that the signal height of the $1b_1$ photoelectron peak has approximately the same height as the features of the low-photon energy spectra; this is a convenient procedure, not based on scientific grounds, but sufficient for the present purpose. All spectra are shifted so as to compensate the difference in photon energy according to $h\nu - VIE_{1b_1}$ ($VIE_{1b_1} = 11.3$ eV). In this presentation it can be immediately seen that the 10–14 eV spectra are composed of a prevailing LET contribution; the true photoemission signal associated with ionization of the water $1b_1$ orbital cannot be identified. Note that the apparent intensity difference between the 14 and 15 eV spectra is a result of the aforementioned intensity scaling procedure. The as-measured spectra (before normalization) are shown in Fig. S6 (ESI[†]). The 15 eV spectrum does exhibit a small $1b_1$ shoulder, and this spectrum can hence be displayed in the same manner as the 20 and 25 eV spectra. On the other hand, no $1b_1$ PE signal can be identified in the 14 eV photoemission spectrum, and this spectrum is scaled in the same way as all the spectra measured at yet lower photon energies.



very onset of the lowest energy, $1b_1$ ionizing transition (extending approximately from +1.5 eV to +3 eV on the relative scale). The energetic range over which $1b_1$ emission can occur increases with increasing photon energy, which is reflected in a wider spectral width, in all cases terminated by the IPED cutoff, as is best seen for the 10 to 14 eV spectra.

The observed transition from unresolvable to resolvable but distorted direct $1b_1$ peak profiles above 14 eV excitation energies in Fig. 3 is particularly notable. This threshold coincides with that observed on the eKE scale, *i.e.*, primary photoelectron impact, shown in Fig. 2, and strongly suggests that a common resonant behavior in liquid water both competes with direct photoionization (see Fig. 3) and effectively electronically inelastically scatters primary photoelectrons (see Fig. 2A) at excitation energies of ~ 14 eV, a point we will return to in a subsequent sub-section.

Considering Fig. 3 more generally, this data cumulatively shows that the water spectrum, *e.g.*, measured at $h\nu = 10$ or 11 eV, is mostly composed of IPED (and potential autoionization signals; possibly, the vibrational scattering CS spikes at $eKE < 2$ eV, if existent in liquid water, may also need to be considered that may be mistaken for the direct $1b_1$ PE feature. Hence, analysis of aqueous solution PES experiments performed so close to the ionization threshold must carefully account for the prevalent fraction of IPED signal (as well as any indirectly produced photoelectrons) *versus* the residual direct, nascent PE signal if spectral misinterpretations are to be avoided.

Photoemission spectra from 3 M NaCl aqueous solution close to a core-level ionization threshold

With the results presented so far, several pertinent questions arise. Is the low eKE behavior described above unique to the valence ionization of liquid water, or is it also observed for aqueous solutes? Further, have the nascent low-kinetic-energy PE peaks vanished, or have they rather been 'hidden' underneath the intense background signal as the primary eKEs were reduced? A related question is whether there is some inherent experimental flaw, such as suppressed electron transmission and detection, when measuring low-energy electrons with a hemispherical electron analyzer, despite application of an electron accelerating bias voltage to the sample. To answer these questions and unequivocally demonstrate the universality of diminishing primary aqueous-phase PE feature intensities at kinetic energies below ~ 10 eV, we conducted electron time-of-flight (TOF) coincidence measurements from a 3 M NaCl aqueous solution liquid jet using soft X-ray photons. Here our focus is on the $Cl^-_{(aq)}$ $2p_{3/2}$ and $2p_{1/2}$ core-level PE spectra. The electron binding energies are 202.1 and 203.6 eV, respectively,³⁸ *i.e.*, much larger than those of the valence features considered above. Experimental results are presented in Fig. 4. Fig. 4A shows the normal (non-coincidence) TOF photoemission spectra of the $Cl^-_{(aq)}$ 2p peak atop the LET spectral component, with the cutoff to the left. Note that electron counts are presented on a logarithmic scale to avoid cutting off the LET intensity for the higher-photon-energy spectra. Upon lowering the photon energy towards the $Cl^-_{(aq)}$ 2p ionization threshold, the 2p peak moves to smaller eKEs, and when approaching ~ 10 –14 eV,

it starts to distort and broaden, and progressively decreases in intensity. This behavior is fully analogous to that shown for the liquid water valence ionization features in Fig. 1.

The LET signal in Fig. 4A mainly consists of inelastically scattered Auger electrons associated with the 2p core-hole decay (with some contribution from high-energy Na^+ and water direct PE electrons), and thus changes only slightly with photon energy. Subtraction of this background reveals the remaining $Cl^-_{(aq)}$ 2p PE signal, as plotted in Fig. 4B, with intensities now presented on a linear y-scale. Respective peak areas (extracted from a fit to the spin-orbit split 2p peak with two Gaussians) are plotted as a function of eKE, as shown by the black data points in Fig. 4C. The peak intensity is observed to rise as the eKE decreases from 18 eV to approximately ~ 12 eV, where the signal intensity suddenly drops towards zero intensity, seemingly highlighting the onset of quasi-elastic and/or resonant electronic scattering at this energy, fully analogous to the findings in Fig. 2A. Furthermore, as in Fig. 2A, the initial smooth signal rise follows the increase of the Cl 2p ionization CS with decreasing photon energy, depicted by the fitted CS curve (purple dashed) associated with the y-scale to the right (where the fit to the CS data is shown in detail in Fig. S7 of the ESI†).

To address the additional questions posed above regarding possible signal detection deficiencies, we also performed electron-electron coincidence measurements from the same solution to effectively reduce the inelastic scattering background. The results are presented in Fig. 4D and are obtained from a two-hit coincidence measurement and analysis, triggered by a fast Auger electron acquisition (150–200 eV) window. By selecting only two-hit events which include (mostly undisturbed) Auger electrons originating from the Cl 2p core-hole decay, the random inelastic background is suppressed by orders of magnitude (note the linear scale in panel D). Similar peak fits to those adopted with the non-coincidence data were applied to the coincidence data, however explicitly including the (unsubtracted) sloping background here (dashed black lines). The resulting eKE dependence of the peak areas is plotted in Fig. 4C (red points) for comparison with the non-coincidence measurement data. We observe the same behavior with eKE, a sudden drop in the direct PE peak area below an eKE ~ 12 eV. We note the similar eKE-dependent ionization trend to that observed with (nearly) neat water close to the valence ionization threshold (see Fig. 2A), and attribute the less abrupt decrease in intensity below eKE ~ 12 eV in the core-level spectra to the smaller photon energy steps used, 2 eV, in comparison to the liquid water valence data, 5 eV.

Collectively considering the aqueous solution data, we can confirm that the discussed inelastic scattering effects are not a property of the detection method. Furthermore, the observation of the same behavior for both the valence solvent and core-level solute features demonstrates that the primary photoelectron peaks are not just masked by a large inelastic scattering background, but really are diminished at low eKEs, as a general effect in photoemission from aqueous solutions. In the next sub-section, we build on these inferences and speculate on the role of indirect ionization processes in the near-threshold PE



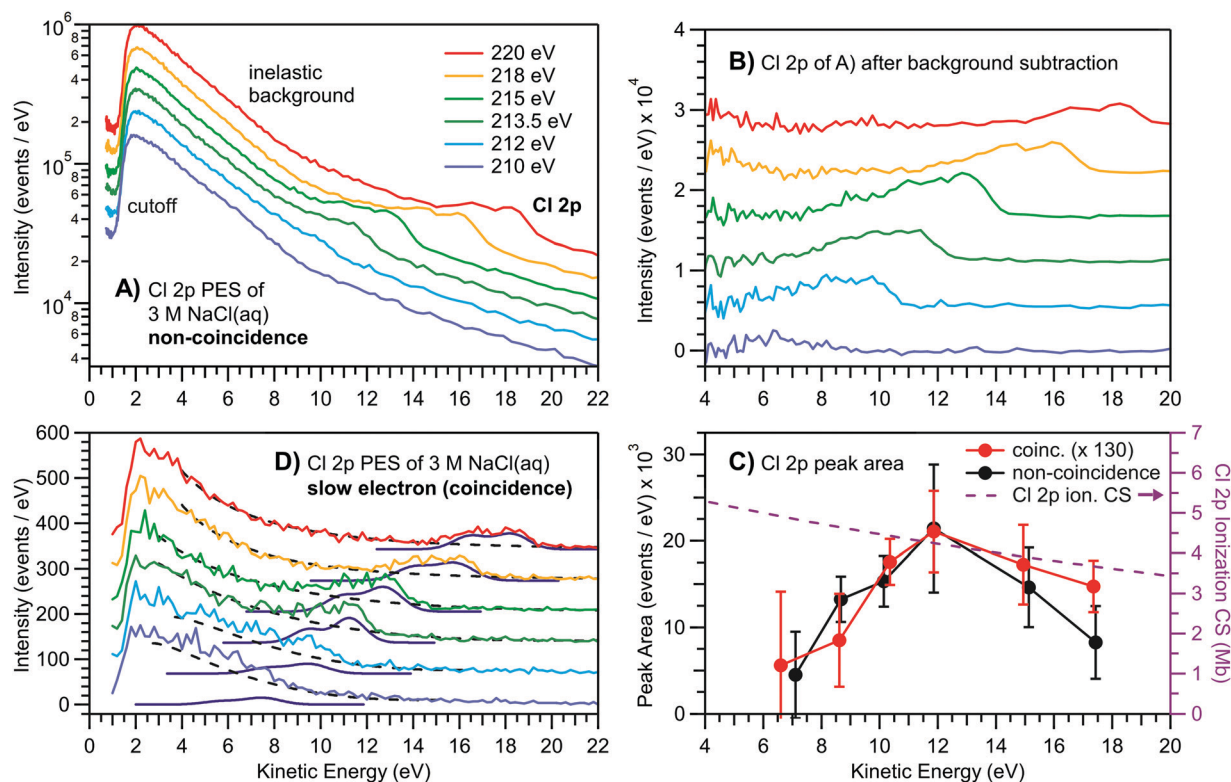


Fig. 4 Time-of-flight-based PE spectra of the Cl 2p doublet peak from 3 M NaCl aqueous solution at various photon energies close to the ionization edge. (A) Non-coincident electron spectrum (log scale) after time-to-energy conversion. The photon energy was successively lowered to bring the peak's eKE towards and below the critical ~ 10 – 14 eV region. The PE peak intensity successively diminishes and eventually almost disappears below ~ 10 eV as the nascent direct PE signal is degraded by scattering. (B) The major inelastic scattering background from liquid water is subtracted, which reveals the leftover Cl 2p signals. Although a peak is still visible at lower eKE, inelastic scattering leads to a broadened and asymmetric shape. (C) Peak areas as extracted from the spectra in panels B and D. A decline of peak intensity below ~ 12 eV is observed, coinciding with the crossing from electronic to vibrational, *i.e.*, quasi-elastic, scattering (compare to Fig. 2C). The Cl 2p photoionization CS is shown for comparison (see text and Fig. S7 in the ESI†). Again, error bars depict the breadth of results obtained from running a least-squares fit of the spectra with varying model parameters and constraints. (D) Cl 2p PE signal of the slow electrons extracted from a two-hit coincidence analysis of the same measurement and data shown in panel A. Here, the inelastic background signal is vastly reduced. Even when suppressing the background signal through coincidence analysis, the nascent 2p feature spectral profiles cannot be retrieved at low eKE values. More specifically, this demonstrates that below ~ 10 eV KE, the PE signals from solutes (which are not strongly surface-active) are distorted and predominantly suppressed.

spectroscopy of liquid water, beyond the observed effects of vibrational inelastic scattering.

Role of superexcited states and autoionization in near-ionization-threshold-excited liquid water

Reviewing the observations reported above, we find that (1) the directly-produced primary $1b_1$ PE peak disappears at photoexcitation energies of $h\nu \leq 14$ eV (see Fig. 3), (2) a step-like decrease in the direct PE peak yields occurs for all direct valence ionization channels below a 10 – 14 eV eKE threshold (see Fig. 2A), (3) a step-like increase occurs in the LET signal as the direct valence PE feature eKEs drop below ~ 13 eV (see Fig. S5, ESI†), and (4) similarly to that described in (2), a step-like decrease occurs in the direct PE signal from an aqueous solute (as opposed to the water solvent) at eKE values of ~ 12 eV, at photon energies ~ 190 eV beyond observations (1)–(3) (see Fig. 4D). These observations collectively and specifically identify a change in the ionization behavior of liquid water below an excitation energy threshold of 12 – 14 eV, with the same threshold being observed on two

different excitation energy scales, *i.e.*, both the $h\nu$ and eKE scales, respectively, associated with photon and electron impact excitation. While the change in the primary, direct PE signals on the eKE scale could be attributed to the transition from predominantly electronic inelastic scattering processes to vibrational alternatives (see Fig. 2C and the explanations above), the similar threshold observed on a $h\nu$ scale cannot; vibrational inelastic scattering process are expected to dominate with similar CSs above and below $h\nu \sim 12$ – 14 eV ($=$ eKE ~ 1 – 3 eV). This suggests that an alternative process is (at least partly) responsible for the loss of primary, direct PE peak intensity below the aforementioned thresholds. We propose that one or more resonant, neutral-state excitation routes exist in liquid water at energies between 10 – 14 eV and that they are (at least partly) responsible for the threshold behaviors. The associated, commonly populated superexcited state (or states) must be efficiently accessible both *via* photoexcitation and electron impact, where electric dipole selection rules will primarily govern the former. Furthermore, observation (3) indicates that the accessed superexcited states



have a measurable autoionization yield and produce low-KE electrons.

Optically-bright, superexcited state resonances at 10–14 eV in liquid water would be expected to contribute to the associated photoabsorption spectrum. While broad absorption peaks are observed in the photoabsorption curve of hexagonal ice at 12.4 eV and 14.5 eV,⁷² those features are found to be inhomogeneously broadened in liquid water and amorphous ice, resulting in a merged profile.^{72,73} The crystalline ice peaks and the broader amorphous ice structure have been respectively attributed to $4a_1 \leftarrow 3a_1$ and $4a_1 \leftarrow 1b_2$ valence-to-conduction-band (electric-dipole-allowed) transitions, with such an assignment likely being extendable to liquid water. Concerning the fate of such superexcited states, autoionization is expected, as described in the following. A related higher-lying amorphous ice absorption feature centered at ~ 28 eV has been assigned to the $4a_1 \leftarrow 2a_1$ transition, with the resulting superexcited state found to decay through an autoionization process.⁵⁸ This process was observed to yield a broad secondary photoelectron spectrum peaking at an eKE of 11 eV and covering the 7–17 eV range, presumably *via* a $1b_2^{-1}$ indirect ionization process (where $VIE_{1b_2(s)}$ is ~ 17.6 eV^{74,75}). We expect similar processes to occur in liquid water following 25–30 eV photon or primary electron impact excitation, where the latter may well be discernible in the $h\nu > 50$ eV data shown in Fig. 1; see the weak and broad secondary PE peaks imposed on the background signals at eKEs of 11–18 eV.

We now return to the four observations listed above. Both $4a_1 \leftarrow 3a_1$ and $4a_1 \leftarrow 1b_2$ photon and electron impact excitations of neutral liquid water are expected to occur between 10–15 eV. The resulting superexcited states are expected to decay through autoionization to produce the $1b_1^{-1}$ and perhaps $3a_1^{-1}$ (energetically accessible^{50,76}) cation states with low-KE electrons spanning 0–5 eV, *via* a similar mechanism as observed following $4a_1 \leftarrow 2a_1$ excitation in amorphous ice⁵⁸ (and potentially identified here in liquid water). Such $1b_1^{-1}$ and/or $3a_1^{-1}$ indirect autoionization processes would be consistent with observation (3), and in concert with vibrational inelastic scattering processes, may be responsible for observations (1), (2), and (4) as well. Notably, the plot in Fig. 2B, related to observation (2), might also be affected by the aforementioned $4a_1 \leftarrow 2a_1$ excitation and $1b_2^{-1}$ indirect autoionization process, given the 25–35 eV photoexcitation energies involved in the critical data plotted in Fig. 2B. Clearly, however, further investigations will be required to confirm and understand such near-threshold, indirect aqueous ionization processes in detail. In any regard, the inference that superexcited states and autoionization phenomena occur close to the ionization threshold in liquid water and are (at least partially) responsible for the loss of direct PE peak structures, further emphasizes the complexity underlying the low excitation energy PE spectra of liquid water. Furthermore, with regard to our division of the LET into SEED and IPED contributions, excitation-energy-dependent indirect ionization channels seemingly need to be additionally included to fully describe our data and the overall LET signal produced at eKEs < 15 eV, and perhaps < 30 eV.

In the following we discuss one further potentially important inelastic scattering process and any effects it may have on our

observations, namely the probability of photoelectrons emitted from the liquid jet colliding with and inelastically scattering from the surrounding gas-phase water molecules.

Role of electron scattering with gas-phase water in a liquid-water-jet PES experiment

Aside from laser-based studies, the majority of previous liquid-jet PES experiments were performed with photon energies considerably above associated ionization thresholds, in which case only electronic scattering is relevant, which does not impair our ability to detect unperturbed (nascent) PE peaks from the liquid phase. In this situation of sufficiently high-KE electrons, the contribution from the gas-phase signal is straight-forward to quantify. This is typically founded on a comparison of the spectrum measured from the liquid water jet and from the surrounding water vapor (the latter being selectively recorded by moving the jet out of the ionizing light beam focus); an example of which is presented in Fig. S1 (ESI[†]) (panel A, green curve *versus* panel B, red curve). Since the characteristic water orbital energies are different for the two phases, it is possible to even measure photoelectron angular distributions (PADs) for each phase.^{47,62} This ability together with the fact that the PADs from the aqueous phase are distinctively different from the gas phase implies that the (Knudsen) gas-phase layer surrounding the jet has a negligibly small effect on the liquid-phase spectra. However, such a distinction of the gas-phase contribution is not as straight-forward at the low eKEs considered here; an issue that has been largely ignored so far. Why is this important? In the case of low-energy-loss channels, low eKEs, and when liquid and gas-phase water photoemission signal contributions are barely spectrally separated, an experimental determination of how much of the LET is due to electron-gas collisions is challenging. It is well-known, and a key aspect in the initial development of the liquid-microjet technology, that elevated gas pressures greatly diminish the PE signal.⁷⁷ With water, the situation is even more complicated as it does not exhibit a sharp boundary to vacuum, and rather the water density gradually decreases to the value of the gas on a length scale of about ~ 5 Å.^{78,79} This implies that in the case of the (low-photon energy and eKE) surface-sensitive PES experiments discussed here, the dense interfacial layer, with intermediate water density, must be inevitably considered as part of the liquid. What then remains to be explored is how much all other gas-phase water molecules on the way to the detector contribute to the LET and hence to the decrease of the initial intensity of the liquid-phase PE signal.

The gas density in the vicinity of the liquid jet quickly diminishes with distance as $1/r$ (where r is the radial distance from the nominal liquid-vapor interface boundary), until entering the skimmer orifice of the detection system where the pressure drops more rapidly (with $1/r^2$).⁸⁰ On this basis, a simple estimation (detailed in the ESI[†]) reveals that the effective thickness of the gas layer surrounding the liquid jet is too small for primary electrons of a few tens of eV KE to generate an appreciable LET signal. This conclusion is in accord with the fact that no LET signal is experimentally observed when probing only the gas layer around the liquid jet, as we demonstrate in Fig. S8 of the ESI[†]. We also recall that the dominance of quasi-elastic scattering translates



into a considerable increase in electron escape depth from the solution, which becomes increasingly 'transparent' as the electrons have insufficient energy to electronically excite liquid water. Possibly in such cases, the detection depth of the inelastically scattered electrons then approaches the optical penetration depth (inverse absorption coefficient) for UV excitation light, which is only on the order of $\sim 20\text{--}60$ nm in the $8\text{--}40$ eV range, but rapidly increases by several orders of magnitude below ~ 7 eV.

Conclusions

From liquid water and aqueous solutions alike, we observe both a rapid decrease in nascent, *i.e.*, undistorted, direct PE peak intensity and a rise of the background signal underlying the peaks when the photoelectron eKE falls below a critical energy of $\sim 10\text{--}14$ eV. This range coincides with the transition from known electronic to vibrational inelastic scattering channels, which vastly enhance quasi-elastic scattering and leads to deterioration of the nascent PE signal. Below the identified energetic threshold, PE features can no longer be reliably extracted (essentially) free from the effects of inelastic scattering, largely preventing the determination of correct VIEs and useful peak areas. Our results provide a reference eKE down to which PE features can still be extracted, largely undisturbed. This problem has only recently come under consideration in the aqueous phase, with sophisticated scattering models being developed with one aim being the retrieval of the nascent PE distribution. Yet, more knowledge of the underlying scattering process in liquid water and influencing factors is needed over an extended eKE range to refine the scattering models.

An additional important inference from this work is that following photon or electron impact excitation close to the ionization threshold of liquid water, indirect autoionization processes seemingly occur at the expense of direct photoemission, leading to effective production of threshold KE electrons, and a disproportionately large LET signal. We suggest that these low-KE electrons are produced *via* valence to $4a_1$ conduction band excitations, forming metastable superexcited states that subsequently autoionize. The specific processes occurring in the $10\text{--}14$ eV photon or electron impact excitation range are thought to form internally excited $3a_1$ and $1b_1$ cation states and electrons in the $0\text{--}5$ eV KE range, which undergo vibrational inelastic scattering prior to detection. Providing direct experimental evidence for these and other autoionizing superexcited valence states in liquid water represents an interesting and potentially important avenue of future research. This is particularly the case given that such processes are driven by some of the highest absorption CSs in liquid water and give rise to slow electrons, which are key contributors to radiobiological damage.^{28,29}

We emphasize that the underlying scattering phenomena discussed here may well be universal for solvents with similarly large band gaps as water, and moreover for all condensed matter exhibiting strong variation in scattering contributions as a function of eKE. Furthermore, one should keep in mind

that quasi-elastic scattering is never completely turned off, and will give an additional error (albeit increasingly small in cases where higher eKEs are tended towards in liquid water) to any determined condensed-phase VIE or peak area. Very likely the scattering discussed here for macroscopic liquid water is different for water clusters and nanodroplets. Indeed, studies from large water clusters have not revealed the existence of a LET signal,¹⁶ which is largely due to the fact that the clusters are significantly smaller in size (about 1 nm in size), resulting in PEs undergoing at most a single scattering event inside the clusters. Furthermore, there is an indication that the LET is significantly smaller in spectra from 100 nm nanodroplets.⁸¹ It remains to be explored how the occurrence of the inelastic scattering background correlates with cluster/droplet size.

Finally, the results reported here imply that great care must be taken when analyzing aqueous-solution PES experiments performed close to a given ionization threshold, for instance when using multiphoton or pump-probe ionization schemes (for example with $\sim 4.6\text{--}6.2$ eV photons). In a related context, these considerations will be extended in a forthcoming publication to evaluate the reported and widely scattered values of the lowest VIE of liquid water,^{45,50,82,83} *i.e.*, the VIE attributed to the $1b_1$ molecular orbital, with particular attention to the KEs of the electrons detected and analyzed in different experiments. Based on the results presented here (as well as those to come), we make a specific recommendation for future liquid-phase PE spectroscopy measurements: where nascent eKEs, associated BEs, and PE peak profiles are to be accurately measured and reported, photon energies ≥ 30 eV above the ionization threshold of interest should be implemented.

Data availability

Data relevant for this study have been deposited at DOI: 10.5281/zenodo.4575281.

Conflicts of interest

There are no conflicts to declare.

Acknowledgements

We would like to thank Ruth Signorell for many stimulating and fruitful discussions, as well as for the critical reading of and comments on this manuscript. S. T. acknowledges support from the JSPS KAKENHI Grant No. JP18K14178 and JSPS KAKENHI Grant No. JP20K15229. S. M., U. H., C. R. and B. W. acknowledge support by the Deutsche Forschungsgemeinschaft *via* projects Wi 1327/5-1 and FOR 1789. F. T., G. M., and B. W. acknowledge support by the MaxWater initiative of the Max-Planck-Gesellschaft. B. W. acknowledges funding from the European Research Council (ERC) under the European Union's Horizon 2020 research and investigation programme (grant agreement No. 883759). D. M. N. and C. L. were supported by the Director, Office of Basic Energy Science, Chemical Sciences Division of the



U.S. Department of Energy under Contract No. DE-AC02-05CH11231 and by the Alexander von Humboldt Foundation. We thank the Helmholtz-Zentrum Berlin für Materialien und Energie for allocation of synchrotron radiation beamtime at BESSY II. Some of the experiments were carried out with the approval of synchrotron SOLEIL (proposals numbers 99190181 and 20190130). Also, support by CalypsoPlus TNA is acknowledged. We thank the technical service personnel of the SOLEIL chemistry laboratories for their helpful support. Open Access funding was provided by the Max Planck Society.

Notes and references

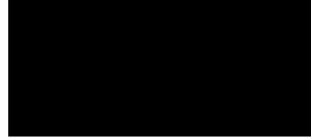
- M. Faubel, B. Steiner and J. P. Toennies, *J. Chem. Phys.*, 1997, **106**, 9013–9031.
- B. Winter and M. Faubel, *Chem. Rev.*, 2006, **106**, 1176–1211.
- R. Seidel, S. Thürmer and B. Winter, *J. Phys. Chem. Lett.*, 2011, **2**, 633–641.
- R. Seidel, B. Winter and S. E. Bradforth, *Annu. Rev. Phys. Chem.*, 2016, **67**, 283–305.
- S. Thürmer, R. Seidel, W. Eberhardt, S. E. Bradforth and B. Winter, *J. Am. Chem. Soc.*, 2011, **133**, 12528–12535.
- R. Seidel, K. Atak, S. Thürmer, E. F. Aziz and B. Winter, *J. Phys. Chem. B*, 2015, **119**, 10607–10615.
- G. Grell, S. I. Bokarev, B. Winter, R. Seidel, E. F. Aziz, S. G. Aziz and O. Kühn, *J. Chem. Phys.*, 2015, **143**, 074104.
- D. Nolting, N. Ottosson, M. Faubel, I. V. Hertel and B. Winter, *J. Am. Chem. Soc.*, 2008, **130**, 8150–8151.
- T. Lewis, B. Winter, A. C. Stern, M. D. Baer, C. J. Mundy, D. J. Tobias and J. C. Hemminger, *J. Phys. Chem. B*, 2011, **115**, 9445–9451.
- N. Ottosson, R. Vácha, E. F. Aziz, W. Pokapanich, W. Eberhardt, S. Svensson, G. Öhrwall, P. Jungwirth, O. Björnehholm and B. Winter, *J. Chem. Phys.*, 2009, **131**, 124706.
- N. Ottosson, J. Heyda, E. Wernersson, W. Pokapanich, S. Svensson, B. Winter, G. Öhrwall, P. Jungwirth and O. Björnehholm, *Phys. Chem. Chem. Phys.*, 2010, **12**, 10693–10700.
- S. Ghosal, J. C. Hemminger, H. Bluhm, B. S. Mun, E. L. D. Hebenstreit, G. Ketteler, D. F. Ogletree, F. G. Requejo and M. Salmeron, *Science*, 2005, **307**, 563–566.
- N. Ottosson, M. Faubel, S. E. Bradforth, P. Jungwirth and B. Winter, *J. Electron Spectrosc. Relat. Phenom.*, 2010, **177**, 60–70.
- H. Ali, R. Seidel, A. Bergmann and B. Winter, *J. Mater. Chem. A*, 2019, **7**, 6665–6675.
- R. Seidel, K. Krafft, A. Kabelitz, M. N. Pohl, R. Kraehnert, F. Emmerling and B. Winter, *Phys. Chem. Chem. Phys.*, 2017, **19**, 32226–32234.
- T. E. Gartmann, S. Hartweg, L. Ban, E. Chasovskikh, B. L. Yoder and R. Signorell, *Phys. Chem. Chem. Phys.*, 2018, **20**, 16364–16371.
- D. Luckhaus, Y. I. Yamamoto, T. Suzuki and R. Signorell, *Sci. Adv.*, 2017, **3**, e1603224.
- C. Adriaanse, J. Cheng, V. Chau, M. Sulpizi, J. VandeVondele and M. Sprik, *J. Phys. Chem. Lett.*, 2012, **3**, 3411–3415.
- A. Bernas, C. Ferradini and J.-P. Jay-Gerin, *Chem. Phys.*, 1997, **222**, 151–160.
- A. P. Gaiduk, T. A. Pham, M. Govoni, F. Paesani and G. Galli, *Nat. Commun.*, 2018, **9**, 247.
- J. Coe, A. D. Earhart, M. H. Cohen, G. J. Hoffman, H. W. Sarkas and K. H. Bowen, *J. Chem. Phys.*, 1997, **107**, 6023–6031.
- J. M. Heller Jr., R. N. Hamm, R. D. Birkhoff and L. R. Painter, *J. Chem. Phys.*, 1974, **60**, 3483.
- F. Williams, S. P. Varna and S. Hillenius, *J. Phys. Chem.*, 1976, **64**, 1549–1554.
- T. W. Marin, I. Janik, D. M. Bartels and D. M. Chipman, *Nat. Commun.*, 2017, **8**, 15435.
- Y. Itikawa and N. Mason, *J. Phys. Chem. Ref. Data*, 2005, **34**, 1–22.
- A. Muñoz, F. Blanco, G. Garcia, P. A. Thorn, M. J. Brunger, J. P. Sullivan and S. J. Buckman, *Int. J. Mass Spectrom.*, 2008, **277**, 175–179.
- M. Michaud, A. Wen and L. Sanche, *Radiat. Res.*, 2003, **159**, 3–22.
- B. Boudaiffa, P. Cloutier, D. Hunting, M. A. Huels and L. Sanche, *Science*, 2000, **287**, 1658–1660.
- C.-R. Wang, J. Nguyen and Q.-B. Lu, *J. Am. Chem. Soc.*, 2009, **131**, 11320–11322.
- R. L. Platzman, *Radiat. Res.*, 1962, **17**, 419.
- F. J. de Heer, *Int. J. Radiat. Phys. Chem.*, 1975, **7**, 137–153.
- Y. Hatano, *Radiat. Phys. Chem.*, 2003, **67**, 187–198.
- G. N. Haddad and J. A. R. Samson, *J. Chem. Phys.*, 1986, **84**, 6623–6626.
- M. U. Kuchiev and S. A. Sheinerman, *Sov. Phys. – Usp.*, 1989, **32**, 569–587.
- P. van der Straten, R. Morgenstern and A. Niehaus, *Z. Phys. D: At., Mol. Clusters*, 1988, **8**, 35–45.
- A. Lindblad, R. F. Fink, H. Bergersen, M. Lundwall, T. Rander, R. Feifel, G. Öhrwall, M. Tchapyguine, U. Hergenbahn, S. Svensson and O. Björnehholm, *J. Chem. Phys.*, 2005, **123**, 211101.
- B. Kassühlke, R. Romberg, P. Averkamp and P. Feulner, *Phys. Rev. Lett.*, 1998, **81**, 2771–2774.
- B. Winter, E. F. Aziz, N. Ottosson, M. Faubel, N. Kosugi and I. V. Hertel, *J. Am. Chem. Soc.*, 2008, **130**, 7130–7138.
- Possible small differences due to changes in scattering cross section caused by the presence of ions in comparison to (nearly) neat water cannot be resolved here.
- L. Nahon, N. de Oliveira, G. A. Garcia, J. F. Gil, B. Pilette, O. Marcouillé, B. Lagarde and F. Polack, *J. Synchrotron Radiat.*, 2012, **19**, 508–520.
- PLÉIADES beamline website, Synchrotron SOLEIL, Saint-Aubin, <https://www.synchrotron-soleil.fr/en/beamlines/pleiades>.
- EASI liquid-jet PES instrument website, Winter group, Fritz-Haber-Institut, Berlin, <https://www.fhi.mpg.de/236287/experimental-methods>.
- K. J. S. Sawhney, F. Senf, M. Scheer, F. Schäfers, J. Bahrtdt, A. Gaupp and W. Gudat, *Nucl. Instrum. Methods Phys. Res., Sect. A*, 1997, **390**, 395–402.
- M. N. Pohl, C. Richter, E. Lugovoy, R. Seidel, P. Slavicek, E. F. Aziz, B. Abel, B. Winter and U. Hergenbahn, *J. Phys. Chem. B*, 2017, **121**, 7709–7714.




- 45 N. Kurahashi, S. Karashima, Y. Tang, T. Horio, B. Abulimiti, Y.-I. Suzuki, Y. Ogi, M. Oura and T. Suzuki, *J. Chem. Phys.*, 2014, **140**, 174506.
- 46 I. Powis, D. M. P. Holland, E. Antonsson, M. Patanen, C. Nicolas, C. Miron, M. Schneider, D. Y. Soshnikov, A. Dreuw and A. B. Trofimov, *J. Chem. Phys.*, 2015, **143**, 144304.
- 47 S. Gozem, R. Seidel, U. Hergenahhn, E. Lugovoy, B. Abel, B. Winter, A. I. Krylov and S. E. Bradforth, *J. Phys. Chem. Lett.*, 2020, **11**, 5162–5170.
- 48 J. Nishitani, C. W. West and T. Suzuki, *Struct. Dyn.*, 2017, **4**, 044014.
- 49 D. Cahen and A. Kahn, *Adv. Mater.*, 2003, **15**, 271–277.
- 50 B. Winter, R. Weber, W. Widdra, M. Dittmar, M. Faubel and I. V. Hertel, *J. Phys. Chem. A*, 2004, **108**, 2625–2632.
- 51 J. Vég, *J. Electron Spectrosc. Relat. Phenom.*, 2006, **151**, 159–164.
- 52 S. Tougaard, *Surf. Interface Anal.*, 1997, **25**, 137–154.
- 53 S. Hüfner, *Photoelectron Spectroscopy: Principles and Applications*, Springer-Verlag, 1995.
- 54 *Encyclopedia of Materials Characterization: Surfaces, Interfaces, Thin Films*, ed. C. R. Brundle, C. A. Evans Jr. and S. Wilson, Butterworth-Heinemann, Boston, 1992.
- 55 Z. J. Ding, H. M. Li, R. Shimizu and K. Goto, *J. Surf. Anal.*, 2008, **15**, 186–194.
- 56 R. Signorell, *Phys. Rev. Lett.*, 2020, **124**, 205501.
- 57 K. F. Dunn, P. F. O'Neill, R. Browning, C. R. Browne and C. J. Latimer, *J. Electron Spectrosc. Relat. Phenom.*, 1996, **79**, 475–478.
- 58 C. D. Wilson, C. A. Dukes and R. A. Baragiola, *Phys. Rev. B: Condens. Matter Mater. Phys.*, 2001, **63**, 121101(R).
- 59 J. W. Gallagher, C. E. Brion, J. A. R. Samson and P. W. Langhoff, *J. Phys. Chem. Ref. Data*, 1988, **17**, 9–153.
- 60 M. S. Banna, B. H. McQuaide, R. Malutzki and V. Schmidt, *J. Chem. Phys.*, 1986, **84**, 4739–4747.
- 61 K. H. Tan, C. E. Brion, Ph. E. Van der Leeuw and M. J. van der Wiel, *Chem. Phys.*, 1978, **29**, 299–309.
- 62 S. Thürmer, R. Seidel, M. Faubel, W. Eberhardt, J. C. Hemminger, S. E. Bradforth and B. Winter, *Phys. Rev. Lett.*, 2013, **111**, 173005.
- 63 H. T. Nguyen-Truong, *J. Phys.: Condens. Matter*, 2018, **30**, 155101.
- 64 C. J. Fecko, J. D. Eaves, J. J. Loparo, A. Tokmakoff and P. L. Geissler, *Science*, 2003, **301**, 1698–1702.
- 65 J. D. Gorfinkiel, L. A. Morgan and J. Tennyson, *J. Phys. B: At., Mol. Opt. Phys.*, 2002, **35**, 543–555.
- 66 K. Ralphs, G. Serna, L. R. Hargreaves, M. A. Khakoo, C. Winstead and V. McKoy, *J. Phys. B: At., Mol. Opt. Phys.*, 2013, **46**, 125201.
- 67 Y. Zheng and L. Sanche, *Appl. Phys. Rev.*, 2018, **5**, 021302.
- 68 M. Matsui, M. Hoshino, H. Kato, F. Ferreira da Silva, P. Limão-Vieira and H. Tanaka, *Eur. Phys. J. D*, 2016, **70**, 77.
- 69 T. Harb, W. Kedzierski and J. W. McConkey, *J. Chem. Phys.*, 2001, **115**, 5507–5512.
- 70 C. E. Melton, *J. Chem. Phys.*, 1972, **57**, 4218–4225.
- 71 K. I. Grais and A. M. Bastawros, *J. Appl. Phys.*, 1982, **53**, 5239–5242.
- 72 K. Kobayashi, *J. Phys. Chem.*, 1983, **87**, 4317–4321.
- 73 H. Hayashi, N. Watanabe, Y. Udagawa and C.-C. Kao, *Proc. Natl. Acad. Sci. U. S. A.*, 2000, **97**, 6264–6266.
- 74 S. Krischok, O. Höfft, J. Günster, J. Stultz, D. W. Goodman and V. Kempter, *Surf. Sci.*, 2001, **495**, 8–18.
- 75 M. A. Henderson, *Surf. Sci. Rep.*, 2002, **46**, 1–308.
- 76 P. Delahay, *Acc. Chem. Res.*, 1982, **15**, 40–45.
- 77 D. F. Ogletree, H. Bluhm, E. D. Hebenstreit and M. Salmeron, *Nucl. Instrum. Methods Phys. Res., Sect. A*, 2009, **601**, 151–160.
- 78 P. Jungwirth and D. J. Tobias, *J. Phys. Chem. B*, 2001, **105**, 10468–10472.
- 79 F. Sedlmeier, D. Horinek and R. R. Netz, *Phys. Rev. Lett.*, 2009, **103**, 136102.
- 80 M. Faubel, S. Schlemmer and J. P. Toennies, *Z. Phys. D: At., Mol. Clusters*, 1988, **10**, 269–277.
- 81 Prof. Dr Ruth Signorell, ETH Zurich, private communication.
- 82 K. Nishizawa, N. Kurahashi, K. Sekiguchi, T. Mizuno, Y. Ogi, T. Horio, M. Oura, N. Kosugi and T. Suzuki, *Phys. Chem. Chem. Phys.*, 2011, **13**, 413–417.
- 83 C. F. Perry, P. Zhang, F. B. Nunes, I. Jordan, A. von Conta and H. J. Wörner, *J. Phys. Chem. Lett.*, 2020, **11**, 1789–1794.
- 84 L. Barreau, A. D. Ross, S. Garg, P. M. Kraus, D. M. Neumark and S. R. Leone, *Sci. Rep.*, 2020, **10**, 5773.
- 85 T. Jahnke, *et al.*, *Chem. Rev.*, 2020, **120**, 11295.



Paper III



Cite this: *Chem. Sci.*, 2021, 12, 10558 All publication charges for this article have been paid for by the Royal Society of Chemistry

Accurate vertical ionization energy and work function determinations of liquid water and aqueous solutions†

Stephan Thürmer, ^{*a} Sebastian Malerz, ^b Florian Trinter, ^{bc} Uwe Hergenbahn, ^b Chin Lee, ^{bde} Daniel M. Neumark, ^{de} Gerard Meijer, ^b Bernd Winter ^{*b} and Iain Wilkinson ^{*f}

The absolute-scale electronic energetics of liquid water and aqueous solutions, both in the bulk and at associated interfaces, are the central determiners of water-based chemistry. However, such information is generally experimentally inaccessible. Here we demonstrate that a refined implementation of the liquid microjet photoelectron spectroscopy (PES) technique can be adopted to address this. Implementing concepts from condensed matter physics, we establish novel all-liquid-phase vacuum and equilibrated solution–metal-electrode Fermi level referencing procedures. This enables the precise and accurate determination of previously elusive water solvent and solute vertical ionization energies, VIEs. Notably, this includes quantification of solute-induced perturbations of water's electronic energetics and VIE definition on an absolute and universal chemical potential scale. Defining and applying these procedures over a broad range of ionization energies, we accurately and respectively determine the VIE and oxidative stability of liquid water as 11.33 ± 0.03 eV and 6.60 ± 0.08 eV with respect to its liquid-vacuum-interface potential and Fermi level. Combining our referencing schemes, we accurately determine the work function of liquid water as 4.73 ± 0.09 eV. Further, applying our novel approach to a pair of exemplary aqueous solutions, we extract absolute VIEs of aqueous iodide anions, reaffirm the robustness of liquid water's electronic structure to high bulk salt concentrations (2 M sodium iodide), and quantify reference-level dependent reductions of water's VIE and a 0.48 ± 0.13 eV contraction of the solution's work function upon partial hydration of a known surfactant (25 mM tetrabutylammonium iodide). Our combined experimental accomplishments mark a major advance in our ability to quantify electronic–structure interactions and chemical reactivity in liquid water, which now explicitly extends to the measurement of absolute-scale bulk and interfacial solution energetics, including those of relevance to aqueous electrochemical processes.

Received 4th April 2021
Accepted 2nd July 2021

DOI: 10.1039/d1sc01908b

rsc.li/chemical-science

Introduction

Knowledge of the electronic structure of liquid water is a prerequisite to understand how water molecules interact with each other and with dissolved solutes in aqueous solution. Here, the valence electrons play a key role because their energetics govern chemical reactions.¹ One quantity of particular interest is water's lowest vertical ionization energy, VIE (or equivalently vertical binding energy, VBE), which is a measure

of the propensity to detach an electron under equilibrium conditions and thus determines chemical reactivity.² More precisely, VIE_{vac} , where the 'vac' subscript refers to energetic referencing with respect to vacuum, is the most probable energy associated with vertical promotion of an electron into the vacuum, *i.e.*, without giving it any excess energy, and with no nuclear rearrangement being involved. Such VIE_{vac} values are most readily accessed using photoelectron spectroscopy (PES) – usually from gases, molecular liquids, or molecular solids – and

^aDepartment of Chemistry, Graduate School of Science, Kyoto University, Kitashirakawa-Oiwakecho, Sakyo-Ku, Kyoto 606-8502, Japan. E-mail: thuermer@kuchem.kyoto-u.ac.jp

^bMolecular Physics Department, Fritz-Haber-Institut der Max-Planck-Gesellschaft, Faradayweg 4-6, 14195 Berlin, Germany. E-mail: winter@fhi-berlin.mpg.de

^cInstitut für Kernphysik, Goethe-Universität, Max-von-Laue-Straße 1, 60438 Frankfurt am Main, Germany

^dChemical Sciences Division, Lawrence Berkeley National Laboratory, Berkeley, CA, 94720 USA

^eDepartment of Chemistry, University of California, Berkeley, CA, 94720 USA

^fDepartment of Locally-Sensitive & Time-Resolved Spectroscopy, Helmholtz-Zentrum Berlin für Materialien und Energie, Hahn-Meitner-Platz 1, 14109 Berlin, Germany. E-mail: iain.wilkinson@helmholtz-berlin.de

† Electronic supplementary information (ESI) available. See DOI: 10.1039/d1sc01908b



are identified as the maximum intensities of primary, directly-produced photoelectron peaks.

Generally, in the condensed phase, PES features cannot be correlated with isolated molecular states, but are instead considered, particularly in crystalline samples, to arise from band structures, dense collections of states born from extended inter-atomic interactions.‡ Broad PES features are most often observed, from which it is often impossible to reliably extract valence VIE values. However, in molecular liquids and molecular solids, peak structures usually remain isolable, with associated VIE_{vac} values regularly being extracted and described within a molecular physics framework. Here, simple molecular orbital formalisms are adopted, with the peak structures ascribed to the liberation of electrons from specific orbitals. Adopting such an approach, the molecular orbitals of the water monomer have been considered to be only weakly perturbed by hydrogen bonding in the liquid phase, without specific regard for inter-monomer interactions or explicit consideration of the aqueous interface. The lowest VIE_{vac} value of water has correspondingly been assigned to ionization of the non-bonding $1b_1$ highest occupied molecular orbital (HOMO) in the gas,³ liquid,⁴ and solid⁵ phases. In fact, this molecular electronic structure description, and a vacuum level energy referencing approach, has almost exclusively been adopted in the interpretation of liquid-phase PES spectra.^{2,6,7} This is in spite of liquid water (and aqueous solutions) exhibiting both molecular^{4,8–11} and dispersed ‘band’^{7,8,12–17} electronic structure signatures. Naturally, this raises the questions of how liquid water should be placed between the aforementioned molecular and condensed matter conceptual frameworks, and specifically what can be learned by applying concepts from the latter to the PES of liquid water and aqueous solutions.

Within a condensed-matter framework and at thermodynamic equilibrium, the available states (or bands) of a system, are separated into occupied and unoccupied components around the Fermi level, E_F . As a precisely defined thermodynamic quantity, energy referencing with respect to E_F engenders direct comparison of system energetics between condensed-phase samples and the ready relation of those energetics to additional thermodynamic quantities. Such a useful energetic reference is readily accessible in metals using PES, where E_F lies within the available states and defines the upper electronic occupation level. In contrast, in semi-conductors, E_F is placed within a ‘forbidden’ band gap (devoid of states) and is thus, directly at least, inaccessible using the PES technique; E_F is notably not an electronic state that can donate or accept electrons here, rather it corresponds to a thermodynamic energy level. Liquid water, like most other liquids, can be classified as a wide-band-gap semiconductor,^{18–20} with a generally inaccessible Fermi level. Upon first consideration, liquid water may, therefore, seem unsuited to an E_F energy referencing scheme. Clearly, the solid-state custom of indirectly energy-referencing semi-conductor PES spectra to E_F via a metallic reference sample is much more difficult to apply to volatile and potentially charged aqueous-phase samples.

The VIE_{vac} values predominantly considered in liquid-phase PES experiments so far, as well as any VIE values determined

with respect to E_F , VIE_{EF} , arise from the cumulative energetics of a photoemission process. This includes the effects of collective phenomena (hydrogen bonding, inhomogeneous broadening *etc.*), electron transport, and an interface (typically liquid-vacuum),^{21–23} where the latter has yet to be explicitly addressed in liquid-phase PES studies. In liquid water, the ionization energies are specifically affected by inhomogeneous and fluxional intermolecular hydrogen bonding interactions. Here, the associated energetics vary over the transition region spanning the aqueous bulk and the liquid interface through which photoelectrons must traverse to escape into vacuum. These properties are closely related to distinctive condensed-matter system descriptors that are of particular relevance to photoemission, such as electrical conductivity, chemical potential (μ , equivalent to E_F), electrochemical potential ($\bar{\mu}$), work function ($e\Phi$), surface dipole, and surface (dipole) potential (χ^d or $e\phi_{outer}$).^{24–26} We present an overview of the relations between these parameters, with a focus on the liquid water system, in Fig. SI-1 of the ESI† and note that even after many years of aqueous-phase PES research, previous evaluations of liquid water's (lowest) VIE_{vac} values^{4,27–29} have barely considered these condensed matter descriptors. In other words, more differential probes of the bulk and interfacial electronic structure properties of liquid water and aqueous solutions have barely been addressed in PES experiments.§

We show here that the application of concepts from condensed-matter physics to liquid-jet (LJ) PES enables a significant expansion of our understanding of the electronic structure of liquid water. Towards that wider goal we pronounce two immediate aims. The first is to determine an accurate value of the lowest vacuum-level-referenced VIE of liquid water, $VIE_{vac,1b1(l)}$ (equivalent to its HOMO or $1b_1$ orbital ionization energy). Perhaps surprisingly, after more than 15 years of research, the value of this quantity remains controversial, mirroring key shortcomings in previous experiments. We address these deficiencies here and identify the need for additional spectroscopic information. For this particular task, the missing quantity is the (yet-to-be-discussed, although previously alluded to^{4,30,31}) low-energy electron cutoff in the liquid-water PES spectrum, a commonly measured parameter in solid-state PES.^{23,32–35} Motivated by a possible depth dependence of $VIE_{vac,1b1(l)}$ (*i.e.*, of neat water), we utilize the cutoff spectral feature to report the first systematic study of $VIE_{vac,1b1(l)}$ over a large range of photon energies, spanning the (vacuum) ionization threshold region up to more than 900 eV above it. We apply the same concepts to determine water's lowest VIE from exemplary aqueous solutions, $VIE_{vac,1b1(sol)}$, in addition, *i.e.*, detecting the solute-induced effect on water's electronic structure. We similarly demonstrate how to extract the VIEs of aqueous solutes, $VIE_{vac,solute}$, over a broad range of concentrations. Our second principal objective is to demonstrate how to measure E_F and $e\Phi$ of liquid water and aqueous solutions. We will discuss the meaning and importance of E_F in the case of the liquid water system, with the main goal of obtaining liquid-phase VIEs referenced to its Fermi level (VIE_{EF}), including those of neat water ($VIE_{EF,1b1}$), the aqueous solvent ($VIE_{EF,1b1(sol)}$), and associated solutes ($VIE_{EF,solute}$). The



successful implementation of this alternative aqueous-phase PES energy referencing scheme permits a direct comparison between liquid- and solid-phase PES results. It further enables more direct derivation of additional thermodynamic quantities from aqueous-phase VIE measurements, including redox energetics. The combination of the VIE_{EF} information with respective VIE_{vac} measurement results allows $e\Phi$ values to be derived and the explicit characterization and quantification of aqueous interfacial effects. Finally, we evaluate the challenges in characterizing Fermi level alignment between solutions and reference metals based on the currently available experimental methods, as we start to bridge the gap between aqueous-phase and solid-phase PES.

LJ-PES from water and aqueous solution

The common experimental approach

We begin with short overviews of the LJ-PES technique, the commonly adopted LJ-PES vacuum energy referencing method, and the current challenges in measuring accurate VIE_{vac} values of liquid water and solutions more generally. We also present some useful considerations on the application of a VIE scale to condensed-phase PE spectra in ESI Section 1,† which we apply from here onwards. Since the experimental breakthroughs in detecting photoelectron spectra from aqueous solutions, marked by the availability of vacuum liquid microjets^{36,37} over 20 years ago, a flurry of LJ-PES measurements has been conducted. Such measurements have greatly advanced our understanding of the electronic structure of aqueous solutions, in the bulk and at the solution–vacuum interface, as has recently been reviewed.³⁸ Notably, however, aside from very few exceptions, previous LJ-PES measurements have garnered the bare minimum spectral information, for which it has sufficed to detect a narrow range of electron kinetic energies, eKEs, of the emitted photoelectron distributions. For example, from aqueous LJs and their evaporating vapor layer, the characteristic eKEs of a solute or liquid water ionization feature of interest, $VIE_{vac,(l)}$, and the lowest energy gas-phase ionization peak, $VIE_{vac,1b1(g)}$, can be simultaneously determined. The latter value is accurately known (12.621 ± 0.008 eV),³ and from the difference of the measured peak positions, $\Delta E_{g-1} = VIE_{vac,1b1(g)} - VIE_{vac,1b1(l)}$, $VIE_{vac,1b1(l)}$ can (in principle) be determined.^{4,28,36} Adopting this procedure, here referred to as Method 1, vacuum-level energy referencing and production of the aqueous-phase photoemission spectrum is achieved without the need for further information. This simple and highly convenient molecular-physics approach, which is however challenging to accurately apply, as we will show below, is illustrated in Fig. 1A. There, we depict the measured valence photoemission spectrum of liquid water, *i.e.*, the kinetic energy distribution curve of the emitted photoelectrons, and the energy difference, ΔE_{g-1} , between the lowest energy liquid-, $1b_{1(l)}$, and gas-phase, $1b_{1(g)}$, water ionization features.

LJ-PES experiments commonly use rather high photon energies, typically some tens or more electron volts above the

relevant ionization thresholds. Such photon energies sufficiently separate directly-produced photoelectron peaks from the low-energy background of inelastically scattered electrons²³ and minimize scattering-induced distortions of the PE peaks themselves³⁰ (owing to the fact that electron scattering is almost exclusively governed by electronic excitations at such photon and kinetic energies³⁹). The vast majority of LJ-PES studies have adopted such photon energies to establish solute *core*-level energies, with the measured chemical shifts serving as a reporter of changes in the chemical environment. Small discrepancies in absolute core-level energies among different laboratories typically have little consequence on the main observations and derived statements. Similarly, the large body of studies of Auger decay and other autoionization processes from the aqueous phase^{40–43} would be barely affected by small uncertainties in absolute electron energies. This is in contrast to the situation with valence LJ-PES, which has been far less explored^{2,44,45} despite the primary importance of the lowest-ionization energies in driving aqueous-phase chemistry.² In this case, after more than 15 years of active high-energy-resolution LJ-PES research,^{38,43} and with concomitant advancement of aqueous electronic structure calculations and spectral simulation methods,^{8,9,41,46–52} an experimental advance and alternative terminology must be adopted to enable unequivocal and accurate valence VIE determinations with respect to the vacuum level. Related developments are needed to permit E_F (or system chemical potential) energy referencing of LJ-PES spectra, robust $e\Phi$ extractions from liquid samples, and direct comparisons of liquid- and solid-phase absolute-scale electronic energetics.

To understand the shortcoming of previous studies it is sufficient to discuss why the exact value of $VIE_{vac,1b1(l)}$ from neat water continues to be debated, spanning a 0.5 eV range between 11.16 ± 0.04 eV⁴ and 11.67 ± 0.15 eV.²⁹ All previously reported reference values were obtained using Method 1, from a mere ΔE_{g-1} measurement which neither requires the determination of absolute eKEs nor an exact calibration of the applied photon energy. However, a seemingly simple measurement of ΔE_{g-1} is difficult to accomplish due to the multiple sample charging effects and contact-potential differences that occur in LJ spectrometer systems (see the Discussion in Section 2 in the ESI and ref. 7, 28, 53 and 54). Accurate ΔE_{g-1} measurements are further complicated by the temporal variation of surface potentials within LJ-PES apparatuses, due to the continuous evaporation of LJs and the establishment of stable, adsorbed surface layers within spectrometers. All of these perturbing influences generate electric fields between the sample and the electron detector, which affect the photoelectrons from the gas and liquid phases differently and have to be precisely accounted for to record the ‘true’ (*i.e.*, undisturbed) ΔE_{g-1} value. As knowledge about the relevant effects and methods for their elimination continues to evolve,^{28,53,54} reported ΔE_{g-1} values, and thus deduced $VIE_{vac,1b1(l)}$ values continue to vary from laboratory to laboratory, which explains the scatter of the reported energies mentioned above.

Efforts to measure accurate ΔE_{g-1} values center around the minimization or even elimination of the effects of perturbing



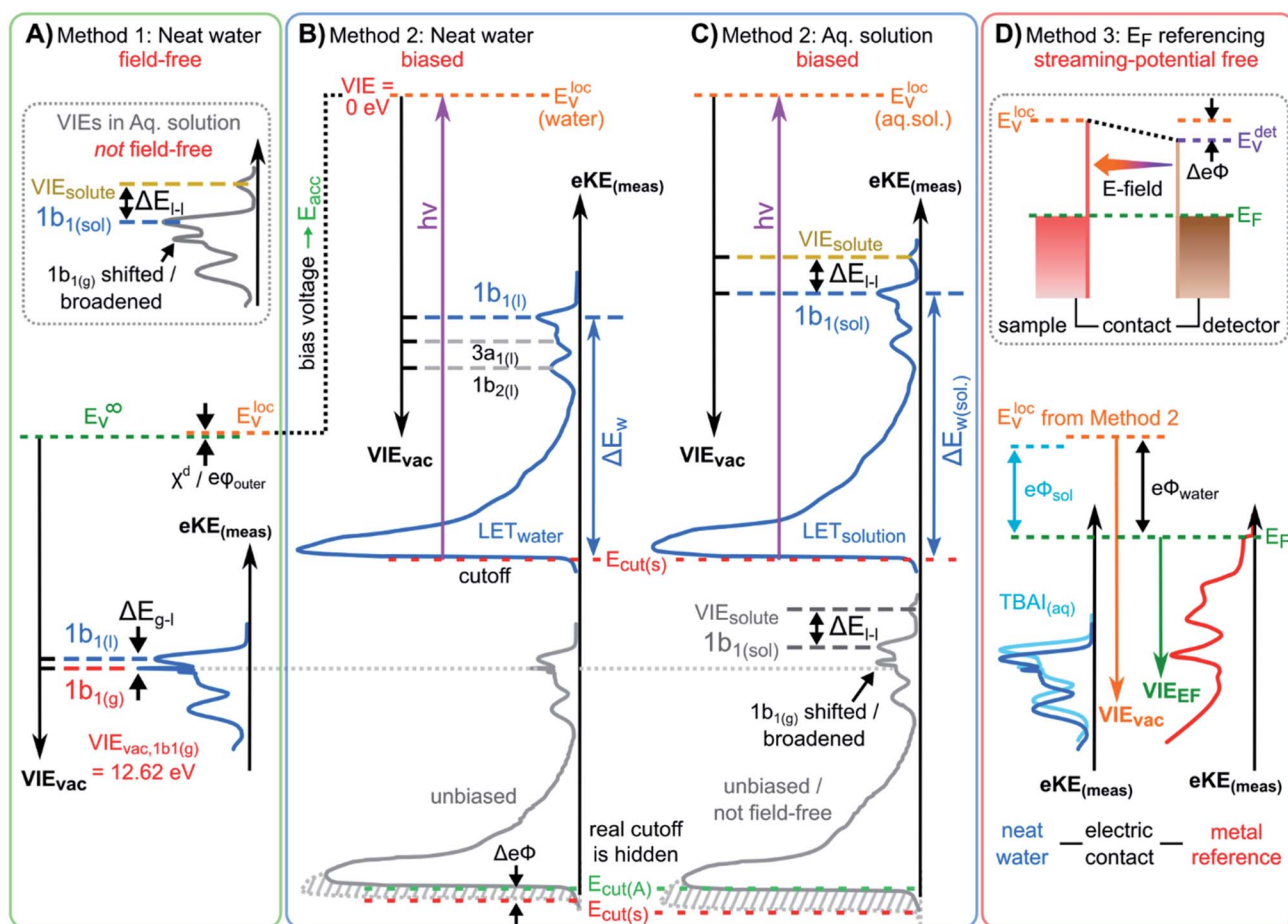


Fig. 1 Schematic electronic energetics for each experimental method described in the main body of the text. (A) Both gas- and liquid-phase water spectral features are measured together on the $eKE_{(meas)}$ scale under field-free conditions (blue spectrum), which makes it possible to use the known gas-phase VIE values (red) as an energy reference; ionization energies, VIE_{vac} , are referenced to the vacuum level at infinity, E_v^∞ . The inset shows the commonly adopted extension of Method 1 to reference solute VIE values by determining the solute peak's energetic distance to the liquid water $1b_1$ peak, ΔE_{g-l} , and (generally inappropriately) using the $VIE_{vac,1b_1}$ value of neat water as a reference value. Any possible changes of $VIE_{vac,1b_1}$ in a solution or the aqueous $e\Phi$ are disregarded in this approach. (B) A bias applied to the LJ shifts all liquid features under the influence of an accelerating field, E_{acc} (blue spectrum); the gas-phase PE signal is smeared out and does not appear here. Biasing reveals the full LET curve and cutoff energy of the sample spectrum, $E_{cut(s)}$. Without bias (grey spectrum), the real cutoff is obscured by the work-function difference between the liquid and analyzer, $\Delta e\Phi$, and one would instead measure a setup-dependent cutoff energy, $E_{cut(A)}$. $E_{cut(s)}$ constitutes a low-energy limit for photoelectrons to still overcome the liquid-surface barrier, and is thus connected to the local vacuum level above the LJ surface, E_v^{loc} . The precisely known photon energy $h\nu$ (vertical purple arrow) is used to map E_v^{loc} onto the measured spectrum and define the VIE_{vac} scale. Note that in general E_v^{loc} will deviate from E_v^∞ due to the intrinsic surface potential $\chi^d/e\phi_{outer}$ (see panel A and the text for details). Any extrinsic potentials are irrelevant in the applied bias case because the only relevant quantity is the energetic separation of the PE features from E_{cut} , ΔE_w (blue arrow). (C) As for (B) but for an arbitrary aqueous solution; here, the spectra are arbitrarily aligned to the cutoff, which at the same time aligns E_v^{loc} . Changes in ΔE_w directly translate to changes in the VIE. The lower part of this panel shows the full unbiased spectrum (compare to the spectra shown in the inset in panel A and bottom part of panel B). (D) The liquid water spectrum (dark blue) is energy-referenced to a common Fermi level, E_F , which defines the ionization energy scale with respect to Fermi, VIE_{EF} . This is achieved by separately measuring a metallic sample (red spectrum) in electrical contact and equilibrium with the liquid. The liquid-phase measurements must be performed with a sufficient amount of dissolved electrolyte to suppress the streaming potential and assure good conductivity. The Fermi-alignment with the apparatus leads to an offset of the local vacuum potentials as shown in the top inset in panel D. This creates an intrinsic potential difference due to the generally different $e\Phi$ values between the sample and the apparatus (detector). Thus, the measurement is usually not performed under field-free conditions, unlike Method 1. The difference between the VIE_{vac} and VIE_{EF} scales yields water's work function, $e\Phi_{water}$. We additionally sketch (light blue), the situation where $e\Phi$ changes and the valence spectrum shifts with respect to E_F upon build-up of a surface dipole arising from adsorbed interfacial anions and cations (here, representative of a surface-active TBAI aqueous solution; although this latter detail is not depicted). TBAI_(aq) is known to exhibit a pronounced surface-dipole layer comprised of slightly spatially separated maxima in the TBA⁺ and I⁻ concentration profiles,⁸⁶ which may lead to a reduction in $e\Phi$. This in turn would shift the position of E_v^{loc} of the TBAI solution with respect to the metallic sample.

potentials, compensating electrokinetic and other forms of charging of the LJ and other local potentials to achieve what we refer to as 'field-free' conditions. The primarily adopted method

achieves this by implementing a small but precisely determined salt concentration in water at a given solution flow rate and temperature.²⁸ Alternatively, the provision of field-free



conditions through application of a compensating bias voltage to a LJ has been discussed.^{29,31} In spite of such compensation efforts, the stabilization of spectrometer potentials occurs on the order of tens of minutes to hours after LJs are started or experimental parameters are adjusted, for example, when cold trap coolant is replenished. As we show in Fig. SI-2,† the apparatus potentials change dramatically (more than 100 meV) over time upon introducing water vapor into the experimental vacuum chamber, while eventually settling into an equilibrium. Unsurprisingly, these effects are difficult to quantify for a given experimental setup and operational conditions.

Here we highlight another potentially crucial and barely realized issue with Method 1, namely the meaning of the vacuum level. We have introduced VIE_{vac} above without providing a sufficiently accurate definition of the relevant vacuum level in a LJ-PES experiment. $VIE_{vac,1b1(g)}$ (like any other gas-phase ionization energy) is necessarily referenced to the vacuum level at infinity, E_v^∞ (used in Fig. 1A), and corresponds to the potential energy of the photoelectron at rest and at infinite separation from the photoionized sample.²⁴ In all previous LJ experiments, it has been implied that this same vacuum level is applicable and accessible upon ionization of liquid water, with existing $VIE_{vac,1b1(l)}$ values being consequently referenced to E_v^∞ via $VIE_{vac,1b1(g)}$. Adopting this assumption, the most probable (vertical) gas- and liquid-phase ionization energies have been taken as the maxima of the gas- and liquid-phase photoelectron (PE) peak fits within an encompassing spectrum. The consequences of this assumption will be further discussed below.

A yet further encountered and momentous oversight in previous LJ-PES studies is the determination of aqueous-phase solute VIE_{vac} values ($VIE_{vac,solute}$) with reference to pre-determined $VIE_{vac,1b1(l)}$ values measured from neat water, ideally under field-free conditions. That is, in (almost) all previous LJ-PES valence and a number of core-level studies spanning a broad range of aqueous solutions,^{2,38} the $VIE_{vac,1b1(l)}$ value (*i.e.*, from neat water) has in fact been used (as is) to calibrate $VIE_{vac,solute}$ values. Specifically, the energy difference between the solute PE peak position and lowest-energy solvent PE peak position, $VIE_{vac,1b1(sol)}$, has been used, under the generally erroneous assumption that $VIE_{vac,1b1(sol)} = VIE_{vac,1b1(l)}$. This is illustrated in the inset of Fig. 1A, where ΔE_{l-1} is the measured energy difference between two liquid-phase peaks, the lowest ionization energy, $1b_{1(l)}$, solvent peak and a solute peak. This energy referencing is generally rendered meaningless when non-negligible solvent-solute interactions and/or solute-induced interfacial electronic structure changes occur. In core-level studies, often the O 1s core-level energy (established for neat water only, again under field-free conditions)⁵⁵ has alternatively been used to similarly energy-reference $VIE_{vac,solute}$ values, with the same fundamental deficiencies. Such practices imply that solute-induced water electronic structure and solution $e\Phi$ changes do not occur, an assumption which has no rigorous foundation and may easily lead to quantitative failure of this extended implementation of Method 1, as recently discussed in ref. 7 and enunciated in ref. 31.

Alternatively, but equally problematic, one could strive for the determination of $VIE_{vac,solute}$ with reference to $VIE_{vac,1b1(g)}$, using the basic variant of Method 1, *i.e.*, the hypothetical field-free variant of what is shown in the main section of Fig. 1A. Yet, as detailed above, only if the region between the LJ interface and detector were field-free, could the measured electron energies from the gas-phase molecules be directly related to those from the liquid phase. For almost all solutions, field-free conditions are not or cannot be established in the experiment, and the same problems remain as for neat water. Thus, any additional field introduced to the solution – *via* electrokinetic charging, ionization-induced charging, or surface dipoles – renders the direct ΔE_{g-1} energy referencing for the solute peaks *via* (extrinsically field-free) values of $VIE_{vac, 1b1(g)}$ questionable. With Method 1, the relative contributions to the sample charging cannot be quantified, and field-free conditions thus only arise from the fortunate mutual compensation of any charging and/or differential $e\Phi$ effects.

Furthermore, and more fundamentally, the effects of any intrinsic and non-negligible interfacial dipole potential, χ^d , at the water liquid-vapor-phase interface⁵⁶ could lead to intrinsic offsets of ΔE_{g-1} from its true value, potentially compromising energy referencing Method 1. The value of the liquid water interfacial surface dipole potential has yet to be directly experimentally determined, although it has been inferred to amount to a few tens of meV in neat water,^{57,58} with associated theoretical predictions^{56,59–62} of χ^d varying significantly. In aqueous solutions, the value of χ^d is expected to be highly solute- and concentration-dependent,⁵⁶ calling the extended Method 1 energy referencing schemes for aqueous solutions further into question. Hence, to uniquely and generally interrogate both solute and solvent electronic structure on an absolute energy scale, a novel and robust experimental procedure that relies on an energy reference other than $VIE_{vac,1b1(g)}$ must be developed.

Condensed-matter approach and absolute energy reference

Above we have seen that an approximate value of $VIE_{vac,1b1(l)}$ from neat liquid water – with up to 0.5 eV uncertainty, depending on the care taken to compensate extrinsic potentials – can be obtained with the conceptually simple Method 1 (Fig. 1A). Adopting a more robust, absolute energy referencing method afforded using the low-energy photoelectron signal cutoff, E_{cut} , as widely applied in solid-state PES,^{23,32–35} the field-free requirement for accurate VIE_{vac} measurements is lifted. We now consider the associated energy-level diagram shown in Fig. 1B to illustrate this more robust and generally applicable experimental approach. In fact, as a requirement for an accurate $VIE_{vac,1b1(l)}$ (or alternative liquid-phase VIE_{vac}) determination, a negative bias voltage should be deliberately applied between the LJ and the electron analyzer orifice, imparting a well-defined additional eKE to the liquid-phase photoelectrons *via* an accelerating field, E_{acc} (indicated as black dotted line in Fig. 1B); we explain why the application of a bias voltage is indispensable below. Hence, a prerequisite for this approach is a sufficiently electrically conductive sample that supports the applied bias, held in direct electrical contact with the electron analyzer *via*



a stable DC power supply. Not only does this allow the unequivocal resolution of the true value of $VIE_{vac,1b1(l)}$ from neat water, the respective value (as well as any associated solute $VIE_{vac,solute}$) can also be accessed from *any* aqueous solution. In fact, the same methodology is also directly applicable more generally, for example, to organic solutions. Moreover, novel information on the solution–vacuum interface is conveniently provided.

The full LJ-PES spectrum from neat liquid water is sketched in Fig. 1B. The case of a photon energy sufficiently in excess of the first three ionizing transition thresholds of liquid water ($1b_1^{-1}$, $3a_1^{-1}$, and $1b_2^{-1}$ in a molecular-physics description) to yield undistorted primary photoelectron peaks is illustrated. Spectra associated with grounded (grey curve) and negatively biased (blue curve) liquid samples are shown. In the biased case, the entire liquid-phase spectrum experiences a rigid energy shift, equivalent to the negative bias voltage (see Fig. S1-3† for an experimental example of this effect). The exact value of the bias voltage is rather irrelevant for the present purpose. Unlike in Fig. 1A, the spectra in Fig. 1B encompass the full low-KE tail, LET, which terminates the spectrum at $eKE = 0$ eV.¶ The LET comprises electrons which have lost most of their energy due to various inelastic scattering processes, and have just enough energy to overcome the surface barrier of the sample. They are accordingly expelled with quasi-zero kinetic energy, signified here by the E_{cut} label, with E_{cut} defining the energetic zero from the perspective of a photoelectron leaving the sample.³⁵ Hence, the concurrent measurement of E_{cut} ($=0$ eV) and the VIE_{vac} values of interest – such as $VIE_{vac,1b1(l)}$ – allows the unique and self-consistent assignment of an eKE reference to the LJ-PES data, irrespective of *any* perturbing potentials, intrinsic or extrinsic. From Fig. 1B, it is seen that the eKE of the $1b_{1(l)}$ peak can be accurately determined *via* its energy separation from E_{cut} , *i.e.*, the spectral width, ΔE_w . The associated VIE is correspondingly determined as $VIE_{vac,1b1(l)} = h\nu - KE_{1b1(l)}$, where E_{cut} is set to 0 eV and it is implied that the photon energy is precisely known (we discuss procedures to precisely determine $h\nu$ for various light sources in the ESI Section 3). This procedure of measuring the *full* PES spectrum (or, at least, the LET region and the PE features of interest under the same conditions) will be referred to as Method 2 in the following. Importantly, gas-phase peaks or referral to $VIE_{vac,1b1(g)}$ are now irrelevant for the accurate extraction of $VIE_{vac,1b1(l)}$, or any other solvent or solute VIE . Furthermore, a favorable side effect of applying a high enough bias voltage is that the liquid-phase PE spectrum can be obtained essentially free from otherwise overlapping gas-phase signal, as is indicated by the missing sharp $1b_{1(g)}$ peak in the blue curve in Fig. 1B. In that case, the varying electrostatic potential between the biased liquid sample and the grounded electron analyzer results in a gas-phase peak broadening and a differential gas–liquid shift which is sufficient to move the gas-phase peak centers out of the liquid phase spectrum. Thus, the gas-phase features can almost be fully pushed out of the spectral range of interest. Notably, however, it is impossible to fully suppress the gas-phase signal at the energy position of the liquid spectrum by applying a bias, as some gas-phase molecules will

always reside directly above the surface and experience the full bias potential.

We have not yet thoroughly motivated the rationale for conducting experiments on a negatively biased sample, which so far was rarely practiced in liquid-phase PES. In the case of an unbiased LJ, the spectrum of the LET is typically obscured by the measurement process, as the PE distribution is modified by additional scattering inside the electron analyzer and then generally arbitrarily terminated at a low-energy cutoff, $E_{cut(A)}$, by the analyzer's own internal work function.^{34,35} This makes an accurate distinction of the true sample cutoff, $E_{cut(s)}$, impossible. The overlapping cutoffs for the unbiased liquid-water jet are correspondingly depicted in the bottom part and grey spectrum in Fig. 1B, with this spectrum being energetically-aligned with that shown in Fig. 1A. As partially highlighted in Fig. 1B, only by applying a sufficiently large negative bias voltage to the liquid jet can the LET curve of the sample and the secondary electron signals produced in the analyzer be well separated, the arbitrary $E_{cut(A)}$ threshold be far exceeded, and $E_{cut(s)}$ be precisely determined.

Thus far we did not comment on the appropriate vacuum reference level for Method 2. As alluded to above, gas-phase and condensed-phase PES measurements in principle refer to different vacuum levels. This is connected to the presence of a surface, through which the photoelectrons have to traverse as the final step in a condensed-phase PE process.²³ E_{cut} marks the minimum energy for a photoelectron to surmount the surface barrier and be placed at rest at a point in free space just outside the surface, overcoming $e\Phi$ (*i.e.*, where the electron image potential at the surface drops to zero and at a distance from the surface that is much smaller than the dimensions of the surface itself).²⁴ This connects all energies inferred with Method 2 to the *local* vacuum level, E_v^{loc} , but not necessarily to E_v^∞ . In aqueous solutions, the offset of E_v^{loc} with respect to E_v^∞ can be related to the outer (Volta) potential $e\phi_{outer}$ or χ^d ,⁵⁹ note the small E_v^{loc} versus E_v^∞ difference labeled $\chi^d/e\phi_{outer}$ in Fig. 1A and B, where the panels connect. Generally, an intrinsic millivolt to volt scale dipolar surface potential, χ^d , is expected to occur at the aqueous liquid–gas interface as the molecular density and hydrogen bond structure of bulk liquid water or an aqueous solution evolves from fully hydrated to partially hydrated and to increasingly isolated molecules in the gas phase. A range of experimental^{57,58,63} and theoretical^{56,59–62} studies have been performed to infer or calculate the net dipolar alignment and associated interfacial potential difference in the neat (or nearly neat) water case. While few tens of meV values have been inferred experimentally,^{57,58} a consensus on the value of χ^d at the water liquid–vapor-phase interface has yet to be reached from a theoretical perspective, and direct experimental measurements have not, to our knowledge, been reported. Relating this to the present discussion, χ^d clearly only emerges within a condensed-matter description of the aqueous-phase electronic structure. Furthermore, any non-negligible χ^d value would differentially affect electrons born at different points across the aqueous bulk to gas-phase transition region. Correspondingly, energy referencing Method 2 and the thus far adopted direct ΔE_{g-1} energy referencing approach, Method 1,



can be expected to yield inherently different $VIE_{vac,1b1(l)}$ values if a significant liquid water χ^d pertains.

Moving beyond our primary consideration of neat liquid water, Method 2 can also be applied without amendment to aqueous (or other) solutions, as shown in Fig. 1C. We can thus determine $VIE_{vac,1b1(sol)}$ with the same high accuracy as $VIE_{vac,1b1(l)}$ for neat liquid water, with the additional possibility of precisely determining other aqueous-phase solvent and solute VIEs. $VIE_{vac,1b1(l)}$, $VIE_{vac,1b1(sol)}$, and $VIE_{vac,solute}$ are again obtained as $VIE_{(l)} = h\nu - KE$ with E_{cut} defining zero KE. A solute-induced change of the former is seen to directly correspond to a change in the measured $1b_1$ ionization feature KE, corresponding to the different values of ΔE_w and $\Delta E_{w(sol)}$. We show an additional high-KE peak in Fig. 1C to exemplify the photoionization of a solute component. We emphasize that in the presence of a solute, surface potentials (in addition to the aforementioned extrinsic fields) are likely to be modified, generally making it impossible to establish the field-free conditions needed to directly apply Method 1. Its extended variant – measurement of ΔE_{l-1} and energy referencing to the field-free value of $VIE_{vac,1b1(l)}$ – as has so far been utilized to obtain reference energies for $VIE_{vac,solute}$ values, is similarly invalidated. Method 2, on the other hand, is not affected and thus permits direct access to absolute VIE changes between aqueous (or alternative) solutions for the first time. We further stress that Method 2 probes VIEs with respect to the local vacuum level E_v^{loc} and that the energetic position of E_v^{loc} with respect to E_v^∞ generally varies depending on the solution (note that the schematic biased spectra in Fig. 1C are arbitrarily aligned to the low-energy cutoff, which simultaneously aligns E_v^{loc}). Analogous to Fig. 1B, we illustrate the spectrum measured from an unbiased aqueous solution at the bottom of Fig. 1C, which highlights the overlapping sample and spectrometer LET curves and depicts the general inaccuracy of unbiased ΔE_{l-1} measurements when energy referenced using previously determined field-free, neat water $VIE_{vac,1b1(l)}$ values, as shown in the inset of Fig. 1A.

Fermi-level referencing and solution work functions

In the following we consider additional steps beyond the absolute, vacuum level energy referencing ability of Method 2 (Fig. 1B and C) and address the interfacial electronic structure information that becomes accessible using a condensed-matter framework and associated experimental approach. This leads us to attempt to determine E_F and $e\Phi$ in both water and aqueous solutions, with the latter providing a means to differentiate between solute-induced changes of (bulk or surface) liquid electronic structure or interfacial effects. Correspondingly, we briefly explain the concepts of E_F and $e\Phi$. E_F is formally equivalent to the chemical potential, μ , and at thermodynamic equilibrium is the energy at which a (potentially hypothetical) electronic state has 50% probability of being occupied at fixed temperature and any given time. The position of E_F throughout matter in electrical equilibrium assumes the same thermodynamic value. This makes E_F an advantageous energy reference in condensed-matter spectroscopies, especially for metallic

samples, in which electrons occupy states up to E_F , and which can be directly measured using photoemission. E_F is conceptually connected to two additional important quantities, the electrochemical potential, $\bar{\mu}$, and the work function, $e\Phi$. $\bar{\mu}$ is the energy required to bring an electron at rest *at* infinity into the bulk of the material. Hence, the sum of E_F and $\bar{\mu}$ is equivalent to E_v^∞ (and in a metal, the energy of $\bar{\mu}$ with respect to E_F is equivalent to the electron affinity). In contrast, $e\Phi$ is the minimum energy required to remove an electron at E_F , deep inside the material, and place it at rest at a point in free space just outside the surface, thus connecting to the local vacuum level, E_v^{loc} . E_v^{loc} and $e\Phi$ are correspondingly local properties of a surface which can change widely depending on the surface conditions.||

Fig. 1D depicts the energetic alignment of E_F for grounded liquid water and a grounded metal, which implies electrical contact between the liquid, the metal sample, and the analyzer. The exact meaning of ‘aligning the Fermi level’ of a solid and a liquid will be detailed in the Discussion section.† To generate accurate PES results, sufficient electrical conductivity must be engineered between all of these elements while suppressing parasitic extrinsic potentials, such as the aforementioned LJ streaming potential. Under these conditions, E_F can be directly measured from a metal, as indicated by the red archetypal spectrum on the right of Fig. 1D. The water sample, which is in direct electrical contact with the metallic reference sample and the analyzer, is then separately probed under the same conditions to produce the blue water spectrum on the left of Fig. 1D (identical to that shown in Fig. 1A). Sequential PES measurements from these two samples accordingly provides a means to formally assign E_F to liquid water (as implied in Fig. 1D), and hence define the energy scale needed to determine water’s ionization energy with respect to the Fermi level, $VIE_{EF,1b1(l)}$.** Such pairwise measurements will be reported here, where extensive efforts have been made to measure the LJ sample and metal reference spectra under as similar conditions as possible, for example by recording the latter in the presence of the LJ in operation to capture any potentially distorting influences of the LJ. The measured E_F position from the metal reference sample was found to remain constant within ~ 2 meV, regardless of conditions inside the vacuum chamber or whether the LJ was on or off. Despite this, our associated experimental approach, referred to in the following as Method 3, does however have a notable deficiency. As the electrons emitted from the metal are measured without crossing the solution–vacuum interface, any parasitic potentials and surface effects uniquely present on the LJ are not captured by Method 3. Extrinsic potentials, such as the streaming potential and light-induced surface charging, which are dependent on the solution and various experimental parameters, pose a new and unique challenge to the Fermi-referencing approach.†† In order to accurately and generally perform the E_F referencing procedure, the electrons from the metal sample would also need to be detected following traversal of the solution–vacuum interface, for example using a PES-compatible solution-on-metal sample system incorporating a continuous solution flow (to avoid sample contamination and cumulative photo-induced degradation). With presently



available experimental techniques (including electron-permeable flow cell windows⁶⁴), such a measurement remains elusive⁶⁵ due to the small electron mean free path in water.^{66,67} This constitutes one of the major challenges in applying PES to study water–solid interfaces. However, although an ideal E_F alignment and single-experiment E_F -referenced liquid-phase PES measurement (as suggested in Fig. 1D) is not yet feasible, E_F alignment can still be achieved *via* analysis of the two separately and carefully measured spectra, as we will discuss below.

Arguably, Method 3 can be applied for Fermi level referencing of aqueous-phase PES spectra under favorable conditions, specifically where parasitic potentials are effectively suppressed. In general, this is *explicitly* a different acquisition condition to the field-free condition required for Method 1. The work functions, $e\Phi$, of the samples and the detection system usually differ, which results in a contact potential difference, $\Delta e\Phi$, between the analyzer, the metallic reference, and/or the LJ sample in the E_F -aligned case; this situation is sketched in the inset of Fig. 1D. For the meaningful application of Method 3, one instead needs to find conditions in which (1) the solution conductivity is sufficiently high to enable alignment of E_F , by the exchange of charge between the solution and the grounding electrode, and (2) adequate suppression of both the streaming potential and ionization-induced sample charging is given. In this case, shifting of the liquid-phase PE features with respect to E_F in the measured spectrum can be avoided, *i.e.*, a direct relationship between the liquid and measured metallic reference spectrum can be established. Thus, after careful elimination of these influences, and the performance of two separate measurements to detect $VIE_{1b1(l)}$ or $VIE_{1b1(sol)}$ from the LJ and the Fermi edge from the reference metal sample, E_F referencing is in principle established. We emphasize – analogous to the gas-phase referencing approach, Method 1 – that if *extrinsic* potentials other than the aforementioned $\Delta e\Phi$ remain, *e.g.*, by insufficient compensation during the experiment, the liquid and metal spectra (*i.e.*, *measured* eKEs) are differentially affected, preventing a common energy referencing based on Method 3.

With $VIE_{vac,1b1(l)}$ determined *via* Method 2, a comparison to $VIE_{EF,1b1(l)}$ determined with Method 3 directly yields $e\Phi_{water}$ with the caveats described in Note ||. A conceptually similar procedure was previously applied by Tissot *et al.*⁶⁸ to extract E_F -referenced VIE values from static, low-vapor pressure, saturated (~ 6 M) NaCl and (~ 11 M) NaI aqueous solutions deposited on a gold substrate. There, the metallic and liquid features were referenced to each other under grounded conditions, with the associated approach further benefitting from being free from streaming potentials due to the static nature of the immobile liquid droplet. A value of $e\Phi$ was subsequently determined by biasing the sample and probing the associated isolated LET signal (see Note ¶). However, organic impurities contained in the solutions and accumulated radiation-induced sample damage may have obfuscated the true value of $e\Phi$; both issues are generally negligibly small when using liquid-microjet sample-delivery methods.³⁷ A subsequent attempt to determine $e\Phi_{water}$ using core-level LJ-PES – from 50 mM NaCl and

0.15 M butylamine aqueous solutions – was reported,³¹ albeit based on the implementation of an inadequate procedure that relied on several questionable assumptions, as detailed in ESI Section 7.†

More recently, we were made aware of a study by Ramírez,⁶⁹ which, building on the two works mentioned above, reports $VIE_{1b1(l)}$ and work function measurements from KCl and Zobell⁷⁰ aqueous solutions to tune the aqueous redox potential; the reasons for and implications of implementing such a redox couple are detailed below when we present our measurements of liquid water's work function. The associated VIE_{vac} , VIE_{EF} , and $e\Phi$ values notably differ from the values reported in the present work and are elaborated on in the Results & discussion section as well as ESI Section 7.†

Methods

Experiments were performed at four facilities, equipped with different setups. Measurements at photon energies of ~ 15 eV, ~ 20 eV, ~ 25 eV, and ~ 30 eV were conducted at the DESIRS VUV beamline⁷¹ of the SOLEIL synchrotron facility, Paris, using a novel LJ-PES apparatus.⁷² The same LJ-PES setup was used for He I α ($= 21.218$ eV), He II α ($= 40.814$ eV), and He II β ($= 48.372$ eV) measurements in our laboratory at the Fritz-Haber-Institute (FHI), Berlin, and for measurements at photon energies of ~ 250 eV, ~ 400 eV, and ~ 950 eV at the P04 soft X-ray beamline⁷³ of the PETRA III synchrotron facility (Deutsches Elektronen-Synchrotron, DESY, Hamburg). Briefly, the LJ-PES apparatus is equipped with a Scienta Omicron HiPP-3 hemispherical electron analyzer (HEA), complete μ -metal shielding, and, when not operated at a synchrotron radiation source, a VUV5k monochromatized plasma-discharge light source (He) for the laboratory experiments. Measurements at photon energies of ~ 123.5 eV, ~ 247 eV, ~ 401 eV, ~ 650 eV, and ~ 867.5 eV were additionally performed using the SOL³PES setup⁷⁴ at the U49-2_PGM-1 soft X-ray beamline⁷⁵ at the BESSY II synchrotron radiation facility in Berlin.

In the low-photon-energy synchrotron experiments at SOL-EIL, the light was linearly polarized perpendicular to the plane of the laboratory floor, which was the plane spanned by the LJ and light propagation axes. The analyzer collected electrons in a backward scattering geometry, forming an angle of 40° to the light polarization direction. An energy resolution of better than 3.5 meV with an on-target spot size of approximately 200 μm horizontal (in the direction of the LJ propagation) and 80 μm vertical was implemented at the LJ in these experiments. The VUV He discharge light source at FHI delivered essentially unpolarized light to the LJ *via* a minimally polarizing ($< 0.1\%$) monochromator system. The energy resolution was limited by the intrinsic width of the emission lines, 1 meV (He I) and 2 meV (He II), and the focal spot size was approximately $300 \times 300 \mu\text{m}^2$ at the LJ. The light propagation axis of the VUV He discharge light source spanned an angle of $\sim 70^\circ$ with respect to the photoelectron detection axis. The associated electron analyzer resolution was better than 40 meV at a pass energy of 20 eV. In the PETRA III experiments, the synchrotron beam was circularly polarized and the electron analyzer collection axis was



aligned at 50° with respect to the light propagation axis (using the same analyzer geometry as in the SOLEIL experiment). The energy resolution was calculated to be 30 meV at 250 eV, 50 meV at 400 eV, 80 meV at 650 eV, and 140 meV at 950 eV with an associated focal spot size of approximately 180 μm horizontal (in the direction of the LJ propagation) and 20 μm vertical at the LJ. In the BESSY II synchrotron experiments, the light propagation axis was aligned orthogonally to the photoelectron detection axis. The U49-2_PGM-1 beamline (BESSY II) supplied linearly polarized soft X-rays with their polarization vector in the plane of the laboratory floor. The LJ and the photon beam propagated in this plane and were mutually orthogonal. The analyzer collection axis was aligned at ~55° with respect to the synchrotron beam polarization axis. The corresponding energy resolutions were 35 meV at ~125 eV, 70 meV at ~250 eV, 120 meV at ~400 eV, and 250 meV at ~868 eV (as determined *via* gas-phase photoemission resolution calibration measurements) with a focal spot size of approximately 100 × 40 μm² at the LJ.

The aqueous solutions were injected into the interaction vacuum chamber through 25–30 μm orifice diameter glass capillaries at the tip of a LJ rod assembly. The liquid flow rate was 0.5–0.8 ml min⁻¹. In the EASI experiments, the temperature was stabilized to 10 °C by water-cooling the LJ rod using a recirculating chiller. In the SOL³PES experiments, the solutions were cooled to 4 °C within a recirculating chiller bath, prior to delivery to the vacuum chamber *via* insulating PEEK tubing. Upon injection into vacuum, the LJs exhibited a laminar flow region extending over 2–5 mm, after which Rayleigh-instabilities caused them to break up into droplets, which were ultimately frozen at a liquid nitrogen trap further downstream. The laminar-flow region was surrounded by an evaporating water gas-sheath in all cases, with rapidly-decaying local gas pressures spanning ~10 mbar at the solution-vacuum interface and descending to the average vacuum chamber pressures with a 1/*r* distance dependence from the cylindrical LJs. The laminar region of the LJs were positioned and ionized in front of the HEA entrance apertures. The liquid-vacuum interface we refer to in the text, *i.e.*, the interface region where water's density rather smoothly decreases from its liquid bulk value to that of the gas in the immediate vicinity of the surface, is thought to evolve over a single-nm length scale.⁷⁶ The associated solutions were prepared by dissolving NaI or NaCl (both from Sigma-Aldrich and of ≥99% purity) in highly demineralized water (conductivity ~0.2 μS cm⁻¹) and were degassed using an ultrasonic bath. Concentrations of 30–50 mM were used for all measurements performed under biased conditions. To measure liquid water spectra under field-free conditions, a conductive electrode was introduced in the electrically conductive liquid stream and electrically connected to the analyzer. In addition, at the beginning of every experimental run, the concentration of NaCl was iteratively varied in ~10 steps to minimize the observed width of the gas-phase photoelectron peaks. Such conditions are obtained when the potential difference between the liquid jet and analyzer entrance cone is zeroed over the liquid-gas-phase sample-light-source interaction region, with field-free conditions correspondingly

pertaining, at least on average. In the EASI instrument, the corresponding optimal NaCl concentration was consistently found to be 2.5 mM at a flow rate of 0.8 ml min⁻¹ and a liquid jet temperature of 10 °C. The LJ rods were mounted into micrometer manipulators for high-precision alignment. The average pressures in the interaction chambers were maintained between 7 × 10⁻⁵ and 1 × 10⁻³ mbar using a combination of turbo-molecular pumping (~2000 or ~2700 l s⁻¹ pumping speed for water vapor in the SOL³PES and EASI instruments, respectively) and two (SOL³PES) or three (EASI) liquid-nitrogen-filled cold traps (up to 18 000 l s⁻¹ pumping speed for water vapor per trap in both instruments). The light-LJ interaction point was set at a 500–800 μm distance from the detector entrance orifice, either a 500 μm (SOL³PES) or 800 μm (EASI) circular differential pumping aperture. In all experiments, the LJ propagation and photoelectron detection axes were orthogonal to each other. For the experiments with the grounded LJ (field-free and streaming-potential-free measurements) all surfaces in the vicinity (at least up to 4 cm away) of the LJ-light interaction point were carefully cleaned and then coated with graphite to equalize the work function of all surfaces and prevent stray potentials: this includes the LJ rod, detector cone including the skimmer, and exit capillary of the VUV plasma-discharge light source. The glass LJ capillary was not coated. We made sure that all new glass LJ capillaries were run with water for at least a day, to passivate the inner surfaces.²⁸

In both the EASI and SOL³PES experiments, solutions were guided through PEEK tubing all the way to the glass capillary, *i.e.*, the liquid did not come in electrical contact with the LJ rod. In the EASI experiments, the liquid flowed through a metallic grounding insert in-between the PEEK tubing prior to injection into the vacuum chamber, *i.e.*, before entering the LJ rod assembly. In the SOL³PES experiments, an electrical contact to the liquid was provided by an electrically insulated platinum disc inside the jet rod just before the glass capillary. This disc was connected *via* an insulated wire to an external electrical feedthrough. Both methods facilitated either the electrical grounding of the liquid to the same potential as the electron analyzer *via* a bridge cable or the deliberate application of a bias voltage to the liquid with respect to the analyzer. We emphasize that this biased the liquid solutions directly, and no external electrodes were used. Identical results were obtained with the two LJ rods. The bias voltages were applied using highly stable Rohde & Schwarz HMP4030 voltage sources. A sketch illustrating the LJ-PES experiment for a grounded and negatively biased water jet is presented in Fig. 2A and B (neat water)/2C (aqueous solution), respectively.

For the Fermi-level measurements, we utilized two metallic reference samples. Firstly, a gold wire in good electrical contact and in close proximity to the LJ (expelled by the aforementioned glass capillary nozzle) was implemented. Alternatively, a grounded platinum-iridium (PtIr) disc was used instead of the glass LJ nozzle to expel the liquid through a metallic pinhole. The PtIr disc was thus in direct electrical contact with the liquid expelled as a LJ, similar to the original LJ-PES setup utilized in ref. 4. In the SOL³PES experiments, both the liquid nozzle and the gold wire were mounted together on the same manipulator assembly



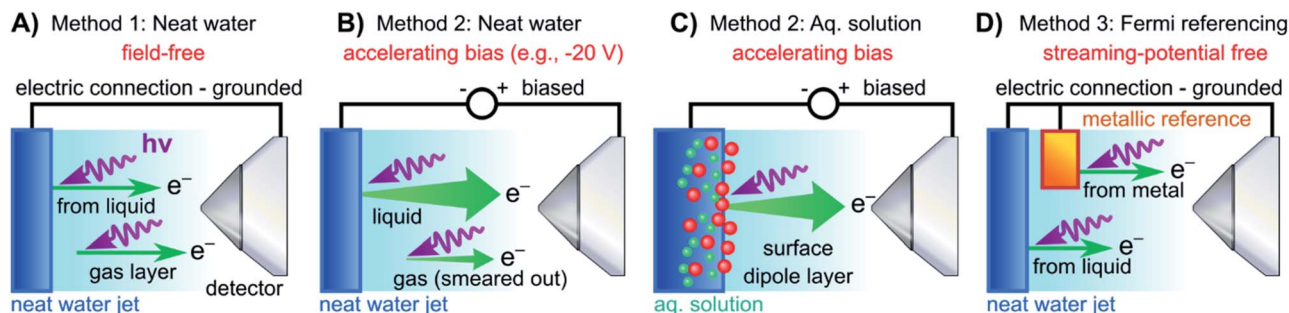


Fig. 2 Schematic setups for the measurement procedures introduced in Fig. 1. (A) Electrically grounded (nearly) neat water LJ with a precisely tuned salt concentration to achieve a field-free condition for gas-phase referencing. (B) Negatively biased LJ used to reveal E_{cut} in the liquid spectrum for energy referencing; gas- and liquid-phase PE contributions are energetically separated in the field gradient. (C) Same as (B) but for an aqueous solution (here, featuring a surface-active solute). Changes in VIEs can be directly observed. (D) Similar to (A) but with the addition of a metallic reference sample held in electrical contact to and mounted within the vicinity of the LJ. The liquid water spectrum can be referenced to the Fermi edge of a metal sample under field-free conditions. Note that the metallic reference sample surface is probed separately from the LJ in the experiments reported here, and thus is not directly affected by any changes at the surface of the solution.

and were moved in unison. The metal spectrum was measured with the LJ running after slightly relocating the whole assembly to bring the gold wire, instead of the LJ, into the synchrotron and detector foci. The EASI setup instead featured a retractable gold wire on a different port. A schematic of the PES measurement from a LJ in electric contact with a grounded gold target is presented in Fig. 2D. The PtIr disc was exposed to ionizing radiation through a cutout in the disc mount that was aligned towards the detector orifice; the disc was brought into the light source focus by slightly moving the rod assembly. All methods yielded the same energetic position of the Fermi level with better than 0.03 eV precision, and no changes in the Fermi-level position were detected when running different solutions.

Results and discussion

The accurate lowest VIE of liquid water, $\text{VIE}_{\text{vac},1b_1}$

We first present results obtained with the measurement schemes introduced in Fig. 1B and 2B, *i.e.*, energy referencing Method 2 introduced above. Fig. 3A shows an exemplary liquid water jet full PES spectrum in red, ranging from $E_{\text{cut(s)}}$ to the eKE maximum, recorded with a 40.814 eV (He II α) photon energy and an applied bias voltage of -20 V. eKEs are presented as recorded by the spectrometer and under the influence of the applied bias on the top abscissa, *i.e.*, the quantity measured in the experiment. On the bottom abscissa, we plot the eKE scale with 20 eV subtracted to compensate for the applied sample bias. $E_{\text{cut(s)}}$ is found at slightly smaller energies than zero eKE when the -20 eV compensation is applied. In general, the bias voltage is slightly reduced (here by about $\sim 2\%$) due to internal resistances between the voltage source and the liquid surface inside the vacuum chamber (for example, see Fig. SI-3†). However, the exact cutoff position can vary widely, as the precise KE scale depends on the particular experimental conditions, including the aforementioned residual resistance, LJ flowrate, electrolyte concentration, ionizing photon flux *etc.* Importantly, the absolute energetic position of $E_{\text{cut(s)}}$ or any valence features in the spectrum is of no concern for our method; we specifically

aim to determine energetic separations here, ΔE_w in Fig. 1B, which are not affected by the effectively applied bias voltage or any other extrinsic potential. The bias must, however, be large enough to separate $E_{\text{cut(s)}}$ from $E_{\text{cut(A)}}$ (where the former may otherwise be obscured by the latter, as illustrated in Fig. 1B), and be stable on the energetic scale of the eKE measurement precision and the timescale of the experiment. Whether the measured LET curve accurately reflects the true shape and intensity of the nascent electron distribution emitted by the liquid sample with respect to the characteristic valence water PES signal intensities (commonly attributed to $1b_1$, $3a_1$, $1b_2$, and $2a_1$ orbital ionization and shown in blue in the $\times 20$ enlarged region of the spectrum), cannot be answered here. Such a determination requires careful and technically demanding calibration of the HEA transmission under the adopted conditions.†‡

Under the -20 V bias conditions employed here in order to utilize Method 2 (see Fig. 1B), most of the gas-phase water contributions are spread out over an energy range which lies below the LET of liquid water. The remaining small tail residing below the LET – accounting for less than 0.5% of the signal, depending on the bias setting and size of the ionizing light spot – has been subtracted from the data shown in Fig. 3 (note that the small signal tail below the sample cutoff feature will generally also have a secondary electron contribution created within the detection system, although modern HEAs adopt measures to minimize such parasitic signals as much as possible). For reference, the inset of Fig. 3A shows the 20–32 eV region of the valence spectrum for the grounded water jet (in green). The unbiased spectrum exhibits simultaneous gas- and liquid-phase contributions, as commonly reported in the LJ literature^{4,6} and somewhat enhanced here due to the relatively large focal spot size of the utilized VUV He discharge light source.

It is of interest to discuss the unbiased spectrum (inset of Fig. 3A) in detail. It exhibits sharp vibrationally resolved gas-phase peaks, which are generally not observed in LJ-PES experiments. Sharp spectra of gaseous molecules are readily



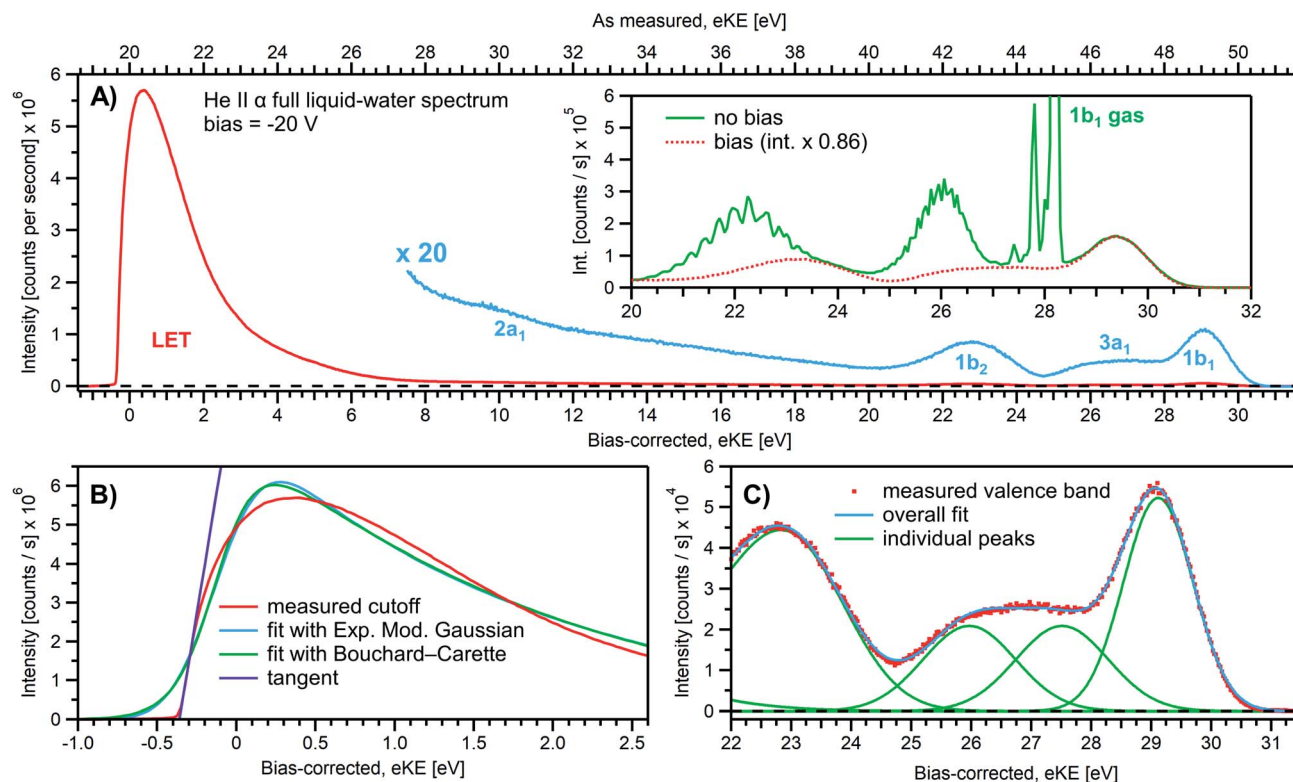


Fig. 3 (A) A representative PE spectrum of liquid water (with 50 mM NaCl added), measured with a monochromatized He II α emission light source ($h\nu = 40.814$ eV). Exemplary associated electron count-rates are presented, as reported by the analyzer measurement software. Note that the count rate calibration is that provided by the analyzer manufacturer, which has not been verified under the acquisition conditions implemented here, and correspondingly should be considered a coarse guide to the overall experimental acquisition conditions only. A bias voltage of -20 V was applied to separate the liquid- and gas-phase contributions as well as to expose the low-KE tail (LET) region. The as-measured eKE is shown on the top x-axis in (A), with the bias-corrected scale shown on the lower x-axis. The same spectrum with the intensity multiplied by 20 shows the full valence band of water. The inset compares the valence region with and without an applied bias, exposing the gas-phase contribution. (B) A close-up of the cutoff region with three analysis methods applied as described in the main body of the text. The bias-corrected x-axis scale is plotted and the residual gas-phase contribution has been subtracted. (C) A close-up on the valence spectral region with a cumulative Gaussian fit to all ionization peaks/molecular orbital contributions, also plotted on the bias-corrected x-axis scale. Only the three highest energy orbitals are visible here.

obtained with our setups if measurements are made without the LJ installed (see, e.g., Fig. SI-2B,[†] where the gaseous $1b_1$ HOMO ionization peak was measured by flowing gaseous water into the vacuum chamber). In that case we are not concerned with any disturbing electric fields. However, in the presence of the LJ, and with associated intrinsic and extrinsic potentials and a potential gradient acting between the LJ and the analyzer, photoelectrons from the gaseous species are accelerated differently depending on their spatial point of origin, and thus the gas-phase spectrum is inevitably broadened. In other words, a sharp gas-phase spectrum measured from water molecules evaporating from the LJ is a good indicator of a vanishing electric field in the experiments that use the relatively large focal spot of our VUV He discharge light source (300 μm beam diameter). Such a field-free condition is a very useful sensor that will be exploited in the present work. A point of caution, however, is that the 'sharpness' or broadening of gaseous PE features in the presence of extrinsic fields distinctively depends on experimental parameters like the spot size of the light source or experimental resolution, and is not a universal indicator of

field-free conditions.^{§§} The liquid spectrum measured with the -20 V bias applied is also shown in the inset of Fig. 3A (red dots), negatively shifted by the bias potential for comparison. Under these experimental conditions, an essentially pure liquid water spectrum is obtained with the gas-phase contribution shifted out of the detected energy range, as explained earlier in the manuscript in the context of Fig. 1. Note that due to experimental-geometry-dependent differences in the relative intensities of the gas versus liquid phase valence ionization features, the energetic positions of the liquid-phase peaks can be easily misidentified in the absence of the applied bias. Different apparent liquid peak heights in the biased and unbiased cases reflect the fact that only the $1b_1$ gas- and liquid-phase ionization signal contributions are well separated spectrally, while for all other valence ionization channels, the two contributions overlap.⁴

We next discuss the accurate determination of $E_{\text{cut}(s)}$ and the position of liquid water's lowest VIE. For the former we analyze the spectral cutoff region and the LET, presented in Fig. 3B. As in Fig. 3A, the measured curve is shown in red. The purple line

is the tangent extracted at the low KE inflection point, which is determined from the first derivative of the LET spectrum. The tangent intersection with the x -axis determines $E_{\text{cut}(s)}$, a standard procedure in solid-state PE spectroscopy (for example, see ref. 77–82) that is correspondingly adopted here. The associated protocol, as well as alternative approaches to defining E_{cut} , are described in ESI Section 5 and illustrated in Fig. SI-4.† For comparison, we apply two additional fit functions to the data shown in Fig. 3B, the Exponentially Modified Gaussian (EMG, blue curve) distribution as originally used by Faubel and co-workers to model the liquid-phase LET curves,³⁶ and the distribution applied by Bouchard and Carette (green curve) as originally introduced for the description of the LET in semiconductors.⁸³ Both of these distributions were previously adopted in the analysis of PES spectra from a stationary droplet of saturated NaCl and NaI solutions.⁶⁸ However, neither of the two functions yield appropriate fits to the narrower experimental LET curves measured in the present work with a LJ sample, unlike in ref. 68, supporting the associated authors' conclusion that their LET is affected by considerable surfactant impurities. Such problems are clearly avoided with a flowing and replenishing LJ, where an intrinsically sharp cutoff spectral region can be accurately measured from a liquid water sample, a similar observation to that reported in ref. 31. We note that the cutoff position extracted through fitting one of the aforementioned functions, or an alternative simple linear fit, often depends on the user-selected fit range, whereas a derivative-based method (like the conventional tangent approach favored here) is purely determined by the data, with no free parameters. Using the tangent method, the directly measured E_{cut} value in our example is determined to be 19.64 ± 0.02 eV (notably including the bias-induced eKE offset; compare to the top axis in Fig. 3A). Again, the fact that this value is smaller than the bias applied at the power supply (-20.000 ± 0.015 V) is primarily assigned to a residual electrical resistance within the LJ, which has no relevance for our method, as outlined above and further discussed below.

In order to determine the position of liquid water's lowest ionization energy, $\text{VIE}_{\text{vac},1b_1(l)}$ (pertaining to the $1b_1$ peak maximum), we fit the valence PES spectrum in accordance with the existing literature, with two Gaussians for the well-established, split second ionization threshold feature, the $3a_1$ upper and lower peaks, and a single Gaussian for the other ionization features, the $1b_1$ and $1b_2$ peaks.^{4,27} Common heights and widths of the split, second VIE ($3a_1$ orbital components) were implemented for spectra recorded with sufficiently high photon energy and bias applied, *i.e.*, in spectra where those peaks were found to be undistorted (such as that shown in Fig. 3A). No other constraints were imposed on the fits. For spectra with distorted peaks and elevated inelastic-scattering background, *i.e.*, spectra recorded with photon energies less than ~ 20 eV, this fit procedure was not applicable (see the next paragraph). The respective fits to the Fig. 3A data, here including the lowest four water ($1b_1$, two-component $3a_1$, and $1b_2$ frontier orbital) ionization contributions, are displayed in Fig. 3C. Again, the red symbols show the measured spectrum, while the green curves are the individual Gaussian fit

components, and the blue curve is the cumulative fit. The lowest VIE ($1b_1$) peak is centered at 49.12 ± 0.01 eV KE, on the as-measured KE scale (Fig. 3A top axis). Here and elsewhere in the manuscript, the eKE peak errors were taken directly from the least-squares fitting outputs and represent one standard deviation with respect to the determined peak positions. Together with the known photon energy, $h\nu = 40.814 \pm 0.002$ eV, we find $\text{VIE}_{\text{vac},1b_1(l)} = h\nu - e\text{KE}_{1b_1(l)} + E_{\text{cut}} = 40.814 \pm 0.002 - 49.12 \pm 0.01$ eV + 19.64 ± 0.02 eV = 11.33 ± 0.02 eV.

Results from analogous analyses of water PES spectra measured at photon energies between ~ 15 eV and ~ 950 eV are shown in Table 1, and plotted in Fig. 4 (blue circles). The respective PES spectra are shown in Fig. SI-5 of the ESI.† With sufficiently high photon energies, an analogous energy referencing can be applied to the O $1s$ core-orbital ionization features. Although less accurate than the $\text{VIE}_{\text{vac},1b_1(l)}$ values for the reasons we discuss below, we extract an average $\text{VIE}_{\text{vac},O1s(l)} = 538.10 \pm 0.05$ eV for a ~ 650 eV photon energy, 538.07 ± 0.07 eV for 867.29 eV, and 538.04 ± 0.08 eV for 950.06 eV, all of which are in excellent agreement with the previous report of 538.1 eV, with an implied uncertainty of ± 0.1 eV.⁵⁵ The error bars and error values respectively shown in Fig. 4 and reported in Table 1, as well as elsewhere in the manuscript, are the cumulative result of all error sources (calculated using standard error propagation procedures), with errors other than those arising from the peak fits being the error of the photon energy determination, error in determining the cutoff energy, and error associated with the bias-voltage shift compensation, if applied.

We make three major observations from the overall photon-energy-dependent $\text{VIE}_{\text{vac},1b_1(l)}$ data shown in Fig. 4: (i) over the large photon energy range spanning 30–400 eV, we extract $\text{VIE}_{\text{vac},1b_1(l)}$ values between 11.31 – 11.34 eV (associated with our minimum error VIE_{vac} determinations, see Table 1), (ii) for photon energies ≤ 30 eV, we observe an apparent significant steady increase of $\text{VIE}_{\text{vac},1b_1(l)}$ values (accompanied by increasing error bars), and (iii) the data indicate a trend towards slightly lower $\text{VIE}_{\text{vac},1b_1(l)}$ values for photon energies up to ~ 650 eV. We start by commenting on the larger error bars determined at high photon energies, which is one aspect of point (i). At higher soft X-ray energies, a lower overall photon flux is often combined with a rapidly decreasing photoionization cross-section, requiring increased signal integration times, increasing the risk of time-dependent changes of the acquisition conditions, or compromises in the implemented acquisition settings (resolution *etc.*) needed to record sufficiently high signal-to-noise ratio data. Additionally, photon energies must be determined under the implemented experimental conditions, with highly precise photon energy calibrations required when higher photon energies are used. Such processes require utmost care and still generally result in photon energy and peak position determinations with higher absolute errors when compared to lower-photon-energy measurements. A detailed discussion of the challenges involved in accurate photon energy calibration can be found in ESI Section 3.† Another important effect to consider is the impact of the bias voltage on the detection system. A bias of several tens of volts is in effect a disturbance of the precisely tuned electron optics of



Table 1 $VIE_{vac,1b1(l)}$ and $VIE_{vac,O1s(l)}$ values of the liquid water valence $1b_1$ band and O 1s core-level peaks, respectively. The values were extracted from the spectra measured at different photon energies using the absolute referencing analysis method, Method 2. These values represent the averages of all measurements performed at the respective photon energy. The values in bold font are deemed to be essentially free of electron scattering based distortions of the measured VIE_{vac} values, while still being minimally affected by spectral distortions associated with the applied bias. The VIE_{vac} values shown in bold font can alternatively be referenced to the Fermi level, VIE_{EF} . Such values can be ascertained by subtracting the work function of liquid water, $e\phi_{water}$, determined here from the VIE_{vac} values. See the main body of the text for further details

| Measured at | $h\nu$ (eV) | | $VIE_{vac,1b1(l)}$ (eV) | | $VIE_{vac,O1s(l)}$ (eV) | |
|------------------------|----------------|-------------------------------|-------------------------|------------------------------|-------------------------|------------|
| DESIRS, SOLEIL | 15.00 | ± 0.03 | 11.82 | ± 0.08 | | |
| DESIRS, SOLEIL | 19.99 | ± 0.03 | 11.58 | ± 0.07 | | |
| Laboratory, FHI Berlin | 21.218 | ± 0.001 | 11.48 | ± 0.05 | | |
| DESIRS, SOLEIL | 24.98 | ± 0.03 | 11.38 | ± 0.04 | | |
| DESIRS, SOLEIL | 29.97 | ± 0.030 | 11.35 | ± 0.04 | | |
| Laboratory, FHI Berlin | 40.814 | ± 0.001 | 11.34 | ± 0.03 | | |
| Laboratory, FHI Berlin | 48.372 | ± 0.001 | 11.35 | ± 0.03 | | |
| U49-2_PGM-1, BESSY II | 123.464 | ± 0.004 | 11.33 | ± 0.03 | | |
| U49-2_PGM-1, BESSY II | 246.927 | ± 0.005 | 11.32 | ± 0.04 | | |
| P04, PETRA III | 249.99 | ± 0.02 | 11.28 | ± 0.04 | | |
| P04, PETRA III | 400.01 | ± 0.03 | 11.31 | ± 0.04 | | |
| U49-2_PGM-1, BESSY II | 400.868 | ± 0.004 | 11.27 | ± 0.05 | | |
| P04, PETRA III | 650.03 | ± 0.03 | 11.27 | ± 0.05 | 538.08 | ± 0.05 |
| U49-2_PGM-1, BESSY II | 649.67 | ± 0.03 | 11.31 | ± 0.06 | 538.13 | ± 0.05 |
| U49-2_PGM-1, BESSY II | 867.29 | ± 0.01 | 11.32 | ± 0.09 | 538.07 | ± 0.07 |
| P04, PETRA III | 950.06 | ± 0.03 | 11.33 | ± 0.09 | 538.04 | ± 0.08 |

a hemispherical energy (and for that matter any alternative electron) analyzer. Indeed, investigating the change in eKES measured with our HEA systems, we find that VIE values for measurements of large eKES can be slightly affected by the bias,

depending on the bias voltage and initial kinetic energy value of the photoelectron. Specifically, it was determined that eKE values are altered by 0.015–0.035% at a bias of -64 V, depending on experimental conditions and geometric details.

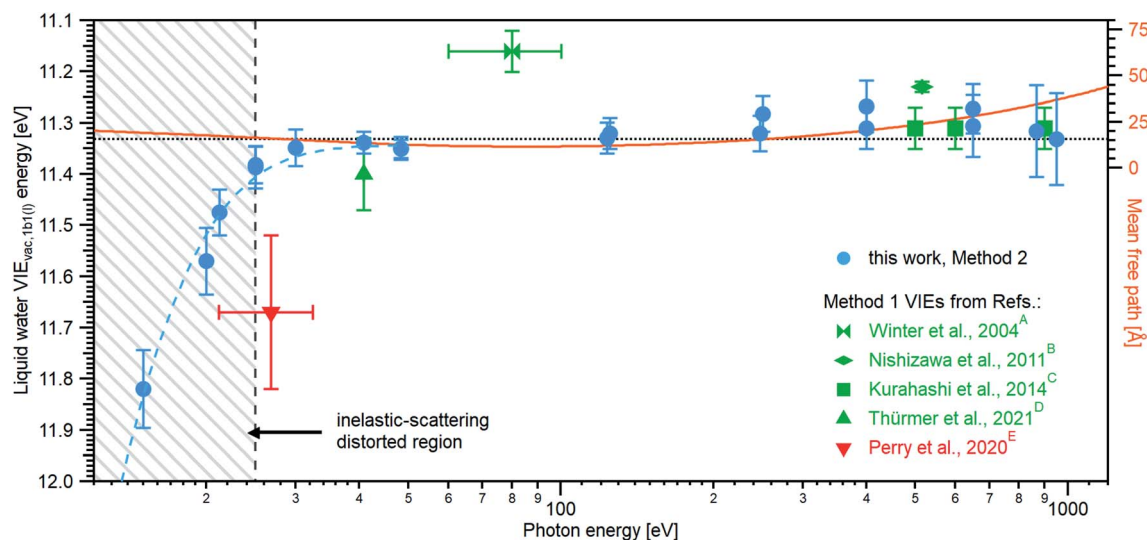


Fig. 4 An overview of the determined $VIE_{vac,1b1(l)}$ values as a function of photon energy. The green squares and green triangle show results obtained with the gas-phase referencing method, Method 1, where the field-free condition was achieved by carefully compensating for all potentials with a specific salt concentration: (A) from ref. 4, (B) from ref. 27, (C) from ref. 28 (where the used photon energies have been confirmed by the authors⁹³), and (D) from ref. 84. The value (E) associated with the red triangle was instead obtained by applying a compensation bias voltage between the detection system and LJ to achieve a field-free condition.²⁹ The values determined in this work, using Method 2, are shown as blue circles. Note that the $VIE_{vac,1b1(l)}$ values *seemingly* shift to higher values at lower photon energies, which corresponds to low eKES for the lowest ionization energy, $1b_1$, photoelectrons (blue dashed line in the gray hatched area). This is, however, an artifact arising from increased inelastic electron scattering at low eKES. The averaged, nascent VIE or binding-energy value – minimally affected by electronic scattering effects – is marked with the black dashed line. Error bars show the confidence interval as reported in the studies/resulting from the analysis of our data. The electron mean free path from ref. 85 is shown as a guide to the eye in orange and on the scale to the right. While we cannot distinguish any depth dependence to $VIE_{vac,1b1(l)}$ with the current error bars, the possibility of slight changes in VIE_{vac} with depth are discussed in the text.



Fig. SI-6† showcases this effect by plotting the measured $VIE_{vac,1b1(l)}$ dependence on the applied bias for exemplary measurements of the lowest-energy VIE at a photon energy of ~ 123.5 eV. While this effect is barely noticeable at smaller photon energies, it can become detrimental to measurements at very high photon energies, resulting in several 100 meV deviations if not properly corrected for. We have corrected all values recorded above a 100 eV photon energy by either measuring the bias-voltage dependent peak-positions directly or by additionally measuring the spectrum of the same PE feature using the residual second harmonic of the beamline and comparing it to the independently calibrated photon energy used in the measurement. This yields a correction factor for the VIE_{vac} values (see ESI Section 6† for details). Finally, we note that, even without such bias-voltage induced shifts, the KE-linearity of the utilized spectrometer may be a concern when the eKEs of the measured features are far apart. In our measurements, we estimate a maximal error of ~ 18 meV for the 950 eV measurements. If very high energy accuracy is required, then the linearity of the spectrometer eKE scale should be energy-calibrated, e.g., by measuring known gas lines over a broad range of eKEs.

The apparent increase of $VIE_{vac,1b1(l)}$ values (point (ii)) for the lower photon energies is an *artifact* caused by a change of electron scattering cross-sections and ionization mechanisms when tending towards lower electron KEs. For the corresponding eKEs, below ~ 18 eV, the direct photoelectrons experience such severe scattering that the nascent photoelectron peak position cannot be reliably extracted.³⁰ However, we deliberately include these misleading values in Fig. 4 to highlight to the reader that utmost care must be taken when trying to determine any meaningful energy in this regime. Solely applying an energy referencing scheme, be it Methods 1 or 2, without consideration of possible energy shifts due to electron scattering, will inevitably lead to erroneous results. We note that the full fit of all valence ionization features is not possible for spectra measured below 30 eV photon energies since spectral features have been considerably distorted by scattering. Accordingly, a simpler fit extracting only the lowest-ionization-energy liquid-water peak position was instead employed within that photon energy range.

From here on, we will restrict our discussion to the meaningful photon energies at and above ~ 30 eV. As shown in Fig. 4, and relating to point (iii) above, the precisely measured $VIE_{vac,1b1(l)}$ value determined using Method 2 in the present work is 11.33 ± 0.03 eV, which is the mean value based on the bold entries in Table 1 (corresponding to the plateau, i.e., energies higher than ~ 30 eV but excluding the results at 650 eV photon energies and above). The new value is in very good agreement with previous values reported by Kurahashi *et al.*²⁸ (green squares in Fig. 4) obtained using soft X-ray photon energies and the traditional Method 1 procedure, depicted in Fig. 1A. This implies that in the experiments of Kurahashi *et al.* all extrinsic surface potentials including electrokinetic charging have been accurately compensated. Indeed, as further discussed below, our own carefully implemented field-free measurements based on energy referencing Method 1 allows us to extract fully consistent $VIE_{vac,1b1(l)}$ values of 11.39 ± 0.08 eV at a 40.814 eV photon energy (see Fig. 5B). Comparison

of our Method 1 and Method 2 results with the Method 1 results of Kurahashi *et al.*²⁸ and Thürmer *et al.*⁸⁴ accordingly indicates that any photon energy dependence of $VIE_{vac,1b1(l)}$ is rather small (related to point (iii) above). These comparisons also suggest that any effect of an intrinsic liquid-water surface-dipole potential is negligibly small or can be adequately compensated by implementing a specific electrolyte concentration that engenders field-free conditions, at least with a cylindrical liquid-microjet source. That is, in our implemented measurement geometry, any differences between E_v^{loc} in the vicinity of (nearly) neat liquid water and E_v^∞ seem to be below our detection limit. Considering the maximum uncertainty with which E_{cut} is defined in our high energy resolution data (see ESI Section 5†) and stressing that direct experimental measurements of the interfacial dipole potential, χ^d , have yet to be reported, our error bars support a <50 meV value of χ^d , in agreement with previous experimental inferences.^{57,58} On a related note, assuming a negligible value of χ^d , the consistency of our Method 2 and properly recorded Method 1 results reinforces the use of the tangent approach to determine E_{cut} from an appropriately recorded LET spectrum. Were we to adopt the inflection point of the LET curve as the E_{cut} value instead of the tangent intersection point with the x-axis, we would determine just 30–100 meV higher $VIE_{vac,1b1(l)}$ values (again see ESI Section 5†). Focusing on our high energy resolution results recorded between 40.814 eV and ~ 401 eV, these offsets are limited to 30–60 meV. Thus, adopting the alternative and non-standard inflection point E_{cut} definition, would result in average and upper limit values of $VIE_{vac,1b1(l)}$ of 11.38 ± 0.03 eV and $VIE_{vac,1b1(l)}$ of 11.41 ± 0.03 eV, respectively.

Our $VIE_{vac,1b1(l)}$ results clearly disagree with the most recently reported value from Perry *et al.*,²⁹ 11.67 ± 0.15 eV (shown in red in Fig. 4). These results were based on Method 1 but were extracted by applying a small (+0.6 V) compensating bias between the jet and time-of-flight electron analyzer, under conditions where the amount of salt was not adjusted to compensate electrokinetic charging. In contrast to the originally implemented variant of Method 1, this biasing procedure seemingly has the benefit of enabling liquid-phase PES energy referencing while lifting any constraints on the concentration or type of solute under investigation (under the proviso that the solution remains sufficiently conductive). In principle, assuming sufficient care is taken to mitigate all possible perturbing potentials with the bias and to appropriately calibrate the spectrometer, this should lead to the same final result as the electrolyte tuning Method 1 scheme. However, this is obviously not the case, and the large $VIE_{vac,1b1(l)}$ value determined by Perry *et al.*²⁹ – approximately 0.3 eV higher than all of those previously reported – probably arises from a combination of inaccurate charge compensation, additional fields caused by the applied bias, and/or the aforementioned electron scattering issues. It is difficult to quantify the relative weight of these contributions *a posteriori*. We emphasize that any attempt to compensate fields by applying a bias voltage may lead to considerable eKE offsets if not properly accounted for during calibration of the energy axis of the employed (ToF) spectrometer, as demonstrated by Nishitani *et al.*⁵⁴ In fact, for an applied bias voltage of



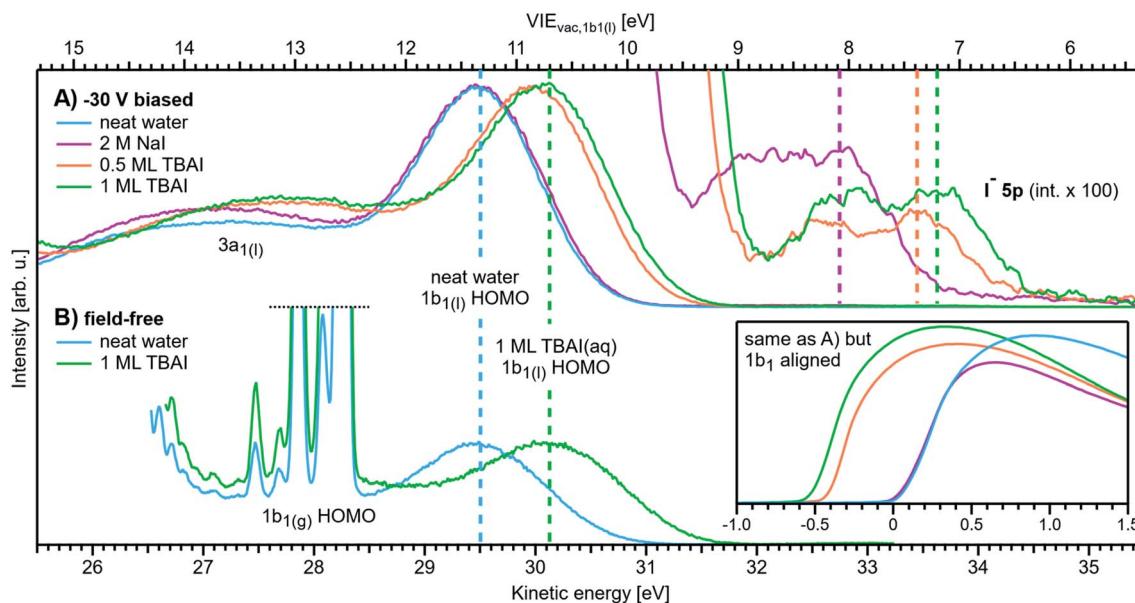


Fig. 5 Changes in $VIE_{vac,1b1}$ for representative aqueous solutions, both with an applied bias and a grounded jet. All spectra were recorded with He II α emission ($h\nu = 40.814$ eV). (A) Spectra measured with a bias voltage of -30 V. Each cutoff position was then aligned to $eKE = 0$ eV, which immediately visualizes VIE_{vac} changes as shifts of the liquid $1b_1$ HOMO position; the top axis shows the corresponding $VIE_{vac,1b1(l)}$ energy scale. The bottom-right inset shows the same spectra aligned to the $1b_1$ HOMO position, which instead show a shift in the cutoff position; both presentations are equivalent. Neat water serves as a reference position (blue line; about 50 mM NaCl was added here, but the precise value is irrelevant for this method). All spectra are normalized to the same $1b_1$ peak height. The spectra are shown multiplied by a factor of 100 (and smoothed with a 5-point boxcar averaging) to reveal the $I^- 5p$ solute feature to the top-right. The position of the $5p_{3/2}$ peak is marked with a dashed line in each case. (B) Spectra measured with a grounded jet. The salt concentration for the (nearly) neat water spectrum (blue line) was precisely tuned to achieve field-free conditions (2.5 mM NaCl was optimal here). The spectra are aligned so that the $1b_1$ position of neat water is matched with (A). The same shift is observed with 1 monolayer (ML) TBAI (green line) as in A, which shows the equivalence of Methods 1 and 2. Here, TBAI aqueous solution serves as a special case, where the field-free condition is preserved even for the solution, which makes a direct comparison possible in the first place. In general, the solutions and delivery conditions generate non-zero extrinsic and intrinsic potentials which impose an unknown additional energy shift to the liquid spectra.

+0.6 V, the determined energy offset reported in ref. 54 for $NaBr_{(aq)}$ yields 0.25 eV, which would push the result of Perry *et al.* down to 11.42 ± 0.15 eV, a value well agreeing with our results (see Fig. 4 and 5B) and those of Kurahashi *et al.*²⁸ Note that the average $VIE_{vac,1b1(l)}$ value of 11.33 ± 0.03 eV found in the present work also notably disagrees with the 11.16 ± 0.04 eV reference value (green diabolo shape) measured more than 15 years ago at intermediate 60–100 eV photon energies within the range spanned in the present study; this is the first LJ-PES reference value reported by one of the present authors.⁴ A likely reason for the offset of the original 11.16 ± 0.04 eV value is again a small effect of uncompensated electrokinetic charging at a time before a precise streaming potential characterization^{28,53} was established.

We next consider photon-energy-dependent variations of the $VIE_{vac,1b1(l)}$ value in more detail. The present study is the first to apply a broad range of photoexcitation energies, connecting the UV to the soft X-ray regime. Naturally, it is intriguing to explore the possibility that $VIE_{vac,1b1(l)}$ may not be exactly the same for surface water molecules and those existing deeper into the bulk solution. The probing depth into an aqueous solution is thought to be at its smallest at around 60–150 eV KE, where the electron inelastic mean free path (IMFP) curve seemingly exhibits a shallow minimum and rises towards higher

energies.^{66,67} Correspondingly, deeper probing into the solution should be enabled at higher photon energies. This raises the barely addressed question whether $VIE_{vac,1b1(l)}$ is eKE -dependent, following the eKE -dependent IMFP in water. Indeed, the observed slight variation in our extracted values – together with the values of Kurahashi *et al.*²⁸ – do not exclude this possibility; the IMFP from ref. 85 is plotted as a right-hand y-scale in Fig. 4 as a guide to the eye. We note that the ~ 50 meV larger $VIE_{vac,1b1(l)}$ value computed at the aqueous interface with respect to the liquid bulk¹³ is consistent with the interfacially-sensitive 125 eV and predominantly bulk-sensitive 650 eV and higher photon energy results reported here. Unfortunately, our current error bounds do not allow us to confirm such an offset though. Based on all available data, the corresponding error bars, and the good agreement between the blue and green data points in Fig. 4 – respectively measured at the low- and high-KE side of the IMFP minimum – it is argued that the KE -dependence of $VIE_{vac,1b1(l)}$ is indeed small, specifically less than 130 meV.

Changes of solvent VIE & solute VIE values in aqueous solutions

Following the exact same Method 2 protocol as described above for neat water, the measurement of $VIE_{vac,1b1}$ of an aqueous



solution (denoted $VIE_{vac,1b1(sol)}$) is straightforward. Aqueous solute VIEs (denoted $VIE_{vac,solute}$) are also readily determined, without assumptions. Such measurements are founded on the schemes introduced in Fig. 1C and 2C.

Fig. 5A compares the neat water valence PE spectrum with that of NaI_(aq) at 2 M concentration and tetrabutylammonium iodide (TBAI), a surfactant, at concentrations of 12.5 mM and 25 mM. These TBAI concentrations yielded approximately one half and one full monolayer (ML) of TBA⁺ coverage at the solution surface, respectively.⁸⁶ We note that the 25 mM TBAI concentration yields approximately the same iodide surface concentrations as obtained in 2 M NaI solutions.⁸⁶ The photoelectron spectra, including the LET and leading valence features, were again measured with a 40.814 eV photon energy, the applied bias voltage was -30 V. The spectra are aligned such that the cutoff position, determined by the tangent method, falls at $eKE = 0$ eV. The bottom axis thus displays the eKEs following their traversal of the solution's surface. We emphasize once more that the measured energy position of the leading photoelectron peaks or E_{cut} alone has no meaning, since solutes may induce several additional potentials which can arbitrarily shift all eKEs associated with different PE features. We also re-emphasize that the effectively applied bias value is not and does not need to be precisely known. The only relevant property in Method 2 is the energetic distance (and changes of this distance) between E_{cut} and a peak of interest, exemplified by ΔE_w in Fig. 1B and C. The inset in Fig. 5 shows LET features of the same data as shown in Fig. 5A but instead with the water $1b_{1(l)}$ peaks aligned; note that this corresponds to the previously adopted and unsatisfactory practice of energy-referencing aqueous solution LJ-PES data to predetermined neat water $1b_{1(l)}$ VIE values. Changes in the overall spectral energy widths now appear as a shift of the cutoff position; both Fig. 5A and the inset presentations are equivalent. Adopting the cutoff spectral positions, the $VIE_{vac,1b1(l)}$ energy scale (top axis) can now be referenced from E_{cut} via the precisely known photon energy. Associated solute-induced changes in the water electronic structure are discussed first, and we later focus on the lowest solute ionization channel, *i.e.*, that attributed to the first I^- 5p atomic orbital which corresponds to the PE features at ~ 33 eV eKE.

When switching from neat water to 2 M NaI, a small and statistically insignificant (*i.e.*, within the error bars) energy shift, accompanied with a slight broadening, of the $1b_1$ peak is observed with respect to neat water; see the purple and blue curves (Fig. 5A). This is a somewhat puzzling result, seemingly at odds with theoretical works on alkali-halide solutions, specifically reporting a larger surface propensity of iodide than the sodium cation, which implies the formation of an interfacial dipole.⁷⁶ Interestingly, the aforementioned work by Tissot *et al.* makes a related observation. Comparing concentrated NaCl and NaI aqueous solutions, which should exhibit a very different surface potential, no differences are found in the spectra;⁶⁸ those authors discussed the possibility of surface impurities obscuring their results. We note that the 2 M NaI concentration used here may still be below the surface-enrichment regime,⁸⁷ and higher concentrations (>6 M) may

in fact lead to a more pronounced shift. However, a concentration-dependent study is beyond the scope of this work. If simple alkali-halide salts do not alter the solution's charge equilibrium at the probed interface, and thus the position of E_{cut} and the valence ionization features, one must assume that inter-ionic dipoles have no net component perpendicular to the solution interface. Unfortunately, there is little data available to clarify this issue, despite multiple works attempting to quantify the interfacial density profiles of different atomic ions in aqueous solutions.^{38,76,88,89} In this context, some of the authors have recently reported that concentrated electrolytes, despite changing the electronic structure of water, do not appear to lead to any significant relative energy shifts between different valence photoelectron peaks.⁷ Rather, the lowest-energy ionization peak ($1b_1$) slightly broadens, with an accompanied apparent narrowing or energy-gap reduction of the split, second ionization feature ($3a_1$), the latter being the more notable spectral change. Both of these behaviors are confirmed in the present data shown in Fig. 5A.

Compared to the NaI results, the TBAI aqueous solutions behave very differently, shifting water's valence electronic structure with respect to E_v^{loc} , as reflected in the higher measured kinetic energies (green and orange curves). This energy shift is approximately 630 meV, judged from the change of the neat water $1b_1$ peak position, in the case of a full ML of TBA⁺ (compare the green and blue spectra). A coverage of 0.5 ML leads to a smaller shift of about 530 meV (orange spectrum). We thus find average $VIE_{vac,1b1(TBAI)}$ values of 10.80 ± 0.05 eV (0.5 ML) and 10.70 ± 0.05 eV (1.0 ML), which are both found to be considerably smaller than $VIE_{vac,1b1(l)}$. This large decrease in VIE could have various causes: (1) resulting from changes of the intrinsic (bulk) electronic structure of the solution (as shown for NaI), (2) a change of the intrinsic electronic structure and associated charge equilibrium at the solution-vacuum interface (*i.e.*, a relative change in the positions of water's electronic bands with respect to a fixed value of E_v^{loc}), or (3) a change in the net aqueous surface-dipole potential and associated value of E_v^{loc} . A change of the bulk-water electronic structure would be hardly expected for this surface-active molecule. However, we may have to consider the possibility of changes of the aqueous electronic structure at the liquid-vacuum interface. Still, such an effect would need to be distinguished from the two other interfacial contributions, requiring establishment of a common and ideally ion-depth-invariant reference level for the two solutions. The Fermi level should be well-suited to this task and can be indirectly measured using the experimental procedure discussed in the context of Fig. 1D. However, before discussing such a referencing procedure in detail, we consider the iodide solute signal, as measured with respect to E_v^{loc} , which is also visible in the spectral range displayed in Fig. 5.

Iodide photoemission gives rise to the small $I^-_{(aq)}$ 5p doublet features (multiplied here by a factor of 100) occurring in the 32.0–34.4 eV KE region in Fig. 5. Applying a 2-Gaussian fit procedure, we determine the respective peak positions at eKEs of ~ 33.6 eV (I^- 5p_{3/2}) and ~ 32.7 eV (I^- 5p_{1/2}) in the case of a 1 ML TBAI_(aq) solution. Slightly lower eKEs of ~ 33.4 eV and ~ 32.5 eV are determined for a 0.5 ML TBAI_(aq) solution. This



corresponds to $VIE_{I5p3/2} = 7.20 \pm 0.1$ eV/ $VIE_{I5p1/2} = 8.11 \pm 0.1$ eV for the 1 ML and $VIE_{I5p3/2} = 7.38 \pm 0.1$ eV/ $VIE_{I5p1/2} = 8.30 \pm 0.1$ eV for the 0.5 ML cases, respectively. In contrast, for a 2 M NaI_(aq) solution we find an eKE of ~ 32.7 eV (I^- 5p_{3/2}) and ~ 31.8 eV (I^- 5p_{1/2}), corresponding to $VIE_{I5p3/2} = 8.08 \pm 0.1$ eV/ $VIE_{I5p1/2} = 8.90 \pm 0.1$ eV; the latter is in excellent agreement with our earlier work.² An important finding from Fig. 5A is, therefore, that the iodide 5p ionization energy is considerably larger in the NaI aqueous solution as compared to the TBAI solution. We note that the observed effect would have been much smaller if we had used Method 1, where only the $VIE_{vac,1b1(l)} - VIE_{I5p}$ energy distance would be accessed but not the change of $VIE_{vac,1b1}$. While this energy separation is indeed different by about ~ 0.1 eV between 0.5 ML and 1.0 ML TBAI and about ~ 0.25 eV between 2 M NaI and 1 ML TBAI (as could have been observed *via* Method 1), the true change of VIE_{I5p} as determined with Method 2 would remain inaccessible. Notably, a previous study⁹⁰ used gas-phase water features as an energy reference for 0.04 m TBAI_(aq) solution PES, and thus circumvented the liquid 1b₁ VIE altogether, arriving at rather accurate $VIE_{I5p3/2} = 7.6$ eV and $VIE_{I5p1/2} = 8.4$ eV values, albeit with a potentially huge margin of error due to unknown and uncompensated extrinsic potentials. Specifically, for NaI_(aq), the energetic separation of water's lowest ionization energy 1b₁ peak to the I^- 5p_{3/2} peak is 3.36 ± 0.05 eV, while for the 5p_{1/2} peak it is 2.41 ± 0.05 eV, in excellent agreement with previous reports.^{28,68,87} Fig. 5 also shows that $VIE_{vac,1b1(TBAI)}$ is slightly smaller in the case of 1.0 ML TBAI coverage in comparison to 0.5 ML coverage. However, the associated energy difference is smaller than the respective changes in the VIE_{I5p} energies. For 1.0 ML TBAI solutions, we see a ~ 0.25 eV increase in the water 1b₁ to I^- peak separations in comparison to the 2 M NaI case. This corresponds to 3.60 ± 0.05 eV and 2.65 ± 0.05 eV separations of the 5p_{3/2} and 5p_{1/2} peaks to the water 1b₁ peak, respectively. This aspect will be considered further below.

We close this sub-section by re-connecting the results reported here to the applicability of Method 1. Fig. 5B presents additional PES spectra from neat water and 1.0 ML TBAI, now measured for grounded solutions, *i.e.*, applying Method 1. We observe the very same positions of $VIE_{vac,1b1(l)}$ as in the upper trace, obtained with Method 2. The reason for this (perhaps surprising) quantitative agreement is that in this particular Method 1 measurement all external fields were successfully compensated. This is true for both neat water and the TBAI solution spectra as judged by the sharp water-gas-phase features; we re-emphasize that the extrinsic fields between the sample and analyzer can only be meaningfully assessed when a sufficiently large gas volume around the LJ is probed. Establishing the necessary field-free conditions to achieve such measurements is however experimentally difficult and time-consuming. More importantly, these conditions are impossible to achieve for most aqueous solutions outside a very limiting concentration range, and only Method 2 will undoubtedly provide the correct ionization energetics. In the next section, we extend our newly applied energy referencing methodology a step further, establishing a common Fermi level for neat water and a metallic reference sample that allows determination of the VIE of liquid water with respect to E_F ,

$VIE_{EF,1b1(l)}$. Furthermore, in combination with the Method 2 results, it provides access to the liquid water $e\Phi$ value, $e\Phi_{water}$.

Fermi-referenced VIEs & work functions of liquid water & aqueous solutions

As argued when describing Fig. 1D and 2D, we can formally introduce Fermi-level referencing when liquid water or an aqueous solution is in electrical equilibrium with a metallic reference sample, an approach we term Method 3. As explained in the introduction, we can measure the valence spectrum from a solution and E_F from a metal in sequential experiments. But exactly what information does this provide? With the two systems in electrical contact, E_F and the bulk chemical potential of the solution and the metal are aligned. However, in the PES experiment, one measures photoelectrons from the solution or metal after they have traversed the sample-vacuum interface and different corresponding surface dipole potentials. Ideally, one would measure the Fermi edge of the metal through a thin sheet of the flowing solution, such that electrons emitted from the metal and the bulk solution would experience the same (intrinsic and extrinsic) solution-vacuum surface potential and E_v^{loc} . However, as of yet, this remains experimentally unfeasible.^{¶¶} Despite this, it can still be argued that a Fermi-level alignment can be achieved between the LJ and metallic reference if *streaming-potential-free* conditions are engineered, *i.e.*, under the experimental conditions depicted in Fig. 1D. We define these conditions as those that preserve the intrinsic liquid solution $\Delta e\Phi$ value with respect to the analyzer, while mitigating the remaining extrinsic potentials. It is important to differentiate these conditions from the field-free alternative discussed in the context of Method 1, where the sum of *all* potentials between the sample and analyzer are compensated to zero. This point is particularly noteworthy as the establishment of field-free conditions has previously been symbolized as ' $\Phi_{str} = 0$ '.²⁸ In general, the optimal solution concentrations for field-free and streaming-potential-free conditions differ, offset by the magnitude of $\Delta e\Phi$ in the experiment. Only if $\Delta e\Phi$ happens to be zero (for a particular experiment) will these two conditions be simultaneously achieved (at a fixed LJ nozzle morphology, jet flow rate, and solution temperature).

In the following, we briefly discuss how streaming-potential-free conditions may be established by considering the streaming current of the aqueous sample, I_{str} , which is the source of the streaming potential, Φ_{str} , and a less ambiguous quantity. I_{str} has been measured independently from Φ_{str} , where it was shown that the aqueous streaming current is minimized at roughly 50 mM alkali halide salt concentrations, with a LJ flow rate of 0.5 ml min⁻¹, and with similar LJ nozzle orifices as implemented here.^{28,53} Accordingly, a 50 mM NaI salt concentration provides a basis for our Fermi-referencing measurements.^{|||} Associated nominally streaming-potential-free liquid water PES results recorded with a photon energy of 40.814 eV are shown in Fig. 6 (blue curve). At higher eKEs, we show the related Fermi-edge spectrum of the metal reference sample (black curve) sequentially recorded under the same conditions, as sketched in Fig. 2D. Here, the liquid water jet was



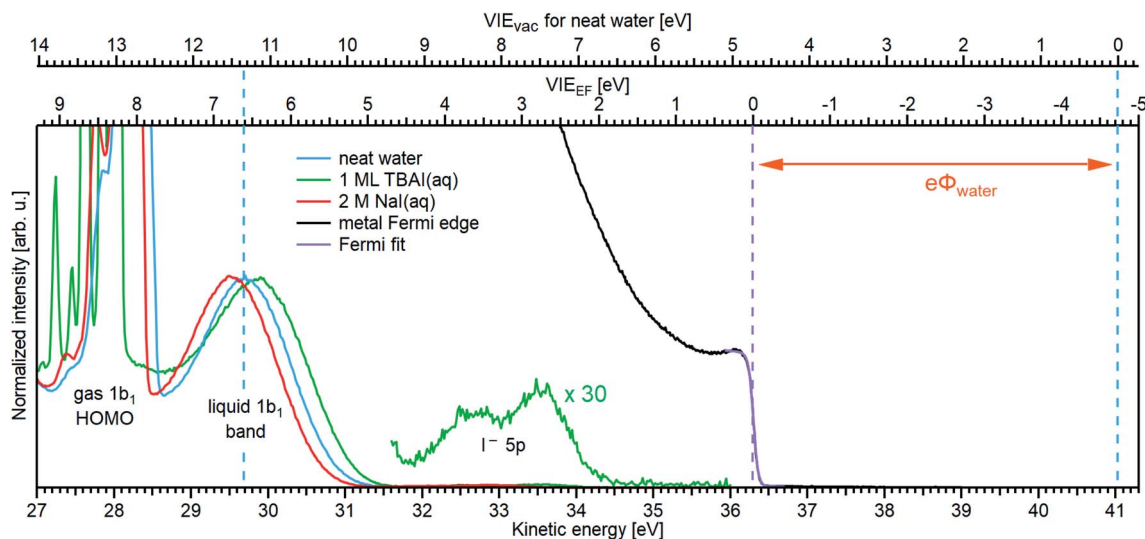


Fig. 6 Determination of $VIE_{EF,1b1(l)}$ for neat water (blue, with an optimal NaCl concentration of 50 mM; see the main body of the text for details) and the limitations of this method for aqueous solutions, exemplified here for 1 ML TBAI(aq) (green) and 2 M NaI(aq) (red) solutions. The relative energy position of liquid water's lowest energy $1b_1$ ionization feature and the Fermi edge of a metallic reference sample were separately recorded using He II α emission ($h\nu = 40.814$ eV). A sample bias was not applied in either case and the bottom axis shows the as-measured kinetic energy scale of the detector. To the right, the highest eKE feature of the metal spectrum is shown in black (only the Fermi edge is visible). The position and spectral shape of the measured metal spectrum was unchanged following the introduction of the LJ and solution. The Fermi edge was fit with a Fermi function²³ (purple line), and its position defines the zero point of the VIE_{EF} energy scale in the spectrum (lower axis scale at the top of the panel). This enables us to determine the $VIE_{EF,1b1(l)}$ value of 6.60 ± 0.08 eV and a $e\Phi_{water}$ value of 4.73 ± 0.09 eV for (almost) neat water. For the 2 M NaI(aq) solution, the $1b_1$ peak is shifted towards lower eKEs (higher VIE_{EF}), which most likely arises from additional extrinsic fields as opposed to a real change of the aqueous electronic structure for this solution (compare to Fig. SI-7[†]); the VIE_{vac} values underwent insignificant changes in going from neat water and 2 M NaI(aq) solutions (compare to Fig. 5). Without proper assessment of additional potentials, such as the streaming potential or surface charge, it is in principle impossible to accurately reference eKEs to E_F or judge associated changes in VIE_{EF} in this case. In the case of TBAI(aq), on the other hand, the $1b_1$ shifts towards higher eKEs (lower VIE_{EF}). It can be argued that this shift is caused by band-bending at the liquid interface (see text for details). Multiplying the TBAI(aq) spectrum by a factor of 30 reveals the I^- 5p solute features around eKE ≈ 33 eV, corresponding to VIE_{EF} values of 3.80 ± 0.10 eV and 2.84 ± 0.10 eV for the $5p_{1/2}$ and $5p_{3/2}$ levels, respectively.

in operation in close proximity to a gold wire or was directly injected from a conductive PtIr disc during these measurements. An associated fit to a Fermi-Dirac distribution is also shown (purple curve), from which we obtain the Fermi-edge position at $eKE_{EF} = 36.296 \pm 0.005$ eV. This position defines the zero of the VIE_{EF} energy and chemical potential scale (lower axis at the top of the figure), to which all liquid-water features can now be referenced. The difference between $VIE_{vac,1b1(l)}$ and E_F , as determined from our fits, corresponds to $VIE_{EF,1b1} = 6.60 \pm 0.08$ eV. Analogous measurements were performed using 125.02 ± 0.03 eV and 649.946 ± 0.005 eV photon energies and yielded the same results.

To examine whether streaming-potential-free conditions were established when recording the liquid water data shown in Fig. 6, and the associated validity of the measured $VIE_{EF,1b1}$ value, a series of aqueous-phase PES spectra in electrical contact with a grounded metallic reference sample were recorded as a function of salt concentration (NaI and NaCl were found to exhibit the same effects). This allowed us to track the shift of aqueous-phase PE features with respect to E_F . The resulting spectra are plotted in Fig. SI-7,[†] with the energetic position of the Fermi level found to be fixed within 0.03 eV, regardless of the type of aqueous solution present. That is, the metallic spectrum appears to be unaffected even by relatively high

extrinsic potentials at the LJ (in some cases exceeding 1 eV). One may speculate that such potentials are effectively screened and thus terminated at the metal, nullifying any field gradients in the region between the metal and the detector. However, in contrast in the liquid water case, the lowest $VIE_{EF,1b1}$ feature shifts dramatically under the influence of the varying salt concentration and streaming potential, displaying the expected behavior and exhibiting a minimum $VIE_{EF,1b1}$ value around 50–100 mM concentrations, *i.e.*, covering the concentration implemented to produce the blue curve in Fig. 6 and where I_{str} (and in turn Φ_{str}) is expected to vanish.^{***} This implies that streaming-potential-free conditions have indeed been achieved in producing the liquid water data shown in Fig. 6.

Recalling our aforementioned determination of the VIE_{vac} energy scale of liquid water using Method 2 (see the upper axis above Fig. 6), we are now set to relate the vacuum and E_F energy scales to each other. Since $e\Phi$ is equivalent to the difference between these two energy scales, *i.e.*, between the ionization energies of any of liquid water's ionization features measured with respect to E_v^{loc} and E_F , we can accordingly determine $e\Phi_{water}$. For example, $VIE_{vac,1b1(l)} - VIE_{EF,1b1(l)} = 11.33 \pm 0.03 - 6.60 \pm 0.08$ eV and yields $e\Phi_{water} = 4.73 \pm 0.09$ eV. By extension, one can further argue in the case of neat water that if the surface dipole/outer potential is zero, near-zero, or averages to zero in



our experiments, then $e\Phi_{\text{water}} \approx \bar{\mu}$, *i.e.*, the determined work function is equivalent to water's electrochemical potential $\bar{\mu}$, which is a generally un-measurable quantity. We again stress that without establishing streaming-potential-free conditions, arbitrary $\text{VIE}_{\text{EF},1\text{b}_1(\text{l})}$ and thus $e\Phi_{\text{water}}$ values would be recorded, depending on the strength and sign of any extrinsic potentials; as demonstrated by Fig. SI-7.† Generally, this will remain a problem whenever the metallic reference spectrum is measured separately from the solution spectrum (*i.e.*, unless the Fermi edge signature and liquid features of interest are recorded in the same spectrum, following ejection *through* the liquid surface). This issue is unfortunately somewhat obscured when the metallic reference sample is used to initially establish an alternative (but nonetheless flawed) reference, such as the analyzer work function, as proposed, *e.g.*, in ref. 31 and 69.

As a further cross-check of our $\text{VIE}_{\text{EF},1\text{b}_1}$ and $e\Phi_{\text{water}}$ results, and that streaming-potential-free conditions are indeed achieved, we extract and utilize our analyzer work function, $e\Phi_{\text{A}}$. To achieve this, we measured PES spectra of the metallic reference sample, either directly recording the Fermi level ($e\Phi_{\text{A}} = h\nu - \text{KE}_{\text{EF}}$) or some other well-calibrated metal energy level such as the gold 4f level ($e\Phi_{\text{A}} = h\nu - \text{BE}_{4\text{f}} - \text{KE}_{4\text{f}}$). The extracted $e\Phi_{\text{A}}$ is an arbitrary value in itself, and only equals the analyzer work function if the measured kinetic energy, $e\text{KE}_{\text{meas}}$, of the detection system has been precisely calibrated using known (gas-phase) reference photon and ionization energies. We briefly describe the procedure to achieve such a calibration and compare the $e\Phi_{\text{A}}$ result to the field-free condition, specifically assuming this corresponds to $\Delta e\Phi = -e\Phi_{\text{str}}$. Using the kinetic energy position of the equilibrated water gas-phase 1b_1 peak (compare to Fig. SI-2†) and the associated reference VIE value of 12.621 ± 0.008 eV,³ we find that the kinetic energy scale of the detector needs to be corrected by $+0.224 \pm 0.008$ eV; note that this value depends on the pass energy setting and detector mode. This yields a corrected Fermi-edge position of $e\text{KE}_{\text{EF}} = 36.520 \pm 0.009$ eV from which we determine $e\Phi_{\text{A}} = 4.293 \pm 0.009$ eV, a value approximately 0.43 eV smaller than $e\Phi_{\text{water}}$. It is intriguing to then compare this value to the shift in the liquid water 1b_1 position when going from our streaming-potential-free (50 mM) to field-free conditions (2.5 mM), *i.e.*, where $\Delta e\Phi = -e\Phi_{\text{str}}$. There we observe that the 1b_1 peak shifts to lower eKEs (compare to Fig. SI-7†) and that the overall shift between these two concentrations matches the expected 0.43 eV. This nicely demonstrates the shift from $\Phi_{\text{str}} = 0$ V conditions to $\Delta e\Phi = -e\Phi_{\text{str}}$ conditions, that the liquid water 1b_1 peak follows the change in potentials one-to-one, and that streaming-potential-free conditions were indeed achieved with 50 mM NaI concentrations (under our implemented conditions). Correspondingly, our values of $\text{VIE}_{\text{EF},1\text{b}_1}$ and $e\Phi_{\text{water}}$ are also confirmed.

Our established experimental value of $e\Phi_{\text{water}}$ is found to be somewhat larger than that reported by Olivieri *et al.*,³¹ 4.65 ± 0.09 eV, who also attempted to determine $e\Phi_{\text{water}}$ using LJ-PES. This work extracted the value of $e\Phi_{\text{water}}$ from the 'midpoint' of the rise of the LET curve (referred to as the SEED in the ref. 31, see Note ¶) as opposed to the tangent method commonly adopted for solid-state samples and in extracting the results reported here. In our data, this E_{cut} determination method has

been shown to result in VIE increases of several 10 meV up to ~ 150 meV (depending on the energy resolution of the experiment and the associated shape of the LET). This would be directly transferred to an increase of our value of $e\Phi_{\text{water}}$, bringing our determination of this value further away from that reported by Olivieri *et al.* With a comparison of these and our own $e\Phi_{\text{water}}$ value determinations in mind, we highlight a number of methodological inconsistencies and inaccuracies in the Olivieri *et al.*³¹ study in ESI Section 7.†

Turning now to an attempted determination of E_{F} and $e\Phi$ from an aqueous solution, we recall that our auxiliary Fermi-referencing procedure, Method 3, is not applicable to, *e.g.*, the 2 M NaI solution considered in Fig. 5, as the streaming current is thought to be non-zero (see ESI Fig. 7†). Although a precise value cannot be determined in this work due to the coupling of higher salt concentrations to Φ_{str} , we can compare $\text{VIE}_{\text{EF},1\text{b}_1(\text{l})}$ (*i.e.*, from water) with the respective value from Tissot *et al.*⁶⁸ for saturated alkali-halide solutions deposited on a gold substrate. There a 0.4 eV smaller $\text{VIE}_{\text{EF},1\text{b}_1(\text{sol})}$ of 6.2 eV was reported. However, we note that for higher concentrations of 2 M NaI (Fig. 6) and 4 M NaI (Fig. SI-7†) the 1b_1 peak notably shifts to higher VIE_{EF} (lower eKEs) values, *i.e.*, even further away from the reported 6.2 eV $\text{VIE}_{\text{EF},1\text{b}_1(\text{sol})}$ value. The shift observed in our high-concentration measurements is likely caused by a non-zero Φ_{str} , and one can only speculate about the true $\text{VIE}_{\text{EF},1\text{b}_1(\text{sol})}$ value in the absence of Φ_{str} . However, a value of 6.2 eV is deemed unlikely. We may speculate that, to some extent, this 6.2 eV determination reflects additional extrinsic surface potentials present at the interface of the concentrated solution in the Tissot *et al.* study.⁶⁸ This is consistent with an observed ~ 0.6 eV energy shift of the O 1s gas peak towards lower eKE (higher VIE) when retracting the sample,⁶⁸ caused either by radiation-induced sample changes or accumulation of surface impurities at the non-replenishing liquid-on-solid sample.

We now return to our TBAI aqueous solution measurements, where we observed large changes in VIE_{vac} . At a bulk concentration of 25 mM, the solution conductivity is sufficient to effectively apply a bias voltage of -30 V, and we can correspondingly assume alignment of E_{F} throughout the solution under unbiased conditions, similar to the 25–50 mM NaCl or NaI aqueous solution cases discussed above. Consequently, we can determine E_{F} following the same steps as for neat water. For that we reproduce the TBAI aqueous solution spectrum from Fig. 5B in Fig. 6 (green curve), and compare it to the Fermi edge spectrum from the metallic sample (black curve), fully analogous to the water experiment. As discussed above, even when measured in the presence of the running TBAI-solution jet, electrically connected to the metallic sample, the same E_{F} reference value is observed as for neat water. Neither I_{str} nor Φ_{str} measurements have been reported for this solute to our knowledge, and are beyond the scope of this work. However, as we argue in the following, Φ_{str} may in fact be immeasurably small or even zero in this particular case. Before explaining this further, we discuss the principal results from the green curves in Fig. 6. Initially assuming $\Phi_{\text{str}} \approx 0$ V, we determine that water's 1b_1 PE peak shifts to 0.15 ± 0.11 eV lower Fermi-referenced VIE values in the TBAI_(aq) solution in comparison



to (nearly) neat water, with $VIE_{EF,1b1(TBAI)} = 6.45 \pm 0.08$ eV. Using the results from Method 2 we can now, analogously to the water case, determine the solution's work function: $e\Phi_{TBAI} = VIE_{vac,1b1(TBAI)} - VIE_{EF,1b1(TBAI)} = 10.70 \pm 0.05 - 6.45 \pm 0.08$ eV = 4.25 ± 0.09 eV. This corresponds to a 0.48 ± 0.13 eV reduction with respect to neat water. Considering the anionic solute components of the solution, we further extract $VIE_{EF,15p}$ values of 3.80 ± 0.10 eV and 2.84 ± 0.10 eV for the $5p_{1/2}$ and $5p_{3/2}$ peaks of the I^- solute feature, respectively.

We have seen that field-free conditions are seemingly achieved for 25 mM TBAI solutions (implied by the sharp water gas-phase spectrum in Fig. 5B and 6), which must mean $e\Phi_{TBAI(aq)} - e\Phi_A \approx -\Phi_{str}$. Recalling that $e\Phi_A = 4.293 \pm 0.009$ eV, it follows that $e\Phi_{TBAI(aq)} = 4.25$ eV $\approx e\Phi_A$, *i.e.*, the E_V^{loc} levels at the sample and analyzer are aligned, implying $\Phi_{str} \approx 0$ V. We have also observed that $\Phi_{str} \neq 0$ V for the 2 M NaI_(aq) solutions, as can be seen in Fig. 6 from the offset of the spectrum towards slightly higher apparent $VIE_{EF,1b1}$ values. However, Method 3 does not reveal whether $e\Phi_{TBAI(aq)}$ or Φ_{str} is compensating the extrinsic potential, implying that the observed shift in $VIE_{EF,1b1}$ may come from an active Φ_{str} and that the field-free condition achieved here is just a coincidence. The origin of the observed energy shift, *i.e.*, the change of $VIE_{vac,1b1(l)}$, in Fig. 5 and 6 thus remains unresolved and cannot be confirmed with the currently available experimental tools. However, we briefly discuss how a real change in $VIE_{EF,1b1}$, *i.e.*, under the premise that $\Phi_{str} = 0$ V, would be realized below.

Dissolution of a salt in water produces hydrated anions and cations, which can be viewed as ionized dopants freely moving in the aqueous solution. At the interface to vacuum this would give rise to the band bending (BB) phenomenon commonly encountered in the semiconductor literature, and illustrated in Fig. SI-1B.† In the present case, BB is argued to be induced in response to TBAI accumulation, which changes the charge distribution at the liquid – vacuum interfacial layer. Briefly, BB occurs if there is a local imbalance of charge near the surface which leads to the build-up of a local field.^{26,35,91,92} Arguably, we observe an upward BB, *i.e.*, in the direction of lower VIEs, which is caused by a depletion of the solvent's electron density near the surface. The hydrophobic TBAI⁺ molecules which reside near the solution's surface are thought to draw I^- ions into this surface region.⁸⁶ It can then be argued that the solvation of I^- reduces water's local electronic density, leading to the observed effect. Notably, the Fermi level remains fixed (the Fermi level is pinned) within the solution at its bulk value and aligned with the metal reference and analyzer, as shown in Fig. SI-1B.† Some intriguing observations support this interpretation. The $1b_1$ HOMO peak slightly broadens when moving from 50 mM NaI_(aq) to 25 mM TBAI_(aq) solutions, which may indicate that an interfacial region with a solution-depth-dependent potential energy gradient of the $1b_1$ band is probed, implying different effective $1b_1$ energies within this so-called space-charge layer. Also, the I^- 5p peaks are shifted the farthest, which would be plausible given that most of the iodide resides directly at the surface, where the most disturbance of the bulk equilibrium occurs. One might correspondingly ask whether the neat water surface is already subject to BB, keeping in mind that intrinsic

surface BB caused by the presence of surface defect states is a common phenomenon for semiconductors.⁹² While we cannot rule out this possibility completely, it is important to note that the water surface is very different from an abruptly terminated crystal lattice, and the dynamic nature of liquid water is likely to compensate for any charge imbalance, unless such charge accumulation is forced as in the case of surface-active species such as TBAI. Thorough exploration and characterization of such effects using photon-energy- and thus solution-depth-dependent Fermi-referenced LJ-PES measurements is an associated interesting future line of research directly enabled by the work reported here.

Until now we have adopted surface-science concepts to interrogate and interpret aqueous-phase PES data, providing a useful methodological advancement to access an explicit descriptor of solution interfacial electronic properties, namely the work function *via* joint determinations of VIEs with respect to E_V^{loc} and E_F . In the following, we briefly discuss the impact of this accomplishment in the wider context of interfacial chemistry and electrochemical processes, in particular at the metal-electrode – electrolyte system. This very ensemble of a LJ electrically connected with a metal sample (again, see Fig. 2D) represents a single electrode immersed into an electrolyte. As we have explained above, connection of a metal to a sufficiently conductive liquid water or aqueous solution sample (both classifiable as semiconductors) yields a common Fermi level. In the case of an electrolyte containing both forms of a redox couple (representing vacant and populated energy levels within the band gap, separated by E_F^{15}), the redox level, E_{redox} , can be equated to E_F in the solution and aligned with E_F of the metal.²⁶ This implies that E_F of the solution shifts with charge flow across the interface until $E_F = E_{redox}$, where the two energy scales for the aqueous solution and the potential scale for the electrode are connected through the theoretical value of the Fermi level of the standard hydrogen electrode. This route has been explored in a very recent LJ-PES study,⁶⁹ determining E_F *via* the aqueous-phase ferricyanide/ferrocyanide redox couple (in a Zobell⁷⁰ solution), and reporting values of $VIE_{EF,1b1(l)} = 6.94$ eV and $e\Phi = 4.60$ eV, both of which differ from our results for neat liquid water. Furthermore, a much larger $VIE_{vac,1b1(l)}$ value of 11.55 eV was reported for the Zobell solution. We highlight a number of potential issues with the methodology adopted in ref. 69 in ESI Section 7,† which we believe may be responsible for the discrepancies between our and their results. We also note that most of these problems could be circumvented by rigorously applying Method 2, as presented in this work.

In a more general context, and not requiring introduction of redox couples, it will be possible to use known electrode potentials and measured Fermi levels to locate the band edges of liquid water and select aqueous solutions on the chemical potential scale.²⁶ This is not only of uttermost importance for advancing our understanding of chemical reactions at electrode-electrolyte systems but it also enables future routes to develop a common interpretation of thus far seemingly disconnected quantities specific to the molecular and condensed-matter descriptions of electronic structure. One pressing example is how the band gap of liquid water



conceptually connects with the molecular-physics or orbital information accessed by LJ-PES, including an experimental determination of liquid water's electron affinity.¹³

Conclusions

Liquid microjet photoelectron spectroscopy (LJ-PES) is an indispensable experimental tool for the characterization of electronic–structure interactions in liquid water and aqueous solutions. This includes the determination of valence electron energetics, which is key to understanding chemical reactivity. And yet, the full potential of this method is just about to be exploited, entailing several important benefits, discussed in the present work. This includes the measurement of *absolute* solute and solvent energetics and the accessibility of a specific interfacial property descriptor, the work function (something that is routinely obtained in solid-state PES). Specifically, we have demonstrated the necessity of measuring the liquid-phase low-energy cutoff spectrum along with the photoelectron peak of interest. This approach has several major advantages over the formerly adopted LJ-PES energy referencing scheme and correspondingly has far-reaching implications. With the help of the cutoff energy, E_{cut} , absolute solute and solvent energies can be robustly, accurately, and precisely measured without assumptions, no longer requiring the long-practiced and unsuitable energy referencing to the lowest-energy VIE_{1b1} of *neat* liquid water. Using the methodology introduced here, we find an average VIE_{vac,1b1} of 11.33 ± 0.03 eV (with respect to $E_{\text{v}}^{\text{loc}}$) for neat water, and attribute several previously measured and offset values to the effects of perturbing surface charges, with various condition-dependent potential origins. *Via* a broad photon energy dependent study of VIE_{vac,1b1}, spanning the UV and a large portion of the soft X-ray range, there is a further indication of a small photon energy dependence of VIE_{1b1}, although a definitive answer has to be postponed until the challenge of precisely measuring VIEs with a small error at high photon-energies can be overcome. We further demonstrated the emergent ability to measure solute-perturbed VIE_{vac,1b1} values from aqueous solutions, *i.e.*, solute-induced effects on water's electronic structure. With the same experimental approach, solute energies can be accurately measured, something which is exemplified here using aqueous iodide solutions. Extending our proposed energy referencing approach to deeper-lying electronic states, we have additionally reconfirmed and more precisely defined water's O 1s core-level binding energy, extracting a value of VIE_{vac,O1s} = 538.10 ± 0.05 eV at a ~ 650 eV photon energy.

Regarding the interfacial properties of water and aqueous solutions, we have described and applied a procedure that allows the formal determination of the Fermi level of neat water and select aqueous solutions. Our approach is based on the measurement of LJ-PES spectra under conditions where the streaming potential associated with the flowing LJ has been mitigated. It further relies on the separate measurement of the Fermi edge spectrum from a metal sample in good electrical contact with the electrolyte and electron analyzer. This allowed us to accurately determine VIE_{EF,1b1} = 6.60 ± 0.08 eV. Building

on this approach and the separate accurate measurement of vacuum-level-referenced VIEs (as discussed above), interface-specific aqueous-phase work functions have been extracted, including that of liquid water. Here, $e\Phi_{\text{water}}$ was accurately determined to be 4.73 ± 0.09 eV. Based on the collective electronic structure information accessed both with respect to $E_{\text{v}}^{\text{loc}}$ and E_{F} over the course of this study, we have carefully discussed the observed solution-specific energy shifts of the E_{cut} feature and/or VIE values, which have allowed us to differentiate solution work function and solute-induced (bulk) electronic structure changes. This included quantification of a nearly 0.5 eV aqueous solution $e\Phi$ reduction upon dissolution of a known surfactant (25 mM TBAI).

Still, our study also highlights current shortcomings in state-of-the-art liquid-phase experimental methodologies, particularly the difficulties in E_{F} -referencing arbitrary, free-flowing aqueous solutions and determining their work functions. This primarily stems from the challenges associated with mitigating solution streaming potentials, irrespective of solute concentrations, surface dipole potentials, and the employed experimental conditions. In the particular case of liquid water, we have shown that the aforementioned limitations can be circumvented by measuring and zeroing streaming potentials, while taking advantage of liquid water's small χ^{d} value, or small effective χ^{d} value in our experimental geometry. Here, the inaccuracies of this approach have been determined to amount to less than 50 meV, notably within our VIE_{EF,1b1} and $e\Phi_{\text{water}}$ error ranges. However, in the case of concentrated aqueous salt solutions, such an approach could not be adopted, specifically due to the presence of unknown streaming potentials *and* χ^{d} values. To overcome these limitations, an alternative and more general E_{F} -referencing method would need to be realized. An intriguing associated approach would be the detection of photoelectrons from a solid sample (specifically a metal) covered with a thin layer of flowing electrolyte, engendering metal- and solution-born electron collection *via* the same, generally charged liquid interface. This, however, remains a formidable challenge, particularly for PES studies aiming to resolve the microscopic (electronic) structure and chemical processes occurring at solid–solution interfaces.⁶⁵ Irrespective of the various technical hurdles ahead, the work presented here is a major enrichment of the LJ-PES technique, enabling the general, direct, and accurate measurement of absolute electron energetics within the liquid bulk and at liquid-vacuum interfaces of aqueous solutions. Concurrently, this work brings us a step closer to bridging the gap between solid-state and liquid-phase PES, and more importantly the surface science and (photo)electrochemistry research disciplines.

Note added in proof

We were made aware of another liquid jet X-ray photoelectron spectroscopy study of aqueous solutions concerned with cutoff and Fermi-level energy referencing, which is currently in press.⁹⁷ This work summarizes some of the results within ref. 69, where a number, although not all, of our associated points raised in section 7 in the ESI have been addressed.



Data availability

The data of relevance to this study have been deposited at the following DOI: 10.5281/zenodo.5036382.

Author contributions

S. T., B. W., and I. W. designed the experiments and, together with S. M., F. T., and with occasional assistance from C. L., performed the measurements. S. T., B. W., S. M., and I. W. analyzed the data. S. T., B. W., and I. W. wrote the manuscript and the ESI† with critical feedback from all co-authors.

Conflicts of interest

There are no conflicts to declare.

Acknowledgements

S. T. acknowledges support from the JSPS KAKENHI Grant No. JP18K14178 and JP20K15229. S. M., U. H., and B. W. acknowledge support by the Deutsche Forschungsgemeinschaft (Wi 1327/5-1). F. T., G. M., and B. W. acknowledge support by the MaxWater initiative of the Max-Planck-Gesellschaft. B. W. acknowledges funding from the European Research Council (ERC) under the European Union's Horizon 2020 research and investigation programme (grant agreement No. 883759). D. M. N. and C. L. were supported by the Director, Office of Basic Energy Science, Chemical Sciences Division of the U.S. Department of Energy under Contract No. DE-AC02-05CH11231 and by the Alexander von Humboldt Foundation. We thank the Helmholtz-Zentrum Berlin für Materialien und Energie for allocation of synchrotron radiation beamtime at BESSY II and Robert Seidel for his support during the associated measurements. We acknowledge DESY (Hamburg, Germany), a member of the Helmholtz Association HGF, for the provision of experimental facilities. Parts of this research were carried out at PETRA III and we would like to thank Moritz Hoesch in particular as well as the whole beamline staff, the PETRA III chemistry laboratory and crane operators for assistance in using the P04 soft X-ray beamline. Beamtime was allocated for proposal II-20180012 (LTP). Some of the experiments were carried out with the approval of synchrotron SOLEIL (proposal number 20190130). We thank Laurent Nahon and Sebastian Hartweg in particular, as well as the technical service personnel of the SOLEIL chemistry laboratories for their assistance.

Notes and references

‡ Note that the term 'band' for the assignment of 'spectral bands' in molecular spectroscopy has a different meaning to that applied within the band-structure context of condensed matter.

§ Although the importance of the determination of the cutoff energy in liquid-jet photoelectron spectra, with the aim of quantifying work functions from aqueous solutions, has been accented already in 2003,⁹⁴ this approach was barely further considered for the subsequent 10–15 years. Arguably, the reason is a combination of the gas-phase-references being such an easy and convenient (although problematic) method, and difficulties in the technical realization of low-energy

electron detection with liquid-jet PES setups. For a significant time, and this remains true in many cases, LJ-PES (liquid jet photoelectron spectroscopy) experiments with HEAs were barely designed to detect low-kinetic energy electrons, typically due to insufficient magnetic shielding and likely because it had yet to be demonstrated that liquid phase PES is capable of accessing characteristic condensed-matter properties. Finally, the ability to properly apply a bias voltage to a liquid jet had to be thoroughly explored, an issue with remaining open questions, such as the degree of the deleterious effects of biasing an entire sample delivery assembly, as opposed to just the liquid stream.

¶ We will refer to the inelastic scattering tail as the low-KE tail or LET curve throughout the manuscript, in contrast to the often-used term secondary electron energy distribution (SEED) curve described in previous studies. This is consistent with the fact that at lower photon energies, when the kinetic energy of the primary electron is too low for efficient secondary electron generation *via*, *e.g.*, impact ionization, the inelastic scattering background is not fully comprised of secondary electrons. Thus, the term SEED cannot be used for aqueous solution spectra recorded at ~ 20 eV photon energies and below.³⁰ The term LET is adopted to avoid misleading connotations about the origin of this low energy signal.

|| In fact, it is possible to deliberately modify $e\Phi$, *e.g.*, by adsorption of molecules on the sample surface, which typically induces or alters a pre-existing surface dipole, the associated value of χ^d , and necessarily the value of E_v^{loc} .^{24,35,91} This creates or modifies the energetic barrier for the photoelectrons escaping from the sample into vacuum, and can be detected as a change in KE of the emitted electrons. For a sample with a truly uncharged, amorphous, apolar surface, we note that $E_v^\infty = E_F + \bar{\mu} = E_F + e\Phi$. However, if an intrinsic dipolar surface potential exists, the first equality holds, and the second generally will not. In such a case, and depending on the geometry of the liquid surface and its overlap with an ionizing light source, condensed phase VIEs or binding energies will be offset by an experimental-geometry-averaged amount with respect to E_v^∞ due to the average offset of E_v^{loc} .

** Here we contrast the electronic structure of liquid water with that of metallic, ionic, or covalent macroscopic solids, where delocalized electronic states are formed *via* atomic valence energy level interactions that generate quasi-continua of energy levels, termed bands. An important consequence of this behavior is that PES spectra recorded from non-molecular systems generally exhibit broad valence features that elude association with specific VIEs. Thus, VIE is a quantity less typically encountered in a condensed-matter electronic structure context, with band edge electronic structure descriptors more commonly being reported. It is of great interest to explore how these different descriptors and experimental observables interconnect within a unified 'band structure' description of typical solids, liquid water, and aqueous solutions, although this is beyond the scope of the present study.

†† The problem of ionization-induced charging is well-known in solid insulator studies and is usually sufficiently counteracted using neutralization instrumentation such as electron flood guns.⁹⁵ Notably, the charging of the surface of a volatile, flowing aqueous solution in a low-vacuum environment cannot be compensated in this way.

‡‡ The transmission function of the HEA generally influences the relative signal intensities over larger energy ranges, and especially at very small eKEs, the electron signal is distorted as slow electrons are particularly affected by stray fields (which is another reason to apply an accelerating bias). This makes it difficult to compare exact relative intensities over an energy range larger than about 30–40 eV, something which is beyond the scope of the findings presented here. Any feature within a smaller energy window, such as the valence band region or the cutoff region can be separately analyzed without further correction, since the transmission function will vary minimally over such a small energy range (assuming the cutoff electrons are sufficiently accelerated by an applied bias). A particularly important aspect is the potential effect of the analyzer electron transmission function on the LET shape upon application of a bias voltage. We find, however, that this effect has a negligibly small impact on the value of the extracted absolute VIE values, as detailed in Fig. SI-3.

§§ A tightly focused ionizing beam – such as those provided by synchrotron or laser light sources – primarily probes gaseous molecules in the immediate vicinity of the LJ surface. The associated spectra may be only mildly energetically broadened in a field gradient and the relatively low potential difference spanning the probed volume. Consequently, associated measurements may present an



apparently sharp gas-phase PE signal, despite the presence of an extrinsic field gradient between the sample and electron analyzer.

¶¶ Such a measurement would be forced to deal with a further complication: the electrons from the metal would experience both the metal-solution interfacial potential and the aqueous-vacuum potential, whereas the solution phase electrons would experience the latter only. It can still be argued, however, that E_F would be equilibrated throughout this system as long as the solution was sufficiently conductive. Considering alternative methodologies for the co-determination of solution- and solid-phase electron energetics, application of the 'dip-and pull' PES method may seem appropriate.⁹⁶ However, a significant associated challenge lies in achieving sufficient control over the composition and cleanliness of the solution-vacuum interface, as well as the composition of the solution bulk following solution pulling and under a significant cumulative ionizing radiation load.

||| Note that an optimal concentration of 30 mM (at a flow rate of 0.5 ml min⁻¹ and at room temperature) has also been reported to establish field-free conditions,²⁸ which however depends on experimental parameters like the size and sign of the sample-spectrometer contact potential or work function difference, $\Delta e\phi$. We remind the reader that our field-free conditions were established under rather different conditions with a 2.5 mM NaI concentration, a flow-rate of 0.8 ml min⁻¹, and a tapered fused silica capillary nozzle with a 28 μ m orifice diameter.

**** Such a nonlinear shift in the streaming potential has been observed before. However, no explanation has been given for the high-concentration behavior.²⁸

- 1 P. Atkins, J. de Paula and J. Keeler, *Atkins' Physical Chemistry*, Oxford University Press, 11th edn, 2018.
- 2 R. Seidel, B. Winter and S. E. Bradforth, *Annu. Rev. Phys. Chem.*, 2016, **67**, 283–305.
- 3 S. Y. Truong, A. J. Yench, A. M. Juarez, S. J. Cavanagh, P. Bolognesi and G. C. King, *Chem. Phys.*, 2009, **355**, 183–193.
- 4 B. Winter, R. Weber, W. Widdra, M. Dittmar, M. Faubel and I. V. Hertel, *J. Phys. Chem. A*, 2004, **108**, 2625–2632.
- 5 K. Kobayashi, *J. Phys. Chem.*, 1983, **87**, 4317–4321.
- 6 B. Winter and M. Faubel, *Chem. Rev.*, 2006, **106**, 1176–1211.
- 7 M. N. Pohl, E. Muchová, R. Seidel, H. Ali, S. Sršeň, I. Wilkinson, B. Winter and P. Slaviček, *Chem. Sci.*, 2019, **10**, 848–865.
- 8 P. Hunt, M. Sprik and R. Vuilleumier, *Chem. Phys. Lett.*, 2003, **376**, 68–74.
- 9 A. P. Gaiduk, M. Govoni, R. Seidel, J. H. Skone, B. Winter and G. Galli, *J. Am. Chem. Soc.*, 2016, **138**, 6912–6915.
- 10 S. Gozem, R. Seidel, U. Hergenbahn, E. Lugovoy, B. Abel, B. Winter, A. I. Krylov and S. E. Bradforth, *J. Phys. Chem. Lett.*, 2020, **11**, 5162–5170.
- 11 T. Fransson, Y. Harada, N. Kosugi, N. A. Besley, B. Winter, J. J. Rehr, L. G. Pettersson and A. Nilsson, *Chem. Rev.*, 2016, **116**, 7551–7569.
- 12 D. Prendergast, J. C. Grossman and G. Galli, *J. Chem. Phys.*, 2005, **123**, 014501.
- 13 A. P. Gaiduk, T. A. Pham, M. Govoni, F. Paesani and G. Galli, *Nat. Commun.*, 2018, **9**, 247.
- 14 C. Adriaanse, J. Cheng, V. Chau, M. Sulpizi, J. VandeVondele and M. Sprik, *J. Phys. Chem. Lett.*, 2012, **3**, 3411–3415.
- 15 A. Shimkevich, *World J. Condens. Matter Phys.*, 2014, **04**, 243–249.
- 16 A. Nilsson, D. Nordlund, I. Waluyo, N. Huang, H. Ogasawara, S. Kaya, U. Bergmann, L. Å. Näslund, H. Öström, P. Wernet, K. J. Andersson, T. Schiros and L. G. M. Pettersson, *J. Electron Spectrosc. Relat. Phenom.*, 2010, **177**, 99–129.
- 17 J. Cheng and M. Sprik, *Phys. Chem. Chem. Phys.*, 2012, **14**, 11245–11267.
- 18 F. Williams, S. P. Varna and S. Hillenius, *J. Phys. Chem.*, 1976, **64**, 1549.
- 19 A. Bernas, C. Ferradini and J.-P. Jay-Gerin, *Chem. Phys.*, 1997, **222**, 151–160.
- 20 C. G. Elles, A. E. Jailaubekov, R. A. Crowell and S. E. Bradforth, *J. Chem. Phys.*, 2006, **125**, 044515.
- 21 C. N. Berglund and W. E. Spicer, *Phys. Rev.*, 1964, **136**, A1030.
- 22 C. N. Berglund and W. E. Spicer, *Phys. Rev.*, 1964, **136**, A1044.
- 23 S. Hüfner, *Photoelectron Spectroscopy: Principles and Applications*, Springer Berlin Heidelberg, 3rd edn, 2010.
- 24 W. F. Egelhoff Jr, *Surf. Sci. Rep.*, 1987, **6**, 253–415.
- 25 S. Trasatti, *Surf. Sci.*, 1995, **335**, 1–9.
- 26 H. Baumgärtel, *Electrochemistry: A Guide for Newcomers*, De Gruyter, 1st edn, 2019.
- 27 K. Nishizawa, N. Kurahashi, K. Sekiguchi, T. Mizuno, Y. Ogi, T. Horio, M. Oura, N. Kosugi and T. Suzuki, *Phys. Chem. Chem. Phys.*, 2011, **13**, 413–417.
- 28 N. Kurahashi, S. Karashima, Y. Tang, T. Horio, B. Abulimiti, Y.-I. Suzuki, Y. Ogi, M. Oura and T. Suzuki, *J. Chem. Phys.*, 2014, **140**, 174506.
- 29 C. F. Perry, P. Zhang, F. B. Nunes, I. Jordan, A. von Conta and H. J. Wörner, *J. Phys. Chem. Lett.*, 2020, **11**, 1789–1794.
- 30 S. Malerz, F. Trinter, U. Hergenbahn, A. Ghrist, H. Ali, C. Nicolas, C.-M. Saak, C. Richter, S. Hartweg, L. Nahon, C. Lee, C. Goy, D. M. Neumark, G. Meijer, I. Wilkinson, B. Winter and S. Thürmer, *Phys. Chem. Chem. Phys.*, 2021, **23**, 8246–8260.
- 31 G. Olivieri, A. Goel, A. Kleibert, D. Cvetko and M. A. Brown, *Phys. Chem. Chem. Phys.*, 2016, **18**, 29506–29515.
- 32 R. Schlaf, *Calibration of Photoemission Spectra and Work Function Determination*, 2014, <http://rsl.eng.usf.edu/Documents/Tutorials/PEScalibration.pdf>.
- 33 O. Klyushnikov, *J. Struct. Chem.*, 1998, **39**, 944–947.
- 34 M. G. Helander, M. T. Greiner, Z. B. Wang and Z. H. Lu, *Appl. Surf. Sci.*, 2010, **256**, 2602–2605.
- 35 D. Cahen and A. Kahn, *Adv. Mater.*, 2003, **15**, 271–277.
- 36 M. Faubel, B. Steiner and J. P. Toennies, *J. Chem. Phys.*, 1997, **106**, 9013–9031.
- 37 M. Faubel, *Photoelectron Spectroscopy at Liquid Surfaces*, in *Photoionization And Photodetachment*, World Scientific, 2000, pp. 634–690.
- 38 R. Dupuy, C. Richter, B. Winter, G. Meijer, R. Schlögl and H. Bluhm, *J. Chem. Phys.*, 2021, **154**, 060901.
- 39 Y. Itikawa and N. Mason, *J. Phys. Chem. Ref. Data*, 2005, **34**, 1–22.
- 40 S. Thürmer, M. Ončák, N. Ottosson, R. Seidel, U. Hergenbahn, S. E. Bradforth, P. Slaviček and B. Winter, *Nat. Chem.*, 2013, **5**, 590–596.
- 41 P. Slaviček, B. Winter, L. S. Cederbaum and N. V. Kryzhevoi, *J. Am. Chem. Soc.*, 2014, **136**, 18170–18176.
- 42 P. Slaviček, N. V. Kryzhevoi, E. F. Aziz and B. Winter, *J. Phys. Chem. Lett.*, 2016, **7**, 234–243.
- 43 T. Jahnke, U. Hergenbahn, B. Winter, R. Dörner, U. Frühling, P. V. Demekhin, K. Gokhberg, L. S. Cederbaum,



- A. Ehresmann, A. Knie and A. Dreuw, *Chem. Rev.*, 2020, **120**, 11295–11369.
- 44 E. Pluhařová, C. Schroeder, R. Seidel, S. E. Bradforth, B. Winter, M. Faubel, P. Slaviček and P. Jungwirth, *J. Phys. Chem. Lett.*, 2013, **4**, 3766–3769.
- 45 C. A. Schroeder, E. Pluhařová, R. Seidel, W. P. Schroeder, M. Faubel, P. Slaviček, B. Winter, P. Jungwirth and S. E. Bradforth, *J. Am. Chem. Soc.*, 2015, **137**, 201–209.
- 46 E. Muchová and P. Slaviček, *J. Phys.: Condens. Matter*, 2019, **31**, 043001.
- 47 Z. Tóth, J. Kubečka, E. Muchová and P. Slaviček, *Phys. Chem. Chem. Phys.*, 2020, **22**, 10550–10560.
- 48 N. Ottosson, K. J. Borge, D. Spangberg, H. Bergersen, L. J. Saethre, M. Faubel, W. Pokapanich, G. Öhrwall, O. Björneholm and B. Winter, *J. Am. Chem. Soc.*, 2011, **133**, 3120–3130.
- 49 D. Yepes, R. Seidel, B. Winter, J. Blumberger and P. Jaque, *J. Phys. Chem. B*, 2014, **118**, 6850–6863.
- 50 G. Grell, S. I. Bokarev, B. Winter, R. Seidel, E. F. Aziz, S. G. Aziz and O. Kühn, *J. Chem. Phys.*, 2015, **143**, 074104.
- 51 D. Ghosh, A. Roy, R. Seidel, B. Winter, S. Bradforth and A. I. Krylov, *J. Phys. Chem. B*, 2012, **116**, 7269–7280.
- 52 E. Pluharova, M. Ončák, R. Seidel, C. Schroeder, W. Schroeder, B. Winter, S. E. Bradforth, P. Jungwirth and P. Slaviček, *J. Phys. Chem. B*, 2012, **116**, 13254–13264.
- 53 N. Preissler, F. Buchner, T. Schultz and A. Lübcke, *J. Phys. Chem. B*, 2013, **117**, 2422–2428.
- 54 J. Nishitani, S. Karashima, C. W. West and T. Suzuki, *J. Chem. Phys.*, 2020, **152**, 144503.
- 55 B. Winter, E. F. Aziz, U. Hergenhausen, M. Faubel and I. V. Hertel, *J. Chem. Phys.*, 2007, **126**, 124504.
- 56 S. M. Kathmann, I.-F. W. Kuo, C. J. Mundy and G. K. Schenter, *J. Phys. Chem. B*, 2011, **115**, 4369–4377.
- 57 J. R. Farrell and P. McTigue, *J. Electroanal. Chem.*, 1982, **139**, 37–56.
- 58 C. V. Nguyen, H. Nakahara, O. Shibata and C. M. Phan, *J. Mol. Liq.*, 2020, **298**, 112076.
- 59 S. M. Kathmann, I.-F. W. Kuo and C. J. Mundy, *J. Am. Chem. Soc.*, 2008, **130**, 16556–16561.
- 60 S. M. Kathmann, I.-F. W. Kuo and C. J. Mundy, *J. Am. Chem. Soc.*, 2009, **131**, 17522.
- 61 J. R. Cendagorta and T. Ichiye, *J. Phys. Chem. B*, 2015, **119**, 9114–9122.
- 62 C. Zhang and M. Sprik, *Phys. Chem. Chem. Phys.*, 2020, **22**, 10676–10686.
- 63 Q. Du, R. Superfine, E. Freysz and Y. R. Shen, *Phys. Rev. Lett.*, 1993, **70**, 2313.
- 64 A. Kolmakov, D. A. Dikin, L. J. Cote, J. Huang, M. K. Abyaneh, M. Amati, L. Gregoratti, S. Günther and M. Kiskinova, *Nat. Nanotechnol.*, 2011, **6**, 651–657.
- 65 B. Winter, *Nat. Chem.*, 2015, **7**, 192–194.
- 66 S. Thürmer, R. Seidel, M. Faubel, W. Eberhardt, J. C. Hemminger, S. E. Bradforth and B. Winter, *Phys. Rev. Lett.*, 2013, **111**, 173005.
- 67 Y.-I. Suzuki, K. Nishizawa, N. Kurahashi and T. Suzuki, *Phys. Rev. E: Stat., Nonlinear, Soft Matter Phys.*, 2014, **90**, 010302(R).
- 68 H. Tissot, J.-J. Gallet, F. Bournel, G. Olivieri, M. G. Silly, F. Sirotti, A. Boucly and F. Rochet, *Top. Catal.*, 2016, **59**, 605–620.
- 69 L. P. Ramírez, Electronic structure of interfaces studied by in situ real-time XPS, doctoral thesis, Sorbonne Université, 2020.
- 70 D. K. Nordstrom, *Geochim. Cosmochim. Acta*, 1977, **41**, 1835–1841.
- 71 L. Nahon, N. de Oliveira, G. A. Garcia, J. F. Gil, B. Pilette, O. Marcouillé, B. Lagarde and F. Polack, *J. Synchrotron Radiat.*, 2012, **19**, 508–520.
- 72 EASI liquid-jet PES instrument website, Winter group, Fritz-Haber-Institut, Berlin, <https://www.fhi.mpg.de/236287/experimental-methods>.
- 73 J. Viehhaus, F. Scholz, S. Deinert, L. Glaser, M. Ilchen, J. Seltmann, P. Walter and F. Siewert, *Nucl. Instrum. Methods Phys. Res., Sect. A*, 2013, **710**, 151–154.
- 74 R. Seidel, M. N. Pohl, H. Ali, B. Winter and E. F. Aziz, *Rev. Sci. Instrum.*, 2017, **88**, 073107.
- 75 T. Kachel, *Journal of Large-Scale Research Facilities*, 2016, **2**, A72.
- 76 P. Jungwirth and D. J. Tobias, *Chem. Rev.*, 2006, **106**, 1259–1281.
- 77 O. Abdulrazzaq, S. E. Bourdo, V. Saini, F. Watanabe, B. Barnes, A. Ghosh and A. S. Biris, *RSC Adv.*, 2015, **5**, 33–40.
- 78 J. Yoo, J. Jeong, K. Jung, G. Hyun, M. Kim, H. Lee and Y. Yi, *Appl. Surf. Sci.*, 2019, **476**, 435–441.
- 79 R. Ishikawa, P. J. Ko, M. Bando, Y. Kurokawa, A. Sandhu and M. Konagai, *Nanoscale Res. Lett.*, 2013, **8**, 534.
- 80 I. M. Dharmadasa, O. K. Echendu, F. Fauzi, H. I. Salim, N. A. Abdul-Manaf, J. B. Jasinski, A. Sherehiy and G. Sumanasekera, *J. Mater. Sci.: Mater. Electron.*, 2016, **27**, 5039–5046.
- 81 A. Mezzi, P. Soltani, S. Kaciulis, A. Bellucci, M. Girolami, M. Mastellone and D. M. Trucchi, *Surf. Interface Anal.*, 2018, **50**, 1138–1144.
- 82 M. M. Beerbom, B. Lägél, A. J. Cascio, B. V. Doran and R. Schlaf, *J. Electron Spectrosc. Relat. Phenom.*, 2006, **152**, 12–17.
- 83 C. Bouchard and J. D. Carette, *Surf. Sci.*, 1980, **100**, 251–268.
- 84 S. Thürmer, T. Shinno and T. Suzuki, *J. Phys. Chem. A*, 2021, **125**(12), 2492–2503.
- 85 H. T. Nguyen-Truong, *J. Phys.: Condens. Matter*, 2018, **30**, 155101.
- 86 B. Winter, R. Weber, P. M. Schmidt, I. V. Hertel, M. Faubel, L. Vrbka and P. Jungwirth, *J. Phys. Chem. B*, 2004, **108**, 14558–14564.
- 87 R. Weber, B. Winter, P. Schmidt, W. Widdra, I. Hertel, M. Dittmar and M. Faubel, *J. Phys. Chem. B*, 2004, **108**, 4729–4736.
- 88 P. Jungwirth and D. J. Tobias, *J. Phys. Chem. B*, 2002, **106**, 6361–6373.
- 89 N. Ottosson, M. Faubel, S. E. Bradforth, P. Jungwirth and B. Winter, *J. Electron Spectrosc. Relat. Phenom.*, 2010, **177**, 60–70.



- 90 H. Bergersen, R. R. T. Marinho, W. Pokapanich, A. Lindblad, O. Björneholm, L. J. Sæthre and G. Öhrwall, *J. Phys.: Condens. Matter*, 2007, **19**, 326101.
- 91 H. Ishii, K. Sugiyama, E. Ito and K. Seki, *Adv. Mater.*, 1999, **11**, 605–625.
- 92 H. Lüth, *Surfaces and Interfaces of Solid Materials*, Springer-Verlag Berlin Heidelberg, 3rd edn, 2013.
- 93 T. Suzuki, Kyoto University, private communication.
- 94 R. Weber, Photoelectron spectroscopy of liquid water and aqueous solutions in free microjets using synchrotron radiation, doctoral thesis, Freie Universität Berlin, 2003.
- 95 D. R. Baer, K. Artyushkova, H. Cohen, C. D. Easton, M. Engelhard, T. R. Gengenbach, G. Greczynski, P. Mack, D. J. Morgan and A. Roberts, *J. Vac. Sci. Technol., A*, 2020, **38**, 031204.
- 96 S. Axnanda, E. J. Crumlin, B. Mao, S. Rani, R. Chang, P. G. Karlsson, M. O. M. Edwards, M. Lundqvist, R. Moberg, P. Ross, Z. Hussain and Z. Liu, *Sci. Rep.*, 2015, **5**, 9788.
- 97 L. Pérez Ramírez, A. Boucly, F. Saudrais, F. Bournel, J. Gallet, E. Maisonhaute, A. R. Milosavljevi, C. Nicolas and F. Rochet, *Phys. Chem. Chem. Phys.*, 2021, DOI: 10.1039/D1CP01511G.



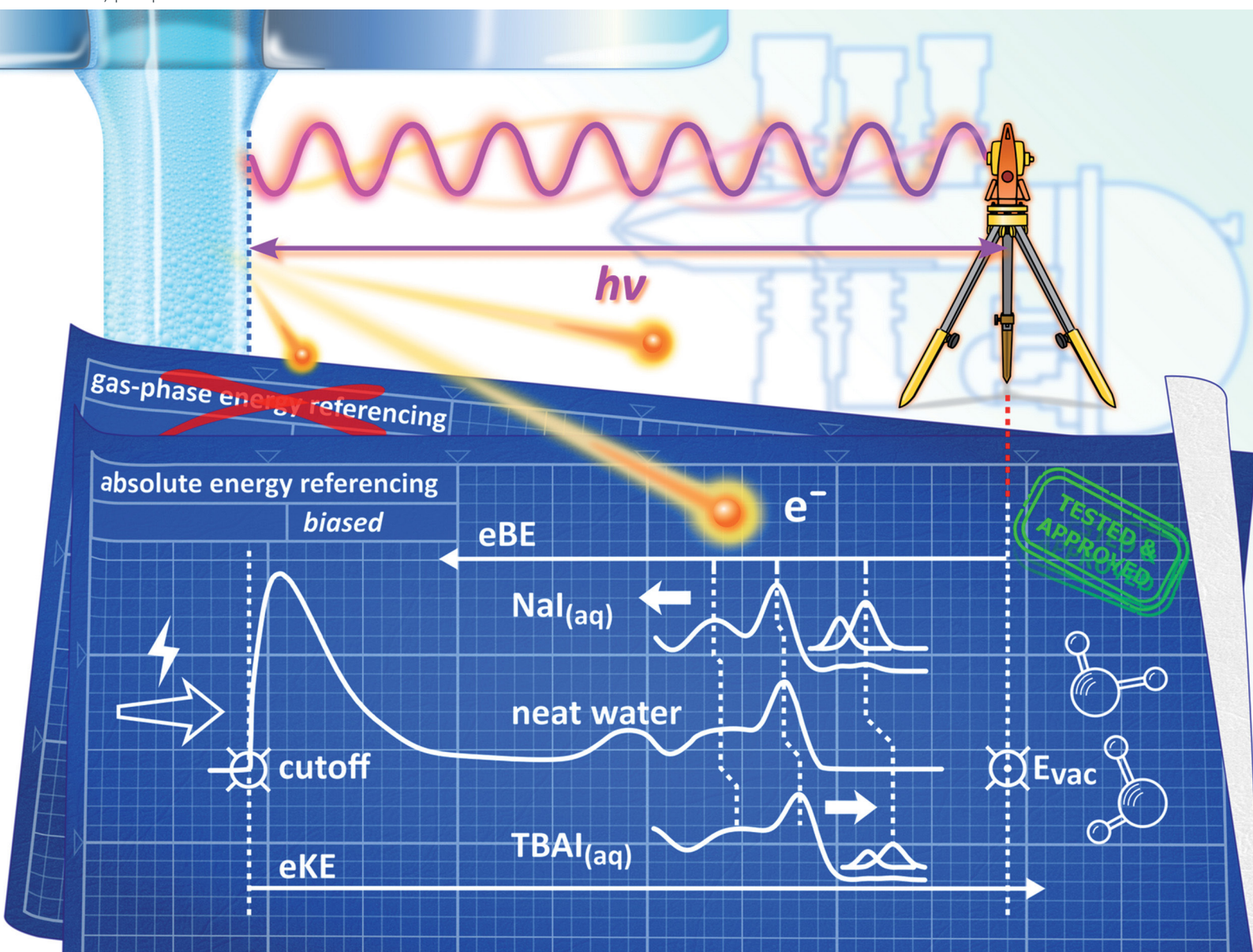
Paper IV



PCCP

Physical Chemistry Chemical Physics

rsc.li/pccp



ISSN 1463-9076

PAPER

Stephan Thürmer, Bernd Winter *et al.*
Quantitative electronic structure and work-function changes
of liquid water induced by solute


 Cite this: *Phys. Chem. Chem. Phys.*,
2022, 24, 1310

Quantitative electronic structure and work-function changes of liquid water induced by solute†

 Bruno Credidio,^{ab} Michele Pugini,^a Sebastian Malerz,^a Florian Trinter,^{ac} Uwe Hergenhahn,^a Iain Wilkinson,^d Stephan Thürmer^{*,e} and Bernd Winter^{*,a}

Recent advancement in quantitative liquid-jet photoelectron spectroscopy enables the accurate determination of the absolute-scale electronic energetics of liquids and species in solution. The major objective of the present work is the determination of the absolute lowest-ionization energy of liquid water, corresponding to the $1b_1$ orbital electron liberation, which is found to vary upon solute addition, and depends on the solute concentration. We discuss two prototypical aqueous salt solutions, $\text{NaI}_{(\text{aq})}$ and tetrabutylammonium iodide, $\text{TBAI}_{(\text{aq})}$, with the latter being a strong surfactant. Our results reveal considerably different behavior of the liquid water $1b_1$ binding energy in each case. In the $\text{NaI}_{(\text{aq})}$ solutions, the $1b_1$ energy increases by about 0.3 eV upon increasing the salt concentration from very dilute to near-saturation concentrations, whereas for TBAI the energy decreases by about 0.7 eV upon formation of a TBAI surface layer. The photoelectron spectra also allow us to quantify the solute-induced effects on the solute binding energies, as inferred from concentration-dependent energy shifts of the I^- 5p binding energy. For $\text{NaI}_{(\text{aq})}$, an almost identical I^- 5p shift is found as for the water $1b_1$ binding energy, with a larger shift occurring in the opposite direction for the $\text{TBAI}_{(\text{aq})}$ solution. We show that the evolution of the water $1b_1$ energy in the $\text{NaI}_{(\text{aq})}$ solutions can be primarily assigned to a change of water's electronic structure in the solution bulk. In contrast, apparent changes of the $1b_1$ energy for $\text{TBAI}_{(\text{aq})}$ solutions can be related to changes of the solution work function which could arise from surface molecular dipoles. Furthermore, for both of the solutions studied here, the measured water $1b_1$ binding energies can be correlated with the extensive solution molecular structure changes occurring at high salt concentrations, where in the case of $\text{NaI}_{(\text{aq})}$, too few water molecules exist to hydrate individual ions and the solution adopts a crystalline-like phase. We also comment on the concentration-dependent shape of the second, $3a_1$ orbital liquid water ionization feature which is a sensitive signature of water–water hydrogen bond interactions.

 Received 12th July 2021,
Accepted 21st September 2021

DOI: 10.1039/d1cp03165a

rsc.li/pccp

1. Introduction

Experimental access to absolute binding energies (BEs) from aqueous solutions has been a principal goal in liquid-jet

photoelectron spectroscopy (LJ-PES) but can only now be accomplished thanks to a recent extension of the method's capabilities, by acquiring additional spectral information. In particular, here we make use of a novel energy referencing scheme, which has been described in detail in our recent publication¹ and is briefly summarized in the following. The key concept is to not only measure a desired photoelectron peak, *i.e.*, the respective kinetic energy (KE) associated with a given ionization feature, but to also measure the distribution of the spectral low-energy tail (LET) arising from various electron scattering processes,² and especially the energy of the cutoff feature, E_{cut} , of this scattering distribution. Briefly, this spectral cutoff indicates the lower bound of electron KEs within the liquid which can still overcome the surface barrier and be expelled from the solution. An electron imparted with an energy equivalent to the BE *via* photoabsorption will be found outside

^a Molecular Physics Department, Fritz-Haber-Institut der Max-Planck-Gesellschaft, Faradayweg 4-6, 14195 Berlin, Germany. E-mail: winter@fhi-berlin.mpg.de

^b Institute for Chemical Sciences and Engineering (ISIC), École Polytechnique Fédérale de Lausanne (EPFL), 1015 Lausanne, Switzerland

^c Institut für Kernphysik, Goethe-Universität, Max-von-Laue-Straße 1, 60438 Frankfurt am Main, Germany

^d Department of Locally-Sensitive & Time-Resolved Spectroscopy, Helmholtz-Zentrum Berlin für Materialien und Energie, Hahn-Meitner-Platz 1, 14109 Berlin, Germany

^e Department of Chemistry, Graduate School of Science, Kyoto University, Kitashirakawa-Oiwakecho, Sakyo-Ku, Kyoto 606-8502, Japan. E-mail: thuermer@kuchem.kyoto-u.ac.jp

† Electronic supplementary information (ESI) available. See DOI: 10.1039/d1cp03165a



the solution with zero KE, under the proviso that electron does not undergo an inelastic scattering event as it escapes the solution. E_{cut} correspondingly serves as a liquid-phase reference point for quantifying BEs. In the experiment, however, E_{cut} is revealed by the large signal background of inelastically scattered electrons, whose signal intensity is cut off by the surface-barrier limit. Such measurements are routinely performed in solid-state systems but were only performed with aqueous solutions many years after the invention of the volatile-liquid-microjet technique in 1997³ and the early development of the LJ-PES research field in approximately 2004.⁴ Although the first measurement of E_{cut} was reported as early as 2003,⁵ the approach was only recently re-introduced^{6,7} and accurately applied.¹

The reasons for this sluggish development were recently reviewed in detail by some of the authors.¹ So far, the LJ-PES community largely relied on known reference photoelectron peak BEs in the respective solvent signal to determine other liquid-phase BEs. One rather involved method to achieve this is to use gas-phase signals to determine liquid-phase BEs, with the former having well-known BEs and inevitably appearing in the spectrum together with the liquid-phase signals due to evaporation from the target. The main complication with this practice is that the surface charge of the liquid jet is difficult to quantify, and as a result, the energy calibration of a measured liquid-water photoelectron peak with respect to the corresponding and known gas-phase ionization energy is only approximate. The error depends on the degree of surface charge, which can vary widely from solution to solution, and hence on the magnitude of the electric field between the liquid jet and the grounded electron detector. Accordingly, liquid-phase (nearly) neat solvent peak BEs have been carefully pre-calibrated using the aforementioned methodology and subsequently used as liquid-phase energy references for aqueous solutions, assuming that the reference solvent BEs are invariant with solute concentration. Here, water's highest occupied molecular orbital (HOMO) $1b_1$ band BE has acted as the reference for the valence spectral region, with the O $1s$ BE being regularly used as a BE reference for core-level spectra. The simplicity of this approach resulted in it becoming a convenient and well-established, although flawed, BE calibration procedure for LJ-PES. A major associated consequence is that all PES studies from aqueous solutions to date, other than our own recent study,¹ did not and could not measure the solute-induced effects on the lowest $1b_1$ ionization energy of liquid water, or absolute-energy-scale changes to its electronic structure more generally. Hence, the systematic errors of previously reported solute ionization energies have the potential to be substantial, particularly when high bulk or local solute concentrations are implemented. Indeed, electrolytes are expected to induce significant electrostatic effects and disruptions of the hydrogen-bonding network in liquid water, particularly for highly concentrated solutions (see ref. 8 and references therein), where the iodide anion has been reported to have an especially large influence on the extended hydrogen-bonding network.⁹ In such solutions, the highly unsatisfactory situation of being unable to quantify any possible energy shifts of the water $1b_1$ orbital energy, and absolute-scale

water electronic energetics in general, has been accentuated only recently⁸ after decades of LJ-PES research. However, with the additional determination of E_{cut} in LJ-PES experiments, such measurements now become possible and BEs of both solvent and solute can be determined absolutely, without assumption, and without relying on a gas-phase-referencing method.

An equally important and recent LJ-PES methodology development permits the accurate determination of surface properties of liquid solutions, such as work functions ($e\Phi_s$).¹ Thus far, the LJ-PES community has largely neglected the characterization of such surface properties, with just four exceptions.^{1,6,7,10} In fact, this field of research has largely been discussed within the domain of molecular physics. However, in order to explicitly account for the liquid surface and accurately determine liquid-phase BEs and surface potentials, condensed-matter concepts must be invoked, as further demonstrated here.

In the present study, we apply the new experimental tools discussed above to quantify the solute-induced evolution of water's valence electronic structure and the lowest ionization energy of the solute. This is exemplified *via* concentration-dependent NaI and tetrabutylammonium iodide (TBAI) aqueous solution LJ-PES measurements, spanning dilute to near-saturated bulk and supersaturated solution concentrations, respectively. The solubility limit of NaI in water is ~ 12.3 M at room temperature,¹¹ and at such high concentrations there are approximately only five water molecules per Na^+/I^- pair, implying extensive solution-structure and composition changes, as well as ion pairing. An associated expectation is that such bulk-solution structure modifications would be reflected in the liquid water and iodide ($\text{I}^- 5p$) valence PES spectra, as explored in an earlier work by some of the authors.⁸ This previous study reported similar LJ-PES measurements to those reported here, also spanning concentrations between 0.5 M and 8.0 M but recorded with photon energies of 180 eV and 650 eV using a synchrotron radiation source. In the present study, a laboratory 40.814 eV (He II α) photon source is alternatively implemented, with no observable effect on the relative peak energetics extracted in the previous study. In fact, the previous PES spectra are almost replicas of those to be presented here, except for the relative spectral signal intensities arising from photon-energy-dependent photoionization cross-sections. Yet, the decisive difference is that we now also measure E_{cut} from which, together with the accurately known photon energy, absolute solvent and solute binding energies can be accurately determined.¹ In the previous Pohl *et al.* study,⁸ on the other hand, the PES spectra measured at different NaI concentrations were aligned at the positions of the water $1b_1$ peaks. This approach was justified by the fact that the entire photoelectron spectrum experienced an average uniform energetic shift as if a bias voltage had been applied to the sample. With that, any signature of electronic structure change could be quantified solely with respect to a fixed water $1b_1$ energy. Nevertheless, the Pohl *et al.* study did reveal a number of water-orbital-specific, relative energy changes that were interpreted with the help of high-level electronic-structure calculations. One of the conclusions from the theoretical data was that the liquid water $1b_1$ peak position essentially remains unaltered (*i.e.*, changes were very small) with



increasing electrolyte concentration, which to some extent would justify the experimental energetic referencing procedure. This latter aspect partially explains the particular interest in water's absolute $1b_1$ BE, as well as the fact that this peak is generally well isolated in the photoelectron spectrum for both the liquid- and gaseous phase. More importantly, this energy is a determining factor for chemical reactivity with the solvent in aqueous solution.¹² Yet, regarding the molecular structure of liquid water more generally, a particularly sensitive fingerprint is the water $3a_1$ PES peak shape, which will also be addressed here. This is connected with a pair of orbital components that are primarily associated with intermolecular bonding and anti-bonding interactions between water molecules, and represent orbitals that are affected by explicit water-water and ion-water interactions. Shining new light on exactly these aspects is a major goal of the present work. A secondary aim is to provide more accurate absolute-energy-scale experimental water $1b_1$ and $3a_1$ as well as iodide $I^- 5p_{(aq)}$ BEs to enable a direct comparison between measured experimental data and the results of high-level electronic-structure theory and associated spectral simulations.

In the case of the TBAI surfactant – where bulk-solution concentrations are much lower but sufficient to achieve surface (super)saturation – we may expect that water $1b_1$ energies correlate with the formation and magnitude of a molecular surface dipole. There may also be correlations of surface-dipole effects with the $I^- 5p$ energy. Hence, the crucial difference between the NaI and TBAI systems is that the latter will allow primary and specific exploration and quantification of $e\Phi$, an explicit surface property, from an aqueous solution. In fact, the present TBAI_(aq) study, performed using the new experimental capabilities, can be compared to one of the very early LJ-PES studies^{4,5} – also on TBAI – where experimental conditions did not permit the current questions to be addressed. Further interest in this particular surfactant system arises from its use as a highly efficient phase-transfer catalyst.¹³

Since our experiments aim at the characterization of the solution interface with concurrent sensitivity to the bulk of the solutions, a sufficiently large probing depth of our generally surface-sensitive method must be assured. At the photon energy of 40.814 eV applied here, the leading water valence photoelectrons have a ~ 30 eV KE, which is thought to correspond to a 1–2 nm electron inelastic mean free path (eIMFP) in neat water.^{14–16} Corresponding values for the solutions are not accurately known but we assume that the experiment probes several layers into solution, exponentially attenuated with the IMFP (or more precisely, an effective attenuation length)¹⁷ for a given electron KE; probing depth in 10 M NaI aqueous solution has been estimated to decrease by $\sim 30\%$ as compared to pure water at 65 eV KE.¹⁸ The aforementioned length scale is well-matched to that over which bulk conditions pertain in aqueous salt solutions.¹⁹ Indeed, the similarity of the relative NaI_(aq) solution energetics reported here and previously at significantly higher photon energies of 180 eV and 650 eV,⁸ corresponding to 1–4 nm probing depths,^{14–16} indicates that the photon energy implemented in this study provides sufficient depth sensitivity to interrogate the interface and bulk solution behavior. One other

crucial aspect is that the 40.814 eV photon energy is large enough to produce valence photoelectrons with energies larger than a threshold KE of approximately 10–15 eV below which quasi-elastic electron scattering in solution causes peak distortions, and binding energies can no longer be determined.²

II. Experimental

All photoelectron experiments were performed with the EASI setup.²⁰ It comprises a state-of-the-art near-ambient-pressure capable hemispherical electron analyzer (HEA, HiPP-3, Scienta-Omicron) which detects electrons generated upon ionization of a 28 μm diameter liquid jet formed from a glass capillary at the exact photon energy of 40.814 ± 0.002 eV. This energy is provided by a VUV laboratory He-discharge light source (VUV5k, Scienta-Omicron), with the emission line being selected and pre-focused *via* a curved diffraction grating. The discharge lamp emits essentially unpolarized light which is only minimally polarized ($<0.1\%$) by the monochromator system as it is delivered to the LJ. The photon-energy resolution was limited by the intrinsic width of the emission line, He II α , of 2 meV. After the monochromator, the light is further collimated *via* an exit capillary down to a focal spot size of approximately $300 \times 300 \mu\text{m}^2$ at the LJ sample. The light propagation axis spanned an angle of $\sim 70^\circ$ with respect to the photoelectron detection axis; LJ propagation and photoelectron detection axes were orthogonal to each other. The electron analyzer resolution was better than 40 meV at a pass energy of 20 eV. For all measurements, we used the so-called VUV lens mode. In this work, we were mainly interested in detecting the water $1b_1$ and $I^- 5p$ photoelectron peaks and the low-energy tail, including E_{cut} . Measurement of the latter necessitates the application of a negative bias voltage at the jet, -25 V for all measurements reported here. This separates the cutoff energy of the solution from that of the electron detector. A beneficial side effect is that liquid-phase spectra can be obtained with nearly no gas-phase contributions.¹ Liquid jet biasing is accomplished by placing a metallic tube in between the high-pressure liquid PEEK lines that feed the glass capillary. This piece, which is thus in direct contact with the liquid approximately 55 cm upstream of the capillary, can either be electrically connected to the grounded HEA or to a highly stable Rohde & Schwarz HMP4030 power supply.

Liquid flow rates for all solutions other than 8 M NaI_(aq) were set to 0.8 mL min^{-1} , which translates to an approximately $\sim 20 \text{ m s}^{-1}$ jet velocity. For 8 M NaI_(aq) we used 1.2 mL min^{-1} ($\sim 30 \text{ m s}^{-1}$) to maintain better jet stability. The solution bath temperature, as regulated by a chiller unit, was typically 10°C for all solutions other than 8 M NaI_(aq), where we used 15°C to avoid precipitation. Upon injection into vacuum, the LJ is formed with a laminar flow region extending over 2–5 mm, which is positioned $\sim 800 \mu\text{m}$ away from the HEA entrance aperture, with an $800 \mu\text{m}$ entrance aperture diameter. The jet was ionized right in front of the HEA. At this short distance, electrons emitted from the liquid phase can reach the differentially pumped electron-detection chamber unperturbed at an



increased transfer length of ~ 1 mm under typical experimental conditions. The average pressure in the interaction chamber during liquid-jet operation was approximately 7×10^{-5} mbar, accomplished with two turbo-molecular pumps (with a total pumping speed of ~ 2600 L s^{-1} for water) and three liquid-nitrogen cold traps (with a total pumping speed of $\sim 35\,000$ L s^{-1} for water). The pumping speed, S , per surface area (*i.e.*, in L s^{-1} cm^{-2}) of the latter was estimated as $S = 3.64 \sqrt{T_{\text{gas}}/M}$,²¹ where $T_{\text{gas}} \approx 273$ K is the temperature of the water vapor and $M = 18$ is the molar mass of water, which yields $S \approx 14.2$ L s^{-1} cm^{-2} . Experimental details, including collection of the liquid and emerging droplet spray, jet fine-positioning, relevant HEA features, and vacuum pumping system are described in ref. 1. Aqueous solutions were prepared by dissolving NaI or TBAI (both Sigma-Aldrich and of +99% purity) in highly demineralized water (conductivity ~ 0.2 $\mu\text{S cm}^{-1}$) and were degassed in an ultrasonic bath for ~ 5 – 10 minutes. The solution was delivered using a Shimadzu LC-20 AD HPLC pump that incorporates a four-channel valve for quick switching between different solutions. The equipped in-line degasser (Shimadzu DGU-20A5R), which is connected between the sample reservoir and the low-pressure side of the HPLC pump, was used as well during operation.

III. Results and discussion

III.1 Near- E_{cut} and valence PES spectra from NaI aqueous solutions as a function of concentration

Fig. 1 presents PES spectra from NaI aqueous-solution micro-jets for several concentrations spanning 50 mM to 8.0 M; the lowest concentration of 50 mM is added to maintain sufficient conductivity for PE experiments but is otherwise considered

indistinguishable from neat water.⁴ Measurements were made from a 28 μm diameter liquid jet, biased at -25 V, and using a photon energy of $h\nu = 40.814 \pm 0.002$ eV. Fig. 1A presents the high-resolution LETs of the photoemission spectra with the characteristic low-energy cutoff, where we have applied the tangent method to plot the spectra on a common, bias-corrected KE scale (where $E_{\text{cut}} = 0$ eV; see the Introduction) and calibrated BE scale for the valence region;¹ signal intensities are normalized to yield the same cutoff slope. The BE scale is established *via* the relation $BE = h\nu - KE$. We note that this equation implicitly uses the spectral width, ΔE_w , to determine the KE term, which we define as the energy distance from E_{cut} to the PE feature of interest, *i.e.*, $\Delta E_w = KE_{\text{measured}} - E_{\text{cut}}$. If E_{cut} is not aligned to zero beforehand, then rather $BE = h\nu - \Delta E_w$. Corresponding valence spectra are plotted in Fig. 1B, where the displayed spectral range covers the water $3a_1$, $1b_1$, and spin-orbit split iodide Γ $5p_{3/2,1/2}$ doublet^{8,12,22} signals occurring at KEs (bottom axis) of ~ 26 – 28 eV, ~ 29 – 30 eV, 31 – 34 eV and electron BEs (top axis) of ~ 13 – 15 eV, ~ 11 – 12 eV, 7 – 10 eV, respectively. Signal intensities are normalized to the $1b_1$ peak height for better visual comparability. As-measured spectra are shown in Fig. S1 in the ESI;† the maximal signal intensities were $\sim 0.4 \times 10^6$ – 1.2×10^6 counts per second for the cutoff region and $\sim 0.4 \times 10^4$ – 1.0×10^4 counts per second for the valence band, respectively.

The series of spectra shown in Fig. 1B is analogous to the respective data presented in Pohl *et al.*,⁸ with the insignificant difference that at the lower $h\nu$ used in the present study, relative differences in ionization cross-sections yield somewhat larger water $1b_1$ -to- Γ $5p$ and $1b_1$ -to- $3a_1$ signal intensity ratios. Another difference, which can be considered an improvement for a detailed analysis, but is otherwise irrelevant in the present context, is that the PES spectra in Fig. 1B contain no gas-phase

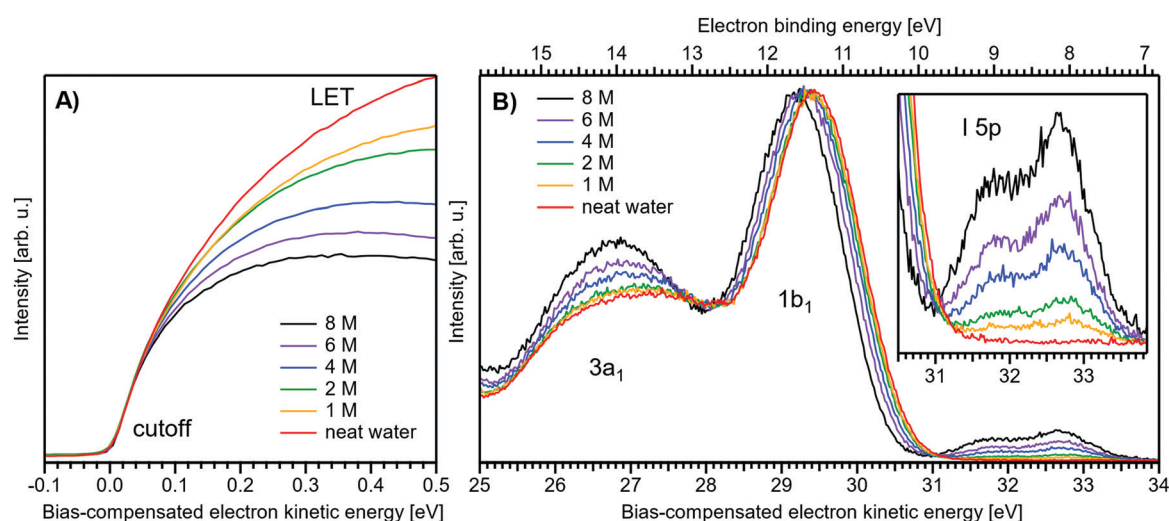


Fig. 1 Series of experimental spectra for NaI aqueous-solutions of varying salt concentration, spanning neat water (50 mM salt added only for the purpose of maintaining conductivity) to 8 M. All spectra have been energy-shifted to yield $E_{\text{cut}} = 0$ eV after applying the tangent-method, *i.e.*, the bottom energy scale shows the KE of the electrons with just enough energy to traverse the liquid surface. (A) Low-energy tail (LET) spectra with the characteristic cutoff; spectra have been normalized to produce the same tangent slope. An overview of the changes in the wide-range LET shape is shown in Fig. 4. (B) Valence region with the prominent water $3a_1$ and $1b_1$ bands; spectra have been normalized to the same height of the $1b_1$ peak for visualizing the subtle shifts of the $1b_1$ peak and the shape change of the $3a_1$ peak with increasing concentration. The inset shows an enlarged view of the Γ $5p$ lowest ionization features of the solute. As-measured spectra are plotted in Fig. S1 in the ESI.†



water signal contributions. The reason is that the applied bias voltage between the liquid jet and detector orifice causes a potential which increases with distance, and only partially accelerates electrons liberated from the gaseous species some distance away from the liquid surface. As a result, the gas-phase signal is energetically smeared out and separated from the liquid-phase signal.¹ At most, the gas-phase contribution adds a broad background to the biased spectrum which, however, was negligible in our experiments. Following the spectral evolution, from the lowest to highest salt concentration, one observes an increase of the I^- 5p signal intensity. However, the important finding is that the position of the $1b_1$ peak (and, on closer inspection, the I^- 5p peak; see below) is not constant in energy, exhibiting a ~ 260 meV total shift towards lower KEs (higher BEs). Furthermore, a significant change of the water $3a_1$ peak shape is observed, arising from weakened intermolecular $3a_1$ - $3a_1$ interaction upon addition of salt.⁸ In the coming sections of this manuscript, we will present and discuss the absolute values of the various orbital binding energies for the two salt solutions and the respective concentrations. It is convenient (and consistent with a previous notation)¹ to interchangeably refer to vertical ionization energies, VIEs, which are a measure of the propensity to detach an electron under equilibrium conditions and are equivalent to the (vertical) binding energies. In both cases, the measured energy is related to the position of the maximum of the respective photoelectron peak. Thus, the $1b_1$ BE from neat liquid water is the same quantity as $VIE_{1b_1, \text{water}}$, the water $1b_1$ BE from solution corresponds to $VIE_{1b_1, \text{sol}}$, and the analogues for the water $3a_1$ and iodide I^- 5p BEs are $VIE_{3a_1, \text{sol}}$ and $VIE_{I^- 5p, \text{sol}}$, respectively, with the subscript 'sol' either referring to NaI or TBAI aqueous solutions.

To extract the quantitative evolution of individual spectral features, concerning both peak position and area, we employed a fit with 4–6 peaks (4 peaks for the neat water spectrum where the I^- 5p signal is absent). Gaussians were used for all peaks other than the $1b_1$ peak. We find that for spectra measured with sufficiently high resolution, as employed here, the simplified assumption of a 'Gaussian' $1b_1$ peak shape is insufficient to describe the asymmetric peak shape correctly. The asymmetry arises from vibrational structure which is not resolved in the liquid-phase spectra due to inhomogeneous (configurational) broadening;²³ see Fig. 3 for an exemplary water gas-phase valence photoelectron spectrum. We thus opt to describe the $1b_1$ peak by an exponentially modified Gaussian shape,²⁴ where the asymmetry τ is fixed to a value of -0.3 eV; asymmetry values

of -0.2 to -0.3 have been found to describe the spectral envelope of the gaseous $1b_1$ peak well. The $3a_1$ split feature is constrained to yield the same height and width for both Gaussians.^{4,8} Furthermore, the I^- $5p_{3/2}$ and $5p_{1/2}$ double peaks were constrained to yield the expected 1:2 peak area ratio. Exemplary fits, for all peaks, are plotted in Fig. S3 (ESI[†]), and the fit results are summarized in Table 1. The analogous analysis has been performed for the TBAI aqueous solutions (discussed later), and the results are summarized in Table 2.

Before quantifying and interpreting the observed energy shifts in Fig. 1B, one important conclusion that can already be drawn at this point is that all effects primarily reflect bulk-solution properties. This is inferred from the water $1b_1$ and I^- 5p signal intensities, specifically the areas from the peak fitting, as a function of concentration (bottom axis), as shown in Fig. 2A. The as-measured $1b_1$ signal intensity (black open triangles) is seen to monotonically decrease over the entire concentration range (also compare Fig. S1, ESI[†]), while the relative, *i.e.*, $1b_1$ -peak-area normalized, I^- 5p signal (red full triangles) monotonically increases. Such a quantitative balance results from the decreasing number of water molecules and the increasing number of ions in a given probing volume as the solute concentration is increased, which is possibly accompanied by increased electron scattering that further diminishes the water signal. That said, it is well established that heavier halide anions preferably accumulate at the liquid interface, with iodide being pushed out of the water network due to its large size and polarizability, resulting in a particularly high halide ion surface activity.^{18,19,25,26} The cation is correspondingly pulled towards the interface and a surface concentration enhancement is established for the two ionic species, with characteristic peaked, but slightly offset, density profiles.²⁵ We attempt to quantify the observed I^- peak intensity increase using the well-known BET (Brunauer, Emmett, and Teller) isotherm,²⁷ which was developed for multi-layer gas adsorption but has been shown to be equally applicable to describe water activity in concentrated electrolyte solutions by viewing hydration as an adsorption of multiple water shells around the electrolyte.²⁸ Here, we repurpose the equation to describe the buildup of ion concentration as an irregular 'multi-layer adsorption' at the water interface:

$$\text{Int}_{I^- 5p} = \text{Int}_{\text{sat}} \frac{cX}{(1+X)[1+(c+1)X]} \quad (1)$$

with $X = [c]/[c]_{\text{sat}}$ being the fractional bulk-solute concentration to saturation concentration (which is about 12.3 M for NaI_(aq) at

Table 1 VIE values of the liquid water valence $1b_1$ and split $3a_1$ bands (denoted as $3a_1$ H and $3a_1$ L; see text) as well as the solute I^- 5p doublet peak as extracted from fits to the spectra of solutions with various NaI concentrations. The right-most column shows the change in energetic distance between the $3a_1$ H and $3a_1$ L bands, which increases with increasing NaI concentration. Errors are one standard deviation as derived from the fits

| Conc. | VIE_{1b_1} (eV) | $VIE_{3a_1, L}$ (eV) | $VIE_{3a_1, H}$ (eV) | $VIE_{I^- 5p_{1/2}}$ (eV) | $VIE_{I^- 5p_{3/2}}$ (eV) | $3a_1$ split (eV) |
|-------|-------------------|----------------------|----------------------|---------------------------|---------------------------|-------------------|
| 50 mM | 11.33 ± 0.02 | 13.09 ± 0.05 | 14.53 ± 0.05 | — | — | — |
| 1 M | 11.37 ± 0.02 | 13.14 ± 0.06 | 14.54 ± 0.06 | 9.00 ± 0.13 | 8.02 ± 0.15 | -0.06 ± 0.09 |
| 2 M | 11.39 ± 0.02 | 13.17 ± 0.05 | 14.53 ± 0.05 | 9.03 ± 0.07 | 8.05 ± 0.07 | -0.09 ± 0.07 |
| 4 M | 11.44 ± 0.02 | 13.26 ± 0.07 | 14.53 ± 0.07 | 9.06 ± 0.04 | 8.10 ± 0.03 | -0.18 ± 0.09 |
| 6 M | 11.51 ± 0.02 | 13.35 ± 0.07 | 14.53 ± 0.08 | 9.12 ± 0.03 | 8.14 ± 0.03 | -0.26 ± 0.11 |
| 8 M | 11.60 ± 0.02 | 13.50 ± 0.07 | 14.55 ± 0.07 | 9.16 ± 0.02 | 8.16 ± 0.02 | -0.41 ± 0.10 |



Table 2 VIE values of the liquid water valence $1b_1$ and split $3a_1$ bands ($3a_1$ H and $3a_1$ L; see text) as well as the solute I^- 5p doublet peak as extracted from fits to the spectra of solutions with various TBAI concentrations. The right-most column shows the full-width at half maximum (FWHM) of the $1b_1$ band, which increases with increasing TBAI concentration; this is deemed to be representative of an overall broadening of all water bands. Errors are one standard deviation as derived from the fits

| Conc. | VIE $_{1b_1}$ (eV) | VIE $_{3a_1L}$ (eV) | VIE $_{3a_1H}$ (eV) | VIE $_{I5p_{1/2}}$ (eV) | VIE $_{I5p_{3/2}}$ (eV) | $1b_1$ FWHM (eV) |
|-------|--------------------|---------------------|---------------------|-------------------------|-------------------------|------------------|
| 0 mM | -11.33 ± 0.02 | 13.12 ± 0.03 | 14.52 ± 0.03 | — | — | 1.40 ± 0.01 |
| 5 mM | -11.08 ± 0.02 | 12.85 ± 0.03 | 14.25 ± 0.04 | 8.63 ± 0.25 | 7.63 ± 0.23 | 1.41 ± 0.01 |
| 10 mM | -10.86 ± 0.02 | 12.61 ± 0.04 | 14.01 ± 0.04 | 8.35 ± 0.12 | 7.39 ± 0.10 | 1.44 ± 0.01 |
| 15 mM | -10.73 ± 0.02 | 12.47 ± 0.05 | 13.87 ± 0.05 | 8.19 ± 0.12 | 7.21 ± 0.12 | 1.45 ± 0.02 |
| 20 mM | -10.65 ± 0.02 | 12.40 ± 0.06 | 13.80 ± 0.06 | 8.12 ± 0.11 | 7.16 ± 0.11 | 1.46 ± 0.02 |
| 25 mM | -10.63 ± 0.02 | 12.33 ± 0.05 | 13.73 ± 0.05 | 8.05 ± 0.10 | 7.08 ± 0.09 | 1.46 ± 0.02 |
| 30 mM | -10.61 ± 0.02 | 12.29 ± 0.05 | 13.69 ± 0.05 | 8.03 ± 0.12 | 7.08 ± 0.10 | 1.47 ± 0.02 |
| 35 mM | -10.60 ± 0.02 | 12.25 ± 0.06 | 13.65 ± 0.05 | 8.02 ± 0.10 | 7.05 ± 0.09 | 1.48 ± 0.02 |
| 40 mM | -10.59 ± 0.02 | 12.34 ± 0.05 | 13.74 ± 0.05 | 7.99 ± 0.10 | 7.03 ± 0.08 | 1.51 ± 0.02 |

room temperature)¹¹ ratio and the BET parameter $c = \exp(\Delta\epsilon_{\text{ads}}/RT)$ relating to the energetics of adsorption $\Delta\epsilon_{\text{ads}}$ in relation to the product of the gas constant R and temperature T , *i.e.*, the thermal energy. Here we assume $RT = 24$ meV (0.562 kcal mol⁻¹, at 10 °C). $\Delta\epsilon_{\text{ads}} = E_1 - E_L$ is composed of the heat of adsorption at the interface E_1 and the heat of liquefaction/vaporization E_L , representing the strength of interaction of the adsorbing species with the interface and with itself, respectively. Int_{I5p} and Int_{sat} is the observed and the maximal expected intensity of the I^- 5p peaks, respectively. In our context, the ‘adsorption’ (interface enrichment) happens at the liquid–vacuum interface and is driven by the increase in bulk concentration. Even though we primarily concern ourselves with the I^- peak intensity here, as the Na^+ peaks are severely perturbed or not observable at the photon energy implemented here, an analogous behavior is expected for the cation. Na^+ is pulled towards the interface by the attraction of the anion, *i.e.*, both anion and cation intensities increase in unison²² and the anion peak intensity in our analysis is representative of the behavior of both species. A fit of the concentration-dependent iodide-5p-to-water- $1b_1$ peak-area ratio data shown in Fig. 2A to eqn (1) yields an excellent match to the data, with a value of $c \sim 4.2 \pm 0.6$ being extracted, corresponding to $\Delta\epsilon_{\text{ads}} = 0.8 \pm 0.08$ kcal mol⁻¹. This value is comparable to, *e.g.*, adsorption of cold (90 K) nitrogen on various surfaces such as silica gel,²⁷ and hints at a moderate-to-low, unfavorable buildup of ion density at the interface. A more detailed analysis of this behavior is beyond the scope of this work, however. More importantly for the following discussion, we argue that the observed surface enrichment does not lead to a significant change to liquid water’s nascent surface dipole and/or a buildup of an appreciable surface dipole perpendicular to the surface, *i.e.*, the additional solute charges are largely compensated in the perpendicular direction. In particular, we emphasize that an interface enrichment is necessarily followed by ion depletion in the subsurface region so as to maintain thermodynamic equilibrium, and the net effect is still a lower ion concentration in the overall interfacial region.²⁵ Thus, any differential segregation, implying the formation of an electric double layer (separating the anions and cations by approximately 3 Å), is counter-balanced by the subsurface, and the net effect is that the majority of photoelectrons (born in deeper layers) only experience a minor deceleration field. This

will be detailed below when we discuss the analogous, but very different, results from $\text{TBAI}_{(\text{aq})}$.

Fig. 2B presents the quantitative evolution of $\text{VIE}_{1b_1, \text{NaI}}$ (blue open circles; left axis). At the lowest salt concentration $\text{VIE}_{1b_1, \text{NaI}} = \text{VIE}_{1b_1, \text{water}} = 11.33$ eV,¹ with this value increasing to 11.6 eV at the highest concentrations. The associated error bars are small, and are included in the figure; the highly precise values presented here are a result of using consistent, high-resolution settings throughout the whole measurement series. The VIE increases analogous to the trend of interfacial ion concentration, *i.e.*, the I^- peak signal, with an essentially linear increase until approximately 4 M concentration, followed by a somewhat steeper rise towards higher concentrations. This trend, and the 1:1 correspondence to the I^- peak-signal increase, is confirmed when comparing the BET curve from panel A with the change in $\text{VIE}_{1b_1, \text{NaI}}$ in panel B; we reproduced this curve in blue which was scaled/offset as a visual guide. Again, an excellent match is observed. One may speculate that at higher bulk concentration, *i.e.*, where the interfacial ion concentration rises rapidly, a major solution structure-change occurs, which would seem plausible since the associated water-to-ion ratio is approximately 7:1. With a reported water hydration-shell number of 8 for I^- ,^{29,30} and 4.5–6.0 for Na^+ ,²⁹ this 4 M concentration coincides with an increasing probability of solvent-shared hydration configurations. Indeed, theoretical calculations reveal an increasing number of solvent-shared ion pairs and contact-ion pairs – see, *e.g.*, ref. 8 and 31 – and noticeably the total fraction of ion-pair structures increases significantly when passing from 3 M to 8 M solution.⁸ At 3 M concentration, for instance, the coordination numbers of the ions around water are 0.450 for an iodide anion and 0.329 for a sodium cation. Also, the water structure is slightly altered in the 3 M solution,^{8,31} assuming less tetrahedral character compared to bulk water. More dramatic effects occur for the 8 M solution, judged from the distance of the closest water molecules, quantified by the O–O radial distribution functions. The observed +260 meV energy shift (Fig. 2B) can be compared with the +200 meV calculated shift in Fig. 9 of ref. 8. To be more specific, the calculations find a <100 meV energetic shift relative to $\text{VIE}_{1b_1, \text{water}}$ when going from zero to 3 M concentration, and the effect increases to ~ 200 meV, corresponding to $\text{VIE}_{1b_1, \text{NaI}} = 11.53$ eV, when going to 8 M. Arguably, this



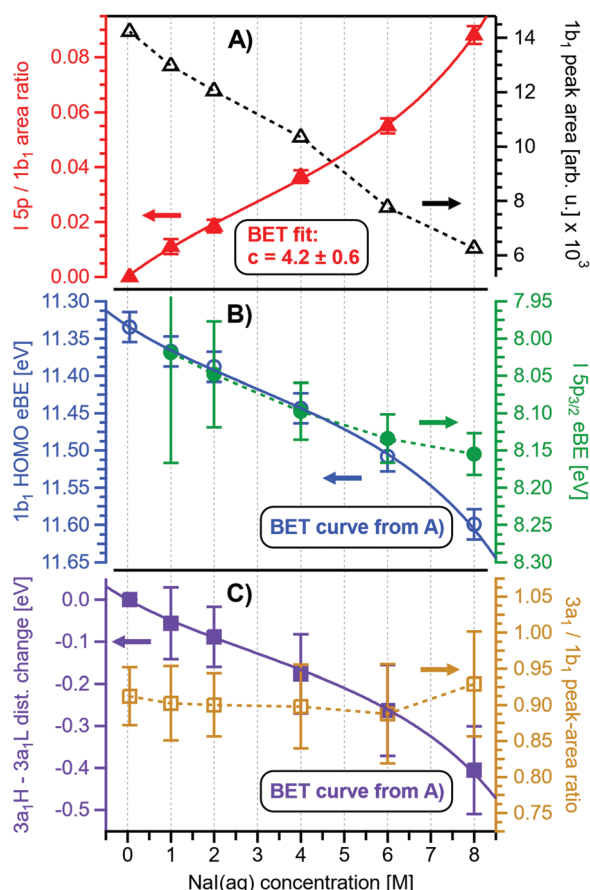


Fig. 2 Results for NaI(aq) solutions extracted from fits to the spectra plotted as a function of salt concentration (bottom axis). (A) Solute I^- 5p peak area normalized by the $1b_{1(0)}$ peak area in red (full triangles; left axis) and absolute $1b_{1(0)}$ peak area in black (open triangles; right axis). The I^- 5p peak successively increases in relative intensity while the liquid-water features (represented by the $1b_1$ intensity) diminish due to reduced relative concentration and enhanced scattering in the surface layer. No saturation behavior is observed for the NaI solute, and instead the trend rather steepens at concentrations above 4 M. A BET (Brunauer, Emmett, and Teller) isotherm was fitted to the data (red line), which yields an excellent agreement with the experimental results (see text for details). (B) Electron binding energy (eBE) of water's $1b_{1(0)}$ peak in blue (open circles; left axis) and the I^- 5p peak in green (full circles; right axis). Both features shift slightly towards higher eBEs by the same amount but deviate somewhat towards very high concentrations. The $1b_{1(0)}$ peak eBE follows the surface enrichment of I^- 5p 1:1, which is apparent from the excellent match to the BET curve (reproduced here as blue curve by shifting and scaling the red fit curve from panel A). In case of the saturation-like behavior of the I^- 5p peak, it can be assumed that the large surface enrichment above 4 M concentration significantly diminishes the solvation of I^- , which partly compensates the increase in eBE. (C) Change in energetic splitting of the $3a_1$ double peak in purple (full squares; left axis) and $3a_1/1b_1$ peak-area ratio in orange (open squares; right axis). The overall peak splitting decreases rapidly with increasing concentration while the peak-area ratio stays constant, *i.e.*, the $3a_1$ feature only seems to increase in relative height because of the diminishing peak distance. Again, the BET curve was reproduced in purple for comparison. The observed narrowing of the $3a_1$ -peak split is in excellent agreement with the values of ref. 8.

observation appears to coincide with the steeper energetic changes (Fig. 2B). We thus find that the observed energy shift is almost fully explained by electronic structure changes, and, considering the

very small discrepancy to theory (~ 0.07 eV at 8 M), a change in the solution's work function is, if occurring at all, very small. The remaining discrepancy may well be explained by a small solution surface-dipole change at very high concentrations, originating from a charge imbalance perpendicular to the interface and/or reorientation of water molecules driven by the present surface charge. In the former case, the dipole between I^- directly at the surface and Na^+ in the immediate sub-layer leads to a somewhat higher $e\Phi$, which translates to a small additional increase in VIE_{1b_1} at very high concentrations. It is interesting to note that the remaining discrepancy of ~ 70 meV agrees well in absolute value and direction with the change in surface potential of about ~ 40 – 50 mV when going from neat water to highly concentrated NaI(aq) as reported by Nguyen *et al.*³² However, considering the assumptions made and error intervals involved, we are unable to draw any definitive conclusions here. Regarding the overall slight changes of VIE_{1b_1} , we conclude that fixing the $1b_1$ energy, as done in the Pohl work, with the aim of determining solute BE turns out to work rather well in the case of $VIE_{I5p,NaI}$. It does not mean, however, that fixing the $1b_1$ energy is a generally valid approach; $TBAI_{(aq)}$ in fact will be shown to exhibit a very different behavior. The reason for the (unexpected at the time before publishing ref. 8) small $1b_1$ energy change in the case of NaI(aq), despite the transitioning from essentially hydrogen-bonded neat liquid water to crystalline-like liquid phase, has been attributed to an isolation and stabilization of the non-bonding $1b_1$ electron by the charge-dense sodium cation. This is accompanied by the destabilization of the water $1b_2$ electron by the iodide anion, which is not considered in the present study. Pohl *et al.* have also discussed the possible effect of concentration-dependent variations of the dielectric constant on $VIE_{I5p,NaI}$, but establishing such a relationship requires additional experimental studies.

Associated $VIE_{I5p,NaI}$ are plotted in Fig. 2B (green color; shown for I^- 5p_{3/2}). The $VIE_{I5p,NaI}$ energy shift is also linear, of almost the same magnitude as for $VIE_{1b_1,NaI}$, and exhibits a similar small departure from linearity at the same 4 M concentration, but this time the energies increase at a slightly slower rate. We emphasize that any possible change in the solution streaming potential with solute concentration is irrelevant here, the additional potential would simply add to that associated with the bias voltage and equally offset the spectral cutoff and valence ionization features used to calculate the VIEs, see the beginning of Section III.1 and ref. 1 for details. Hence, since there is no obvious experimental reason that could cause the observed opposing trends of the two independently measured quantities, we once more corroborate the occurrence of structure changes that are reflected in the PES spectra of both the water solvent and the iodide anion. It is noted that the $VIE_{I5p,NaI}$ values in the present study (Fig. 2B) are somewhat larger than found in ref. 8, which simply arises from the fact that $VIE_{1b_1,NaI} \neq VIE_{1b_1,water}$. A quantitative understanding of the $VIE_{I5p,NaI}$ shifts must await theoretical calculations and, at this point, we conclude with a previous statement that the shifts might be caused by the electrolyte-induced hydrogen-bonding network disruption and associated changes in charge donation by the polarizable I^- anions to the water

anti-bonding, $\sigma^*(\text{O-H})$, orbitals as the electrolyte concentration is increased.⁹

Aforementioned solute-induced effects on the water $3a_1$ peak shape will be only briefly addressed here because the findings are exactly the same as reported in ref. 8. Furthermore, the analysis largely concerns the quantification of the energetic split of the two $3a_1$ components, and absolute energetics provides marginal new information on this particular aspect. Nevertheless, it is useful to present the data here for a direct comparison of the analogous measurements from $\text{TBAI}_{(\text{aq})}$ where the hydrogen-bonding network and its changes would be expected to play a minor role. For that, we recall the origin of the water $3a_1$ flat-top spectral profile (see also Fig. S3C, ESI[†]), which is typical for neat liquid water, and what causes its narrowing and the observation of a broad peak maximum when the NaI concentration is increased. This can be readily seen in Fig. 1B. The flat-top shape in the case of neat water results from the contribution of two $3a_1$ orbitals, each of which can be represented by a Gaussian of the same width and height, at BEs of 13.09 ± 0.05 eV and 14.53 ± 0.05 eV for neat water, primarily associated with intermolecular bonding and anti-bonding interactions between water molecules. The lower-BE-energy peak is referred to as the $3a_1$ L band and the other contribution as the $3a_1$ H band. The (nearly) neat water $3a_1$ peak splitting reduces by 450 ± 90 meV for the highest NaI concentration, as can be seen in Fig. 2C, with the decreasing energy splitting causing the observed change of peak shape, in excellent agreement with ref. 8. Fig. 2C suggests a linear decrease of the peak splitting and, as in Fig. 2B, there might be an indication of

departure from linear behavior near a concentration of 4 M. Such $3a_1$ H- $3a_1$ L energy narrowing, upon addition of salt, has been attributed to weakened $3a_1$ - $3a_1$ intermolecular electronic interactions, modulated through the replacement of water units by ions.⁸

Related to the decrease of the quantitative water-water hydrogen-bonding interactions for sufficiently high NaI concentrations already addressed above, we present another spectral analysis, based on two experimental observables, which descriptively map the evolution from the water gas-phase spectrum into the 8 M NaI solution spectrum. We start with the well-studied gas-phase water spectrum, shown in Fig. 3 (grey-dotted curve), here presented on the KE scale, as measured in the experiment. Note that such a spectrum can be readily measured from the water gas-phase molecules near the liquid jet, where their density is largest. For that, the liquid jet is slightly moved downwards so that the VUV light barely intersects with the liquid. Vibrational resolution, as achieved here, is however only possible if the liquid jet surface is not charged which corresponds to electron detection under field-free conditions; this has been discussed in great detail in ref. 1. The respective neat water liquid-phase spectrum, black-dashed curve, has been simulated by convolution of the gas-phase spectrum with a Gaussian of FWHM = 1.45 eV, in accordance with the liquid $1b_1$ peak width reported in ref. 4, and shifted by 1.02 eV to higher electron KEs (lower eBEs), which corresponds to the gas-liquid shift of 1.28 eV (12.62 – 11.34 eV)¹ for neat liquid water, and corrected by the 0.26 eV shift after adding 8 M NaI. Furthermore, a simple Shirley-type background³³ has been added to include the effect

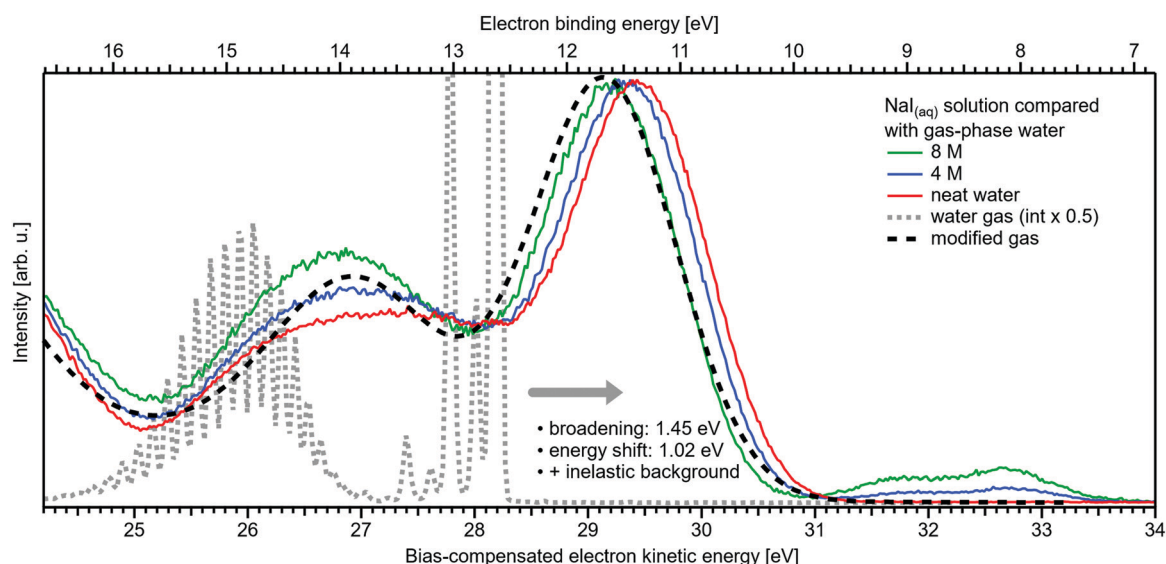


Fig. 3 Selected spectra from Fig. 1B for neat water (red), and concentrations of 4 M (blue) as well as 8 M (green) of $\text{NaI}_{(\text{aq})}$ in comparison with water gas-phase spectra. A high-resolution gas-phase spectrum is plotted as gray dotted line. Some modifications are applied to this spectrum to yield the spectrum plotted as black dashed line: the gas-phase spectrum was convoluted with a Gaussian of FWHM = 1.45 eV, in accordance with the liquid $1b_1$ peak width reported in ref. 4, and shifted by 1.02 eV to higher electron KEs (lower BEs), which corresponds to the gas-liquid shift of 1.28 eV (12.62 – 11.34 eV)¹ for neat liquid water corrected by the 0.26 eV shift after adding 8 M NaI. This modification simulates the unspecific configuration interaction and polarization screening inside the liquid environment. Furthermore, a simple Shirley-type background has been added to include the effect of inelastic scattering for better comparability. The measured 8 M $\text{NaI}_{(\text{aq})}$ spectrum (green trace) and the transformed gas-phase spectrum show excellent agreement. Note that any hydrogen-specific effects are absent in the latter, which hints at strongly reduced hydrogen bonding in the 8 M solution.



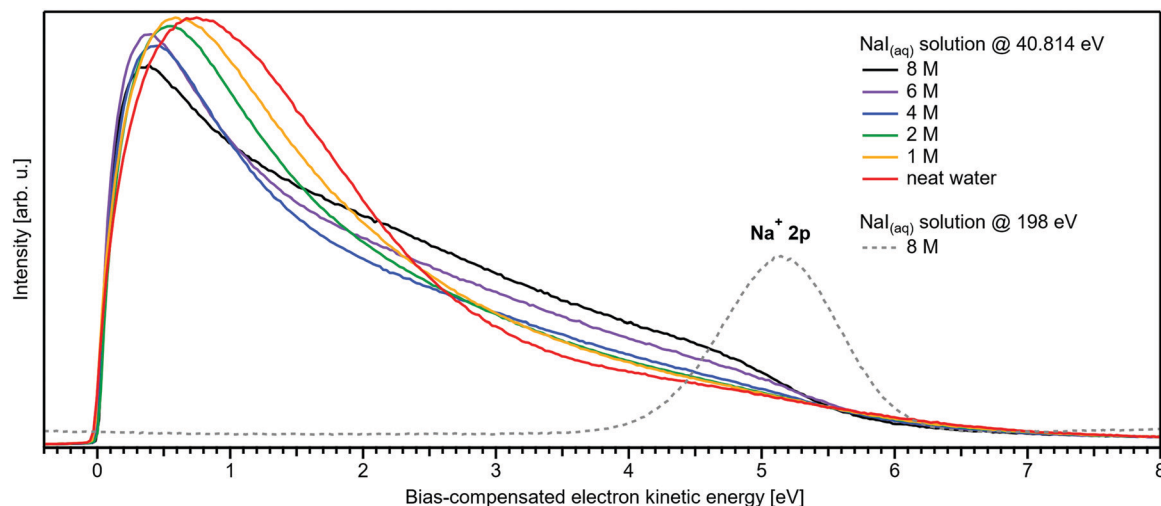


Fig. 4 Wide-range measurement of the LET for different concentrations of NaI aqueous solution; spectra were normalized to the same scaling factor as in Fig. 1B, *i.e.*, to yield the same height for the $1b_{1(1)}$ peak feature (not visible here). A pronounced shape change is observed with increasing salt concentration, especially in the 1–5 eV region. Comparison with data of 8 M NaI_(aq) measured at 198 eV (from our previous study)⁸ reveals the origin of this signal: the intense Na⁺ 2p solute feature would appear at ~ 5.1 eV for the implemented photon energy of 40.814 eV. However, this is already below the critical energy limit of ~ 10 –13 eV to observe undisturbed peak features in liquid water, as recently reported in ref. 2, and electrons at lower electron KE are subject to strong inelastic scattering, which heavily distorts and diminishes the Na⁺ peak observed here.

of inelastic scattering for better comparability. Our simple modification of the water gas-phase spectrum solely accounts for the unspecific structural inhomogeneity, *i.e.*, peak broadening due to the statistical distribution associated with different configurations, and polarization screening inside the liquid environment, associated with an empirical change of the dielectric function when going from water to highly concentrated NaI. The result is found to be in an excellent agreement with the 8 M NaI_(aq) spectrum. Having fully neglected any hydrogen-bonding-specific effects in our simple modeling approach, Fig. 3 directly shows that water hydrogen bonding in the 8 M solution is absent or at least vastly reduced. Furthermore, our data provide the necessary energetic information against which theoretical modeling of concentration-dependent dielectric functions can be gauged, as was also alluded to in ref. 8. Another noteworthy implication of our comparison in Fig. 3 is that the same peak widths, which are characteristic of inhomogeneous structural broadening in neat liquid water, can be used to model the 8 M solution spectrum. It seems that the energetic distribution in the fluxional hydrogen-bonding network is balanced by inter-ionic interactions in the more viscous environment.

We conclude the section on NaI solutions by inspecting the LET shape over a wider range, up to 8 eV above E_{cut} ; see Fig. 4. At low salt concentrations, this distribution exhibits a rather broad, approximately 2 eV wide, structureless peak with a maximum near ~ 0.8 eV from E_{cut} . This is the typical shape observed for neat liquid water.² Upon increasing the concentration, this peak narrows and its maximum shifts closer to E_{cut} , and this is accompanied by an edge evolving near 5 eV KE; it seems that the two effects are quantitatively balanced. This spectral evolution is, however, unrelated to the electronic structure aspects that we are interested in, but is of interest for a different reason: it relates to a comment earlier in this

paper on the ability to extract accurate binding energies if the respective photoelectron peak is at a KE less than 10 eV. Then, strong quasi-elastic scattering leads to a build-up of a broad signal background at the position of the associated photoelectron peak.² Qualitatively, this is exactly what we observe in Fig. 4, however, with the new aspect that electron scattering is now probed in highly concentrated aqueous solutions, where the probability of electron scattering with atomic ions is large, and dominating at the very large concentrations. Theoretical modeling of LET shapes, containing information on the active scattering mechanisms and their probability, from both neat liquid water and aqueous solutions is an ongoing challenge.² The specific photoelectron peak that occurs near the origin of the photoemission spectrum is associated with the Na⁺ 2p_(aq) ionization channel, with ~ 35 eV BE.^{8,22} This poses an intriguing example of the strongly enhanced quasi-elastic scattering in the < 10 –13 eV region, in addition to the cases presented in ref. 2. The Na⁺ 2p is a particularly strong signal, easily dominating the spectrum at high concentrations,²² which enables us to directly observe the deterioration in shape of a mostly (initially) Gaussian-shaped PE feature, in addition to the inevitable reduction in signal intensity. So far, the

‡ Note that alternative explanations for a plateau feature of the intensity observed in the LET curve region shown in Fig. 4 – such as electron-impact-induced electronic transitions to the charge-transfer-to-solvent (CTTS) bands in the I⁻_(aq) anion⁵⁵ – can be readily excluded as primary origins of these features. As shown in Fig. 4 and 8 and further discussed below, the ~ 3 eV plateau features are absent from the neat water spectra and the most concentrated TBAl_(aq) solution spectra, which correspond to surface iodide concentrations locally equivalent to 3 M bulk iodide concentrations. Consequently, the plateau feature in Fig. 4 can be directly related to the Na⁺_(aq) cation. We further note that there is no evidence for a 5–7 eV electron KE loss channel associated with the dominant, directly emitted water 1b₁ photoelectron peak.



presented examples in ref. 2 had a rather small intensity to begin with, which made a close inspection of the peak shapes after suffering strong quasi-elastic scattering difficult. In Fig. 4, one can clearly observe that the initial peak with a FWHM ≈ 1.23 eV is smeared out to a broad plateau spanning more than 4 eV. It can be expected that all PE features will be distorted in a similar way, reinforcing our conclusion in ref. 2 that PE features in liquid water and aqueous solutions cannot be reasonably extracted below an electron KE of 10–13 eV.

III.2 Near- E_{cut} and valence PES spectra from TBAI aqueous solutions as a function of concentration

Fig. 5A and B present LETs and associated valence PES spectra from a microjet of a TBAI aqueous solution for several concentrations, 0 to 40 mM. Experimental conditions were the same as stated above when presenting analogous results from NaI_(aq); we also applied the same bias voltage of -25 V and display the same spectral ranges. LETs (Fig. 5A) are again presented as normalized to yield the same cutoff slope and aligned to $E_{\text{cut}} = 0$ eV. The zero position of the energy scale, E_{cut} , then determines the KE position of the individual valence spectra (Fig. 5B). Qualitatively, the spectra are rather similar to the ones from NaI_(aq) (Fig. 1B), exhibiting the water $3a_1$ and $1b_1$, and the iodide $5p$ photoelectron features. A major difference, most directly reflecting the hydrophobic interactions between water molecules and the TBA⁺ alkyl chains, is the much larger water-to-iodide signal-intensity ratio for a given concentration, corresponding to an effective segregation factor of approximately 70.³⁴ An even larger factor of 300 has been reported in an ionization threshold study by Watanabe *et al.*,³⁵ which, however, is most likely an artefact of the employed measurement and analysis method. We find that the $\text{VIE}_{\text{I}5p}$ is much lower for

TBAI_(aq) than that for NaI_(aq), which will give a proportionally larger photoelectron yield for TBAI_(aq) in the 7.0–7.8 eV photon-energy range used by Watanabe *et al.* The shift in threshold energy with increasing TBAI concentration was observed in their study, but apparently not correlated to an increased ionization probability for this species, which may well have led to an overestimation of the segregation factor.

The most important differences between the TBAI_(aq) and NaI_(aq) solution energetics are (i) the considerably larger spectral energy shifts of the former, which are in fact rigid shifts of the spectrum as a whole, that trend in the opposite direction to the concentration-dependent shifts observed for NaI_(aq), towards larger KEs/lower VIEs, and (ii) the absence of a pronounced change of the $3a_1$ peak shape. Our observations are quantified in Fig. 6, based on the peak-fitting analysis described above. Before detailing the energetics, we consider the evolution of the iodide signal intensity in Fig. 6A (red symbols), which reveals adsorption characteristics of a strong surfactant. Unlike in the case of NaI_(aq) (Fig. 2A), the iodide signal intensity rises rather linearly up to approximately 20 mM TBAI concentration, and then turns over into another seemingly linearly growing regime with reduced growth rate. We will invoke a Langmuir isotherm adsorption model to describe the data below. The results of Fig. 6A are in full agreement with earlier reports.^{5,34} The initial near-linear iodide signal increase is attributed to the regime of sub-monolayer coverage, with the single segregation monolayer being completed near ~ 20 mM concentration. Subsequent shallower signal evolution arguably corresponds to the filling of remaining cavities within the surface layer, and likely some slight increase of bulk-ion concentration.³⁴ Qualitatively, this behavior is further reflected in the accompanying water-signal attenuation shown in Fig. 6A (black symbols), which is also in

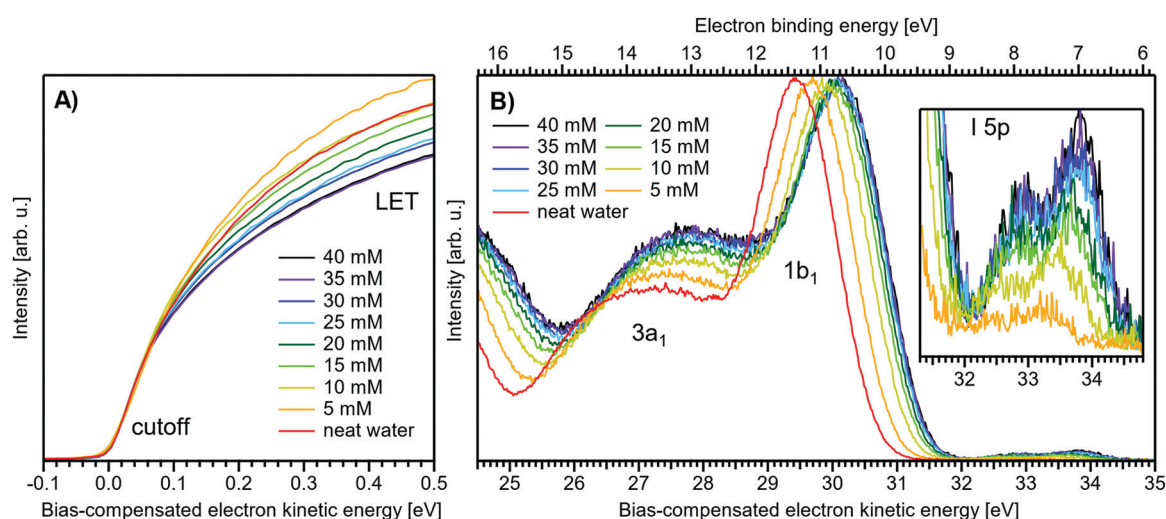


Fig. 5 Series of TBAI aqueous-solution spectra spanning neat water (with 50 mM NaI added only for the purpose of maintaining conductivity) to 40 mM surface-active salt concentrations in 5 mM steps. The energy scale of all spectra has been shifted to yield $E_{\text{cut}} = 0$ eV after applying the tangent method, *i.e.*, the bottom energy scale shows the kinetic energy of the electrons just after leaving the liquid surface. (A) Low-energy tail (LET) spectra with the characteristic cutoff; spectra have been normalized to the same tangent slope. An overview of changes in the wide-range LET-shape is shown in Fig. 7. (B) Valence region with the prominent water $3a_1$ and $1b_1$ bands; spectra have been normalized to the same height of the $1b_1$ peak for visualizing the $1b_1$ peak shifts and $3a_1$ peak-shape changes with increasing concentration. The saturation behavior where the spectra converge to a final form is apparent. The inset shows an enlarged view on the I $5p$ lowest ionization feature of the solute. Fig. S2 of the ESI† shows the as-measured spectra.



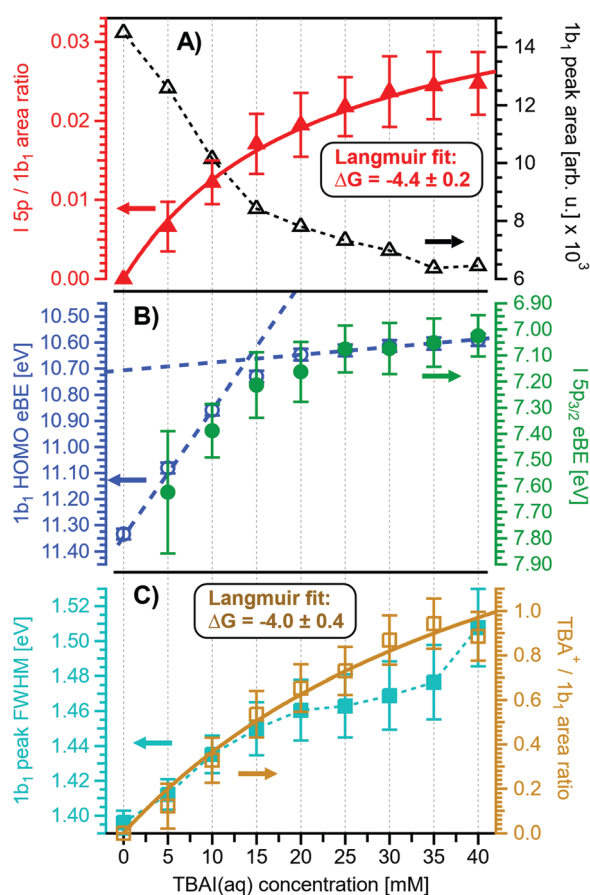


Fig. 6 Results for TBAI_(aq) solutions extracted from fits to the spectra plotted as a function of salt concentration (bottom axis), similar to Fig. 2. (A) Solute I[−] 5p peak area normalized by the 1b₁ peak area in red (full triangles; left axis) and absolute 1b₁ peak area in black (open triangles; right axis). The I[−] 5p peak successively increases in relative intensity, while the liquid-water features (represented by the 1b₁ intensity) diminish due to enhanced scattering in the surface layer. Saturation behavior is observed for both signals above 20 mM. The I[−] 5p peak-area data has been fitted to a Langmuir adsorption isotherm (red line; see text for detail). (B) Electron binding energy (eBE) of water's 1b_{1(l)} peak in blue (open circles; left axis) and the I[−] 5p peak in green (full circles; right axis). Both features shift rapidly towards lower eBEs by the same amount. A steep decrease is observed at lower concentrations, coinciding with the filling of the first monolayer, and then increases only slowly afterwards (blue dashed lines added as a guide to the eye). (C) Change in 1b₁ peak width in cyan (full squares; left axis) and the TBA⁺/1b₁ peak-area ratio in orange (open squares; right axis). Here, the TBA⁺ signal is taken from the difference spectra between neat water and various concentrations of TBAI_(aq), the difference spectra are plotted in Fig. 7. The normalized TBA⁺ feature increases in intensity similar to the I[−] 5p peak, this data has been fitted to a Langmuir curve as well (orange line). It is inferred that all water PE features get broader with increasing solute concentration, which is exemplified by the increasing 1b₁ peak FWHM. The width increase of all features in the spectrum may originate from altered scattering behavior on the surface layer of the solution or an increase in the hydration configurations sample as the interfacial concentration is increased. The evolution in shape of the valence spectra is shown in Fig. S4 of the ESI.†

excellent agreement with the early studies^{5,34} and results from the successive replacement of interfacial water molecules by solute ions.

An arguably more accurate description can be garnered in terms of a Langmuir adsorption isotherm model, which allows the surface-adsorption behavior of the solute ions to be analyzed and the extraction of the Gibbs free energy of adsorption, ΔG_{ads} . Here we used the Langmuir adsorption model adapted to aqueous electrolyte solutions, which has previously been successfully applied to surface-active species in solution:^{36–39}

$$\begin{aligned} \text{Int}_{\text{I}5\text{p}} &= \text{Int}_{\text{sat}} \frac{K c_{\text{TBAI}}}{K c_{\text{TBAI}} + c_{\text{W}}} \\ &\approx \text{Int}_{\text{sat}} \frac{c_{\text{TBAI}}}{c_{\text{TBAI}} + 55.5 \text{ M} \exp(\Delta G_{\text{ads}}/RT)} \end{aligned} \quad (2)$$

Here, K is the equilibrium constant for surface adsorption, c_{TBAI} and c_{W} are the bulk solute and water concentration, respectively, and $RT = 24 \text{ meV}$ ($0.562 \text{ kcal mol}^{-1}$, at 10°C) is again the product of the gas constant and temperature. Indeed, a good fit to the data is obtained with eqn (2), shown as a solid red line in Fig. 6A, with the fit parameter $\Delta G_{\text{ads}} = -0.19 \pm 0.01 \text{ eV}$ per molecule ($-4.4 \pm 0.2 \text{ kcal mol}^{-1}$). Note that the surface-adsorbing species is TBA⁺ in this case, with I[−] in the sub-layer drawn to the surface by the TBA⁺ cations. The valence TBA⁺ signal arises at BEs greater 10.5 eV, as will be further discussed below. A Langmuir fit to this TBA⁺ signal (Fig. 6C) yields a similar $\Delta G_{\text{ads}} = -0.17 \pm 0.02 \text{ eV}$ per molecule ($-4.0 \pm 0.4 \text{ kcal mol}^{-1}$), which shows the expected simultaneous surface enrichment of both ion species; the larger error reflects the fact that the TBA⁺ signal was extracted from difference spectra with greater associated uncertainties in relative scale. Both values are in good agreement with previous reports on TBAI_(aq).⁴⁰ Notably, the value for TBAI_(aq) is smaller than the ΔG_{ads} of $-0.26 \pm 0.01 \text{ eV}$ per molecule ($-6.1 \pm 0.2 \text{ kcal mol}^{-1}$) and $-0.27 \pm 0.01 \text{ eV}$ per molecule ($-6.3 \pm 0.2 \text{ kcal mol}^{-1}$) observed for similar bulk concentrations of NaI_(aq) and KI_(aq), respectively (0–70 mM, as compared to our TBAI range of 0–40 mM), which was extracted from measurements of the I[−] charge-transfer-to-solvent (CTTS) transition *via* UV light from second-harmonic generation.³⁹ In the case of these simple, relatively low-concentration salts, the iodide ion is instead preferentially pushed to the surface, which leads to significant initial surface enrichment.

We next discuss the quantitative evolution of $\text{VIE}_{1\text{b}_1, \text{TBAI}}$, $\text{VIE}_{3\text{a}_1, \text{TBAI}}$, and $\text{VIE}_{\text{I}5\text{p}, \text{TBAI}}$, summarized in Fig. 6B and Table 2. It is seen that $\text{VIE}_{1\text{b}_1, \text{TBAI}} = \text{VIE}_{1\text{b}_1, \text{water}} = 11.33 \text{ eV}$ at zero TBAI concentration, with $\text{VIE}_{1\text{b}_1, \text{TBAI}}$ decreasing to 10.60 eV at the highest concentration, 40 mM, which is a much larger energy shift and in the opposite direction than that of the NaI_(aq) solute data shown in Fig. 1B. Furthermore, changes in $\text{VIE}_{1\text{b}_1, \text{TBAI}}$ approach saturation with high concentration, as opposed to the $\text{VIE}_{1\text{b}_1, \text{NaI}}$ data trend. In fact, the data indicate two different regimes, one below 20 mM and the other above that concentration, seemingly correlating with the adsorption curve of Fig. 6A, as will be detailed below. Analysis of $\text{VIE}_{3\text{a}_1, \text{TBAI}}$ and $\text{VIE}_{\text{I}5\text{p}, \text{TBAI}}$ changes reveal the same energy shifts (within the error bars), presented in Fig. 6B and Table 2, implying that the spectra rigidly shift as a whole, with no indication of differential behavior. These findings disagree with the earlier

conclusion³⁴ that the water (as well as iodide) BEs do not change upon addition of salt but are qualitatively consistent with the interpretation in ref. 5. This discrepancy is connected to the problems with the gas-phase energy referencing used at the time, which insufficiently characterized surface charging, and a flawed measurement of E_{cut} (where a bias voltage was used here to energetically separate E_{cut} from the analyzer cutoff, unlike in ref. 5). In this context, we mention another PES study from 0.04 m (molal) TBAI_(aq) microjets, reporting the VIE of the $\Gamma^- 5p$ from 0.04 m TBAI_(aq) solution using gas-phase energy referencing.⁴¹ The authors found somewhat higher values of $\text{VIE}_{\Gamma^- 5p_{3/2}} = 7.6$ eV and $\text{VIE}_{\Gamma^- 5p_{1/2}} = 8.4$ eV (no confidence interval was given) as compared to our results of 7.03 ± 0.08 eV and 8.0 ± 0.1 eV, respectively. The likely reason is a systematic error due to unknown and uncompensated extrinsic potentials from surface charging or the streaming potential as explained above and in ref. 1.

Regarding possible effects on the water $3a_1$ peak shape, no narrowing of the $3a_1$ L– $3a_1$ H energy splitting is observed as opposed to NaI_(aq). This may either imply that the electronic structure of the interfacial water molecules does not change (which is unlikely), or the effect is not detected over the probing depth of the experiment. Although the eIMFP is expected to be rather small (see the Experimental section), the largest fraction of the detected water signal apparently still comes from molecules with undisturbed electronic structure. What further complicates the analysis of the $3a_1$ peak shape (see Fig. 6C) is that this peak overlaps with a valence peak from TBA⁺ (see Fig. 7), which is the reason for the observed overall signal intensity increase in the water $3a_1$ spectral region.³⁴ This prohibits accurate isolation of a potential small $3a_1$ peak narrowing. Hence, with the available experimental information, it remains unresolved whether TBAI has an effect on the water $3a_1$ orbital. The TBA⁺ signal underlying

the $3a_1$ peak is not considered in our fit, and we opted to constrain the $3a_1$ peak split to 1.4 eV (the value for neat water) in all fits to the TBAI_(aq) spectra and instead report the peak width of the $1b_1$ peak as a function of concentration in Fig. 6C (full squares; left axis), assuming this to be exemplary for the overall broadening observed for all water features in the PE spectrum (also compare to Fig. S4 in the ESI[†]). We still attempted to isolate the TBA⁺ signal contribution by taking the difference of the spectrum for each TBAI concentration with the spectrum of neat water. The resulting difference spectra are shown in Fig. 7, and the $1b_1$ -to-TBA⁺ peak-area ratio is shown in Fig. 6C as well (open squares, right axis). The TBA⁺ signal has a rather large contribution to the valence spectrum (almost the same area as the $1b_1$ peak at a concentration of 35 mM) and increases in a similar way to the $\Gamma^- 5p$ signal (compare Fig. 6A and C).

Before discussing the origin of the observed changes in VIE in detail, we briefly comment on the overall LET shape, for which wide-spectral-range measurements are shown in Fig. 8. In contrast to the NaI_(aq) results, no pronounced changes in LET shape are observed, with no solute PE features being expected in this energy region for the TBAI_(aq) solution, which is apparent when comparing spectra measured at higher photon energies (see, e.g., Fig. 1 in ref. 34). Upon close inspection, we find only a slight LET signal increase around an electron KE of ~ 1 –4 eV. We speculate that this increase correlates with the scattered electron signal contribution from TBA⁺ at a (bias-compensated) electron KE of ~ 25 –30 eV (Fig. 7), where the most probable inelastic electron scattering occurs towards 20–25 eV lower electron KEs in water,^{42,43} i.e., into the 0–5 eV region of the spectrum.

What then is the reason for the large negative BE shifts, and what causes their apparent correlation with TBAI surface coverage? As we have seen, in the case of NaI_(aq) the relatively small

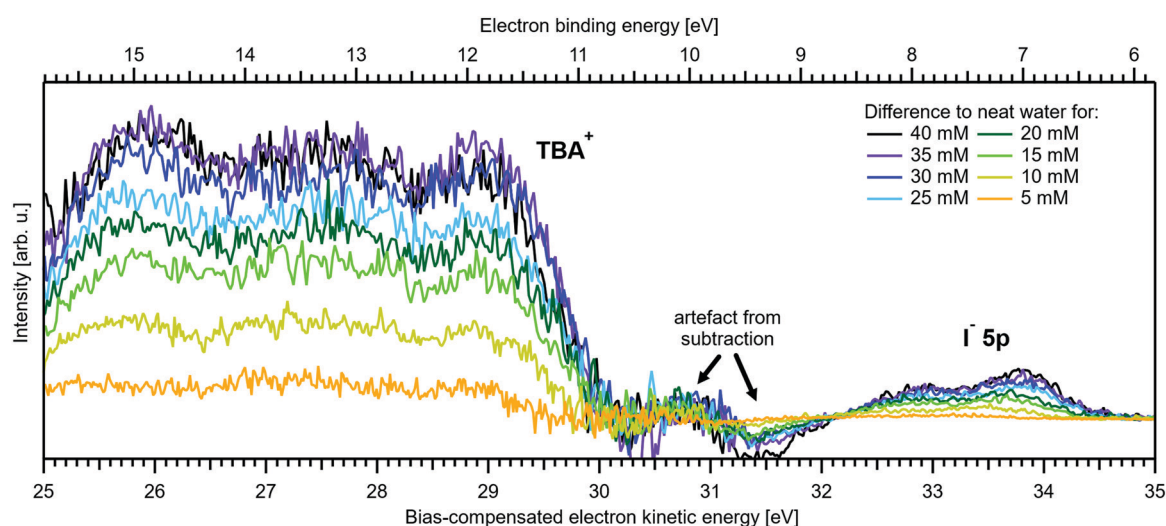


Fig. 7 Difference between the neat water spectrum and spectra for various concentrations of TBAI_(aq) after normalization to the same $1b_1$ peak height, i.e., it is assumed that solute contributions below the $1b_1$ peak are zero. The reference spectrum (not shown, see red curve in Fig. 5B and Fig. S4, ESI[†]) has also been successively Gaussian-broadened before calculating the difference to account for the broadening effect observed with higher TBAI concentration (compare to the $1b_1$ FWHM in Table 2). The signal contribution at an eKE of 25–30 eV is assigned to TBA⁺ and increases in intensity similarly to the $\Gamma^- 5p$ signal at 32–35 eV (see Fig. 6C).



changes of ΔE likely primarily arise from electronic structure changes of the bulk solution, while interfacial molecular dipoles play a smaller role. Our earlier discussion of the $\text{NaI}_{(\text{aq})}$ case highlighted charge neutrality preservation at the solution interface and the ion-density increase at the surface being (over-)compensated by a depleted sub-surface region, which results in an overall lower ion concentration in the interfacial region (see Section III.1). In effect, photoelectron KEs are only minimally affected when traversing such an interface region. However, for surface-active $\text{TBAI}_{(\text{aq})}$, the situation is very different. The high concentration of interfacial solute molecular dipoles will lead to work-function changes which are revealed as rigid spectral shifts, provided there is a considerable net dipole component perpendicular to the solution surface. Yet, the previous, aforementioned study by Watanabe *et al.*,³⁵ which determined concentration-dependent threshold ionization energies of I^- 5p from $\text{TBAI}_{(\text{aq})}$, solely attributed the observed energy shifts, of almost the same magnitude and sign as shown in Fig. 6B, to hydration changes and the decrease of iodide hydration number. Specifically, the authors found a rather complex multi-step variation of the threshold energy which was suggested to reflect the concentration-dependent stepwise dehydration of iodide (and stabilization by TBA^+) from a hydration number of six to four, three, and then two. Work-function effects were not considered, but are suggested here. We argue that they make the major contributions to the observed BE changes, as we explain in the next paragraphs. Note that concentration-dependent electronic structure changes of interfacial water, $\text{VIE}_{1\text{b}_1, \text{TBAI}}$ and $\text{VIE}_{3\text{a}_1, \text{TBAI}}$, have not been quantitatively discussed as of yet; respective computations are not available.

An experimental indication of significant $e\Phi$ effects is revealed from the inferred invariance of the water 3a_1 peak shape (point (ii) above) as well as a slight overall broadening of all spectral features, exemplarily shown for the 1b_1 peak width in Fig. 6C, as discussed above. With the aforementioned expected experimental probing depth and reduced fraction of

interfacial water, with relatively small concentration, essentially remaining undetected on the large signal background from undisturbed bulk water, the large observed spectral shifts are deemed highly unlikely to arise from interfacial electronic structure changes. Indeed, recent 25 mM $\text{TBAI}_{(\text{aq})}$ solution LJ-PES measurements have extracted a $e\Phi_{\text{TBAI}, 25 \text{ mM}}$ value of 4.25 ± 0.09 eV and demonstrated a solute-induced $e\Phi$ reduction of 0.48 ± 0.13 eV with respect to nearly neat water.¹ We thus discuss how $e\Phi$ changes would play out, regarding both the magnitude of the energy shifts and their sign. Qualitatively, a decrease of $e\Phi$ by a negative surface dipole, φ_{dipole} , is associated with a dipole layer with negative charge pointing into the solution and positive charge residing at the top surface. This corresponds to the commonly assumed structure of the TBA^+I^- segregation layer.^{44,45} An emitted electron is hence accelerated within this interfacial dipole field, acquiring a larger kinetic energy, consistent with the experiment (Fig. 6B). The effect scales with concentration, with the observed initial near-linear decrease of both $\text{VIE}_{1\text{b}_1, \text{TBAI}}$ and $\text{VIE}_{1.5\text{p}, \text{TBAI}}$ and increase of the respective KE suggesting that the dipole orientation varies insignificantly until the monolayer is completed. A slightly smaller energy shift of $\text{VIE}_{1.5\text{p}, \text{TBAI}}$ is, however, barely quantifiable given the experimental error but would indeed be expected since the TBA^+ , with its associated iodide counter ion, resides at the very top of the surface and should, hence, be less affected by an interfacial dipole layer. Smaller energy changes that occur at yet higher concentrations, corresponding to denser packing of the solute monolayer, can be associated with increasing dipole-dipole interactions. One might expect considerable variation of the relative position of iodide and TBA^+ , as well as cation re-orientation, in an increasingly sterically hindered dense monolayer packing, but this is not supported by the experiment. With a maximum TBA^+ surface coverage of approximately $n = 1.3 \times 10^{14} \text{ cm}^{-2}$ (arguably corresponding to the completed monolayer near 20 mM concentration),⁴⁴ and $\Delta\varphi_{\text{dipole}, \text{TBAI}} = 0.7$ eV (from Fig. 6B), we can estimate an effective dipole moment of TBAI ,

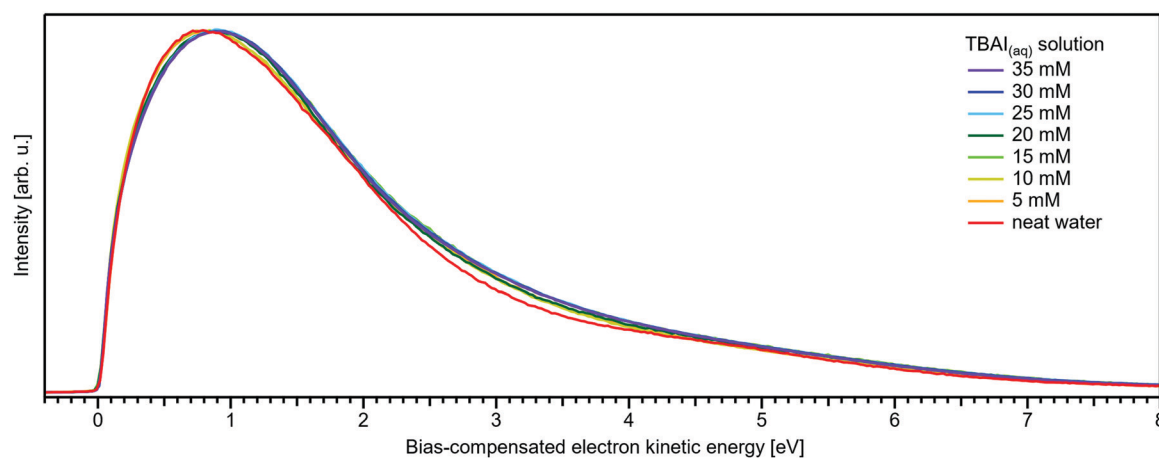


Fig. 8 Wide-range measurement of the LET for different concentrations of $\text{TBAI}_{(\text{aq})}$ normalized to the same maximum height. Only slight changes in LET shape are observed for $\text{TBAI}_{(\text{aq})}$. Most notable is a slight signal rise near ~ 3 eV KE which can be crudely attributed to the corresponding inelastic scattering maximum of the TBA^+ features. This feature increases in intensity in a similar way to the primary TBAI^+ photoelectron peaks and is found at approximately ~ 24 eV higher KE, where 20–25 eV energy loss corresponds to the maximum in the inelastic scattering probability for water.^{42,43}



using the Helmholtz equation $\Delta\phi_{\text{dipole}} = \frac{enm}{\epsilon_r\epsilon_0}$,⁴⁶ where e is the elementary charge, m is the dipole moment, ϵ_0 and ϵ_r are the vacuum and relative permittivity, respectively. This value can then be compared with the actual dipole moment of TBAI ($m = 13$ D, see ref. 47) to infer the average orientation of the dipole moment relative to the solution surface. With the values assumed here, and using $\epsilon_r = 1$ for the liquid–vacuum interface, we get $m = 1.43$ D, which is an order of magnitude lower than the actual dipole moment. The result strongly hints at a molecular arrangement largely in-plane of the solution surface with only a small component in the perpendicular direction, and the charge may be partially screened by the interaction with water. Such a behavior was also observed in MD simulations of 16 TBAI ion pairs in a water slab, where the orientation profiles for the butyl chains spiked at two angles, both of which are primarily in the interfacial plane.³⁴ It was further found that the water-induced and TBA⁺-induced dipoles pointed in opposite directions, resulting in partial compensation. This is to be expected, as it is unlikely that the fluctuating solution interface would support an ordered, perpendicular arrangement of the TBA⁺I[−] dipole, and the system rather is driven towards charge neutrality as far as possible.

A more assertive, although elusive approach to directly measure the concentration-dependence of the eΦs would be to experimentally determine the changes of E_{cut} , as often practiced in solid-state PE spectroscopy, *e.g.*, when assessing eΦ changes of overlayers atop metallic substrates.⁴⁸ This would require the simultaneous measurement of the system Fermi energy and the solution spectra, including the LETs under biased conditions, which is, however, elusive for the following reasons.¹ Water, a large-band-gap semiconductor,^{49–51} does not exhibit a measurable Fermi edge itself (the electron density at the Fermi level/electrochemical potential is zero). Thus, the Fermi edge spectrum of an external (metallic) reference electrode in equilibrated electrical contact with the solution has to be measured separately. The problem lies in relating this external reference spectrum to the spectrum of the solution. This would require correct assessment of the different bias voltages actually applied to the reference electrode and the liquid (the liquid has additional internal resistances) and of the additional extrinsic potentials such as the streaming potential from the solution. An alternative would be to acquire these spectra from a grounded arrangement and under conditions which suppress any extrinsic fields originating from the liquid jet. But without the application of a bias voltage to the solution, E_{cut} cannot be distinguished from the overlapping $E_{\text{cut,HEA}}$ of the electron analyzer. In conclusion, there is currently no feasible method to unequivocally determine eΦ changes from aqueous solutions of arbitrary concentration; a detailed discussion is found in our recent report.¹ The exact origin of the observed energy shifts (change of $\text{VIE}_{1b, \text{TBAI}}$) thus remains unresolved, and arguably cannot be answered with the currently available experimental tools. To complicate things further, rigid spectral shifts are very common for semiconductors, arising from a local imbalance of charge near the surface which leads to

the build-up of a local field.^{48,52–54} Specifically, in the present case, dissolution of salt in water produces hydrated anions and cations which can be viewed as ionized dopants freely moving in the aqueous solution. Charge transfer to the surface leads to a band bending (BB) within a space-charge layer of typically several tens of nm thickness depending on the doping level, manifesting in a rigid spectral energy shift. In the present case, BB is argued to be induced in response to TBAI surface aggregation, which changes the charge distribution at the liquid–vacuum interfacial layer. Arguably, we observe an upward BB, *i.e.*, in the direction of lower VIEs, which is caused by depletion of the solvent's electron density near the surface. The hydrophobic TBA⁺ molecules which reside near the solution's surface are thought to draw I[−] ions into this surface region.³⁴ It can then be argued that the solvation of I[−] reduces water's local electronic density, leading to the observed effect. Notably, the Fermi level remains fixed, or is pinned, within the solution at its bulk value, and aligned with the analyzer; for more details we refer to ref. 1. Notably, there would be a rather straightforward experimental test – at least conceptually – to confirm BB. Specifically, illuminating the liquid jet with photons of energy higher than the band gap would generate electron–hole pairs which separate in the electric field of the space-charge layer. This would partially compensate the band bending and induce a surface photovoltage (SPV). In a two-color pump–probe PES experiment one would thus generate a transient flat band, corresponding to the magnitude of the SPV. Currently, one of our labs is being equipped with a VUV source that would in principle allow such an experiment to be performed.

IV. Conclusions

We have reported a first PES study that quantifies the absolute energetics of aqueous solution ionization as a function of solute concentration. Specifically, lowest vertical ionization energies, VIE, of the water solvent and iodide solute, exemplified for NaI and the surface-active tetrabutylammonium iodide (TBAI) salts, were measured from a liquid microjet using a 40.814 eV photon energy. Our study is a consequent extension of our most recent work that introduced an advanced liquid-jet PES method,¹ based on the measurement of the spectral low-energy cutoff, enabling the determination of absolute ionization energies of solute and solvent. The novelty is that with this more powerful method, previous unsatisfactory gas-phase energy referencing is no longer required. Furthermore, the advanced method enables access to explicit surface and interfacial properties of liquid water and aqueous solutions. For NaI aqueous solution the measured concentration-dependent lowest-ionization energies vary only slightly, up to +260 meV towards larger binding energies in going from dilute to near-saturated solutions. This is largely attributed to associated changes of the bulk-solution electronic structure. The results can be explained with existing theoretical simulations. TBAI, a strong surfactant, exhibits an overall very different behavior, however. Here, VIEs vary to a much greater degree, up to 0.7 eV towards lower binding energies, upon



formation of a complete TBAI surface aggregation layer. Such large changes cannot be attributed solely to a change of solute and water electronic structure within the surface monolayer. We provide evidence, supported by a simple estimate of molecular surface-dipole density and orientation and our previous work,¹ that work-function changes play a crucial role. However, we cannot yet rule out contributions of band bending to the observed shifts. To our knowledge, the latter aspect has not been considered in any previous study, other than our own,¹ and shows the importance of exploring such effects both experimentally and theoretically in the future. In a broader context, the present work demonstrates an example of a systematic study quantifying solute- and concentration-dependent absolute electronic energetic changes in aqueous solutions. Application of the new method to other solutions, aqueous or otherwise, is correspondingly straight-forward.

Data availability

The data of relevance to this study have been deposited at the following DOI: 10.5281/zenodo.5283376.

Conflicts of interest

There are no conflicts to declare.

Acknowledgements

B. C. acknowledges funding by the SNF (project 200021E-171721) and the EPFL-MPG doctoral school. B. C., S. M., U. H., and B. W. acknowledge support by the Deutsche Forschungsgemeinschaft (Wi 1327/5-1). F. T. and B. W. acknowledge support by the Max-Water initiative of the Max-Planck-Gesellschaft. B. W. acknowledges funding from the European Research Council (ERC) under the European Union's Horizon 2020 research and investigation programme (grant agreement no. 883759). S. T. acknowledges support from the JSPS KAKENHI Grant No. JP20K15229.

Notes and references

- S. Thürmer, S. Malerz, F. Trinter, U. Hergenahhn, C. Lee, D. M. Neumark, G. Meijer, B. Winter and I. Wilkinson, *Chem. Sci.*, 2021, **12**, 10558–10582.
- S. Malerz, F. Trinter, U. Hergenahhn, A. Ghrist, H. Ali, C. Nicolas, C.-M. Saak, C. Richter, S. Hartweg, L. Nahon, C. Lee, C. Goy, D. M. Neumark, G. Meijer, I. Wilkinson, B. Winter and S. Thürmer, *Phys. Chem. Chem. Phys.*, 2021, **23**, 8246–8260.
- M. Faubel, B. Steiner and J. P. Toennies, *J. Chem. Phys.*, 1997, **106**, 9013–9031.
- B. Winter, R. Weber, W. Widdra, M. Dittmar, M. Faubel and I. V. Hertel, *J. Phys. Chem. A*, 2004, **108**, 2625–2632.
- R. Weber, Doctoral thesis, Freie Universität, Berlin, 2003.
- H. Tissot, J.-J. Gallet, F. Bournel, G. Olivieri, M. G. Silly, F. Sirotti, A. Boucly and F. Rochet, *Top. Catal.*, 2016, **59**, 605–620.
- G. Olivieri, A. Goel, A. Kleibert, D. Cvetko and M. A. Brown, *Phys. Chem. Chem. Phys.*, 2016, **18**, 29506–29515.
- M. N. Pohl, E. Muchová, R. Seidel, H. Ali, S. Sršeň, I. Wilkinson, B. Winter and P. Slavíček, *Chem. Sci.*, 2019, **10**, 848–865.
- I. Waluyo, D. Nordlund, U. Bergmann, D. Schlesinger, L. G. M. Pettersson and A. Nilsson, *J. Chem. Phys.*, 2014, **140**, 244506.
- L. Pérez Ramírez, A. Boucly, F. Saudrais, F. Bourmel, J.-J. Gallet, E. Maisonhaute, A. R. Milosavljević, C. Nicolas and F. Rochet, *Phys. Chem. Chem. Phys.*, 2021, **23**, 16224–16233.
- A. Seidell, *Solubilities of inorganic and organic compounds: A compilation of quantitative solubility data from the periodical literature*, D. Van Nostrand Company, 1919.
- R. Seidel, B. Winter and S. E. Bradforth, *Annu. Rev. Phys. Chem.*, 2016, **67**, 283–305.
- R. Moberg, F. Boekman, O. Bohman and H. O. G. Siegbahn, *J. Am. Chem. Soc.*, 2002, **113**, 3663–3667.
- S. Thürmer, R. Seidel, M. Faubel, W. Eberhardt, J. C. Hemminger, S. E. Bradforth and B. Winter, *Phys. Rev. Lett.*, 2013, **111**, 173005.
- H. T. Nguyen-Truong, *J. Phys.: Condens. Matter*, 2018, **30**, 155101.
- Y.-I. Suzuki, K. Nishizawa, N. Kurahashi and T. Suzuki, *Phys. Rev. E: Stat., Nonlinear, Soft Matter Phys.*, 2014, **90**, 010302(R).
- N. Ottosson, M. Faubel, S. E. Bradforth, P. Jungwirth and B. Winter, *J. Electron Spectrosc. Relat. Phenom.*, 2010, **177**, 60–70.
- G. Olivieri, K. M. Parry, C. J. Powell, D. J. Tobias and M. A. Brown, *J. Chem. Phys.*, 2016, **144**, 154704.
- P. Jungwirth and D. J. Tobias, *J. Phys. Chem. B*, 2002, **106**, 6361–6373.
- S. Malerz, H. Haak, F. Trinter, A. Stephansen, C. Kolbeck, M. Pohl, U. Hergenahhn, G. Meijer and B. Winter, 2021, arXiv:2109.14365 [physics.chem-ph], arXiv Preprint.
- B. A. Hands, *Vacuum*, 1987, **37**, 621–627.
- R. Weber, B. Winter, P. Schmidt, W. Widdra, I. Hertel, M. Dittmar and M. Faubel, *J. Phys. Chem. B*, 2004, **108**, 4729–4736.
- S. Barth, M. Ončák, V. Ulrich, M. Mucke, T. Lischke, P. Slavíček and U. Hergenahhn, *J. Phys. Chem. A*, 2009, **113**, 13519–13527.
- E. Grushka, *Anal. Chem.*, 1972, **44**, 1733–1738.
- P. Jungwirth and B. Winter, *Annu. Rev. Phys. Chem.*, 2008, **59**, 343–366.
- P. Jungwirth and D. J. Tobias, *J. Phys. Chem. B*, 2001, **105**, 10468–10472.
- S. Brunauer, P. H. Emmett and E. Teller, *J. Am. Chem. Soc.*, 1938, **60**, 309–319.
- R. H. Stokes and R. A. Robinson, *J. Am. Chem. Soc.*, 2002, **70**, 1870–1878.
- Y. Marcus, *Chem. Rev.*, 2009, **109**, 1346–1370.
- H. Ohtaki and T. Radnai, *Chem. Rev.*, 2002, **93**, 1157–1204.
- K. P. Jensen and W. L. Jorgensen, *J. Chem. Theory Comput.*, 2006, **2**, 1499–1509.
- C. V. Nguyen, H. Nakahara, O. Shibata and C. M. Phan, *J. Mol. Liq.*, 2020, **298**, 112076.



- 33 D. A. Shirley, *Phys. Rev. B: Solid State*, 1972, **5**, 4709–4714.
- 34 B. Winter, R. Weber, P. M. Schmidt, I. V. Hertel, M. Faubel, L. Vrbka and P. Jungwirth, *J. Phys. Chem. B*, 2004, **108**, 14558–14564.
- 35 I. Watanabe, N. Takahashi and H. Tanida, *Chem. Phys. Lett.*, 1998, **287**, 714–718.
- 36 A. W. Adamson, *Abstr. Pap. Am. Chem. Soc.*, 2001, **221**, U320–U320.
- 37 S. S. Dukhin, G. Kretzschmar and R. Miller, *Dynamics of adsorption at liquid interfaces: theory, experiment, application*, Elsevier, 1995.
- 38 P. B. Petersen, R. J. Saykally, M. Mucha and P. Jungwirth, *J. Phys. Chem. B*, 2005, **109**, 10915–10921.
- 39 P. B. Petersen and R. J. Saykally, *Annu. Rev. Phys. Chem.*, 2006, **57**, 333–364.
- 40 P. B. Petersen and R. J. Saykally, *J. Phys. Chem. B*, 2006, **110**, 14060–14073.
- 41 H. Bergersen, R. R. T. Marinho, W. Pokapanich, A. Lindblad, O. Björneholm, L. J. Sæthre and G. Öhrwall, *J. Phys.: Condens. Matter*, 2007, **19**, 326101.
- 42 H. Hayashi and N. Hiraoka, *J. Phys. Chem. B*, 2015, **119**, 5609–5623.
- 43 H. Hayashi, N. Watanabe, Y. Udagawa and C.-C. Kao, *J. Chem. Phys.*, 1998, **108**, 823–825.
- 44 S. Holmberg, Z. C. Yuan, R. Moberg and H. Siegbahn, *J. Electron Spectrosc. Relat. Phenom.*, 1988, **47**, 27–38.
- 45 F. Eschen, M. Heyerhoff, H. Morgner and J. Vogt, *J. Phys.: Condens. Matter*, 1995, **7**, 1961.
- 46 K. Christmann, *Introduction to surface physical chemistry*, Springer Science & Business Media, 2013.
- 47 B. Hribar, N. T. Southall, V. Vlasy and K. A. Dill, *J. Am. Chem. Soc.*, 2002, **124**, 12302–12311.
- 48 H. Ishii, K. Sugiyama, E. Ito and K. Seki, *Adv. Mater.*, 1999, **11**, 605–625.
- 49 F. Williams, S. P. Varna and S. Hillenius, *J. Phys. Chem.*, 1976, **64**, 1549.
- 50 A. Bernas, C. Ferradini and J.-P. Jay-Gerin, *Chem. Phys.*, 1997, **222**, 151–160.
- 51 C. G. Elles, A. E. Jailaubekov, R. A. Crowell and S. E. Bradforth, *J. Chem. Phys.*, 2006, **125**, 044515.
- 52 H. Baumgärtel, *Electrochemistry: A Guide for Newcomers*, De Gruyter, 1st edn, 2019.
- 53 D. Cahen and A. Kahn, *Adv. Mater.*, 2003, **15**, 271–277.
- 54 H. Lüth, *Surfaces and Interfaces of Solid Materials*, Springer-Verlag, Berlin Heidelberg, 3rd edn, 2013.
- 55 X. Chen and S. E. Bradforth, *Annu. Rev. Phys. Chem.*, 2008, **59**, 203–231.



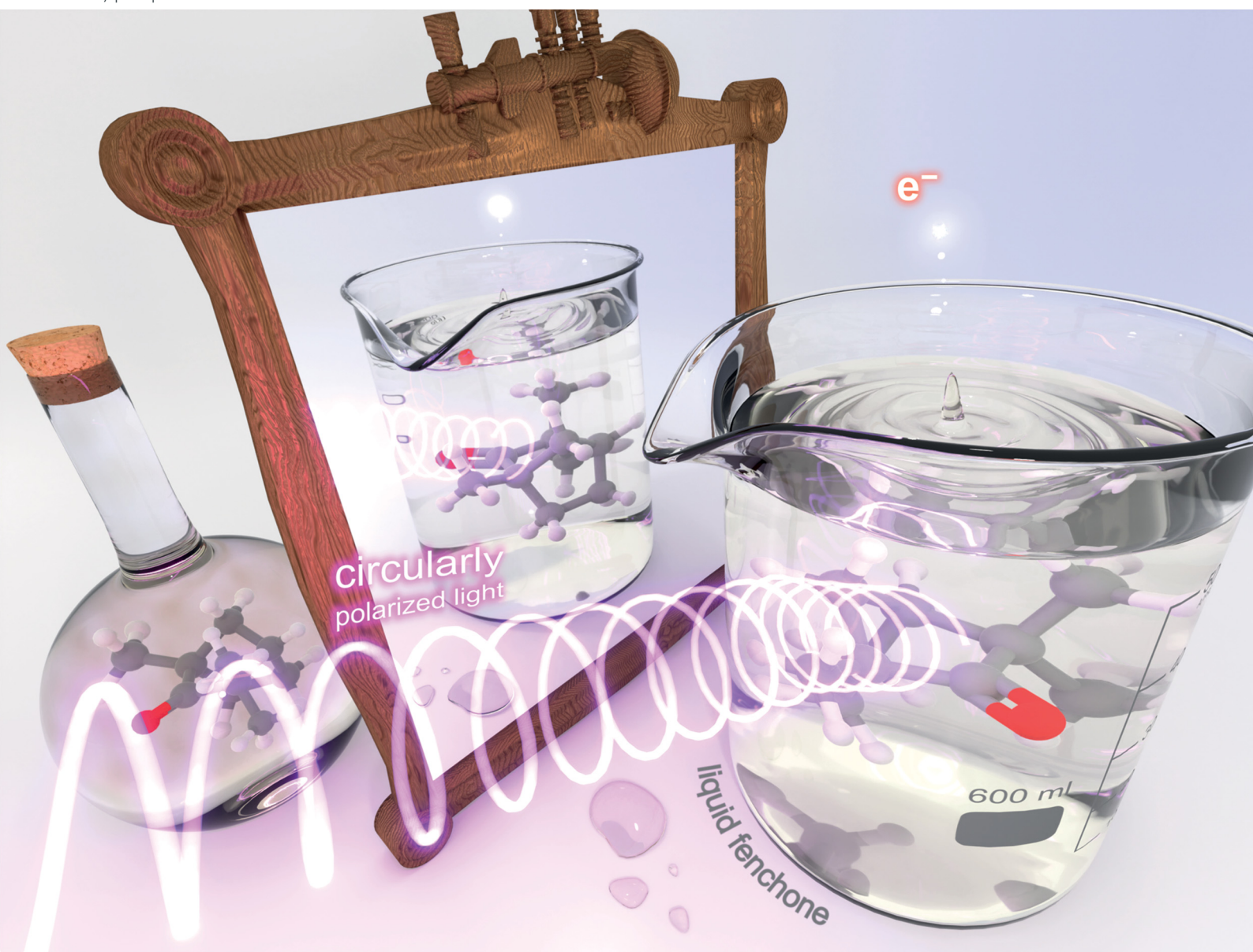
Paper V



PCCP

Physical Chemistry Chemical Physics

rsc.li/pccp




ISSN 1463-9076

PAPER

Uwe Hergenbahn *et al.*
Photoelectron circular dichroism in angle-resolved
photoemission from liquid fenchone


 Cite this: *Phys. Chem. Chem. Phys.*,
2022, **24**, 8081

Photoelectron circular dichroism in angle-resolved photoemission from liquid fenchone†

 Marvin N. Pohl, ^{‡,abc} Sebastian Malerz, ^{‡,a} Florian Trinter, ^{id ad}
Chin Lee, ^{id bc} Claudia Kolbeck, ^{§,a} Iain Wilkinson, ^{id e} Stephan Thürmer, ^{id f}
Daniel M. Neumark, ^{id bc} Laurent Nahon, ^{id g} Ivan Powis, ^{id h} Gerard Meijer, ^{id a}
Bernd Winter ^{id a} and Uwe Hergenhahn ^{id *a}

 Received 16th December 2021,
Accepted 17th February 2022

DOI: 10.1039/d1cp05748k

rsc.li/pccp

We present an experimental X-ray photoelectron circular dichroism (PECD) study of liquid fenchone at the C 1s edge. A novel setup to enable PECD measurements on a liquid microjet [Malerz *et al.*, *Rev. Sci. Instrum.*, 2022, **93**, 015101] was used. For the C 1s line assigned to fenchone's carbonyl carbon, a non-vanishing asymmetry is found in the intensity of photoelectron spectra acquired under a fixed angle in the backward-scattering plane. This experiment paves the way towards an innovative probe of the chirality of organic/biological molecules in aqueous solution.

1 Introduction

Many of the molecules providing the basis of living matter are chiral, that is they may exist in two different 3-D structural forms, which are mirror images of each other. Due to steric effects, these two forms or enantiomers may behave very differently when they interact with other chiral partners. This is chiral recognition, a fundamental metabolic process. Furthermore, the chiral molecular building blocks of terrestrial life, such as amino-acids and sugars, are almost exclusively found as single enantiomers, a fascinating property known as the homochirality of life.¹ As a consequence, it is immensely important to have the means to distinguish between enantiomers at the molecular level, despite them possessing largely

identical physico-chemical properties such as mass, spectra, and energetics (apart from putative tiny electroweak effects²). Therefore, chiral discrimination, or recognition, requires interaction with another chiral entity. A common example is the interaction with circularly polarized light (CPL), which gives rise to the well-known circular dichroism (CD) effect in absorption.^{3,4} Relatedly, chiral (spin-polarized) electrons have also been shown to discriminate for the molecular-level handedness of a sample.^{5,6}

It is of great appeal that elements of these two techniques are combined in yet another effect that discriminates between different enantiomers of a species, namely photoelectron circular dichroism (PECD). This term designates an asymmetry in the angle-resolved photoelectron (PE) flux after ionization of a sample of chiral molecules with circularly polarized light. The effect requires a suitable geometry of the experiment, as it vanishes in the plane perpendicular to the photon propagation direction ('dipole plane'). It can be observed as a difference of photoelectron intensity between two measurements, in which either (1) the same sample is probed by left- *versus* right-handed circularly polarized light, or (2) the same sample is probed by any helicity of the light, and electrons are collected under two different angles, one in the forward and the other in the backward scattering direction, with the two angles being mirror imaged at the dipole plane, or (3) by probing the two different enantiomers of a substance with either helicity, at an angle outside of the dipole plane. Historically, the potential existence of PECD was noted in theoretical papers in the 1970s,^{7,8} but only abstract model systems were considered, and these works received only minor attention at that time. It was over twenty years later that a dedicated numerical simulation on actual molecules by Ivan Powis suggested that this effect could have

^a *Molecular Physics, Fritz-Haber-Institut der Max-Planck-Gesellschaft, Faradayweg 4-6, 14195 Berlin, Germany. E-mail: hergenhahn@fhi-berlin.mpg.de*
^b *Department of Chemistry, University of California, Berkeley, CA 94720, USA*
^c *Chemical Sciences Division, Lawrence Berkeley National Laboratory, Berkeley, CA 94720, USA*
^d *Institut für Kernphysik, Goethe-Universität Frankfurt am Main, Max-von-Laue-Straße 1, 60438 Frankfurt am Main, Germany*
^e *Department of Locally-Sensitive & Time-Resolved Spectroscopy, Helmholtz-Zentrum Berlin für Materialien und Energie, Hahn-Meitner-Platz 1, 14109 Berlin, Germany*
^f *Department of Chemistry, Graduate School of Science, Kyoto University, Kitashirakawa-Oiwakecho, Sakyo-Ku, Kyoto 606-8502, Japan*
^g *Synchrotron SOLEIL, L'Orme des Merisiers, St. Aubin, BP 48, 91192 Gif sur Yvette, France*
^h *School of Chemistry, The University of Nottingham, University Park, Nottingham, UK*

† Electronic supplementary information (ESI) available: Raw data, further details on peak-background separation. See DOI: 10.1039/d1cp05748k

‡ These authors contributed equally to this work.

§ Current address: sonUtec GmbH, Mittlere-Motsch-Straße 26, 96515 Sonneberg, Germany.



an observable magnitude.⁹ In fact, it was simulated to be significantly greater than that of more conventional chiroptical methods, since PECD is already allowed in the pure electric dipole approximation, in contrast to regular CD.¹⁰ Thereafter, the first experimental observations of PECD were reported for valence photoionization,^{11–13} and about two years later, a systematic experimental and theoretical study of PECD in core-level photoionization of gaseous camphor confirmed its existence and several features of its behaviour, including its general manifestation within a few tens of eV of an ionization threshold, where the generated photoelectrons are sensitive to the subtleties of any local chiral potential.¹⁴ Since then, PECD has been studied in the case of one-photon valence and core-level photoionization of gaseous chiral molecules^{15–17} and has been extended to clusters and nanoparticles.^{18–20} Furthermore, its investigation has broadened to include multi-photon^{21–25} and time-dependent^{26,27} ionization processes. Using charged particle coincidence experiments, the underlying molecular-frame photoelectron angular distributions (PADs) were also measured.^{28,29} A profound analysis of the symmetry principles underlying the original PECD mechanism and its variants has appeared recently,³⁰ and the mechanism underlying the build-up of the asymmetric emission in one-photon PECD has been investigated from a fundamental viewpoint.^{31,32}

Here, we present experimental results in the framework of single-photon photoionization processes in a liquid. The primary question we aim to answer is whether PECD can be observed from the photoionization of a liquid composed of chiral constituents. Since the existence of PECD in the gas phase does not require any local molecular ordering, from symmetry principles, this may well be the case. On the other hand, we are not aware of any experiments trying to directly address this question, although a first PECD valence-shell study on pseudo-amorphous nanoparticles of the amino-acid serine revealed a reduced but yet non-vanishing PECD.²⁰ Some of the authors therefore have constructed a new setup dedicated to PECD studies on a liquid microjet, as described elsewhere.³³ Here, we present a complete feasibility study of actual PECD detection using a nearly-neat liquid microjet of fenchone. This work opens up the perspective to use this technique for studying the handedness of chiral molecules in aqueous solution, such as amino acids, their building blocks,³⁴ or sugars.³⁵

Fenchone (C₁₀H₁₆O, 1,3,3-trimethylbicyclo[2.2.1]heptan-2-one) is a chiral bicyclic mono-terpenoid built from a six-membered ring with a single-carbon bridge connecting C1 and C4 and featuring three methyl ligands and a carbonyl (C=O) group adjacent to one of the asymmetrically substituted chiral centres. Its structure is shown in Fig. 1. The (1*R*,4*S*)-(–)-fenchone enantiomer naturally occurs in fennel. Importantly, the C=O carbonyl carbon has a 1s core binding energy shift that allows it to be spectroscopically distinguished from the remaining carbon atoms in a core-level photoelectron spectrum (PES).³³ Moreover, it has been shown to exhibit a sizeable PECD effect in the gas phase.^{33,36} Follow-on studies on this molecule also examined PECD effects in its valence PES,^{37,38} and subsequently targeted multi-photon PECD

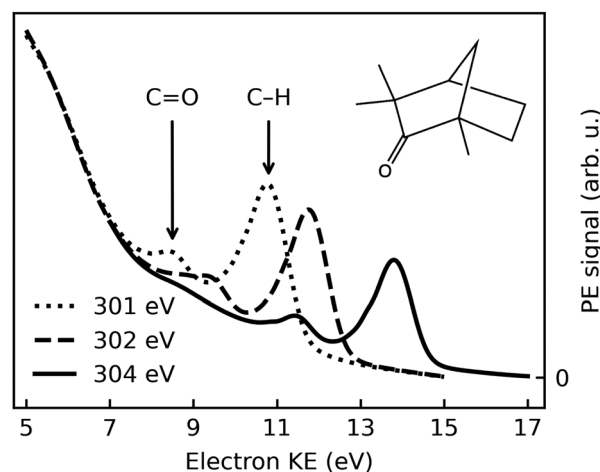


Fig. 1 Electron spectra recorded after photoionization of (1*S*,4*R*)-(+)-fenchone with *l*-CPL at photon energies of 301 eV, 302 eV, and 304 eV; dotted, dashed, and solid lines, respectively. Spectra averaged over a number of sweeps performed at the respective photon energy are shown; no further normalization has been performed. See text for details.

processes^{21,23,39,40} and complex electronic-structure dynamics using ultrafast laser pulses.^{26,41} The choice of fenchone for these prototypical studies has been partially motivated by the relative rigidity of its geometric structure, making conformational isomerism a lesser complication in the interpretation of any associated results, in comparison to those from other similarly-sized chiral systems. In this work, we will address single-photon C 1s core-level PES of fenchone in its native, liquid form, as this presents a clear-cut case for the demonstration of liquid-phase PECD. A small subset of the data from this project was already used for illustrative purposes in an apparatus paper that some of the authors have recently published.³³

2 Experimental

Photoionization experiments on a liquid microjet of fenchone were performed using circularly polarized synchrotron radiation from an undulator, and a hemispherical electron analyzer arranged in the backward-scattering plane. Data were acquired over two measurement campaigns with a setup, *EASI*, described recently.³³ Details of the experimental setup are as follows:

2.1 Synchrotron radiation

The experiments used synchrotron radiation in the soft X-ray range provided by the P04 beamline of the PETRA III storage ring at DESY, Hamburg (Germany). This beamline is equipped with an APPLE-II-type undulator⁴² allowing experiments with high-purity CPL.⁴³ A VLS (variable line spacing) monochromator's planar grating of 400 l mm⁻¹ spacing and 15 nm groove depth (campaign 1) or 1200 l mm⁻¹ spacing and 9 nm groove depth (campaign 2) was used with typical exit-slit settings of 100–120 μm, yielding an energy resolution of approximately 90 meV (400 l mm⁻¹) or 30 meV (1200 l mm⁻¹) at photon energies slightly above the carbon K-edge. The minimum spot



size of the beamline (using smaller exit-slit openings than 30 μm) has been measured as $10 \times 10 \mu\text{m}^2$ ($h \times v$) in the nominal focus position of the optics.^{44,45} For our experiment, due to spatial constraints, the interaction region had to be placed approximately 220 mm downstream of that position; the vertical focus however was shifted accordingly using a pair of Kirkpatrick–Baez mirrors.⁴³ We correspondingly estimate the beam spot size at the point of interaction to be $180 \times 35 \mu\text{m}^2$ ($h \times v$).

The photon-energy scale of the monochromator was calibrated by a standard procedure that optimizes the pitch angle for specular reflection. We estimate the residual error after this procedure as ± 0.2 eV in the photon-energy range used in this work.

Circularly polarized radiation of either helicity was produced by shifting the magnet blocks of the APPLE-II undulator accordingly. In a separate experiment, the polarization of the ensuing radiation has been analyzed by measuring the PADs of various gases in the plane perpendicular to the light propagation direction.^{46,47} Measurements were performed for both signs of the undulator geometric shift, corresponding to both output radiation helicities. The shift was varied in small steps in the spectral region of interest, preferentially yielding circularly polarized light. Then the Stokes parameter for circular polarization was calculated as the complement to the Stokes parameters for the residual amount of linear polarization. Experiments were carried out with the 400 l mm^{-1} , 15 nm groove depth grating and yielded absolute values for the circular Stokes parameter, S_3 , larger than 0.98 for photon energies between 550 and 1250 eV, and in an interval of values of the undulator shift about 5 mm wide. The photon energies of interest in this work are somewhat lower, however, namely in the vicinity of the carbon K-edges of fenchone, slightly below 300 eV. In this energy region, some degradation of the purity of circular polarization has been observed in experiments on another APPLE-II undulator beamline, and was attributed to carbon contamination of the optical elements.⁴⁸ In any case, on that occasion $|S_3|$ was still found to be > 0.92 . Despite the lack of direct measurements for our setup, we consider it fair to assume similar or lesser circular polarization degradation here. Correspondingly, no further normalization of the measured PECD magnitude has been applied.

By carrying out a PECD measurement on the fenchone gaseous phase evaporating from the liquid jet, we established a correspondence of the geometric shift with negative sign to left-handed circularly polarized light (*l*-CPL), according to the 'optical' convention.^{33,36,49}

2.2 Liquid microjet

Both enantiomers of fenchone were obtained commercially (Sigma-Aldrich, purity $\geq 98\%$) and were used without further purification. A microjet was produced by pushing the liquid through a glass capillary nozzle with an inner diameter of 28 μm by a commercial HPLC pump (Shimadzu LC-20AD). A flow rate of 0.6–0.8 ml min^{-1} at pressures of 11–14 bar was typically used. The sample was made conductive by addition of

75 mM tetrabutyl-ammonium nitrate salt (TBAN), to prevent charging by the photoionization process.³³ Our liquid-jet holder features a cooling jacket that was stabilized to 10 $^\circ\text{C}$. Since it, however, does not extend up to the nozzle tip, a slightly higher temperature of the injected liquid cannot be ruled out. The liquid stream was directed horizontally, perpendicular to the light propagation axis. After passing the interaction region, the jet was collected on a cold trap cooled by liquid nitrogen, thus maintaining the interaction chamber pressure below 10^{-3} mbar. A bias voltage could be applied to the liquid microjet *via* a gold wire brought in contact with the liquid approximately 550 mm upstream of the expansion nozzle;^{33,50} this wire was connected to the chamber ground potential, unless otherwise stated. Comparison measurements were performed using the same equipment to produce a jet of high-purity liquid water, made conductive by the addition of NaCl to 50 mM concentration.

2.3 Electron detection

Photoelectrons produced from the liquid fenchone jet by circularly polarized synchrotron radiation were collected in a backward-scattering geometry under an angle of 130 $^\circ$ with respect to the light propagation direction, and of 90 $^\circ$ relative to the liquid jet direction.³³ Electrons were detected by a near-ambient-pressure hemispherical electron analyzer (HEA, Scienta-Omicron HiPP-3) with a lens mode adapted to specifically enable the measurement of electrons at low kinetic energies (KEs, below 30 eV). For the same purpose, μ -metal shielding was added to the interaction chamber housing the liquid jet. Electrons passed a first skimmer into the HEA with an opening of 800 μm diameter and set to the ground potential of the setup, and were accelerated immediately thereafter to diminish scattering losses at the elevated background pressure produced by evaporation from the liquid jet. The distance of the liquid jet to this opening was approximately equal to the skimmer aperture diameter. Under these conditions, photoelectrons from a liquid jet can be observed down to very low KEs, though they appear atop of an intense background of low-energy electrons produced by scattering of photoelectrons created inside the bulk liquid.⁵¹ This point will be further discussed in detail below.

The slit restricting the entrance into the hemispheres was set to 800 μm , adapted to the size of the skimmer opening. Electron spectra were measured with a pass energy of 20 eV, and electrons were detected by a stack of two microchannel plates and a fluorescence screen, read out by a CCD camera. The so-called ADC (analog-to-digital conversion) mode of the control software was used, in which the gray-scale camera image is interpreted to yield the underlying electron detection rates.

Spectra were acquired in swept mode. In order to minimize loss of acquisition time by shifting the undulator structure and switching the X-ray beam helicity, spectral sweeps were typically repeated ten to thirty times for each photon helicity, and several pairs of spectra were acquired for both helicities at each photon energy. A set of individual sweeps that were



averaged to produce a spectrum are shown in Fig. S1 of the ESI.† Some amount of sweep-to-sweep variation is seen, concerning both intensities and peak energies. The typical extent and time-scale of intensity fluctuations is further illustrated by Fig. S2 and S3 of the ESI.† While the exact origin of these effects is still under investigation, the occurrence of small variations of the jet position (much smaller than the focus size, that is on a length scale of one–two μm) likely contributes significantly to these observations. Before analysing the intensity difference between *l,r*-CPL, the raw data were checked for sweep-to-sweep variations of intensity or KE, and sweeps identified as clear outliers were removed. Intensities were always determined from sweep-averaged spectra, to make up for the fact that a different amount of sweeps may pass the quality criterion for *l*- vs. *r*-CPL. Between 3–30% of sweeps were dropped. In some cases, small KE drifts over the course of data acquisition (50 meV or less) were numerically corrected. Methods for peak-area determination and peak-to-background separation were an essential part of the data analysis and will be detailed below.

3 Results

3.1 The C 1s photoelectron spectrum of liquid fenchone

Fig. 1 shows typical C 1s photoemission spectra from liquid (1*S*,4*R*)-(+)-fenchone, measured at 301 eV, 302 eV, and 304 eV photon energies with *l*-CPL. Two features due to C 1s photoionization can be readily identified and strongly resemble earlier results for gaseous fenchone.³⁶ The less intense peak at lower KE (higher binding energy) is correlated with ionization of the single carbon from the C=O double-bond carbonyl group, while the larger peak at higher energy arises from the cumulative ionization of the remaining nine carbon atoms at the primary, secondary, and tertiary sites. This leads to rather similar C 1s binding energies, which cannot be spectroscopically separated.

No discernible features can be attributed to gas-phase contributions to the spectrum. This is unusual compared to photoelectron spectra of other substances probed in liquid microjet experiments, most notably water,⁵² but also, *e.g.*, methanol,⁵³ acetic-acid solutions,⁵⁴ and liquid ammonia.⁵⁵ In principle, two explanations are conceivable: The gas-phase contributions are too low in intensity to become apparent, or they overlap—in this case—with the features stemming from the liquid phase. The vapour pressure of fenchone in the temperature range relevant for this experiment is 0.33 mbar at 10 °C, more than a factor of ten lower than that of liquid water.⁵⁶ Typical gas-phase contributions in O 1s spectra of liquid water with the *EASI* setup at beamline P04 amount to 5–20% of the signal in the O 1s liquid core level peak, depending on the conditions. Hence, a small gas-phase contribution to the fenchone spectra can be expected. In our previous work, we deduced an upper limit for the gas-phase contribution of 14%, based on spectra recorded with a small negative bias applied to the jet in order to separate the gas- and liquid-phase features.³³

From the same analysis, we concluded that gas- and liquid-phase C 1s features indeed energetically overlap in the current case. This is a rather non-trivial result, as even in the valence spectrum of liquid fenchone (unpublished data from our own work), or of other non-polar, liquid solvents,^{57,58} ionization energies are typically lower in the liquid in comparison to the gas phase. In a crude manner, the gas-liquid shift was rationalized by considering the Born free energy of solvation of a positive charge (the vacancy created by photoionization) in the bulk liquid, described by its polarizability, ϵ , at optical frequencies.⁵⁹ The quantity ϵ , taken as the square of the refractive index, does not differ qualitatively between fenchone and liquid water.⁶⁰ Therefore, we suggest that the small or vanishing gas-liquid shift for the inner-shell levels of fenchone is coincidental; it may result from a cancellation of various factors, *e.g.*, electronic charge redistribution following ionization *versus* electronic structure changes due to nuclear rearrangement. In this study, we additionally append the previously-determined gas-phase binding energies of 292.6 eV (C=O site) and 290.3 eV (CH site) to the analogous liquid phase peaks.³⁶

In addition to the C 1s main lines, an unstructured background of low-KE electrons can be seen (low KE tail, LET). This phenomenon is well known from photoemission studies on bulk solid samples⁶¹ and has recently been described in detail for a liquid water jet by some of the authors.⁵¹ Briefly, in our study on aqueous solutions, an intense LET was found, atop of which no discernible structures could be resolved in electron spectra below kinetic energies of approximately 10 eV. This is a general result, valid not only for emission out of water's orbitals, but also for features resulting, *e.g.*, from electronic levels of solutes.⁵¹ While its exact nature is not fully understood at this moment, it is attributed to a strong increase of the importance of quasi-elastic, *e.g.*, vibrational scattering channels, particularly at electron kinetic energies for which electron-impact ionization channels are closed. Adding to that is an influence of excitation into neutral resonant states lying above the nominal ionization potential.⁵¹

Strictly speaking, the nature of the LET and the phenomenon of diminishing peak intensities may very well be of a different nature in fenchone, *e.g.*, less or more intense and with a different energetic threshold, since in liquids little is known about the LET dependence on the ionized substance. Fig. 1 suggests that peak features are observable with acceptable spectral distortion down to KEs of 8 eV in liquid fenchone, which is similar or slightly lower compared to water. This result is of great importance for our work, as in gas-phase studies it has been learned that PECD only leads to significant asymmetries in the threshold region, *i.e.*, at photoelectron kinetic energies below 20 eV. Notably, a comparison of the results on low-KE electron emission from liquid water in ref. 51, giving a lower KE bound at which liquid-phase photoemission peaks from aqueous solutions are discernible, with the gas-phase data by Ulrich *et al.*,³⁶ giving an upper KE bound at which PECD is still sizeable, suggests that the energy window shown in Fig. 1 spans a range offering good prospects for the identification of PECD in a liquid.



3.2 Observed dichroism in the angle-resolved spectra

In order to demonstrate the functionality of our *EASI* apparatus, the PECD of gas-phase fenchone, as sampled by lowering the liquid jet out of the synchrotron-radiation focus, was recorded and the literature results of Ulrich *et al.*³⁶ were reproduced with an improved energy resolution and a shorter acquisition time. These tests are described in our recent apparatus description and characterization paper.³³

We now turn to an analysis of the differences in photoemission spectra recorded with different helicities of the ionizing photons. Conceptually, we will distill an intensity asymmetry due to PECD from pairs of spectra recorded in the energy range shown in Fig. 1 by taking the following three steps: (1) peak-to-background separation and background subtraction, (2) calculation of the asymmetry from a pair of spectra at equal KE, and (3) correction of this raw value for any apparatus asymmetry.

As the first step, quantifying the amount of background present underneath the two C 1s peaks turned out to be the most problematic as obviously the C 1s signal is outweighed by the background contribution. Modelling it by an analytic procedure recommended for UPS (ultraviolet photoelectron spectroscopy) data⁶² did not yield a satisfactory representation. We therefore tested several *ad hoc* approaches to background subtraction, and compare them in detail below.

An exemplary background-corrected pair of sweep-averaged spectra of (1*S*,4*R*)-fenchone measured at 301 eV with *l*- and *r*-CPL is shown in Fig. 2, for all three background models used. Before we detail the various background-subtraction methods further, we would like to discuss dichroic properties of these two spectra and our approach to apparatus asymmetry correction.

In panel (A) of Fig. 2, we show a pair of spectra, averaged over two equally long sets of sweeps for each helicity after deletion of outlier traces and correction of (small) energy drifts. A visible apparatus asymmetry due to a small mismatch in photon intensities produced by the undulator in its two opposite settings has been corrected for in the figure as detailed below. The deviation of the intensity ratio from unity by this effect is practically invariant over the narrow photon-energy interval targeted in this paper, and is constant over a measurement campaign. Uncorrected spectra are shown in Fig. S4 of the ESI;† the intensity mismatch can also be seen in the general trend of the per-sweep total intensities in Fig. S2 of the ESI.† In order to correct for this apparatus-induced effect, we have used the helicity-dependent intensity of the C–H peaks in the spectra as an internal light-intensity monitor. This follows a practice from gas-phase studies of PECD in several terpenoids featuring a single C=O double bond, where it was noted that an asymmetry associated with the sum of overlapping hydrocarbon site signals in the more intense C–H peak can reasonably be assumed to cancel out.¹⁴ It was therefore postulated that the asymmetry of the latter peak vanishes exactly, and the C=O asymmetry was correspondingly measured relative to it.¹⁴ While this started out as an *ad hoc* assumption, this tenet was experimentally verified after work on the data-acquisition methodology allowed the measurement of gas-phase PECD free from a baseline error.^{36,48} We have, therefore, determined the

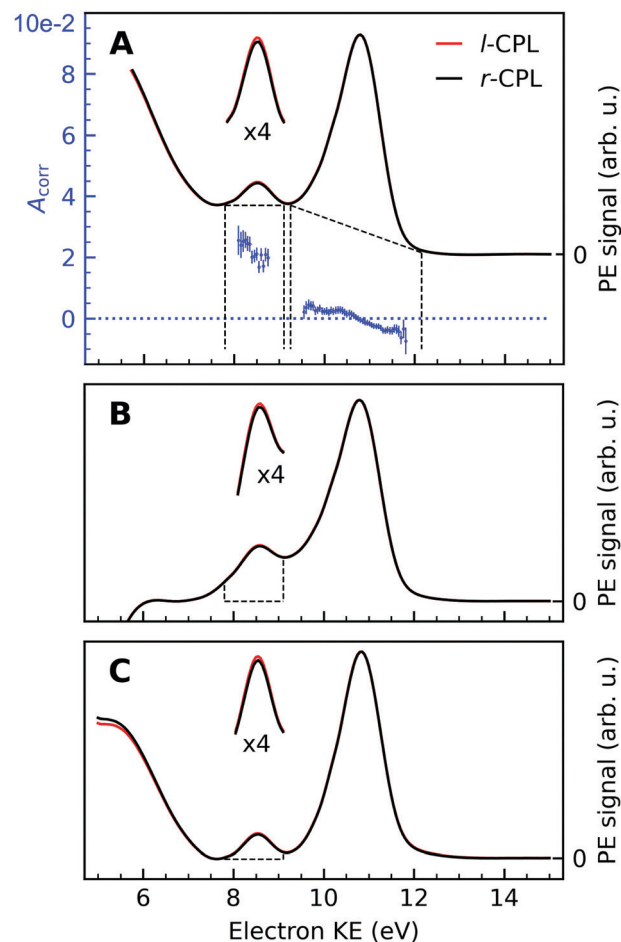


Fig. 2 Background-corrected photoemission spectra of (1*S*,4*R*)-(+)-fenchone measured at 301 eV with *l*- and *r*-CPL. Panels (A) to (C) show the results of various models by which to subtract the background contribution from a pair of spectra; spectra in Fig. 1 were instead displayed as measured for *l*-CPL. Background contributions were calculated by (A) fitting an exponential function to the high kinetic end of the spectrum, and subtracting an additional linear background ('roi'-approach); or (B) by fitting a linear combination of an exponential and a linear function to the high- and low-KE ends of the spectra ('exp'-approach). For (C), an exponential function has been fitted and subtracted from the raw data. Then, the 'total background' function⁶² is applied to the remaining spectrum ('sum'-approach). Blue points in panel (A) indicate the experimental asymmetries, $A_{\text{corr}}(130^\circ)$ (plotted versus the left y-axis) for the peaks originating from C=O and C–H K-edge photoionization, obtained as the difference divided by two times the mean of *r*- and *l*-CPL (eqn (2)), together with associated error bars. The areas marked with dashed lines in panels (B) and (C) indicate the width of the C=O peak, which is used for the asymmetry calculations. Expanded ($\times 4$) views of these peaks are drawn above the full spectra to get a clearer view on the magnitudes of the *l*–*r* asymmetry.

asymmetry of the C–H peak as explained below. For the purpose of illustration, we have used this information to normalize the pair of traces shown in Fig. 2 such that they correspond to the outcome of a measurement that is free from apparatus-induced asymmetry. Here and in the following we use the ratio

$$A = \frac{L - R}{L + R} = \frac{r - 1}{r + 1} \text{ with } r \equiv \frac{L}{R} \quad (1)$$



to calculate the asymmetry, A , from the intensities L and R recorded with l -CPL and r -CPL, respectively. If we include a correction for the apparatus asymmetry, the corrected asymmetry A_{corr} , determined from a measured intensity ratio r' and a correction factor γ is then:

$$A_{\text{corr}} = \frac{r'\gamma - 1}{r'\gamma + 1}, \quad (2)$$

where γ can be determined from the measured asymmetry A'_0 of an isotropically emitted line (intensities L'_0 , R'_0) by:

$$\gamma = \frac{1 - A'_0}{1 + A'_0} = \frac{R'_0}{L'_0}. \quad (3)$$

In that terminology, panel (A) of Fig. 2 shows the traces $L\gamma$ and R . An exponential function fitted only to the part of the spectrum at higher KE than the C–H main line has also been subtracted from the data.

An intensity difference in the traces corrected for apparatus asymmetry, shown in Fig. 2A, can be seen in the region of the C=O C 1s line at a KE of ~ 8.5 eV. In order to exclusively analyse the intensity that can be attributed to C 1s photoemission, we have subtracted a further, linear background, as indicated by the dashed lines. Within the main C 1s peaks, we have then calculated the corrected asymmetry $A_{\text{corr},i}$ for every KE channel i . The resulting values are shown in Fig. 2A, plotted against the left-hand axis in a blue color. The error bars were derived as follows: We arranged all sweeps made with l - and with r -CPL into pairs. Labelling the pairs with the index k , we then calculated the distribution $A_{\text{corr},i}^k$, and give the standard deviation of its mean as an error to the data point $A_{\text{corr},i}$. More details of the data processing steps are provided in ESI† Section 1.3 and Supplementary Fig. S4 and S5 (ESI†).

Trivially, channel-wise asymmetries $A_{\text{corr},i}$ are equal or very near to zero in the range of the major C–H peak (showing the consistency of the baseline correction). Whether the rising trend of the asymmetry data pointing from slightly negative to slightly positive values in going towards smaller KEs is significant cannot be definitively ascertained at this moment. A word of caution is needed about its interpretation, as minute differences in the peak profile as a function of KE may occur *e.g.* due to small pointing differences for the left-handed *versus* right-handed undulator radiation, and can readily produce the apparent trend. On the contrary, asymmetry values for the C=O peak clearly show an asymmetry which is significantly different from zero. Still, with the current data and uncertainty limits, we refrain from (over-)interpreting the trend of the C=O asymmetry data across the low-KE C 1s peak.

3.3 Analysis of the C 1s peak areas

No clear-cut approach to peak-to-background separation is applicable to our spectra (see Fig. 1), to the best of our knowledge. As this point is nevertheless essential, we used different methods in parallel and will compare their results in subsection 3.5. Panels (A)–(C) in Fig. 2 serve to illustrate these methods.

As explained above, an exponential background was subtracted in Fig. 2A. Subsequently, peak areas were determined as integrated counts between the range marked with the vertical dashed lines, minus a linear background as indicated by the approximately horizontal dashed lines. Using the term ‘region of interest’ for these ranges, we term this the ‘roi’ method.

The spectra in Panel (B) were constructed by selectively fitting a linear combination of an exponential and a linear function to the data points containing the LET contribution only, specifically at the low- and high-KE ends of the spectra. After subtraction of the estimated background, the spectra were normalized to the C–H peak maximum. Asymmetries have then been calculated from the integrated PE intensities in a 1.4 eV energy range around the C=O peak, as indicated by the areas enclosed by the dashed lines in Panel (B) of Fig. 2. We use the label ‘exp’ for this method.

The approach adopted to produce Panel (C) follows a similar procedure to that used to produce Panel (B), with the difference that the background was constructed by first fitting an exponential function to the high-KE side of the spectra and then applying the ‘total background’ function⁶² (also known as non-iterative Shirley method⁶³) in order to estimate the LET background. This procedure iterates from the high- to the low-KE end of the spectra while aggregating (‘summing’) spectral intensity and is thus referred to as ‘sum’-approach.

More detail on the various background-signal separation methods is provided in the ESI.†

3.4 Parametrization of the measured results

In order to connect our results to other experiments and to calculations, it is important to resort to parametrized forms of the differential photoionization cross section, which is the quantity measured here. Building on the earlier work of Ritchie,^{7,8} Ivan Powis showed that within the electric-dipole approximation, for chiral molecules the differential photoionization cross-section can be cast in the following form:^{9,10}

$$I^p(\theta) = \frac{\sigma}{4\pi} [1 + b_1^p \cos(\theta) + b_2^p P_2(\theta)]. \quad (4)$$

Here, the intensity has been written as a function of the angle θ measured from the photon propagation vector to the electron emission vector, for the left-handed circular ($p = 1$) or right-handed circular ($p = -1$) pure polarization states. P_2 denotes the second Legendre polynomial. The second-order coefficient b_2 turns out to be independent of the handedness of circular polarization, and can be expressed *via* the more familiar β -parameter as $b_2^{+1} = b_2^{-1} = -\beta/2$. A similar equation can be written for linearly polarized ($p = 0$) light, with the understanding that the angular coordinate in this case refers to the major axis of the polarization ellipse. In the latter case, the first-order coefficients vanish ($b_1^0 = 0$) and the second-order coefficient becomes $b_2^0 = \beta$. Higher-order and magnetic terms in the interaction of the radiation field with the molecule or liquid have been presented,⁸ but based on experimental results, they seem to have been unimportant in earlier gas-phase work.¹⁴ The first-order coefficient b_1 vanishes for non-chiral molecules,



and undergoes a sign change upon changing the chiral handedness of the molecule or swapping the light helicity; it is therefore the chiroptical parameter defining the PECD-induced asymmetry. Correspondingly, we can identify the corrected asymmetry (2) as follows:

$$A_{\text{corr}} = \frac{I^{+1}(\theta) - I^{-1}(\theta)}{I^{+1}(\theta) + I^{-1}(\theta)} = \frac{b_1^{+1} \cos \theta}{1 - (\beta/2)P_2(\cos \theta)}. \quad (5)$$

Here, the symmetry relation $b_1^{+1} = -b_1^{-1}$ has been used.^{7,9} It is interesting that, in the general case, A_{corr} depends on both the chiral parameter b_1 and the conventional angular distribution. In earlier gas-phase PECD experiments based on measurements performed at a single electron collection angle,¹⁴ or a pair of angles mirrored in the dipole plane,⁶⁴ the so-called magic angle-geometry of $\theta = 54.7^\circ$ was used. This geometry was adopted to ensure that the denominator in eqn (5) becomes identical to unity and the dependence on β ceases. Another option is to use imaging techniques collecting electrons over the full 4π sr emission solid angle, directly allowing the cosine dependence of the asymmetry to be extracted.^{12,65}

In our case, a rigorous determination of b_1 from our experiment would require a separate measurement of β , which however was outside the scope of this work. In the following, we will therefore estimate the potential influence of the deviation of our setup from the magic-angle geometry. Similarly, an estimate of the potential influence of non-complete circular polarization is in order. Inserting the limiting values of β (-1 and $+2$) into $[1 - (\beta/2)P_2(\cos \theta)]^{-1}$, we find that this factor may range from 0.94 to 1.14 for our $\theta = 130^\circ$ detection geometry. In the few works on the angular distribution parameter in photoemission from liquids, however, a trend towards small absolute β values has been found at low kinetic energies.⁶⁶ Given the results of that study on the O 1s orbital of water, a $\beta \sim 0.5$ might be a plausible but conservative estimate for our case of C 1s emission, which would lead to a factor of 1.03, resulting from the denominator in eqn (5).

Further, consideration of polarization impurities requires a look at the full angular-distribution function, which can be written as:

$$I(S, \theta, \phi) = \frac{\sigma}{4\pi} \left[1 - S_3 b_1^{+1} \cos \theta - \frac{\beta}{2} \left(P_2(\cos \theta) - \frac{3}{2} (S_1 \cos 2\phi + S_2 \sin 2\phi) \sin^2 \theta \right) \right], \quad (6)$$

with the understanding that the first θ -dependent term is only present for chiral molecules.^{9,67} The polarization state of the radiation is now represented by the three-component Stokes vector S , with S_1 and S_2 representing linear polarization measured with horizontal and vertical, or 45° and 135° polarizers, and S_3 defining the degree and type of circular polarization. The angle ϕ is measured from the horizontal axis in the dipole plane to the electron spectrometer, and amounts to 90° in our experiment. As explained in the Experimental section, polarimetry results in the photon-energy range of interest are not

available for the P04 beamline yet. However, the degree of linear polarization and the direction of the polarization ellipse were measured between 550 and 1250 eV, as a function of the undulator shift.⁴⁷ The complement of the linear polarization degree was attributed to circular polarization, neglecting the presence of an unpolarized fraction of radiation. This is supported by full polarimetry results associated with another APPLE-II undulator beamline.⁶⁸ In all data sets recorded, when the circular component was maximized, a remaining Stokes parameter of linear polarization with magnitude 0.04 or smaller was found, which almost exclusively had S_2 character. As, from eqn (6), S_2 -dependent terms cannot play a role in our geometry, we will neglect the residual linear components entirely, although this is not fully rigorous. Including a finite angular acceptance of our electron analyzer (see ref. 33) in a discussion of eqn (6) leads to corrections that vanish, to first order, and are essentially independent of the enantiomer and helicity of the light. We therefore deem it safe to assume that the impact of such effects is much smaller than the others we have explicitly considered above.

To summarize this discussion, we find that optical polarimetry at the carbon edge, to determine the on-target radiation state, and a photoelectron angular-distribution measurement on liquid fenchone would be desirable for a quantitatively accurate determination of the b_1 -parameter in our experiment. However, for the moment we will retain the simple relation, $b_1^{+1} = A_{\text{corr}}/\cos \theta$, and will make an appropriate adjustment to the error bar with respect to the influence of β and any residual non-circular soft X-ray beam polarization.

3.5 Averaged and corrected results

A compilation of the b_1^{+1} values as obtained from the described analysis procedure is provided in Fig. 3. The results in the figure have a rather large spread between different data sets and different analysis methods. Nevertheless, for most photon energy values, the chiral asymmetry parameter b_1^{+1} is clearly different from zero, with the b_1^{+1} values having an opposite sign for the two different enantiomers. This expected mirroring of the chiroptical data attests that we are indeed measuring, with a reasonable error bar, an enantio-specific observable.

If we scrutinize the data points in Fig. 3, we find that they neither group by analysis method nor by data set. We therefore believe that the scatter between points does not result from a systematic effect leading to preferentially higher or lower asymmetry values as a function of time or associated with peak-background separation method. In order to arrive at consolidated values, we performed a simple average over all data points for the same photon energy and enantiomer. The results are compiled in Table 1. The scatter in our data points, perceived as coming from fluctuations in the signal and background of the spectra rather than from the data treatment, is represented by the standard deviation of the individual data points leading to each table entry. In the table, we also include two potentially important b_1^{+1} corrections, namely one for the presence of gaseous components in the C 1s spectra and another for the potential influence of a non-zero β -parameter,



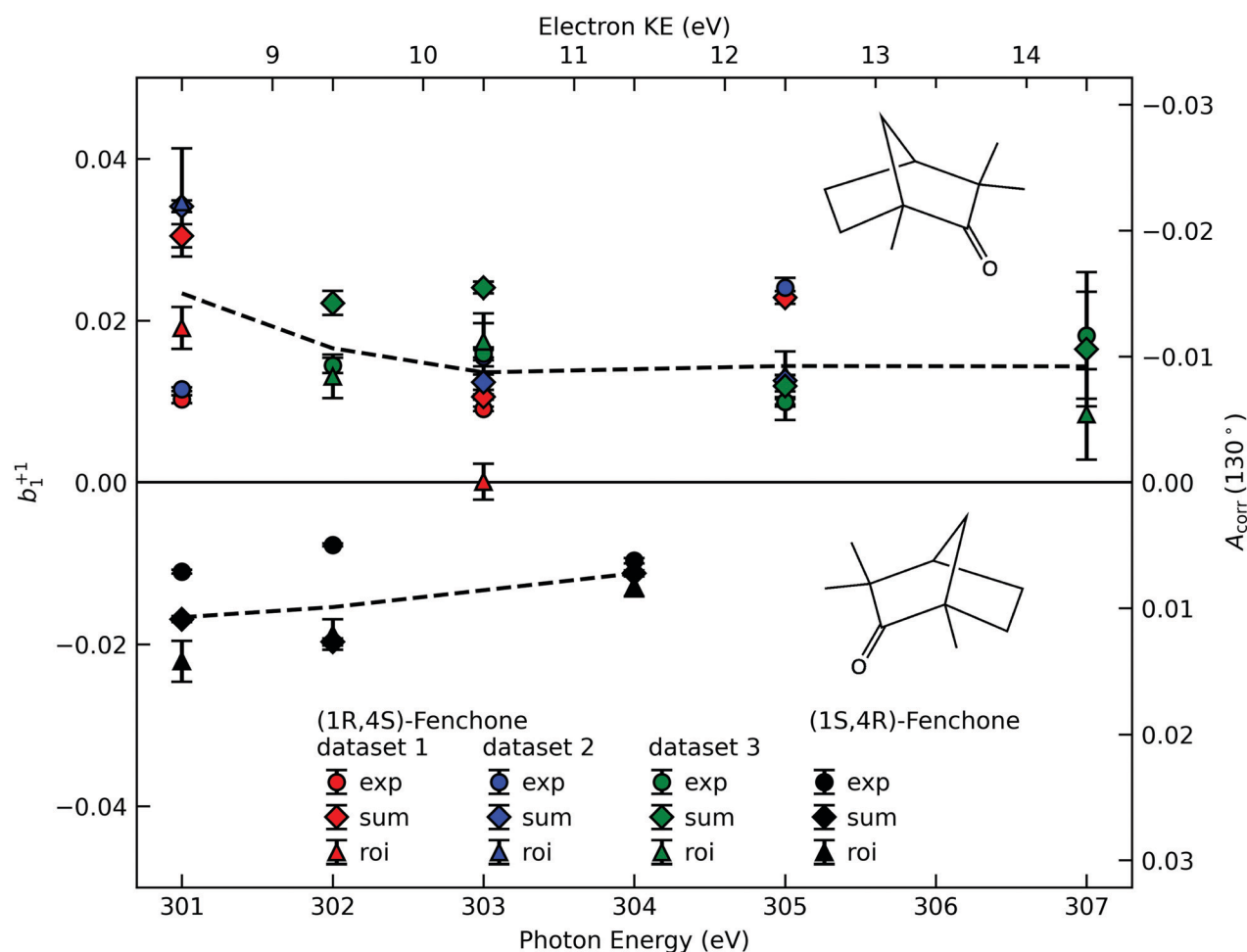


Fig. 3 The corrected asymmetry, A_{corr} , and the resulting chiral angular-distribution parameter b_1^{+1} as a function of photon energy. We use black symbols for the (1S,4R)- and colored symbols for the (1R,4S)-enantiomer. For the latter, the results from three data sets, acquired in two different measurement campaigns, are shown to indicate the stability of our experiment. Different approaches to subtract the LET and, possibly, a residual background are differentiated by the symbol shape, with diamonds referring to the 'total background' approach (Fig. 2C, 'sum'), circles to the linear-exponential approach (Fig. 2B, 'exp') and triangles to the region-of-interest ('roi') approach (Fig. 2A). To guide the eye we indicate the averaged values detailed in Table 1 by dashed lines. Values in the figure are not corrected for any possible gas-phase contributions and angular-anisotropy effects (see Table 1).

Table 1 Recommended b_1^{+1} values calculated as the averages of the values shown in Fig. 3. In round brackets, the standard deviation of all values pertaining to the same enantiomer and photon energy is shown. The rows labelled 'measured' are not corrected for the possible presence of gaseous fenchone nor the β -dependence of the relationship between measured asymmetry and chiral parameter, b_1 (see eqn (5)). In rows labelled 'corrected', the expected maximum correction of the b_1 values has been applied for both factors. See the main body of the text for details

| | 301 eV | 302 eV | 303 eV | 304 eV | 305 eV | 307 eV |
|------------------|-----------|-----------|----------|-----------|----------|----------|
| Measured | | | | | | |
| (1R,4S)-Fenchone | 0.023(11) | 0.017(5) | 0.014(7) | — | 0.014(6) | 0.014(5) |
| (1S,4R)-Fenchone | −0.017(6) | −0.015(7) | — | −0.011(2) | — | — |
| Corrected | | | | | | |
| (1R,4S)-Fenchone | 0.014(12) | 0.010(5) | 0.010(7) | — | 0.011(6) | 0.012(6) |
| (1S,4R)-Fenchone | −0.008(6) | −0.009(7) | — | −0.008(2) | — | — |

which would affect the connection between the measured anisotropy and b_1 values (eqn (5)). As explained above, although no visible presence of a gaseous component has been observed in the PECD measurements, a separate experiment with an electrically biased jet, albeit at slightly different conditions,

suggested that this might result from an inconvenient overlap of liquid-phase and gas-phase C 1s peak features.³³ Referring to that work, we estimate a gas-phase fraction g between negligible, which is expected from the low vapour pressure of fenchone, and $g = 0.14$, which is the finding of the aforementioned



biased jet experiment. As the gas-phase contribution has a b_1 -parameter of larger magnitude, correction for the gas-phase contribution would reduce the liquid phase parameter $b_{1,l}^p$ according to:

$$b_{1,l}^p = \frac{b_{1,m}^p - g b_{1,g}^p}{1 - g}, \quad (7)$$

where subscripts m and g designate the measured and gas-phase values of b_1^p , the latter being taken from ref. 36 with interpolation where necessary. For the correction due to the β -dependent denominator in eqn (5), we expect a value between unity (no correction), for a $\beta = 0$, and multiplication by 0.94, for a $\beta = 1$. Accordingly, the table contains two lines for each parameter stating the averaged, but uncorrected value, and the values corrected downwards by the factors quantified above, which we believe gives the maximum plausible extent of the gas-phase contribution and β parameter effects.

We note two further effects that we cannot quantify at this moment, but could be present to some extent. The exact enantiomeric excess (ee) of the samples supplied was not specified and we were unable to have this independently checked, but previous reports have found commercial samples of (1R,4S)-(-)-fenchone to have a lower ee than (1S,4R)-(+)-fenchone samples. In principle, the measured PECD asymmetry should scale linearly with ee values but these are unknown. However, such adjustments are here expected to be within the current error bars, and so have not been applied. The same applies to a correction for an unpolarized fraction of radiation at our sample, which could be slightly increased at the photon energies used in this experiment because of an influence of carbon contamination on the beamline optics. If present, both factors would lead to a correction of the values of b_1 extracted from the measured asymmetry towards larger absolute values.

4 Discussion

It is interesting to discuss the reduction in b_1^{+1} relative to gas-phase experiments. In the case of fenchone, the reduction in b_1^{+1} amounts to roughly a factor of five. This reduction can be compared to results on the conventional angular distribution, represented by the β parameter. A few experiments for the β parameter of photoemission peaks from liquids are available.^{66,69–71} In comparison with gas-phase water, a general reduction of β has been observed,^{66,71} but only the study on the O 1s β parameter of water by Thürmer *et al.* extended down to the KEs of interest here. For their lowest data point at about 12 eV KE, the measured β -values are approximately $\beta_g = 0.92$ and $\beta_l = 0.28$, which implies a reduction by a factor of 3.3 (with subscripts g and l designating the gas and liquid phase, respectively).⁶⁶ Fully consistent with that, the onset of the reduction in β upon aggregation of individual molecules was also observed in an experiment on water clusters.⁷² A plausible explanation for the reduction in β is the elastic or quasi-elastic scattering of photoelectrons in the liquid bulk, before

traversing the liquid-vacuum interface. Due to the random nature of the associated collisions, this would tend to produce an isotropic angular distribution, and the explanation would equally hold for the reduction in b_1 . It could not be shown in ref. 66, however, that this is the sole explanation for the β reduction, due to a lack of accurate knowledge of the elastic and inelastic mean free paths of electrons in water. Note that electron scattering was also pointed out as the main source of PECD reduction (by about a factor of five) between nanoparticles and gas phase serine.²⁰ This effect may be partly compensated by an increased local order in the nanoparticles or fewer associated conformers in the aggregated state. The former explanation may also be applicable to the case of liquid fenchone. Elastic electron scattering on the water or fenchone vapour surrounding the liquid jets may additionally contribute to the more isotropic angular distributions from liquids, as the cross-sections for elastic scattering for low-KE electrons on gas-phase water are considerable.^{51,73} As these cross-sections are also strongly peaked at low scattering angles, this will likely be a smaller effect, though. A redistribution of intensity from the forward- into the backward-scattering plane, which would be necessary for a reduction of b_1 , is not fully excluded for a cylindrical jet, but seems relatively implausible.

5 Conclusions

A full report on an experiment to measure PECD from the chiral liquid fenchone has been presented. We have shown a non-vanishing effect of opposite sign for the two enantiomers, with a convincing mirroring attesting to the overall quality of the data. Akin to studies on the angular-distribution parameter β from liquids, and to PECD from homochiral nanoparticles, a substantial reduction of the chiral parameter, b_1 , has been found relative to the gas-phase sample. This can be explained to a large or full degree by elastic scattering of the outgoing photoelectrons inside the liquid. Our study opens up prospects to investigate the solution-phase chemistry of chiral substances in their native environment. The *in vivo* study of biomolecules in water with simultaneous site- and chemical-specificity, *via* an analysis of core-level shifts,³⁵ and the chiral handedness, *via* PECD measurements, is an especially exciting and important example.

Data Availability

Data relevant for this study are available at DOI: 10.5281/zenodo.5996526.

Author contributions

Conceptualization: B. W., U. H., L. N., I. P.; methodology: S. M., I. W., S. T., B. W.; investigation (including data acquisition): M. N. P., S. M., F. T., C. L., C. K., L. N., I. P., I. W., B. W.; data analysis (formal analysis): M. N. P., S. T., U. H.; visualization,



writing – original draft: U. H., M. N. P.; writing – review & editing: all authors; supervision: B. W.; funding acquisition: B. W., U. H., S. M., D. M. N.

Conflicts of interest

There are no conflicts to declare.

Acknowledgements

The authors would like to acknowledge help from Sebastian Kray and Stefan Schlichting in setting up the experiment, and from Dana Bloss in data acquisition. We would like to thank André Knie for his contributions in the early stages of this work. B. W. acknowledges funding from the European Research Council (ERC) under the European Union's Horizon 2020 research and investigation programme (grant agreement No. 883759). F. T. and B. W. acknowledge support by the MaxWater initiative of the Max-Planck-Gesellschaft. S. T. acknowledges support from the JSPS KAKENHI Grant No. JP20K15229. D. M. N., M. N. P., and C. L. were supported by the Director, Office of Basic Energy Science, Chemical Sciences Division of the U.S. Department of Energy under Contract No. DE-AC02-05CH11231 and by the Alexander von Humboldt Foundation. We acknowledge DESY (Hamburg, Germany), a member of the Helmholtz Association (HGF), for the provision of experimental facilities. Parts of this research were carried out at PETRA III and we would like to thank Moritz Hoesch in particular, as well as the whole beamline staff, the PETRA III chemistry laboratory and crane operators for their assistance in using the P04 soft X-ray beamline. The beamtime that enabled this work was allocated for proposal II-20180012 (LTP). Open Access funding provided by the Max Planck Society.

References

- U. Meierhenrich, *Amino Acids and the Asymmetry of Life*, Springer, 1st edn, 2008.
- V. Letokhov, *Phys. Lett. A*, 1975, **53**, 275–276.
- L. Pasteur, *Ann. Chim. Phys.*, 1848, **24**, 442–459.
- Circular Dichroism: Principles and Applications*, ed. N. Berova, K. Nakanishi and R. W. Woody, Wiley-VCH, 2nd edn, 2000.
- S. Mayer and J. Kessler, *Phys. Rev. Lett.*, 1995, **74**, 4803–4806.
- B. Göhler, V. Hamelbeck, T. Z. Markus, M. Kettner, G. F. Hanne, Z. Vager, R. Naaman and H. Zacharias, *Science*, 2011, **331**, 894–897.
- B. Ritchie, *Phys. Rev. A: At., Mol., Opt. Phys.*, 1976, **13**, 1411–1415.
- B. Ritchie, *Phys. Rev. A: At., Mol., Opt. Phys.*, 1976, **14**, 359–362.
- I. Powis, *J. Phys. Chem. A*, 2000, **104**, 878–882.
- I. Powis, in *Advances in Chemical Physics*, ed. J. Light, Wiley, New York, 2008, vol. 138, pp. 267–329.
- N. Böwering, T. Lischke, B. Schmidtke, N. Müller, T. Khalil and U. Heinzmann, *Phys. Rev. Lett.*, 2001, **86**, 1187–1190.
- G. A. Garcia, L. Nahon, M. Lebeck, J. C. Houver, D. Dowek and I. Powis, *J. Chem. Phys.*, 2003, **119**, 8781–8784.
- T. Lischke, N. Böwering, B. Schmidtke, N. Müller, T. Khalil and U. Heinzmann, *Phys. Rev. A: At., Mol., Opt. Phys.*, 2004, **70**, 22507–22512.
- U. Hergenbahn, E. E. Rennie, O. Kugeler, S. Marburger, T. Lischke, I. Powis and G. Garcia, *J. Chem. Phys.*, 2004, **120**, 4553–4556.
- L. Nahon, G. A. Garcia and I. Powis, *J. Electron Spectrosc. Relat. Phenom.*, 2015, **204**, 322–334.
- S. Turchini, *J. Phys.: Condens. Matter*, 2017, **29**, 503001.
- R. Hadidi, D. K. Bozanic, G. A. Garcia and L. Nahon, *Adv. Phys.: X*, 2018, **3**, 1477530.
- L. Nahon, G. A. Garcia, H. Soldi-Lose, S. Daly and I. Powis, *Phys. Rev. A: At., Mol., Opt. Phys.*, 2010, **82**, 032514.
- I. Powis, S. Daly, M. Tia, B. Cunha de Miranda, G. A. Garcia and L. Nahon, *Phys. Chem. Chem. Phys.*, 2014, **16**, 467–476.
- S. Hartweg, G. A. Garcia, D. K. Božanić and L. Nahon, *J. Phys. Chem. Lett.*, 2021, **12**, 2385–2393.
- C. Lux, M. Wollenhaupt, T. Bolze, Q. Liang, J. Köhler, C. Sarpe and T. Baumert, *Angew. Chem., Int. Ed.*, 2012, **51**, 5001–5005.
- C. S. Lehmann, N. B. Ram, I. Powis and M. H. Janssen, *J. Chem. Phys.*, 2013, **139**, 234307.
- A. Kastner, T. Ring, B. C. Krüger, G. B. Park, T. Schäfer, A. Senftleben and T. Baumert, *J. Chem. Phys.*, 2017, **147**, 013926.
- R. E. Goetz, T. A. Isaev, B. Nikoobakht, R. Berger and C. P. Koch, *J. Chem. Phys.*, 2017, **146**, 24306.
- M. H. M. Janssen and I. Powis, *Phys. Chem. Chem. Phys.*, 2014, **16**, 856–871.
- A. Comby, S. Beaulieu, M. Boggio-Pasqua, D. Descamps, F. Légaré, L. Nahon, S. Petit, B. Pons, B. Fabre, Y. Mairesse and V. Blanchet, *J. Phys. Chem. Lett.*, 2016, **7**, 4514–4519.
- S. Beaulieu, A. Comby, A. Clergerie, J. Caillat, D. Descamps, N. Dudovich, B. Fabre, R. Généaux, F. Légaré, S. Petit, B. Pons, G. Porat, T. Ruchon, R. Taïeb, V. Blanchet and Y. Mairesse, *Science*, 2017, **358**, 1288–1294.
- M. Tia, M. Pitzer, G. Kastirke, J. Gatzke, H.-K. Kim, F. Trinter, J. Rist, A. Hartung, D. Trabert, J. Siebert, K. Henrichs, J. Becht, S. Zeller, H. Gassert, F. Wiegandt, R. Wallauer, A. Kuhlins, C. Schober, T. Bauer, N. Wechselberger, P. Burzynski, J. Neff, M. Weller, D. Metz, M. Kircher, M. Waitz, J. B. Williams, L. P. H. Schmidt, A. D. Müller, A. Knie, A. Hans, L. Ben Ltaief, A. Ehresmann, R. Berger, H. Fukuzawa, K. Ueda, H. Schmidt-Böcking, R. Dörner, T. Jahnke, P. V. Demekhin and M. Schöffler, *J. Phys. Chem. Lett.*, 2017, **8**, 2780–2786.
- K. Fehre, N. M. Novikovskiy, S. Grundmann, G. Kastirke, S. Eckart, F. Trinter, J. Rist, A. Hartung, D. Trabert, C. Janke, G. Nalin, M. Pitzer, S. Zeller, F. Wiegandt, M. Weller, M. Kircher, M. Hofmann, L. P. H. Schmidt, A. Knie, A. Hans, L. B. Ltaief, A. Ehresmann, R. Berger, H. Fukuzawa, K. Ueda, H. Schmidt-Böcking, J. B. Williams, T. Jahnke, R. Dörner, M. S. Schöffler and P. V. Demekhin, *Phys. Rev. Lett.*, 2021, **127**, 103201.



- 30 A. F. Ordonez and O. Smirnova, *Phys. Rev. A*, 2018, **98**, 63428.
- 31 A. F. Ordonez and O. Smirnova, *Phys. Rev. A*, 2019, **99**, 043416.
- 32 A. F. Ordonez and O. Smirnova, *Phys. Rev. A*, 2019, **99**, 043417.
- 33 S. Malerz, H. Haak, F. Trinter, A. B. Stephansen, C. Kolbeck, M. Pohl, U. Hergenhahn, G. Meijer and B. Winter, *Rev. Sci. Instrum.*, 2022, **93**, 015101.
- 34 D. Nolting, N. Ottosson, M. Faubel, I. V. Hertel and B. Winter, *J. Am. Chem. Soc.*, 2008, **130**, 8150–8151.
- 35 S. Malerz, K. Mudryk, L. Tomanik, D. Stemer, U. Hergenhahn, T. Buttersack, F. Trinter, R. Seidel, W. Quevedo, C. Goy, I. Wilkinson, S. Thürmer, P. Slavíček and B. Winter, *J. Phys. Chem. A*, 2021, **125**, 6881–6892.
- 36 V. Ulrich, S. Barth, S. Joshi, U. Hergenhahn, E. Mikajlo, C. J. Harding and I. Powis, *J. Phys. Chem. A*, 2008, **112**, 3544–3549.
- 37 I. Powis, C. J. Harding, G. A. Garcia and L. Nahon, *ChemPhysChem*, 2008, **9**, 475–483.
- 38 L. Nahon, L. Nag, G. A. Garcia, I. Myrgorodska, U. Meierhenrich, S. Beaulieu, V. Wanie, V. Blanchet, R. Géneaux and I. Powis, *Phys. Chem. Chem. Phys.*, 2016, **18**, 12696–12706.
- 39 A. Kastner, G. Koumariou, P. Glodic, P. C. Samartzis, N. Ladda, S. T. Ranecky, T. Ring, S. Vasudevan, C. Witte, H. Braun, H.-G. Lee, A. Senftleben, R. Berger, G. B. Park, T. Schäfer and T. Baumert, *Phys. Chem. Chem. Phys.*, 2020, **22**, 7404–7411.
- 40 D. P. Singh, J. O. Thompson, K. L. Reid and I. Powis, *J. Phys. Chem. Lett.*, 2021, **12**, 11438–11443.
- 41 S. Beaulieu, A. Comby, D. Descamps, B. Fabre, G. A. Garcia, R. Géneaux, A. G. Harvey, F. Légaré, Z. Mašín, L. Nahon, A. F. Ordonez, S. Petit, B. Pons, Y. Mairesse, O. Smirnova and V. Blanchet, *Nat. Phys.*, 2018, **14**, 484–489.
- 42 S. Sasaki, *Nucl. Instrum. Methods Phys. Res., Sect. A*, 1994, **347**, 83–86.
- 43 J. Viefhaus, F. Scholz, S. Deinert, L. Glaser, M. Ilchen, J. Seltmann and P. Walter, *Nucl. Instrum. Methods Phys. Res., Sect. A*, 2013, **710**, 151–154.
- 44 F. Scholz, I. Shevchuk, K. Bagschik, J. Buck, J. Seltmann and M. Hoesch, unpublished data.
- 45 K. Bagschik, J. Wagner, R. Buß, M. Riepp, A. Philippi-Kobs, L. Müller, J. Buck, F. Trinter, F. Scholz, J. Seltmann, M. Hoesch, J. Viefhaus, G. Grübel, H. P. Oepen and R. Frömter, *Opt. Express*, 2020, **28**, 7282–7300.
- 46 J. Buck, K. Bagschik, L. Glaser, F. Scholz, J. Seltmann and J. Viefhaus, *AIP Conf. Proc.*, 2019, **2054**, 060057.
- 47 K. Bagschik, J. Buck, M. Hoesch, F. Scholz, J. Seltmann, F. Trinter and J. Viefhaus, unpublished data.
- 48 C. J. Harding, E. Mikajlo, I. Powis, S. Barth, S. Joshi, V. Ulrich and U. Hergenhahn, *J. Chem. Phys.*, 2005, **123**, 234310.
- 49 M. Born, E. Wolf, A. B. Bhatia, P. C. Clemmow, D. Gabor, A. R. Stokes, A. M. Taylor, P. A. Wayman and W. L. Wilcock, *Principles of Optics: Electromagnetic Theory of Propagation, Interference and Diffraction of Light*, Cambridge University Press, 7th edn, 1999.
- 50 S. Thürmer, S. Malerz, F. Trinter, U. Hergenhahn, C. Lee, D. M. Neumark, G. Meijer, B. Winter and I. Wilkinson, *Chem. Sci.*, 2021, **12**, 10558–10582.
- 51 S. Malerz, F. Trinter, U. Hergenhahn, A. Ghrist, H. Ali, C. Nicolas, C.-M. Saak, C. Richter, S. Hartweg, L. Nahon, C. Lee, C. Goy, D. M. Neumark, G. Meijer, I. Wilkinson, B. Winter and S. Thürmer, *Phys. Chem. Chem. Phys.*, 2021, **23**, 8246–8260.
- 52 B. Winter, E. F. Aziz, U. Hergenhahn, M. Faubel and I. V. Hertel, *J. Chem. Phys.*, 2007, **126**, 124504.
- 53 C.-M. Saak, I. Unger, B. Brena, C. Coleman and O. Björneholm, *Phys. Chem. Chem. Phys.*, 2019, **21**, 15478–15486.
- 54 J. P. Bruce, K. Zhang, S. G. Balasubramani, A. R. Haines, R. P. Galhenage, V. K. Voora, F. Furche and J. C. Hemminger, *J. Phys. Chem. B*, 2021, **125**, 8862–8868.
- 55 T. Buttersack, P. E. Mason, R. S. McMullen, T. Martinek, K. Brezina, D. Hein, H. Ali, C. Kolbeck, C. Schewe, S. Malerz, B. Winter, R. Seidel, O. Marsalek, P. Jungwirth and S. E. Bradforth, *J. Am. Chem. Soc.*, 2019, **141**, 1838–1841.
- 56 V. Štejfa, M. Fulem, K. Růžicka and C. Červinka, *J. Chem. Thermodyn.*, 2014, **79**, 272–279.
- 57 L. Longetti, M. Randulová, J. Ojeda, L. Mewes, L. Miseikis, J. Grilj, A. Sanchez-Gonzalez, T. Witting, T. Siegel, Z. Diveki, F. van Mourik, R. Chapman, C. Cacho, S. Yap, J. W. G. Tisch, E. Springate, J. P. Marangos, P. Slavíček, C. A. Arrell and M. Chergui, *Phys. Chem. Chem. Phys.*, 2020, **22**, 3965–3974.
- 58 H. C. Schewe, K. Brezina, V. Kostal, P. E. Mason, T. Buttersack, D. M. Stemer, R. Seidel, W. Quevedo, F. Trinter, B. Winter and P. Jungwirth, *J. Phys. Chem. B*, 2022, **126**, 229–238.
- 59 S. Barth, M. Ončák, V. Ulrich, M. Mucke, T. Lischke, P. Slavíček and U. Hergenhahn, *J. Phys. Chem. A*, 2009, **113**, 13519–13527.
- 60 CRC Handbook of Chemistry and Physics, *ch. Physical Constants of Organic Compounds*, ed. J. R. Rumble, CRC Press/Taylor & Francis, Boca Raton, FL., 102nd edn, 2021.
- 61 S. Hüfner, *Photoelectron Spectroscopy: Principles and Applications*, Springer, 2003.
- 62 X. Li, Z. Zhang and V. E. Henrich, *J. Electron Spectrosc. Relat. Phenom.*, 1993, **63**, 253–265.
- 63 J. Végh, *J. Electron Spectrosc. Relat. Phenom.*, 2006, **151**, 159–164.
- 64 S. Turchini, N. Zema, G. Contini, G. Alberti, M. Alagia, S. Stranges, G. Fronzoni, M. Stener, P. Decleva and T. Prospero, *Phys. Rev. A: At., Mol., Opt. Phys.*, 2004, **70**, 14502–14504.
- 65 L. Nahon, G. A. Garcia, C. J. Harding, E. A. Mikajlo and I. Powis, *J. Chem. Phys.*, 2006, **125**, 114309.
- 66 S. Thürmer, R. Seidel, M. Faubel, W. Eberhardt, J. C. Hemminger, S. E. Bradforth and B. Winter, *Phys. Rev. Lett.*, 2013, **111**, 173005.
- 67 V. Schmidt, *Electron Spectrometry of Atoms Using Synchrotron Radiation*, Cambridge University Press, 2005.



- 68 H. Wang, P. Bencok, P. Steadman, E. Longhi, J. Zhu and Z. Wang, *J. Synchrotron Radiat.*, 2012, **19**, 944–948.
- 69 J. Nishitani, C. W. West and T. Suzuki, *Struct. Dyn.*, 2017, **4**, 044014.
- 70 T. Lewis, B. Winter, S. Thürmer, R. Seidel, A. B. Stephansen, J. A. Freites, D. J. Tobias and J. C. Hemminger, *J. Phys. Chem. C*, 2019, **123**, 8160–8170.
- 71 S. Gozem, R. Seidel, U. Hergenhahn, E. Lugovoy, B. Abel, B. Winter, A. I. Krylov and S. E. Bradforth, *J. Phys. Chem. Lett.*, 2020, **11**, 5162–5170.
- 72 S. Hartweg, B. L. Yoder, G. A. Garcia, L. Nahon and R. Signorell, *Phys. Rev. Lett.*, 2017, **118**, 103402.
- 73 M. Matsui, M. Hoshino, H. Kato, F. F. da Silva, P. Limão-Vieira and H. Tanaka, *Eur. Phys. J. D*, 2016, **70**, 77.



Paper VI



THE JOURNAL OF PHYSICAL CHEMISTRY **A**

A JOURNAL OF THE AMERICAN CHEMICAL SOCIETY

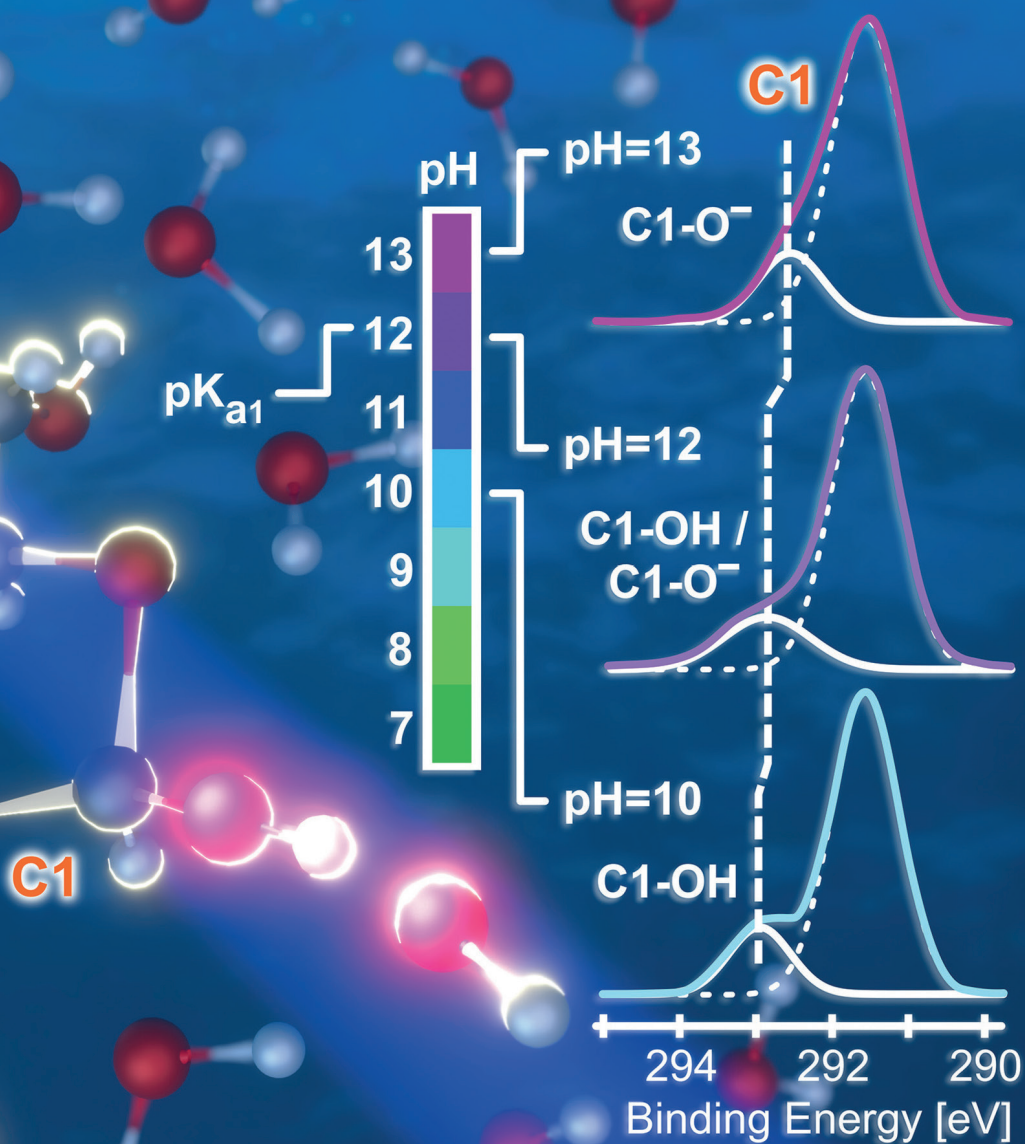


August 19, 2021

Volume 125

Number 32

pubs.acs.org/JPCA



Following in Emil Fischer's Footsteps: A Site-Selective Probe of Glucose Acid–Base Chemistry

Published as part of *The Journal of Physical Chemistry virtual special issue "Daniel Neumark Festschrift"*.

Sebastian Malerz,[◆] Karen Mudryk,[◆] Lukáš Tomaník, Dominik Stemer, Uwe Hergenbahn, Tillmann Buttersack, Florian Trinter, Robert Seidel, Wilson Quevedo, Claudia Goy, Iain Wilkinson, Stephan Thürmer, Petr Slavíček,^{*} and Bernd Winter^{*}



Cite This: *J. Phys. Chem. A* 2021, 125, 6881–6892



Read Online

ACCESS |



Metrics & More

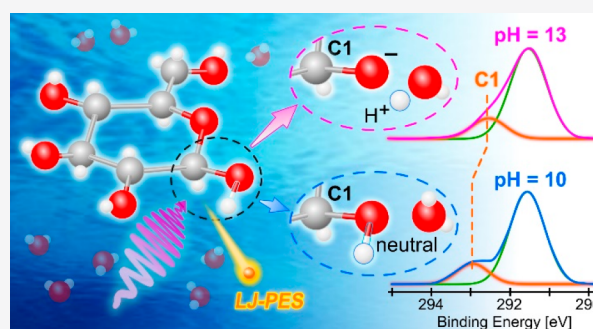


Article Recommendations



Supporting Information

ABSTRACT: Liquid-jet photoelectron spectroscopy was applied to determine the first acid dissociation constant (pK_a) of aqueous-phase glucose while simultaneously identifying the spectroscopic signature of the respective deprotonation site. Valence spectra from solutions at pH values below and above the first pK_a reveal a change in glucose's lowest ionization energy upon the deprotonation of neutral glucose and the subsequent emergence of its anionic counterpart. Site-specific insights into the solution-pH-dependent molecular structure changes are also shown to be accessible via C 1s photoelectron spectroscopy. The spectra reveal a considerably lower C 1s binding energy of the carbon site associated with the deprotonated hydroxyl group. The occurrence of photoelectron spectral fingerprints of cyclic and linear glucose prior to and upon deprotonation are also discussed. The experimental data are interpreted with the aid of electronic structure calculations. Our findings highlight the potential of liquid-jet photoelectron spectroscopy to act as a site-selective probe of the molecular structures that underpin the acid–base chemistry of polyprotic systems with relevance to environmental chemistry and biochemistry.



INTRODUCTION

Glucose is a ubiquitous monosaccharide of major significance in living organisms.^{1,2} It is the precursor of many oligo- and polysaccharides that mediate cell–cell communication,³ build up the scaffold of cells,^{4–6} or serve as energy storage units.^{7–10} It is a natural energy source synthesized via the conversion of solar energy into chemical energy by plants during photosynthesis.^{11,12} Consequently, it plays a central role in the metabolic pathways that govern the flow of energy and matter that sustain life.¹³ As a result, it has also become relevant in the investigation of renewable energy technologies that seek to mimic nature, in particular, with the demonstration of alkaline glucose fuel cells.^{14,15}

The chemistry associated with the use of glucose as a fuel source, in both living organisms and technological devices, is inherently related to the nature of its structure–function relationship and acid–base chemistry in aqueous solution. Despite this, there remains much to be learned about the acid–base properties of this fundamental molecule. This is perhaps surprising because the structure of glucose has been intensively studied since the turn of the 19th century, when Emil Fischer (Nobel Prize in Chemistry 1902) reported the chemical synthesis of D-(+)-glucose and demonstrated its

stereoisomeric forms.^{16,17} But it is only with advancing experimental and theoretical methods,^{18–21} in particular, photoelectron spectroscopy (PES) from an aqueous solution,^{22–25} that previously inaccessible molecular structural details can now be resolved.

With an elemental composition of $C_6H_{12}O_6$, glucose is an aldohexose with an aldehyde group at the C1 position in the Fischer projection. In aqueous solution, glucose predominantly adopts the six-membered closed-ring pyranose structure (>99%), in which the C1 atom forms a hemiacetal linkage to the C5 atom. In smaller quantities, the five-membered, closed-ring furanose (<0.5%) and linear (<0.05%) forms are also present.^{26,27} Traditionally, the stereochemistry in glucose molecules is denoted by the relative orientation of the hydroxyl group at the C5 site, which points to the left in the L form and to the right in the D form, as viewed in the Fischer

Received: May 28, 2021

Revised: July 14, 2021

Published: July 30, 2021

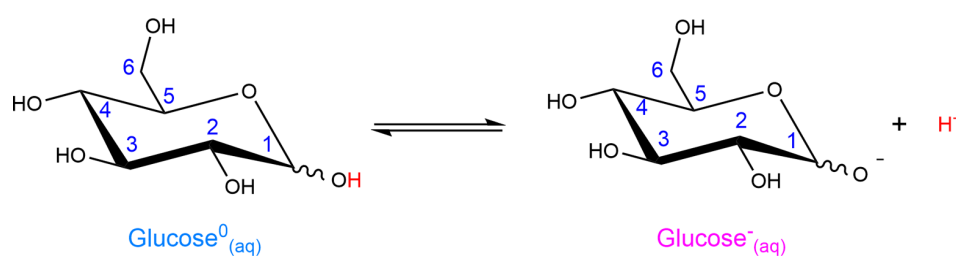


Figure 1. Schematics of the predominantly adopted six-membered closed-ring protonated ($\text{glucose}^0_{(\text{aq})}$) and deprotonated ($\text{glucose}^-_{(\text{aq})}$) structures of glucose in aqueous solution.^{40,42} C–OH sites are labeled 1–6, and the nomenclature is used throughout the text. The zigzag line is used to indicate the two possible orientations of the hydroxyl group at the C1 site, downward or upward, in the α and β anomeric forms, respectively.

projection. As with many biomolecules, such as amino acids, proteins, and DNA, glucose exhibits a remarkable degree of homochirality. In nature, the right-handed D form dominates.^{28,29} Upon cyclization into the pyranose form, a new stereocenter emerges at the C1 site. At this anomeric center, the stereochemistry is denoted depending on the relative orientation of the hemiacetal hydroxyl group as α or β . Because there are multiple stereocenters within the molecule, α - and β -glucose are diastereomers, which exhibit different physicochemical properties. In solution, the α and β forms of glucose are in equilibrium with the open-ring form and therefore constantly interconvert through a process known as mutarotation,³⁰ with β -glucose being favored ($\sim 38\%$ α -glucose vs $\sim 62\%$ β -glucose) due to the anomeric effect;^{27,31} however, this equilibrium can be shifted by tuning the solution pH³² or through the addition of inorganic salts.³³ Glucose is also known to readily isomerize under alkaline conditions to fructose and mannose via Lobry de Bruyn–Alberda van Ekenstein transformations, a process of significance in the preparation of liquid hydrocarbon fuels.^{34,35}

Glucose is a weak acid with at least two reported acid-ionization (*i.e.*, deprotonation) equilibria and acidity constants ($\text{p}K_{\text{a}}$) of 12.1 ($\text{p}K_{\text{a}1}$) and 13.9 ($\text{p}K_{\text{a}2}$),^{36,37} which highlight its enhanced reactivity in alkaline media.^{38,39} Previous determinations of glucose $\text{p}K_{\text{a}}$ values involved the use of site-insensitive high-performance liquid chromatography³⁹ and titration-based methods.^{36,40,41} Consequently, ambiguity remains regarding the extent to which the transition defined at $\text{p}K_{\text{a}1}$ involves charge sharing with C–OH groups beyond the C1 site.⁴² Schematic representations of both the neutral ($\text{glucose}^0_{(\text{aq})}$) and deprotonated ($\text{glucose}^-_{(\text{aq})}$) forms^{40,42} of aqueous glucose are shown in Figure 1.

Whereas site-sensitive methods such as X-ray PES have been applied to study glucose in the solid phase,^{43–45} this approach is unable to access the behavior of aqueous-phase glucose, which is expected to be significantly affected by intra- and intermolecular hydrogen bonding.^{32,40,46} In this context, a local, site-selective, solution-phase characterization of the molecular structure of glucose is needed to better understand its acid–base behavior. To meet this challenge, we leverage the unique experimental capabilities of liquid-jet PES (LJ-PES),^{22,47} which enable us to probe the overall and local electronic structure of protonated and deprotonated solvated glucose via valence and site-specific measurements, respectively. This approach has been previously applied to investigate pH-dependent electronic-structure changes and protonation sites in amino acids.^{48,49}

Herein, we present a combined experimental and theoretical study of the molecular structure of glucose in the pH range from 2 to 13. Utilizing soft X-ray LJ-PES, we monitor (mostly

alkaline) pH-dependent changes in the solution-phase valence and C 1s PES spectra of glucose. Specifically, we probe aqueous-phase binding energy (BE) shifts associated with the most acidic C–OH group(s) and determine the $\text{p}K_{\text{a}1}$ value. To gain insight into the existence of single or multiple deprotonation equilibria related to $\text{p}K_{\text{a}1}$, we investigate the associated chemical structures and confirm principal spectral assignments with the aid of electronic-structure calculations. Our work highlights LJ-PES as a methodology to site-selectively probe ionization equilibria in solvated species, in contrast with previous site-unspecific measurements.

METHODS

Experiments. Glucose aqueous solutions of 1 M concentration were prepared at room temperature by dissolving α -D-(+)-glucose crystals (Acros Organics, >99% purity, anhydrous) in Millipore water (55 nS/cm). Measurements were performed from both freshly prepared and several-hour-old solutions, yielding identical spectra and implying that α and β anomers cannot be distinguished in the present experiments. The pH was varied by the dropwise addition of either HCl (10% and 37% w/w) or NaOH (1 M and 10 M) aqueous solutions under constant magnetic stirring. The solution pH was monitored with a pH meter (VWR, pHenomenal 1100L) to produce 1 M samples at pH values of 2.0, 7.4, 10.0, 10.5, 11.0, 11.5, 12.0, 12.5, and 13.0. Glucose aqueous solutions of 1 M concentration without prior pH adjustment were found to exhibit a pH of 4.8 ± 0.2 . Because of the protonated, nonionic nature of pure glucose, NaCl (Aldrich, $\geq 99\%$) in 25–50 mM concentration was added to those samples to ensure sufficient solution conductivity and minimize sample charging due to streaming potentials.⁵⁰ LJ-PES experiments were performed at the U49/2 PGM-1 beamline⁵¹ at BESSY II using the SOL³PES setup⁵² and the P04 beamline⁵³ at PETRA III using the EASI setup.⁵⁴ Although the majority of the measurements were conducted at the P04 beamline, spectra from glucose solutions at two complementary pH values (11 and 12) were subsequently recorded at BESSY II. The latter yielded somewhat lower electron count rates due to the lower photon flux. At BESSY II, experiments were performed with horizontally polarized light, whereas P04 provided circularly polarized light. Both setups were equipped with differentially pumped hemispherical electron analyzers that detected photoelectrons emitted from the sample either at 0° with respect to the light polarization (SOL³PES) or at 50° with respect to the light propagation (EASI). The samples were introduced into the experimental chamber in the form of liquid microjets⁵⁵ using glass capillary nozzles of 25–35 μm inner diameter and 0.6–0.8 mL/min sample flow rates. In the SOL³PES setup, the (vertical) liquid-

jet flow direction was orthogonal with respect to the light polarization and the electron analyzer detection axes. In the EASI setup, the (horizontal) liquid-jet flow was at 90° with respect to both the light propagation (floor plane) and the electron detection (at an angle of 50° to the floor plane) directions. The liquid jet was electrically connected and grounded to the experimental setup by means of a gold wire immersed in the electrically conductive solution (in the case of SOL³PES) or by a small metallic tube inserted into the main polyether ether ketone (PEEK) liquid delivery line (in the case of EASI). Valence and C 1s spectra were recorded as a function of pH using photon energies of 600 eV and 850 eV, respectively. Such photon energies enabled us to produce photoelectrons with approximately 590 eV (valence) and 560 eV (C 1s) kinetic energies, thus ensuring sufficiently large probing depths into the liquid jet⁵⁶ (*i.e.*, probing of fully hydrated glucose molecules). At PETRA III, the overall experimental energy resolution was 230 meV (for 600 eV photon energy) and 280 meV (for 850 eV photon energy), respectively. The complementary measurements at BESSY II had a somewhat lower overall resolution of 380 meV (850 eV only).

Computations. Valence vertical ionization energies (VIEs), that is, BEs, were calculated for glucose structures optimized at the density functional theory (DFT) level using the CAM-B3LYP⁵⁷ functional and the 6-31+G* basis set. All of the optimized structures were confirmed as energy minima via frequency analysis. The polarizable continuum model (PCM)^{58,59} was used to mimic the presence of the water solvent. In particular, the nonequilibrium PCM⁶⁰ was used to describe the fast photoelectron ionization process. To account for specific intermolecular interactions, several nearest water molecules were considered explicitly. Calculations were performed in Gaussian 09 (revision D.01)⁶¹ using the default parameters for the PCM. VIEs were calculated with the DFT-based delta self-consistent field (Δ SCF) approach, followed by a time-dependent DFT (TDDFT) evaluation of the BEs for deeper-lying electrons. The VIEs were then calculated as⁶²

$$\text{VIE}_i = \text{VIE}_{\text{HOMO}} + E_{\text{exc}}(i \rightarrow \text{SOMO})$$

where VIE_i is the VIE of the i th electron and E_{exc} is the excitation energy, restricted to excitations into the singly occupied molecular orbital (SOMO).

Core-level VIEs were calculated using the maximum overlap method (MOM)⁶³ in the Q-Chem 4.3 software.⁶⁴ This approach is centered on ground-state electronic structure techniques while avoiding the variational collapse of the wave function and providing reliable core-electron BEs for solvated systems.⁶⁵ Calculations were performed using the CAM-B3LYP functional and the cc-pVTZ split basis set for all of the H atoms in glucose. For the C and O atoms, the aug-cc-pCVTZ basis set was used. The parameters in the non-equilibrium PCM were set to match those in Gaussian 09, revision D.01⁶¹ (atomic radii from Universal Force Field⁶⁶ and scaling factor $\alpha = 1.1$). C 1s PES spectra were modeled from the calculated VIEs at the optimized geometries via the empirical broadening scheme. In that way, each modeled spectrum was calculated considering six energies originating from six C atoms in the molecule, and the corresponding sum of six Gaussian components was centered at the respective VIEs. The width of each Gaussian is characterized by a standard deviation (σ) of 0.45 eV, which is reasonable for PES spectra of solvated systems.⁶⁷ This value was found to fit the

experimental PES data of fully protonated glucose (*i.e.*, data recorded at pH 10; see Figure 3) and was thus subsequently used as a constant to simulate similar PES spectra for the different deprotonated forms (*i.e.*, considering the deprotonation of different hydroxyl groups).

Calculations of $\text{p}K_{\text{a}}$ values were performed using Gaussian 09 (revision D.01)⁶¹ and implementing two different approaches. The first approach was based on a thermodynamic cycle including the deprotonation of glucose in the gas phase. Within that methodology, aqueous-phase deprotonation energetics (*i.e.*, changes in Gibbs free energies, $\Delta G_{\text{(aq)}}$) were calculated by evaluating their gas-phase counterpart ($\Delta G_{\text{(g)}}$) and adding solvation energies ($\Delta G_{\text{(solv)}}$). Thus the energies associated with the solvation of gas-phase reactants ($\Delta G_{\text{(solv,react.)}}$) and products ($\Delta G_{\text{(solv,prod.)}}$) were used to calculate $\Delta G_{\text{(aq)}}$ as

$$\Delta G_{\text{(aq)}} = \Delta G_{\text{(g)}} + \Delta G_{\text{(solv,prod)}} - \Delta G_{\text{(solv,react)}}$$

The gas-phase energetics were evaluated using CAM-B3LYP/aug-cc-pVTZ at a temperature of 298.15 K using frequency calculations to obtain the gas-phase free energies. Solvation energies of protonated and deprotonated glucose were calculated using the PCM. The solvation energy of the proton was taken from the literature to be -265.9 kcal/mol.⁶⁸ The second, more straightforward approach consisted of the implementation of the methodology proposed by Thapa and Schlegel.⁶⁹ This method uses a polarizable solvation model to directly evaluate aqueous-phase free-energy changes. According to the authors, reasonable results can be obtained when using a combination of the ω B97XD⁷⁰ method with a 6-31+G* basis set and the solvation model based on solute electron density (SMD).⁷¹

RESULTS AND DISCUSSION

Valence PES Spectra from Protonated and Deprotonated Aqueous-Phase Glucose. Valence PES spectra from 1 M glucose aqueous solutions at pH 10 (below $\text{p}K_{\text{a1}}$, bottom) and 13 (above $\text{p}K_{\text{a1}}$, top) are shown in Figure 2. The spectra are representative of protonated (glucose⁰_(aq)) and deprotonated (glucose⁻_(aq)) molecules. The data are presented on a BE scale calibrated according to the 1b₁ BE of neat liquid water.⁴ The spectra are almost identical, dominated by the contributions from liquid water corresponding to the ionization of water's 1b₁, (split) 3a₁, and 1b₂ leading orbitals (as labeled in Figure 2; see ref 72 for details). Small contributions from gaseous water from the vapor layer surrounding the liquid jet can also be observed (mainly from 1b_{1(g)} photoelectrons; see a somewhat sharper peak at ~ 12.5 eV).

We expected that a change in the charge state of glucose upon deprotonation, from glucose⁰_(aq) at pH 10 to glucose⁻_(aq) at pH 13, would lead to a change in the lowest VIE of the molecule (as demonstrated in previous experiments on the pH-dependent changes in the lowest VIEs of aqueous imidazole,^{73,74} phosphate,⁷⁵ and phenol/phenolate⁷⁶). A small but decisive difference between the pH 10 and pH 13 data is the occurrence of a photoelectron signal near 8.5 eV BE in the pH 13 spectrum. Enlarged views of this spectral region are presented in the figure inset. Gaussian peaks from a cumulative fit analysis highlight the spectral contributions from glucose⁻_(aq) (at 8.5 ± 0.3 eV, magenta fill), added hydroxide (OH⁻_(aq), striped fill, fixed at 9.2 eV BE, as reported in ref 77),

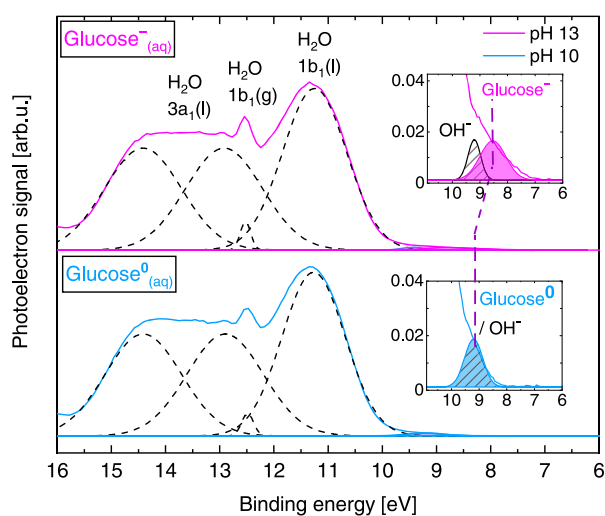


Figure 2. Valence PES spectra of 1 M glucose aqueous solutions at pH 10 (bottom, light blue curve) and 13 (top, magenta curve) measured at a 600 eV photon energy. The dashed lines are Gaussian curves representing signal contributions from water's leading orbitals, $1b_1$ and (split) $3a_1$; liquid (l) and gas-phase (g) signals are assigned.⁷² Spectra intensities are displayed to yield the same height as the $1b_{1(l)}$ peak. The figure insets show enlarged views of the photoelectron features associated with the lowest vertical ionizing transitions in $\text{glucose}^0_{(\text{aq})}$ (light blue peak) and $\text{glucose}^-_{(\text{aq})}$ (magenta peak) as well as from $\text{OH}^-_{(\text{aq})}$ (peak with striped fill). The BE of the latter was fixed during the fitting procedure according to the value reported in ref 77.

and $\text{glucose}^0_{(\text{aq})}$ (light blue fill, overlapping with the $\text{OH}^-_{(\text{aq})}$ feature). Note that lifetime broadening effects are negligible in the case of valence ionization, and a cumulative Gaussian fit approach is thus appropriate. The overall error is a combination of the fitting error reported from the least-squares fitting procedure, the experimental resolution (from both the light source and the electron analyzer) of ~ 0.23 eV, and the error associated with the calibration of the BE scale. As previously stated, the BE scale is referenced to the $1b_1$ BE of neat liquid water, which, however, may deviate slightly from the $1b_1$ BE value of the solution. Solute-induced changes in the electronic structure of water and the work function of the solution may occur, which shift the BE of the photoelectron features. A slight shift of the liquid $1b_1$ peak for very high (up to 8 M) concentrations of NaI has been discussed lately by some of the coauthors⁷⁸ and is being further investigated by our group. Notably, we do not expect any detectable reference-level changes from the 1 M glucose solute, similarly from the small amounts of $\text{HCl}_{(\text{aq})}$ and $\text{NaOH}_{(\text{aq})}$ added to the solutions. On this basis, we estimate cumulative valence peak BE errors of 0.3 eV. Our interpretation of the spectral changes observed upon changing the solution pH from 10 to 13 was corroborated by our calculations, which revealed $\text{glucose}^-_{(\text{aq})}$ to be the prevalent species at pH 13, as opposed to $\text{glucose}^0_{(\text{aq})}$ at pH 10, as shown in the following.

We have evaluated the respective valence VIEs for the minimum-energy structures of protonated and deprotonated glucose in both the α and β anomeric forms. The calculated structures are consistent with the energetic minima previously published,^{79,80} showing only minor energy differences between the α and β forms for both gas- and aqueous-phase glucose. (See Table S1 in the Supporting Information (SI) for details.) Because of the very high charge density at the O atom, the

addition of explicit solvent molecules is required to reach quantitatively correct values in calculations of the electron BEs for $\text{glucose}^-_{(\text{aq})}$. (The calculated results are not sensitive to the explicit solvent addition for $\text{glucose}^0_{(\text{aq})}$.)⁸¹ The highest occupied molecular orbital (HOMO), associated with the lowest VIE, is of π character and is delocalized over the whole molecule for neutral $\text{glucose}^0_{(\text{aq})}$. However, the HOMO is more localized on the single C and single O of the deprotonated hydroxyl group in $\text{glucose}^-_{(\text{aq})}$.

The first VIE of fully protonated glucose ($\text{glucose}^0_{(\text{aq})}$), with the explicit inclusion of close-range water interactions represented by two water molecules, was calculated to be 9.09 eV (Table 1), in good agreement with the onset of the

Table 1. Calculated First Three Vertical Ionization Energies (VIEs) of Fully Protonated ($\text{glucose}^0_{(\text{aq})}$) and Singly Deprotonated ($\text{glucose}^-_{(\text{aq})}$) Aqueous-Phase Glucose in Electronvolts^a

| | $\text{glucose}^0_{(\text{aq})}$ | $\text{glucose}^-_{(\text{aq})}$ |
|-----------------|----------------------------------|----------------------------------|
| 1. VIE (HOMO) | 9.09 | 7.95 |
| 2. VIE (HOMO-1) | 9.40 | 8.87 |
| 3. VIE (HOMO-2) | 9.66 | 9.44 |

^aCalculations were performed by applying the hybrid model with two or six explicitly solvating water molecules for $\text{glucose}^0_{(\text{aq})}$ and $\text{glucose}^-_{(\text{aq})}$, respectively.

spectrum at pH 10. The solvent shift (*i.e.*, the difference between the gas- and solution-phase VIEs) is ~ 1 eV. For $\text{glucose}^-_{(\text{aq})}$, the calculated first VIE is at 7.95 eV (using six explicit water molecules; the larger number of explicit solvating molecules is needed due to a slower BE convergence compared with the neutral species; see Table S1 in the SI), >1 eV lower than that of $\text{glucose}^0_{(\text{aq})}$, in reasonable agreement with the 8.5 eV feature observed from the experimental data recorded at pH 13. (A solvent shift of almost 2 eV is observed in this case.) Note that the calculated VIEs without the inclusion of specific water interaction are much lower (6.75 eV). The VIEs for the various deprotonation sites and for the different anomers are rather close in energy, as presented in Table S1 in the SI for both α and β anomers.

Overall, we conclude that the valence PES spectrum recorded at pH 13 (*i.e.*, above $\text{p}K_{a1}$) reflects the acid ionization of glucose's hydroxyl groups. However, site-specific insights into the molecular structural changes that take place upon deprotonation, that is, which C–OH groups are involved in the deprotonation equilibria, cannot be inferred from the valence spectra. The reason is that the valence energies of the different hydroxyl groups are too similar to be resolved, and the signal contributions from the solvent as well as the $\text{OH}^-_{(\text{aq})}$ solution component overlap with the primary feature of interest. Site-specific and more differential information is revealed in the C 1s core-level PES spectra, which thus serve as a probe of more specific acid–base properties of glucose, as will be presented in the following.

C 1s Core-Level PES Spectra from Aqueous-Phase Glucose: pH-Dependent Changes. Figure 3 shows C 1s PES spectra from 1 M glucose aqueous solutions in the 2–13 pH range. As in Figure 2, the data are presented on a BE scale, but this time they are calibrated based on the liquid water O 1s BE⁸² measured from each solution.^a In this way, (pH-dependent) sample surface-charging effects are canceled out, and the observed small energy shifts (up to ~ 300 meV; see the

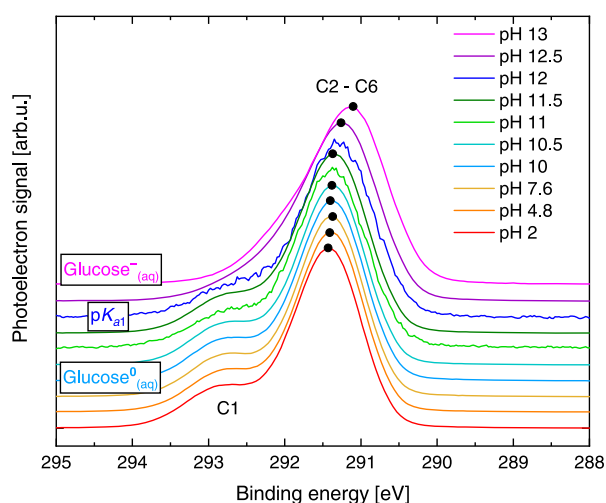


Figure 3. C 1s PES spectra from 1 M glucose aqueous solutions, with pH ranging from 2 to 13, measured at an 850 eV photon energy. The spectra are scaled to yield the same height of the 291.5 eV BE peak and are additionally presented with a vertical offset to highlight the pH-dependent spectral changes. The black dots at the peak of each spectrum serve as a guide for the energy change of the main (C2–C6) peak as a function of pH. Spectra at pH 11 and 12 were measured at the lower-photon-flux beamline and correspondingly have lower signal-to-noise levels. (See the Methods section.) These spectra are manually shifted such that the respective C2–C6 peak centers match the trend of peak maxima (highlighted using black dots).

black dots at the peak of each spectrum to guide the eye) of the overall C 1s spectra are argued to reflect true pH-dependent BE changes, as similarly observed and confirmed by our calculations, see the next section. We further stress that the amounts of $\text{HCl}_{(\text{aq})}$ and $\text{NaOH}_{(\text{aq})}$ solutes added for pH adjustment are too small to lead to a detectable change in the electronic structure of water.⁷⁸

With reference to available PES studies from solid-phase (crystalline) glucose⁴³ and carbon spheres grown from glucose solutions,⁴⁴ the glucose C 1s aqueous-phase spectral features can be crudely assigned to ionization from the C1 and C2–C6 atoms, as labeled in Figure 3. In the 2–10 pH range, we observe a main C 1s peak near 291.5 eV BE accompanied by a higher energy shoulder near 293.0 eV, with no noticeable pH-dependent spectral changes. The latter implies the (near-sole) existence of a single-charge-state species, that is, neutral glucose ($\text{glucose}^0_{(\text{aq})}$) up to pH 10. At pH values higher than 10, the higher energy shoulder becomes less clear, as it appears to move toward lower BEs, consistent with observations from the valence data presented in the previous section. This is indicative of an increase in the fraction of deprotonated glucose molecules up to pH 13 (above $\text{p}K_{\text{a}1}$), when $\text{glucose}^-_{(\text{aq})}$ becomes the prevalent species. (Considering a $\text{p}K_{\text{a}2}$ of 13.9,^{36,37} a fraction of doubly ionized molecules should also be present.)

Qualitatively, the larger C 1s BE of the higher-energy shoulder in $\text{glucose}^0_{(\text{aq})}$ with respect to $\text{glucose}^-_{(\text{aq})}$ reflects the additional positive charge at the specific C site in the former. The observations described here highlight pH-dependent, C-site-specific spectral changes in the C 1s PES data, that is, a site-selective probe of molecular structure changes in glucose upon deprotonation. Details regarding the identity of the C–OH groups involved in the acid dissociation process

highlighted in the data are provided by our calculations, as presented in the following section.

Assignment of the C 1s PES Spectrum of Glucose: Electronic Structure Theory Calculations. The C 1s BEs of each individual C atom (C1–C6) were evaluated using the MOM method combined with the CAM-B3LYP/aug-cc-pCVTZ approach. The BEs were calculated in the gas and aqueous phases for both the α - and β -glucose forms, focusing on the C 1s BE changes taking place upon deprotonation. The calculations considered microsolvation of glucose by the addition of a single explicit water molecule; the addition of further water molecules did not lead to any significant change in the BE. The calculated BEs are summarized in Table S2 in the SI. As follows, we will exclusively discuss the results for the β anomer; the results for the α anomer are very similar.

Simulated C 1s PES spectra for $\text{glucose}^0_{(\text{aq})}$ and $\text{glucose}^-_{(\text{aq})}$ are presented in Figure 4. The corresponding experimental

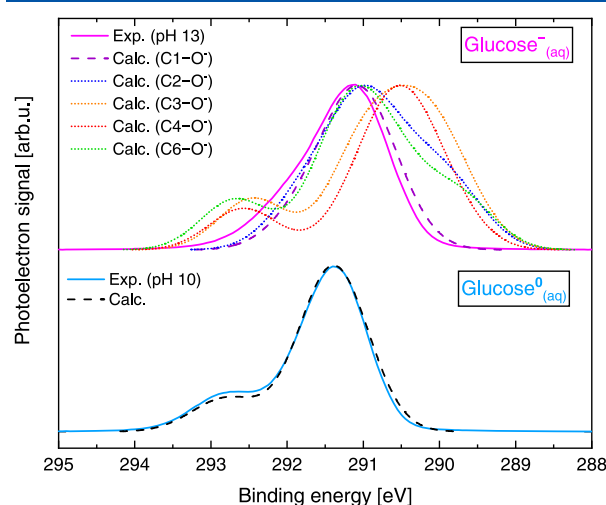


Figure 4. Comparison of experimental (full line) and calculated (dashed and dotted lines) C 1s PES data for $\text{glucose}^0_{(\text{aq})}$ (pH 10, bottom) and $\text{glucose}^-_{(\text{aq})}$ (pH 13, top). All calculated curves were shifted in binding energy by an offset value determined such that the main $\text{glucose}^0_{(\text{aq})}$ peak overlaps with the experimental data at pH 10, as explained in the text. Calculated spectra considering deprotonation at different C sites are shown in the top panel. Note that there is no C5–OH group to deprotonate in the cyclic form.

data (C 1s PES spectra recorded at pH 10 and 13, respectively, as shown in Figure 3) are plotted for comparison. For $\text{glucose}^0_{(\text{aq})}$ (bottom panel), the main C 1s feature in the calculated spectra is overlapped with the experimental data. The same spectral shift was applied to the calculated $\text{glucose}^-_{(\text{aq})}$ curves (top panel), which were produced considering deprotonation at different C–OH sites. The BE shift of the C 1s main feature between the experimental and calculated spectra amounted to 240 meV. Such a magnitude accounts for the (expected) few hundred millielectronvolts shift between theory and experiment due to the known shortcomings of DFT calculations in providing core-level BEs on an absolute scale. (We assume that the absolute value is shifted due to the localized nature of the C 1s electron, yet the differences between various forms are faithfully described.) Nonetheless, consistent with the experimental data, our calculations show that all BEs are shifted toward lower values when going from $\text{glucose}^0_{(\text{aq})}$ to $\text{glucose}^-_{(\text{aq})}$. (See Figure 3.)

For glucose⁰_(aq), the shape of the calculated, fully protonated (cyclic glucose, pyranose form) spectrum (black dashed line) matches that of the experimental data (light-blue full line). For glucose⁻_(aq), a match in spectral shape is observed only with the spectrum calculated considering deprotonation at C1 (purple dashed line). Our calculations show that if we deprotonate any of the other C sites (blue, orange, red, and green dotted lines), then we are left with a separated minor peak at higher energies or a broad shoulder at lower energies. These features are, however, not observed experimentally. Consequently, the experimentally observed higher energy shoulder discussed in the previous section can be safely assigned to the C1 group, whereas the main C 1s feature stems from five close-lying (protonated) components. A more detailed spectral decomposition analysis will be discussed in the next section, with contributions from both theory and experiment.

Our computations were complemented by quantifying the BEs of the energetically unfavorable noncyclic forms of glucose.⁴² The results are presented in Figure 5, with the

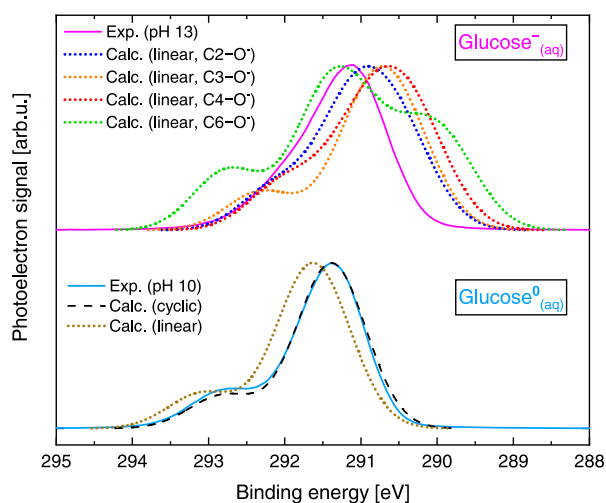


Figure 5. Comparison of experimental (full line) and calculated cyclic and linear (dashed and dotted lines, respectively) C 1s PES spectra of glucose⁰_(aq) (pH 10, bottom) and glucose⁻_(aq) (pH 13, top). The simulated spectral curves were all shifted by the same value, chosen to overlap the pH 10 data, as explained in the text. Calculated spectra of the linear forms of glucose considering deprotonation at different C sites are shown in the top panel.

computed spectra aligned on the BE scale, as discussed for Figure 4. The absolute calculated BE values are shown in Table S2 in the SI but are not considered in the interpretation of the experimental data because an error on the order of few hundreds of millielectronvolts is expected from DFT-based calculations, as performed here. However, more information can be inferred from the structure of the peak. On the basis of a comparison of experimental and calculated spectral shapes for glucose⁰_(aq) (bottom panel), the difference between the cyclic and linear forms is minor. (The linear form has a somewhat larger splitting between the two peaks.) For glucose⁻_(aq) (top panel), spectra from linear structures with a deprotonated hydroxyl group at the C3 and C6 sites exhibit rather pronounced shoulders that are not observed experimentally. Note also that spectra corresponding to acid ionization at C2 and C4 are too wide, and the linear structure

deprotonated at the C5 position does not represent a stable energy minimum. (Calculations for C1 are not shown because there is no C1–OH group in the noncyclic form.) Furthermore, according to our calculations, noncyclic forms are at least 26 kJ/mol (0.27 eV) higher in energy than the cyclic form, so the relative fraction of noncyclic forms should be <0.003%.

Spectral Decomposition of the C 1s PES Spectrum of Glucose. With the aim of identifying the individual spectral contribution from the C1–OH group in the experimental data, we performed a cumulative Gaussian fit analysis of the pH 10 and pH 13 glucose C 1s PES spectra from Figure 3 (glucose⁰_(aq) and glucose⁻_(aq), respectively). The results are presented in Figure 6.

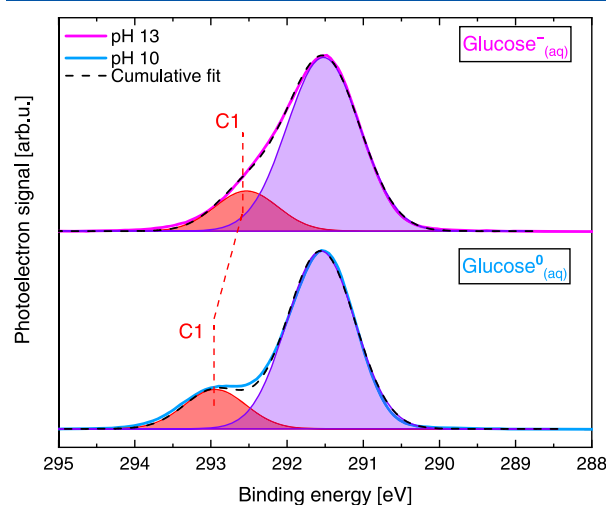


Figure 6. PES spectra of 1 M glucose aqueous solutions at pH 10 and 13, reproduced from Figure 3. The dashed lines indicate cumulative Gaussian fits. Red and purple fills highlight the associated C1 fit component and single-fit component accounting for C2–C6, respectively.

Both the pH 10 (Figure 6, bottom) and pH 13 (Figure 6, top) spectra were fit using two Gaussian curves with the area ratio between the C1 (higher energy shoulder) and the main C2–C6 feature constrained to 1:5. This is indeed a sensible approach because in the pH 10 spectrum, the C1 contribution (highlighted in red) is sufficiently separated from the signal of all of the other C sites (in agreement with our calculations, which indicate a 1.2 eV peak separation; see Table S2 in the SI). The main feature (highlighted in purple) is composed of five C contributions, that is, a convolution of the C2–C6 site signals. The obtained C1 and C2–C6 component BEs are 292.9 ± 0.2 and 291.5 ± 0.2 eV for glucose⁰_(aq) and 292.5 ± 0.2 and 291.5 ± 0.2 eV for glucose⁻_(aq). The 0.4 eV C1 energy shift toward lower BEs in going from glucose⁰_(aq) to glucose⁻_(aq) reflects the larger electron density at the respective carbon site due to the deprotonation of the associated hydroxyl group. As for the valence spectra, the overall error is a combination of the fitting error reported from the least-squares fitting procedure, the experimental resolution, and the error associated with the calibration of the BE scale (calibrated using liquid water's O 1s core level). Because of the somewhat higher photon energy used, the experimental energy resolution is slightly worse, amounting to 0.28 eV (PETRA III) and to 0.38 eV (BESSY II). However, for the C 1s BE values, the

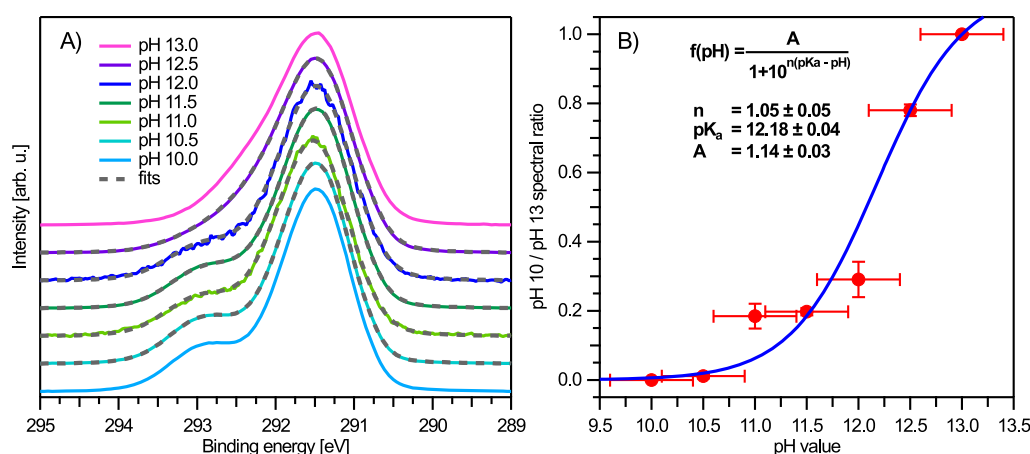


Figure 7. (A) Fits to C 1s PES spectra for intermediate pH values (10.5–12.5) with a model combining the pH 10 (light blue) and pH 13 (magenta) spectra; see the text for details. All spectra were area-normalized and shifted in energy to match the pH 10 spectrum prior to fitting. The vertical offset is added for clarity. (B) Resulting ratio (pH 10/pH 13 spectral contribution) from the fits in panel A as a function of pH value. A fit of a rearranged Henderson–Hasselbalch equation⁸⁴ yields a pK_{a1} value of 12.18 ± 0.04 , but considering uncertainties in the pH values when preparing the solutions, 12.2 ± 0.2 is deemed a reasonable result.

calibration errors for the BEs are less of a concern because one can reasonably expect that the O 1s core level is hardly affected by the solute (at least when non-surface-active solutes like glucose are studied). Furthermore, the relative shift of the C1-associated peak can be determined independent of any energy-scale calibration.

The choice of Gaussian fit functions is justified because the aqueous-phase signals are predominantly subject to inhomogeneous (environmental) broadening, yielding principal Gaussian energy broadening terms. We also performed cumulative Voigt-profile fits to capture possible lifetime broadening in core-level photoionization,⁸³ but the results did not converge due to the greater number of degrees of freedom in those fits. However, with an expected 80–100 meV lifetime broadening component of the C 1s peak, which is one order of magnitude smaller than the Gaussian broadening contribution, we do not expect a Voigt fit (either unconstrained or constrained to known lifetime-broadened widths) to yield any appreciable difference in our fit results. In a related context, we have also performed fitting analyses where each C site was represented by a Gaussian with essentially the same peak area and width. Although such a procedure can accurately reproduce the experimental PES spectra, the fits are not unique, and they yield very large fitting errors due to the similar energies of several components. Accordingly, an experimentally meaningful distinction between the individual C2 to C6 BEs is not possible. This explains the use of a single C2–C6 Gaussian in Figure 6, which yields meaningful fitting errors below 100 meV.

Our analysis implies that the C 1s photoionization cross-sections are taken to be identical for the six C sites, which can be considered a reasonable assumption over such a narrow BE range, well above the photoionization threshold. Note that at the near-magic-angle electron collection geometry adopted in the majority of our experiments, the differential photoionization cross-section becomes essentially independent of the β parameter, which could vary with the molecular shape and character at the different C sites.⁵⁶

Determination of pK_{a1} and Associated Deprotonated Structures. To determine the pK_{a1} value purely from the C 1s PES data, we took the representative experimental spectra of

glucose⁰_(aq) (pH 10) and glucose[−]_(aq) (pH 13) to act as basis curves to fit the spectra associated with the intermediate pH values (10.5–12.5) and determined the ratios of the glucose⁰_(aq) versus glucose[−]_(aq) spectral contributions. All spectra were area-normalized, and the main C 1s feature was overlapped in energy prior to fitting. The basis curves were fit to each spectrum, with the relative basis curve ratio defined as a fitting parameter using the following relation: $\text{Signal}_{\text{pH } 10} \cdot \text{ratio} + \text{Signal}_{\text{pH } 13} \cdot (1 - \text{ratio})$. The results of the fits are shown in Figure 7A, whereas the resulting ratio values are plotted in Figure 7B; the latter can be considered a “photoemission spectroscopy titration”. We also fit the data shown in Figure 7B with a rearranged Henderson–Hasselbalch equation.⁸⁴ The resulting pK_{a1} value was found to be 12.18 ± 0.04 . Considering additional uncertainties in the pH values when preparing the solutions, a precision of 0.2 , yielding 12.2 ± 0.2 , is reasonable. This result is in excellent agreement with the value reported from titration-based methods (pK_{a1} values in the 12.1 to 12.5 range^{36,37,39–41}). The novelty of our LJ-PES approach is the simultaneous determination of the actual deprotonation site, which allows us to associate site-selective spectral changes with a particular acid-ionization constant. Note that our data do not encompass the second acidity constant pK_{a2} , which is expected at a pH of 13.9.^{36,37} This is also the likely reason that the curve in Figure 7B does not end in a plateau and that rather aqueous-phase glucose is already starting to transition into the double-deprotonated species at higher pH values. Our simple analysis thus does not cover the full picture and is rather meant as a first demonstration of the feasibility of this approach.

To further confirm the assignment of the deprotonation site, we calculated pK_a values of glucose upon acid ionization at different C–OH groups. Our results show a robust trend: The pK_a value corresponding to acid ionization at C1 is always 1–3 pK_a units below the others, irrespective of the method used; the second most easily ionizable C–OH group is located at the C4 site. The calculated values are shown in Table 2, and further analysis is presented in the SI in Table S3. Our results are in agreement with findings by Feng et al.,⁸⁵ who showed that C1 is the best proton donor and is associated with the highest acidity, followed by C4. Notably, though, we observe

Table 2. Glucose Acidity Constants Calculated Using the Thapa and Schlegel⁶⁹ Approach and Assuming a Mixed Explicit/Implicit Model with a Single Solvating Molecule

| | C1–OH | C2–OH | C3–OH | C4–OH | C6–OH |
|----------------------|-------|-------|-------|-------|-------|
| calculated pK_{a1} | 11.3 | 15.4 | 15.5 | 14.3 | 17.3 |

no significant differences in the acidity constants between the two anomeric forms. This latter finding is in contradiction with the report by Feng et al.,⁸⁵ who found pK_{a1} values for C4 and C6 sites to vary between the anomeric forms by more than 2 and 4 pK_a units, respectively. Whereas charge sharing between the two most acidic (C1 and C4) sites has been suggested by Lewis and Schramm³⁹ and cannot be completely excluded based on the C 1s PES experimental data, the present calculations show that C4-deprotonation contributions to the pK_{a1} equilibrium would be negligibly small. The second acid dissociation constant (pK_{a2}) of glucose, assuming deprotonation at C1 followed by deprotonation at C4, was also calculated, yielding a value of 20.8, which is well-separated from the pK_{a1} value.

The values of the acidity constants are controlled by the energetics of the glucose anion produced during deprotonation, which are strongly influenced by the presence of the hydrogen-bonding network, including both glucose–glucose and glucose–water interactions.^{40,46,79,86–88} A summary of the different calculated deprotonated structures of glucose[−](aq), together with the respective energies, is shown in Figure 8. Using a relative energy scale, it can be seen that the C1-deprotonated form is energetically preferred.

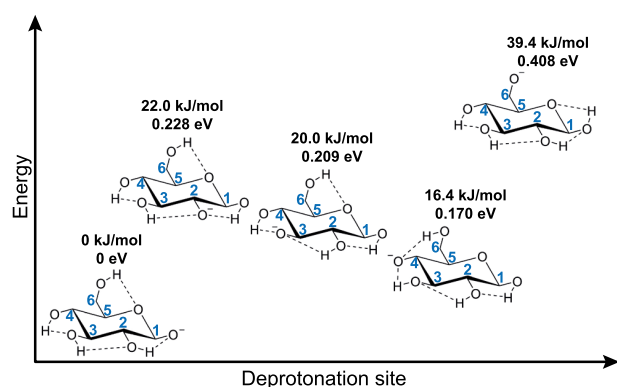


Figure 8. Calculated molecular structures of aqueous-phase β -glucose deprotonated at different C–OH groups. Relative energies (kJ/mol and eV) are also shown and were obtained using free-energy calculations. The presented structures were found as local energetic minima.

CONCLUSIONS

We have investigated the pH-dependent molecular structure changes in glucose by performing LJ-PES experiments over the valence and C 1s spectral regions. With the support of electronic structure calculations, we show how aqueous-phase PES data can be applied to determine the first acid dissociation constant (pK_{a1}) and, more importantly, to unambiguously identify the deprotonation site.

We reported the lowest vertical ionization energies (VIEs), that is, binding energies (BEs) of aqueous-phase glucose from 1 M solutions at pH values below and above pK_{a1} as 9.09 and

7.95 eV, respectively. In addition, our calculations confirmed the signatures of protonated (glucose⁰(aq)) and deprotonated (glucose[−](aq)) species in the experimental data. An experimental VIE of ~ 8.5 eV was determined for glucose[−](aq), almost 1 eV lower than that for its protonated counterpart, glucose⁰(aq).

We have also reported two C 1s PES fingerprints of aqueous glucose: a main C 1s photoelectron feature with a BE of 291.5 eV and a less intense, higher energy feature at 293 eV. Our calculations show that the latter originates from the photoionization of the C1–OH group in glucose. We found that the C1–OH C 1s BE shifts by 0.4 eV toward lower values upon the deprotonation of glucose, as evident from data recorded at pH values below and above pK_{a1} as well as from our calculations. Our combined experimental and theoretical approach confirms that at pK_{a1} deprotonation occurs almost exclusively at the C1 site (in contrast, deprotonation at the C4 site is negligibly small) and that a cyclic deprotonated structure prevails.

The sensitivity of LJ-PES to local chemical environments enables us to identify spectral fingerprints of pH-dependent, site-specific deprotonation in glucose. In particular, our studies provide a deeper understanding of the correlation between the molecular structure and the biological function in aqueous-phase glucose as well as in other pyranose-based sugars more generally. Thus we demonstrate the use of solution-phase PES as a general methodology to determine pK_a values, expanding on the capabilities of the technique to investigate the acid–base chemistry and structure–function relationship of polyprotic acids.

ASSOCIATED CONTENT

Supporting Information

The Supporting Information is available free of charge at <https://pubs.acs.org/doi/10.1021/acs.jpca.1c04695>.

Calculated valence VIEs for aqueous-phase glucose α - and β -anomers in their protonated (glucose⁰(aq)) and deprotonated (glucose[−](aq)) forms. Table S1. Calculated C 1s VIEs for aqueous-phase α - and β -glucose as well as linear (noncyclic, n-) glucose in their protonated (glucose⁰(aq)) and deprotonated (glucose[−](aq)) forms. Table S2. First and second acidity constants (pK_{a1} and pK_{a2} , respectively) calculated for different C–OH groups in α - and β -glucose. Table S3. Sample input for calculations of valence VIEs. Cartesian coordinates of the structures used to calculate valence VIEs. Sample input for calculations of C 1s VIEs. Cartesian coordinates of the structures used to calculate C 1s VIEs. Sample input for calculations of pK_a values. Cartesian coordinates of the structures used to calculate pK_a values via the thermodynamic cycle. Cartesian coordinates of structures used to calculate pK_a values via a thermodynamic cycle (PDF)

AUTHOR INFORMATION

Corresponding Authors

Petr Slaviček – Department of Physical Chemistry, University of Chemistry and Technology, Prague 6 16628, Czech Republic; orcid.org/0000-0002-5358-5538; Email: petr.slavicek@vscht.cz

Bernd Winter – Fritz-Haber-Institut der Max-Planck-Gesellschaft, 14195 Berlin, Germany; orcid.org/0000-0002-5597-8888; Email: winter@fhi-berlin.mpg.de

Authors

Sebastian Malerz – Fritz-Haber-Institut der Max-Planck-Gesellschaft, 14195 Berlin, Germany; orcid.org/0000-0001-9570-3494

Karen Mudryk – Fritz-Haber-Institut der Max-Planck-Gesellschaft, 14195 Berlin, Germany; orcid.org/0000-0002-9046-9915

Lukáš Tomanik – Department of Physical Chemistry, University of Chemistry and Technology, Prague 6 16628, Czech Republic; orcid.org/0000-0003-2547-2488

Dominik Stemer – Fritz-Haber-Institut der Max-Planck-Gesellschaft, 14195 Berlin, Germany; orcid.org/0000-0002-5528-1773

Uwe Hergenroth – Fritz-Haber-Institut der Max-Planck-Gesellschaft, 14195 Berlin, Germany; orcid.org/0000-0003-3396-4511

Tillmann Buttersack – Fritz-Haber-Institut der Max-Planck-Gesellschaft, 14195 Berlin, Germany; orcid.org/0000-0002-4547-2656

Florian Trinter – Fritz-Haber-Institut der Max-Planck-Gesellschaft, 14195 Berlin, Germany; Institut für Kernphysik, Goethe-Universität, 60438 Frankfurt am Main, Germany; orcid.org/0000-0002-0891-9180

Robert Seidel – Operando Interfacial Photochemistry, Helmholtz-Zentrum Berlin für Materialien und Energie, 12489 Berlin, Germany; Institut für Chemie, Humboldt-Universität zu Berlin, 12489 Berlin, Germany; orcid.org/0000-0003-2613-4106

Wilson Quevedo – Operando Interfacial Photochemistry, Helmholtz-Zentrum Berlin für Materialien und Energie, 12489 Berlin, Germany; orcid.org/0000-0002-5222-6891

Claudia Goy – Centre for Molecular Water Science (CMWS), Photon Science, Deutsches Elektronen-Synchrotron (DESY), 22607 Hamburg, Germany; orcid.org/0000-0001-5771-8564

Iain Wilkinson – Department of Locally-Sensitive & Time-Resolved Spectroscopy, Helmholtz-Zentrum Berlin für Materialien und Energie, 14109 Berlin, Germany; orcid.org/0000-0001-9561-5056

Stephan Thürmer – Department of Chemistry, Graduate School of Science, Kyoto University, Kyoto 606-8502, Japan; orcid.org/0000-0002-8146-4573

Complete contact information is available at: <https://pubs.acs.org/10.1021/acs.jpca.1c04695>

Author Contributions

◆ S.M. and K.M. contributed equally.

Notes

The authors declare no competing financial interest. Data relevant for this study have been deposited at [10.5281/zenodo.4777079](https://zenodo.org/record/4777079).

ACKNOWLEDGMENTS

We thank Gerard Meijer, Kevin Pagel, and Maike Lettow for fruitful discussions and critical comments on the manuscript. K.M. acknowledges Nair M. Eguibar for insightful discussions about the biochemistry of glucose. L.T. and P.S. acknowledge

support by the Czech Science Foundation, project no. 21-26601X (EXPRO). L.T. acknowledges Specific University Research grant no. A2_FCHI_2021_028. F.T. and B.W. acknowledge support from the MaxWater initiative of the Max-Planck-Gesellschaft. B.W. acknowledges funding from the European Research Council (ERC) under the European Union's Horizon 2020 research and investigation programme (grant agreement no. 883759). R.S. and W.Q. acknowledge funding from the German Research Foundation through an Emmy-Noether grant (SE 2253/3-1). S.T. acknowledges support from the JSPS KAKENHI grant no. JP20K15229. We thank Helmholtz-Zentrum Berlin for the allocation of synchrotron radiation beamtime at BESSY II. We acknowledge DESY (Hamburg, Germany), a member of the Helmholtz Association HGF, for the provision of experimental facilities. Parts of this research were carried out at PETRA III, and we thank Moritz Hoesch, in particular, as well as the whole beamline staff, the PETRA III chemistry laboratory and crane operators for assistance in using the P04 soft X-ray beamline. Beamtime was allocated for proposal I-20200682.

ADDITIONAL NOTE

“This is the commonly applied procedure in LJ-PES experiments where solute and solvent energies from aqueous solutions are determined from the energy difference between a solute/solvent peak position and the well-known energies of simultaneously measured water gas-phase $1b_1$ or $1a_1$ (O 1s) peak features. More precisely, the gas-phase referenced ionization energy of liquid water $1b_{1(l)}$ (or O $1s_{(l)}$) has been used as an internal aqueous-solution reference, although the reference was only determined for neat liquid water. As discussed in ref 89, this gas-phase referencing method generally does not produce accurate absolute liquid-phase BEs because of the typically ill-defined charging of the solution surface. Accurate BEs can, however, be obtained when measuring the respective photoelectron peak along with the so-called low-energy spectral cutoff. Note, though, that accurately determined $1b_1$ and O 1s BEs from liquid water would still not serve as useful references to infer solute energies, as they neglect any solute-induced effects on the electronic structure of neat liquid water. Despite this, C 1s BEs reported in the present work are expected to be accurate within 200–500 meV of the true values.

REFERENCES

- (1) Seeberger, P. H. Monosaccharide Diversity. In *Essentials of Glycobiology*, 3rd ed.; Varki, A., Cummings, R., Esko, J., Eds.; Cold Spring Harbor Laboratory Press: Cold Spring Harbor, NY, 2017.
- (2) Varki, A. Biological roles of oligosaccharides: all of the theories are correct. *Glycobiology* **1993**, *3* (2), 97–130.
- (3) Krauss, G. *Biochemistry of Signal Transduction and Regulation*; 5th ed.; Wiley-VCH: 2014.
- (4) Hon, D. N. S. Cellulose: a random walk along its historical path. *Cellulose* **1994**, *1* (1), 1–25.
- (5) McNeil, M.; Darvill, A. G.; Fry, S. C.; Albersheim, P. Structure and function of the primary cell walls of plants. *Annu. Rev. Biochem.* **1984**, *53* (1), 625–663.
- (6) Marszalek, P. E.; Oberhauser, A. F.; Pang, Y.-P.; Fernandez, J. M. Polysaccharide elasticity governed by chair–boat transitions of the glucopyranose ring. *Nature* **1998**, *396* (6712), 661–664.
- (7) Beck, E.; Ziegler, P. Biosynthesis and Degradation of Starch in Higher Plants. *Annu. Rev. Plant Physiol. Plant Mol. Biol.* **1989**, *40* (1), 95–117.

- (8) Smith, A. M.; Zeeman, S. C.; Smith, S. M. Starch degradation. *Annu. Rev. Plant Biol.* **2005**, *56* (1), 73–98.
- (9) Adeva-Andany, M. M.; González-Lucán, M.; Donapetry-García, C.; Fernández-Fernández, C.; Ameneiros-Rodríguez, E. Glycogen metabolism in humans. *BBA clinical* **2016**, *5*, 85–100.
- (10) Adeva-Andany, M. M.; Pérez-Felpete, N.; Fernández-Fernández, C.; Donapetry-García, C.; Pazos-García, C. Liver glucose metabolism in humans. *Biosci. Rep.* **2016**, *36* (6), e00416.
- (11) Leegood, R. C. Photosynthesis. In *Encyclopedia of Biological Chemistry*, 2nd ed.; Lennarz, W. J., Lane, M. D., Eds.; Academic Press: Waltham, MA, 2013; pp 492–496.
- (12) Bassham, J. A. Energy capture and conversion by photosynthesis. *J. Theor. Biol.* **1963**, *4* (1), 52–72.
- (13) Pischetsrieder, M. Chemistry of Glucose and Biochemical Pathways of Biological Interest. *Peritoneal Dial. Int.* **2000**, *20* (2 suppl), 26–30.
- (14) Chen, J.; Zhao, C. X.; Zhi, M. M.; Wang, K.; Deng, L.; Xu, G. Alkaline direct oxidation glucose fuel cell system using silver/nickel foams as electrodes. *Electrochim. Acta* **2012**, *66*, 133–138.
- (15) Zhao, C. X.; Wang, K.; Yan, H.; Xu, G. Output Current Increase in Alkaline Glucose Fuel Cells. *J. Electrochem. Soc.* **2011**, *158* (9), B1055.
- (16) Hudson, C. S. Emil Fischer's discovery of the configuration of glucose. A semicentennial retrospect. *J. Chem. Educ.* **1941**, *18* (8), 353.
- (17) Lichtenthaler, F. W. Emil Fischer's Proof of the Configuration of Sugars: A Centennial Tribute. *Angew. Chem., Int. Ed. Engl.* **1992**, *31* (12), 1541–1556.
- (18) Marianski, M.; Supady, A.; Ingram, T.; Schneider, M.; Baldauf, C. Assessing the Accuracy of Across-the-Scale Methods for Predicting Carbohydrate Conformational Energies for the Examples of Glucose and α -Maltose. *J. Chem. Theory Comput.* **2016**, *12* (12), 6157–6168.
- (19) Delbianco, M.; Kononov, A.; Poveda, A.; Yu, Y.; Diercks, T.; Jiménez-Barbero, J.; Seeberger, P. H. Well-Defined Oligo- and Polysaccharides as Ideal Probes for Structural Studies. *J. Am. Chem. Soc.* **2018**, *140* (16), 5421–5426.
- (20) Hofmann, J.; Hahm, H. S.; Seeberger, P. H.; Pagel, K. Identification of carbohydrate anomers using ion mobility–mass spectrometry. *Nature* **2015**, *526* (7572), 241–244.
- (21) Liu, J.; Cukier, R. I.; Bu, Y.; Shang, Y. Glucose-Promoted Localization Dynamics of Excess Electrons in Aqueous Glucose Solution Revealed by Ab Initio Molecular Dynamics Simulation. *J. Chem. Theory Comput.* **2014**, *10* (10), 4189–4197.
- (22) Seidel, R.; Winter, B.; Bradforth, S. E. Valence Electronic Structure of Aqueous Solutions: Insights from Photoelectron Spectroscopy. *Annu. Rev. Phys. Chem.* **2016**, *67* (1), 283–305.
- (23) Williams, H. L.; Erickson, B. A.; Neumark, D. M. Time-resolved photoelectron spectroscopy of adenosine and adenosine monophosphate photodeactivation dynamics in water microjets. *J. Chem. Phys.* **2018**, *148* (19), 194303.
- (24) Erickson, B. A.; Heim, Z. N.; Pieri, E.; Liu, E.; Martinez, T. J.; Neumark, D. M. Relaxation Dynamics of Hydrated Thymine, Thymidine, and Thymidine Monophosphate Probed by Liquid Jet Time-Resolved Photoelectron Spectroscopy. *J. Phys. Chem. A* **2019**, *123* (50), 10676–10684.
- (25) Ramasesha, K.; Leone, S. R.; Neumark, D. M. Real-Time Probing of Electron Dynamics Using Attosecond Time-Resolved Spectroscopy. *Annu. Rev. Phys. Chem.* **2016**, *67* (1), 41–63.
- (26) Angyal, S. J. The Composition and Conformation of Sugars in Solution. *Angew. Chem., Int. Ed. Engl.* **1969**, *8* (3), 157–166.
- (27) Zhu, Y.; Zajicek, J.; Serianni, A. S. Acyclic Forms of [1–¹³C]Aldohexoses in Aqueous Solution: Quantitation by ¹³C NMR and Deuterium Isotope Effects on Tautomeric Equilibria. *J. Org. Chem.* **2001**, *66* (19), 6244–6251.
- (28) Bonner, W. A. The origin and amplification of biomolecular chirality. *Origins Life Evol. Biospheres* **1991**, *21* (2), 59–111.
- (29) Cintas, P.; Viedma, C. On the physical basis of asymmetry and homochirality. *Chirality* **2012**, *24* (11), 894–908.
- (30) Brønsted, J. N.; Guggenheim, E. A. Contribution to the theory of acid and basic catalysis. The mutarotation of glucose. *J. Am. Chem. Soc.* **1927**, *49* (10), 2554–2584.
- (31) Cui, S. W. *Food Carbohydrates: Chemistry, Physical Properties, and Applications*; Taylor & Francis Group: 2005.
- (32) Sugiyama, H.; Usui, T. The Anomeric Equilibrium of Glucose in Acidic and Basic Media. *Agric. Biol. Chem.* **1980**, *44* (12), 3001–3002.
- (33) Mayes, H. B.; Tian, J.; Nolte, M. W.; Shanks, B. H.; Beckham, G. T.; Gnanakaran, S.; Broadbelt, L. J. Sodium Ion Interactions with Aqueous Glucose: Insights from Quantum Mechanics, Molecular Dynamics, and Experiment. *J. Phys. Chem. B* **2013**, *118* (8), 1990–2000.
- (34) Zhao, S.; Guo, X.; Bai, P.; Lv, L. Chemical Isomerization of Glucose to Fructose Production. *Asian J. Chem.* **2014**, *26*, 4537–4543.
- (35) Climent, M. J.; Corma, A.; Iborra, S. Conversion of biomass platform molecules into fuel additives and liquid hydrocarbon fuels. *Green Chem.* **2014**, *16* (2), 516–547.
- (36) Urban, F.; Shaffer, P. A. The acidic property of sugars. *J. Biol. Chem.* **1932**, *94* (3), 697–715.
- (37) Urban, F.; Williams, R. D. The acidic property of sugars II. *J. Biol. Chem.* **1933**, *100* (1), 237–241.
- (38) Shaffer, P. A.; Friedemann, T. E. Sugar activation by alkali: I. Formation of lactic and saccharinic acids. *J. Biol. Chem.* **1930**, *86* (1), 345–374.
- (39) Lewis, B. E.; Schramm, V. L. Isotope Effect-Mapping of the Ionization of Glucose Demonstrates Unusual Charge Sharing. *J. Am. Chem. Soc.* **2003**, *125* (26), 7872–7877.
- (40) Beenackers, J. A. W. M. B.; Kuster, B. F. M.; van der Baan, H. S. Ionisation and solvation of d-glucose. *Carbohydr. Res.* **1985**, *140* (2), 169–183.
- (41) Degani, C. Ionization constants of sugars: a predominant factor in the cyanogen-induced phosphorylation of sugars. *Carbohydr. Res.* **1971**, *18* (2), 329–332.
- (42) de Wit, G.; Kieboom, A. P. G.; van Bekkum, H. Ionization and mutarotation of hexoses in aqueous alkaline solution as studied by ¹³C-NMR spectroscopy. *Tetrahedron Lett.* **1975**, *16* (45), 3943–3946.
- (43) Stevens, J. S.; Schroeder, S. L. M. Quantitative analysis of saccharides by X-ray photoelectron spectroscopy. *Surf. Interface Anal.* **2009**, *41* (6), 453–462.
- (44) Li, M.; Li, W.; Liu, S. Hydrothermal synthesis, characterization, and KOH activation of carbon spheres from glucose. *Carbohydr. Res.* **2011**, *346* (8), 999–1004.
- (45) Qiao, H.; Xiao, L.; Zheng, Z.; Liu, H.; Jia, F.; Zhang, L. One-pot synthesis of CoO/C hybrid microspheres as anode materials for lithium-ion batteries. *J. Power Sources* **2008**, *185* (1), 486–491.
- (46) El Khadem, H. S.; Ennifar, S.; Isbell, H. S. Evidence of stable hydrogen-bonded ions during isomerization of hexoses in alkali. *Carbohydr. Res.* **1989**, *185* (1), 51–59.
- (47) Winter, B.; Faubel, M. Photoemission from Liquid Aqueous Solutions. *Chem. Rev.* **2006**, *106* (4), 1176–1211.
- (48) Nolting, D.; Aziz, E. F.; Ottosson, N.; Faubel, M.; Hertel, I. V.; Winter, B. pH-Induced Protonation of Lysine in Aqueous Solution Causes Chemical Shifts in X-ray Photoelectron Spectroscopy. *J. Am. Chem. Soc.* **2007**, *129* (45), 14068–14073.
- (49) Ottosson, N.; Børve, K. J.; Spångberg, D.; Bergersen, H.; Sæthre, L. J.; Faubel, M.; Pokapanich, W.; Öhrwall, G.; Björneholm, O.; Winter, B. On the Origins of Core–Electron Chemical Shifts of Small Biomolecules in Aqueous Solution: Insights from Photoemission and ab Initio Calculations of Glycine_{aq}. *J. Am. Chem. Soc.* **2011**, *133* (9), 3120–3130.
- (50) Kurahashi, N.; Karashima, S.; Tang, Y.; Horio, T.; Abulimiti, B.; Suzuki, Y.; Ogi, Y.; Oura, M.; Suzuki, T. Photoelectron spectroscopy of aqueous solutions: streaming potentials of NaX (X = Cl, Br, and I) solutions and electron binding energies of liquid water and X. *J. Chem. Phys.* **2014**, *140* (17), 174506.

- (51) Kachel, T. The plane grating monochromator beamline U49/2 PGM1 at BESSY II. *Journal of Large-Scale Research Facilities* **2016**, *2*, A72.
- (52) Seidel, R.; Pohl, M. N.; Ali, H.; Winter, B.; Aziz, E. F. Advances in liquid phase soft-x-ray photoemission spectroscopy: A new experimental setup at BESSY II. *Rev. Sci. Instrum.* **2017**, *88* (7), 073107.
- (53) Viehhaus, J.; Scholz, F.; Deinert, S.; Glaser, L.; Ilchen, M.; Seltnann, J.; Walter, P.; Siewert, F. The Variable Polarization XUV Beamline P04 at PETRA III: Optics, mechanics and their performance. *Nucl. Instrum. Methods Phys. Res., Sect. A* **2013**, *710*, 151–154.
- (54) EASI Liquid-Jet PES Instrument Website. Fritz-Haber-Institut, Max-Planck-Gesellschaft, Berlin. <https://www.fhi.mpg.de/236287/experimental-methods> (accessed May 28, 2021).
- (55) Winter, B. Liquid microjet for photoelectron spectroscopy. *Nucl. Instrum. Methods Phys. Res., Sect. A* **2009**, *601* (1–2), 139–150.
- (56) Thürmer, S.; Seidel, R.; Faubel, M.; Eberhardt, W.; Hemminger, J. C.; Bradforth, S. E.; Winter, B. Photoelectron Angular Distributions from Liquid Water: Effects of Electron Scattering. *Phys. Rev. Lett.* **2013**, *111* (17), 173005.
- (57) Yanai, T.; Tew, D. P.; Handy, N. C. A new hybrid exchange–correlation functional using the Coulomb-attenuating method (CAM-B3LYP). *Chem. Phys. Lett.* **2004**, *393* (1), 51–57.
- (58) Mennucci, B.; Tomasi, J. Continuum solvation models: A new approach to the problem of solute's charge distribution and cavity boundaries. *J. Chem. Phys.* **1997**, *106* (12), 5151–5158.
- (59) Cancès, E.; Mennucci, B.; Tomasi, J. A new integral equation formalism for the polarizable continuum model: Theoretical background and applications to isotropic and anisotropic dielectrics. *J. Chem. Phys.* **1997**, *107* (8), 3032–3041.
- (60) Muchová, E.; Slaviček, P. Beyond Koopmans' theorem: electron binding energies in disordered materials. *J. Phys.: Condens. Matter* **2019**, *31* (4), 043001.
- (61) Frisch, M. J.; Trucks, G. W.; Schlegel, H. B.; Scuseria, G. E.; Robb, M. A.; Cheeseman, J. R.; Scalmani, G.; Barone, V.; Petersson, G. A.; Nakatsuji, H.; et al. *Gaussian 09*, revision D.01; Gaussian, Inc.: Wallingford, CT, 2016.
- (62) Pluhařová, E.; Slaviček, P.; Jungwirth, P. Modeling Photoionization of Aqueous DNA and Its Components. *Acc. Chem. Res.* **2015**, *48* (5), 1209–1217.
- (63) Gilbert, A. T. B.; Besley, N. A.; Gill, P. M. W. Self-Consistent Field Calculations of Excited States Using the Maximum Overlap Method (MOM). *J. Phys. Chem. A* **2008**, *112* (50), 13164–13171.
- (64) Shao, Y.; Gan, Z.; Epifanovsky, E.; Gilbert, A. T. B.; Wormit, M.; Kussmann, J.; Lange, A. W.; Behn, A.; Deng, J.; Feng, X.; et al. Advances in molecular quantum chemistry contained in the Q-Chem 4 program package. *Mol. Phys.* **2015**, *113* (2), 184–215.
- (65) Hollas, D.; Pohl, M. N.; Seidel, R.; Aziz, E. F.; Slaviček, P.; Winter, B. Aqueous Solution Chemistry of Ammonium Cation in the Auger Time Window. *Sci. Rep.* **2017**, *7* (1), 756.
- (66) Rappe, A. K.; Casewit, C. J.; Colwell, K. S.; Goddard, W. A.; Skiff, W. M. UFF, a full periodic table force field for molecular mechanics and molecular dynamics simulations. *J. Am. Chem. Soc.* **1992**, *114* (25), 10024–10035.
- (67) Schroeder, C. A.; Pluhařová, E.; Seidel, R.; Schroeder, W. P.; Faubel, M.; Slaviček, P.; Winter, B.; Jungwirth, P.; Bradforth, S. E. Oxidation Half-Reaction of Aqueous Nucleosides and Nucleotides via Photoelectron Spectroscopy Augmented by ab Initio Calculations. *J. Am. Chem. Soc.* **2015**, *137* (1), 201–209.
- (68) Marenich, A. V.; Ho, J.; Coote, M. L.; Cramer, C. J.; Truhlar, D. G. Computational electrochemistry: prediction of liquid-phase reduction potentials. *Phys. Chem. Chem. Phys.* **2014**, *16* (29), 15068–15106.
- (69) Thapa, B.; Schlegel, H. B. Density Functional Theory Calculation of pKa's of Thiols in Aqueous Solution Using Explicit Water Molecules and the Polarizable Continuum Model. *J. Phys. Chem. A* **2016**, *120* (28), 5726–5735.
- (70) Chai, J.-D.; Head-Gordon, M. Long-range corrected hybrid density functionals with damped atom–atom dispersion corrections. *Phys. Chem. Chem. Phys.* **2008**, *10* (44), 6615–6620.
- (71) Marenich, A. V.; Cramer, C. J.; Truhlar, D. G. Universal Solvation Model Based on Solute Electron Density and on a Continuum Model of the Solvent Defined by the Bulk Dielectric Constant and Atomic Surface Tensions. *J. Phys. Chem. B* **2009**, *113* (18), 6378–6396.
- (72) Winter, B.; Weber, R.; Widdra, W.; Dittmar, M.; Faubel, M.; Hertel, I. V. Full Valence Band Photoemission from Liquid Water Using EUV Synchrotron Radiation. *J. Phys. Chem. A* **2004**, *108* (14), 2625–2632.
- (73) Jagoda-Cwiklik, B.; Slaviček, P.; Cwiklik, L.; Nolting, D.; Winter, B.; Jungwirth, P. Ionization of Imidazole in the Gas Phase, Microhydrated Environments, and in Aqueous Solution. *J. Phys. Chem. A* **2008**, *112* (16), 3499–3505.
- (74) Jagoda-Cwiklik, B.; Slaviček, P.; Nolting, D.; Winter, B.; Jungwirth, P. Ionization of Aqueous Cations: Photoelectron Spectroscopy and ab Initio Calculations of Protonated Imidazole. *J. Phys. Chem. B* **2008**, *112* (25), 7355–7358.
- (75) Pluhařová, E.; Ončák, M.; Seidel, R.; Schroeder, C.; Schroeder, W.; Winter, B.; Bradforth, S. E.; Jungwirth, P.; Slaviček, P. Transforming Anion Instability into Stability: Contrasting Photoionization of Three Protonation Forms of the Phosphate Ion upon Moving into Water. *J. Phys. Chem. B* **2012**, *116* (44), 13254–13264.
- (76) Ghosh, D.; Roy, A.; Seidel, R.; Winter, B.; Bradforth, S.; Krylov, A. I. First-Principle Protocol for Calculating Ionization Energies and Redox Potentials of Solvated Molecules and Ions: Theory and Application to Aqueous Phenol and Phenolate. *J. Phys. Chem. B* **2012**, *116* (24), 7269–7280.
- (77) Winter, B.; Faubel, M.; Hertel, I. V.; Pettenkofer, C.; Bradforth, S. E.; Jagoda-Cwiklik, B.; Cwiklik, L.; Jungwirth, P. Electron Binding Energies of Hydrated H₃O⁺ and OH⁻: Photoelectron Spectroscopy of Aqueous Acid and Base Solutions Combined with Electronic Structure Calculations. *J. Am. Chem. Soc.* **2006**, *128* (12), 3864–3865.
- (78) Pohl, M. N.; Muchová, E.; Seidel, R.; Ali, H.; Sršň, Š.; Wilkinson, I.; Winter, B.; Slaviček, P. Do water's electrons care about electrolytes? *Chemical Science* **2019**, *10* (3), 848–865.
- (79) Cramer, C. J.; Truhlar, D. G. Quantum chemical conformational analysis of glucose in aqueous solution. *J. Am. Chem. Soc.* **1993**, *115* (13), 5745–5753.
- (80) Alonso, J. L.; Lozoya, M. A.; Peña, I.; López, J. C.; Cabezas, C.; Mata, S.; Blanco, S. The conformational behaviour of free d-glucose—at last. *Chemical Science* **2014**, *5* (2), 515–522.
- (81) Tomaník, L.; Muchová, E.; Slaviček, P. Solvation energies of ions with ensemble cluster-continuum approach. *Phys. Chem. Chem. Phys.* **2020**, *22* (39), 22357–22368.
- (82) Winter, B.; Aziz, E. F.; Hergenahn, U.; Faubel, M.; Hertel, I. V. Hydrogen bonds in liquid water studied by photoelectron spectroscopy. *J. Chem. Phys.* **2007**, *126* (12), 124504.
- (83) Campbell, J. L.; Papp, T. Widths of the atomic K–N7 levels. *At. Data Nucl. Data Tables* **2001**, *77* (1), 1–56.
- (84) Hasselbalch, K. A. Die Berechnung der Wasserstoffzahl des Blutes aus der freien und gebundenen Kohlensäure desselben, und die Sauerstoffbindung des Blutes als Funktion der Wasserstoffzahl. *Biochemische Zeitschrift* **1917**, *78*, 112–144.
- (85) Feng, S.; Bagia, C.; Mpourmpakis, G. Determination of Proton Affinities and Acidity Constants of Sugars. *J. Phys. Chem. A* **2013**, *117* (24), 5211–5219.
- (86) Molteni, C.; Parrinello, M. Glucose in Aqueous Solution by First Principles Molecular Dynamics. *J. Am. Chem. Soc.* **1998**, *120* (9), 2168–2171.
- (87) Çarçabal, P.; Jockusch, R. A.; Hünig, I.; Snoek, L. C.; Kroemer, R. T.; Davis, B. G.; Gamblin, D. P.; Compagnon, I.; Oomens, J.; Simons, J. P. Hydrogen Bonding and Cooperativity in Isolated and Hydrated Sugars: Mannose, Galactose, Glucose, and Lactose. *J. Am. Chem. Soc.* **2005**, *127* (32), 11414–11425.

(88) Suzuki, T. The hydration of glucose: the local configurations in sugar–water hydrogen bonds. *Phys. Chem. Chem. Phys.* **2008**, *10* (1), 96–105.

(89) Thürmer, S.; Malerz, S.; Trinter, F.; Hergenbahn, U.; Lee, C.; Neumark, D. M.; Meijer, G.; Winter, B.; Wilkinson, I. Accurate Vertical Ionization Energy and Work Function Determinations of Liquid Water and Aqueous Solutions. *Chem. Sci.* **2021**, DOI: 10.1039/D1SC01908B.













Paper VII





Cite this: DOI: 10.1039/d2cp00227b

Probing aqueous ions with non-local Auger relaxation†

 Geethanjali Gopakumar, ^{‡*a} Eva Muchová, ^{‡b} Isaak Unger, ^{id ac}
 Sebastian Malerz, ^{id d} Florian Trinter, ^{id de} Gunnar Öhrwall, ^{id f} Filippo Lipparini, ^{id g}
 Benedetta Mennucci, ^{id g} Denis Céolin,^h Carl Caleman, ^{id ac} Iain Wilkinson, ^{id i}
 Bernd Winter, ^{id d} Petr Slavíček, ^{id *b} Uwe Hergenbahn ^{id *d} and Olle Björneholm^a

Non-local analogues of Auger decay are increasingly recognized as important relaxation processes in the condensed phase. Here, we explore non-local autoionization, specifically Intermolecular Coulombic Decay (ICD), of a series of aqueous-phase isoelectronic cations following 1s core-level ionization. In particular, we focus on Na⁺, Mg²⁺, and Al³⁺ ions. We unambiguously identify the ICD contribution to the K-edge Auger spectrum. The different strength of the ion–water interactions is manifested by varying intensities of the respective signals: the ICD signal intensity is greatest for the Al³⁺ case, weaker for Mg²⁺, and absent for weakly-solvent-bound Na⁺. With the assistance of *ab initio* calculations and molecular dynamics simulations, we provide a microscopic understanding of the non-local decay processes. We assign the ICD signals to decay processes ending in two-hole states, delocalized between the central ion and neighbouring water. Importantly, these processes are shown to be highly selective with respect to the promoted water solvent ionization channels. Furthermore, using a core-hole-clock analysis, the associated ICD timescales are estimated to be around 76 fs for Mg²⁺ and 34 fs for Al³⁺. Building on these results, we argue that Auger and ICD spectroscopy represents a unique tool for the exploration of intra- and inter-molecular structure in the liquid phase, simultaneously providing both structural and electronic information.

 Received 14th January 2022,
Accepted 22nd March 2022

DOI: 10.1039/d2cp00227b

rsc.li/pccp

1 Introduction

The recent exploration of the molecular structure in soft condensed matter and liquids forced a revision of a number of

previously helpful paradigms and revealed novel, hitherto unobserved effects.^{1–3} In the context of the interaction of radiation and liquids, the discovery of Intermolecular Coulombic Decay^{4–6} (ICD) is probably one of the most exciting phenomena. Upon first glance, ICD shows similarities with the well-known Auger decay, however, it is a decay mechanism characteristic of condensed systems only. It takes place in an atom or molecule after an inner-valence or inner-shell vacancy is created. The vacancy is refilled with a valence electron and the released energy ionizes a neighbouring atom or molecule. The whole process leads to an energetically favourable delocalized two-hole state {Center⁺...Surrounding⁺} in contrast to an Auger decay, where a higher energy {Center²⁺} state is formed.

ICD and other non-local Auger-type processes have entered the field of X-ray science relatively recently and have primarily been discussed in the context of their role in radiation chemistry or X-ray photochemistry.^{7–9} The simultaneous ionization of neighbouring species leads to completely new reaction channels that should be considered within the overall radiolysis mechanisms.¹⁰ Non-local Auger phenomena also offer new possibilities to probe liquid-phase molecular structure, as the decay processes are highly dependent on the intermolecular distances. Some of us have already suggested that the analysis

^a Department of Physics and Astronomy, Uppsala University, Box 516, SE-751 20 Uppsala, Sweden. E-mail: geethanjali.gopakumar@physics.uu.se

^b Department of Physical Chemistry, University of Chemistry and Technology, Technická 5, Prague 6166 28, Czech Republic. E-mail: petr.slavicek@vscht.cz

^c Center for Free-Electron Laser Science, DESY, Notkestraße 85, 22607 Hamburg, Germany

^d Molecular Physics Department, Fritz-Haber-Institut der Max-Planck-Gesellschaft, Faradayweg 4-6, 14195 Berlin, Germany. E-mail: hergenbahn@fhi-berlin.mpg.de

^e Institut für Kernphysik, Goethe-Universität Frankfurt am Main, Max-von-Laue-Straße 1, 60438 Frankfurt am Main, Germany

^f MAX IV Laboratory, Lund University, Box 118, SE-22100 Lund, Sweden

^g Department of Chemistry and Industrial Chemistry, University of Pisa, Via Giuseppe Moruzzi 13, 56124 Pisa, Italy

^h Synchrotron SOLEIL, L'Orme des Merisiers, Saint-Aubin, BP 48, 91192 Gif-sur-Yvette Cedex, Paris, France

ⁱ Department of Locally-Sensitive & Time-Resolved Spectroscopy, Helmholtz-Zentrum Berlin für Materialien und Energie, 14109 Berlin, Germany

† Electronic supplementary information (ESI) available. See DOI: 10.1039/d2cp00227b

‡ These authors contributed equally to this work.



of electron spectra after autoionization of an ionic metal centre could be interpreted with respect to the environment of the respective ion.^{11,12} Moreover, in the liquid state, ICD spectra of metals involving surrounding water molecules have already been observed.^{6,13,14} In fact, the sensitivity of electronic relaxation spectra to the chemical environment of the emitter started to be discussed immediately after the discovery of ICD.^{15,16} Much like Förster energy transfer, ICD also exhibits a $1/R^6$ dependence on the intermolecular distance, R (ref. 6). The impact of ICD, however, is much broader than Förster transfer, since every atom or molecule may act as the receiving end of an inter-centre energy transfer, leading to the ejection of a secondary electron. Corresponding X-ray spectroscopies thus represent a relatively new tool to reveal liquid structure, complementing more conventional techniques such as dielectric spectroscopy or neutron scattering. Previously, the latter methods have been used in conjunction with molecular dynamics (MD) simulations to infer the arrangement of anions and cations in an electrolyte solution.¹⁷ X-ray-based spectroscopies and associated theoretical treatments represent an alternative to these well-established techniques due to their ability to directly and atom-specifically probe the electronic structure of the sample, while simultaneously delivering comparable information about the geometrical microstructure. With the combination of bright high-energy light sources, accurate electron analyzers, and liquid-microjet approaches, we can now relate the liquid structure to its signature in electron spectroscopy.¹⁸ Hand-in-hand with advances in X-ray-based experimental techniques for probing liquids' electronic structure, also the methods to simulate such structures have advanced immensely.^{19–23}

Despite the enormous interest in the non-local Auger-like decay processes in the last decade, their application to elucidate liquid-phase molecular structure remains scarce. In the cases probed so far, these non-local signatures were weak, and since LVV Auger decay was considered, they consisted of a convolution of the water and metal valence shells.^{13,24} This complicated the interpretation of the spectral signatures. In the present work, we focus on the ICD signatures in the K-shell spectra. Such measurements provide a clear-cut case: the signal should be dominated by a valence vacancy of the surrounding and an L-shell vacancy in the metal centre, with a fairly well-defined energy.

We present experimental K-shell Auger and ICD spectra of aqueous-phase Al, Mg, and Na ions, associated with AlCl_3 , MgCl_2 , and NaCl solutions. These cations were selected because they are isoelectronic but represent different types of interaction with neighbouring molecules. While the sodium cation is only weakly bound to neighbouring water molecules, dicationic magnesium is more strongly coordinated and the aluminium ion forms a regular coordination-covalent bond; the ICD signal is shown to reflect this diversity. The measurements are accompanied by molecular dynamics (MD) simulations and *ab initio* calculations, which aid in the interpretation of the experimental data and allow for an in-depth analysis of the spectra.

2 Methods

2.1 Experimental methods

The Auger and ICD electron spectra were measured using the EASI photoemission setup,²⁵ equipped with a liquid microjet and a hemispherical electron energy analyzer, at the P04 beamline of the synchrotron radiation facility PETRA III, DESY, Hamburg.²⁶ The beamline has a high on-target photon flux of about 2×10^{12} photons s^{-1} at a resolving power of 10 000, with a photon-energy tuning range spanning 250–3000 eV, and variable circular polarization.²⁷ The beamline's 1200 lines per mm grating yields a photon-energy resolution of 250 meV at 1200 eV photon energy and 350 meV at 1500 eV, using an exit-slit opening of 100 μm . At these settings, the vertical spot size amounts to approximately 35 μm . The general properties of the liquid-microjet system are described elsewhere.^{25,28} The liquid microjet of the sample solutions was introduced into the vacuum chamber using an HPLC pump at a flow rate of 0.8 ml min^{-1} with a backing pressure of ≤ 12 bar, and was directed horizontally. The glass capillary nozzle used to introduce the sample into the chamber had an inner diameter of 28 μm . The synchrotron radiation was incident perpendicular to the flow of the solution. A near-ambient-pressure hemispherical electron analyzer (Scienta Omicron HiPP-3), mounted at a 50° backward-scattering angle with respect to the beamline (near magic angle), was used to measure the electron kinetic energy.²⁵ The solutions were prepared by dissolving commercially purchased AlCl_3 , MgCl_2 , and NaCl (Sigma-Aldrich with purity $> 98\%$) salts in MilliQ ($18.2 \text{ M}\Omega \text{ cm}^{-1}$) water. Aqueous solutions of MgCl_2 and NaCl had a concentration of 1 M, while that for AlCl_3 was 2 M. At $\text{pH} \leq 4$, the aluminium is predominantly present as the aluminium hexahydrate cation ($[\text{Al}(\text{H}_2\text{O})_6]^{3+}$), *i.e.*, the Al^{3+} surrounded by six water molecules.²⁹ The utilised aluminium chloride solutions were highly acidic ($\text{pH} < 2$), which results in the exclusion of large amounts of chloride from direct contact with Al^{3+} .

The kinetic energy of the electrons produced in the decay processes, both local (Auger) and non-local (ICD), are independent of photon energy ($h\nu$). Therefore, to distinguish the decay features from the photoelectron peaks, electron spectra were measured for two photon energies differing by 3 eV in all cases. Hemispherical-electron-analyzer pass energies of 100 or 200 eV were used together with an analyzer slit width of 800 μm , leading to an estimated analyzer resolution between 0.2 and 0.4 eV.

Photon energies and kinetic energies were calibrated as detailed in the ESI,[†] in part making use of additional measurements carried out at the U49-2_PGM-1 beamline of the BESSY II synchrotron-radiation source at the Helmholtz-Zentrum Berlin für Materialien und Energie, using the SOL³PES setup for liquid-jet photoemission spectroscopy.^{28,30}

The observed ICD features were interpreted by a line-shape analysis using Voigt profiles in the SPANCF (Spectrum Analysis by Curve Fitting) macro package³¹ for Igor Pro (Wavemetrics, Inc., Lake Oswego, USA). In our case, either a 2p or 2s electron of the cation recombines with the 1s hole following direct



photoemission, and the released energy leads to the secondary emission of electrons from the water valence states. The multiplex structure of each individual ICD feature (see Fig. 2) thus arises from the release of electrons from different valence states. During the data fitting process, the kinetic energy, the intensity of the peaks, and the Gaussian width were free to vary and the Lorentzian width was considered to be that of the cation 2p orbital (see Fig. 4). The relative kinetic energy differences of these peaks are almost the same as the relative binding energies of the water valence-band peaks.³² The main KLL Auger peak notably has a higher-kinetic-energy asymmetric tail that could be modelled by a PCI (post-collision interaction) profile, as originally developed for gas-phase work.

2.2 Theoretical methods

Molecular dynamics. Classical molecular dynamics (MD) simulations were performed to sample the configurational space. MD simulations were performed for 1 M NaCl and MgCl₂, and 2 M AlCl₃ solutions to match the experimental conditions. The classical non-polarizable force fields were employed to generate large-scale structural snapshots for subsequent QM/MMPol calculations. The details of the classical MD simulations are summarized in the ESI.†

Ab initio calculations. For the *ab initio* calculations, the systems were divided into relatively small quantum (QM) and extensive molecular mechanics (MM) parts. In this work, we employed the QM/MMPol embedding scheme^{33,34} with the AMOEBA polarizable force field.^{35,36} In the polarizable force fields, each atom is described by a static point charge and an isotropic polarizability; more sophisticated force fields such as AMOEBA also contain higher multipoles. Recently, Lipparini *et al.*^{37,38} have introduced an efficient implementation for polarizable QM/MMPol based on the Fast Multipole Method,³⁹ which makes the calculation of even very large systems affordable. In our case, the MMPol part was a 20 Å-radius sphere of the respective solution surrounding the QM part. All structures were taken from classical molecular dynamics calculations. The binding energies of the aluminium cation and of a chloride anion were also checked for a 30 Å-radius sphere; the calculated values were within the error bars for smaller systems, *i.e.*, the values for a 20 Å sphere can be considered converged. The present model acknowledges the granularity of the solvent around the solute, takes into account the effect of varying ionic strength of the solutions, and allows us to control the convergence of the energetics with the increasing size of the simulation box. Importantly, the model provides an optimal treatment of electronic polarization which is instrumental for a correct description of the ionization energetics.

For the QM part, we considered two models – (1) a minimal model containing a single cation and a single water molecule (or chloride anion), (2) the first solvation-shell model containing one cation and six water molecules, which corresponds to the water coordination numbers for the investigated cations.^{40–46} The considered QM/MMPol systems are shown in Fig. 1.

The core-level energies, binding energies (BEs) and energies of the lowest two-hole final states (of a triplet multiplicity) were

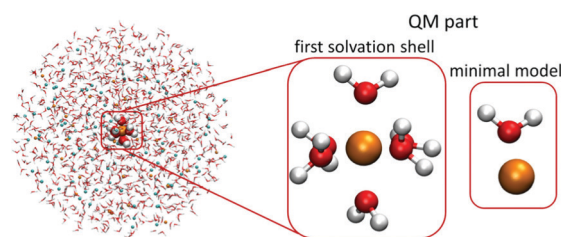


Fig. 1 Scheme of the two QM/MMPol models employed in the present study. The QM part contained one metal cation and six water molecules or one cation and one water molecule (minimal model), the remainder of the 20 Å-radius sphere was treated at the polarizable embedding MM level.

calculated by the Maximum Overlap Method (MOM).⁴⁷ This approach allows the variational convergence of states with specifically localized hole(s) with any ground-state method. In this work, we performed the MOM calculations at the LC- ω PBE level with the range-separated parameter set to a default value of 0.4 bohr⁻¹ with the cc-pCVTZ basis set for a cation and the cc-pVTZ basis set for all other atoms. We did not tune the ω parameter for particular systems or geometry since we mainly aim at pointing out the relative differences in spectra and energies.

Yet, the method has some limits, in clusters with a high density of energetically close-lying electronic states, the convergence of the MOM method can be poor. The BEs and energies of the final two-hole states were calculated for a set of 20 geometries selected from the classical molecular-dynamics simulations. The BEs were calculated as an energy difference of the ground and singly ionized states, the energies of the final two-hole states were evaluated relative to the ground state.

The valence photoemission spectra for cations and their first solvation shell were also calculated with a recently introduced ionization-as-an-excitation-into-a-distant-center (IEDC) approach.^{23,48,49} The method is based on modelling the ionization from a selected orbital space as an excitation into a continuum using time-dependent density functional theory (TDDFT), similarly as was previously suggested by Stanton and Gauß⁵⁰ as well as Coriani and Koch.⁵¹ As DFT is in principle an exact many-body theory, we can obtain correlated orbital energies. Similar to the MOM method, the IEDC approach was performed in the QM/MMPol arrangement at the same level of theory with a sodium cation as a distant centre (placed at a distance of 1000 Å from the system). Because in the QM/MMPol model the distant centre was not solvated, we shifted the excitation energies so that the lowest-energy TDDFT transition agrees with the first ionization energy of the cluster in the MMPol embedding scheme. In this setting, the choice of a sodium cation as a distant centre is arbitrary. A 200-frame set of 20 Å spheres was cut from the classical molecular dynamics, the QM part contained one cation and six neighbouring water molecules. Excitation energies were calculated at the LC- ω PBE/cc-pVTZ level; the ω parameter was set to 0.4 bohr⁻¹.

The population analysis was performed for [Al(H₂O)₆]³⁺ and [Mg(H₂O)₆]²⁺ complexes optimized at the BH&HLYP 6-31 + g* level in the polarizable continuum. The Löwdin reduced orbital



population per molecular orbital was performed in ORCA 4.2.0.⁵² All other *ab initio* calculations were performed using the locally modified current development version of Gaussian 16.⁵³ All classical MD simulations were performed with the GROMACS 5.1.2 package.^{54,55}

3 Results and discussions

Experimental manifestation of ICD

The K-shell Auger and ICD spectra investigated in this work are produced by 1s photoionization of a metal cation in the respective electrolyte. Inner-shell photoelectron spectra resulting from this primary process were measured to determine the binding energies of the respective core levels, and are shown in Fig. S3 of the ESI.† The secondary-electron spectra measured above the metal ion 1s ionization thresholds of the NaCl,

MgCl₂, and AlCl₃ aqueous solutions are the main subject of this article. In order to maximise their intensity, photon energies near the respective K-shell thresholds were chosen to measure the spectra shown in Fig. 2. The secondary-electron spectra associated with each sample were measured with two different photon energies to distinguish peaks from different processes: The kinetic energies of the primary photoelectron peaks disperse with photon energy, whereas the kinetic energies of the Auger and ICD features remain constant. For all three ions, the KLL Auger spectra are shown in the left panels and 2s⁻¹ and 2p⁻¹ photoelectron peaks are seen in the right panels of Fig. 2. In the case of Mg and Na solutions, a different baseline height (resulting from scattered electrons) was found at the two photon energies probed, probably because spectra were recorded in the proximity of the respective K-shell thresholds. To enable comparison of the ICD features, spectra were scaled and shifted on the intensity scale appropriately, which leads to most or all of the apparent difference in Mg 2p and 2s intensity for the two photon energies shown in Fig. 2b. For Na⁺, the water valence-band peaks (w⁻¹) are also in the selected kinetic energy range. Note that the Na⁺ 2p peak coincides in energy with one of the water valence-band peaks, 2a₁⁻¹. The peaks with constant kinetic energy are due to different 1s⁻¹ core-hole decay processes, which we outline in Fig. 3.

Among the peaks with constant kinetic energy, the most intense ones for all three ions are due to the local KLL Auger decay, shown in the leftmost panels of Fig. 2. The three ions are isoelectronic with configuration 1s²2s²2p⁶, which implies that their KLL Auger spectra resulting from the 1s⁻¹ → 2p⁻² + e_{Aug}⁻ decay process should be (and are) relatively similar in terms of multiplet pattern, with the two peaks in this energy range representing the ¹S and ¹D states of the 2p⁻² configuration. Similar decays ending up in 2s⁻² and 2s⁻¹2p⁻¹ states occur at lower kinetic energies, although they are not shown in Fig. 2.

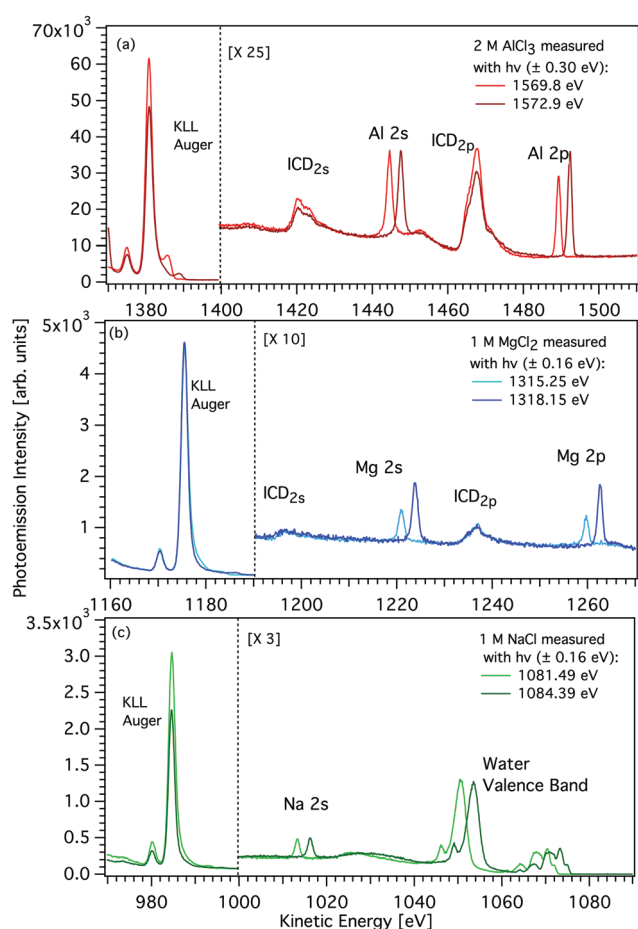


Fig. 2 Photoemission spectra of aqueous solutions of AlCl₃, MgCl₂, and NaCl (panels a–c). Two photon energies were selected and implemented slightly above the respective K-edge of the metal and the resulting spectra are compared. In each panel, the left-hand side shows the main (KLL) Auger peak, and the right-hand side photoemission peaks due to direct L-shell ionization and due to K-shell ICD involving an L-shell electron (see labels). In the case of Na, no ICD peak can be observed, and the water valence band extends into the observed spectral region. Right-hand side spectra were scaled to improve visibility. See text for details.

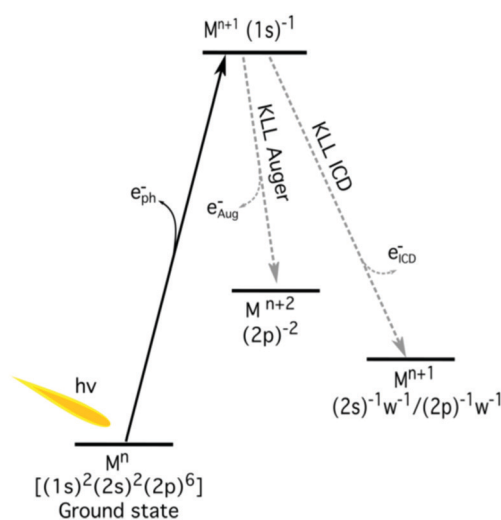


Fig. 3 The schematic energy-level diagram of the relaxation of a 1s core hole in aqueous metal (M) ions. The local decay channel (KLL Auger decay) and non-local decay (ICD) are shown. The neighbouring water molecules are indicated by 'w'.



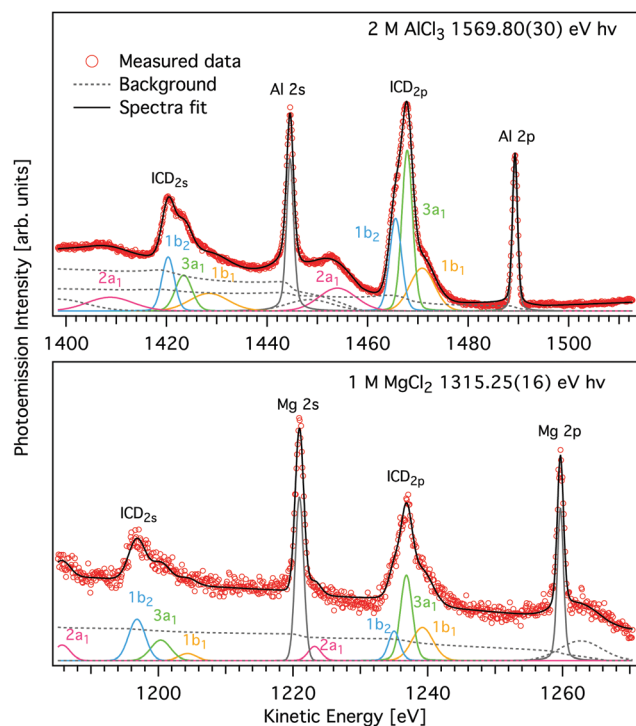


Fig. 4 Magnified view of the L-shell photoelectron and ICD peaks of AlCl_3 (upper panel) and MgCl_2 (lower panel) aqueous solutions shown in Fig. 2 (symbols). Spectra were measured with $h\nu = 1569.8$ eV and 1315.25 eV, respectively. A decomposition of the ICD features into components pertaining to final states of different energy, modelled by Voigt profiles and found by least squares curve fitting is shown by coloured traces (see text for details). Subcomponents of the ICD structure correspond to different water valence-band orbitals, namely $1b_1$ (yellow), $3a_1$ (green), $1b_2$ (blue), and $2a_1$ (purple) and appear for both ICD_{2p} and ICD_{2s} . The peak fits to the two spectra measured with higher $h\nu$ are given in Fig. S2 of the ESI†

In addition to the main KLL Auger decay, the intermediate $M 1s^{-1}$ state can also relax by filling the core hole by the electrons from the $2s$ or $2p$ orbitals and emitting an electron from one of the neighbouring molecules. This ICD process can be described as $M 1s^{-1} \rightarrow M 2s^{-1}X^{-1} + e_{\text{ICD}}^{-}$ (ICD_{2s}) or $M 1s^{-1} \rightarrow M 2p^{-1}X^{-1} + e_{\text{ICD}}^{-}$ (ICD_{2p}), with M and X designating the metal ion and a neighbouring molecule, respectively. These ICD electrons form the non-dispersing, broad, multipeak structures observed in the right-hand panels of Fig. 2 for the Mg^{2+} and Al^{3+} ions, but not for the Na^+ ions. The energetics of the former features are further discussed in the *Binding energies and ICD energies* Section of the ESI† and compiled in Table S1 (ESI†).

ICD takes place between the ion and water

We will start by examining the species involved in the ICD process. The structure of the observed ICD signal should reflect the states corresponding to charge delocalization between the central ion and a neighbouring molecule (either a water molecule, as shown in Fig. 3, or a chloride anion). We assessed the contribution of the chloride anion in the ICD spectra of Al^{3+} and Mg^{2+} with the help of MD simulations. In the case of Al^{3+} , our simulations showed only a very limited number of

$[\text{Al}(\text{H}_2\text{O})_5\text{Cl}]^{2+}$ complexes at 2 M concentration: Only 1.5% of the observed structures featured a chloride anion in the first coordination shell. The majority of these structures also contained a second chloride anion, resulting in an average coordination number for chloride in the first hydration shell of only 0.04. For Mg^{2+} , the MD simulations revealed that the fraction of contact ion pairs in solution is practically zero, in agreement with previous simulations as well as available neutron scattering and X-ray diffraction data.^{40,56–58} The sodium cation forms a limited number of contact ion pairs, however, no ICD signal was observed, preventing the study of states in which the generated charge is delocalized between the central ion and the chloride anion. In the following discussion, in accord with the above, we assume that the ICD signal observed for Mg^{2+} and Al^{3+} is dominated by water molecules in the first solvation shell.

ICD intensity depends on the metal–ligand distance

We will compare the Na^+ , Mg^{2+} , and Al^{3+} ICD spectra and focus on peak intensities next. Fig. 2 shows that the ratio of ICD intensities to the Auger signal is very different for each of the cations studied. Al^{3+} exhibits the highest relative ICD intensity, for Mg^{2+} the ICD intensity is significantly smaller, and for Na^+ the ICD peaks effectively disappear. To quantify the differences, we compare the integrated intensities of the KLL Auger peaks (final state $2p^{-2}$) to the ICD_{2p} peaks (final state $2p^{-1}w^{-1}$), *i.e.*, we determine the intensity ratio of ICD to local Auger decay. We find that the intensity ratio $I(\text{ICD}_{2p})/I(\text{KLL})$ is $\sim 0\%$ for Na^+ , $\sim 2.6\% \pm 0.5\%$ for Mg^{2+} , and $\sim 5.1\% \pm 1\%$ for Al^{3+} . The theory of ICD predicts that the intensity should be asymptotically proportional to $1/R^6$, with R being the distance between the centres. The local solvation patterns around the three metal ions can be conveniently described by MD simulations *via* radial distribution functions (see Fig. S4 in the ESI†). The peak positions for the cation–water oxygen distribution are summarized in Table 1 together with respective coordination numbers. The mean of the distance between a cation and the instantaneously closest water oxygen is also provided in Table 1 as r_{min} . These results highlight the tighter coordination of the solvent to the metal ion in going from Na^+ to Mg^{2+} to Al^{3+} . In other words, the increasing charge of the cation correlates with

Table 1 Structural parameters of the hydration shell for sodium, magnesium, and aluminium cations, according to MD simulations (this work). $+O R_{\text{max}}$ refers to the position of the first maximum in the cation–oxygen radial distribution function, $+O R_{\text{min}}$ is the position of the first minimum in that function, $+O n_{\text{O}}$ is the coordination number of water molecules, $+O r_{\text{min}}$ is the mean distance between the cation and the closest water molecule and $\pm R_{\text{max}}$ is the position of the maximum in the radial distribution function between the respective cation and a chloride anion. All distances are in Å. $\pm R_{\text{max}}$ for Mg^{2+} is not given because this species does not form ion pairs

| | Na^+ | Mg^{2+} | Al^{3+} |
|----------------------|---------------|------------------|------------------|
| $+O R_{\text{max}}$ | 2.28 | 2.04 | 1.86 |
| $+O R_{\text{min}}$ | 3.12 | 2.78 | 2.16 |
| $+O n_{\text{O}}$ | 5.58 | 6.00 | 6.00 |
| $+O r_{\text{min}}$ | 2.21 | 1.90 | 1.82 |
| $\pm R_{\text{max}}$ | 2.86 | — | 2.30 |



a decrease of the intermolecular distance between the cation and neighboring water molecules. Accordingly, based on the MD simulations, the ICD signatures should be 1.3 times more intense for Al^{3+} than for the Mg^{2+} and 3.2 times more intense than for Na^+ . These ratios are reasonably consistent with the experimentally observed values. We note that the binding of water to a sodium cation is rather loose. Hence, although a large number of water molecules surround the Na^+ ions, they barely contribute to the solute secondary ionization, *i.e.* ICD, signals.

Having discussed how the change in ion–water distance from Na^+ to Al^{3+} affects the total ICD intensity, we will now proceed to discuss a second observation related to the intensity, namely that the ICD_{2p} feature has about four times higher intensity than ICD_{2s} for both Mg^{2+} and Al^{3+} . The two processes can be schematically written as $1s^{-1} \rightarrow 2s^{-1}w^{-1} + e_{\text{ICD}}^-$ (ICD_{2s}) and $1s^{-1} \rightarrow 2p^{-1}w^{-1} + e_{\text{ICD}}^-$ (ICD_{2p}). On a qualitative level, there are two reasons for this intensity difference. First, the 2s and 2p orbitals have different numbers of electrons, six in 2p and two in 2s. The number of ICD channels involving 2p is, therefore, higher than that of 2s. Second, as we mentioned before, the ICD probability scales as $1/R^6$ and the 2s and 2p orbitals have different spatial extents which is then reflected in relative ICD probability. Moreover, different directionality of the 2s and 2p orbitals also plays a role, for example, directional 2p orbitals might be oriented more favourably for ICD than the spherically symmetric 2s orbital.

The ICD process takes tens of femtoseconds

The observed $I(\text{ICD}_{2p})/I(\text{KLL})$ intensity ratios depend on the relative branching ratios, and thus the relative timescales of the different decay channels. The $1s^{-1}$ state lifetime t_{1s} is ~ 2.3 fs for Na^+ , ~ 2.0 fs for Mg^{2+} , and ~ 1.7 fs for Al^{3+} ,⁵⁹ and we found the experimentally observed $I(\text{ICD}_{2p})/I(\text{KLL})$ intensity ratios as $\sim 0\%$ for Na^+ , $\sim 2.6\%$ for Mg^{2+} , and $\sim 5.1\%$ for Al^{3+} . This allows us to use the core-hole clock, in which the core-hole lifetime is used as an internal timescale for the secondary decay processes.^{60–63} We can then estimate the timescale for ICD as t_{1s} divided by the $I(\text{ICD}_{2p})/I(\text{KLL})$ ratio, which results in ~ 76 fs for Mg^{2+} and ~ 34 fs for Al^{3+} . The non-observation of ICD for Na^+ supports the aforementioned weaker solute–solvent interaction and suggests that the ICD process occurs much more slowly for Na^+ compared to Mg^{2+} and Al^{3+} . Similar ICD processes following 2s ionization have been reported for Na^+ , Mg^{2+} , and Al^{3+} .²⁴ By line-shape analysis of the photoemission peaks, timescales of the IC-decays following 2s ionization were found as 3.1, 1.5, and 0.98 fs for Na^+ , Mg^{2+} , and Al^{3+} , respectively. These results follow the same trend as the lifetimes in the present case of ICD following 1s ionization: The decay channel becomes more efficient with a decrease in the ion–water distance, and with increasing nuclear charge Z . On an absolute level, the timescales of ICD following 2s ionization, however, are all substantially shorter. We tentatively interpret it as a consequence of a Coster–Kronig-like process – one of the final state holes, $2p^{-1}$, is in the same shell as the primary $2s^{-1}$ hole which makes the decay much more rapid. Radial matrix

elements tabulated for the normal Auger decay of 1s and 2s holes in the metals in question do show an order of magnitude higher rate for the 2s decay.⁶⁴ Another contributing factor may be that the overlap between the water orbitals is larger with the $2s^{-1}$ hole than the $1s^{-1}$ hole.

ICD peaks reveal electronic structure of neighboring molecules

For both Mg^{2+} and Al^{3+} ions, we can see that the ICD_{2p} and ICD_{2s} channels exhibit a substructure (see Fig. 4 containing enlarged views of the Al^{3+} and Mg^{2+} ICD peaks). The final states of the two channels are $2s^{-1}w^{-1}$ and $2p^{-1}w^{-1}$, respectively. The w^{-1} hole can be produced in any of the water valence orbitals, *i.e.*, $1b_1$, $3a_1$, $1b_2$, or $2a_1$. Their shape, for the $[\text{Al}(\text{H}_2\text{O})_6]^{3+}$ complex, is exemplified in Fig. 5. The figure shows how the orientation of the orbital relative to the metal ion differs between the states. The observed substructure of the ICD peaks then corresponds to localization of the final-state hole in these different orbitals. The relative positions of the peaks used for fitting the ICD structure were found practically identical to the water valence-band peaks observed in photoemission.

The observed relative intensities of the peaks associated with the different water orbitals, however, are different for ICD_{2p} , ICD_{2s} , and the valence photoemission spectrum of the respective salt solution. (A valence-band spectrum for NaCl solution at the photon energy of our measurements is shown in the ESI,† Fig. S1.) For both Mg^{2+} and Al^{3+} , the strongest contribution in ICD_{2p} is from the water $3a_1$, followed by $1b_1$ and $1b_2$, with the $2a_1$ orbital contribution being relatively low. In ICD_{2s} , however, the $1b_2$ orbital peak has a slightly higher intensity than the $3a_1$ orbital for both ions. This shows that the ICD process selects electrons from specific molecular orbitals in a way that differs from photoemission and even depends on the orbital involved in the metal ion.

A straightforward theoretical assignment of the ICD peaks would require calculations of decay rates (*e.g.*, by means of the Fano theory^{65,66}). This is unfortunately intractable for the condensed phase. However, a hint about the observed shape of the ICD spectra can be provided by a simple orbital analysis; in our case, we selected the Löwdin population analysis. The preference for ICD electrons from specific molecular orbitals can conveniently be demonstrated for various molecular orbitals of water. The strongest ICD signal among the water molecular orbitals should arise from the $3a_1$ -type orbitals

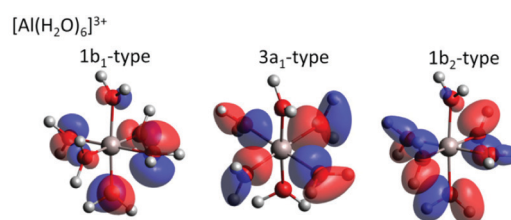


Fig. 5 Selected molecular orbitals for the $[\text{Al}(\text{H}_2\text{O})_6]^{3+}$ complex. The Löwdin reduced orbital population per molecular orbital was performed at the BH6HLYP 6-31 + g^* level in the polarizable continuum, respective molecular orbitals are depicted with an isovalue of 0.05 e.



because they are aligned along the connecting line between water oxygen and the central metal ion (typical contribution amounts to 10–11%). The percentage describes a contribution of the water molecular orbitals on a given atomic orbital of a metal atom.⁶⁷ On the contrary, the $1b_1$ -type and $1b_2$ -type orbitals are oriented perpendicular to the connecting line between water oxygen and the metal ion, which is reflected in a much smaller orbital overlap (up to 2% at maximum). Reviewing the data and fits shown in Fig. 4, the orbital-overlap analysis is consistent with the observed relative intensities of the ICD_{2p} features, but the different relative intensities of the ICD_{2s} peaks show that the nature of the metal orbital also plays an important role. This calls for further research, especially as the present results indicate that ICD spectroscopy can represent a sort of ‘orbital tomography’ – in principle, it is possible to reconstruct dominant features of orbital shapes by a careful analysis of the ICD spectra following ionization of core electrons from different atoms.

It is interesting to compare this result to earlier work on core-level de-excitation processes involving several centres. A related decay mode of core-excited states is Electron Transfer Mediated Decay (ETMD), in which the energy transfer from centre to ligand, which is characteristic for ICD, is accompanied by an *electron* transfer to the centre ionized initially. This process has been studied, *e.g.*, in the de-excitation of Li^{2+} core holes in aqueous Li^+ electrolyte solutions by some of the authors.^{11,12} Since solvated Li^+ is devoid of any valence electrons, a $1s$ core hole (with a binding energy of 60.4 eV, ref. 12) can only decay when an electron is transferred from the solvation shell. Ionization by the excess energy released in this transfer has been experimentally observed, and similar to our current results showed a propensity for creating $3a_1$ vacancies in the Li solvation shell, as found by accompanying calculations.¹¹ Since in that work a theoretical framework quite different from this article was used, a one-to-one comparison is not possible, but we consider it very plausible that in both cases the shape of the $3a_1$ orbital is particularly suited to create overlap with the core hole which lends efficiency to this particular decay channel. As ETMD involves electron transfer, it is clear that it can only proceed if orbital overlap is given. In ICD, orbital overlap plays a minor role: In principle, the decay is possible for two completely separated entities, rather overlap may accelerate a decay channel which is open in any case.^{6,68} Our work shows that this phenomenon can have an important impact on the shape of ICD spectra. This is reminiscent of results on the decay spectra of core holes in molecules featuring strongly electro-negative, *e.g.*, fluorine, ligands. Here a strong, ICD-like involvement of the ligands in the core-hole decay was seen⁶⁹ and the orbital contributions of the ligands at the core-ionized centre were even found to determine the shape of the decay spectrum in some cases.⁷⁰

Water ligands differ from bulk water

Let us now discuss to what extent the electronic structure of the water molecules in the first solvation shell is affected by a neighbouring ion. It has been observed previously^{23,71,72} that

the presence of an electrolyte has only a minor effect on the photoemission spectrum of water, even for a very high concentration of the uni-univalent electrolyte. In the valence photoemission measurements, the signal is dominated by bulk water, and the electronic structure of water molecules in the first solvation shell is very difficult to identify. In contrast, the ICD process involves practically only water molecules in the first solvation shell of the core-ionized cation. This opens up the possibility to selectively probe the electronic structure of these bound water molecules, to see how they differ from bulk water. Here, we compare the valence photoemission spectrum of bulk water and photoemission spectra of the water molecules in the first solvation shell, as simulated by the IEDC technique.

The calculated valence photoemission spectra of pure water and water molecules directly coordinated to the cations are shown in Fig. 6, the respective peak positions are collected in Table S5 of the ESI.† It can be seen that the calculations reproduce the experimental binding energies for pure water within tenths of eV. We can observe that the cations significantly influence the binding energies of the closest water molecules. For the magnesium cation, the binding energies are shifted towards higher values (by about 0.3–0.5 eV), and the effect of the aluminium cation is even stronger, the values are shifted by about 0.6–1.3 eV. In both cases, the six water molecules forming the solvation shell are more strongly bound to the cation than to another water molecule. In the case of aluminium, the $3a_1$ peak forms a double-peak structure, the interpretation of which is unclear. Such an increase of binding energies can be expected by taking into account the electric field of a (positively charged) metal ion. This claim, however, is too simplistic, as the sodium cation exhibits the opposite effect. For Na^+ , the energies are shifted towards lower energies by

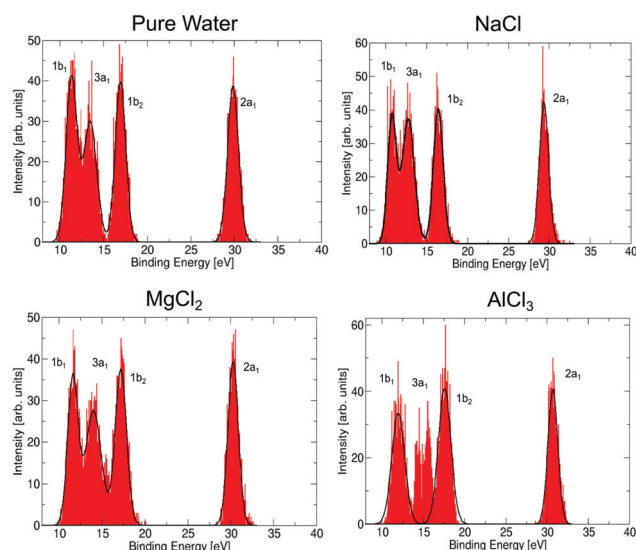


Fig. 6 Simulated photoemission spectrum for pure water, and for water molecules directly coordinated to a metal cation in NaCl, $MgCl_2$, and $AlCl_3$ solutions. Spectra were calculated by the QM/MMPol IEDC approach at the LC- ω PBE/cc-pVTZ level.



0.5–0.7 eV because Na⁺ ‘breaks’ the structure of liquid water, *e.g.*, it forms weaker bonds with water.⁷³ Note that the shift in binding energies of water in the solvation shell, $\Delta E_{b,vi}$ should be taken into account in the theoretical interpretation of ICD spectra, *e.g.*, experimental values for water valence-band peaks should not be used.

Energetics of the ICD process

We now further discuss the energetics of the ICD process, $M 1s^{-1} \rightarrow M 2s/2p^{-1}w^{-1} + e_{ICD}^{-}$. As can be seen in Fig. 3, the kinetic energy of the ICD electron upon 1s ionization (E_k) can be expressed as the difference between the intermediate $M 1s^{-1}$ (E_{1s}) and $M 2s^{-1}/2p^{-1}w^{-1}$ two-hole final state energies (E_{2h})

$$E_k = E_{1s} - E_{2h}. \quad (1)$$

We can obtain the energy of the final two-hole states from the experimental data as

$$E_{2h} = E_{1s} - E_k. \quad (2)$$

The resulting two-hole energies for both the Auger and ICD final states of Mg²⁺ and Al³⁺ are shown in Fig. 7 and collected in Tables S2 and S3 in the ESI.† For Mg²⁺ (Al³⁺), the experimentally obtained two-hole energies are seen to decrease from 134 (187) eV for the localized 2p⁻² final states of the Auger decay to 70 (96) eV for 2p⁻¹1b₁⁻¹, the lowest delocalized two-hole state reached in the ICD process. This decrease in energy is an important driving force for the ICD process, and for the localized 2p⁻² final states this has been predicted to lead to secondary delocalization *via* the ETMD processes.⁷⁴

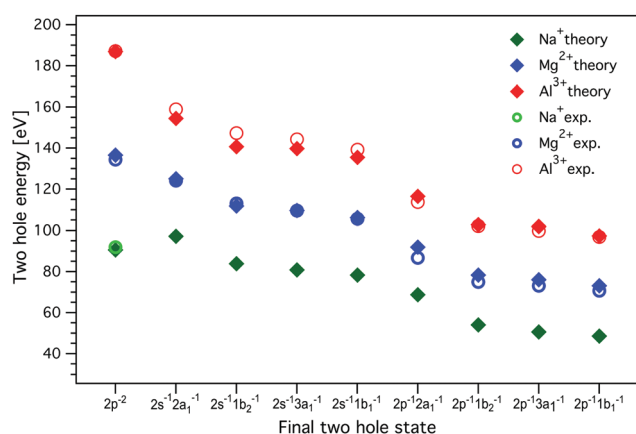


Fig. 7 The energies of the two-hole ICD final states for Al³⁺, Mg²⁺, and Na⁺. The experimental values, measured with 1569.8 eV and 1315.25 eV photon energies for Al³⁺ and Mg²⁺, respectively, were determined from the curve fitting of the measured spectra. MOM/LC- ω PBE/cc-pVTZ (with cc-cPVTZ basis for the cation) energies were obtained for a minimal model containing one cation and one water molecule; the dimer was solvated by a 20 Å sphere of molecules treated at the MMPol level. The values of experimental and calculated energies are collected in Tables S2, S3, and S6 in the ESI.† Experimental errors are approximately equal to or smaller than the symbol size. No experimental values for delocalized final states are given for Na⁺, as ICD leading to the respective two-hole states could not be observed.

To quantitatively understand this energy lowering, we can conceptually decompose the energy of the final two-hole states into three contributions

$$E_{2h} = E_{b,v1} + E_{b,v2} + E_{Cp}, \quad (3)$$

where $E_{b,vi}$ is the binding energy of the i^{th} electron participating in this process and E_{Cp} is the Coulomb penalty, which can be understood as the electrostatic potential energy of the positively charged metal and water ions in a close proximity. The values of $E_{b,vi}$ and E_{Cp} are not directly experimentally accessible; the experiment provides bulk water valence-band peaks only. Ignoring this difference, the Coulomb penalty is generally found in the range of 3–6 eV, with a tendency towards somewhat lower values if states of s-character are involved. This is in contrast with the Coulomb penalty found for the ETMD process following the Li⁺ ionization where the Coulomb penalty was found to be very small.¹¹

Theoretically, we model the energetics with the MOM approach in the minimal model containing one cation and one water molecule for Na⁺, Mg²⁺, and Al³⁺ in a polarizable embedding. In this way, we obtain the binding energies of the i^{th} electron $E_{b,vi}$, the two-hole state energies, and the Coulomb penalty. The calculated energies are presented in Fig. 7 and collected in Tables S2 and S3 in the ESI.†

As seen in Fig. 7, the calculations reproduce the experimental values for the final two-hole energies for Mg²⁺ and Al³⁺ very well. It is important to note here that the calculated E_{2h} values correspond to the low-energy onset of the fitted ICD peaks (the MOM approach provides only the energies of the lowest triplet two-hole states). For Mg²⁺ and Al³⁺, the Coulomb penalty is found in the range 4–6 eV, which is reasonably consistent with the experimental estimate.

For Na⁺, there are no experimental values since we did not observe any ICD-related spectral features, but based on the good agreement between the calculation including solvation and experiment for Mg²⁺ and Al³⁺, we can use the calculated values for Na⁺. One interesting observation is that the energy difference between the localized 2p⁻² final state to the delocalized 2p⁻¹w⁻¹ states is much smaller for Na⁺ than for Mg²⁺ and Al³⁺. If we regard this lowering of the two-hole state energy as a driving force for the ICD process, this may be another reason why ICD is less efficient for Na⁺ than for Mg²⁺ and Al³⁺.

As can be inferred from Table S6 in the ESI,† the theoretically predicted Coulomb penalty E_{Cp} is higher for Al³⁺ and Mg²⁺ than for Na⁺, which is due to the formation of highly charged pairs of Al⁴⁺ H₂O⁺ and Mg³⁺ H₂O⁺ compared to Na²⁺ H₂O⁺ as the final ICD states. The energy difference between the ions is however rather minor, most probably due to a large amount of screening by the surrounding water.

Screening effects of water

The two-hole energies for the minimal system in the gas phase are collected in Table S8 in the ESI,† respective one-electron binding energies are provided in Table S9 (ESI†). These energies exhibit the same trend for energy lowering upon delocalization as the minimal system with solvation, but the absolute



two-hole energies are much higher, ≈ 20 eV for Na^+ , ≈ 40 eV for Mg^{2+} , and ≈ 60 eV for Al^{3+} . These large differences observed in the gas phase further highlight the huge screening effect of water, which minimizes the Coulomb penalty and the binding-energy shifts. The Coulomb penalty in the gas phase is a factor 1.5–2 larger than in solution; the binding-energy shifts are around 7 eV for Na^+ , 15 eV for Mg^{2+} , and more than 20 eV for Al^{3+} in the gas phase compared to less than 1.3 eV in the aqueous phase. The large reduction of the two-hole energies illustrates the importance of including the solvent effects when considering the energetics of ICD.

4 Conclusions

X-ray photoemission spectroscopy, molecular dynamics, and *ab initio* calculations have been combined to investigate ICD channels during the decay of 1s core holes in aqueous-phase Al^{3+} , Mg^{2+} , and Na^+ in chloride solutions. We observed two individual ICD features originating from the relaxation involving either the 2s or 2p levels of the cations and mostly water valence states. Importantly, each of these features displays a substructure, which has been shown to originate from the participation of different water valence orbitals. According to our calculations and the analysis of our data, transitions including the water $3a_1$ level contribute the largest share of the overall ICD signal. This is caused by the orbital overlap between the water valence states and the cation. The orientation of the water molecules toward the cation enhances the orbital overlap of the water $3a_1$ orbital, whereas the water $1b_1$ and $1b_2$ orbital overlaps are disfavoured. However, ICD channels that lead to $1b_2$ orbital emission appear to be favoured in the specific cases of Mg^{2+} and Al^{3+} ICD_{2s} processes relative to ICD_{2p}, indicating that also the electronic structure of the core-hole-excited species plays a role. If chloride is present in the first solvation shell (forming a contact ion pair), we expect a significant overlap of one of the Cl^- 2p orbitals, too. However, according to our calculations and the experimental data, this is rarely the case. Contributions from Cl^- states were not discernable in the experiments.

The charge of the cation has been found to have a profound impact on the overall strength of the ICD transitions. For example, the higher the charge on the cation, the stronger the ICD signal. ICD is pronounced in the decay of 1s holes in Al^{3+} and Mg^{2+} , while only Auger decay is observable in Na^+ . The enhancement of the ICD signal with the charge of the cation reflects the intermolecular distances between the cation and the water molecules in the first solvation shell, as ICD scales with $1/R^6$, with R being the distance between the interacting entities (see entries r_{min} in Tab. 1 for calculated, averaged values). Accordingly, the strongest ICD_{2p}/Auger branching ratio could be determined for Al^{3+} with about $\sim 5\%$ relative ICD efficiency. This number is about a factor of 10 higher than ICD rates, *e.g.*, in Ar clusters.⁷⁵ A $\sim 5\%$ intensity ratio also allows us to estimate the timescale of the ICD_{2p} transition to about 34 fs, based on the core-hole lifetime in Al 1s of about 1.7 fs.

Note that this is about 20 times slower than the ICD decay of much shallower Al 2s holes.¹⁴

We have shown that the substructure of ICD spectra hinges on the electronic structure of the valence levels of the partner species during the de-excitation. One may regard the ICD spectrum as a projection of the valence states, but with the relative intensities and peak widths modified by the orbital overlap and the geometry of the reaction partners. If used under this premise, ICD can serve as a quasi-tomographic tool to explore the combined electronic structure and local geometry of aqueous solutes and their first hydration shell simultaneously.

From a radiation-chemistry perspective it is interesting to follow the further relaxation of the ICD final state. We provide a speculative outlook here: A Coulomb explosion will immediately follow the ICD in the gas phase⁶ and in aggregates of inert species.⁷⁶ However, we suggest that the process is more complicated in the liquid phase. An ionized water molecule, H_2O^+ , is an extremely short-lived species; in less than 50 fs, H_2O^+ gives up a proton to another water molecule, forming H_3O^+ and a hydroxyl radical.⁷⁷ Besides, we can speculate that a charge transfer from another water molecule to the metal cation might follow;⁷⁴ this process would give rise to another ionized water molecule and another proton transfer would follow. The overall result would then be formation of two OH radicals and two H_3O^+ , which would later slowly diffuse.

Data Availability

Data relevant for this study are available at DOI: 10.5281/zenodo.6372662.

Author contributions

G. G. and O. B. conceived the project, G. G., S. M., F. T., I. W., O. B., and B. W. performed the experiments, G. G., I. U., G. Ö. and U. H. analyzed the data, E. M. and P. S. performed all the *ab initio* calculations, B. M. and F. L. adjusted and implemented MOM into the polarizable force field, G. G., E. M., P. S., O. B., and U. H. wrote the manuscript that was discussed by all authors.

Conflicts of interest

The authors declare no competing financial interest.

Acknowledgements

The authors would like to thank Chin Lee, Dana Bloß, Karen Mudryk, Wilson Quevedo, Tillmann Buttersack, and Clemens Richter for their help in data acquisition, and Robert Seidel for his help with the SOL³PES setup. We acknowledge DESY (Hamburg, Germany), a member of the Helmholtz Association HGF, for the provision of experimental facilities. Parts of this research were carried out at PETRA III and we would like to



thank Moritz Hoesch and his team for assistance in using beamline P04. We also thank HZB for the allocation of synchrotron-radiation beamtime. F. T. and B. W. acknowledge support by the MaxWater initiative of the Max-Planck-Gesellschaft. B. W. acknowledges funding from the European Research Council (ERC) under the European Union's Horizon 2020 research and innovation program under grant agreement No. 883759. P. S. and E. M. thank the Czech Science Foundation for the support *via* project number 21-26601X (EXPRO project). E. M. acknowledges that the research leading to the results was supported by the European Structural and Investment Funds, OP RDE-funded project 'CHEMFELLS III' (CZ.02.2.69/0.0/0.0/19_074/0014006) funding her MCSA-IF proposal. O. B. acknowledges funding from the Swedish Research Council (VR) for the project VR 2017-04162. C. C. acknowledges the Swedish Research Council, project 2018-00740, and the Helmholtz Association through the Center for Free-Electron Laser Science at DESY. Open Access funding provided by the Max Planck Society.

Notes and references

- P. Jungwirth and D. J. Tobias, *Chem. Rev.*, 2006, **106**, 1259–1281.
- N. F. A. van der Vegt, K. Haldrup, S. Roke, J. Zheng, M. Lund and H. J. Bakker, *Chem. Rev.*, 2016, **116**, 7626–7641.
- O. Björneholm, M. H. Hansen, A. Hodgson, L.-M. Liu, D. T. Limmer, A. Michaelides, P. Pedevilla, J. Rossmeisl, H. Shen, G. Tocci, E. Tyrode, M.-M. Walz, J. Werner and H. Bluhm, *Chem. Rev.*, 2016, **116**, 7698–7726.
- L. S. Cederbaum, J. Zobeley and F. Tarantelli, *Phys. Rev. Lett.*, 1997, **79**, 4778.
- S. Marburger, O. Kugeler, U. Hergenbahn and T. Möller, *Phys. Rev. Lett.*, 2003, **90**, 203401.
- T. Jahnke, U. Hergenbahn, B. Winter, R. Dörner, U. Fröhling, P. V. Demekhin, K. Gokhberg, L. S. Cederbaum, A. Ehresmann, A. Knie and A. Dreuw, *Chem. Rev.*, 2020, **120**, 11295–11369.
- K. Gokhberg, P. Kolorenč, A. I. Kuleff and L. S. Cederbaum, *Nature*, 2014, **505**, 661–663.
- F. Trinter, M. S. Schöffler, H.-K. Kim, F. P. Sturm, K. Cole, N. Neumann, A. Vredenburg, J. Williams, I. Bocharova, R. Guillemin, M. Simon, A. Belkacem, A. L. Landers, T. Weber, H. Schmidt-Böcking, R. Dörner and T. Jahnke, *Nature*, 2014, **505**, 664–666.
- P. Slaviček, N. V. Kryzhevoi, E. F. Aziz and B. Winter, *J. Phys. Chem. Lett.*, 2016, **7**, 234–243.
- S. Thürmer, M. Ončák, N. Ottosson, R. Seidel, U. Hergenbahn, S. E. Bradforth, P. Slaviček and B. Winter, *Nat. Chem.*, 2013, **5**, 590–596.
- I. Unger, R. Seidel, S. Thürmer, M. N. Pohl, E. F. Aziz, L. S. Cederbaum, E. Muchová, P. Slaviček, B. Winter and N. V. Kryzhevoi, *Nat. Chem.*, 2017, **9**, 708–714.
- M. N. Pohl, C. Richter, E. Lugovoy, R. Seidel, P. Slaviček, E. F. Aziz, B. Abel, B. Winter and U. Hergenbahn, *J. Phys. Chem. B*, 2017, **121**, 7709–7714.
- W. Pokapanich, H. Bergersen, I. L. Bradeanu, R. R. T. Marinho, A. Lindblad, S. Legendre, A. Rosso, S. Svensson, O. Björneholm, M. Tchapyguine, G. Öhrwall, N. V. Kryzhevoi and L. S. Cederbaum, *J. Am. Chem. Soc.*, 2009, **131**, 7264–7271.
- N. Ottosson, G. Öhrwall and O. Björneholm, *Chem. Phys. Lett.*, 2012, **543**, 1–11.
- S. Barth, S. Marburger, S. Joshi, V. Ulrich, O. Kugeler and U. Hergenbahn, *Phys. Chem. Chem. Phys.*, 2006, **8**, 3218–3222.
- E. Fasshauer, M. Förstel, S. Pallmann, M. Pernpointner and U. Hergenbahn, *New J. Phys.*, 2014, **16**, 103026.
- A. A. Chialvo and L. Vlcek, *Fluid Phase Equilib.*, 2016, **407**, 84–104.
- B. Winter and M. Faubel, *Chem. Rev.*, 2006, **106**, 1176–1211.
- B. Winter, R. Weber, I. V. Hertel, M. Faubel, P. Jungwirth, E. C. Brown and S. E. Bradforth, *J. Am. Chem. Soc.*, 2005, **127**, 7203–7214.
- D. Ghosh, A. Roy, R. Seidel, B. Winter, S. Bradforth and A. I. Krylov, *J. Phys. Chem. B*, 2012, **116**, 7269–7280.
- A. P. Gaiduk, M. Govoni, R. Seidel, J. H. Skone, B. Winter and G. Galli, *J. Am. Chem. Soc.*, 2016, **138**, 6912–6915.
- T. A. Pham, M. Govoni, R. Seidel, S. E. Bradforth, E. Schwegler and G. Galli, *Sci. Adv.*, 2017, **3**, e1603210.
- M. N. Pohl, E. Muchová, R. Seidel, H. Ali, Š. Sršeň, I. Wilkinson, B. Winter and P. Slaviček, *Chem. Sci.*, 2019, **10**, 848–865.
- G. Öhrwall, N. Ottosson, W. Pokapanich, S. Legendre, S. Svensson and O. Björneholm, *J. Phys. Chem. B*, 2010, **114**, 17057–17061.
- S. Malerz, H. Haak, F. Trinter, A. B. Stephansen, C. Kolbeck, M. Pohl, U. Hergenbahn, G. Meijer and B. Winter, *Rev. Sci. Instrum.*, 2022, **93**, 015101.
- J. Viefhaus, F. Scholz, S. Deinert, L. Glaser, M. Ilchen, J. Seltmann, P. Walter and F. Siewert, *Nucl. Instrum. Methods Phys. Res., Sect. A*, 2013, **710**, 151–154.
- P04 beamline parameters, https://photon-science.desy.de/facilities/petra_iii/beamlines/p04_xuv_beamline/beamline_parameters/index_eng.html, Accessed: 2021-09-23.
- R. Seidel, M. N. Pohl, H. Ali, B. Winter and E. F. Aziz, *Rev. Sci. Instrum.*, 2017, **88**, 073107.
- J. Duan and J. Gregory, *Adv. Colloid Interface Sci.*, 2003, **100–102**, 475–502.
- Helmholtz-Zentrum Berlin für Materialien und Energie, *Journal of Large-Scale Research Facilities*, 2016, **2**, A72.
- E. Kukk, *Spectrum Analysis by Curve Fitting (SPANCF) macro package for Igor Pro*, 2012.
- B. Winter, R. Weber, W. Widdra, M. Dittmar, M. Faubel and I. V. Hertel, *J. Phys. Chem. A*, 2004, **108**, 2625–2632.
- D. Loco, É. Polack, S. Caprasecca, L. Lagardère, F. Lipparini, J.-P. Piquemal and B. Mennucci, *J. Chem. Theory Comput.*, 2016, **12**, 3654–3661.
- M. Bondanza, M. Nottoli, L. Cupellini, F. Lipparini and B. Mennucci, *Phys. Chem. Chem. Phys.*, 2020, **22**, 14433–14448.
- J. W. Ponder, C. Wu, P. Ren, V. S. Pande, J. D. Chodera, M. J. Schnieders, I. Haque, D. L. Mobley, D. S. Lambrecht, R. A. DiStasio, Jr., M. Head-Gordon, G. N. I. Clark,



- M. E. Johnson and T. Head-Gordon, *J. Phys. Chem. B*, 2010, **114**, 2549–2564.
- 36 P. Ren and J. W. Ponder, *J. Phys. Chem. B*, 2003, **107**, 5933–5947.
- 37 F. Lipparini, L. Lagardère, C. Raynaud, B. Stamm, E. Cancès, B. Mennucci, M. Schnieders, P. Ren, Y. Maday and J.-P. Piquemal, *J. Chem. Theory Comput.*, 2015, **11**, 623–634.
- 38 F. Lipparini, *J. Chem. Theory Comput.*, 2019, **15**, 4312–4317.
- 39 L. Greengard and V. Rokhlin, *J. Comput. Phys.*, 1987, **73**, 325–348.
- 40 E. Duboué-Dijon, P. E. Mason, H. E. Fischer and P. Jungwirth, *J. Phys. Chem. B*, 2018, **122**, 3296–3306.
- 41 E. Cauët, S. A. Bogatko, E. J. Bylaska and J. H. Weare, *Inorg. Chem.*, 2012, **51**, 10856–10869.
- 42 T. S. Hofer, B. R. Randolph and B. M. Rode, *J. Phys. Chem. B*, 2008, **112**, 11726–11733.
- 43 I. S. Joung and T. E. Cheatham, *J. Phys. Chem. B*, 2008, **112**, 9020–9041.
- 44 G. Lamoureux and B. Roux, *J. Phys. Chem. B*, 2006, **110**, 3308–3322.
- 45 H. Yu, T. W. Whitfield, E. Harder, G. Lamoureux, I. Vorobyov, V. M. Anisimov, A. D. MacKerell, Jr. and B. Roux, *J. Chem. Theory Comput.*, 2010, **6**, 774–786.
- 46 Y. Marcus, *Chem. Rev.*, 1988, **88**, 1475–1498.
- 47 A. T. B. Gilbert, N. A. Besley and P. M. W. Gill, *J. Phys. Chem. A*, 2008, **112**, 13164–13171.
- 48 M. Rubešová, E. Muchová and P. Slavíček, *J. Chem. Theory Comput.*, 2017, **13**, 4972–4983.
- 49 E. Muchová and P. Slavíček, *J. Phys.: Condens. Matter*, 2019, **31**, 043001.
- 50 J. F. Stanton and J. Gauss, *J. Chem. Phys.*, 1999, **111**, 8785–8788.
- 51 S. Coriani and H. Koch, *J. Chem. Phys.*, 2015, **143**, 181103.
- 52 F. Neese, *Wiley Interdiscip. Rev.: Comput. Mol. Sci.*, 2018, **8**, e1327.
- 53 M. J. Frisch, G. W. Trucks, H. B. Schlegel, G. E. Scuseria, M. A. Robb, J. R. Cheeseman, G. Scalmani, V. Barone, G. A. Petersson, H. Nakatsuji, X. Li, M. Caricato, A. V. Marenich, J. Bloino, B. G. Janesko, R. Gomperts, B. Mennucci, H. P. Hratchian, J. V. Ortiz, A. F. Izmaylov, J. L. Sonnenberg, D. Williams-Young, F. Ding, F. Lipparini, F. Egidi, J. Goings, B. Peng, A. Petrone, T. Henderson, D. Ranasinghe, V. G. Zakrzewski, J. Gao, N. Rega, G. Zheng, W. Liang, M. Hada, M. Ehara, K. Toyota, R. Fukuda, J. Hasegawa, M. Ishida, T. Nakajima, Y. Honda, O. Kitao, H. Nakai, T. Vreven, K. Throssell, J. A. Montgomery, Jr., J. E. Peralta, F. Ogliaro, M. J. Bearpark, J. J. Heyd, E. N. Brothers, K. N. Kudin, V. N. Staroverov, T. A. Keith, R. Kobayashi, J. Normand, K. Raghavachari, A. P. Rendell, J. C. Burant, S. S. Iyengar, J. Tomasi, M. Cossi, J. M. Millam, M. Klene, C. Adamo, R. Cammi, J. W. Ochterski, R. L. Martin, K. Morokuma, O. Farkas, J. B. Foresman and D. J. Fox, *Gaussian Development Version Revision J.06+*, Gaussian Inc., Wallingford CT, 2020.
- 54 M. J. Abraham, T. Murtola, R. Schulz, S. Páll, J. C. Smith, B. Hess and E. Lindahl, *SoftwareX*, 2015, **1-2**, 19–25.
- 55 S. Pronk, S. Páll, R. Schulz, P. Larsson, P. Bjelkmar, R. Apostolov, M. R. Shirts, J. C. Smith, P. M. Kasson, D. van der Spoel, B. Hess and E. Lindahl, *Bioinformatics*, 2013, **29**, 845–854.
- 56 S. Friesen, G. Hefter and R. Buchner, *J. Phys. Chem. B*, 2019, **123**, 891–900.
- 57 K. M. Callahan, N. N. Casillas-Ituarte, M. Roeselová, H. C. Allen and D. J. Tobias, *J. Phys. Chem. A*, 2010, **114**, 5141–5148.
- 58 F. Bruni, S. Imberti, R. Mancinelli and M. A. Ricci, *J. Chem. Phys.*, 2012, **136**, 064520.
- 59 J. Campbell and T. Papp, *At. Data Nucl. Data Tables*, 2001, **77**, 1–56.
- 60 O. Björneholm, A. Nilsson, A. Sandell, B. Hernnäs and N. Mårtensson, *Phys. Rev. Lett.*, 1992, **68**, 1892–1895.
- 61 W. Wurth and D. Menzel, *Chem. Phys.*, 2000, **251**, 141–149.
- 62 P. A. Brühwiler, O. Karis and N. Mårtensson, *Rev. Mod. Phys.*, 2002, **74**, 703–740.
- 63 A. Föhlisch, P. Feulner, F. Hennies, A. Fink, D. Menzel, D. Sanchez-Portal, P. M. Echenique and W. Wurth, *Nature*, 2005, **436**, 373–376.
- 64 M. H. Chen, F. P. Larkins and B. Crasemann, *At. Data Nucl. Data Tables*, 1990, **45**, 1–205.
- 65 U. Fano, *Phys. Rev.*, 1961, **124**, 1866–1878.
- 66 H. Feshbach, *Rev. Mod. Phys.*, 1964, **36**, 1076–1078.
- 67 P.-O. Löwdin, *J. Chem. Phys.*, 1950, **18**, 365–375.
- 68 V. Averbukh, I. B. Müller and L. S. Cederbaum, *Phys. Rev. Lett.*, 2004, **93**, 263002.
- 69 T. D. Thomas, C. Miron, K. Wiesner, P. Morin, T. X. Carroll and L. J. Saethre, *Phys. Rev. Lett.*, 2002, **89**, 223001.
- 70 F. O. Gottfried, L. S. Cederbaum and F. Tarantelli, *J. Chem. Phys.*, 1996, **104**, 9754–9767.
- 71 S. Thürmer, S. Malerz, F. Trinter, U. Hergenhahn, C. Lee, D. M. Neumark, G. Meijer, B. Winter and I. Wilkinson, *Chem. Sci.*, 2021, **12**, 10558–10582.
- 72 B. Credidio, M. Pugini, S. Malerz, F. Trinter, U. Hergenhahn, I. Wilkinson, S. Thürmer and B. Winter, *Phys. Chem. Chem. Phys.*, 2022, **24**, 1310–1325.
- 73 I. Waluyo, C. Huang, D. Nordlund, U. Bergmann, T. M. Weiss, L. G. M. Pettersson and A. Nilsson, *J. Chem. Phys.*, 2011, **134**, 064513.
- 74 V. Stumpf, K. Gokhberg and L. S. Cederbaum, *Nat. Chem.*, 2016, **8**, 237–241.
- 75 A. Hans, C. Küstner-Wetekam, P. Schmidt, C. Ozga, X. Holzapfel, H. Otto, C. Zindel, C. Richter, L. S. Cederbaum, A. Ehresmann, U. Hergenhahn, N. V. Kryzhevoi and A. Knie, *Phys. Rev. Res.*, 2020, **2**, 012022(R).
- 76 F. Wiegandt, F. Trinter, K. Henrichs, D. Metz, M. Pitzer, M. Waitz, E. Jabbour al Maalouf, C. Janke, J. Rist, N. Wechselberger, T. Miteva, S. Kazandjian, M. Schöffler, N. Sisourat, T. Jahnke and R. Dörner, *Phys. Rev. A*, 2019, **100**, 022707.
- 77 Z.-H. Loh, G. Doumy, C. Arnold, L. Kjellsson, S. H. Southworth, A. Al Haddad, Y. Kumagai, M.-F. Tu, P. J. Ho, A. M. March, R. D. Schaller, M. S. Bin Mohd Yusof, T. Debnath, M. Simon, R. Welsch, L. Inhester, K. Khalili, K. Nanda, A. I. Krylov, S. Moeller, G. Coslovich, J. Koralek, M. P. Minitti, W. F. Schlotter, J.-E. Rubensson, R. Santra and L. Young, *Science*, 2020, **367**, 179–182.



Paper VIII



Imaging of Chemical Kinetics at the Water–Water Interface in a Free-Flowing Liquid Flat-Jet

H. Christian Schewe,[#] Bruno Credidio,[#] Aaron M. Ghrist,[#] Sebastian Malerz, Christian Ozga, André Knie, Henrik Haak, Gerard Meijer, Bernd Winter, and Andreas Osterwalder^{*}



Cite This: *J. Am. Chem. Soc.* 2022, 144, 7790–7795



Read Online

ACCESS |



Metrics & More



Article Recommendations



Supporting Information

ABSTRACT: We present chemical kinetics measurements of the luminol oxidation chemiluminescence (CL) reaction at the interface between two aqueous solutions, using liquid jet technology. Free-flowing liquid microjets are a relatively recent development that have found their way into a growing number of applications in spectroscopy and dynamics. A variant thereof, called flat-jet, is obtained when two cylindrical jets of a liquid are crossed, leading to a chain of planar leaf-shaped structures of the flowing liquid. We here show that in the first leaf of this chain, the fluids do not exhibit turbulent mixing, providing a clean interface between the liquids from the impinging jets. We also show, using the example of the luminol CL reaction, how this setup can be used to obtain kinetics information from friction-less flow and by circumventing the requirement for rapid mixing by intentionally suppressing all turbulent mixing and instead relying on diffusion.



INTRODUCTION

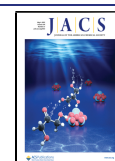
Fast-flowing liquid microjets are a powerful tool for the preparation of volatile liquids, including water, even in high-vacuum environments.^{1–5} They recently gained much interest in particular for in-vacuum applications, where the jet travels freely for some millimeters before decaying into droplets and freezing. One of the prime factors that make them interesting tools is the free flow through air or vacuum, which permits unobstructed optical access to a liquid and thus enables a wide range of spectroscopic detections that are incompatible with many solid container materials. Recent applications include X-ray photoelectron spectroscopy,^{1,6–14} evaporation dynamics,^{15–21} attosecond-pulse generation,^{22,23} and liquid–gas scattering.^{24,24,25} The most common implementation is a single cylindrical jet, obtained by forcing a liquid at a pressure of a few bars through a 10–50 μm -diameter nozzle, which results in a laminar jet with a flow velocity of tens of m/s.

Many experiments demand a planar surface in order to avoid unwanted averaging over effects resulting from the angle-dependent surface normal.^{24,26} Different arrangements exist to produce laminar-flow planar surfaces,^{27,28} among which a widely used setup is the crossing and impinging of two cylindrical jets.²⁹ For a large enough Reynolds number, this produces a chain of few-micron-thin leaf-shaped sheets, each bound by a relatively thick fluid rim and stabilized by an interplay of surface tension and fluid inertia. More specifically, at the crossing point of the two cylindrical jets, the aqueous solution is pushed outwards, continuing to move in an overall forward direction. However, this outward motion is counteracted by the solutions' surface tension, such that after some distance the outer boundaries of this structure merge. The resulting flow leads to a fluid chain of mutually orthogonal, thin, linked, and stable leaf-shaped sheets bound by relatively

thick fluid rims, each providing a planar water surface.³⁰ Individual links in the chain decrease successively in size until the chain coalesces into a cylindrical stream through the action of viscosity. Whether or not stable sheets can be generated, or sheets rather destabilize, break, or disintegrate into a spray of droplets is governed by surface tension, viscous, inertial, and aerodynamic forces.³¹ Consecutive sheet planes are perpendicular to each other. The stability and geometry of this structure are governed by solution properties such as surface tension and viscosity and by controlled parameters such as the flow rate and jet diameter.^{29,31} An important question about such objects is whether the first leaf of the chain contains a turbulent mixture of the fluids from the two jets or if these flow alongside each other, yet we are not aware of any experimental study addressing this question. Indeed, the second option implies that a well-defined liquid–liquid interface is generated, which is of great interest in the case of two different solvents but also for identical solvents of different compositions. Previous studies have shown that in microfluidic devices, it is possible to prepare well-defined interfaces between miscible and immiscible fluids by keeping the liquid flow laminar, and these devices have been used in studies targeting structural and dynamical aspects of interfaces.^{32,33} In contrast to free-flowing flat-jets, microfluidics inherently require a container material which, on the one hand, imposes limitations on the systems in terms of flow dynamics, because friction on the walls leads to

Received: January 31, 2022

Published: April 26, 2022



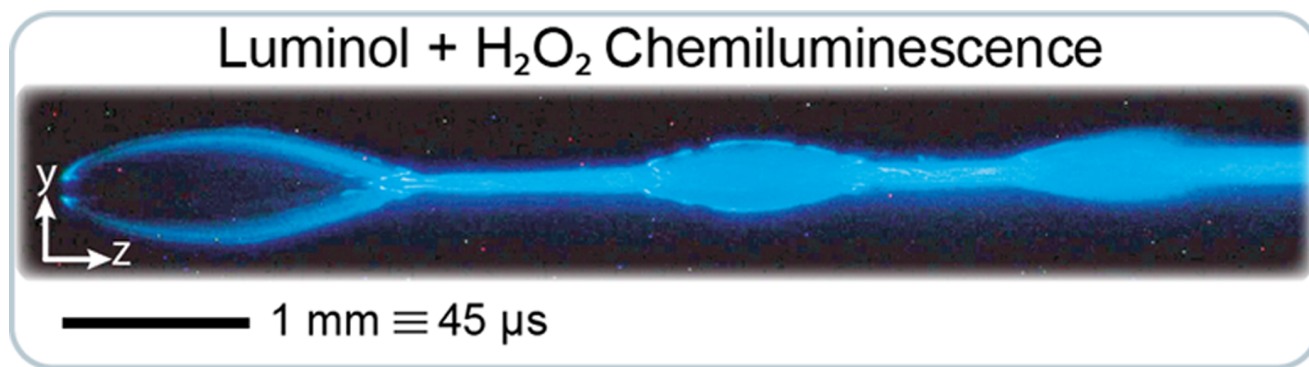


Figure 1. Photograph of a water flat-jet glowing blue as a result of chemiluminescence.

modified flow patterns, and on the available spectroscopic tools, on the other hand, because the container material itself absorbs electromagnetic radiation in ranges that may be critical for the system under investigation.

We here demonstrate that impinging, but free-flowing, jets do produce a leaf structure, where the fluids flow alongside each other in the first leaf and thus represent a tool to gain access to the liquid–liquid interface of miscible fluids. This finding demonstrates an important aspect of free-flowing microjets, which makes them a powerful borderless alternative to microfluidics and opens the door toward the investigation of chemical reactions and in-vacuum studies at liquid–liquid interfaces, with the option of using extreme ultraviolet and X-ray radiation that is only limited by the absorption spectrum of the solvent itself. Species in either solution diffuse across the interface while flowing downstream, thereby creating a steady-state system with an increasingly overlapping region, where chemical reactions can take place. Based on this, here, we also demonstrate a technique for chemical kinetics studies under completely controlled conditions, which explicitly avoids the necessity for rapid mixing and benefits from the free-flowing jets that are not perturbed by friction on container walls.³⁴ By combining two jets with different reactants and applying a suitable spectroscopic detection scheme, the flow axis of the jet represents the time to see and image directly the progress of the reaction. Typical leaf surface dimensions are 1.5 mm \times 0.5 mm with flow velocities of a few 10 m/s corresponding to a flow time through the first leaf of around 50–100 μ s, thus covering a time scale for chemical kinetics that currently is difficult to access by other methods. Indeed, conventional stopped-flow techniques are best suited for studies on time scales around a millisecond, while laser-induced techniques work best on faster time scales.

The present experiment detects photons from a chemiluminescence (CL) reaction, allowing at the same time the proof for the controlled formation of the liquid–liquid interface and the imaging of the chemical reaction kinetics. Our sample reaction is the oxidation of 5-amino-2,3-dihydro-1,4-phthalazinedione, known as luminol, which is oxidized by H_2O_2 in the presence of a transition metal ion.^{35,36} The reaction product is an electronically excited state of deprotonated 3-aminophthalic acid (AP^*), which relaxes to the electronic ground state by emitting a blue photon.^{37–39} This reaction is thus well suited for the main purpose of the present study, fulfilling the requirements of being straightforward to prepare, sufficiently fast to be observed here, and detectable with a common camera setup.

Injecting the principal reactants through individual jets yields a liquid flat-jet that luminesces exclusively where the liquids mix. Figure 1 is the resulting photograph of the glowing flat-jet, where the cylindrical jets enter from the left and flow to the right. Such an image provides a direct visualization of the dynamics in the flat-jet: from the intensity distribution of the emitted light, we can immediately conclude that there is no turbulent mixing in the flat region of the first leaf and infer information on the kinetics. Complete mixing of the solutions leads to a uniform blue glow as it is observed in rims and onward from the second leaf. However, the first leaf displays a gradual increase of the luminescence, indicative of diffusion across the well-defined interface and determined by the relative rates of diffusion, chemical reaction kinetics, and luminescence. The luminol– H_2O_2 reaction has been found to be sufficiently fast to yield diffusion-limited reaction kinetics in the present setup. Our imaging setup allows for a time resolution of around 2 μ s, and as shown in the Supporting Information, on this time scale the reaction takes place instantaneously. This system is thus ideally suited for spatial mapping of solution mixing and the demonstration of the feasibility of reaction kinetics measurements.

EXPERIMENTAL SECTION

In the present experiment, described in detail in the Supporting Information, we generate the flat-jet by colliding two liquid jets in atmosphere, one containing an aqueous H_2O_2 solution, and the other containing luminol and copper ions. More details on the experimental setup, and a computer rendering of the mounted capillaries, are provided in Figure SI-2 of the Supporting Information

A photograph of a typical flat-jet, but with no chemical reaction, used in the present experiments is shown in Figure 2A. Rims and turnover point to the second leaf are clearly visible. Color structures on the leaf surface are optical interferences resulting from the sample illumination. Figure 2B shows a cross section of the flat-jet in the plane of the two original jets, sketching the merged structure formed by the two flat-jets of solutions #1 and #2, joined by the interface. Here, the two cylindrical jets are represented by the two arrows crossing at angle α . The downstream increase of the interfacial layer thickness, indicated as the dark blue area, results from diffusion of species across the boundary (see the Supporting Information for calculations of the resulting concentration distributions).

RESULTS AND DISCUSSION

Figure 3A shows a false-color plot of the CL intensity in the $y - z$ plane, from the first leaf in Figure 1, with the camera oriented along the x -axis (see Figure 2B). Two 50 μ m jets enter from the left, in the $x - z$ plane. The first leaf in this arrangement has dimensions of $l = 1.5$ mm and $w = 0.3$ mm,

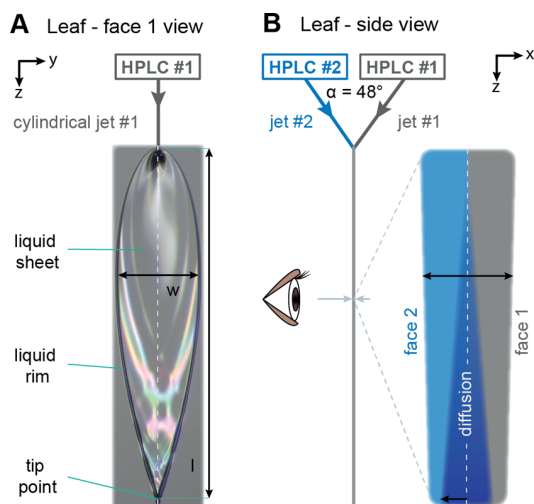


Figure 2. Experimental arrangement to generate the flat-jet. Two cylindrical liquid microjets, operated by separate HPLC pumps, are crossed at an angle of $\alpha = 48^\circ$. One contains a luminol solution and Cu^{2+} ions, the second an aqueous H_2O_2 . (A) View at the face of the first leaf. The plane spanned by the two cylindrical jets is vertical to the leaf plane. This image was taken with pure water and no chemical reaction. (B) Sketch showing the geometry used for CL detection and a cross section of the first leaf. A CCD camera faces the leaf surface and collects the CL.

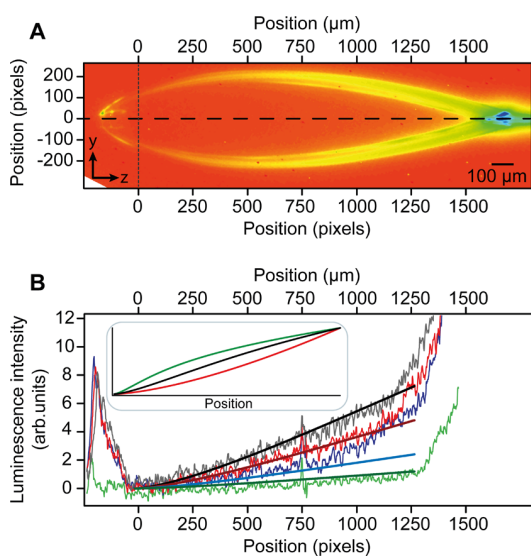


Figure 3. (A) False-color image of the measured CL intensity within the first leaf of the flat-jet (blue is high intensity; red is zero intensity). (B) CL signal intensity along the z -direction at $y = 0$, indicated by the dashed horizontal line in A, for luminol concentrations of 6 g/L (black line), 4 g/L (red line), 2 g/L (blue line), and 1 g/L (green line), respectively. Thick solid lines are numerical results. Inset: calculated results for cases with extreme (red and green) ratios and the results found here (black) between reaction and diffusion rates.

respectively, and a flow speed of 23 m/s. They are not visible because no luminescence is emitted from the individual reactant jets, which impinge at around $z = -100 \pm 100$ pixels and $y = 0 \pm 50$ pixels. Calibration of the pixel scale and conversion to the μm scale at the top is obtained using the known cylindrical-jet diameter in Figure 2A. The flat-jet origin is defined as the point where a laminar flat-jet forms and CL

starts to be observable. CL intensity at negative z values and in the rims mirrors the turbulences in those regions. Here, the observed relative signal increase along the flow is due to the fact that for small z -values, less liquid accumulates in the rims. Mixing in this region is likely by turbulences but possibly also involving complex surface migrations. In contrast, in the flat region only a slight intensity increase, starting at zero luminescence, is observed along the flow direction. The specific form of this increase is defined by the overall dynamics of the process and is used to extract information on the rates of the involved processes. The CL intensity as a function of the downstream coordinate (along the z -axis at $y = 0$; dashed line in Figure 3A) is shown in Figure 3B. Results are plotted for four different solutions with luminol concentrations of 6 g/L (grey), 4 g/L (red), 2 g/L (blue), and 1 g/L (green), respectively (all other reactants in this solution are scaled accordingly). These graphs, along with Figures 1 and 3A, reveal the following: (1) all leaves except the first one exhibit uniform CL intensity of similar magnitude in the flat parts and in the rims, indicating complete mixing of the two liquids. (2) The CL intensity observed at $z < 0$ first decreases to zero before gradually increasing. (3) The CL intensity in the first leaf increases toward positive z , supporting the assumption of reagent diffusion across the interface. Point 2 is an important confirmation that the CL reaction, including the final luminescence step, proceeds fast on the time scale in comparison with flow speed, diffusion, and reaction kinetics, and that at the origin a purely laminar flow is established (also see the Supporting Information). We note that the luminescence lifetime of AP^* is not known precisely, and a measurement through, for example, excitation with a short laser pulse and monitoring of the luminescence would be of high interest. However, such a study is beyond the scope of the present work.

The overall kinetics are assessed by theoretically reproducing the measured CL profiles of Figure 3B, using a simple kinetics model that includes the diffusion, the principal reaction steps (detailed in the Supporting Information), and luminescence. The photon flux Φ from CL results from the decay of AP^*

$$\Phi = k_p[\text{AP}^*](t) \quad (1)$$

where k_p is the rate coefficient for CL and $[\text{AP}^*](t)$ is the time-dependent product concentration. AP^* is formed in a series of chemical reactions outlined in the Supporting Information.^{35,38,40–42} The rate of this process can be written as a function of the limiting reactant concentrations

$$d[\text{AP}^*]/dt = k_R[\text{H}_2\text{O}_2][\text{LH}^-] \quad (2)$$

where k_R is a collective rate coefficient for the chemical reaction sequence that incorporates the various steps leading to AP^* . The required high pH of the luminol solution indicates that it is present exclusively in the deprotonated form LH^- , conditions that have been found to be favorable for the reaction.^{43,44}

Applying the coordinate system introduced in Figures 2 and 3A, the relevant spatial dimensions thus are both the z -axis (which translates into a time axis, t) and the x -coordinate perpendicular to the leaf surface, which is the principal direction of diffusion and hence mixing of the reactants. The concentration distribution $c(x, t)$ is derived from the initial concentrations, c_0 , using Fick's law.⁴⁵ In the model of the two-solution flat-jet, the initial concentration distributions, $c(x = 0, t = 0)$, are step-functions, where the concentration of either

reactant is c_0 on its original side and zero elsewhere. As time progresses, the diffusion-determined profile for each species i is described by an error-function Γ

$$c_i(x, t) = \frac{c_{0,i}}{2} \left\{ 1 - \Gamma \left(\frac{x}{2\sqrt{D_i t}} \right) \right\} \quad (3)$$

where D_i is the diffusion coefficient for species i and t is the time, which is defined by the flow velocity v and the position along the jet propagation as $t = z/v$. As the reaction progresses, the reactants are consumed, and this is taken into account globally by adjusting $c_{0,i}$ for both species after each time step by the amount of products that have been formed. Through this approximation, we explicitly take into account minor changes of both reactant concentrations and assume that the reaction happens uniformly across the entire interface.

In a second step, the concentration profiles from eq 3, expressed as a function of z , are convoluted with each other and fed into eq 2, thus incorporating diffusion into the kinetic model. This yields the final profile for $[AP^*]$ along the z axis, and eq 1 is then used to calculate the CL intensity

$$\frac{\Delta[AP^*]}{\Delta z} = \frac{1}{v} [-k_p[AP^*] + k_R\Omega(z)] \quad (4)$$

here, $\Omega(z)$ is the integral along z of the convoluted concentration profiles along x , and it thus accounts for the widening of the interface downstream in the jet (see the Supporting Information). The terms in brackets are the rate of decrease of $[AP^*]$ due to CL, in accordance with eq 1, and of increase due to the chemical reaction, eq 2.

The resulting expression is then numerically integrated to yield synthetic luminescence traces along the jet axis, and rate coefficients are fitted to reproduce the experimental results from Figure 3B, as is shown by thick solid lines in the same graph. In the current proof-of-principle study, we are not able to extract absolute rate coefficients because some of the rates are correlated and because in this case a calibration of the luminescence measurement was not attempted. Here, we present a simplified analysis that reproduces the shape of the traces that depends on the relative magnitudes of the rates of diffusion, luminescence, and chemical kinetics. In the Supporting Information, we elaborate on a procedure that will enable a quantitative analysis for future experiments, where a calibration will be included.

From the results in Figure 3B, we extract the following: the interplay and relative magnitudes of diffusion, reaction kinetics, and fluorescence rates determine the overall magnitude of the CL signal but in particular also the profile of the intensity along the z axis. The global shape of the curve is an asymmetric sigmoidal evolution, and depending on the relative magnitudes of the different rates, we probe different parts of that curve, as shown in the inset of Figure 3B. The curve starts with a positive curvature, which is emphasized in the red curve, where we artificially reduced the diffusion coefficients. It converges, showing a negative curvature, on a threshold, as is clearly seen in the green curve, where we artificially slowed down the luminescence. The intermediate regime, shown in black, provides a near-linear evolution as is also observed experimentally. Interestingly, the reaction rate coefficient itself merely leads to an overall scaling of the signal but without affecting the shape, thus underlining that for a qualitative understanding, calibrated measurements seem unimportant: even without it, the shape of the curve reveals principal aspects

of the dominating kinetics. The curvature also does not depend on the concentrations, and nearly identical results to those shown in Figure 3 are obtained by linearly scaling a single calculation with concentration.

CONCLUSIONS

A free-flowing liquid flat-jet has been produced from two different solutions to form a controlled liquid–liquid interface with uninhibited optical access from both sides. Using the CL reaction of luminol-oxidation by H_2O_2 , we created a marker for the temporal evolution of the mixing in the interfacial layer. By measuring the CL intensity distribution from the surface of the first leaf, we demonstrate that the individual cylindrical jets merge into a laminar regime, and mixing between the two solutions within this leaf happens solely due to diffusion. We further show that the obtained CL image reveals reaction kinetics on the sub-ms timescale. We observe a linear dependence of CL on reactant concentrations, indicative of first order kinetics in the rate-limiting substances. By modeling the experimental data theoretically, and by including diffusion, chemical kinetics, and luminescence, we were able to qualitatively replicate the quasilinear increase of the CL intensities measured experimentally as well as to quantitatively reproduce the concentration dependence.

This study demonstrates the potential buried in the free-flowing flat-jet technology for the investigation of liquid–liquid interfaces and interfacial chemical reactions for identical solvents. The flat-jet represents a steady-state system, wherein the time axis is transformed into a spatial coordinate, and imaging provides direct access to time-dependent phenomena. In contrast to otherwise equivalent experiments using microfluidics, free-flowing jets are not limited by the presence of containers. These affect the flow dynamics and impose restrictions on the range of wavelengths applicable to spectroscopic studies. Investigations of liquid–liquid interfaces using free-flowing fluids on the other hand can be extended to X-ray spectroscopies on vacuum flat-jets to access electronic structure, exploiting the unique element specificity and sensitivity to chemical environment of these techniques, and the controlled preparation of interfaces now offers possibilities for the study of, for example, transfer processes, chemical dynamics, or catalysis.

ASSOCIATED CONTENT

Supporting Information

The Supporting Information is available free of charge at <https://pubs.acs.org/doi/10.1021/jacs.2c01232>.

Details of the target reaction, experimental setup, luminescence lifetime, as well as additional information on the calculation of concentration gradients and kinetics, and an alternative mathematical approach to fit the experimental results to extract quantitative information (PDF)

AUTHOR INFORMATION

Corresponding Author

Andreas Osterwalder – Institute for Chemical Sciences and Engineering (ISIC), Ecole Polytechnique Fédérale de Lausanne (EPFL), 1015 Lausanne, Switzerland;
orcid.org/0000-0001-7346-4808;
Email: andreas.osterwalder@epfl.ch

Authors

H. Christian Schewe – Fritz-Haber-Institut der Max-Planck-Gesellschaft, 14195 Berlin, Germany; Institute of Organic Chemistry and Biochemistry, Czech Academy of Sciences, 16610 Prague 6, Czech Republic; orcid.org/0000-0003-3232-5486

Bruno Credidio – Institute for Chemical Sciences and Engineering (ISIC), Ecole Polytechnique Fédérale de Lausanne (EPFL), 1015 Lausanne, Switzerland

Aaron M. Ghrist – Fritz-Haber-Institut der Max-Planck-Gesellschaft, 14195 Berlin, Germany; Department of Chemistry, University of Southern California, Los Angeles, California 90089-0482, United States; orcid.org/0000-0003-2196-9278

Sebastian Malerz – Fritz-Haber-Institut der Max-Planck-Gesellschaft, 14195 Berlin, Germany; orcid.org/0000-0001-9570-3494

Christian Ozga – Institut für Physik und CINSaT, Universität Kassel, 34132 Kassel, Germany

André Knie – Institut für Physik und CINSaT, Universität Kassel, 34132 Kassel, Germany; orcid.org/0000-0002-2208-8838

Henrik Haak – Fritz-Haber-Institut der Max-Planck-Gesellschaft, 14195 Berlin, Germany

Gerard Meijer – Fritz-Haber-Institut der Max-Planck-Gesellschaft, 14195 Berlin, Germany; orcid.org/0000-0001-9669-8340

Bernd Winter – Fritz-Haber-Institut der Max-Planck-Gesellschaft, 14195 Berlin, Germany; orcid.org/0000-0002-5597-8888

Complete contact information is available at: <https://pubs.acs.org/10.1021/jacs.2c01232>

Author Contributions

[#]H.C.S., B.C., and A.M.G. contributed equally

Notes

The authors declare no competing financial interest.

ACKNOWLEDGMENTS

This work was funded by the SNF (project 200021E-171721), the DFG in the context of a D-A-CH collaboration, and by the EPFL-MPG doctoral school. We thank Marco Picasso and François Gallaire (both EPFL) for useful discussions.

REFERENCES

- (1) Faubel, M. *Photoionization and Photodetachment*; Advanced Series in Physical Chemistry; World Scientific, 2000; Vol. 10; pp 634–690.
- (2) Faubel, M.; Steiner, B.; Toennies, J. P. Photoelectron Spectroscopy of Liquid Water, Some Alcohols, and Pure Nonane in Free Micro Jets. *J. Chem. Phys.* **1997**, *106*, 9013–9031.
- (3) Faubel, M.; Siefertmann, K. R.; Liu, Y.; Abel, B. Ultrafast Soft X-Ray Photoelectron Spectroscopy at Liquid Water Microjets. *Acc. Chem. Res.* **2012**, *45*, 120–130.
- (4) Winter, B.; Faubel, M. Photoemission from Liquid Aqueous Solutions. *Chem. Rev.* **2006**, *106*, 1176–1211.
- (5) Faubel, M.; Schlemmer, S.; Toennies, J. P. A Molecular Beam Study of the Evaporation of Water from a Liquid Jet. *Z. Phys. D: At, Mol. Clusters* **1988**, *10*, 269–277.
- (6) Ali, H.; Seidel, R.; Bergmann, A.; Winter, B. Electronic Structure of Aqueous-Phase Anatase Titanium Dioxide Nanoparticles Probed by Liquid Jet Photoelectron Spectroscopy. *J. Mater. Chem. A* **2019**, *7*, 6665–6675.
- (7) Buttersack, T.; Mason, P. E.; McMullen, R. S.; Martinek, T.; Brezina, K.; Hein, D.; Ali, H.; Kolbeck, C.; Schewe, C.; Malerz, S.; Winter, B.; Seidel, R.; Marsalek, O.; Jungwirth, P.; Bradforth, S. E. Valence and Core-Level X-Ray Photoelectron Spectroscopy of a Liquid Ammonia Microjet. *J. Am. Chem. Soc.* **2019**, *141*, 1838–1841.
- (8) Fransson, T.; Harada, Y.; Kosugi, N.; Besley, N. A.; Winter, B.; Rehr, J. J.; Pettersson, L. G. M.; Nilsson, A. X-Ray and Electron Spectroscopy of Water. *Chem. Rev.* **2016**, *116*, 7551–7569.
- (9) Jungwirth, P.; Winter, B. Ions at Aqueous Interfaces: From Water Surface to Hydrated Proteins. *Annu. Rev. Phys. Chem.* **2008**, *59*, 343–366.
- (10) Lewis, T.; Faubel, M.; Winter, B.; Hemminger, J. C. CO₂ Capture in Amine-Based Aqueous Solution: Role of the Gas-Solution Interface. *Angew. Chem., Int. Ed.* **2011**, *50*, 10178–10181.
- (11) Winter, B. Liquid Microjet for Photoelectron Spectroscopy. *Nucl. Instrum. Methods Phys. Res., Sect. A* **2009**, *601*, 139–150.
- (12) Karashima, S.; Yamamoto, Y.-i.; Suzuki, T. Ultrafast Internal Conversion and Solvation of Electrons in Water, Methanol, and Ethanol. *J. Phys. Chem. Lett.* **2019**, *10*, 4499–4504.
- (13) Suzuki, T. Time-Resolved Photoelectron Spectroscopy of Non-Adiabatic Electronic Dynamics in Gas and Liquid Phases. *Int. Rev. Phys. Chem.* **2012**, *31*, 265–318.
- (14) Suzuki, T. Ultrafast Photoelectron Spectroscopy of Aqueous Solutions. *J. Chem. Phys.* **2019**, *151*, 090901.
- (15) Ryazanov, M.; Nesbitt, D. J. Quantum-State-Resolved Studies of Aqueous Evaporation Dynamics: NO Ejection from a Liquid Water Microjet. *J. Chem. Phys.* **2019**, *150*, 044201.
- (16) Faust, J. A.; Sobyra, T. B.; Nathanson, G. M. Gas–Microjet Reactive Scattering: Collisions of HCl and DCl with Cool Salty Water. *J. Phys. Chem. Lett.* **2016**, *7*, 730–735.
- (17) Hahn, C.; Kann, Z. R.; Faust, J. A.; Skinner, J. L.; Nathanson, G. M. Super-Maxwellian Helium Evaporation from Pure and Salty Water. *J. Chem. Phys.* **2016**, *144*, 044707.
- (18) Lancaster, D. K.; Johnson, A. M.; Kappes, K.; Nathanson, G. M. Probing Gas–Liquid Interfacial Dynamics by Helium Evaporation from Hydrocarbon Liquids and Jet Fuels. *J. Phys. Chem. C* **2015**, *119*, 14613–14623.
- (19) Sobyra, T. B.; Melvin, M. P.; Nathanson, G. M. Liquid Microjet Measurements of the Entry of Organic Acids and Bases into Salty Water. *J. Phys. Chem. C* **2017**, *121*, 20911–20924.
- (20) Murdachew, G.; Nathanson, G. M.; Halonen, L. Deprotonation of Formic Acid in Collisions with a Liquid Water Surface Studied by Molecular Dynamics and Metadynamics Simulations. *Phys. Chem. Chem. Phys.* **2016**, *18*, 29756–29770.
- (21) Faust, J. A.; Nathanson, G. M. Microjets and Coated Wheels: Versatile Tools for Exploring Collisions and Reactions at Gas–Liquid Interfaces. *Chem. Soc. Rev.* **2016**, *45*, 3609–3620.
- (22) Jordan, I.; Jain, A.; Gaumnitz, T.; Ma, J.; Wörner, H. J. Photoelectron Spectrometer for Liquid and Gas-Phase Attosecond Spectroscopy with Field-Free and Magnetic Bottle Operation Modes. *Rev. Sci. Instrum.* **2018**, *89*, 053103.
- (23) Yin, Z.; Luu, T. T.; Wörner, H. J. Few-Cycle High-Harmonic Generation in Liquids: In-Operando Thickness Measurement of Flat Microjets. *J. Phys.: Photonics* **2020**, *2*, 044007.
- (24) Lancaster, D. K.; Johnson, A. M.; Burden, D. K.; Wiens, J. P.; Nathanson, G. M. Inert Gas Scattering from Liquid Hydrocarbon Microjets. *J. Phys. Chem. Lett.* **2013**, *4*, 3045–3049.
- (25) Artiglia, L.; Edebeli, J.; Orlando, F.; Chen, S.; Lee, M.-T.; Corral Arroyo, P.; Gilgen, A.; Bartels-Rausch, T.; Kleibert, A.; Vazdar, M.; Andres Carignano, M.; Francisco, J. S.; Shepson, P. B.; Gladich, I.; Ammann, M. A Surface-Stabilized Ozonide Triggers Bromide Oxidation at the Aqueous Solution–Vapour Interface. *Nat. Commun.* **2017**, *8*, 700.
- (26) Thürmer, S.; Seidel, R.; Faubel, M.; Eberhardt, W.; Hemminger, J. C.; Bradforth, S. E.; Winter, B. Photoelectron Angular Distributions from Liquid Water: Effects of Electron Scattering. *Phys. Rev. Lett.* **2013**, *111*, 173005.

- (27) Galinis, G.; Strucka, J.; Barnard, J. C. T.; Braun, A.; Smith, R. A.; Marangos, J. P. Micrometer-Thickness Liquid Sheet Jets Flowing in Vacuum. *Rev. Sci. Instrum.* **2017**, *88*, 083117.
- (28) Koralek, J. D.; Kim, J. B.; Bruža, P.; Curry, C. B.; Chen, Z.; Bechtel, H. A.; Cordones, A. A.; Sperling, P.; Toleikis, S.; Kern, J. F.; Moeller, S. P.; Glenzer, S. H.; DePonte, D. P. Generation and Characterization of Ultrathin Free-Flowing Liquid Sheets. *Nat. Commun.* **2018**, *9*, 1353.
- (29) Ekimova, M.; Quevedo, W.; Faubel, M.; Wernet, P.; Nibbering, E. T. J. A Liquid Flatjet System for Solution Phase Soft-x-Ray Spectroscopy. *Struct. Dyn.* **2015**, *2*, 054301.
- (30) Bush, J. W. M.; Hasha, A. E. On the Collision of Laminar Jets: Fluid Chains and Fishbones. *J. Fluid Mech.* **2004**, *511*, 285–310.
- (31) Chen, X.; Ma, D.; Yang, V.; Popinet, S. High-Fidelity Simulations of Impinging Jet Atomization. *Atomization Sprays* **2013**, *23*, 1079–1101.
- (32) Atencia, J.; Beebe, D. J. Controlled Microfluidic Interfaces. *Nature* **2005**, *437*, 648–655.
- (33) Ismagilov, R. F.; Stroock, A. D.; Kenis, P. J. A.; Whitesides, G.; Stone, H. A. Experimental and Theoretical Scaling Laws for Transverse Diffusive Broadening in Two-Phase Laminar Flows in Microchannels. *Appl. Phys. Lett.* **2000**, *76*, 2376–2378.
- (34) Song, H.; Ismagilov, R. F. Millisecond Kinetics on a Microfluidic Chip Using Nanoliters of Reagents. *J. Am. Chem. Soc.* **2003**, *125*, 14613–14619.
- (35) Rose, A. L.; Waite, T. D. Chemiluminescence of Luminol in the Presence of Iron(II) and Oxygen: Oxidation Mechanism and Implications for Its Analytical Use. *Anal. Chem.* **2001**, *73*, S909–S920.
- (36) Matsumoto, R.; Yoshida, K.; Matsuo, R. Diffusion in Microchannel Analyzed by Chemiluminescence. *J. Therm. Sci. Technol.* **2013**, *8*, 448–459.
- (37) Merenyi, G.; Lind, J.; Eriksen, T. E. The Equilibrium Reaction of the Luminol Radical with Oxygen and the One-Electron-Reduction Potential of 5-Aminophthalazine-1,4-Dione. *J. Phys. Chem.* **1984**, *88*, 2320–2323.
- (38) Merényi, G.; Lind, J.; Eriksen, T. E. Luminol Chemiluminescence: Chemistry, Excitation, Emitter. *J. Biolumin. Chemilumin* **1990**, *5*, 53–56.
- (39) Merenyi, G.; Lind, J.; Eriksen, T. E. The Reactivity of Superoxide (O₂⁻) and Its Ability to Induce Chemiluminescence with Luminol. *Photochem. Photobiol.* **1985**, *41*, 203–208.
- (40) Burdo, T. G.; Seitz, W. R. Mechanism of Cobalt Catalysis of Luminol Chemiluminescence. *Anal. Chem.* **1975**, *47*, 1639–1643.
- (41) Gaikwad, A.; Silva, M.; Pérez-Bendito, D. Selective Stopped-Flow Determination of Manganese with Luminol in the Absence of Hydrogen Peroxide. *Anal. Chim. Acta* **1995**, *302*, 275–282.
- (42) Ojima, H. In *Advances in Catalytic Activation of Dioxygen by Metal Complexes*; Simándi, L. I., Ed.; Catalysis by Metal Complexes; Springer US, 2002.
- (43) Menzi, S.; Knopp, G.; Al Haddad, A.; Augustin, S.; Borca, C.; Gashi, D.; Huthwelker, T.; James, D.; Jin, J.; Pamfilidis, G.; Schnorr, K.; Sun, Z.; Wetter, R.; Zhang, Q.; Cirelli, C. Generation and Simple Characterization of Flat, Liquid Jets. *Rev. Sci. Instrum.* **2020**, *91*, 105109.
- (44) O'Sullivan, D. W.; Hanson, A. K.; Kester, D. R. Stopped Flow Luminol Chemiluminescence Determination of Fe(II) and Reducible Iron in Seawater at Subnanomolar Levels. *Mar. Chem.* **1995**, *49*, 65–77.
- (45) Steinfeld, J. I.; Francisco, J. S.; Hase, W. L. *Chemical Kinetics and Dynamics*, 2nd ed.; Pearson: Upper Saddle River, NJ, 1998.

Curriculum Vitae

Name: Sebastian Malerz

Education:

06/2017 – 09/2022 Doctoral candidate at Fritz-Haber-Institut der Max-Planck-Gesellschaft, Department of Molecular Physics

10/2014 – 05/2017 Master studies in chemistry at Freie Universität Berlin, M. Sc. Chemistry (topic of the master thesis: "*Structural Investigation of Amyloid Oligomers via IM-MS and Infrared-Spectroscopy*", accomplished in the research group of Prof. Dr. Kevin Pagel at Freie Universität Berlin in cooperation with Fritz-Haber-Institut der Max-Planck-Gesellschaft)

05/2016 – 09/2016 Guest scientist at Fritz-Haber-Institut der Max-Planck-Gesellschaft

04/2011 – 12/2014 Bachelor studies in chemistry at Freie Universität Berlin, B. Sc. Chemistry (topic of the bachelor thesis: "*Synthese und Funktionalisierung von Porphyrinen für eine Verknüpfung mit hochverzweigtem Polyglycerol*", accomplished in the research group of Prof. Dr. Rainer Haag at Freie Universität Berlin in cooperation with Biolitec®)

Work experience:

04/2007 – 02/2011 Chemical laboratory assistant at Mercedes-Benz Ludwigsfelde GmbH (Production monitoring, quality assurance and analytics)

02/2007 – 03/2007 Chemical laboratory assistant at the Landesbetrieb für Hochwasserschutz und Wasserwirtschaft Sachsen-Anhalt (LHW) (inorganic and organic wet chemical and instrumental analysis)

Apprenticeship:

08/2003 – 02/2007 Training as a chemical laboratory assistant at the Landesbetrieb für Hochwasserschutz und Wasserwirtschaft Sachsen-Anhalt (LHW), Germany

School education:

1993 - 2003

Grundschule Trebitz / Realschule Kemberg, Germany

Graduation:

Erweiterter Realschulabschluss (07/2003)

Statutory Declaration

I, Sebastian Malerz, confirm that I have prepared the thesis "*Advances in Liquid-Jet Photoelectron Spectroscopy: Determination of Absolute Energetics and Probing Chirality in Solution*" independently and entirely by myself using only the referred sources and support. I additionally assert that this thesis has not been part of another, or a failed doctoral procedure.

Berlin, 23rd May 2022

Sebastian Malerz

Acknowledgment

Since the first lessons of biology, physics, and chemistry in school, I got hooked and aimed to learn as much as I can about natural processes in physics and most of all in chemistry. This led me to the decision to apply for an apprenticeship as a laboratory worker (Chemielaborant) in 2003 in a public-service organization. During my apprenticeship, I had a lot of training and gained a lot of practice with new and modern instrumental analytic devices and methods. At this time, I started to wonder who developed such complex instruments and methods, which give us an insight of the structure of molecules, their environment, and their reactions.

In 2007, after successfully finishing my apprenticeship, I started working for Mercedes-Benz, where I was faced with the reality of economy. However, getting a deeper insight and understanding of used methods was difficult and almost impossible due to company's secrets. During the financial crisis of 2008, my ambition for a better understanding arose once more and I started to look for new opportunities for further job qualifications. Unfortunately, without an "Abitur certificate", there were several obstacles I had to overcome, in order to get access to further qualification, let alone to go studying. It took almost three years until I found the possibility to study chemistry at the Freie Universität Berlin. A severe hindrance, beside the abdication of a permanent salary, was the fact that I had to proof my knowledge in a probation period of two semesters. I put all my efforts into passing the probation and accomplished it in a shorter period of time, thus earning my permanent student acceptance after just one semester. In the end, I was allowed to complete my studies in chemistry at the Freie Universität Berlin and acquired a bachelor's and a master's degree.

Within an internship during my master studies, I got in touch with the Fritz-Haber-Institut for the first time. After two internships and after my master thesis, I got the opportunity to work on a topic for my doctoral thesis, which included to design and to development a new instrument and method. In fact, when you start to build and develop a scientific instrument and a scientific method from scratch, you meet many people without whose help and expertise such a project is difficult to implement. Nevertheless, I would like to try at this point to thank everyone without whom I would not have been able to accomplish my thesis.

First, I would like to thank my first supervisor Gerard Meijer. Due to his confidence in me, I had the opportunity to pursue my projects with a large degree of independence. He gave me the chance to deepen my interest in photoelectron spectroscopy, technical development of “my”[∇] machine, and working in the impressive scientific environment of the Fritz-Haber-Institut. Further, I would like to thank my second supervisor Eckart Rühl for his willingness to evaluate my work on behalf of the Freie Universität Berlin. I attended some of his lectures during my studies, which further increased my interest in spectroscopy and had a great impact on my work.

An extraordinary and very big thanks goes to my advisor Bernd Winter. I always felt welcome in his office. He supported me in all aspects of my work and always had time for me, both in scientific and in general matters. His broad and vast knowledge of liquid-jet photoelectron spectroscopy inspired me to face new challenges and showed me that it is good to change the point of view on many problems. He shared the hard, exhausting, and long shifts during beamtimes and was always fully involved in all of my projects, and guided me back on track if I lost the focus of the important aspects. He did not accept the fact that I do not like to travel, which led me to my first journey to Japan (and I liked it) and many more. His enthusiasm for his research and his lightheartedness is contagious, and I am very grateful for the time we spend together, scientifically as well as casually.

I had the pleasure to work with Uwe Hergenbahn. He always was accessible for me not just regarding questions of our projects, but also regarding other physical topics. He never got tired of giving me context on topics new to me, also after long and exhausting beamtime shifts and of correcting some of the chapters in this thesis.

I will never forget the long technical and casual discussions with Henrik Haak about the realization of “my” setup and the fruitful discussions for improvements of it. Also a big thanks to Sebastian Kray, not only for his helpful hand with the shipping of “my” setup and his technical support at all times. I am also grateful for his help with my gardening projects at home.

[∇] “my” instrument is given with the fully consciousness that *EASI* never will be my own.

Stephan Thürmer has my special acknowledgment for his long breath (not only for proof-reading this thesis) to help with data analysis and also with his 24/7 support regarding our analysis software Igor Pro. His advice during long beamtimes helped to stay on track and to be focused on the import measurements.

A special acknowledgment goes to Iain Wilkinson. He was always there to take over long night shifts and supported me in all my concerns. I appreciate his critical way of thinking and his ability to stay focused after a 20-hour shift. A big thanks to Florian Trinter for the organization of many beamtimes at DESY, for his support with the P04 beamline during long shifts with a lack of sleep and of course for his detailed proof reading of this thesis.

Also a big thanks goes to Claudia Kolbeck. Although we only worked together for two years, I would like to thank you for your help and support in the building phase of *EASI*. During my (long) time at the FHI, I met many people who contributed directly or indirectly to my work, be it scientific or just casual discussions, writing, proof-reading, or just a helpful hand during the build-up phase or during beamtimes. I want to mention in particular Hanns Christian Schewe, Petr Slavíček, Robert Seidel, Laurent Nahon, Claudia Goy, Marvin Pohl, Karen Mudryk, Mallory Green, Michele Pugini, Dominik Stemer, Dennis Hein, Garlef Wartner, Hanna Trzesniowski, Anne B. Stephansen, Isaak Unger, Lanhai He, Simon Hoffsäss, Johannes Seifert, Klaus-Peter Vogelgesang, Andreas Liedke, all the other MP-members I forgot here, and last but not least all the staff from our workshops. Without their expertise and help it would not have been possible to build *EASI*. I wish each of them all the best!

I would like to thank all my friends for their support and for patiently enduring my sometimes professional and boring monologues.

Special thanks go to my parents and my brother with his family, who supported me lovingly and without exception; not only during my school years and apprenticeship, but also throughout my studies and the subsequent doctoral phase. They were always there for me and I am more than grateful to have them in my life.

My biggest thanks go to my lovely wife Patricia, who always supported me with love and devotion, gave me support throughout the entire course, showed a lot of understanding, and

built me up mentally and morally with motivating words and some constructive criticism. The last sentence is dedicated to my beloved daughter Elisabeth: although I came home late very often and was on beamtimes for long stretches of time, you were always with me in my heart.

